

HOT DEFORMATION CHARACTERISTICS OF
OXIDE/SULPHIDE INCLUSIONS IN LOW CARBON STEELS

by

JAMES CLARENCE BOADI ASANTE

A THESIS SUBMITTED FOR THE DEGREE
OF DOCTOR OF PHILOSOPHY

THE UNIVERSITY OF ASTON IN BIRMINGHAM

January 1980

NAME: JAMES CLARENCE BOADI ASANTE

SUBMITTED FOR THE DEGREE: DOCTOR OF PHILOSOPHY 1 1980

SUMMARY

Studies have been made of the effect of sulphur contents between 0.02 and 0.2% on the composition of the oxides and oxy-sulphides produced by deoxidation of a low carbon (<0.04%) steel with aluminium-manganese-silicon alloys.

The inclusions were analysed by Quantimet for size distribution and Microscan V for composition. Hot rolling of the suction cast bars was achieved on a 2 high-rolling mill. Samples were taken at 50%, 70% and 90% total reductions in thickness and temperature of rolling was between 800 and 1300°C. Deformation of the inclusions was measured by optical microscopy.

It was shown that at 0.56% Mn in the steel increasing sulphur decreased the manganese oxide content of the inclusions but with higher manganese contents (>1.5% Mn) little or no effect was observed. The average size of both the oxide and sulphide inclusions increased with increasing sulphur content in the steel.

The relative plasticity indices of inclusions have been related to inclusion size, matrix strain, composition and the rolling temperature. It was shown that inclusions less than about 2 μm in diameter did not exhibit any deformation characteristics under all working conditions. It was also shown that the relative plasticity index value was lowered as the matrix strain increased. Spheroidisation of the inclusions partly contributed towards the decrease in relative plasticity index with decreasing inclusion size.

Oxide inclusions rolled at the lower temperatures behaved in a rigid or brittle manner. There was a rapid transition from non-deformable to deformable behaviour over a narrow range of temperature. The transition temperatures for the inclusions were observed to be well below the liquidus temperatures of any of the oxide compositions. The non-deformable/deformable transition temperature was decreased with increasing sulphur content of the steel, reflecting the change in composition of oxides shown above. A ternary oxide ($\text{Al}_2\text{O}_3\text{-MnO-SiO}_2$) diagram has been produced to predict the transition temperatures for the oxide inclusions within the composition range studied. Deformation of sulphide inclusions decreased with increasing rolling temperatures.

It was shown that the equations (for estimation of inclusion strain in a third plane if the inclusion strain in the other planes are known; width spread, ϵ_z ; plane strain plasticity index, (v_p^*)) are valid and can be useful for volume plasticity index determination.

It was found that ductility of the steel decreased with increasing percentage area of both oxide and sulphide inclusions. Directionality was found to be pronounced in steels containing type II MnS inclusions.

(Deoxidation, oxides, sulphides, rolling, plasticity-index)

C O N T E N T S

Page

SECTION 1 INTRODUCTION

1.0	Introduction	1
1.1	Oxygen and sulphur in steel	1
1.2	The purpose of the present work	4

SECTION 2 LITERATURE REVIEW

2.1	Deoxidation thermodynamics	6
2.1.1	Deoxidation by manganese	6
2.1.2	Deoxidation by silicon	7
2.1.3	Deoxidation by aluminium	9
2.1.4	Deoxidation by aluminium and manganese	9
2.1.5	Deoxidation by silicon and manganese	10
2.1.6	Deoxidation by manganese-silicon-aluminium	11
2.2.0	Kinetics of formation and elimination of inclusions in steel	13
2.2.1	Formation of inclusions in steel	14
2.2.2	Elimination of inclusions	16
2.3.0	Nature of inclusions commonly found in steels deoxidised by Al-Si-Mn alloys	22
2.3.1	Silica, SiO_2	22
2.3.2	Alumina, Al_2O_3	23
2.3.3	Iron-Manganese Oxides $(\text{Fe, Mn})\text{O}$	23
2.3.4	Iron-manganese-alumino-silicates $[\text{Fe, Mn})\text{O}-\text{Al}_2\text{O}_3-\text{SiO}_2]$	24
2.3.4.1	$(\text{Fe, Mn})\text{O}-\text{SiO}_2$	24
2.3.4.2	$(\text{Fe, Mn})\text{O}-\text{Al}_2\text{O}_3-\text{SiO}_2$ (Silicates)	24
2.3.5	Sulphide inclusions in steel	27
2.3.5.1	Manganese sulphides (MnS)	27
2.3.5.2	Sulphide modification	31

	<u>Page</u>	
2.4.0	Deformability of inclusions during hot working	32
2.4.1	Analytical methods of inclusion deformation	32
2.4.2.0	Factors affecting inclusion relative plasticity index	38
2.4.2.1	Degree of deformation	38
2.4.2.2	The effect of the ratio of (inclusion-matrix) flow stresses	41
2.4.2.3	Temperature	46
2.4.2.3.1	The behaviour of manganese sulphides	46
2.4.2.3.2	The behaviour of oxide inclusions	51
2.4.2.4	Inclusion size	54
2.4.2.5	Inclusion composition	54
2.4.2.6	Strain rate	55
2.5.0	The effect of inclusions on the mechanical properties of steel	57
2.5.1	Micro-mechanism of ductile fracture	57
2.5.2.0	Theoretical aspects	60
2.5.2.1	Void nucleation	60
2.5.2.2	Void growth	63
2.5.2.3	Void coalescence	65
2.5.3	Matrix-particle bonding	66
2.5.4	Inclusion deformation	67
2.5.5	Interparticle spacing and volume fraction	69
2.5.6	Notch effect in fracture	70

SECTION 3 EXPERIMENTAL PROCEDURE

3.0	Experimental procedure	74
3.1	Deoxidation alloy preparation	75

		<u>Page</u>
3.2	Experimental melts	76
3.2.1	Preparation of cast bars	76
3.2.1.2	Melting procedure	76
3.2.1.3	Sampling, addition of Fe_2O_3 and FeS deoxidation procedure and suction casting	77
3.3	Oxygen analysis	79
3.4	Sectioning of cast bars	79
3.5	Rolling procedure	80
3.6	Metallographic examination	82
3.6.1	As cast bars	82
3.6.2	Rolled samples	82
3.6.3	Inclusion distribution analysis	83
3.7	Heat treatment	84
3.8	Verification of Wardle's equation (100) and variation of height to width ratio	86
3.9	Chemical analysis	87
3.10	Electron probe micro-analysis	87
3.11	Scanning electron microscopy	88
3.11.1	Specimen preparation	89
3.12.0	Notch tensile testing	89
3.12.1	Testing procedure	90
3.12.2	Further developments of notch tensile testing experiments	90
3.12.2.1	Testing procedure	91
3.12.2.2	Strain and stress measurements	91
3.12.2.3	Measurements of void sizes and the number of voids per unit area	92

SECTION 4 EXPERIMENTAL RESULTS

4.0	Analysis of the Japanese-Electrolytic iron	94
4.1	Oxygen analysis	94
4.2	Chemical analysis	95
4.3	Metallographic examination	97
4.3.1	'As cast' inclusions	97
4.3.1.1	Products of deoxidation alloys A6 and A7	97
4.3.1.2	Products of deoxidation alloys A12, A15, D1, D2 and D3	98
4.3.1.3	Products of deoxidation alloy D4	99
4.3.2	Inclusion size analysis	99
4.3.3	Rolled structures	99
4.3.3.1	Melt A6 (sulphur levels of 0.07, 0.10, 0.2%)	99
4.3.3.2	Melt A7 (sulphur levels of 0.07, 0.10, 0.2%)	100
4.3.3.3	Melt A12 (sulphur levels of 0.07, 0.10, 0.2%)	102
4.3.3.4	Melt A15 (sulphur levels of 0.07, 0.10, 0.2%)	103
4.4	Microprobe analysis of inclusions	104
4.5	Deformation of inclusions	105
4.6	Heat treatment	106
4.7	Verification of Wardle's equations and the effect of height to width ratio on inclusion deformation	107
4.8	Notch tensile test	112

SECTION 5 DISCUSSION OF RESULTS

5.1	Composition of deoxidation products	114
5.1.1	The effect of Mn:Si ratio (deoxidant) on deoxidation product compositions	114
5.1.2	Variation of inclusion composition with size	117
5.1.3	Sulphide inclusions morphology	119
5.1.4	Effect of sulphur content of melt on oxide inclusion composition	121
5.1.5	Inclusion distribution	123
5.1.5.1	Sulphide inclusion distribution	124
5.1.5.2	Oxide inclusion distribution	127
5.2	The effect of hot rolling on deformation of inclusions	129
5.2.1	The variation of inclusion mean plasticity index with temperature	129
5.2.1.1	Melts A6 and A7 (deoxidised with Mn-Si alloys) (Different sulphur contents of melts ~ 0.07%, 0.10% and 0.2%)	130
5.2.1.2	Melt A12 (deoxidised with Mn-Si-Al alloy)	133
5.2.1.3	Melt A15 (deoxidised with Mn-Si-Al alloy)	136
5.2.1.4	Factors affecting the transition from non-deformable to deformable behaviour	138
5.2.1.5	Deformation of inclusions at temperatures higher than the transition temperature	139

	<u>Page</u>	
5.2.2	Variation of inclusion composition with plasticity index	141
5.2.2.1	Rolling temperature 800°C (Figs. 65c and 70a)	142
5.2.2.2	Rolling temperature 900°C (Figs. 65a, 67 and 70b)	143
5.2.2.3	Rolling temperature 1000°C (Figs. 65b, 68a and 71a)	143
5.2.2.4	Rolling temperature 1100°C (Figs. 66a, 68b and 71b)	143
5.2.2.5	Rolling temperature 1200°C and 1300°C (Figs. 66b, 68c, 69, 71c and 72)	143
5.2.3	Relative plasticity determination and factors affecting inclusion deformation	144
5.2.3.1	Representation of inclusion size	144
5.2.3.2	Variation of inclusion relative plasticity index with inclusion size	146
5.2.3.2.1	Spheroidisation of deformed inclusions	147
5.2.3.2.2	Sectioning problem	148
5.2.3.2.3	Surface energy criterion	150
5.2.3.3	The influence of total matrix reduction upon relative plasticity index	151
5.2.3.3.1	Matrix constraint	152
5.2.3.3.2	Temperature rise	153
5.3	Verification of Wardle's equations and the effect of height to width ratio on inclusion deformation	154
5.4	Notch tensile test	155
5.4.1	Effect of sulphide and oxide inclusions on the fracture behaviour of the steels (D)	155

		<u>Page</u>
5.4.2	Notch effect on fracture	159
5.5	Practical implications	161
5.5.1	Machinability	163
5.5.2	Surface finish of rolled products	164
5.5.3	Influence of inclusions on mechanical properties	165

SECTION 6

6.1	As cast inclusion composition and distribution	166
6.2	Inclusion deformation	168
6.3	Estimation of inclusion strain in the third dimension	171
6.4	Influence of inclusions on notch ductility measurements	172
6.5	Recommendations for further work	174

Acknowledgements 177

Table 4.0	Electrolytic iron composition	94
Table 4.1	Total oxygen analysis	94
Table 4.2	Chemical analysis of 'as cast' bars	95
Table 4.3	Deoxidation alloy composition	97
Table 4.4	Results of Wardle's equations	108
Table 5.1	Relationship between $[\%Mn]:[\%Si]$ (Deoxidant) ratio and $N_{(MnO)}^2:N_{(SiO_2)}$ ratio of deoxidation products	115
Table 5.4		161

	<u>Page</u>
Appendix 1.1.0 Calculation of deoxidation alloy composition	178
Appendix 1.1.1 Calculation of Fe ₂ O ₃ addition	180
Appendix 1.1.2 Calculation of FeS addition	180
Appendix 1.2 Calculated deoxidation alloy compositions	181
Appendix 2 : Tables	183
Table 4.5 Sulphide inclusion distribution	183
Table 4.6 Oxide inclusion distribution	184
Table 4.7 Inclusion distribution	185
Table 4.8 Mean 'as cast' inclusion composition	186
Table 4.9 Mean inclusion plasticity index	190
Tables 4.10-4.11 Heat treatment results	194
Tables 4.12-4.14 Notch tensile test results	196
Appendix 3 Wardle's equations	204
Appendix 4 The calculation of theoretical temperature rise during rolling	215
Figures 1-32 Literature survey	218-238
Figures 33-39 Experimental procedure	239-243
Figures 40-51 Inclusion distribution analysis	244-249
Figures 52-64 'As cast' oxide inclusion composition analysis	250-255
Figures 65-76 Oxide inclusion composition after rolling	256-263

	<u>Page</u>
Figures 77-123 Relative plasticity index versus size	264-302
Figures 124-127 Effect of rolling temperature on relative plasticity of MnS inclusions	303-304
Figures 128-131 The effect of sulphur content on the transition temperature of the oxide inclusions	305-306
Figures 132-133 Spheroidisation of inclusions	307
Figures 134-155 Notch tensile test results	308-319
Figures 156-160 Variation of 'as cast' oxide inclusion composition with inclusion size	320-324
Figure 161 Distribution of the radii appearing in planes cutting spherical grain of radius R_0	325
Figure 162 Plasticity index (or factor) versus matrix height strain	326
Figure 163 Influence of ingoing thickness on mean rate of deformation	327
Figure 164 Mechanism of the ductile fracture when elongated inclusions are involved	328
Plates 1-12 As cast inclusion structures	329-331
Plates 13-41 Deformed inclusion structures	332-341
Plates 42-58 X-ray distribution	342-346
Plates 59-64 Spheroidisation of inclusions	344-348

		<u>Page</u>
Plates 65-67	Fracture surfaces	349-350
Plates 68-71	Coalescence of inclusions	351
Plates 72-76	Shearing or splitting of deformed inclusions	352-353
Plates 77-79	Distribution of inclusions	353-355
Plates 80-82	Sectioning problem	356
	References	357

Two kinds of non-metallic inclusions are generally recognised; those which are entrapped in the steel unintentionally, and those which separate from it because of a change in temperature or steel composition. The first type originate almost exclusively from particles of non-metallic matter that are entrained in the steel while it is in the molten state. The second type is produced either in the molten or the solid state by the separation from the steel of oxide, sulphide or other non-metallic compounds in the form of droplets or particles, when these compounds are produced in such amounts (by reactions or temperature changes) that their solubility in the steel is exceeded. Since the latter type of inclusions are the products of chemical reactions within the steel, they are inherent constituents of it. Such inclusions cannot be entirely eliminated from the steel by the ordinary processes of manufacture. The best that can be done is to control the type and amount of these constituents within such limits that the steel is free from those inclusions which are considered to be injurious to final properties; or to ensure that the steel contain those inclusions, such as the sulphides which impart machinability.

1.1 Oxygen and Sulphur in Steel

In steelmaking most of the impurities (C, Si, Mn, P) are removed by oxidation. Their oxidation is usually achieved by either blowing large volumes of oxygen through or onto the melt or by the action of an oxidising slag.

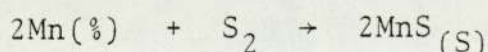
The solubility of oxygen in molten iron is about 0.25% at 1650°C. During solidification this decreases markedly and is only 0.0086% at 1500°C (1). Most of the elements which may be present in molten steel lower the solubility of oxygen. When the molten steel solidifies, the excess oxygen is rejected from solution and combines with the other elements present to form oxides. If the carbon in the molten steel combines with the excess oxygen to form carbon monoxide, some of this carbon monoxide escapes but some gas bubbles remain trapped in the solid metal causing extensive porosity. This porosity can be controlled by adding to the cooling melt elements which have greater affinity for oxygen than carbon at steelmaking temperatures and which do not produce volatile products. This process is known as deoxidation. Curves for the elements relevant to steelmaking have been given in Fig. 1 (from Muan and Osborn (2)). During deoxidation the additions added for this purpose normally form liquid oxides.

In practice some of the oxides formed during deoxidation escape to the surface of the solidifying casting, but the majority are entrapped and remain within the metal as inclusions. It has been suggested by Kiessling (3) that one tonne of ordinary carbon steel contains about 10^{12} - 10^{13} oxide inclusions. It has been shown that about 80-90% of the non-metallic inclusions in an ingot results directly from deoxidation (4).

Like oxygen, sulphur is soluble in molten steel, but its solubility in the solid steel phase is very low. It is precipitated in the form of metal sulphides during solidification of the steel and the precipitation pattern is influenced by its strong segregation tendency.

The stability of the different metal sulphides relative to the elements is indicated by the curves for the standard free energy of formation against temperature. A graph showing this for a number of sulphides important in steel-making is shown in Fig. 2 (from Muan and Osborn). Fig. 2, as well as the corresponding graph for oxides in Fig. 1, gives the ΔG^0 values, i.e. the conditions for the pure elements when the activity is unity. Furthermore, activities may be increased or decreased when additional elements are dissolved in iron by their individual interactions. The activity of sulphur, for example, is strongly and positively influenced by carbon, silicon, and phosphorus. The diagrams in Figs. 1 and 2 should therefore only be used as guidelines.

The sulphur potential-temperature diagrams for sulphides in iron and steelmaking processes may be corrected giving equilibrium lines for contents usual in steel practice. Such corrections have been made by Jorgensen ⁽⁵⁾ for the reaction:



Corrected ΔG^0 diagrams have been calculated for contents of 1% and 0.5% manganese in iron. The results are shown in Fig.3, where the ΔG^0 values for FeS formation from pure iron

have also been shown. It is evident from this diagram that the sulphur potential/temperature relationships diagrams for MnS under actual steelmaking conditions have been moved due to the lower Mn- activity in the steel as compared with pure Mn and are closer to the FeS equilibrium line. The equilibrium lines for MnS and FeS at actual steelmaking conditions now intersect in the temperature range 1600-1800°C instead of at temperatures higher than 2000°C. The implication of this is that the tendency for the formation of FeS and MnS at steelmaking concentrations and temperatures is about the same, but that MnS is the more stable phase at room temperature. In contrast, according to the ΔG° equilibrium curves (Fig. 2), FeS should never be formed except in Mn-free steels.

1.2 The Purpose of the Present Work

The aim of this work was to investigate the behaviour of oxide and sulphide inclusions during hot working and their effect on notch ductility. An iron melt containing oxygen and sulphur was deoxidised using alloys from the manganese-silicon-aluminium system.

It was hoped to provide information on:-

- (i) The effect of sulphur content in the steel on
 - (a) composition of the oxide inclusions,
 - (b) the transition between rigid and fluid behaviour of silicate inclusions,
 - (c) type and deformation behaviour of sulphide inclusions.
 - (d) the distribution of sulphide and oxide inclusions respectively.

- (ii) The effect of manganese content in the steel on sulphide inclusion distribution.
- (iii) The effect of composition on the deformation of inclusions.
- (iv) The effect of prolonged soaking treatments at high temperatures on deformed inclusions in steel.
- (v) Mechanism of fracture and dissemination of brittle types of silicate inclusions.
- (vi) The effect of inclusions on notch ductility of some of the materials investigated and their relationship to the plasticity index of inclusions in the longitudinal and long transverse directions respectively.
- (vii) The effect of different height to width ratio of the steel matrix on inclusion deformation.
- (viii) Test the validity of equations derived by Wardle⁽¹⁰⁰⁾ for the plasticity of inclusions in the third plane if plasticity in two planes are known, i.e. the estimation of the plasticity of inclusions in the third plane from the known inclusion plasticity in the other two planes and the estimation of corrected inclusion plasticity index for plane strain condition. Full derivation of the equations are given in Appendix 3.

Although this investigation was primarily concerned with the effect of sulphur content in the steel on composition of the oxide inclusions, and the deformation of oxide and sulphide inclusions, it was thought that the work would be incomplete if the current views concerning the main features (as discussed below) which have significant effect on the inclusion composition and deformation are not reviewed.

2.1 Deoxidation Thermodynamics

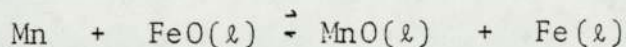
Numerous investigations have been carried out on the thermodynamics of deoxidation which have been reviewed previously (6-10). However, it must be noted the data was obtained for elements in their standard states and single binary and ternary systems. Due to the short time between deoxidation, casting and the rapid solidification obtained in this present work; the validity of the above data pertinent to the present work is questionable. The data available (10,12,13) has been used, however, as the basis of deoxidant alloy calculations and is reviewed briefly.

2.1.1 Deoxidation by manganese

Manganese alone is not a powerful deoxidiser as can be seen from the free energy diagram (Fig. 1). It is added primarily for its desired effect on sulphide inclusions, but it may also significantly modify deoxidation by silicon or aluminium.

Korber and Oelsen⁽¹⁴⁾ described the phase relations, for simple deoxidation by manganese and this was updated by

Fischer and Fleischer ⁽¹⁵⁾. The oxides of iron and manganese form almost ideal solid and liquid solutions, at the low oxygen pressures typical of steelmaking. As indicated by the equilibrium constant for the reaction:



An increase in manganese content of the metal increases the ratio of MnO to FeO in the oxide mixture and this in turn raises its liquidus temperature. It can be seen from the diagram (Fig. 4) that only a range of MnO-FeO compositions are liquid at steelmaking temperatures, thus showing a further disadvantage of manganese as a deoxidant.

2.1.2 Deoxidation by silicon

From free energy-temperature diagram (Fig. 1), silicon is seen as a relatively stronger deoxidant than manganese. The influence of silicon as a deoxidant has been based upon the equilibria reaction:



The phase relations pertinent to deoxidation by silicon have been analysed independently by Forward and Elliott ⁽¹⁶⁾ and Iyengar and Philbrook ⁽¹⁷⁾ with similar conclusions. The pseudo-binary FeO-SiO₂ diagram (Fig. 5) indicates the composition of the deoxidation products. The most common condition in deoxidation by silicon is that the initial metal composition lies above the hypereutectic liquidus surface in the region where SiO₂ of virtually stoichiometric composition is the primary deoxidation product.

Gokcen and Chipman (18) proposed that:

- (1) the activity coefficient of oxygen is reduced by addition of silicon,
- (2) in dilute solutions the activity coefficient of silicon increases with its concentration.

From their work they concluded that for pure Fe-Si-O melts containing less than 2 wt% Si the change in silicon activity coefficient (f_{Si}) with oxygen concentration was almost balanced by the change in the oxide coefficient squared, i.e. f_o^2 . The equilibrium constant is given approximately as:

$$K_{Si-O}^1 = \frac{a_{SiO_2}}{[\%Si] [\%O]^2}$$

Since the product (f_{Si})(f_o^2) is approximately constant, they also showed that silica formation is very much dependent on temperature.

The principal difference between silicon and manganese deoxidation lies in the acidic nature of SiO_2 compared with the basic nature of MnO (10). This is underlined by the fact that a_{MnO} increases and a_{SiO_2} decreases as slag basicity is increased.

A melt containing low silicon, high oxygen content within the two-liquids region solidifies by monotectic reaction with the formation of liquid oxide globules. These have variable composition, ranging from silica saturation melt to liquid iron oxide depending on the metal composition and temperature. Globules trapped among the dendrite arms will ultimately freeze as either tridymite plus fayalite or

fayalite plus wüstite, depending on their composition (17).

2.1.3 Deoxidation by aluminium

There have been a number of investigations into the deoxidation of iron-oxygen melts by aluminium (14,15,19-31).

Values of aluminium equilibrium constant have been determined in the range 10^{-9} to 10^{-14} at 1600°C .

Lindon (31) pointed out many experimental difficulties encountered in the $K_{\text{Al-O}}$ determination, although alumina is a very stable oxide. Sloman and Evans (23) found that aluminium addition in stoichiometric excess of the oxygen content produced alumina inclusions whilst additions of less than stoichiometric proportion gave rise to mixed oxide phases containing the spinel phase hercynite, their composition depending on the aluminum to oxygen ratio.

The differences in true and apparent equilibrium constant are thought to be due to a slow rate of approach to equilibrium. Kawawa et al (32) and Lindon (31) observed that the rate of dissolution of aluminium into molten steel is lower than the rate of dissolution of manganese and silicon respectively.

2.1.4 Deoxidation by aluminium and manganese

Manganese and aluminium oxides form the spinel galaxite ($\text{MnO} \cdot \text{Al}_2\text{O}_3$), which is isostructural with hercynite and other spinels, and accommodates a considerable range of stoichiometric and substitution of other elements such as

Fe for Mn or Cr for Al (33-35). Galaxite inclusions are observed in commercial steels lightly deoxidised with aluminium (36). A noteworthy feature of the binary MnO-Al₂O₃ system is the range of composition that may exist as liquid oxide at steelmaking temperatures (37,38). Such liquid inclusions would nucleate more easily than alumina and would coagulate and float out more readily than solid products (32, 38). McLean (33) points out that manganese lowers the oxygen and raises the aluminium concentration for univariant transition from (Fe, Mn) Al₂O₄ to Al₂O₃ as the stable deoxidation product, and the formation of galaxite enhances the deoxidising power of aluminium at low concentration levels. The manganese content of commercial steels therefore significantly enters into the deoxidation reactions with aluminium in lightly deoxidised steel.

2.1.5 Deoxidation by silicon and manganese

It is well known that manganese enhances the deoxidising power of silicon at low silicon concentrations in the steel. Although silicon is a much ^{more} powerful deoxidiser than manganese (Fig. 1), simultaneous addition gives a much lower residual oxygen in solution (14).

Hilty and Crafts (39) and Kawawa et al (32) agree that oxygen equilibrium content decreases with increasing manganese content. Walsh and Ramachandran (40) explained the low final melt oxygen observed by the fact that the deoxidation product was a manganese silicate having a silica activity less than unity. The primary deoxidation

product in this case is not a solid oxide but a liquid manganese silicate, in which the activities of both MnO and SiO₂ are lower than if either element were added alone. Kawawa et al (32) found that liquid inclusions may coalesce and float out more rapidly than smaller solid particles.

Turkdogan (41) also has calculated the residual oxygen content of steels deoxidised by silicon plus manganese and his results agree with the earlier findings by Hilty and Crafts. Turkdogan (42,43) calculated the Mn-Si deoxidation equilibrium data for the reaction: $2\text{MnO} + \underline{\text{Si}}_{\frac{1}{2}} \rightarrow 2\underline{\text{Mn}}_{\frac{1}{2}} + \text{SiO}_2$ For which $K_{\text{Si-Mn}}$ is given by

$$K_{\text{Si-Mn}} = \frac{[\% \text{Mn}]^2}{[\% \text{Si}]} \cdot \frac{a_{\text{SiO}_2}}{a_{\text{MnO}}^2}$$

where a_{MnO} and a_{SiO_2} are the Raoultion activities of oxides in the molten manganese oxide-silica deoxidation product. He also showed that above a critical $[\% \text{Si}]$ to $[\% \text{Mn}]^2$ ratio for a given temperature solid silica will form (Fig. 6).

2.1.6 Deoxidation by manganese-silicon-aluminium

There is very limited data available for the MnO-SiO₂-Al₂O₃ system (Figs. 7 and 8). Lindon (31) working on the MnO-SiO₂-Al₂O₃ system pointed out that the presence of alumina in the product of deoxidation would lead to a decrease in the activity coefficients of both manganese oxide and silica. He also indicated that manganese-alumina-silicate slag would equilibrate with a lower oxygen level for a given manganese to silicon ratio.

Kawawa and Ohkubo ⁽³²⁾ working on this system observed a remarkable decrease in total oxygen content immediately after the addition of the deoxidant. They attributed the low total oxygen levels to the rapid floating up of MnO-SiO₂-Al₂O₃ inclusions with a high degree of coalescence.

2.2.0 Kinetics of Formation and Elimination of Inclusions in Steel

Early studies on deoxidation of steel was dominated by thermodynamics aspects, although kinetic influences have occasionally been referred to in passing.

Plöckinger and Wahlster (44,45) conducted the first extensive investigation into deoxidation reaction kinetics involving the formation, growth and separation of inclusions. They observed that alumina inclusions separate more rapidly than silica inclusions, and that agitation or stirring of the steel generally favours the elimination of inclusions. Since, the kinetics and fluid dynamics of deoxidation have been studied intensively (46) and highlighted by recent review papers (41,47-51). The sequence of events in deoxidation kinetics is thought to be divided into four elementary stages which can be studied separately (41,46,47,49,51-53):

- (i) dissolution and mixing of the deoxidiser in the melt,
- (ii) nucleation of deoxidation products,
- (iii) growth of the nuclei to inclusions of an initial size distribution,
- (iv) floating out of the inclusions with concurrent growth.

In practice these stages overlap to a large extent and therefore, it is convenient that the first three steps will be discussed under general heading of 'formation' and the last step as 'elimination' of inclusions in steel.

2.2.1 Formation of inclusions in steel

It is well known that inclusions originate from liquid steel by the process of nucleation and growth (41,46,49-51, 54-57). For several reasons, it is difficult to apply classical nucleation theory quantitatively. Initial conditions involve fluctuation in composition and temperature on macroscopic scale which is dependent upon the way in which the deoxidants are mixed with the steel. In the case of deoxidation with aluminium Olette et al (58) showed the influence of the method of introducing the deoxidant on the kinetics of deoxidation. The degree of supersaturation necessary for nucleation to occur at a finite rate is very sensitive to the interfacial free energy between the liquid steel and the inclusion phase. Due to this, the phase that nucleates is not necessarily the equilibrium phase. Homogeneous nucleation may occur in regions of high supersaturation formed during mixing of the deoxidant. Thus homogeneously formed nuclei may subsequently be carried by convection into regions not sufficiently supersaturated for nucleation but capable of contributing to growth. Substrates for heterogeneous nucleation may normally be abundant from impurities carried in by the additions of deoxidants. Numerous workers have contributed to the formulation and explanation of these concepts.

Turpin and Elliott (56) studied the application of homogeneous nucleation of oxide phases from liquid steel. They calculated the necessary critical supersaturations, and from estimated interfacial tensions and experimental results deduced the conditions for nucleation of pure silica or liquid silicates

in the Fe-Si-O system and of Al_2O_3 , hercynite, or iron-aluminate in the Fe-Al-O system. Forward and Elliott (59) studied the nucleation of silica and iron-silicates during solidification (60). Melts containing less than about 0.02% oxygen may not nucleate homogeneously if a silicon addition is mixed in. If supersaturation is achieved rapidly, depending on the density of particles, homogeneous nucleation may occur during deoxidation even in the presence of heterogeneous nuclei. It must be pointed out that neither Turpin and Elliott (56) nor Torssell, Gatellier and Olette (61-63) were able to achieve a sufficient degree of supersaturation by rapid cooling to cause homogeneous nucleation in Fe-Si-O melts.

A number of investigators have observed that the nucleation and precipitation of silica inclusions are completed within a second, giving an initial distribution of inclusions of narrow size range of approximately 4 or 5 μm diameter, corresponding to a population density of the order of 10^7 - 10^8 per cm^3 . The rapid growth of nuclei to inclusion size has been fitted by diffusion models (41,46,48,52,53-55), although Sakagami et al (65) postulated rate control by reaction at the particle surface rather than by diffusion. It has been suggested that neither Brownian Collisions nor Ostwald ripening contribute significantly to growth at this stage (41,52,66).

The addition of solid aluminium does not lower the dissolved oxygen content of liquid steel as rapidly as deoxidation by silicon; the size of alumina inclusions as measured by

Quantimet is closely distributed about a peak of 3-4 μm and the particles do not coarsen with time as silica inclusions do (47-49,67). Gattellier and Olette (47) explained the slower reaction of solid aluminium by the delay caused in the homogenisation of the deoxidising metal as a result of a layer rich in small alumina particles, holding back the diffusion of the deoxidising agent introduced. Schenck et al (68) reported that the precipitation of Al_2O_3 was slower than calculated for control by diffusion, and attributed this to poisoning of the alumina surface. However, the initial rate of deoxidation depends on how the deoxidant and steel are mixed, and it is increased significantly if liquid instead of solid alumina is used (63,48,51). Sigworth and Elliott (57) suggested that the faster reaction is the result of a greater density of nuclei obtained with the more rapid mixing that is possible with the liquid addition.

The fact that homogeneous nucleation is possible for strong deoxidisers does not imply that all inclusions from deoxidation with aluminium, for example, will be precipitated homogeneously. Supersaturations required for heterogeneous nucleation are always less than those of homogeneous nucleation. It should be pointed out that, in industrial practices, heterogeneous nucleation is the more important.

2.2.2 Elimination of inclusions

Several investigators have contributed towards explaining the coarsening or coalescence, rise, and eventual elimination of inclusions and to clarify suspected deviations from

Stoke's law. Miyashita et al ⁽⁶⁹⁾ concluded that the rising velocity of silica inclusions in a tranquil bath is in agreement with Stoke's law. The rising velocity of a particle not wetted by the steel may be at the most, 50% faster than the Stoke's velocity of a wetted particle ^(69,70). The separation of inclusions from agitated bath is more rapid and the rate of elimination depends upon the crucible material.

Torssell and Lindborg ⁽⁵²⁾ developed a collision model which describes the observations on the growth and separation of inclusions. On the basis of theoretical and experimental results, these authors suggested schematic representation of their result (Fig. 9).

Iyengar and Philbrook ⁽⁷⁰⁾ found that natural convection currents caused recirculation and retention of some inclusions longer than predicted by Stoke's law. The ultimate removal of inclusions depends upon their emergence at the free surface of the metal or their assimilation by slag or crucible wall. It must be pointed out that the latter step in turn depends upon the interfacial free energy effects ^(67,71,72), and the time required for rupture and drainage of the metal film between the particle and the interface ⁽⁷³⁾.

Turkdogan ⁽⁵⁵⁾ using a theoretical model showed that the growth of oxide inclusions as they rise in the melt is dependent upon the number of nuclei initially produced by deoxidation (Fig. 10). The larger the initial number of nuclei, the slower the rate of elimination. Turpin and

Elliott (56) suggested that strong deoxidisers results in a large number of nuclei-formation due to high degree of supersaturation. Weaker deoxidants result in fewer stable nuclei which grew into large inclusions therefore enhancing inclusion separation. From Turkdogan's model, if the number of nuclei, Z is less than the critical value Z_m , the relatively large inclusions float out of the melt quickly leaving behind unreacted high residual oxygen in solution. If the number of nuclei, Z , is greater than the critical value, Z_m , the inclusions attain their full growth in a relatively short time, i.e. the residual oxygen in solution approaches equilibrium value in short time. Under these conditions, the inclusions are small in size and hence their separation from the melt takes a longer time as shown in diagram (Fig. 11). He also showed that small inclusions did not float from the melt readily when a large number of nuclei were present because the inclusions attained a constant velocity within a short time due to the speed of the diffusion controlled reaction.

Evolution of gas during deoxidation results in an increase rate of inclusion removal, due to the adhesion of gas bubbles onto inclusions aiding buoyancy (a phenomenon made use of in the argon rinsing process (74) although inclusions surface properties promote particle adhesion).

The importance of size and composition on inclusion removal was shown by Herty et al (34,35). They showed that the cleanest steel produced by manganese-silicon deoxidation

occurred when the ratio of Mn to Si was between 4 and 7. The product composition was found to be in the low liquidus range of the MnO-FeO-SiO₂ (Fig.12) at 35-45% SiO₂, 45-55% MnO and approximately 10% FeO. This led to the conclusion that low melting point inclusions were advantageous, their high level of fluidity allowed them to coalesce and float out easily.

The separation of inclusions within the MnO-SiO₂-Al₂O₃ system was studied by Lindon and Billington (75). They observed that the rate of separation of inclusions within the system increased with increasing Mn:Si and Al:Si ratios of the deoxidants added. Where they observed silica rich inclusions they observed concurrent low removal rates, coalescence of such inclusions being delayed due to the higher viscosity of silica rich inclusions. They also observed that fluid manganese-alumina-silicates separated at slower rate than anticipated by Stoke's law and attributed this to a low interfacial energy between the inclusion phase and the melt. They concluded that the rates of separation of inclusions increased as a result of increasing the melt-oxide interfacial energy, which confirmed Plöckinger and Wahlster results. Kozakevitch and Olette (67) and Kozakevitch and Lucas (72) demonstrated the importance of surface phenomenon upon inclusion coalescence and separation.

Waudby (76) pointed out that an inclusion rising through a liquid metal may behave in the following manner when it approaches the surface of the metal:

- (i) remain just below the surface without emergence in which case the inclusion may be pushed into the metal by descending currents (the inclusion thoroughly wetted by the liquid metal).
- (ii) escape and float on the surface (no wetting of the inclusion)..

It has been pointed out by Kozakevitch and Olette (67) and Waudby (76) that emergence can take place spontaneously only if it results in lessening of the free energy, G , of the system, $\Delta G < 0$: $\Delta G_s = \gamma_s - \gamma_m - \gamma_{sm}$ where γ_s is the surface energy of the inclusion, γ_m that of the metal, and γ_{sm} , the interfacial energy at the inclusion-metal interface. Under steelmaking conditions ΔG is always less than zero, hence there will always be some emergence of inclusions to the surface of the melt. Dyson (77) found that the surface tension of iron melt is strongly influenced by sulphur and other impurities in the melt (78) (Figs. 13 a and b).

It is well known that γ_s and γ_m can be determined experimentally. The metal-inclusion interfacial tension, γ_{sm} , can be calculated based on γ_m and γ_s and using vector analysis. Thus γ_{sm} can be calculated from the relation: $\gamma_{sm} = \gamma_s - \gamma_m \cos \theta$ where θ is the contact angle between the liquid metal and its support.

Kozakevitch and Olette (67) determined contact angles for several systems and summarised their conclusions as follows:

- (i) when the contact angle, θ , metal-oxide is given as $0 < \theta < 90^\circ$, primary contact between inclusions is possible but the agglomerates would not be stable because the contact surface would be too small.
- (ii) when $\theta > 90^\circ$, the natural result is the spontaneous retreat of the metal from the space still separating the neighbouring inclusions after the establishment of the contact points, and formation of stable agglomerates become possible. The probability of this phenomenon obviously increases with an increase in the value of θ , thus the emergence of inclusions is promoted.

A recent analysis of hydrodynamics and collisions of small particles in turbulent melts has been made by Linder ⁽⁷⁹⁾. His results confirmed some of the earlier findings.

Recent experiments by Lindskog and Sandberg ⁽⁸⁰⁾, using radioactive silicon, have shown that in the deoxidation of a well stirred bath most of the inclusions are absorbed by the crucible wall rather than floating to the surface. They also found that with aluminium deoxidation, silicon and manganese dissolved in the melt increase the removal rate of alumina inclusions in alumina crucibles.

2.3.0 Nature of Inclusions Commonly Found in Steels Deoxidised by Al-Si-Mn Alloys

The review of some of the inclusions encountered in the (Mn, Fe)O-SiO₂-Al₂O₃ system will be brief. For a more detailed review, the reader is advised to read the reviews by Kiessling and Lange (81,82), Pickering (83) and Robinson (84). The physical properties of oxide and sulphide inclusions can be found in reference (81).

2.3.1 Silica, SiO₂

Several silica modifications are known. Pure silica inclusion is very rarely observed in steels. The following phases are stable at ordinary pressures: quartz, tridymite and cristobalite. Transformations between the phases are fast and reversible. Cristobalite often crystallises as dendrites or rosettes in a glassy or crystallised matrix of various metal silicates (82). Cristobalite also occurs as a scale around inclusions and this phase can dissolve several per cent of alumina and other metal oxides in solid solution.

Tridymite only exists if stabilised by traces of other metal ions present in solid solution. This phase often crystallises as rather dark, thin plates in inclusions.

Quartz phase in steel inclusions has been observed as dark grains which form more or less regular plates in polished sections. Its presence is a strong indication of the exogenous origin of the inclusion (i.e. refractories).

2.3.2 Alumina, Al_2O_3

The most commonly observed oxide in steelmaking is alumina and it is usually observed in the form of corundum ($\alpha-Al_2O_3$). Alumina inclusion of glassy morphology has been reported by Plöckinger. Rege et al (85) showed the dendritic nature of small clusters of alumina inclusions. This dendritic growth or skeletal form of alumina inclusion has since been observed by other workers (83,84). Corundum phase in inclusions is usually pure, or contains traces of most other metal oxides.

2.3.3 Iron - Manganese oxides (Fe, Mn)O

Iron and Manganese oxides form a continuous series of solid solutions and they precipitate from oxygen rich melts as liquid phases within the miscibility gap of Fe-Mn-O system (Fig. 4). (Fe, Mn)O normally precipitates as single phase spherical globules but two phase character of these oxides have been reported (86) and this was attributed to the cooling cycle of the steel. Fischer and Fleischer (87) reported that (Fe, Mn)O inclusions are FeO rich when precipitated but increase in MnO content if the cooling rate is long due to the fact that during steelmaking equilibrium point is not reached. This was supported by Kiessling and Lange (82) who stated that compositional changes may take place upon heat treatment. The MnO rich inclusions have melting points above that of the steel so that they form angular idiomorphic inclusions and sometimes dendrites, while inclusions rich in FeO are still molten and form droplets either present originally in the melt or as very small liquid particles when the metal freezes.

2.3.4 Iron-Manganese-Alumino-Silicates [(Fe,Mn)O-Al₂O₃-SiO₂]

2.3.4.1 (Fe,Mn)O-SiO₂: Most common inclusions found in steels deoxidised by silicon-manganese alloys are iron-manganese-silicates which are glassy and/or crystalline in nature. The number of phases possible within the FeO-MnO-SiO₂ system is dependent upon the oxygen content of the melt, cooling rate and the weight percent of silicon added, (Fig. 12). Low levels of silicon promote manganowustite, (Fe,Mn)O inclusions, whereas high levels aid fayalite or tephroite inclusions formation. Rhodonite (MnO:SiO₂) rarely occurs in commercial steel deoxidised by silicon-manganese alloy (83).

2.3.4.2 (Fe,Mn)O-Al₂O₃-SiO₂ (Silicates): Most of the phases in this system have not been found to exist alone as a single phase inclusion, however it is usual to find precipitates of the phases within manganese-alumino-silicate inclusions. It is common to find manganese rich phase rather than iron rich phase due to the greater stability of MnO relative to FeO, though some iron is present within the inclusions. Phases observed within this system is summarised below:-

Rhodonite, (MnO.SiO₂): This phase is common in steel inclusions. Single-phase rhodonite inclusions, sometimes partially glassy, are often found as round droplets which are easily mistaken for pure silica. In sections of multiphase inclusions, the rhodonite phase is frequently found as broad, rather bright laths. If the mean inclusion composition is close to that of rhodonite, these laths form a dense structure,

often with a fine precipitate of MnS in the grain boundaries.

Tephroite, $(2\text{MnO}\cdot\text{SiO}_2)$: In multiphase inclusions, the tephroite phase forms banded structures. No inclusions with pure tephroite phase have been found, but silicate inclusion has been shown, having banded structure typical of tephroite. MnO in tephroite can be completely substituted by FeO. As an immiscibility gap is reported for low FeO contents, it is not possible to decide if the phase is tephroite with FeO or fayalite with MnO. It is known that this phase can have solid solubility for alumina up to 15 wt-% and the homogeneity range is between about 65-73 wt-% of MnO.

Spessartite, $(3\text{MnO}\cdot\text{Al}_2\text{O}_3\cdot 3\text{SiO}_2)$: This phase forms a featherlike, branched phase in microsections of inclusions. It has the lowest melting point (1195°C) of the different phases present in the MnO- Al_2O_3 - SiO_2 system. This phase was only observed in those steel inclusions which had been hot worked or cooled slowly (81,82). If steel samples with inclusions having a glassy matrix near the spessartite composition range are heat treated below 1195°C , spessartite often crystallises in the matrix.

Mullite, $(3Al_2O_3 \cdot 2SiO_2)$: Mullite has an extended composition range between about 25-28 wt-% SiO_2 . Depending on temperature and pre-history of the mullite phase, the extension of the composition range shows considerable variation.

Galaxite, $(MnO \cdot Al_2O_3)$: The grey galaxite phase often has a cloverleaf appearance. Galaxite is observed frequently in inclusions from different steel types as well as from ferroalloys and it is also common inclusion phase in chromium steels.

Spinels: Spinel is a common phase found in steel inclusions and of the general formula $AO \cdot B_2O_3$ ⁽⁸²⁾. They have various double oxides which show extended composition ranges. The spinels galaxite $(MnO \cdot Al_2O_3)$ and hercynite $(FeO \cdot Al_2O_3)$ are often observed as clusters ⁽⁸³⁾. Hercynite is rarely seen in manganese containing steels where galaxite is promoted, however, the MnO in galaxite may partly be substituted by FeO.

Kiessling and Lange ⁽⁸²⁾ in their review of the $MnO-Al_2O_3-SiO_2$ system concluded that all the mean compositions of the inclusions are situated in that part of the ternary diagram (Fig. 15) which is limited by the lines L_1 and L_2 .

2.3.5 Sulphide inclusions in steel

Sulphur has unlimited solubility in liquid steel at 1600°C however, in solid state this solubility is virtually nil and thus nearly all the sulphur must be precipitated from the metal as it solidifies. In the absence of more stable sulphide forming elements, FeS is the phase precipitated and forms as a low melting point (988°C) eutectic. The presence of this FeS phase leads to the familiar problem of hot shortness. In order to prevent FeS formation, manganese is added which increases the melting point of the inclusions formed above the normal hot working temperatures. This is due to the stability of MnS compared to FeS. The effect of manganese on solubility of manganese sulphide in hot metal is shown in Fig. 16c:

2.3.5.1 Manganese sulphides (MnS)

The morphology of MnS however is dependent upon the steel-making deoxidation practice and its alloy content. Simms and Dahle (88) classified the morphologies of MnS inclusions as types I, II and III.

Type I: randomly dispersed globular sulphides; individual inclusions may be associated with an oxygen rich second phase.

Type II: fan or chain-like distribution of fine inclusions normally described as eutectic and confined to the interdendritic regions.

Type III: randomly dispersed angular inclusions.

Traditionally type II sulphides have been regarded as an eutectic structure being produced by eutectic reaction.

Baker and Charles ⁽⁸⁹⁾ studied the morphology of MnS inclusions in steel and reached the following conclusions:

- (1) All three types of MnS are precipitated in the interdendritic regions,
- (2) Type I are spherical and are associated with varying proportions of an oxide-sulphide eutectic. They are precipitated from the solidifying steel by a monotectic reaction, those formed first having a higher oxygen content than those rejected later,
- (3) Type II are precipitated as extensive interconnected branched rods. Traditionally they are thought to be formed by an eutectic reaction but are more likely to be a co-operative eutectic,
- (4) Type III have an octahedral morphology and are precipitated as a divorced eutectic.

Below a limiting oxygen content of (0.01%), Dahl ⁽⁹⁰⁾ states that only type II sulphides are formed, and there is a gradual transition between types I and II sulphides at oxygen contents between 0.02% and 0.01%. The effect of aluminium ⁽⁹¹⁾ in changing the morphology from type I to type II is generally accepted to be due to the action of aluminium on the reduction of oxygen in solution. However, Fredriksson and Hillert ⁽⁹²⁾ have obtained both type I and type II at low oxygen to sulphur ratios in experimental melts and have suggested that the absence of type II sulphides from the silicon treated steels was due to the silicate droplets being efficient nuclei for the

liquid type I sulphides. Deoxidation by aluminium alone produces a solid oxide which is presumably not an efficient nucleant for liquid MnS. It has been suggested that type I is formed by degenerate monotectic reaction ⁽⁹²⁾, type II being co-operative monotectic reaction ^(89,92), while the type III is by degenerate eutectic reaction ⁽⁹²⁾.

Small alumina particles have been found within type III sulphides and it is possible that alumina may promote the formation of type III sulphides ^(93,94). In steels with very low oxygen levels, example, correctly treated aluminium killed steels, an idiomorphic forms of MnS is formed. These are precipitated in crystalline form directly from the melt. The form of type III MnS indicated that it precipitated from the melt as solid, and several attempts have been made to explain its formation by considering the influence of alloying elements on the Fe-MnS binary diagram ^(95,96) (Figs. 16 a and b). The effect of increased aluminium, carbon, and silicon is to reduce the melting point of iron and increase the activity of sulphur. The eutectic is thus moved closer to the iron side of the diagram. Dahl et al ⁽⁹⁰⁾ assumed that the steel composition (X_1) (Fig. 16a) must be to the right of the eutectic and thus crystalline proeutectic MnS is precipitated. Baker and Charles ⁽⁸⁹⁾ argued that the explanation depends on the ability of the alloying elements to increase the activity of sulphur and hence to move the eutectic to the left of the steel composition and that it should be possible to change a type II MnS into a type III MnS merely by increasing the

sulphur content. Since this is not the case, Baker and Charles assert that type III MnS are unlikely to be formed by proeutectic precipitation, and support the view that this morphology results from a divorced eutectic reaction.

Fredriksson and Hillert ⁽⁹²⁾ observed a fishbone or chinese script morphology which they believed resulted from co-operative eutectic reaction. This they called type IV. This morphology has only been clearly distinguished from type II sulphides in experimental melts containing high sulphur. It is very difficult to distinguish between types II and IV sulphides in commercial steels containing small volume fractions of sulphides.

There is now enough evidence to support the possible mechanism of the different sulphide morphologies. The various types of MnS inclusions are formed by the following reactions:

Type I: degenerate monotectic reaction where MnS forms as liquid.

Type II: co-operative monotectic reaction, where MnS forms as a liquid phase together with the solid Fe-rich phase.

Type III: degenerate eutectic reaction where MnS forms as crystalline phase

Type IV: co-operative eutectic reaction where MnS forms as a crystalline phase together with the solid Fe-rich phase.

2.3.5.2 Sulphide modification

Although sulphide modification can be achieved in steel this aspect will not be reviewed since the present work does not include any sulphide modification experiments.

Manganese sulphides behave plastically, forming elongated thin stringers during hot working, which are very deleterious to the mechanical properties of steel. The modification treatment of sulphides are designed to replace the highly plastic MnS inclusions with a less plastic form and also to ensure that the highly dangerous type II morphology does not occur. The objective of sulphide modification is to produce inclusions which are less plastic during rolling deformation and must not crack. Thus they must be small and must be distributed uniformly throughout the steel, since clusters would also produce deleterious effect on the mechanical properties of the steel.

In recent years the rare earth elements have attracted a considerable amount of attention from steelmakers because of their strong affinity for sulphur and oxygen and their beneficial effects in removing dangerous types of oxide and sulphide inclusions. The resulting oxides and sulphides formed by the usage of rare earths as deoxidants are less plastic and are normally uniformly distributed throughout the steel.

2.4.0 Deformability of Inclusions During Hot Working

Introduction

During hot working the material flows in a certain direction which is dependent upon the working process. Thus any non-metallic inclusion in the material deforms in conjunction with the surrounding matrix. Whether these inclusions do/ or not deform is dependent on a number of factors which will be discussed later.

Non-metallic inclusions in steel after hot rolling may behave in several ways - they may be non-deformable, brittle, plastic or fluid. Inclusions which are brittle, plastic or fluid string out in the direction of imposed flow whether they remain disseminated or intact. The apparent deformation is relative to the matrix in which the inclusion is embedded.

The undesirable effects of non-metallic inclusions on steel properties is known to depend on their amount, type, shape, size and distribution. An examination of the behaviour of inclusions during hot working is therefore of great importance, and the problem of deformation of non-metallic inclusions has been the subject of several investigations (89,97-104).

2.4.1 Analytical methods of inclusion deformation

Scheil and Schnell (98) studied the deformation of inclusions in steel using cylindrical steel specimens deformed in a press. They observed the deformation in sections parallel to the direction of upsetting. Assuming the as-cast spherical inclusions deformed into oblate spheroids (which in the

microsection appeared as ellipses), they measured the aspect ratios of the deformed inclusions as a measure of inclusion strain. Using the ratio of this parameter with the diameter to thickness ratio of the deformed steel sample, they defined an index of deformability of the inclusions as

$$v = \frac{a_i/b_i}{a_m/b_m}$$

where a_i = major semi-axis of the deformed inclusion
 b_i = minor " " " " " "
 a_m = diameter of the compressed steel sample
 b_m = thickness " " " " " "

Assessing the deformability of the inclusions in hot rolled steel bar, Pickering (102) used a similar method. In this case the aspect ratios of the deformed samples were defined as

$$a_m/b_m = (A_o/A_f)^{3/2}$$

where A_o and A_f are the original and final cross-sectional area respectively.

Malkiewicz and Rudnik (99) developed the concept of using the ratio of inclusion strain to matrix strain as the deformability index. They defined the deformability index, v , as

$$v = \epsilon_i/\epsilon_m$$

where ϵ_i is the inclusion strain and ϵ_m is the matrix strain. Assuming that the inclusion is initially spherical and deforms to an ellipsoid during rolling, then for rolling of rod:

$$v = \frac{2 \ln b/a}{3 \ln A_0/A_1}$$

where b = major axis of the inclusion
 a = minor " " " "
 A₀ = initial cross-sectional area
 A₁ = final " " "

In later work Maunder and Charles (104) modified the formula used by Malkiewicz and Rudnik, to take account of strip rolling or plate rolling, which is defined as

$$v = \frac{\ln b/a}{2 \ln H}$$

where $H = h_0/h_1$, h_0 and h_1 are initial and final cross-sectional area respectively. This formula relates plasticity index to plane strain conditions. The formula used by Maunder and Charles has been used by other workers (84,97,100,101,103), although matrix strain has not been measured in the same manner in all the experimental work. Maunder and Charles defined H as the ratio of initial to final cross-sectional area, whereas Ekerot (97) defined H as the ratio of initial to final height in ^{the} plane of compression. In idealised plane strain, these values will be the same, but in practice some deviation from this ideal behaviour can cause problems due to the non-homogeneous deformation of the matrix.

The most common method of measuring inclusion strain is by the measurement of individual inclusion aspect ratio. Although this method is reasonably accurate, it has disadvantages of being time consuming and can be subject to investigator bias unless the inclusions are selected

randomly (105). The advantages of this method are that the investigator has the ability to observe whether the inclusions are behaving in brittle, plastic or fluid manner, and also observe the type of inclusion and whether the inclusions contain precipitates.

In order to eliminate the subjective influence of manual method, Baker and Charles (103) used the advantages of Quantitative Television Microscopy (Q.T.M.) in determining plasticity indices of sulphide inclusions. Baker and Charles showed that inclusion true strain was related to its projected length in the longitudinal plane, by the relations $\epsilon_i = \ln(P/P_0)$ where P_0 and P are the projected lengths per unit area of 'as-cast' and deformed inclusions respectively. The inclusion plasticity index, v , therefore is given by:

$$v = \frac{\log_e P - \log_e P_0}{\log_e H}$$

Unlike previous determinations of inclusion relative plasticity index, the aspect ratio (λ) does not have to be measured directly. This, can, however, be obtained from the square of the ratio of the deformed and 'as-cast' inclusion projected lengths:

$$\lambda = b/a = (a/a_0)^2 = (P/P_0)^2$$

The validity of these relationships depend on the same volume fraction of inclusions being present in each specimen. Although this is not always true, however, since P is directly proportional to N_a , area fraction, (and therefore N_v , volume fraction) this error can be corrected for, if the area fraction can be measured accurately. Where the

difference is due to a difference in the size distribution rather than area distribution, the suggested correction is likely to introduce errors rather than eliminate them. This arises because the area of the inclusions is a function of the square of the radius whilst the projected length is in simple proportion to the radius. In spite of this limitation, the great advantage of the Q.T.M. is that it enables a very large number of inclusions to be analysed.

The determination of projected length which does not include the use of advanced electronic systems was advocated in a recent review by Gladman ⁽¹⁰⁶⁾. He showed that the projected inclusion length per unit area is numerically equal to the number of inclusions per unit length intersected by a line perpendicular to the plane of projection, assuming a random distribution of uniformly sized spheres prior to deformation. This assumption made by Gladman is not true in real situations, so the reliability of this model as an approximation to a true section is questionable.

Recently Robinson ⁽⁸⁴⁾ pointed out that from the normal definition used, the relative plasticity index of an inclusion is the gradient of the chord of the curve of inclusion strain, ϵ_i , versus matrix strain, ϵ_m , from the origin through the point $(\epsilon_m^j, \epsilon_i^j)$ where j is an arbitrary point on the curve (Fig. 17a). He went on further to say that if the inclusion should cease to deform at some stage, having a 'true' relative plasticity of zero, the gradient of the chord would continue to have a finite value and the

inclusion would still exhibit an 'apparent' relative plasticity, v_A . Robinson then defined the 'true' relative plasticity, v_T , as the gradient of the curve ϵ_i vs ϵ_m at the point $(\epsilon_m^j, \epsilon_i^j)$ as

$$v_T = \left. \frac{d\epsilon_i^j}{d\epsilon_m^j} \right|_{\epsilon_m}$$

The 'apparent' relative plasticity, he defined as

$$v_A = \left. \frac{\epsilon_i}{\epsilon_m} \right|_{\epsilon_m}$$

Thus at zero matrix strain, the 'true' and 'apparent' plasticities have equal values and their values are a maximum at this point. Robinson suggested that this is the intrinsic plasticity exhibited by different inclusions and could be used for comparing different inclusions. He also pointed out that the 'true' relative plasticity decreases rapidly compared to the 'apparent' relative plasticity as the matrix strain increases (Fig. 17b).

More recently Wardle ⁽¹⁰⁰⁾ derived equations for the following:

- (i) the estimation of inclusion strain in the third plane if the inclusion strain in the two other planes are known;
 - (ii) the estimation of the inclusion width spread from the measurement of inclusion strain in two planes if non plane strain conditions exist, and
 - (iii) the plane strain corrected plasticity index.
- The equations were obtained by assuming plane strain conditions.

(i) The inclusion strain in the various planes are related by the equation:

$$\epsilon_y^1(xy) = \frac{1}{2}(\epsilon_y^1(xz) + \epsilon_y^1(yz))$$

where $\epsilon_y^1(xy)$ = inclusion strain in the (xy) plane

$\epsilon_y^1(xz)$ = " " " " (xz) "

$\epsilon_y^1(yz)$ = " " " " (yz) "

(ii) For the estimation of the inclusion width spread, ϵ_z , from the measurement of $\epsilon_y^1(xy)$ and $\epsilon_y^1(yz)$ he obtained:

$$\epsilon_z = \frac{2}{3}(\epsilon_y^1(yz) - \epsilon_y^1(xy))$$

Finally he obtained an equation for corrected plane strain plasticity index, from the measurement of inclusion strains in the (xy) and (yz) planes, as

$$v_{P\epsilon}^* = \frac{2\epsilon_y^1(xy) + \epsilon_y^1(yz)}{3\epsilon_m}$$

It must be pointed out that he derived equations for the estimation of ϵ_z and $v_{P\epsilon}^*$ when measurements of inclusion strain were made in any two planes. the full derivation of these equations are given in appendix 3.

2.4.2.0 Factors Affecting Inclusion Relative Plasticity Index

2.4.2.1 Degree of deformation

The behaviour of inclusions in steel has been studied by numerous workers. It is now clearly established that the relative plasticity indices of inclusions decrease as the overall deformation of the steel increases (84,98-100,102,103, 107).

A number of theories have been suggested to explain the observed decrease in relative plasticity of inclusion with increasing matrix strain. Pickering (102) suggested that crystalline mangano-wustite inclusions may work harden much more than the matrix ^{as the} strain increases. Since manganese sulphide inclusions are crystalline at hot working temperatures, the proposal must hold for the observed decrease in the relative plasticity of MnS with increasing matrix strain (89). No evidence has been presented to suggest that MnS and mangano-wustite do work harden appreciably at normal hot working temperatures. It was also suggested by Pickering that as the inclusions become elongated they offer less resistance to the flow of the matrix so that the interfacial forces causing their deformation decrease. However, it must be pointed out that this is applicable to those cases where the inclusions are weakly bonded so that interface sliding can take place. In the case of strongly bonded inclusions the frictional constraint at the interface will increase and the inclusions will behave as dictated by the matrix.

Charles and co-workers (89,105,107) have proposed several reasons why a decrease in plasticity index should occur with increasing strain. They are as follows:-

- (1) the extra energy expended in creating new interface could be responsible for the observed reduction in relative plasticity,

- (2) in the case of inclusions initially less deformable than the matrix, regions of frictional constraint are produced at the inclusion-metal interface. This constraint then impedes the flow of matrix around the inclusion, hence impairs the deformation of the inclusion,
- (3) the steel matrix in the vicinity of the inclusion-matrix interface becomes work hardened to a greater extent than the bulk matrix. The inclusion becomes surrounded by a shell of harder matrix which deforms less than the bulk matrix thus impairing deformation of the inclusion,
- (4) the strain-hardening rate of the inclusion could be higher than that of the matrix at the temperatures involved. If this is the case then the relative flow stresses will increase, and the observed plasticity will decrease.

More recently, Wardle ⁽¹⁰⁰⁾, using a plasticine model supported by experimental evidence, observed that the inclusion strain fell relative to the matrix strain as the matrix strain was increased. He also observed that at low matrix strains the inclusion strain was virtually nil but as the matrix strain was increased there was a rapid rise in inclusion strain until matrix strain of about 0.8 above which the inclusion strain decreased with increasing matrix strain.

2.4.2.2. The effect of the ratio of (inclusion-matrix) flow stresses

Numerous investigators have studied the effect of the ratio of inclusion to matrix strength, β , upon inclusion plasticity. Various relationships between this parameter β and inclusion plasticity have been reported, although the expected trend towards decreasing relative plasticity with increasing relative strength is generally agreed.

Unkle was the first to report the importance of the parameter β , in the non-ferrous field. Warrick and Van Vlack⁽¹⁰⁵⁾ studied the influence of relative flow stresses upon the plasticity of second phase particles during extrusion of non-ferrous materials. Zeisloft and Hosford⁽¹¹⁰⁾ deformed samples containing cylindrical rods and spheres. The material used for the matrix phase was Woods metal or lead. The inclusions phase was synthetic material of known flow stress. By plotting inclusion strain versus matrix strain, values of the relative plasticity (ϵ_i/ϵ_m) were obtained for low matrix strains which were plotted against the flow stress ratio, β , (Figs. 18a and b). These workers observed that as the flow stress ratio tended towards zero, the relative plasticity tended towards 3.0, a value of 2.9 being obtained for the case of water inclusions in Woods metal matrix. As the relative flow stress increased, the relative plasticity decreased.

Sundström⁽¹¹¹⁾ extended the mathematical analysis by McClintock⁽¹¹²⁾ on the deformation of holes, to the case of plastic inclusions in plastic plates. Assuming that

both the inclusion and the matrix behave in accordance with the equation of the form:

$$\sigma = \sigma_0 \epsilon^n$$

where σ = the flow stress, σ_0 = the flow stress at $\epsilon=1$
 ϵ = true strain, and n = work hardening exponent. He obtained a solution

$$v = (\epsilon_i / \epsilon_m) = \frac{2 \sinh(1-n)}{(1-n)} / (2 + [\beta^{1/n} - 1])$$

where v = relative plasticity at zero strain

ϵ_i = inclusion true strain

ϵ_m = matrix true strain

n = work hardening exponent of both the inclusion and the matrix

β = flow stress ratio

This solution predicts that, for materials having low work hardening rates, the inclusion having inclusion-matrix flow stress ratio greater than two will show little tendency to deform, whilst inclusions which are fluid will deform little more than twice as much as the matrix (Fig.19). There is a good agreement between Zeisloft and Hosford's experimental results and Sundström's model at low 'n' values (Fig. 20).

Klevebring ⁽¹¹³⁾ using Mann and Van Vlack's ⁽¹¹⁴⁾ hot hardness of MnS results predicted the plasticity index of MnS as a function of temperature. The plasticity index was obtained using Sundström's equation, he then compared the plasticity index with experimental data at initial strain and true strain equal to 2.1 given by Charles ⁽¹¹⁵⁾. The results show a very good correlation as far as the

shape of the curves are concerned. The deviations may be due to the fact that hot hardness data were measured on pure MnS (Fig. 21).

Gove and Charles ⁽¹⁰⁷⁾ recently working on both models and actual inclusion-matrix systems reported that all inclusions and second phases within an otherwise uniform matrix obey approximately the relationship $v = 2 - H_i/H_m$ ($0 < v < 2$); where v is the plasticity index, and H_i and H_m are the hardness of the inclusion and matrix respectively (Fig. 22). It should be pointed out that the relative plasticity referred to here was obtained by extrapolation to zero deformation where strain hardening is negligible. This can therefore be shown to be in good agreement with Sundström's model for low work hardening rates.

Gay ⁽¹¹⁶⁾ using a model, analysed the deformation of inhomogeneous materials by pure and simple shear. The model adopted was that of a homogeneous newtonian fluid in which are embedded small, circular or elliptical particles. He then concluded that a single elliptical particle which lies with its axes parallel to the pure shear axes, changes shape according to the equation:

$$\ln(a/b) = \ln(a_i/b_i) + [5/(2R+3)] \ln \sqrt{\lambda_1/\lambda_2} \dots\dots(1)$$

where a/b = axial ratio of an ellipse

a_i, b_i = initial semi-axial lengths of a non-rigid ellipse

R = viscosity ratio between a particle and the matrix.

$\sqrt{\lambda_1/\lambda_2}$ = axial ratio of the strained ellipse.

Robinson in his literature review converted these parameters used by Gay to the form normally encountered when working on inclusion deformation and obtained:

$$2\varepsilon_i = 2(\varepsilon_i)_0 + [5/(2\beta + 3)] 2\varepsilon_m$$

where $\varepsilon_i = \frac{1}{2} \ln (a/b) =$ inclusion true strain

$(\varepsilon_i)_0 = \frac{1}{2} \ln (a^i/b_i) =$ initial true strain of the inclusion.

$\beta = R =$ viscosity ratio of the inclusion and the matrix

$\varepsilon_m = \frac{1}{2} \ln (\sqrt{\lambda_1}/\lambda_2) =$ matrix true strain

Assuming $(\varepsilon_i)_0 = 0$, then rearranging he obtained

$$v = \varepsilon_i/\varepsilon_m = 5/(2\beta + 3)$$

Figure 23 shows his results for various β values and compared with Sundström's model for the case of $n = 0.8$ and Zeisloft and Hosford's results. It must be pointed out that Gay's model was based on a non-work hardening newtonian fluid matrix, thus at low temperatures this equation derived by Robinson will not be completely valid in the case of inclusions in steel though it may serve as a useful comparison.

Ashok ⁽¹¹⁷⁾ recently studied the influence of interface adhesion upon the deformation characteristics of second phase particles. Ashok observed that unbonded inclusions of the same phase as the matrix, could have relative plasticities significantly less than unity whilst if the inclusion is strongly bonded to the matrix a relative plasticity of unity was obtained. He showed that there is a marked difference in the behaviour of bonded and unbonded types of inclusions. In the case of bonded

inclusions some deformation occurred up to high inclusion-matrix flow stress ratios (i.e. $\beta = 6$) whilst the unbonded inclusions showed no deformation for flow stress ratios greater than 1.8.

In summary, from the results reported above, an upper limiting relative plasticity is exhibited by second phase particles with relative strength (inclusion-matrix) ratio equal to zero. This upper limit vary from 2.9 (Hosford and Zeisloft) down to 1.7 ⁽⁸⁴⁾. Most investigators tend to favour the upper limit value in the region of 1.9 to 2.3. The influence of adhesive strength becomes increasingly important at higher relative flow stress. The deformation of unbonded inclusions becomes greatly inhibited but there was significant deformation of the bonded inclusions. This may account for the difference between Robinson's ⁽⁸⁴⁾ and Sundström's ⁽¹¹¹⁾ models on the one hand, and Zeisloft and Hosford's ⁽¹¹⁰⁾, and Gove and Charles' ⁽¹⁰⁷⁾ results on the other. The main difference between Gove and Charles', and Zeisloft and Hosford results lie in the region of relative flow stress ratios 0-1.0. This may be due to volume changes in Zeisloft and Hosford's results. From the results and experimental models mentioned, the results which are more likely to be representative of inclusions in steel are Gove and Charles' ⁽¹⁰⁷⁾ and Ashok's ⁽¹¹⁷⁾ results.

2.4.2.3 Temperature

Temperature is probably the most important parameter which influences the behaviour of non-metallic inclusions in steel. The flow stress of both the inclusion and the matrix are greatly dependent upon the rolling temperature. It has already been discussed that changes in the flow stress affects the relative plasticity of the inclusion to a large extent.

Gove and Charles ⁽¹⁰⁷⁾ developed a technique for measuring hot hardness of inclusions in steel. The results of Kiessling ⁽¹¹⁸⁾, and Gove and Charles using hot hardness measurements indicated that hardness of inclusions decreases with temperature (Figures 24 a and b).

The inclusions encountered in this work are MnS and silicates so the effect of temperature on MnS and silicates will be discussed below.

2.4.2.3.1 The behaviour of manganese sulphides

Manganese sulphide inclusions may undergo considerable plastic deformation, this is particularly true when MnS is present within a ductile matrix. The hot hardness of MnS has a considerable influence on the behaviour of the sulphides during deformation. Chao et al ⁽¹¹⁹⁾ reported that the hot hardness of MnS decreases at high temperatures (Figures 25 a and b). They also concluded that although dissolved calcium ions increase the hardness of MnS, the hardness is essentially unchanged when iron ions replace Mn ions but the hardness increases measurably when the

solubility limit of (Mn,Fe)S is exceeded and FeS forms a second phase. Their experiments were performed on single and polycrystalline MnS. The effect of MnO on the hot-hardness of sulphide was observed to be a minimum at temperatures below 800°C but its effect may be more significant at high temperatures (120,121). The authors thought the lack of strengthening by MnO may be due to its low solubility in MnS. The same authors observed that MnS deformed plastically at the hot working temperatures of steel production, whilst at cold working temperatures considerable fracture could and did occur. They concluded that this fracturing was influenced by the inclusion orientation, although fracturing may be initiated within MnS inclusions by compressive loads (120,121). Undoubtedly, however, the fractured inclusions served an important role in initiating metal failure when subsequent stressing was reoriented from the initial compressive pattern.

Schiel and Schnell (98) reported that the deformation of sulphides was practically independent of the forging temperature. They did their investigation on the deformation of slag inclusions over the temperature range -80° to 1250°C.

Later Dahl et al (90), however, observed that the deformation of sulphide inclusions decreased with increasing rolling temperature. They reported that type I sulphides deformed to a lesser extent than type III, although both types exhibited decreasing deformation with increasing rolling temperature. They ignored type II sulphides, because they

were not so well defined due to the formation of long inclusion stringers and the joining of neighbouring inclusions. Dahl and co-workers observations have subsequently been confirmed by other investigators (89,104, 107,122).

Maunder and Charles (104) observed that the relative plasticity of sulphides appeared to be unaffected by differing amounts of reduction, or variation in inclusion size. They also noticed that above 1200°C the sulphide inclusions were less plastic in relation to the steel and deformed less. Baker and Charles (89,122) have reported a detailed study of the effects of temperature on deformation of types I, II and III manganese sulphide inclusions. Generally, they observed that the plasticity index of sulphides decreased with increasing temperature and that the relative plasticity decreased with increasing deformation of the matrix. They also reported that type I MnS deformed less than type III and that maximum observed plasticity for type I occurred at 900°C whilst for type III it occurred at 800°C. The deformability of type II sulphides increased with decreasing rolling temperature but was intermediate between that of type I and of type III sulphides. Gove and Charles (107) studied the effects of temperature of deformation on type I MnS inclusions, and their results confirmed Baker and Charles' results. Gove and Charles' results lie well above those of Baker and Charles and exhibit values more in line with the expected value at zero strain. Some of the results they obtained are shown in Figure 26. Baker and Charles (122) also observed that

during rolling, rotation of the colonies into the rolling plane and their elongation decreased the toughness in the short transverse direction. They found, however, that a short spheroidisation treatment at 1200°C increased the toughness of the weakest rolled strip to that of the cast condition. Subsequent investigations into the effect of high temperature homogenisation on sulphide inclusions have been carried out (123-125).

Gnanamthu et al (123) after studying the effect of high temperature homogenisation on sulphide inclusions arrived at the following conclusions:

- (1) the volume % sulphides did not change significantly with distance from chill,
- (2) during homogenisation of steel in which types II and II-III inclusions coexist, as well as iron-carbon-manganese alloys in which a single type of inclusion exists, substantial coarsening takes place,
- (3) during coarsening the volume % of sulphides remained practically unchanged, whereas their morphology changed, i.e. Type II-type I, breaking into segments and finally formed faceted forms,
- (4) in all cases the number of inclusions per unit volume of matrix decreased with time, whereas the mean overall size increased.

Murty *et al* ⁽¹²⁵⁾ extended the previous work by studying the kinetics of early stage of homogenisation and drew up the following conclusions:

- (i) during early stages of homogenisation MnS inclusions become cylindrical following the kinetics proposed by Nichols and Mullins ⁽¹⁹⁶⁾ of the decay of circumferential perturbation in an infinite rod. 'Spheroidisation' or breaking up of each cylinder into spheres, occurs at later stages;
- (ii) the rate of spheroidisation below 1310°C is controlled by surface diffusion of the rod-like inclusions having a final diameter of the order of 5×10^{-6} M or less;
- (iii) 'Spheroidisation' of the rod-like inclusions mentioned above should also occur by surface diffusion.

Wilson *et al* ⁽¹²⁴⁾ studied the effect of homogenisation on mechanical properties of steel. They observed that transverse ultimate tensile strength and yield strength remain unchanged during homogenisation whereas transverse ductility improves slightly. They also observed that the impact strength in both longitudinal and transverse directions improved appreciably and the variation of reversed bending fatigue strength with homogenisation time exhibited a maximum.

In summary, there is now enough evidence in literature to conclude that the relative plasticity of MnS decreases with increasing temperature. The plasticity of type I MnS is less than that of type III, but the plasticity of type II is intermediate between that of the type I and the type III. The reason for the lesser plasticity value of type I is thought to be due to the higher oxygen content giving high hot hardness. It can also be pointed out that homogenisation leads to coarsening of sulphide inclusions and this takes place by surface diffusion.

2.4.2.3.2 The behaviour of oxide inclusions

Since in this work the oxide inclusion phases investigated are mainly silicates, the review will be limited to only silicates.

Among the first systematic studies of siliceous inclusions and their behaviour during hot rolling were those presented by Pickering ⁽¹⁰²⁾, and Maunder and Charles ⁽¹⁰⁴⁾. They observed that the behaviour of the silicate inclusions depended directly on their rolling temperature. Pickering observed that at low working temperatures the siliceous inclusions behaved either rigidly, in the case of glassy silicates, or in a brittle manner in the case of crystalline duplex silicates. Rapid transition from rigid (or brittle) to plastic (or fluid) behaviour was observed at high working temperatures. Subsequent studies ^(100,104,126,127) have confirmed these observations, although it has now been pointed out that transition from rigid (brittle) to plastic (fluid) behaviour is dependent on the inclusion composition ^(100,126).

The behaviour of siliceous inclusions during hot rolling could be conveniently divided into four parts: where they exhibited fluid, transition, brittle, and plastic behaviour. Maunder and Charles ⁽¹⁰⁴⁾ produced a schematic illustration of siliceous inclusions behaviour (Figure 27).

Kiessling and Lange ⁽⁸³⁾ attempted to show the effect of variation in oxide content on the transition temperature (Figure 28). Due to variations in the effects of composition on solidus and liquidus temperatures, such a simple relationship is unlikely, although the relationship may be more straightforward in the case of glassy inclusions. It has been confirmed, however, that the transition does increase with increasing silica content ^(127,128).

The major factors affecting transition temperature are not well established, although Ekerot ⁽¹²⁶⁾ developed a theory to explain this transition in terms of viscosity in the case of glassy siliceous inclusions which showed a rapid change in plasticity index over a narrow range of temperatures, about 25°C. Assuming that the glassy inclusions behave like a newtonian fluid, then the change in viscosity could be related to the flow stress, i.e.

$$\sigma_A = \eta \dot{\epsilon}$$

where σ_A = apparent flow stress, η = viscosity, and $\dot{\epsilon}$ = strain rate. Ekerot pointed out that the transition temperature of various inclusion phases could be estimated if the viscosity data are known and that if the flow stress ratios could be derived using viscosity data, then using the analysis, the plasticity indices of the inclusions could be determined.

Recently, however, Robinson (84) pointed out that Ekerot's equation relating viscosity to apparent flow stress was not totally correct and that the correct form at zero strain should be $\sigma_A = 4\eta\dot{\epsilon}$ where the symbols are as above. The actual form is given as: $\sigma_A = 4\eta\dot{\epsilon}\cosh\epsilon$ where ϵ = true strain. Using his formula, he showed that the critical viscosity corresponds to a temperature somewhat above the glass softening point.

Rigid - plastic transition behaviour of silicate inclusions over a wide range of composition has been reported by Ekerot (126, 127). Shiraiwa et al (129) has reported the softening temperatures of both crystalline and glassy silicates of similar compositions, as measured by hot hardness test on synthetic slags. From the results of these workers it would appear that in the case of crystalline silicate inclusions the transition temperature will correspond to the solidus temperature, whereas the transition temperature for the glassy silicate may be 100^o-300^o below the solidus temperature.

Ekerot (126,127), Robinson (84) and Wardle (100) found that the relative plasticity of silicates may increase, decrease, or remain constant at temperatures above the transition temperature, whereas Pickering (102) observed that the relative plasticity of silicates remained at a constant value above the transition temperature.

2.4.2.4 Inclusion size

Various investigators (84,100,102,130) have reported that larger inclusions deform to a greater extent than small inclusions. Although extensive work on the effect of size on plasticity had not been reported, there was a consensus of opinion that small inclusions exhibited lower relative plasticities than larger inclusions of the same composition (102, 107,83,89). Baker and Charles (89) suggested that the decrease in plasticity index may be due to the greater surface to volume ratio of smaller inclusions.

Recent work by Segal and Charles (132), Robinson (84), and Wardle (100) have shown the relationship between size and plasticity index which agrees with the results of the previous investigators.

2.4.2.5 Inclusion composition

Inclusion composition can often be the most important factor in determining the behaviour of an inclusion during hot rolling. From the experimental work of Pickering (102) and Uchiyama and Sumita (130) on iron deoxidised with different amounts of Mn, it seems that inclusions of the FeO type become decreasingly plastic, as the temperature increases. Furthermore, with an increase in the Mn-content of the (Fe,Mn)O solid solution their plasticity decreases. Multi-phase crystalline silicates often break up on working at low temperatures becoming disseminated into long stringers (102,104,83). In such cases the mechanism of fracture is by the decohesion of the interfaces of the individual phases.

Maunder and Charles (104) observed the effect of alumina on the behaviour of silicate inclusions and that its presence acted as a strengthening body whose effect depended on the silicate/alumina ratio, the alumina orientation and the temperature of rolling. They also observed that the deformation of the inclusions and the length of the stringers formed was highly dependent on the alumina/silicate ratio.

Later investigations on a wider range of inclusion types have demonstrated that the transition temperatures of silicates is related to the liquidus temperature of the inclusion (126,127,133). Thus iron-manganese-silicates which have relatively low liquidus temperatures continue to deform to about 1000°C. Increasing the SiO₂ content of this type of inclusion increases its liquidus temperature (133) and silica contents above 50% lead to form a two-phase inclusion with the SiO₂-rich phase surrounding the iron-manganese silicate (126,127,133). As a result, these inclusions behave as pure silica inclusions and remain undeformed even after deformation at 1350°C. However, two-phase manganese-silicate inclusions in which the SiO₂ is present as a minor phase have transition temperatures between 1000°C and 1100°C.

2.4.2.6 Strain rate

The influence of strain rate on the deformation of inclusions in steel has been ignored by most investigators, although it is known that the flow stress of the steel matrix is very sensitive to strain rate. It is expected that increase in strain rate should increase the flow

stress of the steel which in turn will increase the values of inclusion deformability index. If the inclusion is affected more by strain rate than the matrix then the relative plasticity may decrease. It must be pointed out that strain rate affects temperature rise within a deforming material ⁽¹³⁴⁾. Thus near the transition temperature region the effect of strain rate may be appreciable causing an inclusion to become more fluid than expected as a result of a higher temperature of deformation being attained. The effect of strain rate must be taken into account when comparing data of different workers. Robinson ⁽⁸⁴⁾ studied the effect of strain rate on inclusion deformation and found that at higher strain rate the inclusions are slightly more deformable.

2.5.0 The Effect of Inclusions on the Mechanical Properties of steel

This subject is so complex and widespread, that only the topics relevant to the present work will be discussed. However, a large amount of work has been carried out, and is summarised in some recent publications (135-138). The present work is concerned with notch ductility so this review will focus on ductility.

2.5.1 Micro-Mechanism of Ductile Fracture

In the last few years the role of inclusions in controlling the mechanism of ductile fracture has been well documented.

There is a considerable amount of experimental evidence to show that second phase particles play an important role in the ductile fracture process by acting as sites for the nucleation of internal cavities. There are two main mechanisms by which second phase particles act as sites for the nucleation of voids:

- (i) the particle can fracture under the induced stress system (139),
- (ii) the normal stress on the walls of the particle may be sufficient to cause a breakdown of the matrix-particle cohesive bond (140). The mechanism of void nucleation will depend on the intrinsic properties of the matrix-particle interface and the second phase particles (141).

Inoue and Kinoshita (142) observed carbide cracking as a nucleation process that was stress dependent and concluded that the strain to void initiation increased as the interparticle spacing increased.

Kozasu and Kubota (143) investigated ductility and ductile fracture of a structural steel and observed that in the course of plastic deformation, extensive cracks developed from cracking of sulphide and the decohesion of sulphide-matrix interface. Kozasu et al (144) later studied the ductility and ductile fracture of 1.4% copper-bearing steels and the results confirmed his earlier findings that initial stage of ductile fracture is cracking of elongated inclusions and decohesion of their interface to form elongated cracks.

Butcher (145) also observed that voids were formed by both cracking of particles and interface decohesion when working on copper-oxygen alloys. He also found that the cracked particles had a larger mean size than those which failed by interface decohesion and that the particles which were still bonded to the matrix had even smaller mean size.

Palmer and Smith (146) and Palmer, Smith and Warda (147) have shown that particles as small as 50 Å in diameter can nucleate voids in internally oxidised copper-silicon alloys. They concluded that there is no indication that this was the minimum size on which a void could nucleate but this was the smallest size observed.

Rogers (148) studied tensile fractures as well as sections of partially fractured bars and observed the following:

- (1) ductile fracture of polycrystalline metals in tension is initiated by the formation of voids approximately at the strain at which necking begins,
- (2) these voids grow with increasing strain and the crack growth takes place by the concentration of strain at the tip of the static crack. He also found that macro-inclusions need not coalesce, but may be linked by sheets of very small voids which form in shear bands between the macro-inclusions. This has been observed also by other workers (143, 144, 149). Cox and Low (149) observed that void growth proceeds more rapidly from larger inclusions. They also found that tensile stress triaxiality does not affect the void nucleation process whereas increased levels of triaxial tension do result in greatly increased rates of void growth.

The available evidence suggests that interface decohesion is the major factor for void nucleation in the case of sulphide particles, and further, that the interfacial bonding is so weak that decohesion occurs at extremely small strains although there is a particle size dependence of the nucleation strain in certain systems (150-153).

Theories of ductile fracture and the effects of second phase particles attach importance to the three sequential events of:

- (1) Void nucleation,
- (2) Void growth, and
- (3) Void coalescence.

2.5.2.0 Theoretical Aspects

2.5.2.1 Void nucleation

Gurland and Plateau ⁽¹⁴⁰⁾ developed a model for void nucleation, using a stored energy criterion, they showed that there was a particle size dependence for void nucleation and that the larger particles formed voids first. They formulated the following relationship for cavity nucleation:-

$$\sigma_{\text{crit}} = 1/q \left(\frac{E\gamma}{a} \right)^{\frac{1}{2}}$$

where σ_{crit} = remote stress to nucleate void
 q = average stress concentration factor
 E = weighted averages of elastic moduli of inclusion and matrix
 a = diameter of particle
 γ = the specific surface energy of the crack.

Tanaka et al ⁽¹⁵⁴⁾ also showed that there was a size relationship where the larger particles would form voids first. Their model was based on the energy calculation in and around the inclusion following Eshelby's transformation problem. They showed that there is a size below which the fracture strain is inversely proportional to the square root of the particle size and there is also a size above which the applied stress causes cavitation without plastic strain. They showed that the critical strain, ϵ_{crit} , to cavitation was given by:

$$\begin{aligned}\epsilon_{\text{crit}} &= \beta (l/d)^{\frac{1}{2}} & \alpha < 1 \\ &= \beta \left(\frac{l}{\alpha d}\right)^{\frac{1}{2}} & \alpha > 1\end{aligned}$$

where α = the ratio of inclusion to matrix Young's moduli.
 β = a function which embraces stored elastic energy.
 d = particle diameter

They predicted that when an inclusion is greater than 200-300Å in diameter, cavitation will be able to begin at the critical strain. They also predicted cavitation around inclusions smaller than that suggested by Gurland and Plateau which is for inclusions larger than 10 μm.

Ashby ⁽¹⁵⁵⁾ derived a model which showed that the strain to void nucleation from a particle varied linearly with the size of that particle. His model also predicted larger particles forming voids first.

Similarly Brown and Stobbs ⁽¹⁵⁶⁾ using the energy criterion gave a very simple estimate of the strain at which plastic cavitation might start: cavitation will not occur unless the elastic energy thereby released was greater than the surface energy created. Then using Eshelby's solution for elastic energy in the particle derived an equation for the critical strain at which plastic cavitation can occur. The equation they derived predicted that smaller particles should form voids at earlier strain than the larger ones which was contrary to their observations.

Klevebring and Mahrs ⁽¹⁵⁷⁾ used very simplified assumptions on the stress generation at ^{the} inclusion-matrix interface to determine the critical inclusion size for formation of micro-cracks or voids at the interface during hot deformation.

The equation of their model is given as:

$$\sigma_c = K \frac{\epsilon r}{b\Omega}$$

where K = constant,

b = Burger's vector,

ϵ = strain,

Ω = the height of the dislocation array, and

σ_c = critical stress.

They then concluded that for every material, fracture will occur at a specific critical stress such that the stress, σ_c , exceeds some interfacial strength and that cracks occur primarily at large inclusions, and as the strain increases, the minimum size for an inclusion showing cracks will decrease.

Sundström⁽¹⁵⁸⁾ applied the finite element method to the problem of micro-crack initiation on cylindrical (spherical) particles in a matrix. He obtained an expression for critical stress, σ_c , as a function of work of adhesion:

$$\sigma_c = \sigma_{c0} \sqrt{(W/d)}$$

where W = work of adhesion,

d = particle size, and

σ_{c0} = the critical stress for a particle of diameter $d_0 = 1 \mu\text{m}$ and for work of adhesion, $W_0 = 1 \text{ J/m}^2$.

This model is limited to particles which are large enough for the application of finite element method. Toya⁽¹⁵⁹⁾ also used a model based on complex variable method to the problem of micro-crack initiation and predicted that the critical pressure for microvoid initiation is inversely proportional to the square root of the radius of the

inclusion which is very similar to Sundström's predictions.

The models, observations and theories of void nucleation are numerous and these are only a selection of some of the theories, models and observations. It can be seen that the theories range from little or no size dependency of nucleation to large particles nucleating voids at lower strains.

2.5.2.2 Void growth

Void growth may be enhanced due to strain concentration in the vicinity of the second-phase particles, caused by the presence of the voids. Numerous equations can be used to describe void growth, each relating to circumstances associated with void nucleation ⁽¹⁶⁰⁾, but each of which depends on the strain concentration in the vicinity of the inclusion being directly proportional to the frontal radius of curvature.

Gladman et al ⁽¹⁶¹⁾ derived a model for void growth following the work of Gurland and Plateau ⁽¹⁴⁰⁾. For the case of spheroidal second phase particle with a length (in the direction of the major stress), $2b$ and width $2a$, the rate of growth of the void with increasing true strain, ϵ , is given by:

$$b = [(L^2 + Ka^2) \exp 2(\epsilon - \epsilon_0) - Ka^2]^{\frac{1}{2}} \dots \dots (1)$$

where L = initial void length

ϵ_0 = void nucleation strain

K = strain concentration factor

The initial limit of 'b' at ϵ_0 depends on the mode of void nucleation. If the second phase cracks, then $L = 0$. If decohesion of the interface occurs then $L = b_0$. In the case of decohesion the void volume includes the inclusion, whereas in the case of particle cracking the void does not include the inclusion. It is generally observed that most inclusions nucleate voids by interface decohesion. Gladman et al, assuming that all second-phase particles behaved in an identical manner, then showed that the total volume fraction of voids, f , can be expressed as:

$$f = f_0 \left[(1 + K/r^2) \exp 2 (\epsilon - \epsilon_0) - K/r^2 \right]^{1/2} \dots\dots(2)$$

- where f_0 = initial volume fraction of inclusions
 r = initial length to width ratio of the inclusions
 K = strain concentration factor.

Clearly the details of void growth is dependent on the stress and strain systems. No evidence of lateral void growth has been observed until the onset of void coalescence, when small second phase particles contents are encountered.

The importance of the model is that the elongation of voids results in a decrease in the lateral spacing of voids, due to both the increasing volume fraction of voids with strain, and the absence of lateral contraction of the voids.

Other models have been developed by McClintock ⁽¹⁶²⁾ and Tracy ⁽¹⁶³⁾ and both models predict that void growth increases with increasing stress triaxiality. It must be pointed out that the general shape of the curves predicted by the various models, is supported by experimental results on ductility obtained by Edelson and Baldwin ⁽¹⁸¹⁾ on copper-base composite alloys.

2.5.2.3 Void coalescence

Void coalescence means a relatively rapid lateral expansion of the voids so that lateral coalescence occurs. This gives rise to a macroscopic crack which has a characteristic dimple feature of a ductile crack.

Various models have been applied to describe the onset of the rapid growth of a ductile fracture ⁽¹⁶⁰⁾. The models take a critical void length to lateral void spacing ratio as the criterion for the onset of propagation of a ductile crack ^(140,146,161,164). Only one of the models will be discussed here.

Gladman et al ⁽¹⁶¹⁾ developed further equation (2) to include a critical volume fraction of voids at which coalescence of voids will occur. The true strain to failure, ϵ_T , for cavities formed by decohesion of second-phase particles is expressed as:

$$\epsilon_T = \epsilon_0 + 0.5 \ln (K^2/f_0^2 + K/r^2)/(1 + K/r^2) \dots (3)$$

where k is the critical volume fraction of voids, the other symbols are as described previously.

It can be seen from the above equation that the true strain to fracture is related to the initial volume fraction of inclusions and the initial shape of the inclusions. Most other models define the critical void size to void spacing required to cause rupture, thus growth is terminated at some value of cavity separation and the voids then coalesce in a single void sheet to give final failure. No prediction of a particle size effect can be seen in any of the models,

and in fact, the Edelson and Baldwin experimental work appears to support this prediction (Figure 29).

2.5.3 Matrix - Particle Bonding

The nucleation of a void around a second phase particle has been attributed to the decohesion of the particle-matrix interface. Gurland and Plateau ⁽¹⁴⁰⁾ examined the role of inclusions in ductile fracture and concluded that interface decohesion can lead to void initiation.

Fischmeister et al ⁽¹⁶⁵⁾ determined the work of adhesion between particles and matrix. They found that particle-matrix bonding is largely dependent on the magnitude of the interfacial energy between an oxide and the matrix, which in turn is dependent on the matrix alloying elements. They concluded that improved interfacial energy in turn increases the ductility of the material.

Knott ⁽¹⁶⁶⁾ pointed out that alumina, most common silicates and manganese sulphide inclusions are weakly bonded to the matrix. The stress concentration at the interface plays an important role in void initiation. If the stress at the inclusion-matrix interface is higher than the interfacial energy of the inclusion and the matrix, decohesion may take place whereas in the case where the latter is stronger the inclusion may relieve itself by fracturing (i.e. carbides). Baker ⁽¹⁶⁷⁾ observed some decohesion at the interface between inclusions and the matrix. Sulphides can be particularly detrimental because they decohere at the sulphide-matrix interface prior to straining ^(122,168).

As discussed earlier Ashok (117) observed the effect of particle-matrix bonding on the deformation of second-phase particle. He observed that the deformation of unbonded inclusions become greatly inhibited but there was significant deformation of the bonded inclusions.

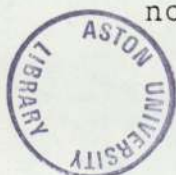
2.5.4 Inclusion Deformation

The effect of hot rolling on inclusion deformation, is either to increase or decrease the plasticity index depending on the rolling temperature.

According to investigations on ductile fracture (143,168-170), apparent phenomena associated with elongated MnS inclusions during the tensile deformation are the cracking of inclusions and the decohesion of inclusion-matrix interface at or around the onset of plastic instability. These damages become more pronounced with plastic deformation. The final fracture takes place by the localised shearing or void sheet formation between neighbouring elongated cracks (143, 149,169). Microvoids associated with small inclusions ($d < 1\mu\text{m}$) which may be responsible for the dimples are observed only to a very limited extent at incipient fracture (143,169,170).

Thomasen (171) observed that elongation, reduction in area, and impact strength values of the as cast specimens were lowered by increasing number of elongated inclusions.

The influence of elongated manganese sulphide inclusions and non-metallic inclusions on ductility and ductile fracture were



studied by Kozasu and Kubota (143) and Kozasu et al (144), and they observed that the initial stage of ductile fracture is cracking of the elongated inclusions and decohesion of their interface to form elongated cracks. The final separation proceeds by microvoid formation from submicron inclusions less than 1.0 to 0.5 μm and their coalescence. The shape of the inclusions are understood to impose geometrical conditions to accelerate the microvoid coalescence and that premature decohesion of sulphide-matrix interface is the governing mechanism in the short transverse direction and the transverse direction.

Scott (172) found that the important factor responsible for directionality of the through thickness ductility and transverse impact properties is the total inclusion length in the direction of fracture propagation. Grange (173) observed that elongated non-metallic inclusions had a greater effect on the directionality than banding.

Gouch and Dulieu (174) observed that fracture behaviour was governed by the deformation of the type II MnS sulphide networks present in the ingot. Mihelich et al (175) found that property anisotropy, particularly ductility, normally present in as rolled steel can be markedly reduced by changing the morphology of inclusions from elongated stringers to discreet globular particles.

Baker et al (131) observed that crack opening displacement (C.O.D.) in short transverse direction was influenced by inclusion aspect ratio and by rolling reduction. Smith and

Knott (176) showed that for free cutting steel the C.O.D. in the longitudinal direction was approximately three times that of the transverse direction.

Farrow (177) and Trigwell (178) showed that the tensile properties of materials tested in the longitudinal, transverse and intermediate directions were not significantly different. They observed very little difference in ductility and strength, this could be due to the fact that the number of samples tested were not enough for them to obtain any conclusive evidence.

2.5.5 Interparticle Spacing and Volume Fraction

Various workers have studied the influence of different types of second phase particles with varying volume fraction and interparticle spacing on the ductile fracture of metals (180-188).

It must be pointed out that since volume fraction may be related to interparticle spacing, the findings of the investigators tell the same story. It has generally been observed that increasing the volume fraction of inclusions markedly decreases the ductility, and to a very good approximation the effects of sulphides, carbides and oxides can be regarded as additive, and all follow the same general relationship which is in agreement with most of the models (161,164), relating volume fraction to the fracture strain (Figure 30).

Gladman (186) showed that increased volume fraction of sulphides and oxides lowered the work hardening rate at high strains in tensile tests and also pointed out that increased volume fraction of carbide had no effect on the work hardening rate at high strains but significantly reduced the tensile ductility.

2.5.6 Notch Effect in Fracture

The introduction of a notch produces changes which have important implications for the fracture of metals. Its introduction results in a stress concentration at the root of the notch. Neuber (189) has given a comprehensive treatment of the elastic stress distribution in the vicinity of notches of various shapes.

The longitudinal tensile stress in a notched tensile bar was found to be no longer uniform but rather, it reaches a maximum at the root of the notch (Figure 31). When yielding occurs at the root of the notch, the stress concentration is reduced. However, transverse and radial stresses are set up in the vicinity of the notch. The radial stress, σ_r , is zero at the free surface at the root of the notch. This situation of triple stresses (all of them tensile) is called triaxiality.

The stress concentration factor, K_t , which is dependent on the specimen geometry (the diameter of the specimen, diameter of the notch section, and the notch root radius) is defined as the ratio of the maximum longitudinal stress to the average stress. Peterson (190) has published a

very useful compilation of diagrams for the determination of elastic stress-concentration factors of a variety of combinations of notch geometries and loading systems. From elastic considerations the stress concentration at the root of the notch can be made extremely high as the radius at the root of the notch approaches zero. When plastic deformation occurs at the root of the notch, the elastic stress concentration is reduced to a low value.

The existence of radial and transverse stresses (triaxial stress state) raises the value of the longitudinal stress at which yielding occurs. For brittle material, rupture occurs when

$$\sigma_{1\max} = K_t \cdot \sigma_{av} (\geq \sigma_{\text{rupture}})$$

For a rigid plastic material, which obeys Tresca's criterion, yielding occurs when: $\sigma_1 - \sigma_3 = 2\tau$, where σ_1 and σ_3 are the maximum and minimum principal stresses, respectively at any point and τ is the shear stress.

Hill and Southwell (191) have found a stress distribution (Figure 31) when ^{the} plastic limit is exceeded, for a rigid plastic material which obeys Tresca's criterion. At the root of the notch (point A), the stress σ_1 is equal to σ_y ; and at the point B, $\sigma_{1\max}^1$ is reached and this value is given as:

$$\sigma_{1\max}^1 = \sigma_y + \sigma_{3\max}^1$$

There exists a plastic zone between points A and B but the material remains elastic between points B and C.

When the tensile stress gets much greater than the yield stress total plastification of the specimen takes place.

This redistribution of stresses within the specimen is dependent on the length of the zone AB at the moment of rupture and this characteristic can be termed notch ductility of the specimen in question. The length of the plastic zone AB is very small compared with the notch root radius (OA) at the moment of fracture if the material is slightly ductile.

Sachs et al (192) have demonstrated that the increase in notch strength of a circumferential notched ductile specimens is related to the notch depth, ND (reduction in area due to the notch) as:

$$\text{N.S.R.} \geq 1 + \text{notch depth}$$

where N.S.R. is defined as the ratio of notched strength to the ultimate tensile strength of unnotched specimen and the notch depth is defined as:

$$\text{notch depth} = \left(\frac{D-d}{D}\right)^2$$

where d = diameter at the notch section and D = the maximum diameter of the notch tensile test bar.

Joubert and Valentin (193) using the relationship between the stress concentration factor (K_t) and experimentally determined N.S.R. values, obtained an analytical expression of the curves (Figure 32) which can be applied to both mild and maraging steel. This expression is:

$$\text{N.S.R.} = \exp[A(r) \times (K_t - 1)^3]$$

where A(r), which is dependent upon the metallurgical properties of the material, is a third degree polynomial in r.

Hancock and Mackenzie (194) have been concerned with the effect of stress state on the effective strain required to initiate ductile fracture in a range of materials. These workers used circumferential notched bars, the notch root radius being varied from 1.27 mm to 6.34 mm. The specimens were pulled in tension to the point of instability. The ductility was measured as:

$$\epsilon_T = 2 \ln(d_0/d)$$

where d_0 is the initial radius of the minimum section of the bar and d is the instantaneous radius of the minimum section of the bar. They concluded that the ductility of high-strength steels depends markedly on the stress-state.

Introduction

The experimental programme of this work was designed to investigate the effect of sulphur on the nature of non-metallic inclusions and their behaviour during hot rolling and also the effect of non-metallic inclusions on notch tensile testing.

Electrolytic iron melts containing a specific amount of oxygen but varying amounts of sulphur were deoxidised at 1600°C and then cast into bars. The 'as-cast' bars were sectioned and then metallographic examination, rolling and inclusion distribution analysis were performed on the various sections. Further, the rolled samples were examined for:

- (i) Relative plasticity;
- (ii) determination of the inclusion composition by Cambridge microscan V (electron probe analyser);
- (iii) determination of the inclusion morphology before and after rolling by scanning electron microscope;
and
- (iv) notch tensile testing and observation of fracture surfaces by scanning electron microscope.

This work was a continuation of Wardle's (100) work on the deoxidation of 'almost' sulphur free melts, the nature of non-metallic inclusions and their behaviour during hot rolling. The experimental techniques used in this work were the same as experimental techniques used in that work.

3.1 Deoxidation Alloy Preparation

It was decided that deoxidation alloys used by Wardle should be used so that the two results could be compared.

The technique used in preparing the deoxidation alloys was as follows: correct proportions of lump silicon and electrolytic manganese flakes were melted in a recrystallised alumina crucible under hydrogen atmosphere using a high frequency induction furnace. Finally, correct proportions of super purity aluminium were added to the molten manganese-silicon melt and the melt allowed to cool under argon atmosphere. The addition of super purity aluminium was omitted in the case of deoxidants not containing any aluminium. The melts were stirred in order to get homogeneity and oxygen absorption prevented by hydrogen atmosphere. The ingots obtained from each melt were crushed to less than micron size and samples of each deoxidation alloy produced were sent for wet analysis.

Assuming

- (a) 100% utilisation of the deoxidant elements;
- (b) appropriate solute equilibrium data at 1600°C, and
- (c) specific initial and final oxygen levels,

the required deoxidant additions were calculated. Appendix (1.1) shows a detailed calculation of a typical deoxidant alloy. The total deoxidant addition was obtained from the individual equilibrium and stoichiometric additions for the various elements present in the alloy. The summary of these values for each of the deoxidants used are shown in appendix 1.2.

3.2 Experimental Melts

3.2.1 Preparation of cast bars

Japanese electrolytic iron was used for the cast bar preparation. Suppliers analysis showed an oxygen content of approximately 0.055% to 0.065% and sulphur content of about 0.007%. In order to produce the desired oxygen content (0.09%) and sulphur contents (0.06%, 0.1%, 0.2%), predetermined amounts of powdered iron oxide (Fe_2O_3) and iron sulphide (FeS) were added to the molten iron.

For each level of sulphur content four cast bars were produced, each deoxidised by one of the deoxidants DA12, DA15, DA6, and DA7 respectively (see Appendix 1.2). For the notch tensile testing experiments, the levels of sulphur were 0.02%, 0.1%, and 0.2%, with the oxygen level remaining constant (0.09%) as in the previous cases. The bars produced for the notch tensile testing were deoxidised by deoxidant D1, D2, and D3 respectively. The experimental procedure was identical for producing all the bars.

3.2.1.2 Melting procedure

The electrolytic iron (1500 gms) was melted under argon atmosphere in a high-frequency induction furnace using recrystallised alumina crucible (Figure 33a).

The alumina crucible was placed in a graphite susceptor in the high-frequency induction furnace. The susceptor was designed to avoid induction turbulence in the melt which would cause loss of inclusions on to the crucible walls. Temperature measurement was by means of two Platinum/Platinum - 13% Rhodium thermocouples connected to a multi-

point pen recorder. The susceptor temperature was measured continuously during melting by one of the thermocouples. The second thermocouple was used for temporary immersion in the melt. When both thermocouples were in use, it was possible to determine directly the temperature difference between the melt and the susceptor by recording alternatively from the two thermocouples. The immersion thermocouple was protected by a silica sheath and access to the melt was obtained through the sampling hole provided in the lid.

3.2.1.3 Sampling, addition of Fe_2O_3 and FeS, deoxidation procedure and suction casting

The charge was observed through the sampling hole in the lid and when the metal became molten, the power input was reduced from 13 kW to 9 kW at which the melt temperature stabilized at approximately 1600°C .

At this point a suction sample was taken to determine the oxygen content of the electrolytic iron melt before any additions were made. This sample was designated with the cast number and the term 'melt out'.

Sampling was done by using 4mm bore silica tube and a hand aspirator to provide the partial vacuum required in the tube. The tube was inserted into the melt through the sampling hole in the lid and withdrawn approximately 1 cm from the bottom of the crucible before taking the sample. Samples were always taken from a similar plane in the melt.

The predetermined amounts of iron oxide (Fe_2O_3) and iron sulphide (FeS) were weighed out and placed in a shim steel

cartridge and attached to the end of a silica plunging rod as shown in Figure 33b. The susceptor lid was removed and the cartridge was stirred into the melt, the silica plunging rod was removed and the lid replaced. The melt was stirred at intervals and a second suction sample taken after about fifteen minutes and designated cast number and 'melt-out' + Fe_2O_3 + FeS.

When the temperature had restabilised at 1600°C the predetermined amount of deoxidation alloy was added in similar manner as the Fe_2O_3 + FeS addition and stirred vigorously. The stirring of the melt was to ensure thorough mixing of the deoxidisers.

The melt was then suction cast about 20 seconds after addition of the deoxidant. This was done by plunging a 25 mm internal diameter silica tube to the base of the crucible whilst the top of the tube was being evacuated with a vacuum pump. The pump was capable of rapidly producing an adequate vacuum to support the column of molten iron, leaving a little in the base of the crucible to prevent the column from falling back. This method of casting was very effective in trapping a considerable amount of the inclusions formed at the place or near the position where the formation took place.

When casting was completed the furnace was turned off and the bar allowed to cool. The vacuum was released when the melt had solidified to some extent. The bar was then examined visually for any signs of unsoundness.

3.3 Oxygen Analysis

The suction samples were prepared for oxygen analysis by removing all oxide scales which might have formed on the surface of the samples.

Oxygen contents were determined by vacuum fusion analysis. The instrument used was the Balzer Exhalograph. Oxygen in the form of carbon monoxide was measured by infra-red absorption cell. Calibration and standardisation of the instrument were done by measuring quantities of pure carbon monoxide introduced into the analytical system.

Samples weighing between 0.2 to 0.3 gm were dissolved in a molten nickel bath saturated in carbon from the graphite crucible. The nickel bath was held at 1750°C under a 10^{-5} torr vacuum. Under these conditions any oxygen in the steel combined with the carbon to produce carbon monoxide. Even stable oxides such as alumina was reduced by carbon under these operating conditions.

Three specimens from each suction sample and three from each of the cast bars were analysed.

3.4 Sectioning of Cast Bars

The bars were sectioned as shown schematically in diagram (Figure 34). Samples taken for 'as cast' metallography, microprobe analysis and scanning electron microscopy analysis were transverse sections. These sections had maximum thickness of 10 mm, due to limitation of the microprobe analyser specimen stage. Samples for hot rolling were about 60 mm in length.

3.5 Rolling Procedure

All rolling was carried out using a two-high mill of 205 mm roll diameter with a rolling speed of 430 mm/sec.

The mill settings were determined such that approximately 10% reduction was obtained for each of the first two passes, then 20% reduction per pass after the initial round bar had been flattened.

Wardle showed that heat loss on transfer of the bar from the furnace to the mill in three seconds caused a temperature drop of 1° - 70° C depending upon the working temperature and the specimen thickness. The transfer times were actually observed to vary between two and five seconds depending on the reduction stage. When the working temperatures were 1000° C and below, a super heat of 20° C was used for reductions up to 50% total, after which 30° C super heat was utilised. At working temperatures 1100° C, 1200° C, and 1300° C, super heat of 30° C was used up to 50% total reduction, after which super heats of 40° C, 50° C and 60° C were used respectively.

Loss of heat to the rolls was ignored due to the complex nature of heat flow pattern. This loss was thought to have been fairly low due to the presence of insulating oxide film on the bar and the relatively short time of contact in the zone of deformation. One of the reasons for ignoring the heat loss to the rolls was the possibility that this heat loss may be compensated for by the heat generated from working.

The range of temperatures employed during this investigation was 800^o-1300^oC. The relevant temperatures used were determined by the type and composition of the inclusions under investigation. The first rolling temperature used was always 1000^oC and samples were obtained at each of the reduction steps of about 50%, 70% and 90% total reduction. Metallographic examination of rolled bars at this temperature determined whether to decrease or increase the rolling temperature for the other bars to be rolled.

The furnace was set at the rolling temperature plus the super heat allowance and allowed to stabilise. The bars to be rolled were then placed in the furnace and given thirty minutes to attain the furnace temperature. In order to flatten the round bar, the bars were first given two 10% reductions, subsequent reductions were about 20% reduction.

A specimen was first cut from the edge of the strip produced after a reduction of about 50% from each bar for the rolling temperature chosen. The remainder of the sample was in each case reheated and re-rolled. Thus, rolled samples were obtained at each rolling temperature and at each of the reduction steps of about 50%, 70% and 90%. At least ten minutes resoaking time was allowed between passes for the strips to reach the furnace 'set' temperature. This resoaking time was increased to 25 minutes following the increase in super heat to ensure that the furnace temperature had restabilised after the adjustment and also after taking a specimen at each of the reduction steps of about 50% and 70%.

Furnaces: For preheating and reheating of the bars between passes two furnaces were used. Both furnaces had the facility for using partially controlled atmospheres (90% N₂ - 10% H₂) to limit oxidation and were electrically heated. The bigger of the two had a maximum operating temperature of 1050°C whilst the smaller furnace had a maximum operating temperature of 1400°C. To prevent the bars to be rolled from sticking to the refractories of the smaller furnace an Inconel support had to be used. Both furnaces 'hot zone' temperature was monitored by Pt/Pt - 13% Rh thermocouples although the furnaces had automatic temperature control.

3.6 Metallographic Examination

All the metallographic specimens (and also probe analysis specimens) were prepared by normal techniques. Polishing time was kept to a minimum to prevent the removal or part removal of inclusions. If this happened the entire polishing process was repeated. All the samples were mounted in conducting bakelite.

3.6.1 As cast bars

All the as-cast bars were examined for the type of inclusions present (single or multiphase, glassy and crystalline). Types of inclusions from two different parts of the as-cast bar were examined and compared. Similarly MnS inclusions types were also identified.

3.6.2 Rolled samples

Samples from the 50%, 70% and 90% total reductions of each strip were examined. The deformed specimens were sectioned at right angles to the rolling plane and micro-examinations

were performed on the longitudinal section as shown in diagram (Figure 35). The samples taken for micro-examination were always taken from the centre of the strips' width. This was because it was in this region that plane strain conditions would have most likely been encountered. Due to the fact that temperature abnormalities at the surface may have been set up during rolling, the top and bottom surfaces of the strips were avoided.

Assuming the deformation to be plane strain and the inclusions to be initially spherical, being deformed to ellipsoids, a study of inclusion deformation was carried out. For each specimen 270 inclusions were selected at random and the major and minor axis of each of the inclusions were measured. The measurements were done by using a projection microscope at $\times 1000$ and measuring with a graph sheet. The accuracy of the measurement was to the nearest $0.5 \mu\text{m}$ in the case of inclusions with diameter or major axis less than $160 \mu\text{m}$ and to within $\pm 4 \mu\text{m}$ for inclusions greater than $160 \mu\text{m}$ (inclusions over $160 \mu\text{m}$ had to be moved in order to measure the major axis). Ninety oxide inclusions (with the square root of the product of their major and minor axes greater than ten microns) and also ninety sulphide inclusions were selected at random and their major and minor axes were measured to determine the mean deformation of oxides and sulphides at 50% total reduction for each of the samples rolled.

3.6.3 Inclusion distribution analysis

A quantitative study of inclusion distribution in four cast bars (A6, A7, A12, A15 with sulphur level in the melts at 0.07%S) was made using a Quantimet Image Analysing Computer B. From each bar two samples were taken and the examination of inclusion size distribution performed on each. For example,

steel A6, the sample taken from the top of the cast bar was designated A6 and the sample taken from the bottom designated A6/3. On each sample 280 fields were selected at random and examined to get a fair idea of inclusion size distribution.

Non-metallic inclusions can be distinguished by separate discriminatory threshold levels for oxides and sulphides but unfortunately the Quantimet Image Analysing computer B used could not discriminate between the oxides and sulphides separately. The instrument was set on maximum resolution and the field size was approximately 0.23 mm by 0.19 mm. In order to determine the size distribution of inclusions with sizes between 0 - 6 μm , the objective lens was changed from x20 to x40 and the field size was approximately 110 μm by 95 μm . For the latter analysis, two cast bars were used (A6 and A15) and on each sample 40 fields were selected at random and examined to get an idea of inclusion size distribution within the range (0 - 6 μm).

By courtesy of G.K.N., a QTM 720 was used to determine area, size and number of sulphide particles in three steels (D1, D2 and D3) with varying sulphur contents (0.02, 0.10, 0.20%) and oxide particle distributions separately. On each sample 120 fields were selected at random and examined to obtain the inclusion distribution in the steels. The field size for this analysis was approximately 0.625 mm^2 .

3.7 Heat Treatment

Samples of rolled bars containing deformed inclusions were cut into specimens of size 30 mm x 12 mm x 12 mm. The steels

used for this experiment were:

- (i) DA12 (with 0.1% sulphur in melt);
- (ii) DA512 (deoxidised by DA12 and the melt containing 50% nickel);
- (iii) DA112 (deoxidised by DA12 and the melt containing 1% nickel).

All the bars were rolled at 900°C. Apart from DA12 which was rolled to 50% total reduction, the other two were rolled to 70% total reduction.

Heat treatment temperatures were 900°, 1000°C and 1100°C. A vacuum furnace was used so that oxidation of specimen surface was prevented. In order to observe the influence of soaking time upon inclusion deformation or spheroidisation, times used were ½ hour, 24 hours and 72 hours. The specimen was placed in a recrystallised alumina crucible and the crucible in turn placed in the vacuum furnace. The unit operated under vacuum greater than 10^{-5} torr. The temperature of the furnace hot zone was continuously monitored by Pt/Pt - 13% Rh thermocouple. The major, a, and minor, b, axes of the inclusions were determined before and after heat treatment. The inclusions in the samples were oxides and sulphides. The spheroidisation of sulphide inclusions were determined separately from that of oxides. The oxide inclusions were grouped in the following size range:

- (i) $\sqrt{ab} < 5\mu\text{m}$,
- (ii) $5\mu\text{m} < \sqrt{ab} < 10\mu\text{m}$, and
- (iii) $\sqrt{ab} > 10\mu\text{m}$.

For each of the oxide groups and also sulphide inclusions, ninety inclusions were selected at random and the major and

minor axes measured before and after heat treatment to determine the extent of spheroidisation.

3.8 Verification of Wardle's Equations ⁽¹⁰⁰⁾ and Variation of Height to Width Ratio

The size of specimens for hot rolling was usually 200 mm x 13 mm x 13 mm. The specimen had to be surrounded by the welded mild steel support shown in diagram (Figure 36). This had the added advantage that it prevented excessive heat loss from the specimen both during handling and rolling and generally stabilised the specimen temperature. Furthermore, it ensured that the deformation was typical of the central region of a rolled plate since any edge effects were minimized. Whilst the size of the specimen remained the same, the height to width ratio of the supported rolling specimen (Figure 36) was varied. The height to width ratio used were 0.5, 1.0, 1.6 and 2.0. The rolling temperature used was 1000°C and the specimens were given 50% total reduction. The type of steel used for this experiment was DA12 with sulphur level of about 0.21%. The deformation of the inclusions in the steel was determined by measuring the major and minor axes of the inclusions. The deformation of the inclusions was determined in all the three planes (Figure 37) for each of the various height to width ratio in order to verify the equations derived by Wardle (as shown in appendix 3). The effect of variation of height to width ratio on the deformation of inclusions in all the three planes were also studied.

3.9 Chemical Analysis

Two samples (one sample from the top, and the other from the bottom, as shown in diagram (Figure 34)) of each of the as-cast bars were analysed for manganese, silicon, aluminium, carbon and sulphur by gravimetric techniques.

3.10 Electron Probe Micro-analysis

The composition of inclusions found was analysed by electron probe micro-analyser. About twenty inclusions were selected at random from each sample and analysed for iron, silicon, manganese, aluminium and sulphur. Oxygen was calculated on stoichiometric ratios. The specimens used were those that had been used for micro-examination in the as-cast condition and those specimens obtained after 50% total reduction.

All the samples were coated with a thin vacuum deposited carbon film (about 300 Å thick). This was to prevent the inclusions from building up an electrostatic charge under the influence of the electron beam. The samples were degreased and cleaned ultrasonically prior to coating. Failure to do this resulted in the contamination of the electron gun and specimen systems which can cause a drastic loss in resolution of absorbed and backscattered electron images.

Both of the instruments' spectrometers were used in analysing the inclusions composition. Iron and manganese content were analysed with a lithium fluoride crystal, whilst silicon and sulphur were analysed on the other spectrometer using a P.E.T. crystal. Aluminium was analysed with a R.A.P. crystal which meant there had to be a crystal change to R.A.P.

The P.E.T. crystal was changed to R.A.P. when it was necessary to analyse for aluminium. Sulphur and aluminium used the same spectrometer, hence resetting of the spectrometer Bragg angle from sulphur to aluminium peak and vice versa for alternate analysis respectively. The analysis was done by comparing scalar counts for each element against those obtained from pure standards of each element. In the case of sulphur the standard used was FeS.

All inclusion analyses reported in this work were obtained using an accelerating voltage of 15 kV. The analyses of the inclusions were done at random, however inclusions less than 10 μm were avoided due to problems of beam penetration. Line or area scans were used in order to obtain an approximate mean composition of the inclusions.

3.11 Scanning Electron Microscopy

In order to obtain a three-dimensional picture of the as-cast inclusions and the deformed inclusions, all specimens examined optically were again examined using scanning electron microscope. The unit used for this work was a Cambridge Stereoscan 150 fitted with a Kevex which allowed a qualitative appraisal of the elements present within an inclusion or precipitate. The inclusions were viewed 'in situ' in a deeply etched matrix.

3.11.1 Specimen preparation

The specimens which were already mounted in conducting bakelite were polished and then etched by submerging in a boiling mixture of 5% bromine in methanol. (Specimens were left submerged in the solution for about 15 minutes). After removal from the solution the deep etched specimens were repeatedly washed in methanol before drying.

The specimens were coated with gold by a gold sputtering technique. The deeply etched samples were stuck to the stub with non stringing clear adhesive. Electrical contact between stub and specimen was made by the application of 'silver dag' (a suspension of silver in a volatile solution).

3.12.0 Notch Tensile Testing

Notch tensile test pieces were machined from the nine types of steel produced by deoxidising the melts containing different sulphur levels (0.02%, 0.1% and 0.2%) with deoxidants D1, D2 and D3. All the samples were rod rolled at 1000°C and were given about 50% total reduction.

Three circumferential notches with different root radii were machined. For each root radii three specimens were machined, thus producing a total of nine specimens for each steel. The dimensions of the notches are as shown in diagram (Figure 38).

The notch root radii of the specimens, r ; the maximum diameter of the tensile test bar, D ; and the diameter at the notch section were measured by a shadowgraph. The elastic stress concentration factors, K_t , were then obtained from standard diagrams (190).

Two No. 14 Hounsfield tensile test pieces were machined from each of the steels so that uniaxial stress-strain data for each of the materials used could be obtained.

3.12.1 Testing procedure

The circumferentially notched tensile specimens were strained, under tension, in a Mand precision tensile machine. The cross-head speed was 0.2 mm/min., and the extension of the specimen was measured by electronic strain gauge; attached on either side of the notch section (on the maximum diameter of the specimen) and assuming that all the extension takes place in the notch region. The extension was recorded against the corresponding applied load on a chart recorder. The maximum load and the load at the point of fracture were recorded.

The fracture surfaces were examined under a scanning electron microscope for the types of fracture, voids and appearance of cracks.

3.12.2 Further developments of the notch tensile testing experiments

Furthermore, notch tensile test pieces were machined from three bigger steel ingots produced at Round Oak Steelworks. The ingot size was about 450 mm x 150 mm x 150 mm. The steels were deoxidised by deoxidants D1 and a new deoxidant D4. The deoxidant D1 was used to deoxidise one melt containing 0.1% sulphur and 0.2% oxygen. The deoxidant D4 was used to deoxidise two melts, one containing 0.1% sulphur and 0.2% oxygen whilst the other melt contained virtually no sulphur but the same oxygen level as in the previous one. As-cast samples were obtained so that circumferential notches

could be machined from them. The rest was then rolled at 1200°C to 50% total reduction. Specimens were machined from both the longitudinal and long transverse directions in the rolled steel plate as shown in Figure 39.

Again three different root radii were machined and for each root radii two specimens were machined. Again the dimensions of the notch tensile specimens were measured by a shadowgraph and the elastic stress concentration factors determined as previously.

Two No. 14 tensile test pieces were machined from each of the steels for the determination of uniaxial stress-strain data.

3.12.2.1 Testing procedure

The testing procedure was virtually the same as in previously, except that 5 tonne Instron tensile machine was used in this case and a strain gauge was attached to the notch section to measure the change in diameter across the notch root.

3.12.2.2 Strain and stress measurements

In the circumferentially notched tensile test pieces, the strains were measured as the change in diameter across the notch root. The effective plastic strain is

$$\bar{\epsilon}_p = 2 \ln (d_0/d)$$

where d_0 = initial diameter of the notch section

d = diameter of the notch section after straining

The true stresses in the notch tensile bars were measured as the ratio of instantaneous load to instantaneous area of the

notch section. Using Bridgman's (195) stress analysis in a pre-notched tensile specimen; the radial stress σ_r , = hoop stress $\sigma_\theta = \bar{\sigma} \ln \left(\frac{d^2 + 2dR - r^2}{2dR} \right)$ where R is the notch root radius and d is the radius of the minimum cross-section and r is the radial co-ordinate. Axial stress, σ_z , = $\sigma_r + \bar{\sigma}$; the stress complexity factor, $(\sigma_m/\bar{\sigma})_{\max}$, in the central region of the bars is defined as

$$(\sigma_m/\bar{\sigma})_{\max} = 1/3 + \ln (d/2R + 1)$$

This stress complexity factor, $(\sigma_m/\bar{\sigma})_{\max}$ was compared with the strain to failure, ϵ_f .

3.12.2.3 Measurements of void sizes and the number of voids per unit area

A series of random photographs were taken of the central area of each fracture surface. The magnifications and beam angles were noted so that accurate quantitative measurements could be made later. For this work, the beam angle was 0° and the magnifications were generally x200, x500 and x2000.

Two sets of measurements were made from the photographs of the central area of the fracture surfaces.

- (1) The size of voids on the photographs were measured and compared with strain to failure.
- (2) The number of voids per unit area for each fracture surface examined were also determined by counting the number of voids on a photograph and dividing the number by the true area of the photograph. This measure could also be expressed as the average nearest neighbour which is defined as the square root of the ratio of the true photograph area to the number

of voids on the photograph. The results were compared with the applied plastic strain to failure.

EXPERIMENTAL RESULTS

4.0 Analysis of the Japanese Electrolytic Iron

The Japanese electrolytic iron used had composition as shown below:

TABLE 4.0 (Electrolytic Iron Composition) in wt. %

C	S	P	Si	Mn	Al	O
0.01	0.01	0.01	0.01	0.01	0.005	0.055-0.075
						Balance iron

4.1 Oxygen Analysis

The analysis of total oxygen contents in the melt before and after Fe_2O_3 and FeS addition and also the total oxygen content for the 'as cast' bars are shown in table 4.1

TABLE 4.1

Total Oxygen Analysis

Melt	Sulphur content %	Melt out (O_T %)	Melt out + Fe_2O_3 +FeS (O_T %)	'As cast' Bar (O_T %)
A6	0.07	0.074	0.150	0.050
A6	0.10	0.078	0.149	0.045
A6	0.20	0.070	0.143	0.048
A7	0.07	0.068	0.147	0.055
A7	0.10	0.065	0.156	0.041
A7	0.20	0.070	0.152	0.058
A12	0.07	0.068	0.137	0.087
A12	0.10	0.074	0.143	0.092
A12	0.20	0.068	0.145	0.082
A15	0.07	0.070	0.144	0.038
A15	0.10	0.067	0.148	0.056
A15	0.20	0.072	0.146	0.046

TABLE 4.1 (Cont'd)

Total Oxygen Analysis

Melt	Sulphur content %	Melt out (O _T %)	Melt out +Fe ₂ O ₃ +FeS (O _T %)	'As cast' Bar (O _T %)
D1	0.02	0.073	0.131	0.055
D1	0.10	0.072	0.141	0.098
D1	0.20	0.068	0.138	0.082
D2	0.02	0.072	0.152	0.031
D2	0.10	0.078	0.152	0.058
D2	0.20	0.075	0.113	0.054
D3	0.02	0.062	0.129	0.038
D3	0.10	0.071	0.121	0.055
D3	0.20	0.067	0.123	0.043

4.2 Chemical Analysis

Table 4.2 shows the results of the chemical analysis of the 'as cast' bars. The chemical analysis of the deoxidants used are given in table 4.3.

TABLE 4.2

Chemical Analysis of 'as cast' bars

Melt	Actual composition % by weight				
	C	S	Si	Mn	Al
A6	0.031	0.069	0.61	1.61	-
A7	0.032	0.069	0.43	2.51	-
A12	0.030	0.069	0.28	0.52	0.005
A15	0.030	0.069	0.22	1.26	<0.001
A6	0.034	0.100	0.61	1.64	-
A7	0.029	0.113	0.43	2.59	-
A12	0.032	0.100	0.32	0.52	0.005
A15	0.033	0.098	0.26	1.26	<0.001
A6	0.06	0.190	0.59	1.51	-
A7	0.06	0.191	0.46	2.51	-
A12	0.06	0.190	0.32	0.49	<0.01
A15	0.06	0.189	0.20	1.16	<0.01

TABLE 4.2 (Cont'd)

Chemical Analysis of 'as cast' bars

Melt	Actual composition % by weight				
	C	S	Si	Mn	Al
D1	<0.01	0.030	0.26	0.44	0.010
D2	0.01	0.030	0.38	0.98	0.010
D3	0.02	0.022	0.32	1.80	0.005
D1	0.03	0.100	0.22	0.41	0.005
D2	0.03	0.100	0.33	0.99	0.005
D3	0.03	0.099	0.44	1.65	0.012
D1	0.06	0.19	0.44	0.47	0.009
D2	0.07	0.19	0.26	0.97	0.008
D3	0.06	0.18	0.43	1.79	0.007
D1**	0.08	0.11	0.55	0.89	0.015
D4**	0.06	0.12	Trace	1.27	0.10
A12 ₁ *	0.02	0.23	0.22	0.39	0.003
A12 ₂ *	0.03	0.22	0.24	0.40	0.007
A12 ₃ *	0.03	0.23	0.23	0.38	0.005
A12 ₄ *	0.03	0.21	0.26	0.40	0.008

* Melts used for the verification of Wardle's equations

** Melts from Round Oak Steelworks

TABLE 4.3

Deoxidation Alloy Composition

Alloy	Aimed For			Analysed		
	%Mn	%Si	%Al	%Mn	%Si	%Al
A6	73.31	26.69	-	74.27* (72.05)	25.74 (28.37)	-
A7	85.90	14.10	-	86.99* (84.70)	13.01 (16.82)	-
A12	58.45	39.27	2.28	62.21* (58.85)	35.69 (37.62)	2.10 (2.23)
A15	81.47	16.87	1.66	83.89* (81.26)	14.68 (17.04)	1.34 (1.92)
D1	58.45	39.27	2.28	61.23*	36.69	2.10
D2	71.38	27.05	1.57	70.99	27.70	1.31
D3	83.30	15.79	0.91	83.10	16.61	0.61

* By difference

Values in brackets are the values obtained by Wardle.

4.3 Metallographic Examination4.3.1 'As cast' inclusions4.3.1.1 Products of deoxidation alloys A6 and A7.

The melts based on deoxidants A6 and A7 were all deoxidised by Mn-Si alloys. In the melts containing 0.07% sulphur, the majority of the oxide inclusions observed were glassy (Plate 3) and appeared to be single phase silicates even though there were significant amounts of opaque oxide inclusions. Some of the small oxide inclusions ($\sim 5 \mu\text{m}$) had MnS cusps or rings around them. Many of the small inclusions ($< 5 \mu\text{m}$) observed were sulphides. These inclusions could not be analysed quantitatively because the 'probe' beam would excite the matrix (steel), but x-ray pictures revealed that they were MnS. These sulphides were type I MnS inclusions (Plate 12).

As the melt sulphur content increased to 0.1% and 0.2%, the majority of the oxide inclusions observed were opaque (Plate 1) and appeared to be single phase silicates whilst very little or no glassy silicates were observed in these melts. Again the small oxide inclusions (this time $\sim < 10 \mu\text{m}$) had MnS cusps or rings around them and the sulphides observed in the melts were type I MnS.

4.3.1.2 Products of deoxidation alloys A12, A15, D1, D2 and D3

These melts were deoxidised by Mn-Si-Al alloys. In the melts D1, D2 and D3 containing very low sulphur ($\sim 0.02\%S$), the majority of the oxide inclusions observed were glassy. These inclusions were easily identifiable, due to the appearance of concentric rings on the inclusion surface. It must be noted that few opaque (single phase) and/or heterogeneous oxide inclusions were observed. The sulphides observed in these melts were type I MnS inclusions.

At higher sulphur contents (0.07%, 0.1% and 0.2%), the majority of the oxide inclusions observed in melts A12, A15, D1, D2 and D3 were opaque and/or heterogeneous (Plates 2, 4-6). Plates 7-10 show the effect of increasing sulphur content of the melt on glassy inclusions in the steel. Again the sulphides observed in these melts were type I MnS inclusions.

4.3.1.3 Products of deoxidation alloy D4

The melt D4 was deoxidised with Al-Mn alloy. The majority of the inclusions found in this melt were type II MnS inclusion (Plate 11). It must be noted that very little or no oxide inclusions were observed in this melt.

4.3.2 Inclusion size analysis

The results of the inclusion size analysis are represented in Figures 40-51. The results of the size distribution studies on the sample of each of the deoxidation alloys have been averaged and the graph of the number of inclusions greater than a given size that can be expected to be found in a field of 1 mm^2 in the 'as cast' sample is plotted against the size. The results are shown in appendix 2 (tables 4.5-4.7).

4.3.3 Rolled Structures

4.3.3.1 Melt A6 (sulphur levels of 0.07, 0.10, 0.2%)

It must be noted that the inclusions in the melts containing different levels of sulphur exhibited very similar structures at all the temperatures involved. The Oxy-sulphides and the oxides behaved in a similar manner.

The oxide and oxy-sulphide inclusions present in the samples hot rolled at 900°C and 1000°C did not deform plastically, even at higher reductions. No glassy inclusions were observed after hot rolling, all the inclusions observed after rolling appeared opaque or heterogeneous. At 50% matrix reduction, however, some of the large oxide inclusions fractured and 'fish tail' cracks or voids (Plate 13) were

present. At 70% and 90% matrix reduction, the fractured particles tended to form discontinuous stringers behind the fractured inclusion. At these rolling temperatures the MnS inclusions appeared readily deformable.

At 1100°C, some of the large oxide inclusions deformed in a plastic/brittle manner (Plate 24). During examination of these inclusions on the S.E.M., it was revealed that they showed the formation of internal voids even at 50% matrix reduction (Plates 14-17).

However, at 1200°C and 1300°C, the large oxide inclusions had deformed considerably and some of the oxide inclusions had joined together. At 1200°C, the oxide inclusions showed internal cracking (Plates 18 and 19) but at 1300°C, the oxide inclusions behaved in a fluid manner (Plate 20). It must be pointed out that MnS precipitates were clearly observed in the oxide inclusions at rolling temperatures of 1200°C and 1300°C whilst nothing was observed at 1100°C. (Plates 21-23). The deformation of MnS inclusions appeared to decrease with temperature increase.

4.3.3.2 Melt A7 (Sulphur levels of 0.07, 0.10 and 0.2%)

The oxide and oxy-sulphide inclusions present in the samples (A7 containing 0.1% S and 0.2% S) hot rolled at 900°C exhibited no deformation even at higher matrix reductions. At 50% reduction, the large oxide inclusions fractured and 'fish tail' cracks were present and at higher reductions the fractured particles tended to form discontinuous stringers behind the fractured inclusion.

Some of the oxide inclusions in sample (A7 [0.1% S]) rolled at 1000°C were deformed (Plates 25 and 26) but the other oxide inclusions present remained undeformed. It was observed that the undeformed inclusions contained fine precipitates whilst the deformed ones were single phase. At 1000°C, the oxide inclusions in the sample (A7 0.2% S) showed very little or no deformation even at higher matrix reductions. It was observed that some of the undeformed oxide inclusions had voids created at the ends of them.

The oxide inclusions in the A7 samples (with sulphur levels 0.07%, 0.10% and 0.20%) behaved in plastic/brittle manner (Plate 24) at the rolling temperature of 1100°C. On examining these inclusions on the S.E.M., the formation of internal voids were observed (Plates 14-17).

The oxide inclusions in the same samples (A7 0.07% S, 0.1% S and 0.2% S) deformed plastically when rolled at 1200°C and 1300°C. The oxide inclusions behaved in a fluid manner at these two temperatures. It must be pointed out that at these two temperatures, MnS precipitates were clearly observed in the oxide inclusions whilst no precipitates were observed at 1100°C (Plates 21-23).

The MnS inclusions appeared to deform to a lesser extent as the rolling temperature increased.

4.3.3.3 Melt A12 (Sulphur levels of 0.07%, 0.1% and 0.2%)

(i) Melt A12 (0.07% S)

When rolled at 900°C, it was observed that the large oxide inclusions (>10 µm) with resolvable precipitates in them exhibited little or no deformation (Plate 27) whilst the single phase oxide inclusions deformed. It must be pointed out that the majority of the inclusions showed little or no deformation. At rolling temperatures of 1000°C and 1100°C, no precipitation was observed in the inclusions. At 1000°C, some of the large oxide inclusions behaved in a brittle manner but the others deformed plastically. When rolled at 1100°C, all the large inclusions deformed plastically.

It was observed that MnS inclusions deformed plastically at all the three rolling temperatures.

(ii) Melt A12 (0.1% S and 0.2% S)

When rolled at 800°C, majority of the oxide inclusions deformed plastically but a few oxide inclusions were not deformed (Plates 28 and 29). S.E.M. Kevex revealed that the undeformed inclusion contained high silicon (Plates 39-41). The oxide inclusions present in the samples rolled at 900°C were all deformed plastically and some of the inclusions were joined (Plate 30). At higher matrix reductions the inclusions exhibited necking and joining of inclusions, and some of the more plastic inclusions showed roping characteristics and were splitting (Plates 31-36). Plates 31-36 show the effect of increasing matrix reduction on inclusion deformation. At rolling temperatures

of 1000°C, 1100°C and 1200°C, the oxide inclusions exhibited considerable necking and deformed/fracture characteristics.

The MnS inclusions deformed plastically at all the rolling temperatures involved.

4.3.3.4 Melt A15 (Sulphur levels of 0.07%, 0.1% and 0.2%)

(i) Melt A15 (0.07% S)

When rolled at 900°C, all the oxide inclusions exhibited little or no deformation even at higher matrix reductions (Plate 37). At 50% matrix reduction, majority of the large oxide inclusions present in the samples rolled at 1000°C behaved in a brittle manner but some of the large oxide inclusions deformed plastically. It was observed that at 70% matrix reduction virtually all the large oxide inclusions were deformed.

All the oxide inclusions were deformed plastically when rolled at 1100°C (Plate 38) except very small oxide inclusions (~2 µm) which remained undeformed.

The MnS inclusions were observed to exhibit plastic deformation at all the rolling temperatures involved.

(ii) Melt A15 (0.1% S and 0.2% S)

All the oxide inclusions exhibited little or no deformation when rolled at 900°C. The oxide inclusions present in the samples rolled at 1000°C exhibited plastic deformation but

at a higher rolling temperature (1100°C), the oxide inclusions exhibited deformed/fracture characteristics.

The MnS inclusions deformed plastically at all the rolling temperatures.

4.4 Microprobe Analysis of Inclusions

The results of the microprobe analysis of inclusions are summarised as Mean 'as cast' compositions for oxide inclusions greater than $10\ \mu\text{m}$ diameter (Appendix 2, table 4.8). Individual inclusion analysis for both the 'as cast' and inclusions in rolled samples are tabulated, a copy of this table is obtainable at the Department of Metallurgy and Materials office.

Figures 52-58 show the individual 'as cast' inclusion analysis (inclusion diameter $> 10\ \mu\text{m}$) indicating the ranges in 'as cast' inclusion composition. The Mean 'as cast' inclusion compositions are shown in figures 59-61. The graphs were produced by scaling of results to give 100% total oxide (that is including sulphur). Figures 62-64 show the graphs of the mean sulphur content of the 'as cast' oxide inclusions plotted against the sulphur content of the melt. Generally it was observed that the sulphur contents of the 'as cast' oxide inclusions (produced by deoxidation with Mn-Si-Al alloys) were low whilst the sulphur contents of the 'as cast' oxide inclusions (produced by deoxidation with Mn-Si alloys) were fairly high comparatively. It was

also observed that increasing sulphur contents of the melts changed the composition of the oxide inclusions considerably when the manganese content of the melt is low (i.e. 0.56%).

The individual oxide inclusion compositions after rolling are shown in figures 65-72. These diagrams show the effect of composition on deformation of oxide inclusions. The mean sulphur content of the oxide inclusions after rolling are plotted against rolling temperature (Figs. 73-76). A minimum sulphur content of oxide inclusions was observed after rolling steels A6 and A7 at 1100°C whilst no significant minimum was observed in steels A12 and A15.

Plates 42-58 show the x-ray pictures revealing qualitatively the distribution of the elements in oxide and sulphide inclusions.

4.5 Deformation of Inclusions

The deformation of inclusions was expressed in terms of the relative plasticity index, ν , which is defined as:

$$\nu = \frac{1}{2} \frac{\ln b/a}{\ln h_0/h}$$

where

- b = major axis of inclusion
- a = minor axis of inclusion
- h_0 = initial height of specimen
- h = final height of specimen

The results of the inclusion deformation studies are shown in figures 77-123. These results indicate that there is a definite reduction in relative plasticity index with

increasing matrix reduction. The results also show that deformation of inclusions is dependent on size. It must be pointed out that the plasticity indices refer to the (xy) section or longitudinal plane and the inclusion size is given by \sqrt{ab} .

Figures 124-127 show the mean plasticity index of MnS inclusions in steels A6, A7, A12 and A15 plotted against rolling temperature for different sulphur levels in melts. All the results show the same general trend that the plasticity index of MnS inclusions decreases with increasing rolling temperature.

The mean plasticity index of oxide inclusions ($\sqrt{ab} \geq 10\mu\text{m}$) in steels A6, A7, A12 and A15 were plotted against rolling temperature for different sulphur levels in the melts (Figs. 128-131). The graphs show that there is an effect of sulphur on the oxide inclusion transition (non-deformable/deformable) temperature, for the oxide inclusions in steels A12 and A15 whilst there is virtually no effect on the transition temperature of the high manganese steels A6 and A7. The mean deformation of both oxides and sulphides are tabulated in table 4.9 (Appendix 2).

4.6 Heat Treatment

Some of the results of the heat treatment experiments are shown in figures 132 and 133. From the results it is evident that spheroidisation of inclusions does occur but the extent of this spheroidisation is dependent on size and time. It was observed that the small inclusions do

spheroidise more than large inclusions. When the homogenisation time was kept constant (72 hours) and the homogenisation temperature was increased, it became evident that while the sulphides stopped spheroidising the smaller oxide inclusions ($<10 \mu\text{m}$) did spheroidise to a greater extent as the homogenisation temperature increased. The results are tabulated in tables 4.10 and 4.11 (Appendix 2).

Plates 59-64 show S.E.M. pictures showing the effect of spheroidisation.

4.7 Verification of Wardle's Equation and the Effect of Height to Width Ratio on Inclusion Deformation

The results of this set of experiments are given in table 4.4. From this experiment it became evident that there is little or no significant difference in the inclusion deformation when the height to width ratio of the specimen to be rolled is changed. From the results it is conclusive that the equations derived by Wardle can be used to estimate the inclusion strain in the third plane if the inclusion strains in the two other planes are known.

TABLE 4.4

Height to width ratio = 0.5

Plane of Measurement	Type of inclusions	Inclusion strain ϵ_i	S.D.	S.E.	N	Estimated value of $\epsilon_y^1(xy)$
Longitudinal	Sulphides	0.69	0.11	0.02	45	0.76
	Oxides $\sqrt{ab} < 5\mu\text{m}$	0.68	0.17	0.03	45	0.66
	" $5 \leq \sqrt{ab} < 10$	0.88	0.19	0.03	46	0.84
	" $\sqrt{ab} \geq 10$	1.20	0.14	0.01	90	1.24
Long Transverse	Sulphides	1.33	0.43	0.06	45	
	Oxides $\sqrt{ab} < 5$	1.29	0.34	0.05	45	
	" $5 \leq \sqrt{ab} < 10$	1.55	0.35	0.05	46	
	" $\sqrt{ab} \geq 10$	2.11	0.26	0.03	90	
Short Transverse	Sulphides	0.19	0.17	0.03	46	
	Oxides $\sqrt{ab} < 5$	0.03	0.08	0.01	45	
	" $5 \leq \sqrt{ab} < 10$	0.12	0.14	0.02	46	
	" $\sqrt{ab} \geq 10$	0.36	0.30	0.03	91	

Height to width ratio = 0.5

Inclusion strains used in the estimation	Type of inclusion	Estimated values	
		v_{pe}^*	ϵ_z
$\epsilon_y^1(xy)$ and	Sulphides	1.31	0.43
	Oxides $\sqrt{ab} < 5$	1.28	0.41
$\epsilon_y^1(yz)$	" $5 \leq \sqrt{ab} < 10$	1.60	0.45
	" $\sqrt{ab} \geq 10$	2.18	0.61
$\epsilon_y^1(xy)$ and	Sulphides	1.24	0.33
	Oxides $\sqrt{ab} < 5$	1.30	0.43
$\epsilon_y^1(xz)$	" $5 \leq \sqrt{ab} < 10$	1.64	0.51
	" $\sqrt{ab} \geq 10$	2.14	0.56
$\epsilon_y^1(yz)$ and	Sulphides	1.38	0.38
	Oxides $\sqrt{ab} < 5$	1.26	0.42
$\epsilon_y^1(xz)$	" $5 \leq \sqrt{ab} < 10$	1.56	0.48
	" $\sqrt{ab} \geq 10$	2.21	0.58

TABLE 4.4 (Cont'd)

Height to width ratio = 1.0

Plane of Measurement	Type of inclusion	Inclusion strain ϵ_i	S.D.	S.E.	N	Estimated value of $\epsilon_y^1(xy)$
Longitudinal	Sulphides	0.56	0.23	0.02	90	0.81
	Oxides $\sqrt{ab} < 5$	0.04	0.09	0.01	90	0.06
	" $5 \leq \sqrt{ab} < 10$	0.30	0.39	0.04	90	0.40
	" $\sqrt{ab} \geq 10$	1.09	0.30	0.03	90	1.19
Long Transverse	Sulphides	1.30	0.35	0.04	90	
	Oxides $\sqrt{ab} < 5$	0.06	0.17	0.02	81	
	" $5 \leq \sqrt{ab} < 10$	0.70	0.25	0.03	90	
	" $\sqrt{ab} \geq 10$	2.26	0.45	0.05	90	
Short Transverse	Sulphides	0.31	0.44	0.04	90	
	Oxides $\sqrt{ab} < 5$	0.05	0.09	0.01	90	
	" $5 \leq \sqrt{ab} < 10$	0.09	0.13	0.01	90	
	" $\sqrt{ab} \geq 10$	0.12	0.16	0.02	90	

Height to width ratio = 1.0

Inclusion strains used in the estimations	Type of inclusion	Estimated values	
		ν_{pe}^*	ϵ_z
$\epsilon_y^1(xy)$ and $\epsilon_y^1(yz)$	Sulphides	1.17	0.49
	Oxides $\sqrt{ab} < 5$	0.07	0.01
	" $5 \leq \sqrt{ab} < 10$	0.63	0.27
	" $\sqrt{ab} \geq 10$	2.14	0.78
$\epsilon_y^1(xy)$ and $\epsilon_y^1(xz)$	Sulphides	0.93	0.17
	Oxides $\sqrt{ab} < 5$	0.05	0.01
	" $5 \leq \sqrt{ab} < 10$	0.54	0.14
	" $\sqrt{ab} \geq 10$	2.05	0.65
$\epsilon_y^1(yz)$ and $\epsilon_y^1(xz)$	Sulphides	1.41	0.33
	Oxides $\sqrt{ab} < 5$	0.08	0.00
	" $5 \leq \sqrt{ab} < 10$	0.72	0.20
	" $\sqrt{ab} \geq 10$	2.24	0.71

TABLE 4.4 (Cont'd)

Height to width ratio = 1.60

Plane of Measurement	Type of inclusion	Inclusion strain ϵ_i	S.D.	S.E.	N	Estimated value of $\epsilon_y^1(xy)$
Longitudinal	Sulphides	0.63	0.19	0.03	45	0.74
	Oxides $\sqrt{ab} < 5$	0.06	0.07	0.01	45	0.10
	" $5 \leq \sqrt{ab} < 10$	0.70	0.26	0.04	41	0.68
	" $\sqrt{ab} \geq 10$	1.19	0.17	0.02	90	1.27
Long Transverse	Sulphides	1.30	0.35	0.05	45	
	Oxides $\sqrt{ab} < 5$	0.13	0.14	0.02	45	
	" $5 \leq \sqrt{ab} < 10$	1.24	0.39	0.06	44	
	" $\sqrt{ab} \geq 10$	2.33	0.33	0.03	90	
Short Transverse	Sulphides	0.17	0.16	0.02	45	
	Oxides $\sqrt{ab} < 5$	0.07	0.12	0.02	45	
	" $5 \leq \sqrt{ab} < 10$	0.12	0.10	0.01	47	
	" $\sqrt{ab} \geq 10$	0.20	0.16	0.02	90	

Height to width ratio = 1.6

Inclusion strains used in the estimations	Type of inclusion	Estimated values	
		ν_{pe}^*	ϵ_z
$\epsilon_y^1(xy)$ and $\epsilon_y^1(yz)$	Sulphides	1.24	0.45
	Oxides $\sqrt{ab} < 5$	0.12	0.05
	" $5 \leq \sqrt{ab} < 10$	1.28	0.36
	" $\sqrt{ab} \geq 10$	2.28	0.76
$\epsilon_y^1(xy)$ and $\epsilon_y^1(xz)$	Sulphides	1.14	0.31
	Oxides $\sqrt{ab} < 5$	0.08	0.01
	" $5 \leq \sqrt{ab} < 10$	1.29	0.39
	" $\sqrt{ab} \geq 10$	2.20	0.66
$\epsilon_y^1(yz)$ and $\epsilon_y^1(xz)$	Sulphides	1.34	0.38
	Oxides $\sqrt{ab} < 5$	0.16	0.02
	" $5 \leq \sqrt{ab} < 10$	1.26	0.37
	" $\sqrt{ab} \geq 10$	2.35	0.71

TABLE 4.4 (Cont'd)

Height to width ratio = 2.0

Plane of Measurement	Type of inclusion	Inclusion strain ϵ_i	S.D.	S.E.	N	Estimated value of $\epsilon_y^1(xy)$
Longitudinal	Sulphides	0.61	0.15	0.02	82	0.61
	Oxides $\sqrt{ab} < 5$	0.03	0.06	0.01	45	0.03
	" $5 \leq \sqrt{ab} < 10$	0.05	0.12	0.02	46	0.06
	" $\sqrt{ab} \geq 10$	1.10	0.29	0.03	75	1.12
Long Transverse	Sulphides	1.10	0.35	0.04	90	
	Oxides $\sqrt{ab} < 5$	0.05	0.09	0.01	45	
	" $5 \leq \sqrt{ab} < 10$	0.08	0.11	0.02	46	
	" $\sqrt{ab} \geq 10$	2.20	0.68	0.07	90	
Short Transverse	Sulphides	0.12	0.19	0.02	90	
	Oxides $\sqrt{ab} < 5$	0.01	0.05	0.01	45	
	" $5 \leq \sqrt{ab} < 10$	0.03	0.07	0.01	46	
	" $\sqrt{ab} \geq 10$	0.04	0.10	0.01	90	

Height to width ratio = 2.0

Inclusion strains used for the estimation	Type of inclusion	Estimated values	
		$\nu_{p\epsilon}^*$	ϵ_z
$\epsilon_y^1(xy)$ and $\epsilon_y^1(yz)$	Sulphides	1.12	0.33
	Oxides $\sqrt{ab} < 5$	0.05	0.01
	" $5 \leq \sqrt{ab} < 10$	0.09	0.02
	" $\sqrt{ab} \geq 10$	2.13	0.73
$\epsilon_y^1(xy)$ and $\epsilon_y^1(xz)$	Sulphides	1.12	0.33
	Oxides $\sqrt{ab} < 5$	0.05	0.01
	" $5 \leq \sqrt{ab} < 10$	0.08	0.01
	" $\sqrt{ab} \geq 10$	2.11	0.71
$\epsilon_y^1(yz)$ and $\epsilon_y^1(xz)$	Sulphides	1.12	0.33
	Oxides $\sqrt{ab} < 5$	0.05	0.01
	" $5 \leq \sqrt{ab} < 10$	0.09	0.02
	" $\sqrt{ab} \geq 10$	2.14	0.72

4.8 Notch Tensile Test

The measured values of the notch geometry were used to calculate the elastic stress concentration factors (K_t) using the standard curves published by Peterson (190).

The specimen geometry were as follows:-

Diameter of specimen = 10.00 mm

Diameter of notch section = 5.00 mm

The notch root radii used were as follows:-

r = 1.00 mm
= 0.26 mm
= 0.175 mm
= 0.16 mm
= 0.125 mm

The notch strength was calculated as the maximum load divided by the notch section cross-sectional area. The notch strength ratio was determined as the ratio of the notch strength to the ultimate tensile strength of unnotched specimen. The ultimate tensile strength for the alloys of steel D was obtained from tensile test carried out on unnotched Hounsfield tensile test pieces and the values are tabulated in tables 4.12 and 4.13 (appendix 2).

In order to verify the equation ($NSR = \exp [A(r) \cdot (K_t - 1)^3]$) published by Joubert and Valentin (193) relating the elastic stress concentration factor (K_t) to the experimentally determined values of N.S.R., the experimentally determined values of N.S.R. were plotted as \log_e N.S.R.

against $(K_t - 1)^3$ (Figs. 134-142 and 146-149). For each notch root radius, the slopes of the curves in the above diagrams were measured in order to relate them to the metallurgical properties of the steel. (Table 4.14, appendix 2).

The total extension to fracture was plotted against the Area fraction of oxide and sulphide inclusions in the steels. The results are as shown in Figures 143-145.

The stress-strain curves for the 'as cast', longitudinal, and long transverse specimens of steels D1* and D4 are shown in Figures 150-155.

For all the samples tested, the examination of the centre of the fracture surface revealed that the fracture was in ductile mode except the 'as cast' samples (D1* and D4) which revealed cleavage fracture. S.E.M. pictures of the fracture surfaces encountered in the experiments are shown in plates 65-67.

5. DISCUSSION OF RESULTS

5.1 Composition of Deoxidation Products

5.1.1 The effect of Mn:Si ratio (Deoxidant) on deoxidation product compositions

The initial oxygen contents of melts aimed for was 0.09 wt% but the measured level of initial oxygen contents of the melts prior to deoxidation were within the range 0.11 to 0.15 wt% (table 4.1).

Various Mn-Si and Mn-Si-Al deoxidation alloy additions with different Mn:Si ratios were made to the melts. It must be pointed out that the maximum aluminium content of the melts after addition of deoxidant was approximately 0.012 wt%. Generally, it appears that as the [%Mn]:[%Si] ratio increased the $N^2_{(MnO)}:N_{(SiO_2)}$ ratio increased (Table 5.1). This agrees with Wardle's ⁽¹⁰⁰⁾ results.

The effect of sulphur on the $N^2_{(MnO)}:N_{(SiO_2)}$ ratio will be limited to the steels D1, D2 and D3 only because the same master deoxidant alloy was used for the deoxidation of each of the steels whilst different master (deoxidation) alloys were used for the other steels in table 5.1. It can be seen from table 5.1 that generally the $N^2_{(MnO)}:N_{SiO_2}$ ratio decreased as the sulphur content of the melt increased. This effect seems to be less pronounced as the [%Mn]:[%Si] ratio of the deoxidant is increased. The reason for this decrease in $N^2_{(MnO)}:N_{(SiO_2)}$ ratio is due to the fact that as the sulphur content of the melt increases, more manganese is required to tie up the sulphur to form manganese sulphide, thus decreasing the amount of manganese oxide in the oxide inclusion composition in the low manganese melts, whilst in

TABLE 5.1

RELATIONSHIP BETWEEN $[\%Mn]:[\%Si]$ (DEOXIDANT) RATIO AND $N^2_{(MnO)}:N_{(SiO_2)}$ RATIO OF DEOXIDATION PRODUCTS

Melt	Sulphur content of melt %	% Al Addition	$\frac{[\%Mn]}{[\%Si]}$ Deoxidant	$\frac{[\%Mn]^2}{[\%Si]}$ Deoxidant	$\frac{N^2_{(MnO)}}{N_{(SiO_2)}}$ Product	S.D.	S.E.	N.
D1	0.02	0.022	1.49	0.84	0.17	0.017	0.003	33
	0.10	0.022	1.49	0.84	0.13	0.013	0.003	20
	0.20	0.022	1.49	0.84	0.13	0.032	0.007	23
D2	0.02	0.022	2.64	2.64	0.45	0.028	0.006	19
	0.10	0.022	2.64	2.64	0.42	0.070	0.010	20
	0.20	0.022	2.64	2.64	0.42	0.050	0.012	20
D3	0.02	0.022	5.28	10.55	0.71	0.074	0.017	20
	0.10	0.022	5.28	10.55	0.71	0.041	0.009	20
	0.20	0.022	5.28	10.55	0.65	0.054	0.012	19
A12	0.10	0.022	1.49	0.84	0.14	0.014	0.003	30
	0.20	0.022	1.49	0.84	0.14	0.021	0.005	20
A15	0.10	0.032	4.83	7.59	0.53	0.020	0.005	15
	0.20	0.032	4.83	7.59	0.68	0.075	0.015	25
A6	0.10	-	2.75	5.30	0.68	0.061	0.014	18
	0.20	-	2.75	5.30	0.78	0.083	0.019	20
A7	0.10	-	6.09	17.40	0.88	0.053	0.012	20
	0.20	-	6.09	17.40	1.01	0.154	0.032	23

the high manganese melts there is enough manganese to cope with the sulphur increase without affecting the oxide inclusion composition to a greater extent (Figs. 52-61).

The analysis of the melts containing aluminium showed pronounced deficiency in the observed alumina content of the oxide inclusion composition compared with calculated values of total oxide formation (Table 4.8).

The observed values of silica contents in the inclusions were higher than the target composition of the oxides whilst the observed values of manganese oxide contents in the inclusions were lower than the corresponding calculated values. The final oxygen content before the addition of deoxidation alloy exceeded the target oxygen content of 0.09 wt%.

The most active deoxidant in the deoxidation alloy is aluminium (Fig. 1), thus the formation of alumina is completed, before the silicon and manganese can combine with the remaining oxygen. The remaining oxygen will be higher than expected to satisfy stoichiometric requirements and the equilibrium amount for the silicon and manganese hence the production of more silica or manganese oxide could occur. The increase in the amount of silica or manganese oxide might have resulted in an apparent decrease in the percentage of alumina observed in the oxide inclusion composition. The observed decrease in manganese oxide content of the oxide inclusions composition is due to the fact that some of the manganese in the melts being tied up with the sulphur to form manganese sulphide inclusions.

The deficiency in the alumina content of the oxide inclusions composition could also be due to alumina rich inclusions agglomerating, coalescing, and floating out to the top of the bath faster. Wardle (190) observed that the inclusions at the uppermost section of the cast bar had higher alumina contents. It must be noted that alumina rich inclusions have high interfacial tension (197) and thus can float out at a faster rate. Even though sulphur does decrease the surface tension of iron melt, it appears that its effect on the emergence of alumina rich inclusions may be small.

For the melts containing no aluminium, the most active deoxidant is silicon. Hence the formation of silica will near completion before the manganese starts to combine with the remaining oxygen. Because the oxygen is higher than expected there is an increase in manganese oxide content in inclusions and a decrease in silica content. The deficiency of silica is not as pronounced as the alumina and this may be due to the separation rates.

5.1.2 Variation of inclusion composition with size

In order to examine the variation in composition with respect to inclusion size, the inclusions were analysed using an area scan of the centre of the 'as cast' inclusions. To eliminate errors in the analysis, the thickness of the area scan was kept to a minimum (~ about 2 mm). It was also important that variations due to matrix excitation were eliminated by making sure that the diameter of inclusions examined were not less than 10 μm . Qualitative analysis by x-ray distribution of

elements in numerous large oxide inclusions (diameter $>10 \mu\text{m}$) showed little or no variation of Mn, Si, and Al in the inclusion (across the diameter) whilst it was clearly visible that the oxide inclusions were surrounded by thick sulphide rings (Plates 42-45). This characteristic is quite pronounced in inclusions of steels deoxidised by Mn-Si-Al deoxidation alloys. The sulphur dissolved in these inclusions was very small whilst the inclusions of steels deoxidised by Mn-Si deoxidation alloys dissolved larger amounts of sulphur. It must be pointed out that the thick sulphide ring persisted in the case of the inclusions of steels deoxidised by Mn-Si alloys although the inclusions dissolved a greater amount of sulphur. Generally, the smaller oxide inclusions had much thicker sulphide rings around them.

Inclusion compositions within melts deoxidised by Mn-Si and Mn-Si-Al deoxidation alloys showed little or no systematic change in composition as the inclusion size increased [(from $10 \mu\text{m}$ onwards) (Figs. 156-160)]. It was observed that inclusions less than $10 \mu\text{m}$ in diameter showed variations in composition. This variation may be partly due to matrix excitation which may cause an apparent increase in FeO content and decrease in MnO, SiO_2 and Al_2O_3 if present. It was also observed qualitatively that the sulphur content of the oxide inclusions increased as the inclusion size decreased.

An explanation of this increase in sulphur content of the oxide inclusions in the case of smaller inclusions may be based on

- (1) early removal of inclusions, and
- (2) matrix excitation.

From thermodynamic data (Figs. 1 and 2), it can be seen that oxide inclusions are more stable than the sulphide inclusions present in steel. It is therefore expected that the sulphide phase would form later in the solidification process and would most likely nucleate on the oxide inclusions present in the steel. It has been shown that initial products of deoxidation have both time and ability to coalesce ⁽⁷⁾ and thus these inclusions are normally the largest in the system and they do emerge from the melt at a faster rate. The small oxide inclusions which are formed in the latter stages of the deoxidation process and hence act as nucleating site for the sulphide inclusions which are the last to form. The other possible explanation is that during the analysis of smaller oxide inclusions, it is more likely to excite the thick sulphide ring around the inclusion hence the increase in sulphur content of the inclusion as the size decreases.

5.1.3 Sulphide inclusions morphology

In all the steels under present investigation, the sulphide inclusions observed were all type I MnS inclusions (Plate 12) except steel D4 which produced type II MnS inclusions (Plate 11).

Increasing the sulphur level in steel can lead to replacement of type I with type II MnS inclusions. The sulphur level at which this occurs depends on the carbon, oxygen, silicon and manganese contents ⁽²⁰¹⁾. It is generally accepted that oxygen plays a very important role since an increase in the concentration of this element (O) produces type I MnS

inclusions in both low and high sulphur alloys. It will be recalled that the aimed for oxygen was 0.09 wt % but the actual determined oxygen was between 0.11 and 0.15 wt % and therefore the melt had excess oxygen compared with the oxygen required by the calculated deoxidation alloys. Increasing the sulphur content of the melt to a maximum of 0.2 wt % will therefore not be able to change the morphology of the type I MnS inclusions observed in the steels to type II MnS inclusions.

The final oxygen content in steel D4 melt before deoxidant addition was not determined because it was not done at the University. The final oxygen content in steel D4 melt before deoxidant addition was assumed to be 0.2 wt % because it was air melted. The amount of aluminium added for deoxidation was such that it would combine with the assumed final oxygen content (~ 0.2 wt%) to form alumina. 1 wt% manganese was added as an alloying element. In this steel it was more likely the residual oxygen in the melt after deoxidation would be very low, hence type II MnS inclusion morphology were seen in D4.

The effect of aluminium in changing the morphology from type I to type II MnS inclusions is generally accepted to be due to the action of aluminium on the reduction of oxygen in solution ⁽⁹¹⁾.

Plates 77-79 show the distribution of both sulphide and oxide inclusions in some of the steels under present investigation. Plate 79 shows how the sulphide form during

solidification of the steel matrix. This reveals that sulphur concentrates at the solidification front and thus precipitate out of the last melt to solidify.

5.1.4 Effect of sulphur content of melt on oxide inclusion composition

From figures 52-61, it appears that for low manganese melts the composition of the oxide inclusions were affected by the increase in sulphur content of the melt whilst no effect on oxide inclusions in high manganese melts was observed. The effect of increase in sulphur changing the oxide inclusion composition is demonstrated by steel D1 (\sim Mn = 0.5 wt%) (Fig. 56).

A possible explanation for this is that in low manganese melts, the presence of sulphur in the melt greatly decreases the activity of manganese as compared to high manganese melts. As the sulphur content increased, the activity coefficient of manganese in the melt decreased and thus the manganese oxide formed will be less than expected. Therefore, the manganese in the low manganese melts becomes less involved in the deoxidation process because some of the manganese combined with the sulphur present to form manganese sulphide inclusions whilst in the case of high manganese melts there is enough manganese to take care of the sulphur increase and also take part in the deoxidation process without changing the oxide inclusion composition.

It was observed that the 'as cast' oxide inclusions in the steels deoxidised with Mn-Si alloys had higher sulphur dissolved in the oxide inclusions and this increased with

increasing sulphur content of the melt (Fig. 63) whilst very low sulphur contents were observed in the 'as cast' oxide inclusions in the steels deoxidised with Mn-Si-Al alloys at all levels of sulphur in the melt [(Figs. 62 and 64), (Plates 42 and 46)]. This may be the reason why no glassy inclusions were observed in all the steels when the sulphur content of the melt was increased.

The increase in sulphur content of the iron-manganese-silicate inclusions may be because of greater sulphur diffusivity and solubility in them as compared to iron-manganese-alumino-silicate inclusions. Kiessling and Lange ⁽³⁾ observed Rhodonite inclusion surrounded by a scale of manganese sulphide which was also finely precipitated in the inclusion matrix in aluminium free melts. It must be noted that the 'as cast' oxide inclusions which had high sulphur contents were in the Rhodonite and Tephroite region of the $MnO-SiO_2$ system. Kor and Turkdogan ⁽¹⁹⁸⁾ observed that sulphur diffusivity and solubility in liquid iron-silicate was quite high. A possible explanation for the low sulphur contents observed in the 'as cast' inclusions in steels deoxidised by Mn-Si-Al alloys may be based upon the lower solubility of sulphur in the liquid iron-manganese-alumino-silicates than the liquid iron-manganese-silicates.

The explanation for the higher sulphur content in the iron-manganese-silicate inclusions than expected may be due to the precipitation of sulphide simultaneously with the production of deoxidation products. Thus oxygen and sulphur are precipitated almost at the same time from the liquid steel. The resulting inclusions were either a result of primary

precipitation of both sulphides and oxides from the liquid steel often in duplex form or a sulphur and oxygen-rich silicate was formed. In the inclusions, manganese sulphide is precipitated from the silicate melt when the temperature falls, followed by crystallisation of the oxide component (manganese-silicate).

5.1.5 Inclusion distribution

The aim of the suction casting process was to obtain uniform distribution of inclusions within the 'as cast' bar. It is interesting to note the actual distribution of inclusions (Figs. 49-51). The diagrams suggest a good degree of agreement of inclusion distribution between the top and bottom positions of the 'as cast' bar. As seen the top of each 'as cast' bar contains more large inclusions than the bottom of the bar. This is expected to some extent, since there is a finite cooling period in which inclusion flotation takes place due to relative density effects. This also agreed with the fact that particles grow during their ascent in the melt by coalescence or agglomeration (Plates 68-71).

Lindon ⁽⁷⁾, applying Fullman's equation, found that the number of particles per unit volume (N_V) was of the order of 10^7 cm^{-3} . He assumed that $N_V = 10^7 \text{ cm}^{-3}$ represents the approximate nuclei concentration. Applying this value to Turkdogan's diffusion model, he obtained a value 1.4 seconds for 99% desaturation. Lindon calculated the maximum value of r_i (r_i = instantaneous radius of a growing inclusion) for complete oxygen desaturation and obtained $r_i = 3.27 \text{ } \mu\text{m}$ from the Turkdogan diffusion model by assuming $r_o = 0.62 N_V$

(r_0 = radius of the spherical diffusion cell). This shows that solute diffusion does not seriously limit the particle growth rate and also that very little growth occurs because of the large number of nuclei present. These results supported Turpin and Elliott's ⁽⁵⁶⁾ predictions of local supersaturation resulting in formation of large numbers of small particles.

Inclusion sizes exceeding 3.27 μm , however, are not accounted for by this nucleation and growth mechanism. The observation of inclusions greater than 3.27 μm in the present work may be explained by assuming that coalescence or agglomeration of particles takes place. This agrees with results obtained by other workers ^(7,100). Evidence supporting growth by coalescence can be found in figures 49-51 (Plates 68-71). These diagrams show curves which are similar in form to that expected from the equation derived by Kawawa et al ⁽²⁰²⁾ from observed inclusion size distribution obtained from a quiescent bath. The equation is as follows: $n = N_0 e^{-A\gamma}$ where n is the number of inclusions per unit area having radius greater than γ , and N_0 and A are constants.

The distribution of sulphide and oxide inclusions were determined separately.

5.1.5.1 Sulphide inclusion distribution

From metallographic data (Figs. 43-45 and Tables 4.5-4.7), it appears that sulphide size distributions were influenced by the sulphur content of the melts. The size distributions

were investigated in terms of number of inclusions greater than a given diameter per unit area and as shown in the previous section this can be influenced by the position from which the samples were taken from the 'as cast' bar. It must be noted that in this instance the samples were taken approximately 9-10 cm from the top of the bar so that sulphide distributions in samples from the various melts could be compared directly.

Generally, it was observed that the number of sulphide inclusions greater than a given diameter per unit area increased as the sulphur contents of the melts increased (Figs. 43-45). This effect was more pronounced in the low manganese melts (i.e. D1 \sim 0.5% Mn, and D2 \sim 1.0% Mn).

The role of surface phenomenon on the emergence of sulphide inclusions has not been widely investigated. It should be noted that the emergence of inclusions is favoured by:

- (a) a high interfacial tension, γ_{SM} ;
- (b) a high surface tension, γ_m , of the liquid metal; and
- (c) a low surface tension, γ_s , of the oxide.

It is generally accepted that the surface tension of the iron melt decreases as the sulphur content of the iron melt increases (77). This implies that in high sulphur melts the emergence of inclusions will be impaired. It is known that the surface tension of oxide inclusions which are of practical

interest appears to be always lower than that of iron with low oxygen and sulphur contents (67). If it is assumed that the surface tension of sulphide inclusions are always lower than that of the iron bath with low oxygen and sulphur contents, then the sulphide inclusions should be able to emerge out of the bath hence resulting in only the small sulphide inclusions being left behind in the melt.

The studies of surface tension of $\text{MnO-SiO}_2\text{-Al}_2\text{O}_3$ slags at 1600°C by Gähler (197) revealed that the values lie in the range 0.3 to 0.5 Joules/ m^2 and Kozakevitch and Olette (67) found the surface tension of solid alumina to be 0.9 Joules/ m^2 . Although no data on sulphide surface tension are known as a first approximation it is assumed that the surface tension of solid sulphide inclusions to be about 0.7 Joules/ m^2 and that of liquid sulphide inclusions to be equal or less than 0.5 Joules/ m^2 . The sulphide inclusions in the present investigation are more likely to be liquid sulphides at 1600°C because Type I MnS inclusions were observed in nearly all the steels investigated. When the sulphur content of the iron melt was increased, to say 0.2%, the surface tension of the iron melt would be reduced to about 1.0 Joules/ m^2 and the interfacial tension between the sulphide inclusions and the iron melt would be reduced but would be high enough to allow emergence of some of the sulphide inclusions. It should be noted that the separation rate of the sulphide inclusions in the higher sulphur iron melts would be slower thanⁱⁿ the lower sulphur melts. The slower rate of separation of the sulphide inclusions in the high sulphur melts, gives the sulphide inclusions more time to grow and hence more

and larger sulphide inclusions should be expected in the high sulphur melts (i.e. 0.2% S).

In the higher manganese melts (D3 ~2% Mn) the effect (the number of sulphide inclusions greater than a given diameter per unit area increasing with increasing sulphur contents of the melts) was not as pronounced as in the case of the low manganese melts. The reason is that the presence of higher manganese reduces the solubility of sulphur in the iron melt and thus reducing the effect of sulphur in reducing the surface tension of the iron melt. The rate of emergence of the sulphide inclusions will therefore not be very different hence there will be a less significant difference in the sulphide size distribution. It is evident from the diagrams (Figs. 41 and 42) that as the manganese content of the melt increases the number of sulphide inclusions less than 3 μm increases. This may be due to the fact that **Manganese** is a strong sulphide former, and the presence of high manganese in the melt enhanced the formation of a lot of sulphide nuclei and hence led to the formation of a lot of small sulphide inclusions as shown in the diagrams.

5.1.5.2 Oxide inclusion distribution

From the diagrams (Figs. 46-48), it appears that sulphur has an effect on the oxide inclusions size distribution. As the sulphur content of the melt increased the number of oxide inclusions greater than a given diameter per unit area increased. The reason for this phenomenon can be explained using similar arguments to those used for the sulphide inclusions, that the increase in sulphur content of the melts

decreased the surface tension of the iron melt thus reducing the rate of emergence of the oxide inclusions. This would enhance the growth of the oxide inclusions, hence the melts containing high sulphur contents would exhibit more larger oxide inclusions because in low sulphur melts the larger inclusions have the chance of escaping to the surface of the melt.

Figures 46-48 exhibit the effect of manganese on the size distribution of oxide inclusions. Generally it can be seen that as the manganese content of the melt increased the number of larger oxide inclusions in the melts decreased (the manganese levels being: D1 $\sim 0.5\%$ Mn; D2 $\sim 1.0\%$ Mn; D3 $\sim 2.0\%$ Mn). The explanation for this is that high manganese melts ($\sim 2.0\%$ Mn) results in high supersaturation and hence more nuclei being formed and because of the short time for the melt to solidify they cannot grow into large inclusions even though some amount of coalescence do take place.

In summary, it appears from the diagrams (Figs. 43-48) that the size distribution of both sulphide and oxide inclusions are influenced by the sulphur contents of the melts. It would seem that the degree of growth of the products of deoxidation was not encouraged when the manganese content of the melt was high. This could be attributed to the fact that the high manganese melts resulted in high supersaturation, thus the formation of large numbers of small inclusion because the solidification time was very short.

5.2 The Effect of Hot Rolling on Deformation of Inclusions

5.2.1 The variation of inclusion mean plasticity index with temperature

The variations of the inclusion mean plasticity index with temperature for both oxides ($\sqrt{ab} > 10 \mu\text{m}$) and sulphides are presented in table 4.9 (appendix 2). These are shown graphically in figures 124-131. Generally, a rapid transition from non-deformable to deformable behaviour (for oxide inclusions) was observed over a narrow range of temperature ($\sim 100^\circ \text{C}$). The observation was in agreement with numerous investigators who have studied the deformation of silicate inclusions over a range of temperatures (84, 100, 102, 125, 127). The exact transition temperatures could not be determined for the different compositions encountered due to shortage of materials but the figures do give the transition temperature within 100°C range.

Generally, it was observed that the deformation of the sulphide inclusions decreased with increasing rolling temperature which is in agreement with results obtained by Charles and Co-workers (89, 103, 104, 107). It was observed that increase in the sulphur content of the melt had no effect on the deformation of the sulphide inclusions.

The following discussion is separated into three parts and the effect of sulphur on the transition temperature of the different silicates are discussed in each section.

- (i) Melts A6 and A7 (deoxidised with Mn-Si alloys)
- (ii) Melt A12 (deoxidised with Mn-Si-Al alloy)
- (iii) Melt A15 (deoxidised with Mn-Si-Al alloy).

5.2.1.1 Melts A6 and A7 (deoxidised with Mn-Si alloys)
(Different sulphur contents of melts ~0.07%,
0.10%, and 0.20%)

Generally the deformation of both oxide and sulphide inclusions in these melts was not affected by the increase in sulphur contents of the melts.

At deformation temperatures of 900°C, and 1000°C the majority of the iron-manganese-silicate inclusions exhibited rigid behaviour, giving rise to the usual conical voids (Plate 13) at low matrix strains (~50% total matrix reduction).

Generally few of the larger oxide inclusions which were fractured at lower strains produced stringers at higher matrix strains (~90% total matrix reduction). Very few of the large iron-manganese silicates deformed when rolled at 1000°C (Plates 25 and 26). It should be pointed out that the glassy inclusions which were observed in the lower sulphur melts did not retain their glassy appearance after hot rolling.

The rapid transition from non-deformable to deformable behaviour occurred on increasing the rolling temperature from 1000°C to 1100°C (Figs. 128 and 129) is a characteristic behaviour of majority of the silicate inclusions which has been reported extensively in the literature (84,100,102,104, 126,127). The transition temperature of 1000°-1100° C lies well below the solidus temperature. This observation is in agreement with other investigators (84,100,126) and may be due to rapid change in the silicate viscosity over a narrow range.

A quite striking change in behaviour of oxide inclusions was observed when the samples were rolled at 1100°C. The iron-manganese-silicate inclusions were deformed in a plastic/brittle manner with characteristic internal voids in the deformed inclusions (Plate 21) examined by ^{the}projection microscope. Scanning electron microscope (S.E.M.) revealed that the inclusions were crystallised (Plates 14-17).

This latter behaviour may be due to the precipitation of less deformable silica (cristobalite) particles in a more deformable matrix. During deformation the silica (cristobalite) particles already formed were pulled apart and the remaining deformable inclusion matrix stretched out between the separated crystalline silica fragments. Generally this observation agrees with Robinson's ⁽⁸⁴⁾ results. He observed this phenomenon during the rolling a steel sample (deoxidised by Mn-Si alloy) at 1275°C.

At a deformation temperature of 1200°C; the iron-manganese silicate inclusions behaved in a plastic manner. These inclusions, by S.E.M. examination revealed that the inclusions exhibited plastic/brittle deformation of a different kind (Plates 18 and 19), with the inclusions showing cracks parallel to their major axes.

The iron-manganese silicate inclusions rolled at 1300°C behaved plastically (fluid). The composition of the inclusions lay very near or within the liquid region of the MnO-SiO₂ system (at 1300°C) and at this temperature the inclusions exhibited fluid behaviour (Plate 20).

The sulphide inclusions showed a general trend of sulphide inclusion deformation decreasing with increasing rolling temperature irrespective of the sulphur content of the melts (Figs. 124 and 125).

The sulphur dissolved in the oxide inclusions was high at all temperatures except at 1100°C (Figs. 73 and 74). Plates 21-23 show the types of inclusion phases observed at rolling temperatures 1100°C, 1200°C and 1300°C respectively. MnS dendrites and fine crystallised MnS can be seen in the iron-manganese-silicate inclusions in the samples rolled at temperatures of 1200°C and 1300°C whilst no MnS could be seen in the iron-manganese-silicate inclusions in samples rolled at 1100°C.

Generally, it was observed that the amount of sulphur dissolved in the oxide inclusions was at its minimum when the samples were rolled at 1100°C (Figs. 73 and 74). This behaviour was well defined when the mean inclusion composition was within the Rhodonite region. The solubility of sulphur in the Rhodonite matrix at the steelmaking temperature can be high depending on the sulphur content of the steel melt, on solidification the sulphur dissolved in the Rhodonite matrix precipitated finely in the matrix. This confirms Kiessling and Lange's ⁽³⁾ observations of finely precipitated MnS in Rhodonite inclusion matrix.

The reason for the observed minimum sulphur in the oxide inclusions is due to the fact that at 1100°C the silica content of the oxide inclusions was observed to have increased,

supporting the proposition that silica precipitated in the oxide inclusions in samples rolled at 1100°C (Figs. 65-72). The silica precipitated in the oxide inclusions in samples rolled at 1100°C would be pushed to the centre of the inclusion because they were less deformable whilst the deformable Rhodonite matrix stretched to fill the gaps between the silica precipitates and the edges of the inclusion. Since all the analyses were carried out at the centre of the inclusions, the sulphur dissolved in the inclusion would appear to be lower than usual.

The mean 'as cast' oxide inclusions compositions are given in table 4.8 (appendix 2).

In summary, it was observed that both oxide and sulphide inclusions deformations were not affected by the increase in sulphur content of the melts. The transition from non-deformable to deformable behaviour occurred with increasing rolling temperature from 1000°C to 1100°C. The characteristic behaviour of oxide inclusion at 1100°C was due to silica precipitation and this brought about the observed decrease in sulphur content of the oxide inclusions. Sulphide inclusion deformation decreased with increasing rolling temperature.

5.2.1.2 Melt A12 (deoxidised with Mn-Si-Al alloy)

(a) Melt A12 (0.07% S)

At the deformation temperature of 900°C, it was observed that the oxide inclusions ($\sqrt{ab} > 10 \mu\text{m}$) with resolvable precipitates in them showed little or no deformation (Plate 27) whilst the single phase oxide inclusions were deformed. The

majority of the oxide inclusions in the sample rolled at 900°C showed little or no deformation. Analysis of the inclusions which showed the latter behaviour revealed that the silica content of those inclusions was higher than the inclusions which deformed at the rolling temperature (Plates 40 and 41).

At rolling temperatures of 1000°C and 1100°C, little or no precipitation was observed in the inclusions. It can be seen that very few of the large oxide inclusions remained undeformed at 1000°C (Fig. 85) and this may have been due to the number of inclusions with precipitates in them being reduced. The transition from non-deformable to deformable behaviour seemed to occur at rolling temperature between 900°C - 1000°C (Fig. 130).

When the steel sample was hot rolled at 1100°C, all the large oxide inclusions in the steel deformed plastically.

It should be noted that the transition from non-deformable to deformable behaviour was not well defined as in the previous case and this may be due to the precipitates in the inclusions.

The sulphide inclusions deformation decreased with increasing rolling temperature (Fig. 126).

(b) Melt 12 (0.1% S and 0.2% S)

The oxide inclusions in the steels with sulphur levels of 0.1% and 0.2% behaved in a similar manner at the rolling temperatures employed

The majority of the oxide inclusions in the high sulphur samples behaved plastically when rolled at 800°C but a few remained undeformed (Plates 28, 29, 40 and 41) even at higher matrix reductions. At higher matrix reductions some of the highly deformable inclusions started splitting up (Plate 29).

At rolling temperature of 900°C, all the oxide inclusions were deformed plastically and at higher matrix reductions the inclusions exhibited necking and joining of inclusions (Plate 30) whilst some of the more plastic inclusions showed roping and splitting characteristics (Plates 31-36).

At rolling temperatures of 1000°C, 1100°C and 1200°C the oxide inclusions exhibited necking and deformed/fracture characteristics. Unfortunately, for these steels the transition from non-deformable to deformable behaviour for the oxide inclusions could not be determined because the oxide inclusions deformed at all the temperatures involved in the experiments (Fig. 130).

The mean 'as cast' oxide inclusions composition are given in table 4.8 (appendix 2).

The sulphide inclusions in melt A12 (0.1%S, and 0.2%S) exhibited deformation characteristics similar to the previous trend of decreasing with increasing rolling temperature (Fig. 126).

In summary, for Melt A12, the behaviour of oxide inclusions during rolling was affected by the sulphur content of the

melt. This behaviour was definitely due to the change of inclusion composition as the sulphur content of the melt was increased (Fig. 60). From the above results it was more likely that the oxide inclusion composition had been pushed into the lower liquidus composition region. Because of manganese's great affinity for sulphur, the manganese in the silicate inclusions was reduced in higher sulphur melts, thus pushing the inclusion composition towards the higher silica or alumina side of the $\text{MnO-SiO}_2\text{-Al}_2\text{O}_3$ system. This effect was more significant in low manganese melts (i.e. A12) as compared to the high manganese melts (i.e. A6 or A7). The sulphide inclusion deformation decreased with increasing rolling temperature.

5.2.1.3 Melt A15 (deoxidised with Mn-Si-Al alloy)

(a) Melt A15 (0.07%S)

All the oxide inclusions in the sample rolled at 900°C exhibited little or no deformation even at higher matrix reductions (Plate 37). The majority of the large oxide inclusions present in the sample rolled at 1000°C (50% total matrix reduction) behaved in a brittle manner whilst few of the large oxide inclusions deformed plastically. At higher matrix reduction ($\sim 70\%$ total matrix reduction) virtually all the large oxide inclusions were deformed.

The oxide inclusions exhibited a transition from non-deformable to deformable behaviour when the rolling temperature was increased from 1000°C to 1100°C (Fig. 131). All the oxide inclusions were deformed when the sample was rolled at 1100°C .

The deformation of the sulphide inclusions decreased with increasing rolling temperature.

The mean oxide inclusions ('as cast') compositions are given in table 4.8 (appendix 2).

(b) Melt A15 (0.1%S and 0.2%S)

The inclusions in the steel samples with sulphur levels of 0.1% S and 0.2% S behaved in a similar manner when rolled at the temperatures used in the experiments.

All the oxide inclusions present in samples rolled at 900°C exhibited little or no deformation. In samples rolled at 1000°C the oxide inclusions exhibited a rapid transition from non-deformable to deformable behaviour, thus exhibiting a transition between 900°C-1000°C. All the oxide inclusions were deformed plastically at rolling temperatures of 1000°C and 1100°C. From figure 131, it is evident that there is a drop in plasticity index at rolling temperatures higher than the transition temperature. This will be discussed in detail in section 5.2.1.5.

The mean 'as cast' oxide inclusions composition are given in table 4.8 (appendix 2).

The sulphide inclusions exhibited deformation characteristics similar to the previous results (Figs. 124-127) of decreasing with increasing rolling temperature.

Summarising, the behaviour of the oxide inclusions during rolling was affected by the sulphur content of the steel melt. This was because the oxide inclusion compositions were changed by increasing the sulphur content of the steel melt. The sulphide inclusion deformation decreased with increasing rolling temperature.

5.2.1.4 Factors affecting the transition from non-deformable to deformable behaviour

(i) Sulphur content of steel melt

Initially, confining the discussion to the transition from non-deformable to deformable behaviour of the oxide inclusions in melts A12 and A15, it was seen that the transition temperature decreased with increasing sulphur content of the melts (Figs. 130 and 131). This was due to the manganese having a great affinity for sulphur, thus in low manganese melt the presence of high sulphur in the melt tended to attract a disproportionate amount of the manganese thus leaving the oxide inclusions with low manganese oxide content. This caused the inclusions ^{to move} into the low liquidus composition region and enhancing deformation of the resulting oxide inclusions at lower rolling temperatures (Figs. 60 and 61).

The transition from non-deformable to deformable behaviour of the oxide inclusions in melts A6 and A7 was not affected by the increase in sulphur content of the melts (Figs. 128 and 129). This was due to the manganese contents of the melts being high enough to contain the increase in sulphur content of the melts without affecting the amount of manganese oxide in the oxide inclusion composition very much and thus the oxide

inclusion composition virtually remained unchanged (Figs. 60 and 61).

It was seen that the transition temperature varied with composition and that the transition temperatures were 200°C or more below the estimated equilibrium solidus temperature. This observation was in agreement with other investigators (84,100,126).

It was seen that the deformation of single phase sulphide inclusions, in all the steels under present investigation, decreased with increasing temperature (Figs. 124-127). This observation confirmed results obtained by Charles and co-workers (89,103,104,107). It must be pointed out that no analysis of the sulphide inclusions were obtained because they were too small to be analysed on the microprobe analyser due to matrix excitation.

(ii) Precipitation

Where dispersed second phase precipitates were observed in the oxide inclusions, the transition from non-deformable to deformable behaviour was less pronounced. This agrees with the observations by Wardle (100).

5.2.1.5 Deformation of inclusions at temperatures higher than the transition temperature

Some of the inclusions which exhibited rapid transition from non-deformable to deformable behaviour showed lower plasticity values at temperatures higher than the transition temperature. This reduction in relative plasticity index has been reported by other investigators (84,100,126,127) but few investigators

have offered an explanation for this phenomenon. Robinson (84) suggested that the increase in temperature did little to lower the viscosity of the inclusion whilst the yield strength of the steel matrix was reduced considerably thus leading to an increase in the inclusion-matrix relative strength, therefore decreasing the value of the relative plasticity. Wardle (100) disagreed with Robinson by suggesting that at the temperatures involved σ_i/σ_m are so low as to have very little effect on the maximum value of the relative plasticity index. He then went on to propose possible mechanisms for this fall in relative plasticity index:

- (i) the onset of internal fluid flow, whereby a proportion of the energy available for deformation is used up;
- (ii) where the inclusions deform in a fully fluid manner, these inclusions may break up and disperse;
- (iii) where there is inter-pass reheating; there may be spheroidisation of the inclusions.

The present author also cannot agree with Robinson (84) in the light of the data on strength/or hardness values for the silicate inclusions and the matrix (Fig. 24). The effect of σ_i/σ_m increase or decrease on the inclusion plasticity index will be very little at this stage and would not be significant. Some of the suggestions put forward by Wardle are possible mechanisms for this fall in plasticity index but spheroidisation of the large inclusions ($\sqrt{ab} > 10 \mu\text{m}$) is

definitely not a possible mechanism. This is because large inclusions do not spheroidise to any appreciable extent and therefore, cannot have any significant effect on the reduction in the plasticity index (Figs. 132 and 133).

The author has obtained possible evidence that the inclusions which deform in a fully plastic or fluid manner may break up and disperse, thus giving lower values of the plasticity index (Plates 55-58), 72-76). The possible mechanism for the break up of the inclusions may be due to the difference in metal flow velocity. If a fluid inclusion happened to be within a boundary of two different flow (metal) velocities, the inclusion would shear thus the side within the region of higher metal flow velocity would move ahead of the side of the inclusion within the slower flow (metal) velocity region, the resulting structures of the inclusions may be as shown in plates 55-58, and 72-76.

5.2.2 Variation of inclusion composition with plasticity index

It was shown in section 5.1.2 that oxide inclusion (diameter $>10 \mu\text{m}$) composition in the steels showed very little or no variation with size. It was clear that there may be variation in the inclusions composition if the sulphur content of the steel is increased (Figs. 52-58) but this is not size dependent.

The measurement of oxide inclusions non-deformable/deformable transition temperatures was attempted relating it to compositional differences. The actual measurements of

deformed inclusion compositions and dimensions were done by microprobe analyser. The results of the compositions and plasticity indices measurements on the microprobe analyser were plotted on composition-plasticity index diagrams at various rolling temperatures (Figs. 65-72). The diagrams showed which inclusions composition were deformable at the rolling temperatures (800°C - 1300°C) involved in the present experiments for different sulphur contents of the melts.

It must be noted that all the samples used in these experiments were soaked for 30 minutes and all reheating times (~ 10 minutes) were constant up to the total matrix strain at which samples were taken [$(\epsilon_m = 0.69)$, (50% total matrix reduction in height)].

5.2.2.1 Rolling temperature 800°C (Figs. 65c and 70a)

The oxide inclusions in the steel (A12 $\sim 0.1\%$ S) were highly deformable at this rolling temperature. The inclusion compositions were within the range of 39-54% SiO_2 , 11-26% Al_2O_3 , the remainder being $\text{FeO} + \text{MnO} + \text{S}$. Very few of the inclusions in this range exhibited plasticity indices less than unity. It can also be seen that these few inclusions exhibited plasticity indices close to unity (Fig. 65c).

The oxide inclusions in the steel (A12 $\sim 0.2\%$ S) were all deformable at this temperature. The composition range was 36-47% SiO_2 , 26-32% Al_2O_3 and the remainder being $\text{MnO} + \text{FeO} + \text{S}$ (Fig. 70a).

5.2.2.2 Rolling temperature 900°C (Figs. 65a, 67 and 70b)

Figures 65a, 67 and 70b show that the oxide inclusions with compositions: 20-40% SiO₂ - 0-20% Al₂O₃, the remainder being MnO + FeO + S, and 50-60% SiO₂ - 0-10% Al₂O₃, the remainder being MnO + FeO + S exhibited little or no deformation whilst the oxide inclusions with compositions 10-30% Al₂O₃ - 40-60% SiO₂ and the remainder being MnO + FeO + S were highly deformable at a rolling temperature of 900°C.

5.2.2.3 Rolling temperature 1000°C (Figs. 65b, 68a, and 71a)

From figures 65b, 68a and 71a, it is evident that the oxide inclusions with more than 10% alumina and about 30-65% SiO₂ were highly deformable whilst the inclusions with compositions:

(i) alumina <10% and silica content of about 30-40%, and

(ii) Rhodonite + Tephroite were not deformed.

The inclusions with very high silica content (>70%) did not deform as would be expected.

5.2.2.4 Rolling temperature 1100°C (Figs. 66a, 68b and 71b)

All the inclusions in this investigation exhibited high relative plasticity indices, however, some of the inclusions with no alumina and a silica content of about 39% were deformed less than unity at this temperature.

5.2.2.5 Rolling temperatures 1200°C and 1300°C (Figs. 66b, 68c, 69, 71c and 72)

All the oxide inclusions exhibited high plasticity indices at these rolling temperatures.

From these composition-plasticity index diagram, the compositions at which non-deformable/deformable transition occurred at different rolling temperatures are summarised in Fig. 76b. The schematic diagram was for a temperature range of 800°C-1300°C. The inclusions of the present series were all deformed at 1100°C so the maximum transition temperature observed was not higher than 1100°C. This figure 76b is only a guide for the inclusions in this series of experiments. The results obtained are very similar to those measured by Wardle ⁽¹⁰⁰⁾ for low sulphur melts. The region with the lowest transition temperature coincides with the lowest liquidus composition region of the MnO-SiO₂-Al₂O₃ ternary diagram (Fig. 14b), thus showing that the estimation is probably accurate if not very accurate.

5.2.3 Relative Plasticity Determination and Factors Affecting Inclusion Deformation

5.2.3.1 Representation of inclusion size

It is generally accepted that inclusion relative plasticity index was influenced by inclusion size. The square root of the product of major (a) and minor (b) axes, obtained by measurement of ellipsoid inclusion (deformed) on the XY plane (Fig. 35) was used as a measure of the original inclusion size.

The inclusion size derivation was based on the assumptions that the inclusions deformed in a manner as described by plane strain (i.e. there was no width spread) and constancy of the inclusion volume. If the inclusions were spheres which after deformation became ellipsoids, then by constancy

of volume: considering a sphere of radius D_0

Volume of sphere = Volume of ellipsoid

$$\frac{\pi D_0^3}{6} = \frac{\pi D_0 ab}{6}$$

$$D_0 = \sqrt{ab}$$

The inclusion relative plasticity index, v , is defined as

$$v = \frac{\epsilon_i}{\epsilon_m} = \frac{\ln \frac{a}{b}}{2\epsilon_m} \quad \text{for plane strain}$$

where ϵ_i is the inclusion strain and ϵ_m is the matrix strain. To relate the inclusion relative plasticity index (v) to the inclusion size defined as \sqrt{ab} , the graphs of inclusion relative plasticity index versus \sqrt{ab} were plotted for several melts. Because the inclusion relative plasticity index, v , is also dependent on the major and minor axes of the ellipsoid inclusion, the plot of v versus \sqrt{ab} results in a family of curves which are dependent on the magnitude of the major and minor axes.

Figure 77a shows the dependency of ϵ_i upon a and b values. The figure indicates that the graphs obtained by plotting v versus \sqrt{ab} will give a series of curves (i.e. Figs. 77-89) if during measurement of inclusions major and minor axes, the operator encounters many inclusions with the same major or the same minor axes.

5.2.3.2 Variation of inclusion relative plasticity index with inclusion size

The diagrams (Figs. 77-123) show the relationship between the inclusion relative plasticity index and inclusion size for several melts. It must be noted that the graphs represent the deformation of both oxide and sulphide inclusions. If it is remembered that the majority of the sulphide inclusions were 5 μm or less in diameter, it can be seen from the diagrams that generally the relative plasticity of the oxide inclusions decrease with ^{decreasing} size. From these diagrams the minimum deformable inclusion size was always greater than 2 μm at all rolling temperatures.

From more quantitative data (table 4.4)^{p.108} it was evident that the inclusion relative plasticity index does decrease with decreasing inclusion size. This confirms reports in the literature of a reduction in relative plasticity index with decreasing inclusion size (84,100,132).

The decrease of inclusion relative plasticity index with size may be due to the following:

- (i) inclusion composition;
- (ii) spheroidisation of deformed inclusions;
- (iii) sectioning problem;
- (iv) surface energy criterion.

Small inclusions composition could not be determined accurately, owing to the thickness or diameter of the inclusion relative to the depth of penetration of the microprobe analyser's electron beam. Therefore, the effect of inclusion composition on the reduction of the relative plasticity cannot be discussed.

5.2.3.2.1 Spheroidisation of deformed inclusions

It was the author's opinion that spheroidisation of inclusions was responsible for the decrease in relative plasticity index as the inclusion size decreases. To study the effect of spheroidisation on relative plasticity index, samples containing deformed inclusions were heat treated and the plasticity indices of inclusions after heat treatment were measured.

Figures 132, 133 and tables 4.10-4.11 (appendix 2) show the influence of both soaking time and temperature on the inclusion relative plasticity index for different inclusion size ranges (oxide) and sulphides.

From figure 132 (table 4.10a), it is evident that the sulphide inclusion mean relative plasticity index decreased as the soaking time increased. The small oxide inclusions ($\sqrt{ab} < 5 \mu\text{m}$) do exhibit significant decrease in the mean relative plasticity index value whilst the large oxide inclusions ($\sqrt{ab} > 10 \mu\text{m}$) showed very little or no decrease in the mean relative plasticity index (Plates 59-64). Thus the greatest effect of spheroidisation was observed to be on the small inclusions. This effect was to be expected since the small inclusions have the highest surface area to volume ratio and will therefore tend to spheroidise in a short time.

The influence of soaking temperature upon spheroidisation of inclusions is shown in figure 133 at constant soaking time (72 hours). The sulphide inclusions exhibited virtually constant relative plasticity index as the soaking temperature

was increased. The inclusions most affected by the variation of the soaking temperature, were the small oxide inclusions (Fig. 133, Table 4.10b (appendix 2)). The effect on the large oxide inclusions ($\sqrt{ab} > 10 \mu\text{m}$) was not as pronounced as small oxide inclusions ($\sqrt{ab} < 5 \mu\text{m}$).

The results agree with results for sulphide inclusions obtained by other workers (123-125). Murty et al (125) found that the rate of spheroidisation was controlled by surface diffusion of the inclusions.

From the results obtained it is evident that inclusions in samples which are repeatedly reheated prior to rolling would spheroidise, and this would contribute to lowering the relative plasticity index of the small inclusions.

5.2.3.2.2 Sectioning problem

Segal and Charles (132) showed that sectioning is one of the important problems encountered in the measurement of inclusion sizes.

The probability that the radius of a circle that is found in a globe (radius = R_0) when cut by a plane at any position will be within r and $r + dr$ is (199)

$$P(r) dr = \frac{1}{R_0} \cdot \frac{r}{\sqrt{R_0^2 - r^2}} dr$$

Masui and Takechi (199) then showed that the appearance probabilities of different radius circles would be

$\int_r^{r+dr} P(r) dr$ when the position of the cutting plane is

varied as shown in fig. 161a and the results are shown in fig. 161b. From the equation obtained by Masui and Takechi, it can be shown that the probability that a circle having a radius of $0.8R_0 - R_0$ will appear in the plane of sectioning is about 60%.

This analysis used by Masui and Takechi may also be applied to ellipsoid inclusions. There would be an error in the values obtained by such a model but it would act as a good approximation. If this is true, then it is useful to know that the probability of the inclusions being cut such that its true dimensions are not obtained is very small. The inclusions which are cut such that they appear less than their actual dimensions will affect the relative plasticity index-size relationship.

Plate 80 shows an inclusion sectioned such that it exhibits its true relative plasticity whilst Plate 81 shows an inclusion sectioned such that it exhibits lower relative plasticity index value than its true value. Plate 82 shows an inclusion sectioned such that it exhibits a relative plasticity index higher than its true value.

It is evident that if the operator encounters inclusions with a sectioning problem such as in plates 81 and 82 the overall mean relative plasticity value would be lower or higher than the actual relative plasticity index value.

Sectioning problems are very difficult to overcome, so the only consolation is that the probability of getting many inclusions with sizes very close to their actual sizes is fairly high. The likely procedure to overcome this problem may be the use of S.E.M. to assess inclusion deformation characteristics.

5.2.3.2.3 Surface energy criterion

Baker and Charles ⁽⁸⁹⁾ suggested that the energy required to create a new interface, as an inclusion deforms, may be responsible for the reported reduction in relative plasticity index with increasing matrix strain. This suggestion may offer an explanation for the observed reduction in the relative plasticity index of smaller inclusions.

Equations have been derived by Robinson ⁽⁸⁴⁾ and Wardle ⁽¹⁰⁰⁾ to study the effect of surface energy criterion on the deformation of inclusions and both of them concluded that surface energy effect was only noticeable at very small inclusion sizes whilst its effect on large inclusions ($>5 \mu\text{m}$) was minimal.

From the present work it is evident that inclusions (silicates and manganese sulphides) smaller than $2 \mu\text{m}$ are not deformed. This has also been observed by other workers ^(84,100,132).

Thus the surface energy criterion can be seen to offer a partial explanation for the observed lower relative plasticity index of smaller inclusions but it is not complete within itself. It is the author's opinion that this surface

energy effect coupled with spheroidisation of the smaller inclusions may offer a more complete explanation for the observed lower relative plasticity index of the smaller inclusions.

5.2.3.3 The influence of total matrix reduction upon relative plasticity index

The influence of matrix deformation upon relative plasticity index of inclusions has been shown by numerous workers (100, 102, 104). Most of the workers used the mean relative plasticity index to illustrate this effect but in the present work this influence is clearly shown (Figs. 77-105) without using the mean relative plasticity index. In general, the relative plasticity index values for the different inclusion phases were higher for the smaller total matrix reduction (50%) than for the larger total matrix reductions employed in the present work. This behaviour was pronounced when the inclusions behaved in a plastic manner. The drop in relative plasticity index values is due to the fact that the relative plasticity index of the inclusion as measured by the ratio of the inclusion strain to that in the steel is always larger for the lower total reductions because of the smaller ingoing to outgoing thickness ratio of the steel (lower localised strain in the matrix whilst the localised strains would be higher at higher matrix total reductions).

Using plasticine model and experimentally determined values, Wardle (100) showed that the relative plasticity index or inclusion strain increased rapidly (reaching a peak at approximately matrix strain, $\epsilon_m = 0.8$) and decreased

gradually (approaching value of 1.0) with increasing matrix strain (Fig. 162). Wardle explained the shape of the inclusion-matrix strain diagram ^{Fig.} (162) partially in terms of strain rate for a multipass situation (i.e. as the matrix strain was increased, the strain rate increased which led to an increased value of apparent inclusion to matrix flow stress ratio). This effectively leads to the inclusions being less deformable at higher matrix strains and therefore flattening the inclusion-matrix strain diagram.

Numerous explanations have been given for the decrease in relative plasticity index with increasing matrix strain (section 2.4.2.1) and the factors mentioned in the literature will not be discussed again. Apart from the factors already mentioned, the other factors which may affect the relative plasticity index are:

- (i) matrix constraint, and
- (ii) temperature rise.

5.2.3.3.1 Matrix constraint

Larke ⁽²⁰⁰⁾ showed that the smaller the ingoing thickness the more dominant the influence of the frictional constraint. Thus at small total matrix reductions the frictional constraint is less dominant whilst at large total matrix reductions this effect would be more pronounced.

Pickering ⁽¹⁰²⁾ suggested that spherical inclusions offer less resistance to the flow of metal than if they were ellipsoids so that the interfacial forces causing deformation decrease, thus the relative plasticity index apparently

decreases. If this is true then it explains why there is a decrease in the relative plasticity index as the total matrix reduction increases.

It could also be explained by the fact that the flow of metal at the centre of the strip decreases as the total matrix reduction increases from the matrix strain at which the maximum inclusion strain occurs. Thus the deformation of the inclusions at the centre of the strip would deform to a lesser extent as compared to the matrix deformation as the total matrix reduction increases.

5.2.3.3.2 Temperature rise

When the deformation of the matrix by rolling is considered, it must be noted that the deformation process is non-homogeneous. Assuming homogeneous deformation, a simple calculation of theoretical temperature rise can give up to about 10°C temperature rise depending on the roll speed. The temperature increase in localised areas may be even much higher, thus inclusions within these areas would, therefore, be of lower viscosity or strength than the other areas and hence will deform more easily.

The influence of ingoing thickness on mean rate of deformation or strain rate is shown in figure 163. This diagram clearly shows that as the ingoing thickness decreases, the mean rate of deformation increases. Appendix 4 shows how temperature rise is dependent on mean rate of deformation and it can be concluded that as the ingoing thickness decreases, the temperature rise increases. At lower matrix reductions the volume of material which undergoes localised deformation is small in comparison with that at higher matrix reductions,

therefore the effect becomes more significant as the amount of matrix reduction is increased.

As the transition temperature is approached this increase in temperature may push an inclusion which behaves in a plastic manner to become liquid and behave in fluid manner. This effect will, therefore, be more dominant at higher matrix reductions since the temperature rise will be higher and will push the inclusions well into the liquid formation temperature hence the decrease in the relative plasticity index at higher matrix reductions.

5.3 Verification of Wardle's Equations and the Effect of Height to Width Ratio on Inclusion Deformation

The derivations of all the equations considered below from Wardle ⁽¹⁰⁰⁾ are given in appendix 3.

From table 4.4, it is evident that the equation derived by Wardle appear to give a good estimation of the inclusion strain, $\epsilon_y^1(xy)$, in the third plane if the inclusion strain in the two other planes are known. The maximum error was not greater than $\pm 9\%$ for the large inclusions ($\sqrt{ab} > 10 \mu\text{m}$). There was no effect of the height to width ratio (of the sample to be rolled) on the estimated inclusion strain.

Again using the equation derived for width spread, ϵ_z , it can be seen from table 4.4 that the large inclusions ($\sqrt{ab} > 10 \mu\text{m}$) exhibited greater width spread when compared to the smaller inclusions ($\sqrt{ab} < 5 \mu\text{m}$). This effect was more pronounced when the height to width ratio (of the sample to be rolled) increased from 0.5 to 2.0. This is expected,

because the sample with height to width ratio about 2.0 should have larger width spread in comparison to the sample with height to width ratio of about 0.5. It is generally accepted that large inclusions do deform more than small inclusions, hence the results obtained.

Wardle derived an equation for the estimation of plane strain inclusion relative plasticity ($v_{p\epsilon}^*$), if non plane strain conditions are operative and if width spread, ϵ_z , is known. Again, plane strain inclusion relative plasticity index ($v_{p\epsilon}^*$) for different size groups and type of inclusions are given in table 4.4. The value of the estimated relative plasticity index ($v_{p\epsilon}^*$) for the large oxide inclusions ($\sqrt{ab} > 10 \mu\text{m}$) was about 2.2. This value is in agreement with the maximum value of relative plasticity index of inclusion behaving in a plastic or fluid manner predicted by models and experimental results (84,107,110,111,117). The height to width ratio (of the sample to be rolled) again affects these results. It must be pointed out that the effect of height to width ratio (of the sample to be rolled) seems to be pronounced on the smaller inclusions ($\sqrt{ab} < 10 \mu\text{m}$).

In summary, the equations derived by Wardle can be a useful guide for the estimation of inclusions strain or plasticity index if plane strain conditions are not operative.

5.4 Notch Tensile Test

5.4.1 Effect of sulphide and oxide inclusions on the fracture behaviour of the steels (D)

The effects of sulphide and oxide inclusions shown in Plates 65-67 are consistent with the traditional views of void

nucleation, void growth, and void coalescence. In the case of sulphides in a ferritic matrix the void nucleation strain is negligibly small and lateral growth is generally associated with the later stage of void coalescence which occurs over a limited strain range. Therefore, the majority of the strain to fracture is associated with the growth of voids in ^{the} tensile test.

It was observed that the void growth was greater in the low sulphur content alloy steel [(D1 and D2) (Plate 66a)] whilst in the high sulphur content alloy steels (D1 and D2) there were several small voids nucleated around very small inclusions as a result of very high local strains required to separate the intervening matrix (Plate 66b).

The high manganese alloy steel (D3) with different sulphur contents exhibited a different fracture surface. However, these steels contained large numbers of small sulphide inclusions. For the low sulphur content steel (D3 - 0.02%S) the fracture surface appeared flatter and S.E.M. examination revealed cleavage fracture at the centre of the material and ductile fracture at the edges (Plate 65a).

In the high sulphur steels (D3 ~ 0.1%S, 0.2%S), the fracture surface revealed local void coalescence producing a super-void which then continued to grow and interact with other voids as shown in Plate 65b.

The total extensions to fracture for the different steels (D1, D2 and D3) were plotted against the percentage area of

the sulphide and oxide inclusions in the steels (Figs. 143-145). The shape of the graph is the same as predicted by models and experimental results (160-164). This confirms the well known relationship between the volume fraction of second phase particles, which may be inclusions, and the total ductility in a tensile test. From figures 143-145, it can be concluded that the ductility is adversely affected by increasing volume fraction of inclusions (because area fraction can be related to volume fraction). Since the volume fraction of inclusions in a particular steel alloy increases with increasing sulphur content in the steel, it would seem reasonable to conclude that ductility decreases with increasing sulphur content of the steel.

The general deleterious effects of MnS inclusions on ductility have been well established by many investigators (143,168-170). MnS inclusions also give rise to the anisotropy of ductility relative to the rolling direction because of its high deformability on hot rolling. It is generally accepted that the deformability of sulphide inclusions do decrease with increasing rolling temperature. Because of this, samples used for subsequent experiments were hot rolled at 1200°C so that the relative plasticity index of the MnS inclusions would not be very high. In order to study the effect of MnS inclusions morphology on ductility, two steels with different sulphide morphology were studied. Figures 150-155 show the stress-strain curves for steel D1* (with type I MnS inclusions) and steel D4 (with type II MnS inclusions). The effect of MnS inclusions

morphology on the strain to fracture is clearly demonstrated by the diagrams. When type II MnS inclusions are present in the steel the strain to fracture in the case of ^{the} 'as cast' notch specimen may be very small as compared to the strain to fracture for the longitudinal notch specimens, the strain to fracture for the long transverse notch specimen was intermediate. Steel containing type I MnS inclusions showed the same effect for the specimens ('as cast', longitudinal, and long transverse) but it was not as pronounced as in the case of type II MnS inclusions containing steels (Figs. 150-155). This observation confirms ^{the} results of other investigators (172-175). Examination of the fracture surfaces of the two steels revealed that the steels containing type I MnS inclusions fractured by greater growth of the voids (Plate 66a) compared to the steels containing type II MnS inclusions (Plate 67).

The mechanism of the ductile fracture when elongated inclusions ~~were~~ involved is shown schematically (Fig. 164). In the long transverse specimen, deformed inclusions lie with their elongated axis perpendicular to the tensile direction. When the inclusions form elongated cracks, their total length (or total area) on the unit area of a cross section parallel to the final separation is larger compared with that of the longitudinal specimen, and this qualitatively leads to the final separation by the localised shearing more easily. In the 'as cast' specimens, apart from inclusions, there may be small pores present in the material and this makes the material weaker than rolled materials (in which these pores are welded).

5.4.2 Notch effect on fracture

The results obtained from the notch tensile tests are given in tables 4.12-4.14.

For the un-notched specimens, table 4.12a generally shows that the increase in sulphur content of the steels decreased the percentage reduction in area of the specimen and the tensile strength. It can also be seen that the tensile strength increased with increasing manganese content of the steels (D1 ~0.5% Mn, D2 ~1.0% Mn, D3 ~2.0% Mn).

It is generally accepted that the introduction of a notch results in a stress concentration at the root of the notch. To study the effect of notches on fracture, the fracture surfaces of the notch specimens tested were examined. All the fractures in the steels D showed the fracture surfaces were all ductile except the specimens of steel D3. An example of ductile fracture observed is shown in Plate 66. Generally the fracture in all the steels were cup and cone type.

For specimens with notches of root radii 1.00 mm and 0.26 mm, the fracture was a combination of normal rupture and shear whilst for the lower root radii specimens ($r = 0.16$ mm and $r = 0.18$ mm), the fracture was generally normal rupture. This shows that the lower root radii notches produced high local strain concentrations at the root of the notch and started cracks at the notch root which propagate inwards, thus accelerating the nucleation and growth of cracks.

Figs. 132-142 and 146-149 show the graphs of \log_e NSR versus $(K_t - 1)^3$, where NSR is the Notch Strength ratio and K_t is the elastic stress concentration factor. The slope, $A(r)$, of each curve in the diagrams (Figs. 132-142 and 146-149) were measured in order to relate them to the metallurgical properties of the steels used for the notch tensile tests. Joubert and Valentin (193) reported that $A(r)$ is a third degree polynomial and is dependent on the metallurgical properties of the steel. From table 4.14 (appendix 2), it can be seen that the effect of the different steels on the polynomial $A(r)$ was pronounced when the notch root radii was small.

For extremely sharp or pointed notches, Neuber's (199) original theory becomes unrealistic. Neuber introduced a new model in which the continuum mechanics solutions are used everywhere except near the root of the notch. The calculations yield the result that the elastic stress-concentration factor of sharp notches can be determined from the equations for the elastic stress-concentration factor based on continuum mechanics, provided that the actual root radius of the notch r is replaced by r^1 , which is given by the equation.

$$r^1 = r + [(2\pi - w)/(\pi - w)]\eta \dots\dots\dots$$

where w is the included angle of the notch and η is assumed to be a material constant. Therefore, according to the above equation, the material constant can only be obtained when $r \rightarrow 0$ or $r = 0$. From the equation $A(r) = a_0 + a_1r + a_2r^2 + a_3r^3$, the material constant can be determined when

$r = 0$. But $A(0) = a_0$, therefore a_0 is the material constant. This agrees with the results obtained that the lower notch root radii reveal the metallurgical properties of the material. The values of a_0 determined for steels D1* and D4, in the case of steel D1* compared with the relative plasticity index of the inclusions (Table 5.4). It can be seen from table 5.4 that the material constant decreases as the inclusions start deforming. This may have an effect on the elastic stress concentration factor of sharp notches.

TABLE 5.4

Steel	ϵ_i	a_0
D1* 'as cast'	0.00	2.086
D1* Longitudinal	0.70	-11.42
D1* Long transverse	1.21	-40.34
D4 'as cast'	-	2.25
D4 Longitudinal	-	-0.63
D4 Long transverse	-	9.33

5.5 Practical Implications

When molten steel solidifies, the excess oxygen present in the steel is rejected from solution and combines with carbon in the steel to form carbon monoxide which leads to blowholes in the cast product. To prevent this it is essential to reduce the oxygen level to a value such that there will be no carbon-oxygen reaction. This can be achieved by adding to the cooling metal elements which have greater affinity for oxygen than the carbon at steel-making temperatures.

Commercially, aluminium is often used for this purpose but it may lead to the production of deleterious alumina and type II MnS inclusions (in the case of high sulphur steels) which cause problems during hot rolling, wire and tube manufacture. In the case of steels for special applications where mechanical properties are very important it may also be injurious to those properties.

The use of Mn-Si-Al deoxidation alloys prevent the formation of alumina and type II MnS inclusions if the deoxidant is chosen carefully. The rate of emergence and the final inclusion size distribution of the products of deoxidation alloys Mn-Si-Al are dependent on the composition of the inclusions produced. The low liquidus composition of the $\text{MnO-SiO}_2\text{-Al}_2\text{O}_3$ system produced inclusions which had the highest rate of emergence. In continuous casting, Al is used often as a final deoxidant in the tundish and the mould, if the complex deoxidants (Mn-Si-Al alloys) considered here were used it is likely that tundish nozzle blockage would be reduced and the final inclusions if trapped would be less detrimental to the final steel mechanical properties.

The studies of inclusions behaviour during hot rolling, and the parameters that influence the inclusion behaviour may provide useful information which may be applied where possible to obtain optimum performance from the steel.

5.5.1 Machinability

It is generally accepted that MnS inclusions have beneficial effects on the machinability of steel. It has also been shown that low liquidus silicates can also be beneficial as far as machinability is concerned.

The effect of sulphur content on the composition of oxide inclusions has also been shown to be pronounced in low manganese steels (i.e. A12) in this present series of experiments. The compositions of the oxide inclusions were pushed into the lowest liquidus regions of the $\text{MnO-SiO}_2\text{-Al}_2\text{O}_3$ system as the sulphur content of the steel increased from about 0.1% up to 0.2%, and the resulting inclusions were deformable at ^arolling temperature of 800°C.

Normally, free cutting steels used for industrial purposes are En1A, En1B, En7 and En8M.

From the present series of experiments, only the high sulphur contents of steel A15 have compositions similar to one of the normally used free cutting steels (i.e. En7). It has been shown that as the sulphur content of steel A15 increased, the non-deformable/deformable transition was reduced, indicating that the oxide inclusion composition had been pushed into a lower liquidus composition region of the $\text{MnO-SiO}_2\text{-Al}_2\text{O}_3$ system as the sulphur content of the steel increased.

It can be seen that the machinability of high sulphur steels may not be only due to the MnS inclusions but may also be due to the fact that lower liquidus oxide inclusions

compositions have also been produced by increasing the sulphur content of the steel (i.e. A15). High sulphur contents of steel A12 may be ideal for machining since it produces the lowest liquidus composition in the present investigation.

The iron-manganese-silicate inclusions were found to dissolve high levels of sulphur but still the transition from non-deformable to deformable behaviour was not affected by the increase in sulphur content of the steel. These steels may require higher values of sulphur content in order to make them machinable at high speeds if at all.

5.5.2 Surface finish of rolled products

The lustre of a polished steel surface is sensitive to surface irregularities. The presence of different types of inclusions in the steel surface has an influence on the degree of finish attainable. The surface finish of flat rolled products is impaired by the presence of inclusions because these inclusions are pulled out of the surface during the polishing operation, which results in scratches and surface drags.

The surface finish may be improved by using a deoxidation practice which gives highly plastic siliceous deoxidation products which do not produce liquid or solid fragments at low rolling temperatures.

5.5.3 Influence of inclusions on mechanical properties

It has been established that the type, size, shape and distribution of inclusions do influence the mechanical properties of the steel. There are different ways in which non-metallic inclusions can nucleate cracks in the steel, and they are dependent on the deformation characteristics of the inclusions.

The studies of their behaviour during hot rolling may be turned to advantage such that improved mechanical properties of the steel may be obtained.

6. CONCLUSIONS

6.1 As Cast Inclusion Composition and Distribution

- (1) It appeared that as the $[\%Mn]^2:[\%Si]$ ratio of the deoxidant increased there was a corresponding increase in the $N_{(MnO)}^2:N_{(SiO_2)}$ ratio of the inclusions (diameter $>10 \mu m$) over the range of compositions encountered in the present investigation.
- (2) For a particular ratio of $[\%Mn]^2:[\%Si]$, the ratio of $N_{(MnO)}^2:N_{(SiO_2)}$ decreased with increasing sulphur content of the melt. This effect was pronounced in the low manganese content melts (i.e. 0.5% Mn) using consistent master deoxidation alloys.
- (3) The inclusion composition of the aluminium containing melts was found to vary slightly with size. Alumina was the only component that varied slightly. In melts containing FeO-MnO-SiO₂ inclusions, there was very little evidence of variation in composition.
- (4) Increase in sulphur content of low manganese melts ($\sim 0.5\%$ Mn) changed the composition of the oxide inclusions to higher silica or alumina side of the (FeMn)O-SiO₂-Al₂O₃ whilst in the case of high manganese melts the oxide inclusion composition remained unchanged with increasing sulphur content of the melt.

- (5) The morphology of sulphide inclusions was found to be very dependent on the dissolved oxygen in the melt. Thus, low dissolved oxygen led to the formation of type II MnS inclusions whilst higher dissolved oxygen led to the formation of type I MnS inclusions.
- (6) Increasing sulphur content of high oxygen melts does not change the morphology of the sulphide inclusions provided the deoxidation practice does not lead to very low dissolved oxygen contents which will not cope with the increase in sulphur.
- (7) Increase in the sulphur content of the melt gave a corresponding increase in the number of sulphide inclusions greater than a given diameter per unit area. This effect was more pronounced in the low manganese melts (D1 and D2).
- (8) Sulphur dissolved in Rhodonite and Tephroite inclusions of the MnO-SiO₂ system was very high compared to the manganese-aluminium-silicate inclusions. This dissolved sulphur in Rhodonite and Tephroite inclusions increased with increasing sulphur content of the iron melt.
- (9) As the sulphur content of the melts increased, it appeared that the number of oxide inclusions greater than a given diameter per unit area increased. This may have been due to reduction in the rate of removal of oxide inclusions by emergence being impaired.

- (10) At higher manganese content ($\sim 2\%$ Mn) of the melt, no oxide inclusions greater than 30 μm were observed. This was due to higher supersaturation and hence more inclusion nuclei formation leading to more small oxide inclusions.

6.2 Inclusion Deformation

- (1) All the sulphide inclusions observed in the steels exhibited decreasing relative plasticity index values with increasing rolling temperature.
- (2) At low rolling temperatures, silicate inclusions exhibited either rigid or brittle behaviour depending upon their composition.
- (3) In the case of more rigid silicate inclusions, the formation of conical voids in association with the inclusion-metal interfaces was observed.
- (4) All the silicate inclusions showed a rapid transition from non-deformable to deformable behaviour on reaching a narrow critical rolling temperature range. This rapid transition was less marked in inclusions which exhibited precipitation at lower rolling temperatures.
- (5) The transition from non-deformable to deformable behaviour normally occurred at temperatures more than 200°C below the estimated liquidus temperature.

- (6) The relative plasticity index of the silicate inclusions decreased as the rolling temperature was increased above the transition temperature range.
- (7) At temperatures well above the transition temperature, the inclusions appeared to break up in a fluid manner.
- (8) The effect of sulphur (content of the melt) in reducing the non-deformable/deformable transition is dependent upon the nature of inclusions. In lower manganese oxide inclusions (of compositions -33% MnO, 52% SiO₂, 10% Al₂O₃, 3% FeO, 2% S, and 54% MnO, 34% SiO₂, 6% Al₂O₃, 2% FeO, 4% S) this effect can be predicted by the change in inclusion composition to the lower liquidus composition in the MnO-SiO₂-Al₂O₃ system as the sulphur content of the melt increases.
- (9) Sulphur has no effect on the non-deformable/deformable transition temperature of oxide inclusions with compositions in the region of Tephroite and Rhodonite.
- (10) The apparent decrease in dissolved sulphur in Rhodonite and Tephroite inclusions at rolling temperatures of 1100°C was due to silica precipitation.

- (11) The relative plasticity index of inclusions decreased as their size decreased. There may be a limiting critical size, under any given set of conditions, below which the inclusions do not exhibit any deformation. In the present investigation the critical size was found to be about 2 μm .
- (12) Spheroidisation of small deformed oxide and sulphide inclusions increased with increasing reheating time. At a constant reheating time, spheroidisation of small oxide inclusions increased with increasing reheating temperature whilst spheroidisation of sulphide inclusions appeared to remain constant. Spheroidisation of small inclusions thus enhance the relative plasticity index-size relationship.
- (13) Sectioning contributes towards the variation of inclusions relative plasticity index with inclusion size.
- (14) All inclusions exhibited lower relative plasticity index values as the matrix strain increased and this is due partially to the following factors:
- (i) At small total reductions the frictional constraint is less dominant whilst at large total reductions this effect is pronounced hence the lower relative plasticity index exhibited by inclusions;

- (ii) For a multipass process, strain rate increased with decreasing ingoing thickness which led to an increase in the value of apparent inclusion to matrix flow stress ratio;
- (iii) At the transition temperature, the temperature rise in the sample contributed towards the decrease in relative plasticity index. It has been shown that the theoretical temperature rise increased with decreasing ingoing thickness.
- (15) From relative plasticity index-composition diagrams the non-deformable/deformable transition temperature has been estimated for oxide inclusion compositions within the range of the present work. It was observed that the lowest temperature for the transition from non-deformable to deformable behaviour occurred when the inclusions composition lay within the low liquidus composition region of the $\text{MnO-SiO}_2\text{-Al}_2\text{O}_3$ system.

6.3 Estimation of Inclusion Strain in the Third Dimension

- (1) It has been shown that the equation derived by Wardle ⁽¹⁰⁰⁾ for the estimation of inclusion strain in the third plane (appendix 3) if the inclusion strain in the two other planes are known gives a very good estimate. The estimation was not affected by changes in the height to width ratio of the sample to be rolled.

(2) The equation derived by Wardle for the estimation of width spread, ϵ_z , (appendix 3) showed that the large oxide inclusions (diameter $>10 \mu\text{m}$) exhibited greater relative width spread compared to the smaller oxide inclusions (diameter $<5 \mu\text{m}$). This effect was pronounced when the height to width ratio of the sample to be rolled increased from 0.5 to 2.0.

(3) Wardle's equation for the estimation of plane strain inclusion plasticity index, v_{pe}^* , assuming non-plane strain conditions are operative and if ϵ_z is known, gave a realistic value of 2.2 for the large oxide inclusions (diameter $>10 \mu\text{m}$). The equation could be a practical means of determining inclusion volume relative plasticity index.

6.4 Influence of Inclusions on Notch Ductility Measurements

- (1) It has been shown that the dependence of the polynomial $A(r)$ on the metallurgical properties of steel can be revealed significantly when the notch root radius tends toward zero.
- (2) From limited results, a possible dependence of $A(r)$ on the relative plasticity index of inclusions has been shown.

- (3) It has been illustrated that the strain to fracture was dependent on the percentage area fraction of both oxide and sulphide inclusions.
- (4) The morphology of MnS inclusions gave rise to the anisotropy of ductility relative to the rolling direction because of its high deformability in hot rolling. Anisotropy is much more pronounced in steels containing type II MnS inclusions than steels containing type I MnS inclusions.
- (5) Increase in sulphur content of the steel led to a corresponding decrease in the percentage reduction in area and the tensile strength of the unnotched steel specimens.

6.5 RECOMMENDATIONS FOR FURTHER WORK

- (1) The effect of strain rate on inclusion deformation should be studied in detail. It has been shown theoretically that increase in strain rate leads to a corresponding increase in temperature rise in the steel upon rolling. The effect of strain rate on inclusion deformation can be studied accurately by the use of a Camm Plastometer.

- (2) In order to study the deformation of small inclusions accurately, scanning electron microscope (S.E.M.) should be used. This is because the resolution limit of S.E.M. is much better as compared to ordinary optical microscope (i.e. Vickers Projection Microscope). The use of S.E.M. will enable, the investigator to give a critical inclusion size under which no deformation takes place. Also the S.E.M. can be used to determine both composition and deformation of inclusions if an electronic circuit can be developed to do the measurement. of inclusion deformation and E.D.A.X. attached for compositional analysis.

- (3) The nucleation and growth of precipitates in inclusions should be studied quantitatively at various heat treatment temperatures for various inclusion compositions.

- (4) The use of hot torsion test to investigate the mode of inclusion deformation at various shear strains from the surface to centre of the specimen.

- (5) The solubility of sulphur in various inclusion compositions should be studied in detail.
- (6) In order to obtain a more detailed interpretation of the physical significance of the polynomial $A(r)$ and its dependence on the metallurgical properties of different steels, notches of root radii less than 0.1 mm should be used. The metallurgical properties can be magnified if the root radii is less than 0.1 mm.
- (7) The dependence of $A(r)$ on the inclusion plasticity index should be studied in detail, so that the matrix constant, a_0 , can be determined and related to the inclusions relative plasticity index.
- (8) The dependence of void growth on different shapes of inclusions (non-deformable and deformable) should be studied in detail so that it can be related to ductility of the material.
- (9) The strain distribution in the matrix during rolling should be analysed critically so that the deformation of inclusions can be determined by the use of the ratio ^{of} inclusion strain to localised matrix strain (the matrix strain around the inclusion).
- (10) It may be interesting to investigate the machinability of steels deoxidised by deoxidant Al₂ (varying the sulphur content of the steel from 0.05% to 0.3%) since the composition of the oxide inclusions

present in the steel is changed by the increase in the sulphur content of the steel. At higher sulphur contents the composition of the oxide inclusions was pushed into the lower liquidus (temperature) composition region of the MnO-SiO₂-Al₂O₃ system.

- (11) The formation of sulphide and oxy-sulphide inclusions formation in steels deoxidised with Mn-Si alloys and Mn-Si-Al alloys should be studied in detail.

- (12) The rolling load during the deformation of the as cast bar should be measured so that the theoretical temperature rise can be found and its effect on inclusion deformation correlated.

ACKNOWLEDGEMENT

The author wishes to thank Dr. J.C. Billington, the project supervisor, for his interest and valuable discussions during the progress of this work.

My sincere thanks are due to my colleague, Mr. G. Wardle, for his advice and the numerous discussions. Thanks are also due to the following technical staff of the Department of Metallurgy and Materials: Mr. G. Reeves, Mr. P. Cox, Mr. D. Webb, Mr. K. Smith and Mr. R. Howell.

The author wishes to express his sincere thanks to the office staff: Mrs. H. Howell, Colette, Gillian and Nancy.

APPENDIX 1

1.1.0 Calculation of Deoxidation Alloy Composition

Consider 'A15'

To calculate the deoxidation alloy composition to obtain a oxide product 30% MnO, 40% SiO₂ and 30% Al₂O₃. Assume 100% utilisation of deoxidation alloy addition and production of 100x10⁻³kg of oxide.

Oxygen combined as MnO in product	=	$\frac{30 \times 16}{71}$	=	6.761x10 ⁻³ kg
" " " SiO ₂ " "	=	$\frac{40 \times 32}{60}$	=	21.333x10 ⁻³ kg
" " " Al ₂ O ₃ " "	=	$\frac{30 \times 48}{102}$	=	14.118x10 ⁻³ kg

Total oxygen per 100x10 ⁻³ kg of deoxidation product	=	42.212x10 ⁻³ kg
---	---	----------------------------

Fraction of total oxygen combined as MnO	=	0.1602
" " " " " " SiO ₂	=	0.5054
" " " " " " Al ₂ O ₃	=	0.3344
		<hr/>
		1.0000
		<hr/>

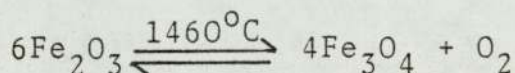
The oxygen available for deoxidation is 0.085% (assuming that an initial level of oxygen in melt to be 0.090% and the residual oxygen level of 0.005%) and it will be distributed between MnO, SiO₂, and Al₂O₃. Thus:

O" as MnO	=	0.085 x 0.1602	=	0.01362%
O" as SiO ₂	=	0.085 x 0.5054	=	0.04296%
O" as Al ₂ O ₃	=	0.085 x 0.3344	=	0.02842%
				<hr/>
				0.08500%
				<hr/>

Calculation of the deoxidation alloys A7, A6, and A12 are identical but the activity data is different for each deoxidation alloy.

1.1.1 Calculation of Fe₂O₃ addition

Assuming the following reaction occurs:



Assuming that the initial oxygen content of the electrolytic iron is 0.06 wt% and the required level is 0.090 wt% then the amount of oxygen to be added is 0.03 wt%. Allowance for

$$\text{reduction of Fe}_2\text{O}_3 : \frac{(3 \times 16)}{(4 \times 16)} \times \frac{6}{4} = \frac{18}{16}$$

$$\text{equivalent O as Fe}_2\text{O}_3 = 0.03 \times \frac{18}{16} = 0.03375\%$$

$$48 \times 10^{-3} \text{ kg of O} = 160 \times 10^{-3} \text{ kg of Fe}_2\text{O}_3$$

$$1 \times 10^{-3} \text{ kg of O} = 3.33 \times 10^{-3} \text{ kg of Fe}_2\text{O}_3$$

$$\text{Hence \% addition of Fe}_2\text{O}_3 = 0.1125\%$$

Therefore in a charge of 1500×10^{-3} kg electrolytic iron,

$$\text{Fe}_2\text{O}_3 \text{ addition} = 1.6875 \approx 1.69 \times 10^{-3} \text{ kg}$$

1.1.2 Calculation of FeS addition

$$\text{FeS} = 56 + 32 = 88 \times 10^{-3} \text{ kg mole wt.}$$

1 part sulphur requires $\frac{88}{32}$ parts FeS. Assuming an initial sulphur content of about 0.005%. To obtain a desired level of 0.1% sulphur requires addition of 0.095% sulphur. The FeS used contained 70% sulphur. Thus the amount required to be added to give a desired level of 0.1% sulphur in a charge of 1500×10^{-3} kg electrolytic iron is:

$$\frac{88}{32} \times \frac{0.095}{0.7} \times \frac{1500}{100} = 5.60 \times 10^{-3} \text{ kg}$$

APPENDIX 1.2

CALCULATED DEOXIDATION ALLOY COMPOSITIONS

Deoxidation Alloy	Element	% Oxide Product	a_{MO} (1600°C)	Stoichiometric wt%	\bar{m} at 1600°C wt%	Total wt%	% Alloy Composition
A6	Mn	55	0.18	0.099	1.829	1.928	73.31
	Si	45	0.68	0.049	0.653	0.702	26.69
	Al	-	-	-	-	-	-
						<u>2.630</u>	
A7	Mn	60	0.27	0.113	2.744	2.857	85.90
	Si	40	0.44	0.046	0.423	0.469	14.10
	Al	-	-	-	-	-	-
						<u>3.326</u>	
A12	Mn	35	0.05	0.056	0.508	0.564	58.45
	Si	45	0.35	0.043	0.336	0.379	39.27
	Al	20	-	0.022	-	0.022	2.28
						<u>0.965</u>	
A15	Mn	30	0.15	0.0468	1.5075	1.5543	81.45
	Si	40	0.30	0.0376	0.2843	0.3219	16.87
	Al	30	-	0.0320	-	0.0320	1.68
						<u>1.9082</u>	

Deoxidation Alloy	Element	% Oxide Product	^a MO (1600°C)	Stoichiometric wt%	at 1600°C wt%	Total wt%	% Alloy Composition
D1*	Mn	35	0.05	0.56	0.508	0.564	58.45
	Si	45	0.35	0.043	0.336	0.379	39.27
	Al	20	-	0.022	-	0.022	2.28
						0.965	
D2*	Mn	-	-	-	-	1.000	71.38
	Si	-	-	-	-	0.379	27.05
	Al	-	-	-	-	0.022	1.57
						1.401	
D3*	Mn	-	-	-	-	2.000	83.30
	Si	-	-	-	-	0.379	15.79
	Al	-	-	-	-	0.022	0.91
						2.401	
D4**	Mn	-	-	-	-	1.000	81.63
	Si	-	-	-	-	-	-
	Al	-	-	-	-	0.225	18.37
						1.225	

* Al2 plus extra or no Mn addition

** Blended deoxidant

APPENDIX 2

TABLE 4.5

Sulphide Inclusion Distribution

Sample	% Sulphur in Melt	Number of inclusions $>D_o^{\dagger} \text{mm}^{-2}$								Number of fields=120	
		1	2	3	4	5	6	8	10	% Area	
D1	0.02	941.5	306.9	82.5	38.7	14.8	10.0	6.0	5.2	0.283	
D1	0.10	1039.5	599.5	188.1	89.3	39.3	24.5	12.8	10.6	0.503	
D1	0.20	1656.9	861.7	268.6	117.6	54.6	31.1	16.3	9.2	0.723	
D2	0.02	655.3	297.1	81.8	34.0	11.2	6.9	4.8	3.7	0.257	
D2	0.10	2052.7	910.0	166.2	64.2	31.1	18.3	7.6	5.2	0.700	
D2	0.20	2623.2	1357.8	381.0	158.9	58.5	28.2	9.6	6.4	0.993	
D3	0.02	1244.6	481.5	120.6	43.6	17.5	12.8	4.8	1.6	0.374	
D3	0.10	2003.5	581.4	87.2	28.7	8.5	4.8	3.2	2.1	0.556	
D3	0.20	3156.2	965.2	173.8	55.8	20.7	11.2	5.3	2.7	0.811	

$^{\dagger}D_o$ = diameter of inclusion (μm)

APPENDIX 2

TABLE 4.6

Oxide Inclusion Distribution

Number of fields = 120

Sample	% Sulphur in Melt	Number of inclusions $>D_o \dagger \text{mm}^{-2}$								% Area
		1	2	5	10	15	20	30	40	
D1	0.02	247.9	208.5	40.3	4.8	0.8	0.4	0.4	-	0.197
D1	0.10	229.6	179.6	40.9	11.2	3.2	0.5	-	-	0.236
D1	0.20	268.6	216.4	48.6	12.8	5.2	2.0	1.2	0.4	0.339
D2	0.02	73.7	58.6	9.2	1.6	0.8	0.8	-	-	0.054
D2	0.10	131.9	100.4	12.4	1.6	0.8	-	-	-	0.114
D2	0.20	149.1	121.6	25.1	8.0	3.6	2.8	1.6	1.2	0.180
D3	0.02	34.5	27.1	6.9	0.5	-	-	-	-	0.029
D3	0.10	35.1	30.8	9.0	4.3	1.1	0.5	-	-	0.048
D3	0.20	26.6	21.8	6.9	1.1	-	-	-	-	0.036

$\dagger D_o$ = diameter of inclusion (μm)

APPENDIX 2

TABLE 4.7

Sample	Inclusion Distribution						Number of fields = 280		
	2	5	10	15	20	25	30	35	40
A6 ₁	345.9	61.8	9.2	5.4	4.1	3.7	3.2	2.6	2.2
A6 ₃	309.0	55.2	7.0	3.9	3.2	2.3	1.8	1.4	1.3
A7 ₁	360.2	68.9	8.3	4.1	2.9	2.5	2.1	1.9	1.8
A7 ₃	456.2	122.8	8.5	3.8	2.7	2.3	1.8	1.5	1.2
A12 ₁	624.9	180.9	23.6	9.8	6.4	5.4	4.2	3.4	3.1
A12 ₃	608.8	171.2	19.0	7.9	6.1	4.6	3.8	3.3	3.0
A15 ₁	356.4	181.5	15.1	5.6	3.3	2.3	1.6	1.4	1.4
A15 ₃	376.3	188.0	17.9	5.6	3.3	2.0	1.1	0.8	0.8

[†]D_o = diameter of inclusion (μm)

Subscript 1 indicates the sample was taken from top of the bar,
 and subscript 3 " " " " " " " " bottom of the bar.

APPENDIX 2

TABLE 4.8

Mean 'as cast' inclusion composition

Melt	% Sulphur in melt	Inclusion phase	MO%	Range	S.D.	S.E.	N
A6	0.07	S ¹	4	2-8	1.74	0.55	10
		FeO ¹	2	1-4	0.91	0.29	
		MnO ¹	56	55-58	1.83	0.58	
		SiO ₂ ¹	38	34-40	0.80	0.25	
A6	0.10	S ¹	6	3-8	1.56	0.38	17
		FeO ¹	2	1-5	1.88	0.46	
		MnO ¹	56	54-59	1.15	0.28	
		SiO ₂ ¹	35	30-39	2.73	0.66	
A6	0.20	S ¹	8	6-11	2.19	0.49	20
		FeO ¹	2	1-3	0.61	0.14	
		MnO ¹	58	55-61	1.40	0.31	
		SiO ₂ ¹	32	28-35	2.55	0.57	
A7	0.07	S ¹	4	3-5	1.37	0.48	8
		FeO ¹	4	3-6	1.02	0.36	
		MnO ¹	59	58-60	0.78	0.27	
		SiO ₂ ¹	33	31-35	1.40	0.50	
A7	0.10	S ¹	6	4-8	1.36	0.30	20
		FeO ¹	3	1-6	2.31	0.52	
		MnO ¹	60	58-62	2.17	0.49	
		SiO ₂ ¹	31	29-33	1.43	0.32	
A7	0.20	S ¹	7	3-11	3.11	0.64	24
		FeO ¹	2	1-4	0.73	0.15	
		MnO ¹	62	56-65	2.45	0.50	
		SiO ₂ ¹	29	24-38	3.74	0.76	

APPENDIX 2

TABLE 4.8 (cont'd)

Melt	% Sulphur in melt	Inclusion phase	MO%	Range	S.D.	S.E.	N
A12	0.07	S ¹	2	1-3	0.68	0.24	8
		FeO ¹	3	2-3	0.34	0.12	
		MnO ¹	33	32-34	1.00	0.35	
		SiO ₂ ¹	52	49-56	2.20	0.79	
		Al ₂ O ₃ ¹	10	8-12	1.02	0.36	
A12	0.10	S ¹	2	1-3	0.49	0.09	29
		FeO ¹	2	1-3	0.40	0.07	
		MnO ¹	31	29-33	1.01	0.19	
		SiO ₂ ¹	46	41-50	2.11	0.39	
		Al ₂ O ₃	19	15-27	2.39	0.44	
A12	0.20	S ¹	1	1-2	0.48	0.11	20
		FeO ¹	3	2-4	0.67	0.15	
		MnO ¹	31	27-33	1.81	0.40	
		SiO ₂ ¹	54	50-57	2.13	0.48	
		Al ₂ O ₃ ¹	11	9-13	1.24	0.28	
A15	0.07	S ¹	4	1-9	2.34	0.68	12
		FeO ¹	2	1-3	0.59	0.17	
		MnO ¹	54	52-58	2.20	0.63	
		SiO ₂ ¹	34	30-39	3.68	1.06	
		Al ₂ O ₃	6	2-10	2.13	0.62	
A15	0.10	S ¹	2	2-3	0.51	0.13	15
		FeO ¹	2	1-4	0.66	0.17	
		MnO ¹	47	46-50	0.86	0.22	
		SiO ₂ ¹	34	32-36	0.85	0.22	
		Al ₂ O ₃	15	12-17	1.53	0.40	

APPENDIX 2

TABLE 4.8 (cont'd)

Melt	% Sulphur in melt	Inclusion phase	MO%	Range	S.D.	S.E.	N
A15	0.20	S ¹	3	2-7	2.54	0.51	25
		FeO ¹	2	2-3	0.41	0.08	
		MnO ¹	53	51-57	1.39	0.28	
		SiO ₂ ¹	33	25-36	2.76	0.55	
		Al ₂ O ₃ ¹	9	8-9	0.44	0.09	
D1	0.02	S ¹	1	1-2	0.31	0.05	33
		FeO ¹	3	2-6	1.26	0.22	
		MnO ¹	30	27-31	1.10	0.19	
		SiO ₂ ¹	44	38-47	1.87	0.32	
		Al ₂ O ₃ ¹	22	20-28	1.69	0.29	
D1	0.10	S ¹	2	1-4	0.72	0.16	20
		FeO ¹	3	2-13	2.36	0.54	
		MnO ¹	30	26-31	1.27	0.29	
		SiO ₂ ¹	55	49-57	2.18	0.50	
		Al ₂ O ₃ ¹	10	8-13	1.37	0.31	
D1	0.20	S ¹	2	2-3	0.92	0.20	23
		FeO ¹	3	2-3	0.35	0.08	
		MnO ¹	30	25-33	2.90	0.62	
		SiO ₂ ¹	54	48-63	3.7	0.79	
		Al ₂ O ₃ ¹	12	10-14	1.11	0.24	
D2	0.02	S ¹	3	2-4	0.62	0.15	19
		FeO ¹	3	2-10	1.71	0.40	
		MnO ¹	47	43-51	1.62	0.38	
		SiO ₂ ¹	38	37-40	1.25	0.29	
		Al ₂ O ₃ ¹	9	6-15	2.02	0.48	

APPENDIX 2

TABLE 4.8 (cont'd)

Melt	% Sulphur in melt	Inclusion phase	MO%	Range	S,D.	S,E.	N
D2	0.10	S ¹	3	2-4	0.99	0.23	20
		FeO ¹	2	1-6	1.14	0.26	
		MnO ¹	45	36-50	2.92	0.67	
		SiO ₂ ¹	37	32-42	2.67	0.61	
		Al ₂ O ₃ ¹	13	4-29	4.81	1.10	
D2	0.20	S ¹	2	1-5	0.84	0.21	17
		FeO ¹	2	2-4	0.37	0.09	
		MnO ¹	45	42-50	2.32	0.58	
		SiO ₂ ¹	39	37-41	1.12	0.28	
		Al ₂ O ₃ ¹	12	6-16	3.12	0.78	
D3	0.02	S ¹	3	2-8	1.39	0.34	18
		FeO ¹	2	1-3	0.60	0.15	
		MnO ¹	51	46-56	2.83	0.69	
		SiO ₂ ¹	31	27-33	1.25	0.30	
		Al ₂ O ₃ ¹	13	6-23	4.27	1.04	
D3	0.10	S ¹	2	2-4	0.70	0.17	19
		FeO ¹	2	1-3	0.55	0.13	
		MnO ¹	51	47-57	2.87	0.68	
		SiO ₂ ¹	30	25-33	1.79	0.42	
		Al ₂ O ₃ ¹	15	6-23	4.66	1.10	
D3	0.20	S ¹	2	2-4	0.57	0.14	18
		FeO ¹	2	1-3	0.66	0.16	
		MnO ¹	48	45-55	3.12	0.74	
		SiO ₂ ¹	30	27-33	2.06	0.48	
		Al ₂ O ₃ ¹	18	9-23	4.32	1.05	

APPENDIX 2

TABLE 4.9

MEAN INCLUSION PLASTICITY INDEX

For the oxides $\sqrt{\text{major axis} \times \text{minor axis}} > 10 \mu\text{m}$

Melt	% Sulphur in melt	Rolling Temp. °C	Type of inclusion	Plasticity index v	S.D.	S.E.	N
A6	0.07	1000	Oxides	0.03	0.04	0.00	90
			Sulphides	0.97	0.20	0.02	91
		1100	Oxides	0.82	0.19	0.02	90
			Sulphides	0.70	0.20	0.02	90
		1200	Oxides	1.41	0.11	0.01	90
			Sulphides	0.49	0.16	0.02	90
		1300	Oxides	1.45	0.15	0.02	51
			Sulphides	0.35	0.16	0.02	90
A6	0.10	900	Oxides	0.05	0.04	0.00	90
			Sulphides	1.27	0.28	0.03	90
		1000	Oxides	0.21	0.19	0.02	90
			Sulphides	0.96	0.19	0.02	90
		1100	Oxides	1.29	0.13	0.01	90
			Sulphides	0.57	0.21	0.02	91
		1200	Oxides	1.48	0.09	0.01	90
			Sulphides	0.41	0.19	0.02	91
A6	0.20	900	Oxides	0.08	0.08	0.01	90
			Sulphides	1.07	0.18	0.02	90
		1000	Oxides	0.11	0.14	0.02	90
			Sulphides	1.03	0.21	0.02	90
		1100	Oxides	0.59	0.24	0.03	90
			Sulphides	0.81	0.17	0.02	90
		1200	Oxides	1.39	0.13	0.01	90
			Sulphides	0.60	0.22	0.02	90
1300	Oxides	1.22	0.21	0.02	90		
	Sulphides	0.45	0.21	0.02	90		

APPENDIX 2

TABLE 4.9 (cont'd)

Melt	% Sulphur in melt	Rolling Temp. °C	Type of inclusion	Plasticity	S.D.	S.E.	N
				index v			
A7	0.07	1100	Oxides	1.31	0.22	0.02	90
			Sulphides	0.59	0.18	0.02	91
		1200	Oxides	1.45	0.14	0.01	90
			Sulphides	0.36	0.15	0.02	90
		1300	Oxides	1.60	0.13	0.01	90
			Sulphides	0.27	0.10	0.01	90
A7	0.10	900	Oxides	0.03	0.02	0.00	90
			Sulphides	1.33	0.18	0.02	90
		1000	Oxides	0.18	0.26	0.03	91
			Sulphides	1.07	0.25	0.03	90
		1100	Oxides	1.48	0.17	0.02	91
			Sulphides	0.73	0.24	0.03	90
		1200	Oxides	1.35	0.10	0.01	90
			Sulphides	0.53	0.19	0.02	90
A7	0.20	900	Oxides	0.07	0.06	0.01	90
			Sulphides	1.07	0.17	0.02	90
		1000	Oxides	0.27	0.27	0.03	90
			Sulphides	0.92	0.18	0.02	90
		1100	Oxides	1.42	0.15	0.02	90
			Sulphides	0.66	0.23	0.02	90
		1200	Oxides	1.52	0.15	0.02	90
			Sulphides	0.43	0.17	0.02	90
		1300	Oxides	1.41	0.16	0.02	90
			Sulphides	0.27	0.13	0.01	90
A12	0.07	900	Oxides	0.28	0.39	0.04	90
			Sulphides	1.07	0.33	0.03	90
		1000	Oxides	0.73	0.39	0.04	90
			Sulphides	0.97	0.22	0.02	90
		1100	Oxides	1.32	0.18	0.02	90
			Sulphides	0.73	0.22	0.02	90

APPENDIX 2

TABLE 4.9 (cont'd)

Melt	% Sulphur in melt	Rolling Temp. °C	Type of inclusion	Plasticity				
				index v	S.D.	S.E.	N	
A12	0.10	800	Oxides	1.16	0.20	0.02	90	
			Sulphides	-	-	-	-	
		900	Oxides	1.55	0.12	0.01	90	
			Sulphides	1.42	0.22	0.02	90	
		1000	Oxides	1.40	0.16	0.02	90	
			Sulphides	1.04	0.22	0.02	92	
	1100	Oxides	1.29	0.13	0.01	90		
		Sulphides	0.80	0.17	0.02	93		
	1200	Oxides	1.16	0.19	0.02	90		
		Sulphides	0.65	0.21	0.02	94		
	A12	0.20	800	Oxides	1.22	0.20	0.02	101
				Sulphides	1.09	0.15	0.02	91
900			Oxides	1.33	0.21	0.02	90	
			Sulphides	1.07	0.20	0.02	90	
1000			Oxides	0.91	0.45	0.05	90	
			Sulphides	0.95	0.24	0.03	90	
1100		Oxides	1.30	0.14	0.02	90		
		Sulphides	0.95	0.22	0.02	90		
1200		Oxides	1.28	0.19	0.02	98		
		Sulphides	0.77	0.21	0.02	90		
A15		0.07	900	Oxides	0.05	0.03	0.00	90
				Sulphides	1.07	0.17	0.02	90
	1000		Oxides	0.39	0.20	0.02	90	
			Sulphides	0.80	0.20	0.02	90	
	1100		Oxides	1.44	0.21	0.02	90	
			Sulphides	0.56	0.18	0.02	90	
A15	0.10	900	Oxides	0.04	0.05	0.01	90	
			Sulphides	1.23	0.24	0.03	90	
		1000	Oxides	1.34	0.22	0.02	90	
			Sulphides	1.06	0.29	0.03	90	
		1100	Oxides	1.18	0.25	0.03	90	
			Sulphides	0.57	0.20	0.02	90	

APPENDIX 2

TABLE 4.9 (cont'd)

Melt	% Sulphur in melt	Rolling Temp. °C	Type of Inclusion	Plasticity index v	S.D.	S.E.	N
A15	0.20	900	Oxides	0.06	0.07	0.01	90
			Sulphides	1.13	0.18	0.02	90
		1000	Oxides	1.42	0.22	0.02	90
			Sulphides	0.84	0.21	0.02	90
		1100	Oxides	1.12	0.14	0.01	90
			Sulphides	0.69	0.21	0.02	90

APPENDIX 2

TABLE 4.10a

HEAT TREATMENT RESULTS

Specimen: A12 (0.1%S) rolled at 900°C : Matrix reduction = 50%

Homogenisation temperature = 900°C

Homogenisation time	Type of inclusion	Mean Plasticity Index \bar{v}	S.D.	S.E.	N
0	Sulphides	1.35	0.26	0.03	92
	Oxides $\sqrt{ab} < 5$	1.05	0.23	0.03	48
	" $5 \leq \sqrt{ab} < 10$	1.33	0.17	0.02	90
	" $\sqrt{ab} \geq 10$	1.55	0.12	0.01	90
30 mins	Sulphides	0.92	0.17	0.02	90
	Oxides $\sqrt{ab} < 5$	0.97	0.20	0.03	45
	" $5 \leq \sqrt{ab} < 10$	1.23	0.18	0.02	90
	" $\sqrt{ab} \geq 10$	1.54	0.12	0.01	92
24 hours	Sulphides	0.79	0.14	0.01	90
	Oxides $\sqrt{ab} < 5$	0.86	0.17	0.03	45
	" $5 \leq \sqrt{ab} < 10$	1.14	0.17	0.02	90
	" $\sqrt{ab} \geq 10$	1.52	0.09	0.01	90
72 hours	Sulphides	0.66	0.17	0.02	90
	Oxides $\sqrt{ab} < 5$	0.75	0.29	0.04	45
	" $5 \leq \sqrt{ab} < 10$	1.10	0.23	0.02	90
	" $\sqrt{ab} \geq 10$	1.43	0.17	0.02	90

TABLE 4.10b

Specimen: A12 (0.1%S)

Homogenisation time = 72 hours

Homogenisation temperature	Type of inclusion	Mean Plasticity Index \bar{v}	S.D.	S.E.	N
1000°C	Sulphides	0.66	0.22	0.02	90
	Oxides $\sqrt{ab} < 5$	0.39	0.18	0.02	90
	" $5 \leq \sqrt{ab} < 10$	0.79	0.26	0.03	90
	" $\sqrt{ab} \geq 10$	1.27	0.16	0.02	90
1100°C	Sulphides	0.59	0.19	0.02	90
	Oxides $\sqrt{ab} < 5$	0.22	0.11	0.01	90
	" $5 \leq \sqrt{ab} < 10$	0.54	0.23	0.02	90
	" $\sqrt{ab} \geq 10$	1.26	0.20	0.02	99

APPENDIX 2

TABLE 4.11a

Specimen: A512 rolled at 900°C : Matrix reduction = 70%

Homogenisation temperature = 900°C

Homogenisation time	Type of inclusion	Mean Plasticity Index \bar{v}	S.D.	S.E.	N
0	Oxides $\sqrt{ab} < 5$	0.13	0.16	0.02	41
	" $5 \leq \sqrt{ab} < 10$	0.21	0.18	0.03	46
	" $\sqrt{ab} \geq 10$	0.28	0.22	0.03	63
72 hours	Oxides $\sqrt{ab} < 5$	0.05	0.08	0.01	91
	" $5 \leq \sqrt{ab} < 10$	0.15	0.19	0.02	90
	" $\sqrt{ab} \geq 10$	0.27	0.22	0.02	90

TABLE 4.11b

Specimen: A112 rolled at 900°C : Matrix reduction = 70%

Homogenisation temperature = 900°C

Homogenisation time	Type of inclusion	Mean Plasticity Index \bar{v}	S.D.	S.E.	N
0	Oxides $\sqrt{ab} < 5$	0.22	0.29	0.04	45
	" $5 \leq \sqrt{ab} < 10$	0.53	0.49	0.07	45
	" $\sqrt{ab} \geq 10$	1.04	0.11	0.02	45
72 hours	Oxides $\sqrt{ab} < 5$	0.14	0.17	0.03	45
	" $5 \leq \sqrt{ab} < 10$	0.43	0.42	0.06	48
	" $\sqrt{ab} \geq 10$	0.96	0.14	0.02	51

APPENDIX 2

TABLE 4.12a

Results of tensile tests on unnotched specimens from the alloys of steel D.

Specimen	% Elongation	% Reduction in area	UTS KN/mm ²
D10 (i)	45	76	355.2
(ii)	45	75	364.5
D11 (i)	44	70	321.2
(ii)	45	70	319.7
D12 (i)	42	65	342.9
D20 (i)	46	80	462.9
D21 (i)	42	68	367.6
(ii)	45	70	362.9
D22 (i)	42	68	344.4
D30 (i)	38	65	418.5
(ii)	40	66	420.1
D31 (i)	42	68	413.9
(ii)	34	66	424.7
D32 (i)	42	65	409.3

TABLE 4.12b

Specimen	Type of specimen	Strain to fracture ϵ_f	UTS (KN/mm ²)
D1*	Longitudinal	0.27	434.5
		0.292	436.2
D1*	Long transverse	0.192	437.3
D1*	'as cast'	0.233	416.7
D4	Longitudinal	0.131	329.2
		0.338	326.1
D4	Long transverse	0.235	324.1
		-	324.1
D4	'as cast'	0.115	118.7

APPENDIX 2

TABLE 4.13

Notch tensile test

Specimen	Notch root radius (r) mms	Stress concentration factor (K_t)	$(K_t - 1)^3$	Notch strength KN/mm ²	Notch strength ratio N.S.R.	Total extension (mms)	% Area of oxides and sulphides
D101	1.02	1.835	0.582	546.9	1.520	1.23	0.48
D102	1.02	1.835	0.582	531.9	1.478	1.30	
D103	1.02	1.840	0.593	531.0	1.476	1.22	
D104	0.26	3.150	9.940	596.5	1.658	1.25	
D105	0.26	3.150	9.940	602.3	1.674	1.30	
D106	0.26	3.100	9.261	609.5	1.694	-	
D107	0.16	3.950	25.670	618.1	1.718	1.26	
D108	0.16	3.950	25.670	619.3	1.721	1.26	
D109	0.16	3.900	24.389	601.8	1.672	1.28	
D111	1.00	1.870	0.650	451.3	1.408	1.26	0.739
D112	1.00	1.850	0.600	413.7	1.291	1.20	
D113	1.00	1.850	0.600	477.8	1.491	1.00	
D114	0.26	3.150	9.940	528.4	1.649	0.90	
D115	0.26	3.150	9.940	532.1	1.660	1.10	
D116	0.26	3.200	10.650	475.2	1.483	0.90	
D117	0.16	3.950	25.670	658.0	2.053	0.65	
D118	0.16	4.00	27.00	497.7	1.553	1.15	
D119	0.16	3.900	24.390	523.1	1.633	1.15	
D121	1.00	1.840	0.593	490.3	1.430	0.90	
D122	1.00	1.840	0.593	485.7	1.417	0.47	
D123	1.00	1.835	0.582	506.2	1.477	0.90	
D124	0.26	3.100	9.261	543.1	1.584	0.61	
D125	0.26	3.150	9.940	411.6	1.201	0.60	
D126	0.26	3.150	9.940	544.3	1.588	0.60	
D127	0.16	3.950	25.670	572.1	1.669	0.73	
D128	0.16	4.00	27.000	536.9	1.566	0.90	

APPENDIX 2

TABLE 4.13 (cont'd)

Specimen	Notch root radius (r) mms	Stress concentration factor (K_t)	$(K_t - 1)^3$	Notch strength KN/mm ²	Notch strength ratio N.S.R.	Total extension (mms)	% Area of oxides and sulphides
D201	1.02	1.835	0.582	540.6	1.490	1.40	0.311
D202	1.02	1.840	0.593	454.1	1.251	1.45	
D203	1.02	1.835	0.582	546.9	1.507	1.37	
D204	0.26	3.150	9.940	597.8	1.647	1.50	
D205	0.26	3.180	10.360	579.4	1.596	1.50	
D206	0.18	3.670	19.034	629.2	1.734	1.50	
D207	0.18	3.670	19.034	636.7	1.754	1.50	
D208	0.18	3.690	19.465	615.7	1.696	1.40	
D211	1.00	1.850	0.614	554.9	1.519	1.10	0.814
D212	1.00	1.850	0.614	535.8	1.467	1.07	
D213	1.00	1.845	0.603	562.8	1.541	1.00	
D214	0.26	3.100	9.261	628.0	1.719	0.91	
D215	0.26	3.150	9.940	597.7	1.637	0.93	
D216	0.26	3.100	9.261	597.2	1.635	0.92	
D217	0.16	4.000	27.000	626.5	1.715	0.71	
D218	0.16	3.950	25.672	613.0	1.678	0.90	
D221	1.00	1.830	0.572	532.6	1.546	0.92	1.173
D222	1.00	1.840	0.593	496.4	1.442	1.08	
D223	1.00	1.840	0.593	516.1	1.499	1.05	
D224	0.26	3.150	9.940	555.7	1.614	0.80	
D225	0.26	3.150	9.940	559.6	1.625	0.81	
D226	0.26	3.150	9.940	562.4	1.633	0.80	
D227	0.16	3.950	25.672	561.2	1.630	0.76	
D228	0.16	4.000	27.000	557.2	1.618	0.90	
D229	0.16	4.000	27.000	562.7	1.634	0.98	

APPENDIX 2

TABLE 4.13 (cont'd)

Specimen	Notch root radius (r) mms	Stress concentration factor (K_t)	$(K_t - 1)^3$	Notch strength KN/mm ²	Notch strength ratio N.S.R.	Total extension. (mm)	% Area of oxides and sulphides
D301	1.00	1.840	0.593	654.2	1.560	1.46	0.403
D302	1.00	1.850	0.614	619.3	1.477	1.50	
D303	0.26	3.100	9.261	725.4	1.730	1.46	
D304	0.26	3.150	9.940	688.2	1.641	1.46	
D305	0.26	3.100	9.261	754.3	1.799	-	
D306	0.16	3.900	24.389	761.6	1.817	1.35	
D307	0.18	3.750	20.797	669.6	1.597	1.46	
D308	0.16	4.000	27.000	660.8	1.576	1.35	
D311	1.00	1.860	0.636	626.8	1.495	0.93	0.604
D312	1.00	1.850	0.614	627.7	1.497	1.05	
D313	0.26	3.100	9.261	707.9	1.688	1.04	
D314	0.26	3.100	9.261	729.9	1.741	0.84	
D315	0.26	3.150	9.940	710.8	1.695	0.93	
D316	0.16	3.950	25.672	749.6	1.788	0.84	
D317	0.16	4.000	27.000	716.8	1.710	0.80	
D321	1.02	1.835	0.582	639.1	1.562	0.71	
D322	1.02	1.838	0.588	-	-	-	
D323	1.02	1.835	0.582	636.7	1.556	0.63	
D324	0.26	3.18	10.360	713.6	1.744	0.60	
D325	0.26	3.19	10.503	686.7	1.678	0.57	
D326	0.26	3.18	10.360	721.3	1.763	0.55	
D327	0.18	3.70	19.683	735.7	1.798	0.63	
D328	0.18	3.73	20.346	697.9	1.705	0.55	
D329	0.18	3.73	20.346	699.1	1.708	0.61	

APPENDIX 2

TABLE 4.13 (cont'd)

Specimen	Notch root radius (r) mms	Stress concentration factor (K_t)	$(K_t - 1)^3$	Notch strength, KN/mm ²	Notch strength ratio	Strain to fracture ϵ_f
D1* Longitudinal	0.125	4.55	44.74	725.4	1.666	0.318
	0.125	4.55	44.74	746.6	1.714	0.385
	0.125	4.25	34.33	738.5	1.696	0.399
	0.150	4.10	29.79	736.3	1.691	0.338
	0.175	3.90	24.39	673.9	1.548	0.311
	0.250	3.30	12.17	697.0	1.601	0.327
D1* Long Transverse	0.125	4.40	39.30	709.2	1.622	0.238
	0.150	4.20	32.77	708.3	1.620	0.268
	0.150	4.20	32.77	706.6	1.616	0.300
	0.175	3.90	24.39	664.9	1.520	0.265
	0.230	3.30	12.17	626.4	1.432	0.250
D1* 'As cast'	0.125	4.60	46.66	672.2	1.613	0.230
	0.140	4.30	35.94	597.9	1.435	0.158
	0.150	4.30	35.94	657.6	1.578	0.221
	0.150	4.25	34.33	661.8	1.588	0.246
	0.175	3.90	24.39	658.1	1.579	0.205
	0.45	2.70	4.913	530.0	1.272	0.260
D4 Longitudinal	0.125	4.55	44.74	406.3	1.240	0.200
	0.125	4.55	44.74	480.2	1.466	0.289
	0.15	4.20	32.77	473.4	1.445	0.301
	0.16	4.00	27.00	458.4	1.399	0.255
	0.25	3.30	12.17	460.8	1.406	0.232
	0.25	3.30	12.17	-	-	-

APPENDIX 2

TABLE 4.13 (cont'd)

Specimen	Notch root radius (r)mms	Stress concentration factor (K_t)	$(K_t - 1)^3$	Notch strength KN/mm ²	Notch strength ratio	Strain to fracture ϵ_f
D4 Long Transverse	0.125	4.55	44.74	417.8	1.289	0.167
	0.150	4.20	32.77	402.5	1.242	0.157
	0.175	3.90	24.39	434.5	1.341	0.182
	0.175	3.90	24.39	501.9	1.549	0.247
	0.230	3.40	13.82	470.0	1.450	0.206
D4 'As cast'	0.15	4.20	32.77	321.2	1.702	0.066
	0.15	4.25	34.33	376.1	1.993	-
	0.175	3.85	23.15	360.3	1.909	-
	0.45	2.70	4.91	286.2	1.517	-
	0.55	2.50	3.38	257.2	1.363	-

APPENDIX 2

TABLE 4.14a

Verification of the Polynomial A(r)

Specimen	%Sulphur content	Values of A(r) for different notch radii			
		r=1.00mm	R=0.26mm	r=0.18mm	r=0.16mm
D1	0.02	12.71	1.04	-	0.45
D1	0.10	12.71	1.00	-	0.42
D1	0.20	12.71	0.96	-	0.36
D2	0.02	12.71	0.93	0.58	-
D2	0.10	14.30	1.05	-	0.40
D2	0.20	14.30	1.02	-	0.36
D3	0.02	14.30	1.23	-	0.41
D3	0.10	14.30	1.11	-	0.42
D3	0.20	14.30	1.07	0.53	-

APPENDIX 2

TABLE 4.14b

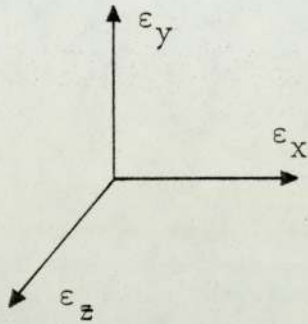
Specimen	Values of A(r) for different notch radii							Inclusion strain, ϵ_i
	r=0.125 mm	r=0.150 mm	r=0.16 mm	r=0.175 mm	r=0.23 mm	r=0.25 mm	r=0.45 mm	
D1* 'as cast'	0.414	0.537	-	0.753	-	-	2.006	0.00
D1* Long Transverse	0.488	0.583	-	0.687	1.183	-	-	1.21
D1* Longitudinal	0.466	0.707	-	0.727	-	1.570	-	0.70
D4 'As cast'	-	1.045	-	1.111	-	-	3.487	-
D4 Long transverse	0.226	0.268	-	0.471	1.063	-	-	-
D4 Longitudinal	0.344	0.454	0.499	-	-	1.120	-	-

APPENDIX 3

WARDLE'S (100) EQUATIONS

Variation in v with respect to the plane of measurement

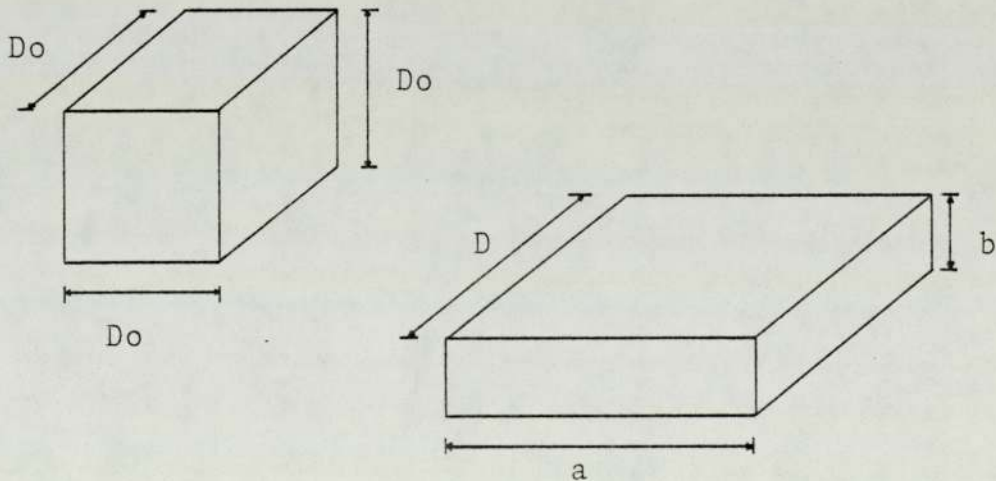
Consider the case of homogeneous deformation such that an applied strain ϵ_y results in the two strains ϵ_x and ϵ_z which may have values $0 \rightarrow \epsilon_y$.



i.e. $\epsilon_y = \epsilon_x + \epsilon_z$
 ϵ_y is the largest strain
 $\epsilon_z \rightarrow 0$

Now consider a block of material of volume D_0^3 being deformed to a parallelepiped of axial lengths a, b, D , assuming also that there is no volume change.

i.e.



Const. vol. $D_0^3 = aD$

True strains may now be given for each of the directions X, Y, Z as

$$\epsilon_x = \ln \frac{a}{D_0}, \quad \epsilon_z = \ln \frac{D}{D_0}, \quad \text{and} \quad \epsilon_y = \ln \frac{D_0}{b}$$

$$\text{i.e.} \quad \ln \frac{a}{D_0} + \ln \frac{D}{D_0} - \ln \frac{D_0}{b} = 0$$

Considering each of the planes on which strains act

$$(XZ) : \epsilon_X \text{ and } \epsilon_Z : \left[\ln \frac{a}{D_0} + \ln \frac{D}{D_0} \right]$$

$$(YZ) : \epsilon_Y \text{ and } \epsilon_Z : \left[\ln \frac{D_0}{b} + \ln \frac{D}{D_0} \right]$$

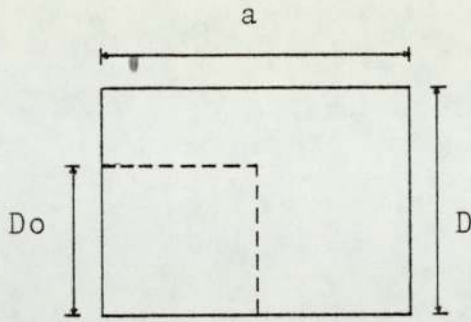
$$(XY) : \epsilon_X \text{ and } \epsilon_Y : \left[\ln \frac{a}{D_0} + \ln \frac{D_0}{b} \right]$$

For non plane strain in terms of physical measurement D_0 cannot be found and aspect ratios involving other axial lengths can only be measured, i.e.

$$\begin{aligned} (XZ) \quad \text{plane} \quad \lambda(XZ) &= a/D \\ (YZ) \quad \text{plane} \quad \lambda(YZ) &= D/b \\ (XY) \quad \text{plane} \quad \lambda(XY) &= a/b \end{aligned}$$

Now consider the relationships between the quantity which can physically be measured, and the strains present on each of the plane.

(XZ) plane

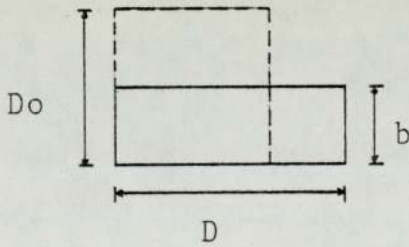


$$\ln \frac{a}{D_0} = \ln \frac{a}{D} + \ln \frac{D}{D_0}$$

i.e. $\epsilon_X = \ln \lambda(XZ) + \epsilon_Z$

$\ln \lambda(XZ) = \epsilon_X - \epsilon_Z$ (i)

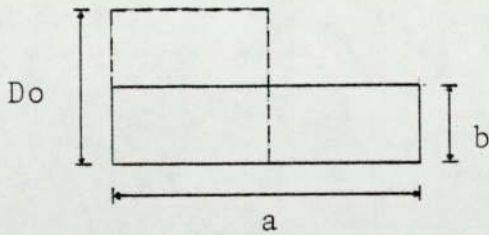
(YZ) plane



$$\ln \frac{D}{b} = \ln \frac{D_0}{b} + \ln \frac{D}{D_0}$$

$\ln \lambda(YZ) = \epsilon_Y + \epsilon_Z$ (ii)

(XY) plane



$$\ln \frac{a'}{b'} = \ln \frac{a'}{D_0} + \ln \frac{D_0}{b}$$

$$\therefore \underline{\underline{\ln \lambda(XY) = \epsilon_X + \epsilon_Y}} \quad \text{(iii)}$$

Taking the limiting case of plane strain $\epsilon_Z = 0$

$$\therefore \epsilon_X = \epsilon_Y$$

(XZ) plane

$$\ln \lambda(XZ) = \epsilon_X - 0 = \epsilon_X = \epsilon_Y$$

(YZ) plane

$$\ln \lambda(YZ) = \epsilon_Y + 0 = \epsilon_Y$$

(XY) plane

$$\ln \lambda(XY) = \epsilon_X + \epsilon_Y = 2\epsilon_Y$$

Estimates of the strain ϵ_Y^1 by measurements on any of the section planes are:

$$\epsilon_Y^1 (XZ) = \ln \lambda(XZ) \quad \text{(iv)}$$

$$\epsilon_Y^1 (YZ) = \ln \lambda(YZ) \quad \text{(v)}$$

$$\epsilon_Y^1 (XY) = \frac{1}{2} \ln \lambda(XY) \quad \text{(vi)}$$

All equal
under P_ϵ
conditions.

These estimates are in fact the equations which are used in practice for measuring inclusion strains during rolling, where plane strain is assumed.

When inclusion strains are measured on the false assumption that plane strain exists, the resultant measured quantities termed ϵ_Y^1 () may be related to the linear strains ϵ_X , ϵ_Y and ϵ_Z , i.e.

$$\epsilon_Y^1(XZ) = \epsilon_X - \epsilon_Z \quad (\text{vii})$$

$$\epsilon_Y^1(YZ) = \epsilon_Y + \epsilon_Z \quad (\text{viii})$$

$$\epsilon_Y^1(XY) = \frac{1}{2}(\epsilon_X + \epsilon_Y) \quad (\text{ix})$$

$$\epsilon_Y^1(XZ) = \epsilon_Y^1(YZ) = \epsilon_Y^1(XY) = \epsilon_Y$$

in the limiting case of P_ϵ when $\epsilon_Z = 0$ & $\epsilon_X = \epsilon_Y$.

From the above equations it also follows that $\epsilon_Y^1(XY)$ may be estimated from measurements of $\epsilon_Y^1(XZ)$ and $\epsilon_Y^1(YZ)$, i.e.

$$\begin{aligned} \epsilon_Y^1(XY) &= \frac{1}{2}(\epsilon_X + \epsilon_Y) \\ &= \frac{1}{2} \left(\left[\epsilon_Y^1(XZ) + \epsilon_Z \right] + \left[\epsilon_Y^1(YZ) - \epsilon_Z \right] \right) \end{aligned}$$

$$\therefore \epsilon_Y^1(XY) = \frac{1}{2}(\epsilon_Y^1(XZ) + \epsilon_Y^1(YZ)) \quad (\text{x})$$

Estimation of width spread (ϵ_Z)

Taking the general case for the estimation of ϵ_Y from measurements on the (XY) plane, using the equations which assume plane strain, i.e. (vi)

$$\epsilon_Y^1 (XY) = \frac{1}{2} \ln \lambda (XY) = \frac{1}{2} \ln \frac{a}{b}$$

Constant volume $D_0^3 = abD$

$$\begin{aligned} \therefore \epsilon_Y^1 (XY) &= \frac{1}{2} \ln \left(\frac{D_0^3}{DbZ} \right) \\ &= \frac{1}{2} \ln \left(\frac{D_0}{b} \right)^2 + \frac{1}{2} \ln \frac{D_0}{D} \end{aligned}$$

i.e. $\epsilon_Y^1 (XY) = \epsilon_Y - \frac{1}{2} \epsilon_Z$ (xi)

Also

$$\epsilon_Y^1 (XZ) = \epsilon_X - \epsilon_Z \quad \text{(vii)}$$

but $\epsilon_X = 2\epsilon_Y^1 (XY) - \epsilon_Y$ from eqn. (ix)

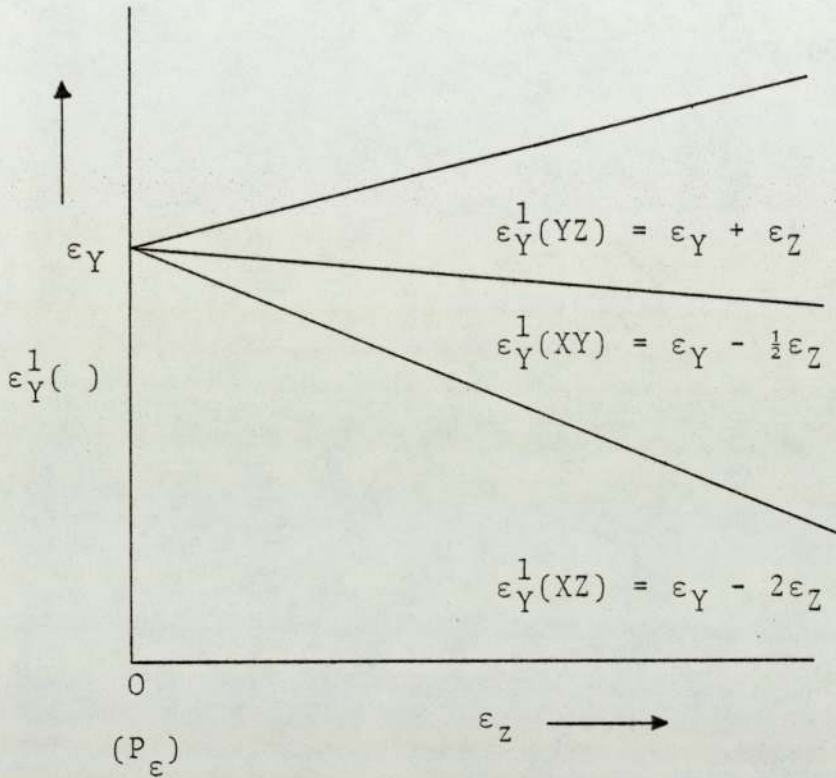
$$\therefore \epsilon_Y^1 (XZ) = 2\epsilon_Y^1 (XY) - \epsilon_Y - \epsilon_Z$$

and $\epsilon_Y^1 (XY) = \epsilon_Y - \frac{\epsilon_Z}{2}$ from eqn. (xi)

$$\therefore \epsilon_Y^1 (XZ) = 2 \left(\epsilon_Y - \frac{\epsilon_Z}{2} \right) - \epsilon_Y - \epsilon_Z$$

i.e. $\epsilon_Y^1 (XZ) = \epsilon_Y - 2\epsilon_Z$ (xii)

Graphically the variation of the measured estimates of ϵ_Y ($\epsilon_Y^1(\)$) for conditions moving away from plane strain are:



from which it is observed that as ϵ_Z increases $\epsilon_Y^1(YZ)$ increases but both $\epsilon_Y^1(XY)$ and $\epsilon_Y^1(XZ)$ decrease.

Estimating ϵ_Z from measurements of $\epsilon_Y^1(XY)$ and $\epsilon_Y^1(YZ)$

Combining equations (viii) and (xi)

$$\epsilon_Y^1(YZ) - \epsilon_Z = \epsilon_Y^1(XY) + \frac{\epsilon_Z}{2}$$

$$\therefore \epsilon_Z = \frac{2}{3} \left[\epsilon_Y^1(YZ) - \epsilon_Y^1(XY) \right] \quad \text{(xiii)}$$

Similarly for the planes $\epsilon_Y^1(XY)$ and $\epsilon_Y^1(XZ)$

Combining equations (xii) and (xi)

$$\begin{aligned} \epsilon_Y^1(XZ) + 2 \epsilon_Z &= \epsilon_Y^1(XY) + \frac{\epsilon_Z}{2} \\ \therefore \epsilon_Z &= \frac{2}{3} \left[\epsilon_Y^1(XY) - \epsilon_Y^1(XZ) \right] \quad \text{(xiv)} \end{aligned}$$

and for $\epsilon_Y^1(XZ)$ and $\epsilon_Y^1(YZ)$

Combining equations (xii) and (viii)

$$\begin{aligned} \epsilon_Y^1(XZ) + 2\epsilon_Z &= \epsilon_Y^1(YZ) - \epsilon_Z \\ \therefore \epsilon_Z &= \frac{1}{3} \left[\epsilon_Y^1(YZ) - \epsilon_Y^1(XZ) \right] \quad \text{(xv)} \end{aligned}$$

Thus it can be seen clearly that by measuring any two strain estimates, the width strain ϵ_Z may be determined.

Derivation of a plane strain corrected plasticity index

From the preceding section it is obvious that measurements of $\epsilon_Y^1()$ on the (XY) plane will vary and become smaller as the amount of width spread increases.

However, by making measurements either on the (XZ) or the (YZ) plane the value of $\epsilon_Y^1(XY)$ at $\epsilon_Z = 0$ may be determined, i.e. $\epsilon_Y (P_\epsilon)$

From equation (xi)

$$\begin{aligned} \epsilon_Y^1(XY) &= \epsilon_Y - \frac{\epsilon_Z}{2} \\ \therefore \epsilon_Y &= \epsilon_Y^1(XY) + \frac{\epsilon_Z}{2} \end{aligned}$$

Now under normal circumstances the relative plasticity index is given by $v = \epsilon_i / \epsilon_m$, i.e. the strain of the inclusion to the overall strain of the matrix. ϵ_Y is the only strain which is a dependent variable.

It is sensible to measure the matrix strain in the Y direction. i.e. ϵ_{mY} .

$$v_{P\epsilon} = \frac{\epsilon_Y}{\epsilon_{mY}} \text{ for } P_\epsilon \text{ conditions } \left(\epsilon_{mY} = \ln \frac{h_0}{h_f} \right)$$

where plane strain conditions do not operate

$$\underline{\underline{v_{P\epsilon}^* = \frac{\epsilon_Y^1(XY)}{\epsilon_{mY}} + \frac{\epsilon_Z}{2\epsilon_{mY}}}} \quad \text{(xvi)}$$

Now earlier in equation (xiii) ϵ_Z was defined for the (XY) and (YZ) planes as

$$\epsilon_Z = \frac{2}{3} \left[\epsilon_Y^1(YZ) - \epsilon_Y^1(XY) \right]$$

and substituting into equation (xvi)

$$\begin{aligned} v_{P\epsilon}^* &= \frac{\epsilon_Y^1(XY)}{\epsilon_m} + \frac{\epsilon_Y^1(YZ) - \epsilon_Y^1(XY)}{3\epsilon_m} \\ \underline{\underline{v_{P\epsilon}^* &= \frac{2\epsilon_Y^1(XY) + \epsilon_Y^1(YZ)}{3\epsilon_m}}} \quad \text{(xvii)} \end{aligned}$$

A similar expression may also be arrived at for $\epsilon_Y^1(XY)$ and $\epsilon_Y^1(XZ)$.

i.e.

$$v_{P\epsilon}^* = \frac{\epsilon_Y^1(XY)}{\epsilon_m} + \frac{\epsilon_Y^1(XY) - \epsilon_Y^1(XZ)}{3\epsilon_m}$$

$$\therefore v_{P\epsilon}^* = \frac{4\epsilon_Y^1(XY) - \epsilon_Y^1(XZ)}{3\epsilon_m} \quad \text{(xviii)}$$

and

$$v_{P\epsilon}^* = \frac{\epsilon_Y^1(XY)}{\epsilon_m} + \frac{\epsilon_Y^1(YZ) - \epsilon_Y^1(XZ)}{6\epsilon_m}$$

but $\epsilon_Y^1(XY) = \frac{\epsilon_Y^1(YZ) + \epsilon_Y^1(XZ)}{2}$

$$\therefore v_{P\epsilon}^* = \frac{2\epsilon_Y^1(YZ) + \epsilon_Y^1(XZ)}{3\epsilon_m} \quad \text{(xix)}$$

APPENDIX 3(a)

Summary of the more useful equations used for the measurement of strains on the various planes

Physical quantities measured are $\lambda(XY)$, $\lambda(YZ)$, $\lambda(XZ)$.

Quantities calculated are the values

$$\epsilon_Y^1(XY) = \frac{1}{2} \ln \lambda(XY)$$

$$\epsilon_Y^1(YZ) = \ln \lambda(YZ)$$

$$\epsilon_Y^1(XZ) = \ln \lambda(XZ)$$

Planes	$\epsilon_Z^1 =$	ϵ_Y Estimate (Plain Strain)
$[(XY):(YZ)]^+$	$\frac{2}{3}[\epsilon_Y^1(YZ) - \epsilon_Y^1(XY)]$	$\frac{1}{3}[2\epsilon_Y^1(XY) + \epsilon_Y^1(YZ)]$
$[(XY):(XZ)]$	$\frac{2}{3}[\epsilon_Y^1(XY) - \epsilon_Y^1(XZ)]$	$\frac{1}{3}[4\epsilon_Y^1(XY) - \epsilon_Y^1(XZ)]$
$[(YZ):(XZ)]$	$\frac{1}{3}[\epsilon_Y^1(YZ) - \epsilon_Y^1(XZ)]$	$\frac{1}{3}[2\epsilon_Y^1(YZ) + \epsilon_Y^1(XZ)]$

+ preferred measurement planes

Also

$$\epsilon_Y^1(XY) = \frac{\epsilon_Y^1(XZ) + \epsilon_Y^1(YZ)}{2}$$

APPENDIX 4

THE CALCULATION OF THEORETICAL TEMPERATURE RISE DURING ROLLING

In Fig. 163, the influence of ingoing thickness upon the mean rate of deformation is shown. From the diagram it can be observed that when the ingoing thickness changes from 24.13 mm to 2.54 mm the mean rate of deformation changes from 2.88 to 8.80 at constant reduction of 10%.

Using the equation below, the resistance to homogeneous deformation, σ , can be calculated by using known values of n and σ_0 .

$$\sigma = \sigma_0 \dot{\epsilon}^n$$

where σ_0 = the stress associated with a rate of deformation equal to unity, n is the strain rate sensitivity index, and $\dot{\epsilon}$ is the mean rate of deformation.

Values of strain rate sensitivity index, and σ_0 , determined by Alder and Phillips (203), at 10% reduction and temperature of 1000°C for 0.17% carbon steel used

$$n = 0.108, \quad \sigma_0 = 89.6 \text{ MN m}^{-2}$$

Inserting these values in the above equation, the resistance to homogeneous deformation can be calculated:

Ingoing thickness	% reduction	$\dot{\epsilon}$	$\dot{\epsilon}^n$	$\sigma = \sigma_0 \dot{\epsilon}^n (\text{MN m}^{-2})$
24.13 mm	10	2.88	1.121	100.4
2.54 mm	10	8.80	1.265	113.3

Rolling load, P , can be defined as

$$P = \sigma b \sqrt{R(h_1 - h_2)} \cdot Q$$

where σ = resistance to homogeneous deformation
 b = width of material
 R = radius of rolls
 h_1 = ingoing thickness
 h_2 = outgoing thickness
 Q = factor, which is dependent on % reduction
and R/h_2

If $R = 102.5$ mm

When the ingoing thickness is 24.13 mm, for 10% reduction the value of $Q = 0.948$; for 2.54 mm ingoing thickness, for 10% reduction the value of $Q = 1.337$. The Q values are quoted from tables in 'The rolling of Strip, Sheet, and Plate' by Larke (200).

Work done per revolution = $4\pi aP = 4\pi a\sigma b\sqrt{R(h_1-h_2)} Q$
where a = lever arm, all other symbols are as stated previously.

Theoretical temperature rise can be defined as

$$\Delta T = \frac{4\pi aP}{PVS}$$

where P = density, S = specific heat, and V = volume of material.

However, the volume, V , rolled in one revolution is

$$V = 2\pi Rbh_2$$

$$\therefore \Delta T = \frac{4\pi aP}{PVS} = \frac{4\pi aP}{PS2\pi Rbh_2} = \frac{2aP}{PSRbh_2}$$

assuming that $a = \frac{1}{3}\sqrt{R(h_1-h_2)}$

then

$$\Delta T = \frac{2aP}{PSRbh_2} = \frac{2/\sqrt[3]{R(h_1-h_2)} \cdot \sigma b \sqrt{R(h_1-h_2)} Q}{PS Rh_2 b}$$

Hence, when the ingoing thickness is 24.13 mm at 10% reduction, $h_2 = 21.717$ mm, $P = 7870 \text{ Kgm}^{-3}$, $S = 150 \text{ J Kg}^{-1}\text{K}^{-1}$.
 $Q = 0.948$

$$\therefore \Delta T = 5.97^\circ\text{C}$$

when the ingoing thickness is 2.54 mm at 10% reduction, $h_2 = 2.286$, $P = 7870 \text{ Kgm}^{-3}$, $S = 150 \text{ J Kg}^{-1}\text{K}^{-1}$, $Q = 1.337$

$$\therefore \Delta T = 9.51^\circ\text{C}$$

The temperature rise calculated is the temperature rise for one revolution.

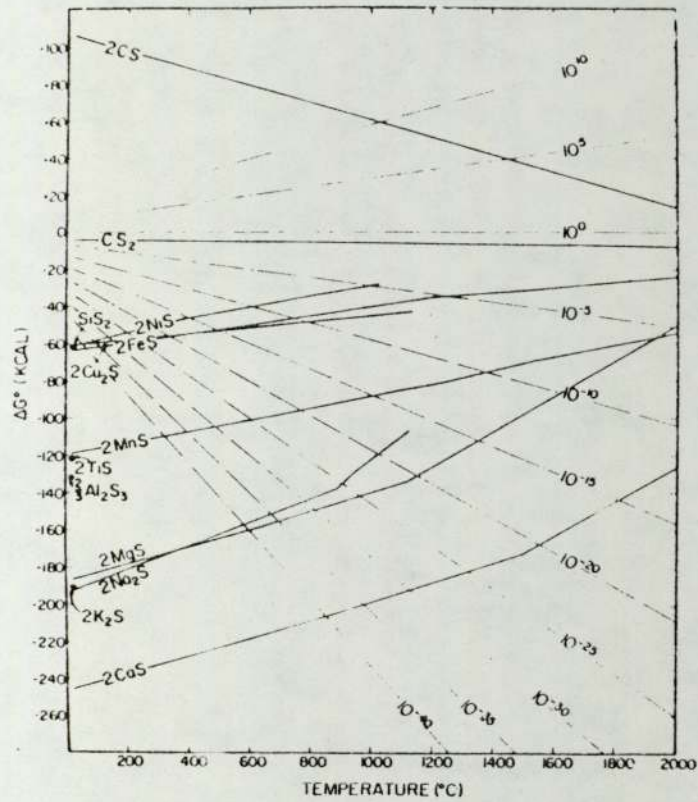


FIGURE 2 : STANDARD FREE ENERGIES OF FORMATION ΔG° (K Cal) FOR VARIOUS SULPHIDES OF THE ELEMENTS AS A FUNCTION OF TEMPERATURE.

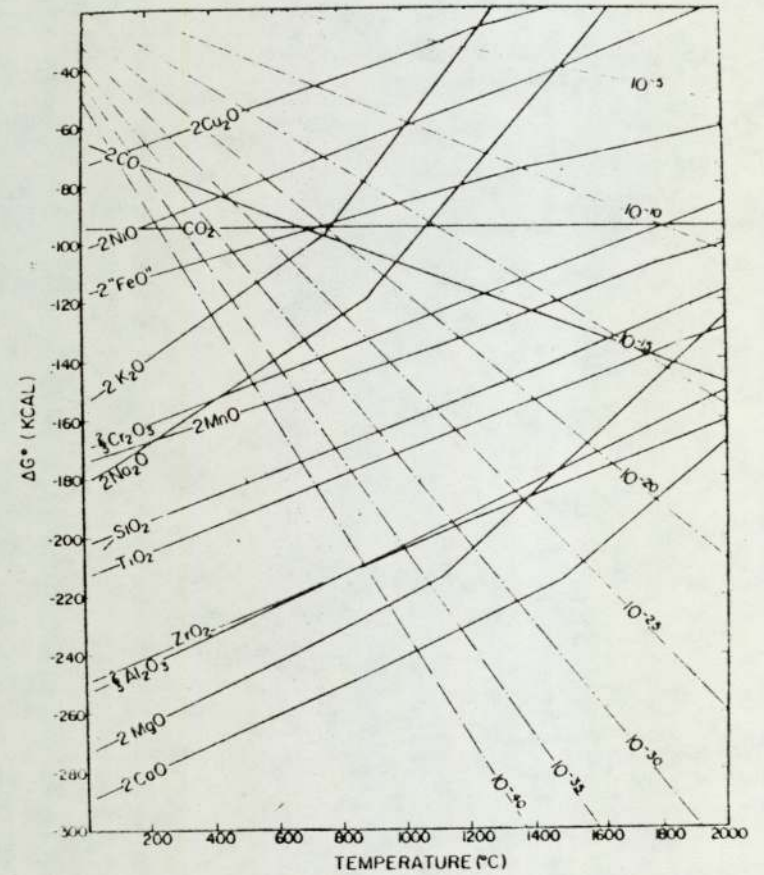


FIGURE 1 : STANDARD FREE ENERGIES OF FORMATION ΔG° (K Cal) FOR VARIOUS OXIDES OF THE ELEMENTS AS A FUNCTION OF TEMPERATURE.

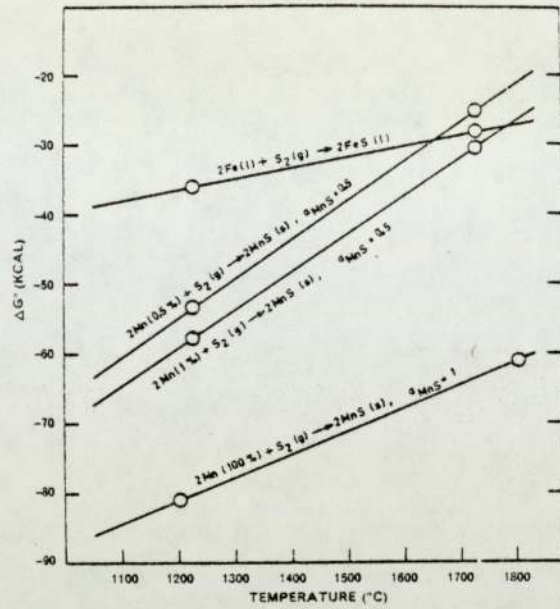


FIGURE 3 : FREE ENERGY OF FORMATION $\Delta G = RT \ln P_{\text{S}_2}$ FOR THE REACTION $2\text{Mn}(\%) + \text{S}_2 \rightarrow 2\text{MnS}(s)$ AS A FUNCTION OF TEMPERATURE

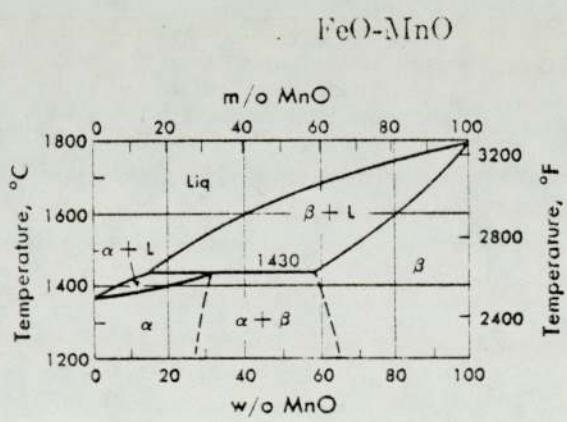


FIGURE 4 : THE FeO - MnO BINARY PHASE DIAGRAM.

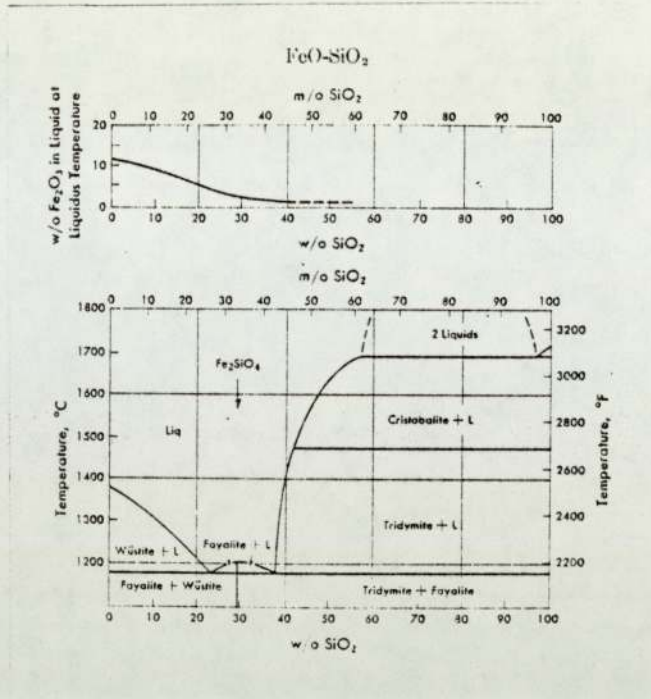


FIGURE 5 : THE FeO - SiO₂ PSEUDO-BINARY PHASE DIAGRAM.

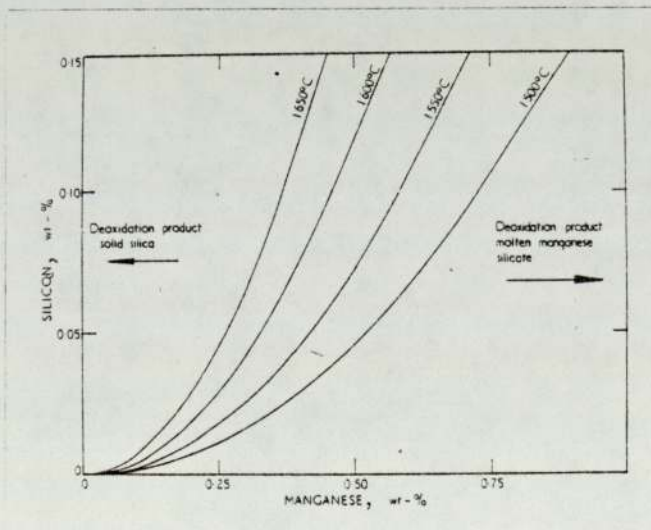


FIGURE 6A : CRITICAL Si AND Mn CONTENTS OF STEEL IN EQUILIBRIUM WITH SILICA-SATURATED DEOXIDATION PRODUCT (MANGANESE SILICATE) AT DIFFERENT TEMPERATURES.

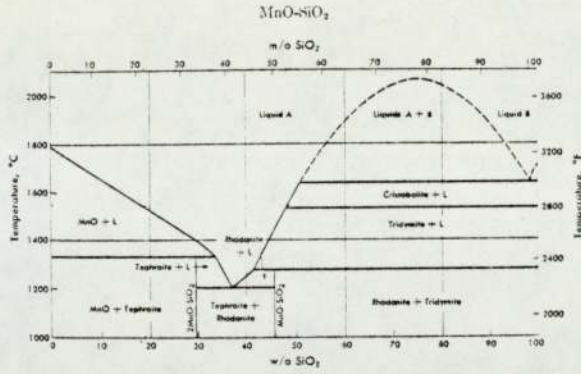


FIGURE 6B : THE MnO - SiO₂ PSEUDO-BINARY PHASE DIAGRAM

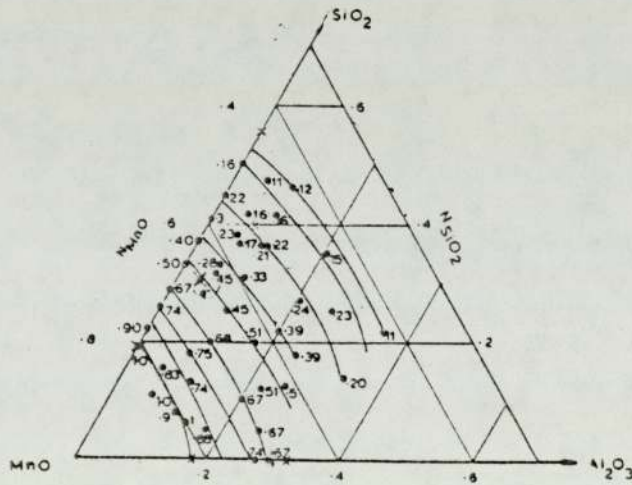


FIGURE 7 : ACTIVITY OF MnO in MnO - SiO₂ - Al₂O₃ PSEUDO - TERNARY SYSTEM, RELATIVE TO PURE SOLID.

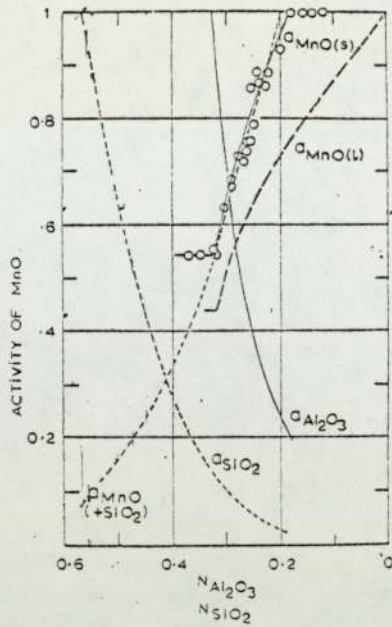


FIGURE 8 : ACTIVITIES IN BINARY OXIDE MELTS

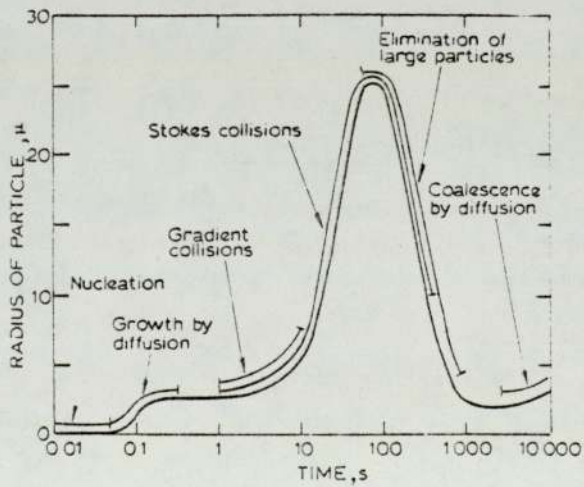


FIGURE 9 : CHARACTERISTIC DIMENSIONS OF SILICA PARTICLES DURING DEOXIDATION

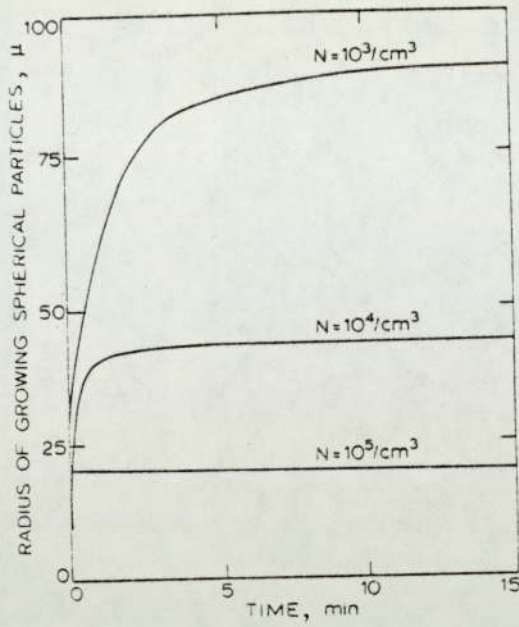


FIGURE 10 : EFFECT OF NUMBER OF NUCLEI ON THE GROWTH RATE

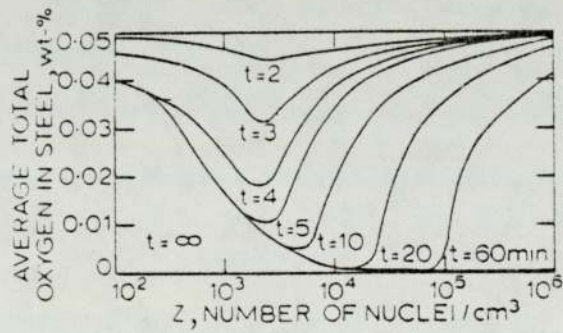


FIGURE 11 : CALCULATED DATA ON AVERAGE TOTAL OXYGEN CONTENT OF STEEL AS FUNCTIONS OF NUMBER OF NUCLEI/ cm^3 IN STAGNANT LIQUID STEEL AND HOLDING TIME AFTER DEOXIDISER ADDITIONS AND DEPTH OF LIQUID STEEL (41)

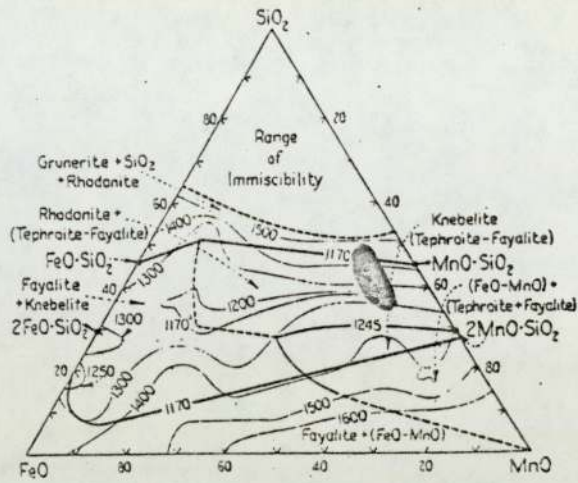


FIGURE 12 : THE $\text{FeO} - \text{MnO} - \text{SiO}_2$ PHASE DIAGRAM

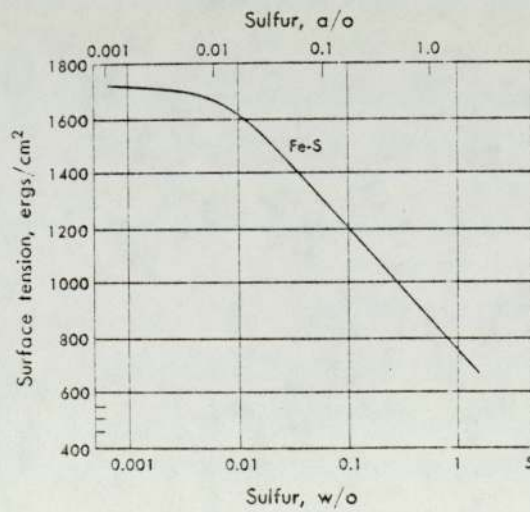


FIGURE 13A : EFFECT OF SULPHUR ON THE SURFACE TENSION OF LIQUID IRON AT 1570°C

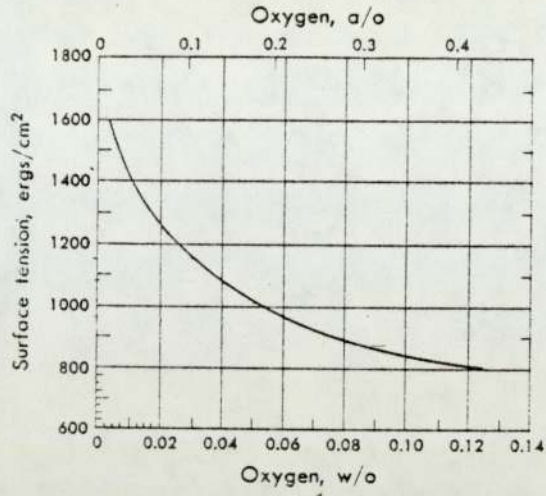


FIGURE 13B : EFFECT OF OXYGEN ON THE SURFACE TENSION OF LIQUID IRON AT 1550°C

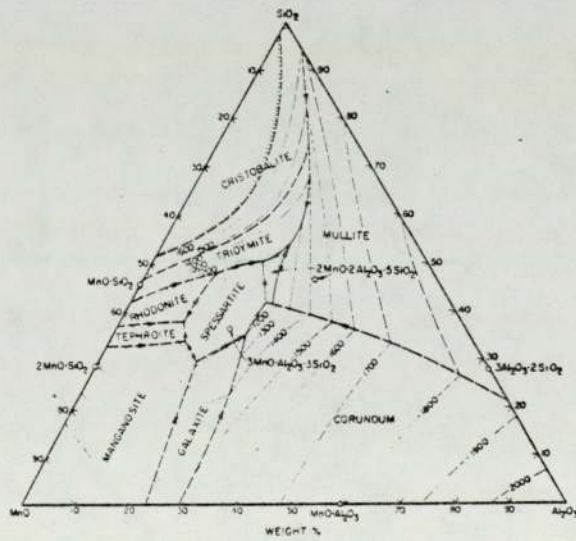


FIGURE 14 : THE $MnO - SiO_2 - Al_2O_3$ PSEUDO-TERNARY PHASE DIAGRAM

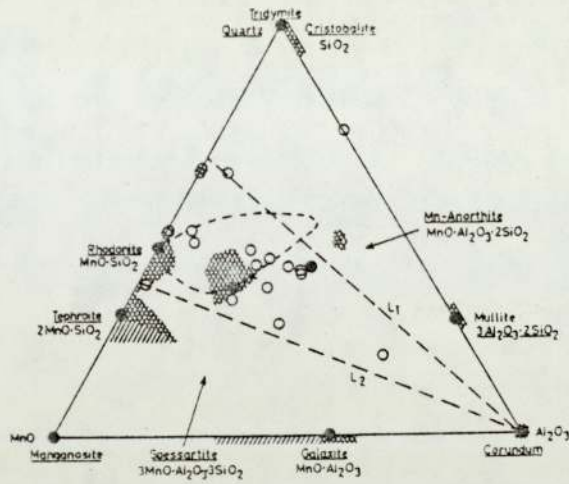


FIGURE 15 : SUMMARY OF THE OCCURRENCE AND HOMOGENEITY RANGES FOR THE DIFFERENT PHASES IN THE $\text{MnO} - \text{SiO}_2 - \text{Al}_2\text{O}_3$ SYSTEM (3)

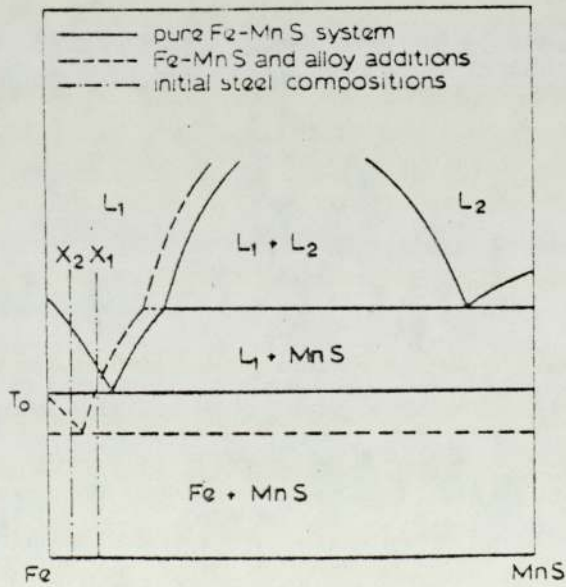


FIGURE 16A : Fe - MnS PSEUDO-BINARY PHASE DIAGRAM (89)

Robinson's definition of true relative plasticity index

FIG.17a

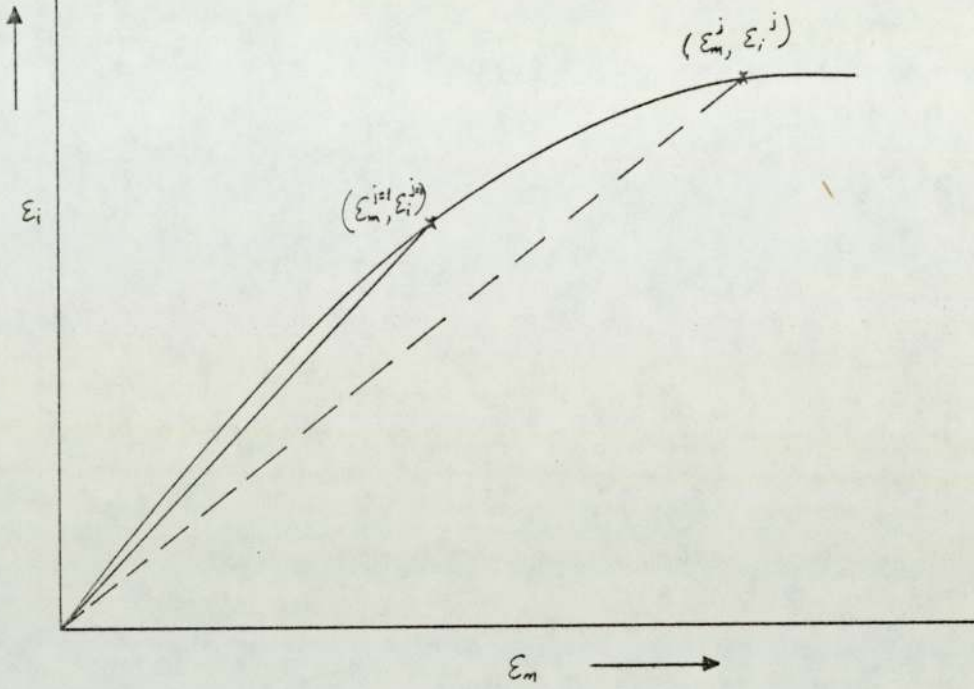
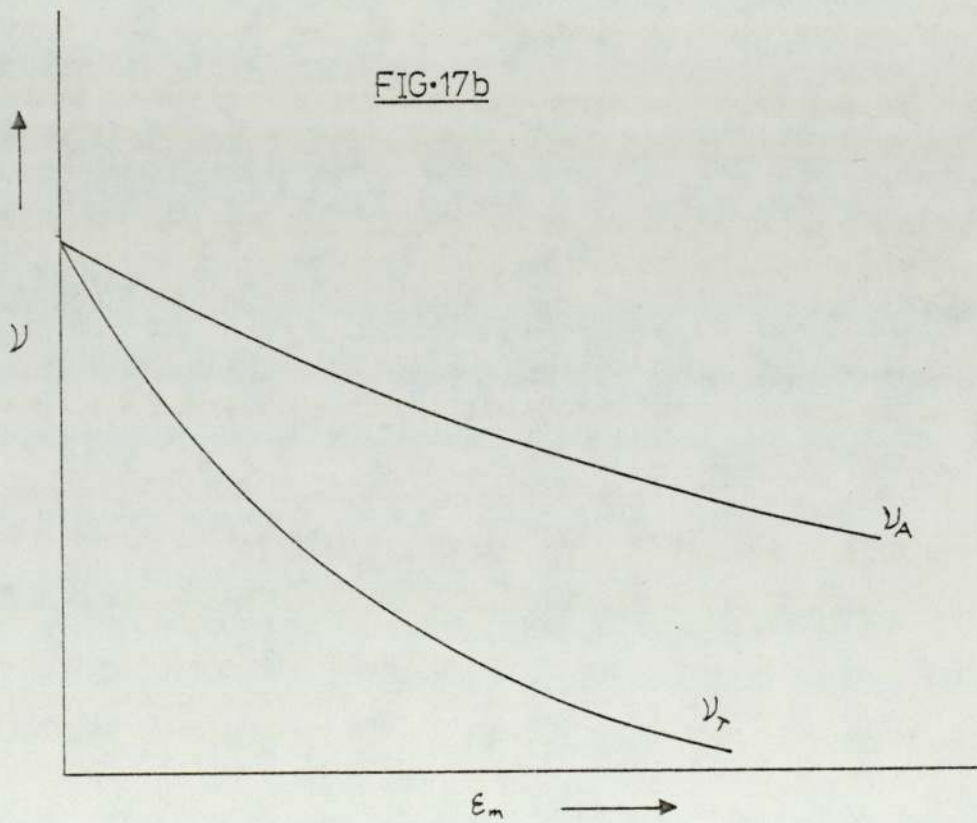


FIG.17b



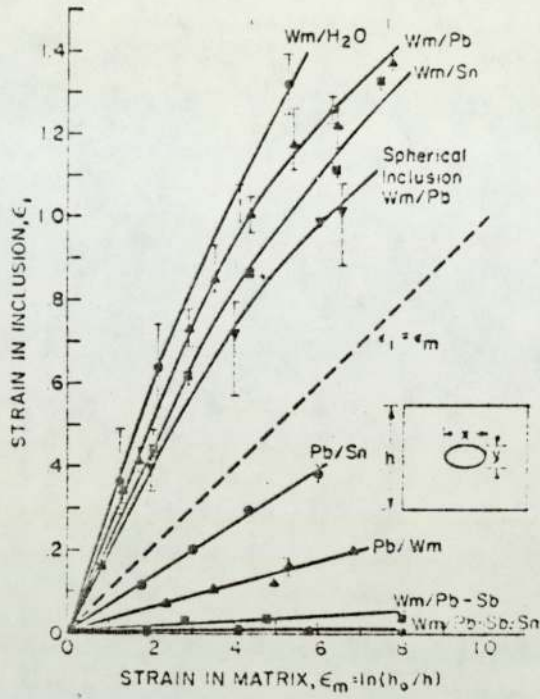


FIGURE 18A : INCLUSION STRAIN VERSUS MATRIX STRAIN FOR VARIOUS SYSTEMS (110)

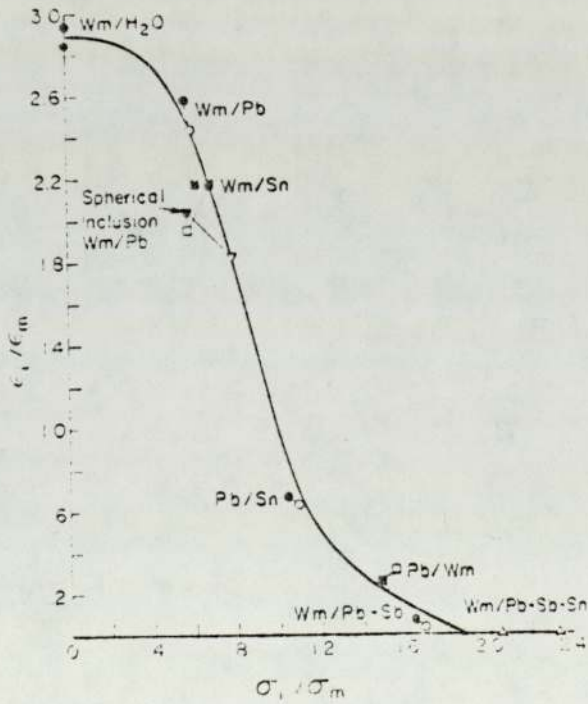


FIGURE 18B : RATIO OF INCLUSION TO MATRIX STRAIN VERSUS A FUNCTION OF THE RATIO OF INCLUSIONS TO MATRIX FLOW STRAIN (110)

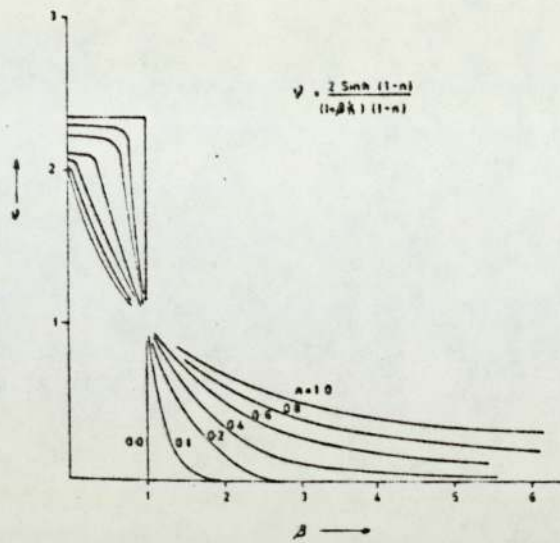


FIGURE 19 : INCLUSION PLASTICITY INDEX
VERSUS RATIO OF INCLUSION TO
MATRIX FLOW STRESS FOR VARIOUS
n VALUES (84)

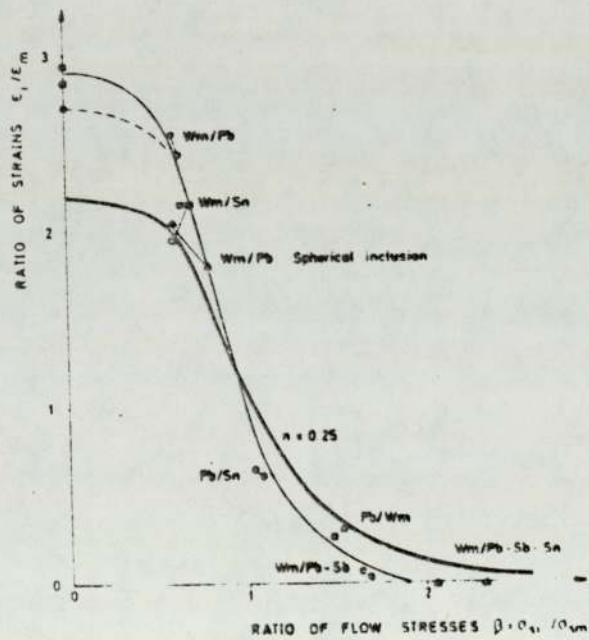


FIGURE 20 : COMPARISON OF THEORETICAL
AND EXPERIMENTAL VALUES ON
 ϵ_i/ϵ_m AS A FUNCTION OF β
(σ_i/σ_m). [111]

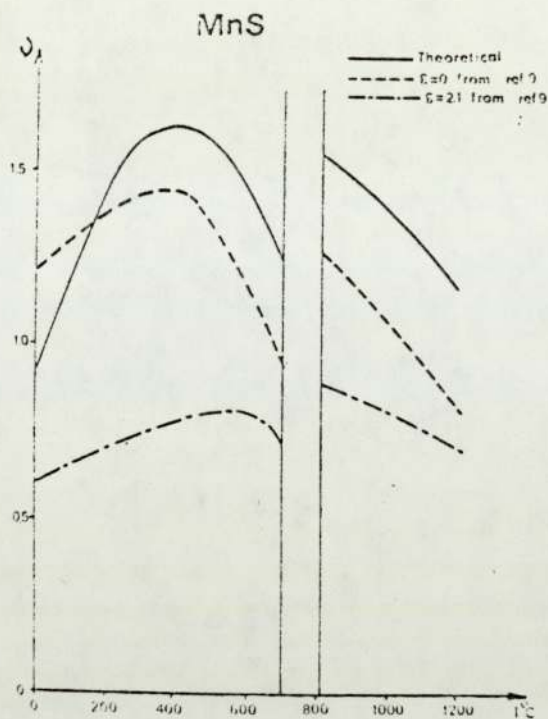


FIGURE 21 : PREDICTED PLASTICITY INDEX, ν , VALUES FOR MnS FROM 600 TO 1200°C. (113)

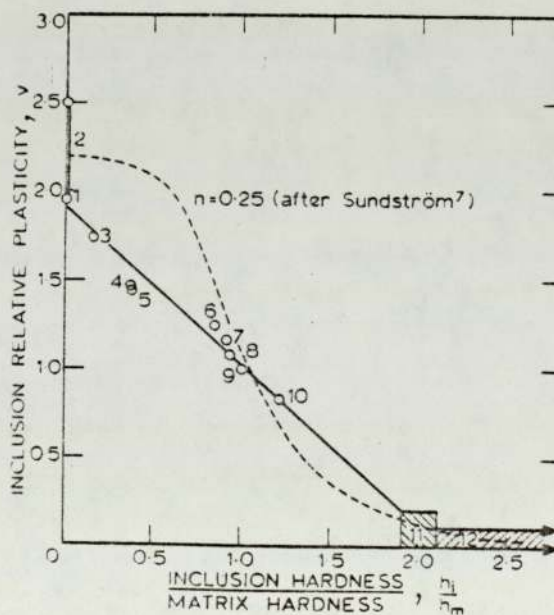
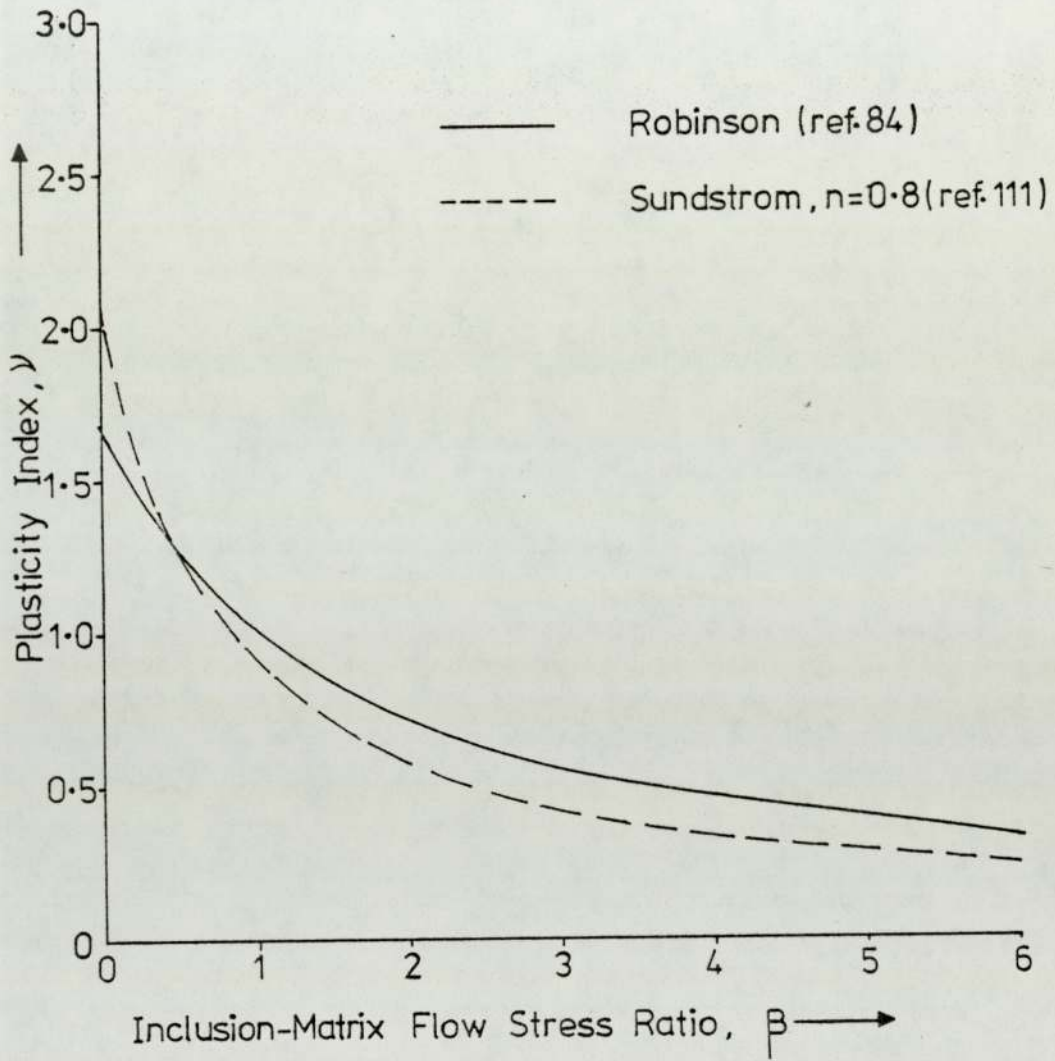


FIGURE 22 : RELATIONSHIP BETWEEN RELATIVE PLASTICITY AND THE RATIO OF INCLUSION TO MATRIX HARDNESS (131)

FIG-23: Variation Of Plasticity Index With
Inclusion-Matrix Flow Stress Ratio



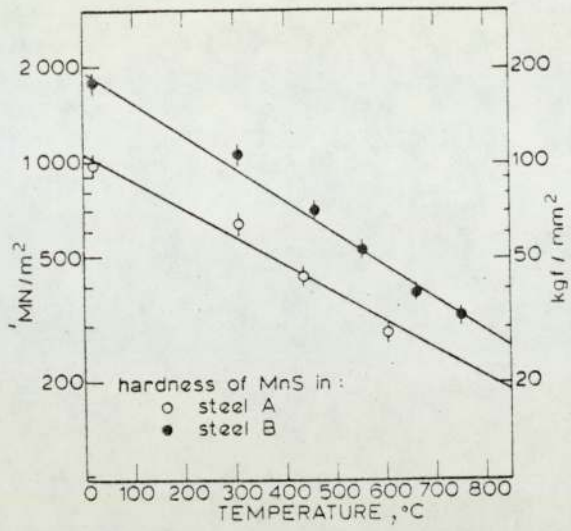


FIGURE 24A : HARDNESS OF TYPE I MnS INCLUSIONS IN RELATION TO TEMPERATURE. (131)

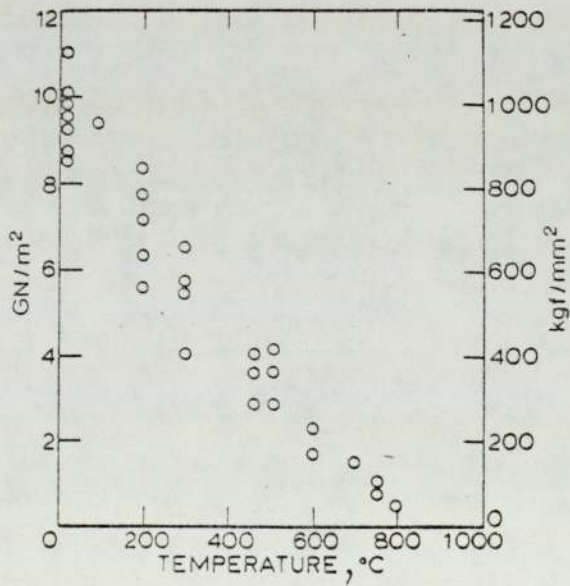


FIGURE 24B : HARDNESS OF SILICATE INCLUSIONS VERSUS TEMPERATURE. (131)

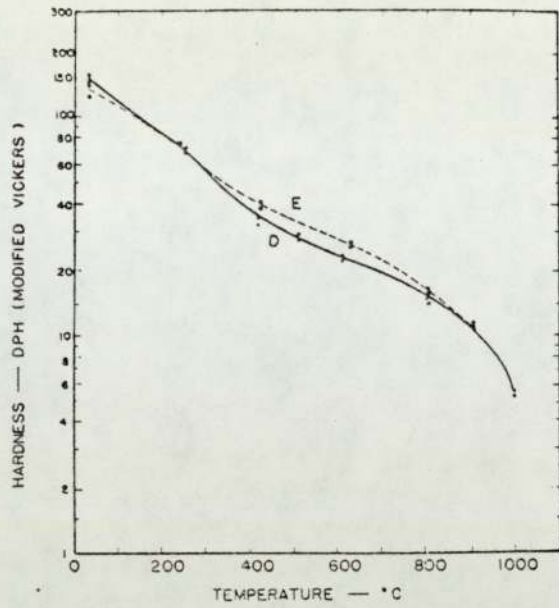


FIGURE 25A : HARDNESS VERSUS TEMPERATURE (D) SINGLE CRYSTAL MnS, (E) POLYCRYSTALLINE MnS. (133)

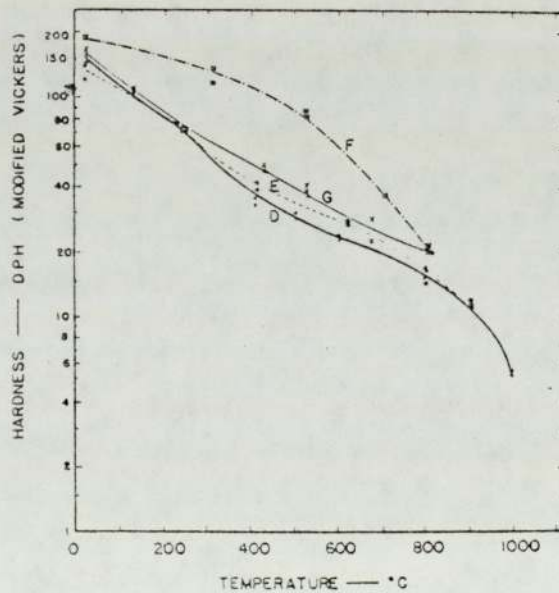


FIGURE 25B : HARDNESS VERSUS TEMPERATURE (D) SINGLE CRYSTAL MnS (PUREST), (E) POLYCRYSTALLINE MnS (PUREST), (F) CRYSTAL MnS (WITH MnO). (133)

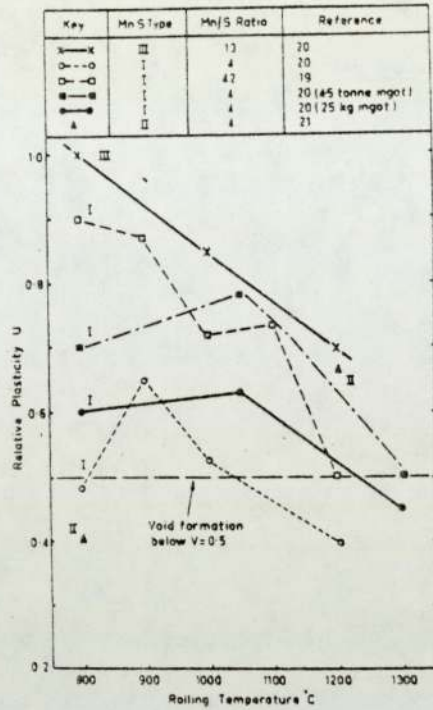


FIGURE 26 : EFFECT OF ROLLING TEMPERATURE ON RELATIVE PLASTICITY OF MnS

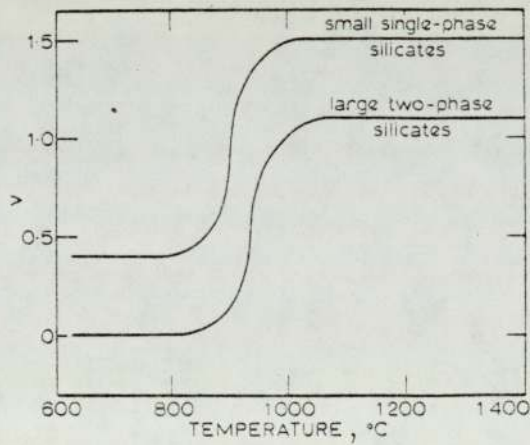


FIGURE 27 : RELATIVE PLASTICITY OF SILICATE INCLUSIONS VERSUS ROLLING TEMPERATURE.

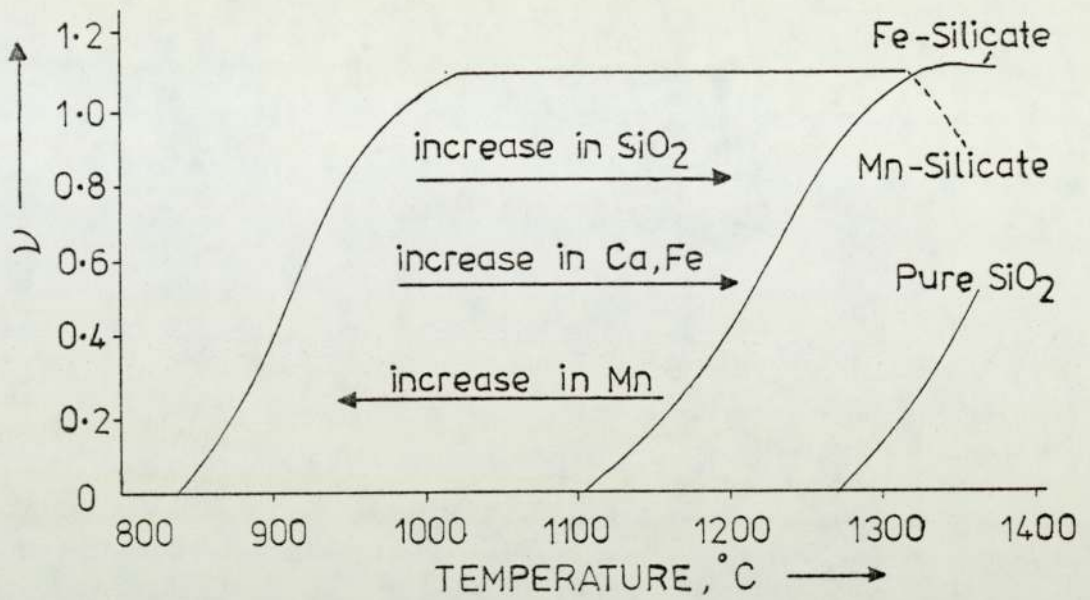


FIGURE 28 : INFLUENCE OF TEMPERATURE ON THE PLASTIC DEFORMATION OF DIFFERENT INCLUSION TYPES (3)

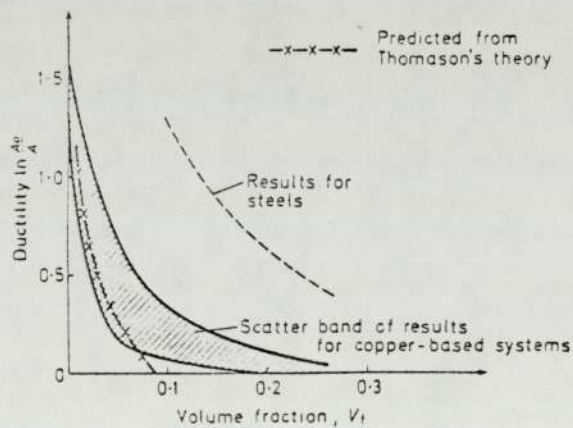


FIGURE 29 : DEPENDENCE OF DUCTILITY ON VOLUME FRACTION OF SECOND - PHASE PARTICLES (COPPER-BASED RESULTS FROM EDELSON AND BALDWIN (182); STEEL RESULTS FROM TURKALO AND LOW (185))

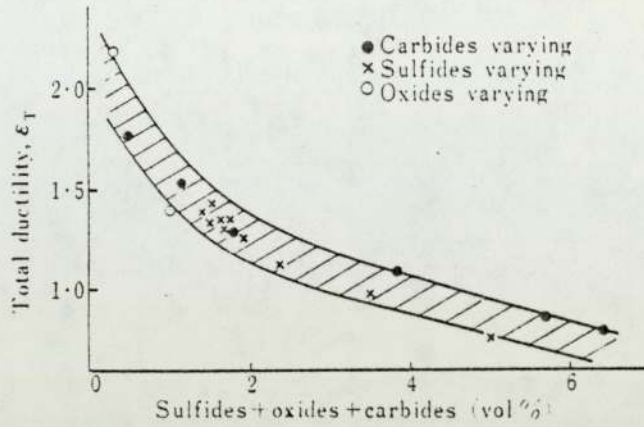


FIGURE 30A : THE EFFECT OF SECOND-PHASE PARTICLES ON ϵ_T

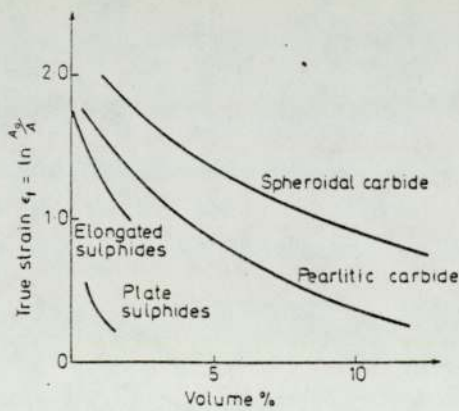


FIGURE 30B : EFFECTS OF TYPE AND SHAPE OF SECOND-PHASE PARTICLES ON THE TENSILE DUCTILITY OF STEEL.
(181)

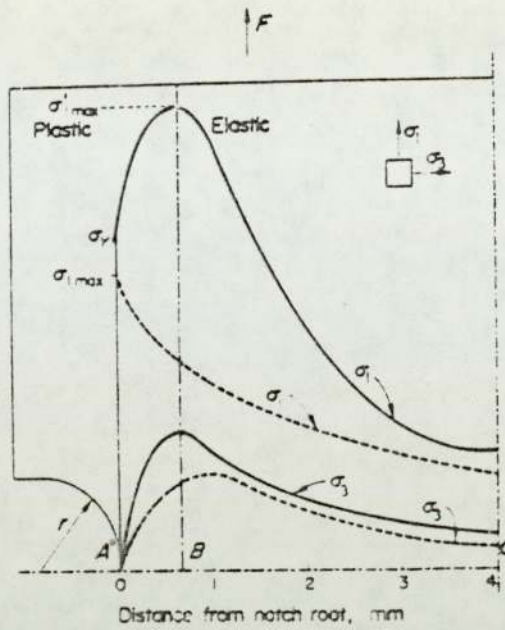
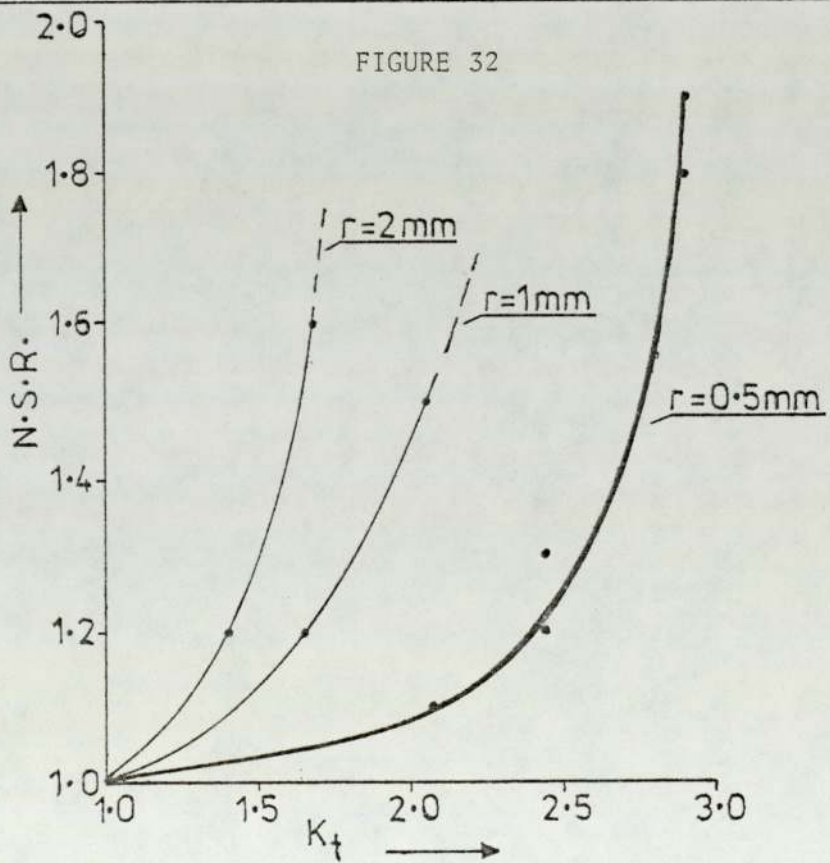
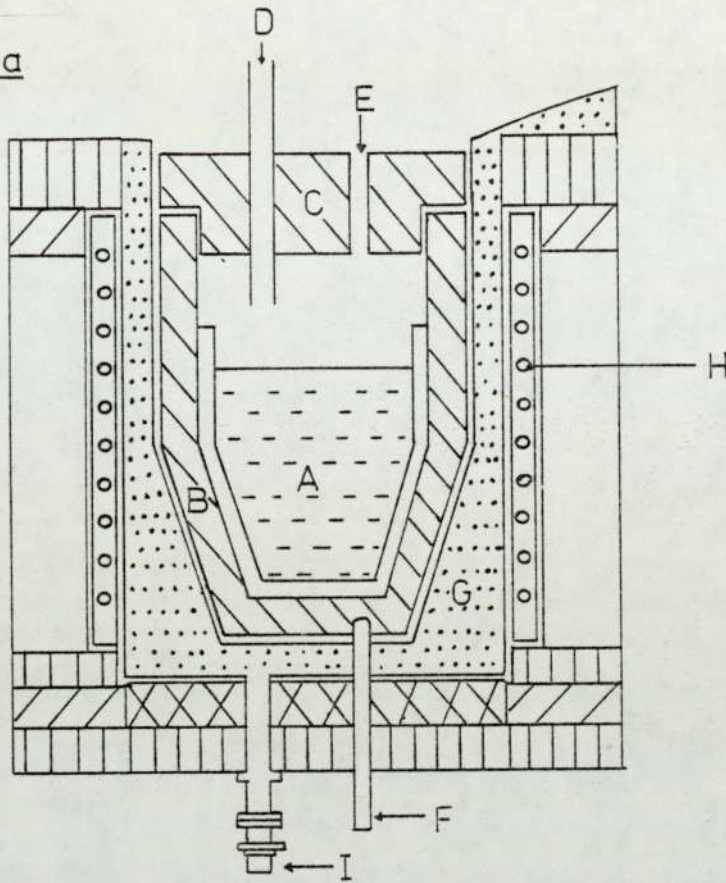


FIGURE 31 : COMPARISON OF THE DISTRIBUTION OF STRESSES WHEN THE SPECIMEN IS ENTIRELY ELASTIC OR PARTIALLY PLASTIC, ---, ELASTIC STRESSES; ———, PLASTIC STRESSES.



FURNACE ASSEMBLY

FIG-33a



- A IRON MELT CONTAINED IN ALUMINA CRUCIBLE
- B GRAPHITE SUSCEPTOR
- C GRAPHITE SUSCEPTOR LID
- D ARGON INLET TUBE
- E THERMOCOUPLE AND SAMPLING HOLE
- F THERMOCOUPLE
- G FURNACE LINING
- H WATER COOLED INDUCTION COIL
- I EARTH LEAKAGE SPIDER

FIG-33b

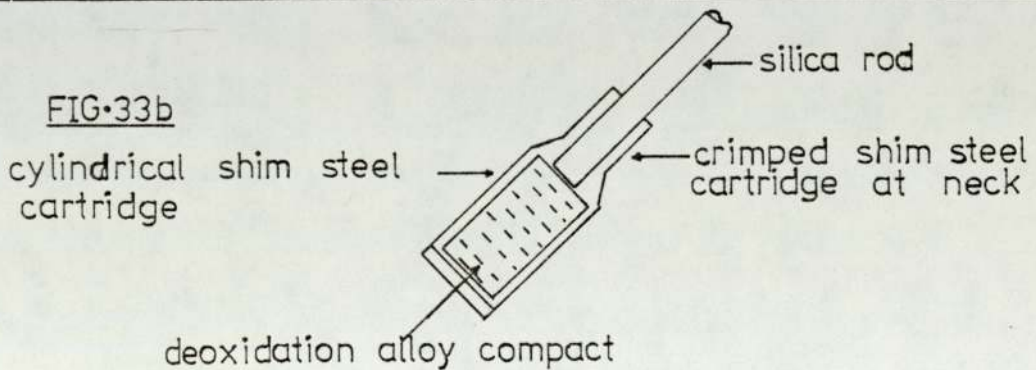


FIG-34 : Sectioning Of As Cast Bars

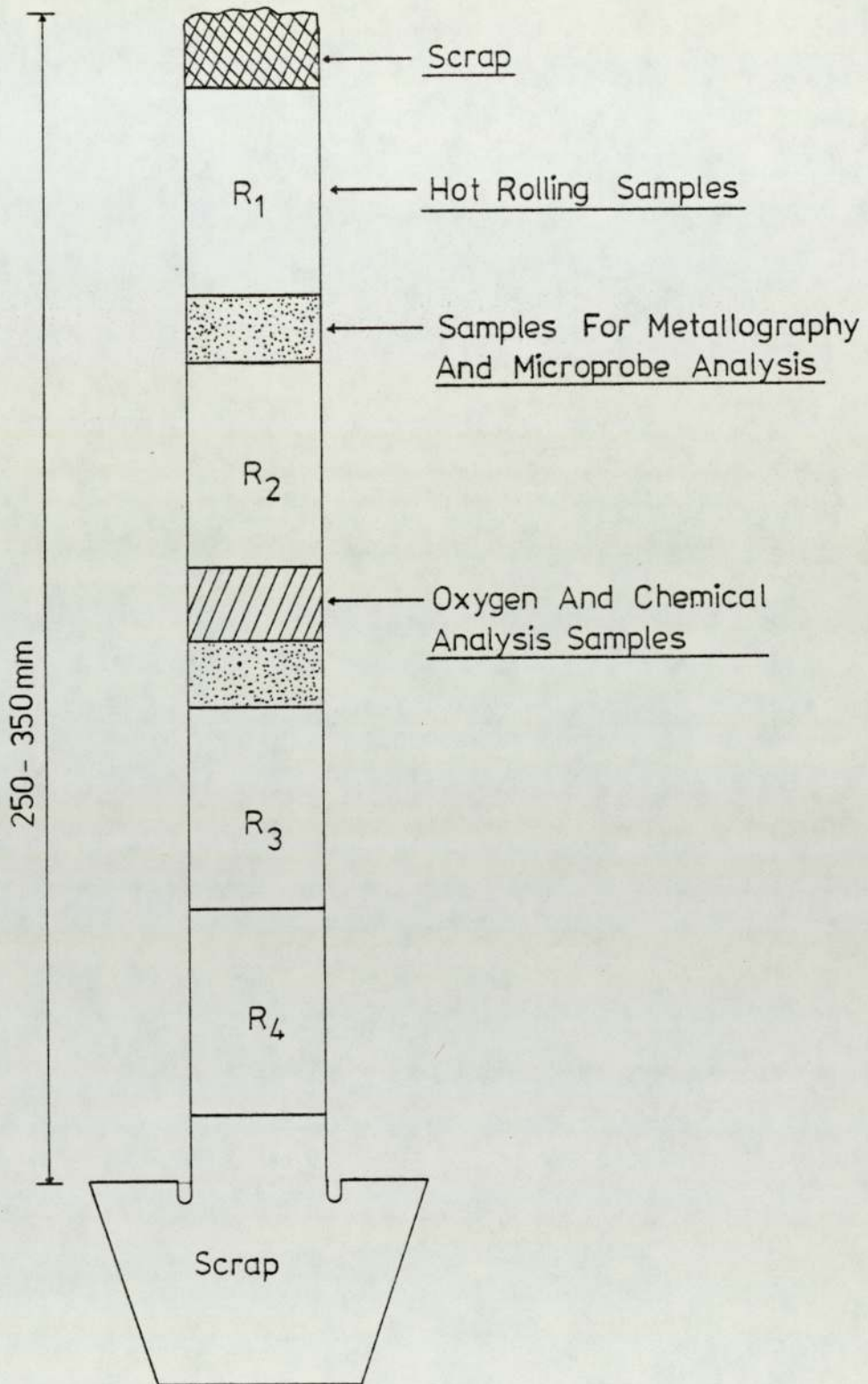
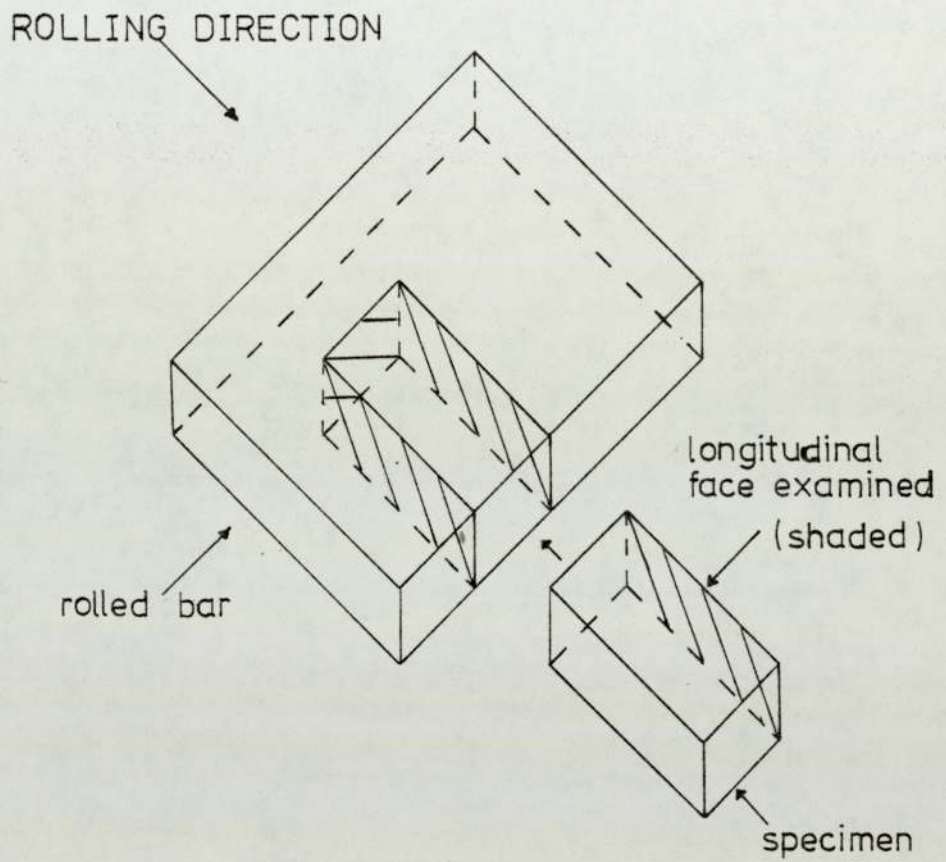
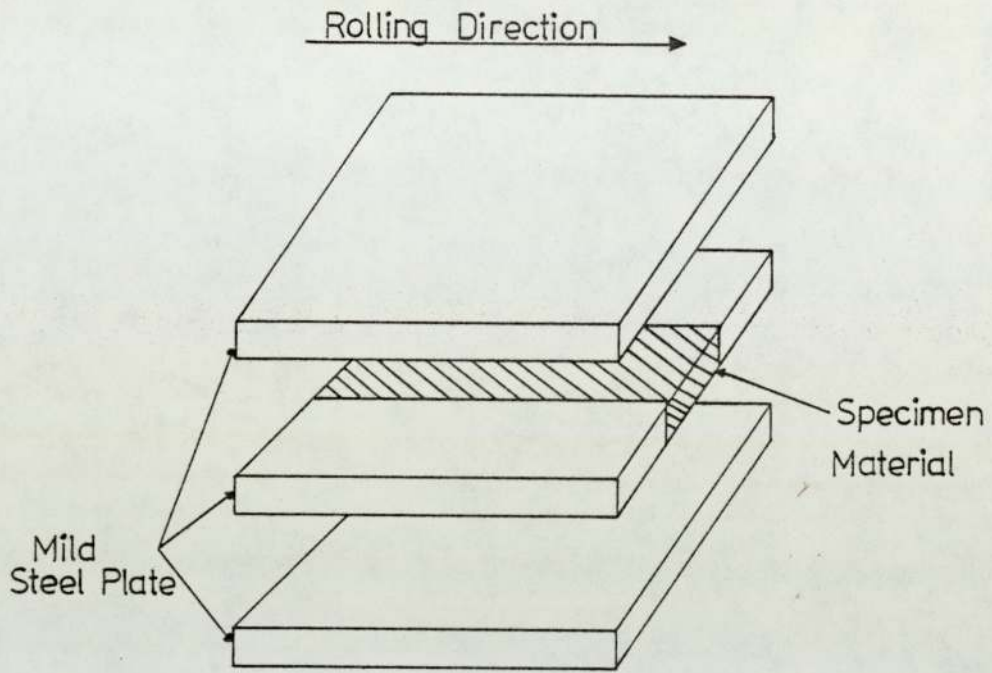


FIG.35: SECTION PLANE USED IN ROLLED BAR



FIG•36: Supported Rolling Specimen



FIG•37: Sectioning Of Rolled Samples

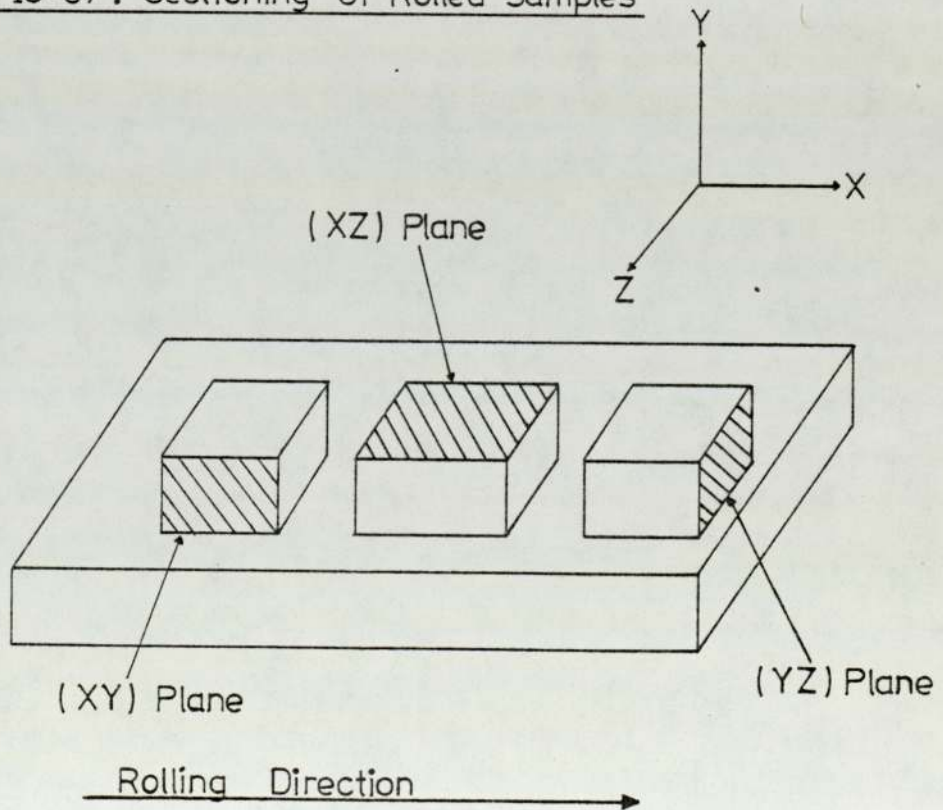


FIG-38 : The Geometry Of The Notch Tensile-Specimens

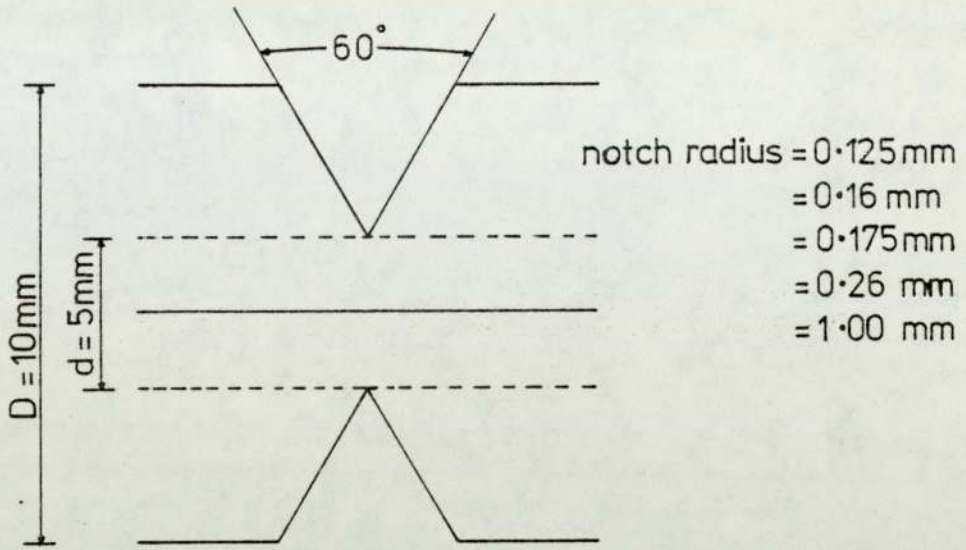
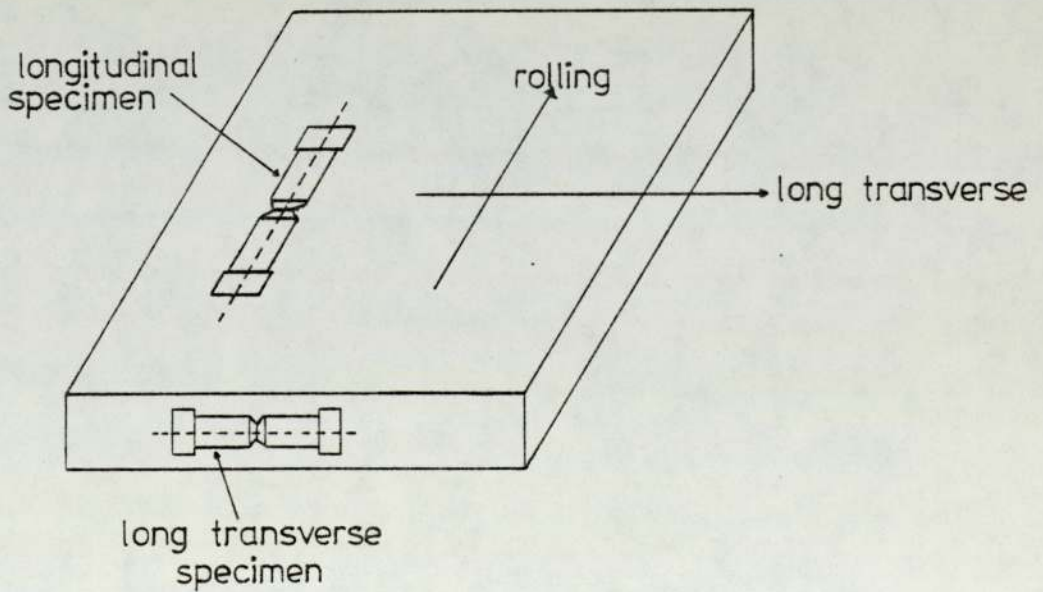
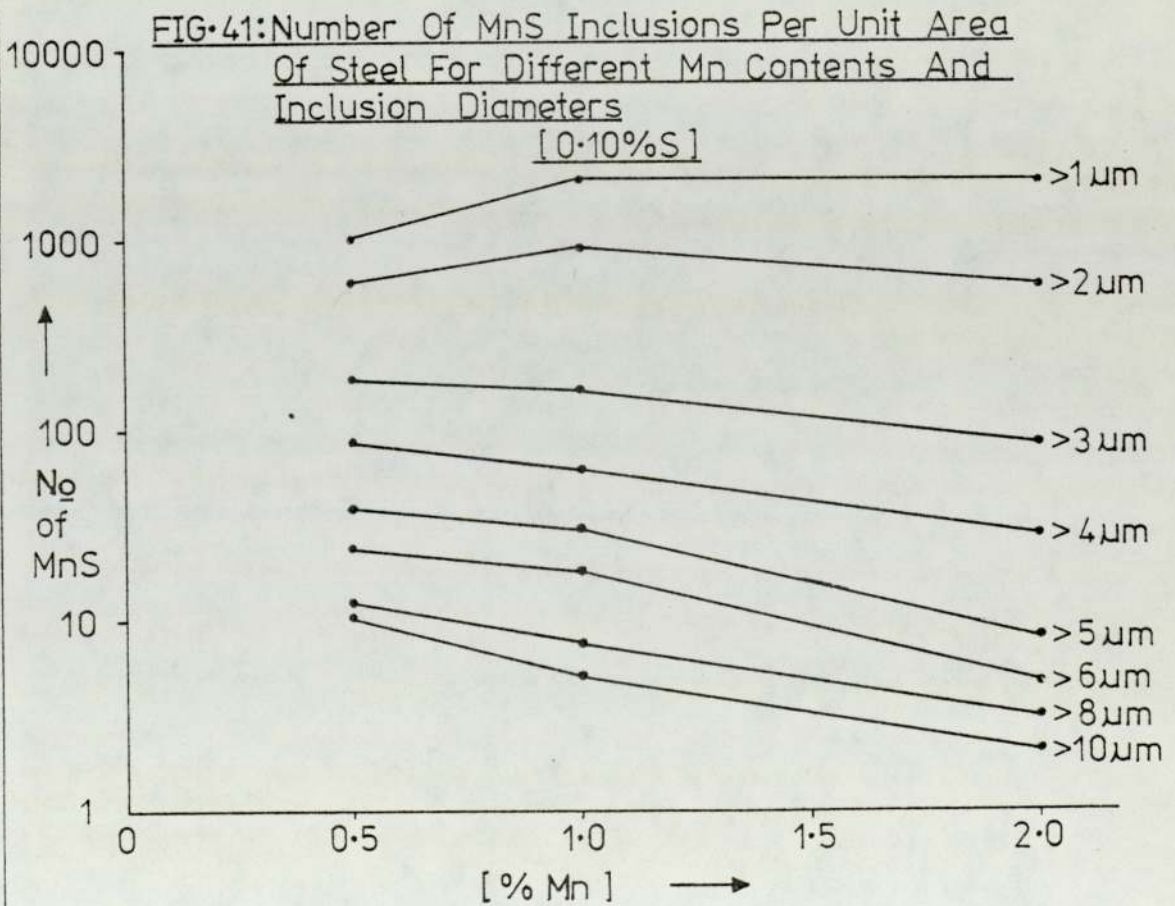
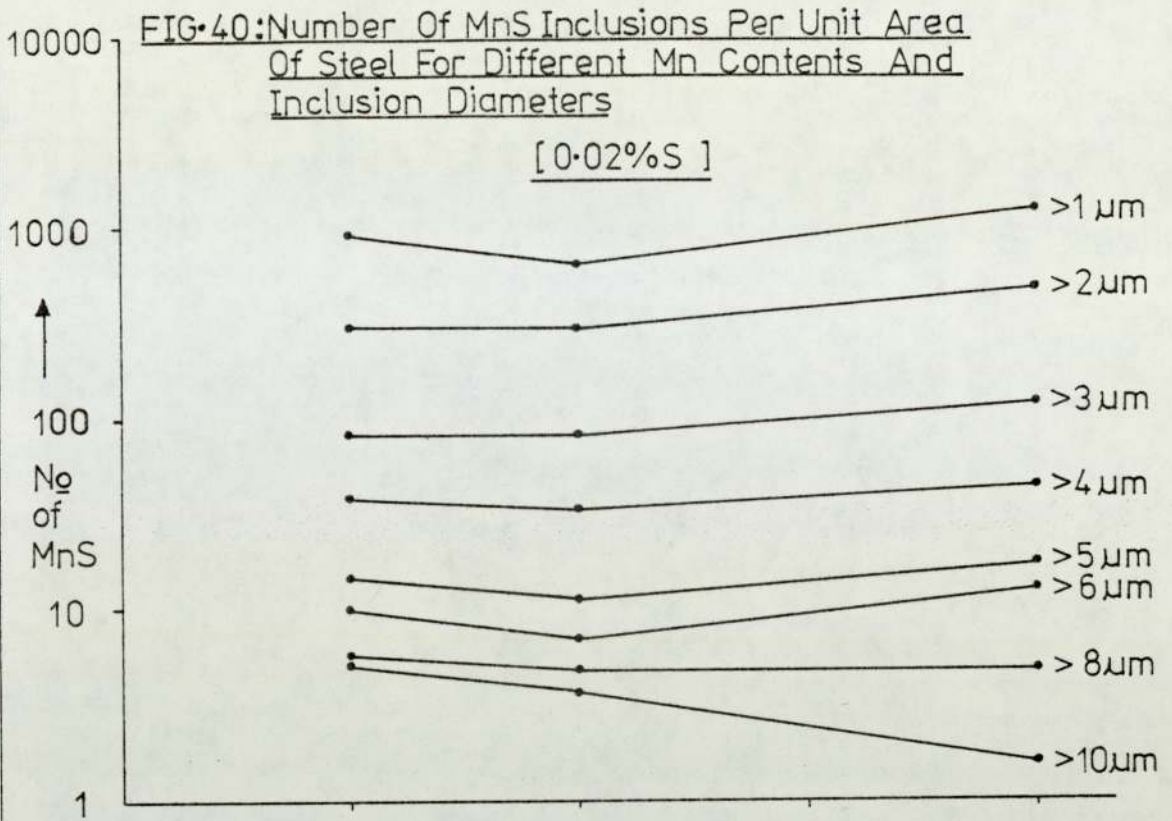


FIG-39 : The Orientation Of The Notch Tensile-Specimens Taken From Rolled Plate





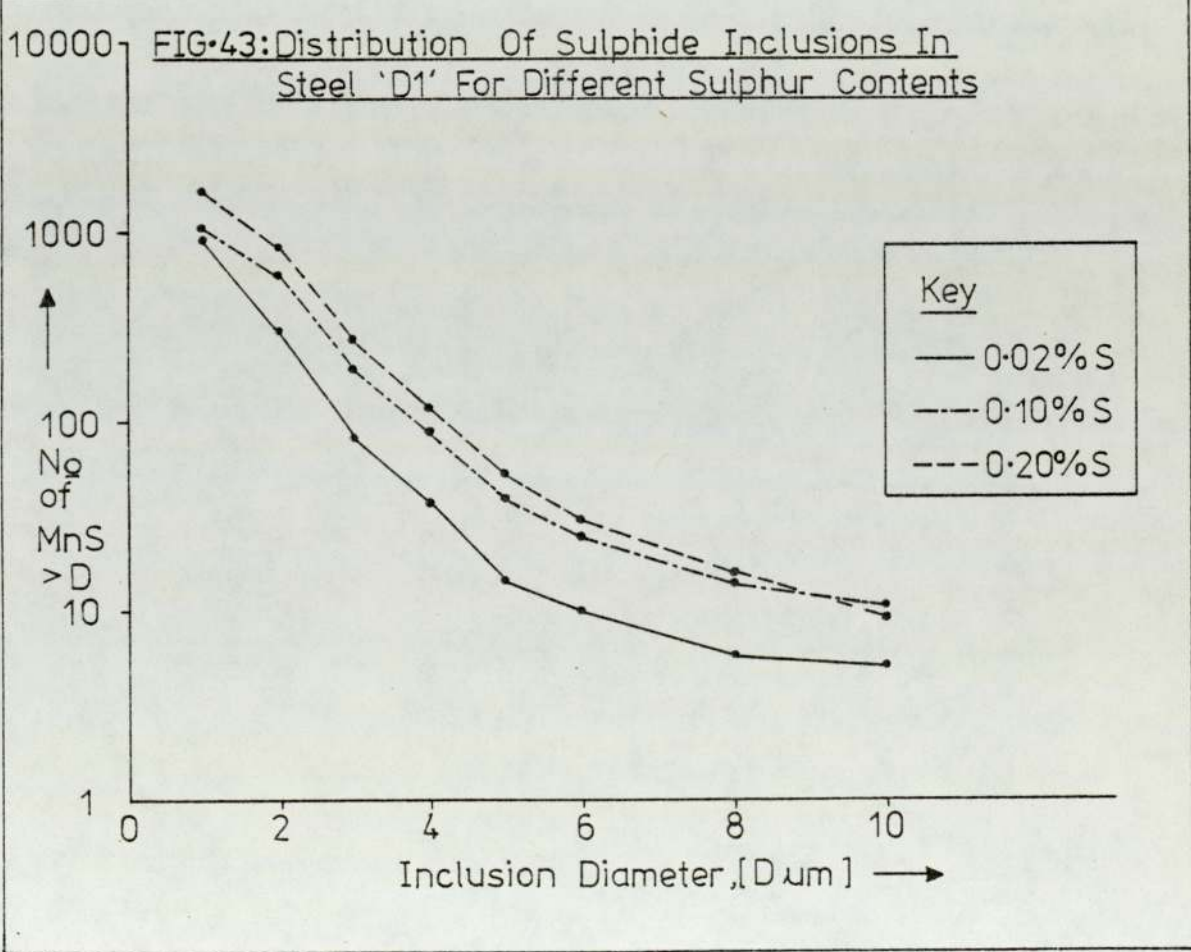
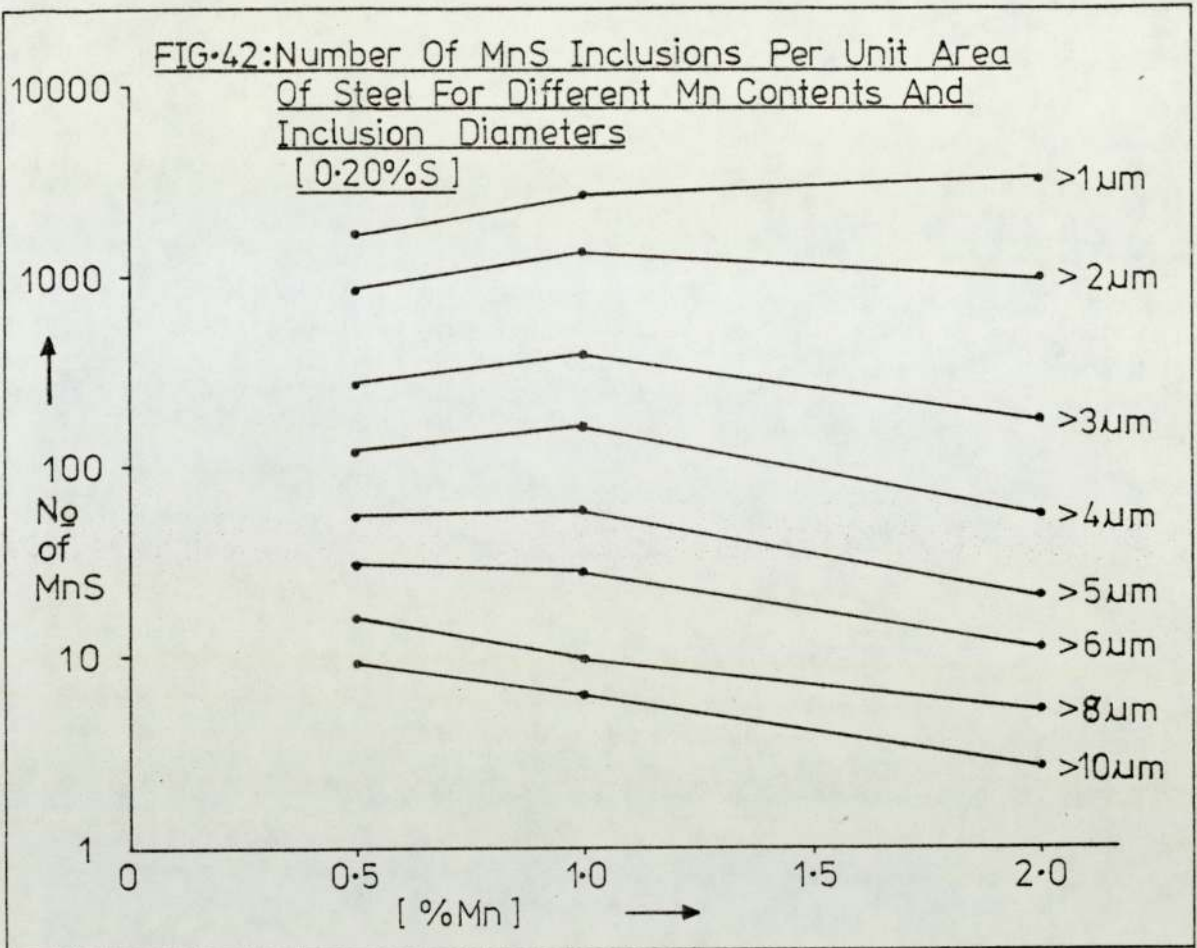


FIG-44: Distribution Of Sulphide Inclusions In Steel 'D2' For Different Sulphur Contents

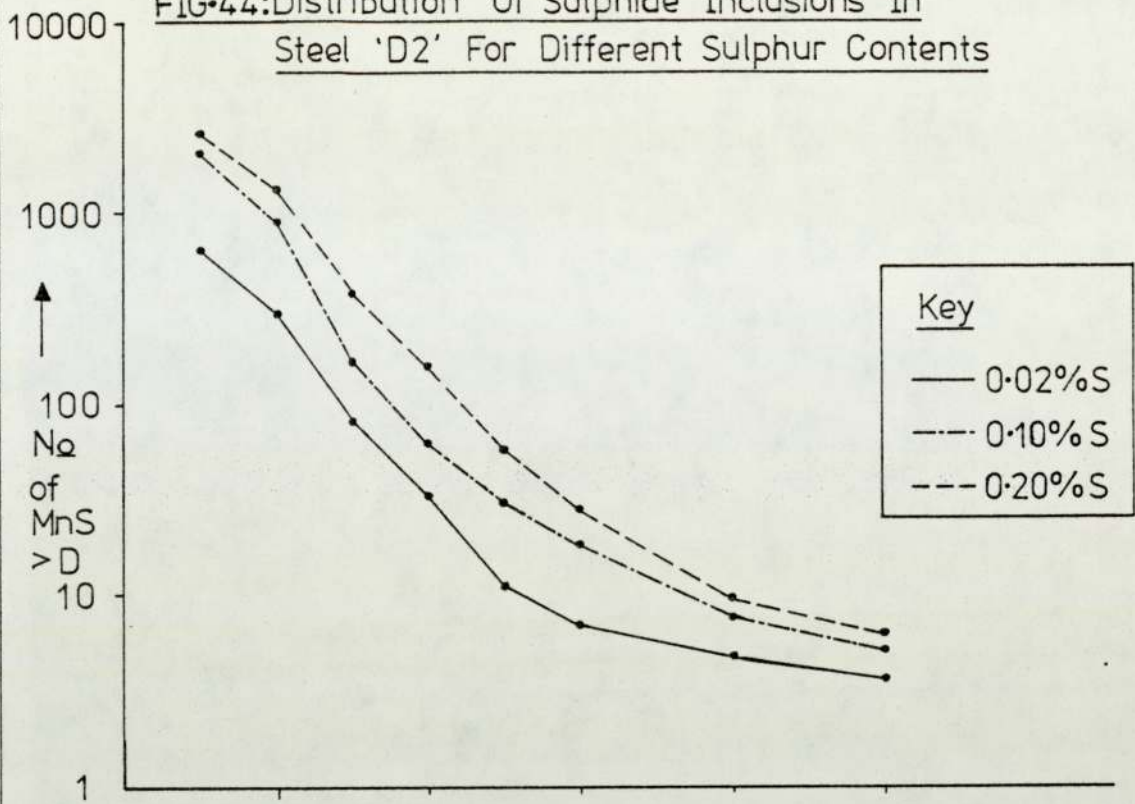


FIG-45: Distribution Of Sulphide Inclusions In Steel 'D3' For Different Sulphur Contents

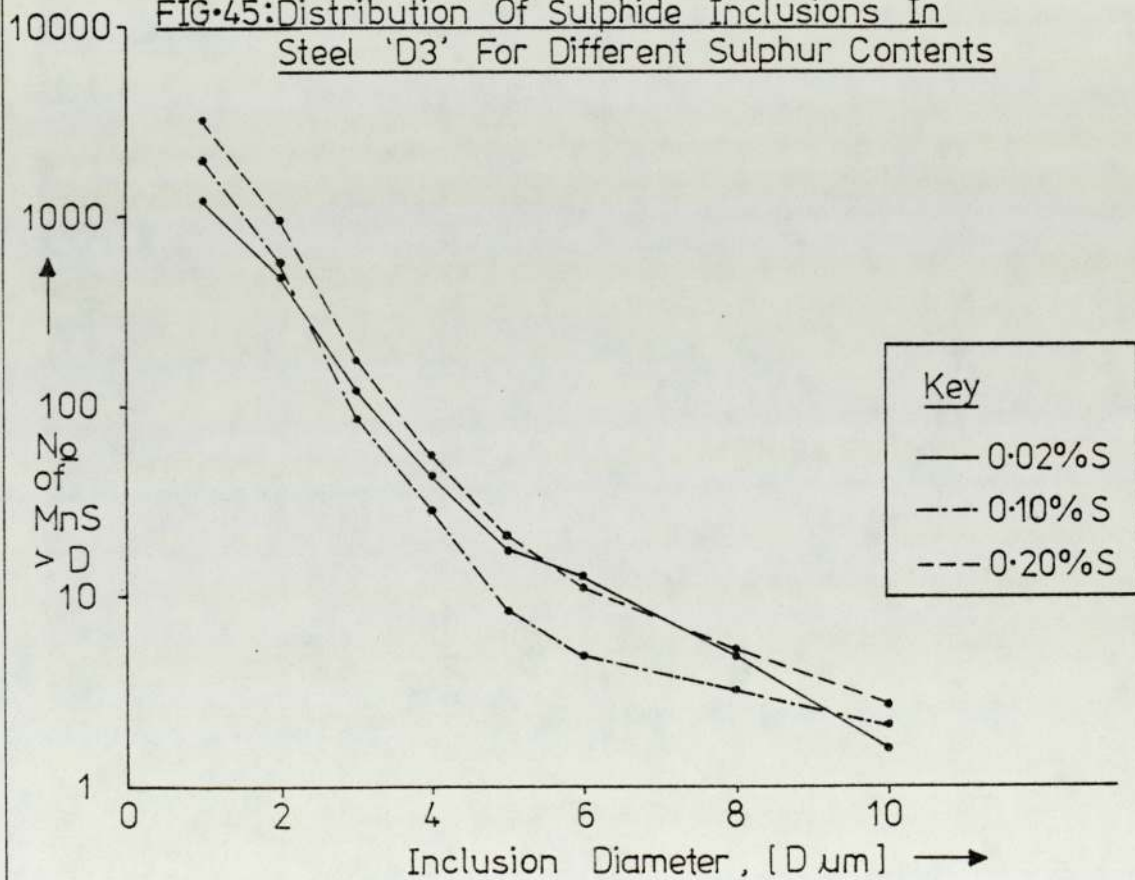


FIG.46:Distribution Of Oxide Inclusions In Steel 'D1' For Different Sulphur Contents

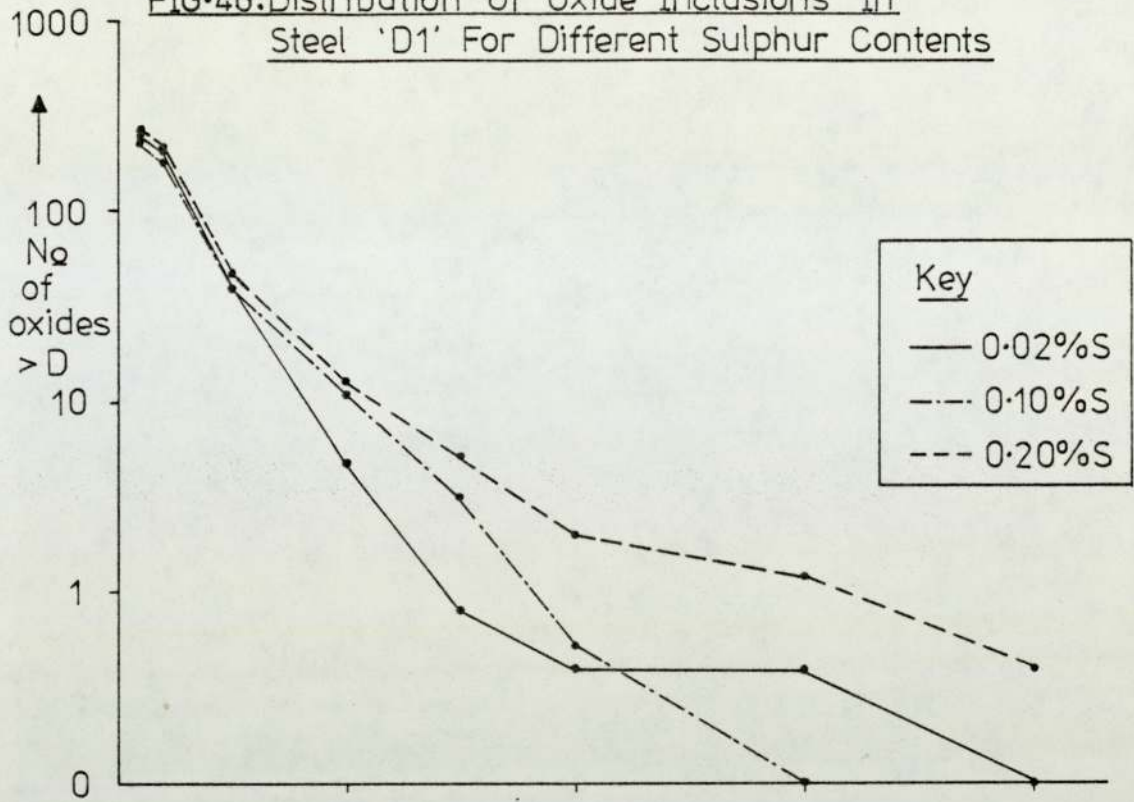
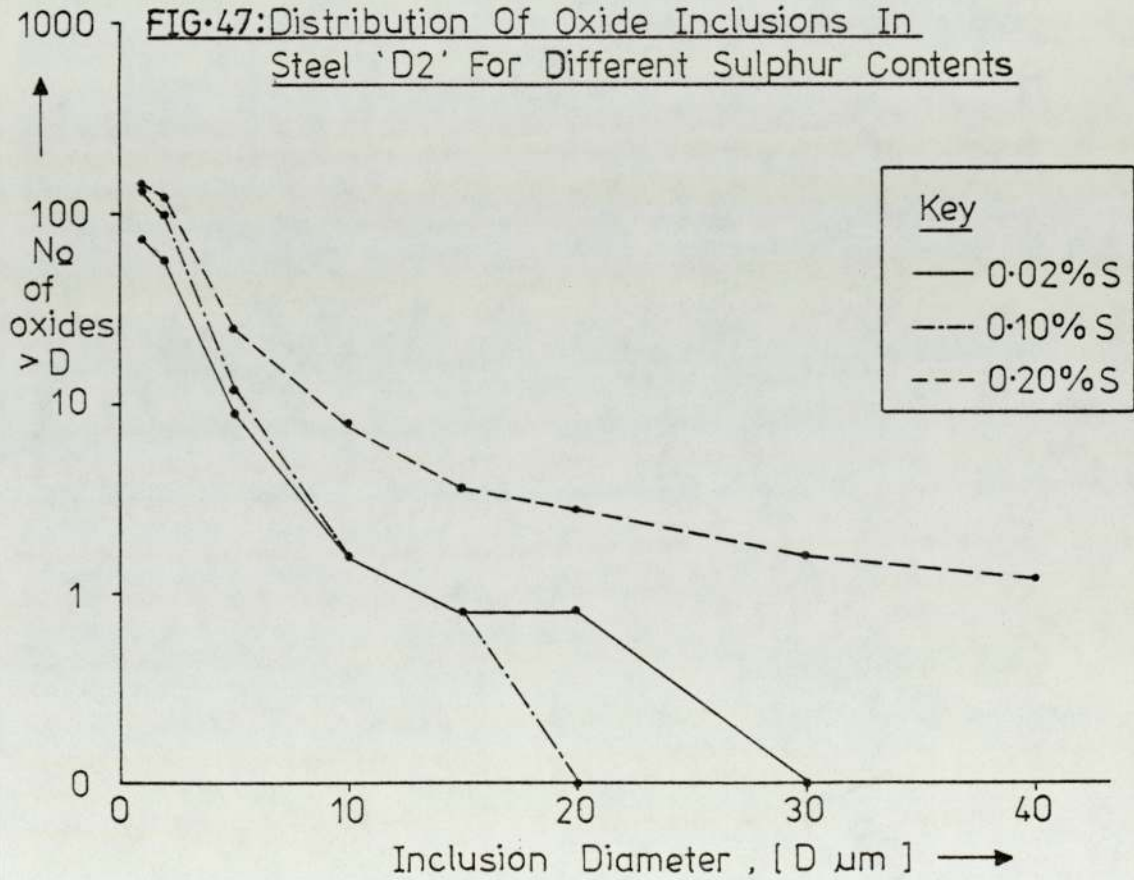


FIG.47:Distribution Of Oxide Inclusions In Steel 'D2' For Different Sulphur Contents



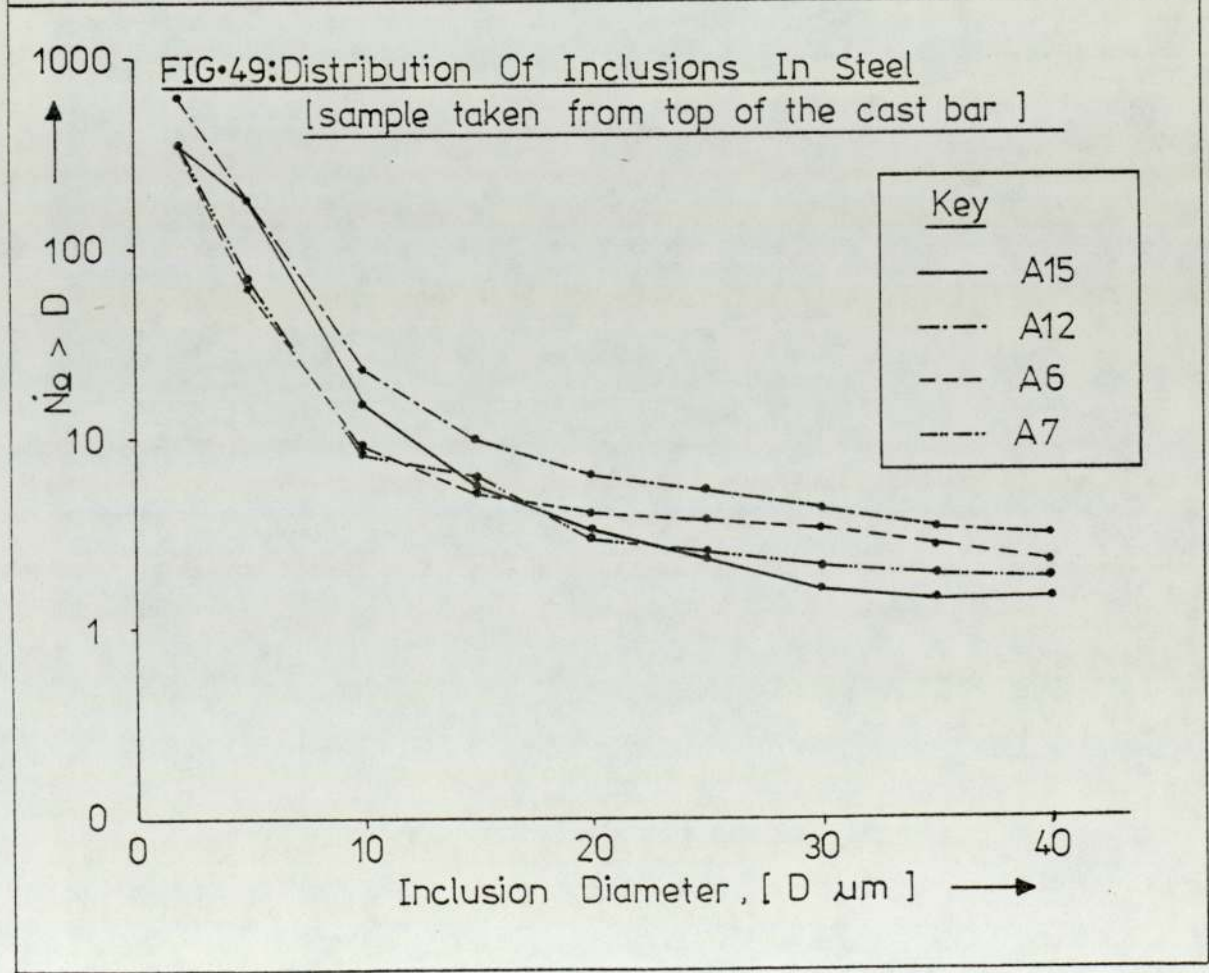
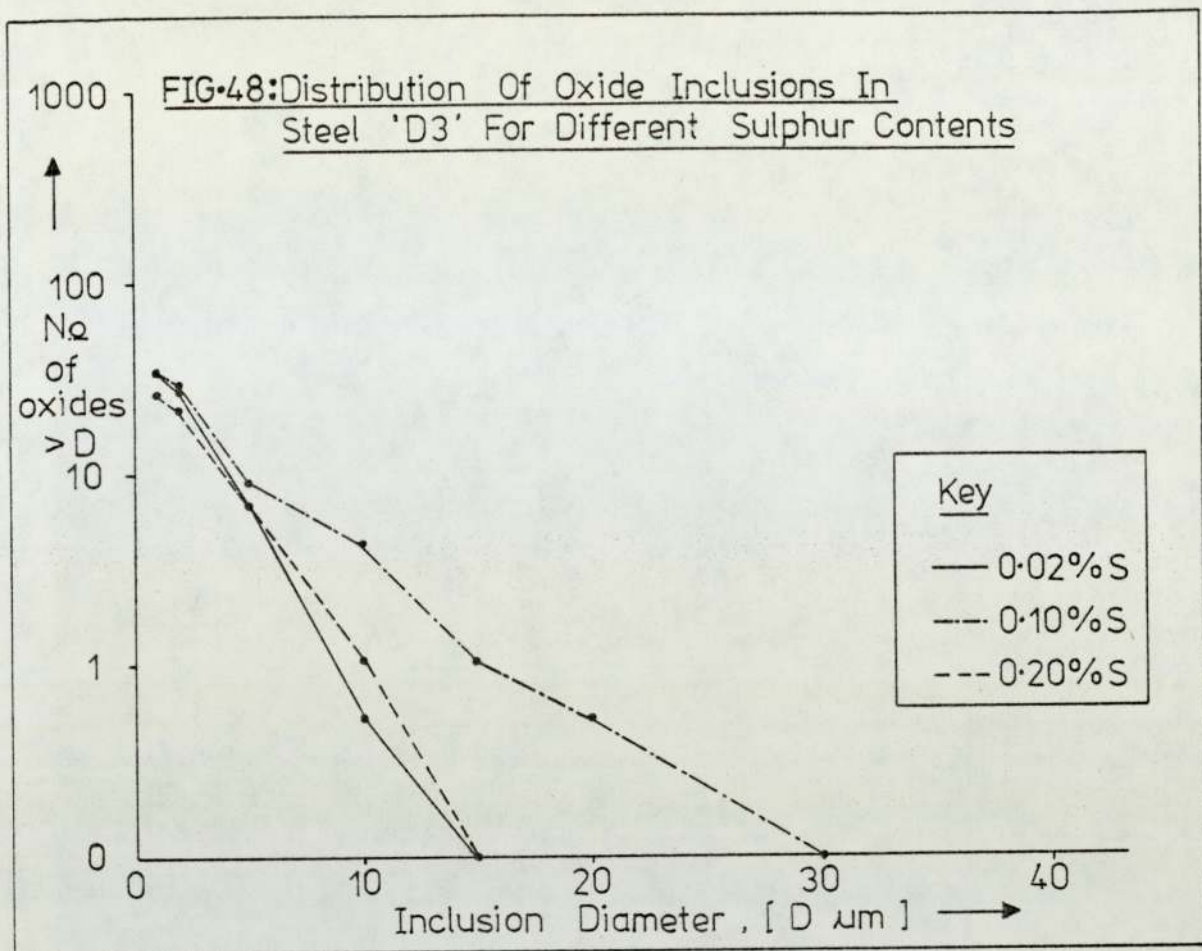


FIG-50: Distribution Of Inclusions In Steel

[sample taken from bottom of the cast bar]

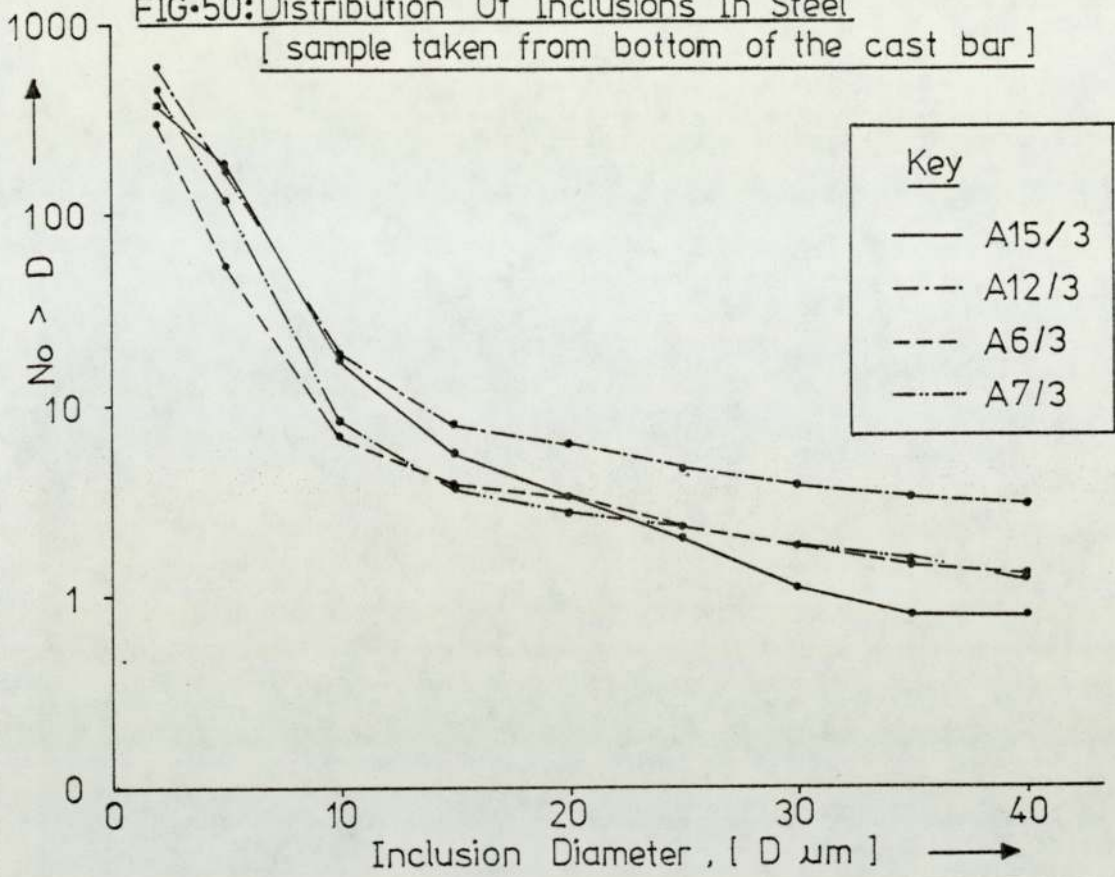


FIG-51: Distribution Of Inclusions In Steel

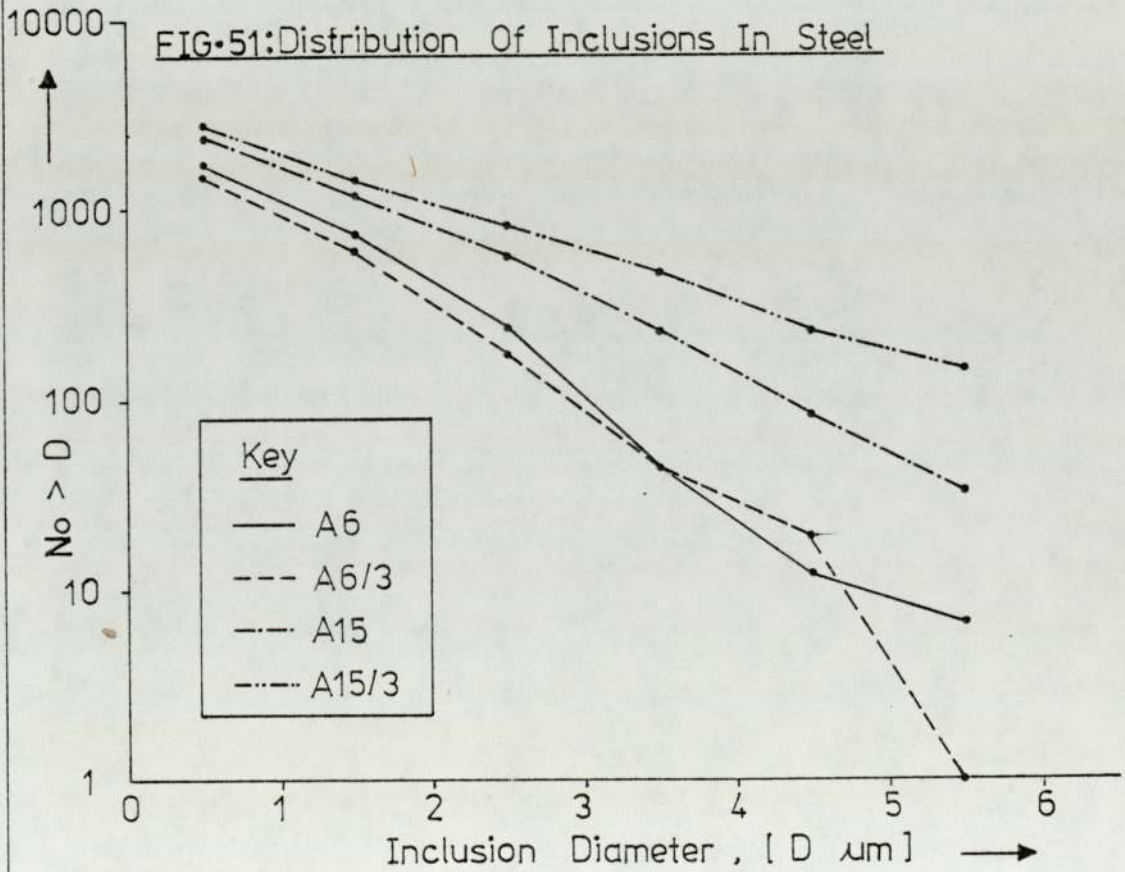


FIG-52: 'As Cast' Oxide Inclusion Compositions In Steel 'A12' For Different Sulphur Contents

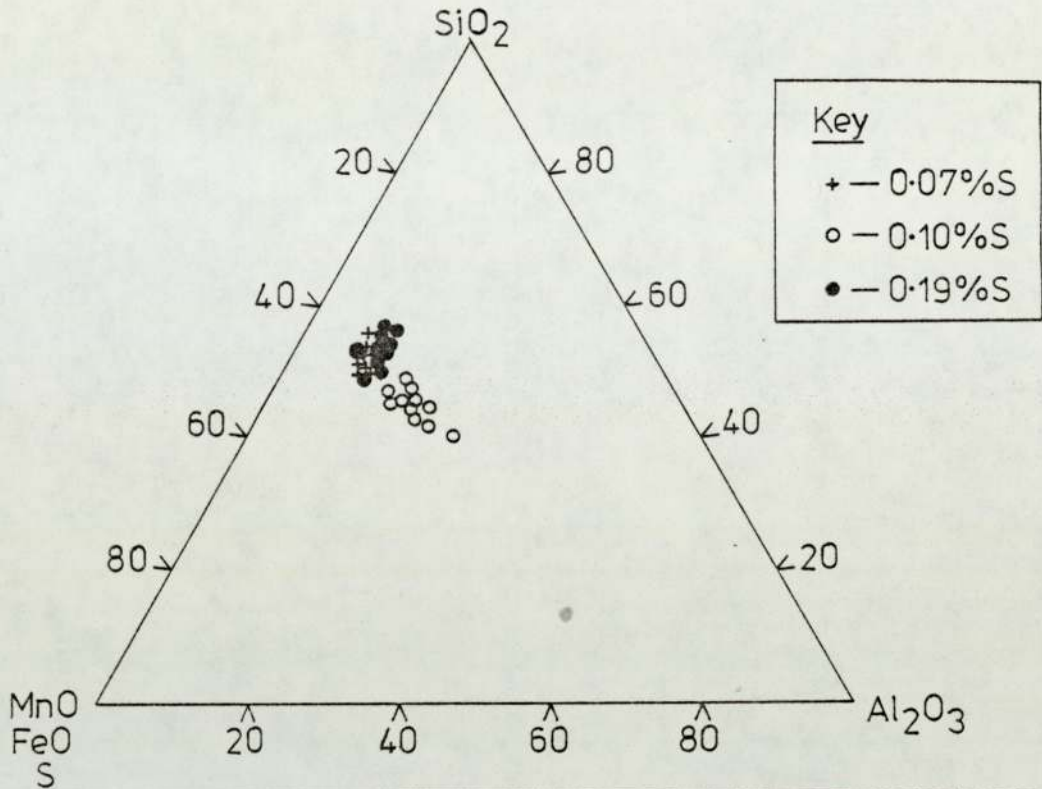


FIG-53: 'As Cast' Oxide Inclusion Compositions In Steel 'A15' For Different Sulphur Contents

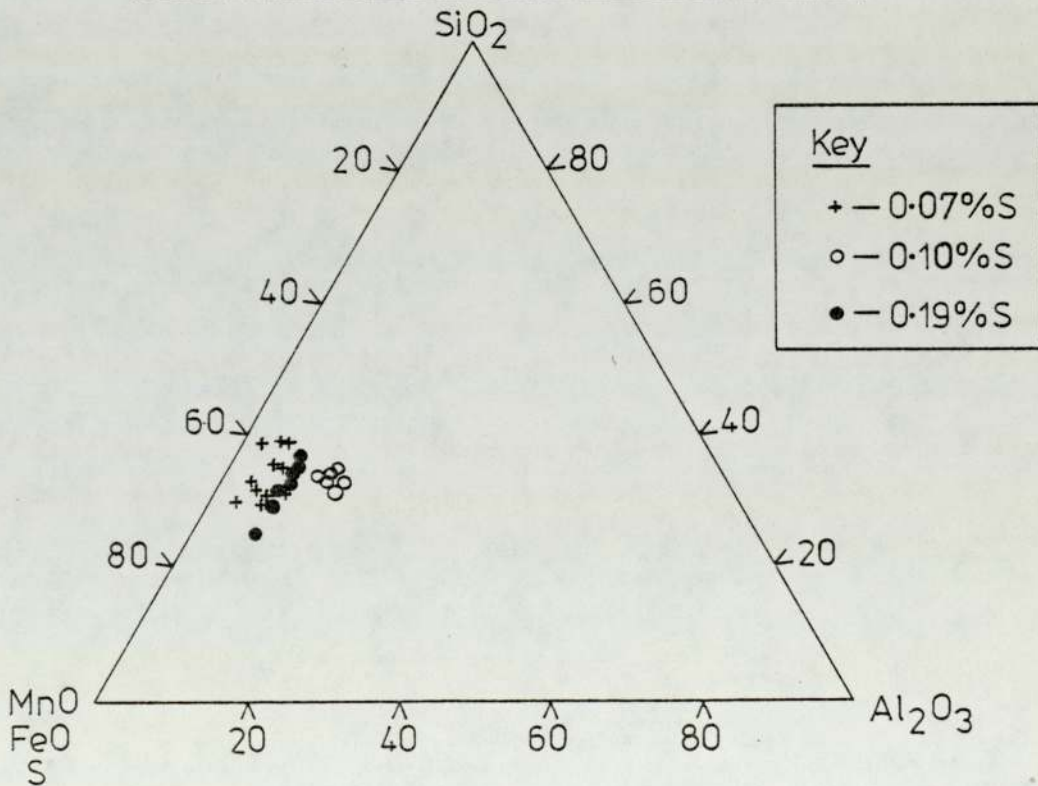


FIG-54: 'As Cast' Oxide Inclusion Compositions In Steel 'A6' For Different Sulphur Contents

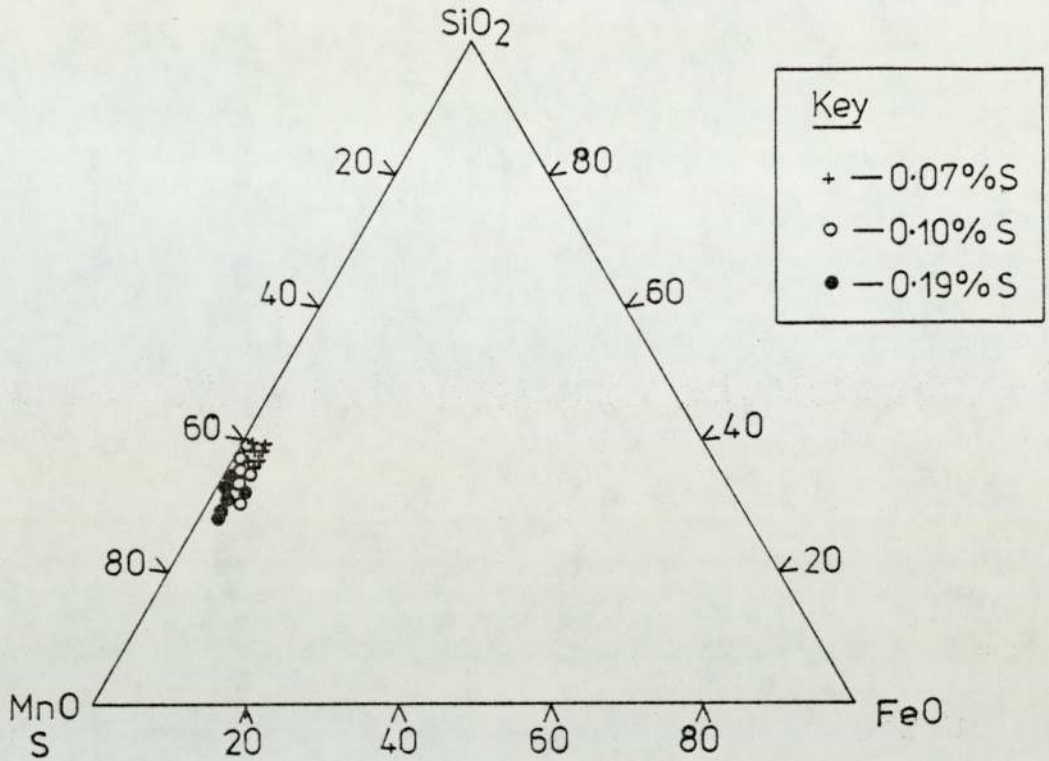


FIG-55: 'As Cast' Oxide Inclusion Compositions In Steel 'A7' For Different Sulphur Contents

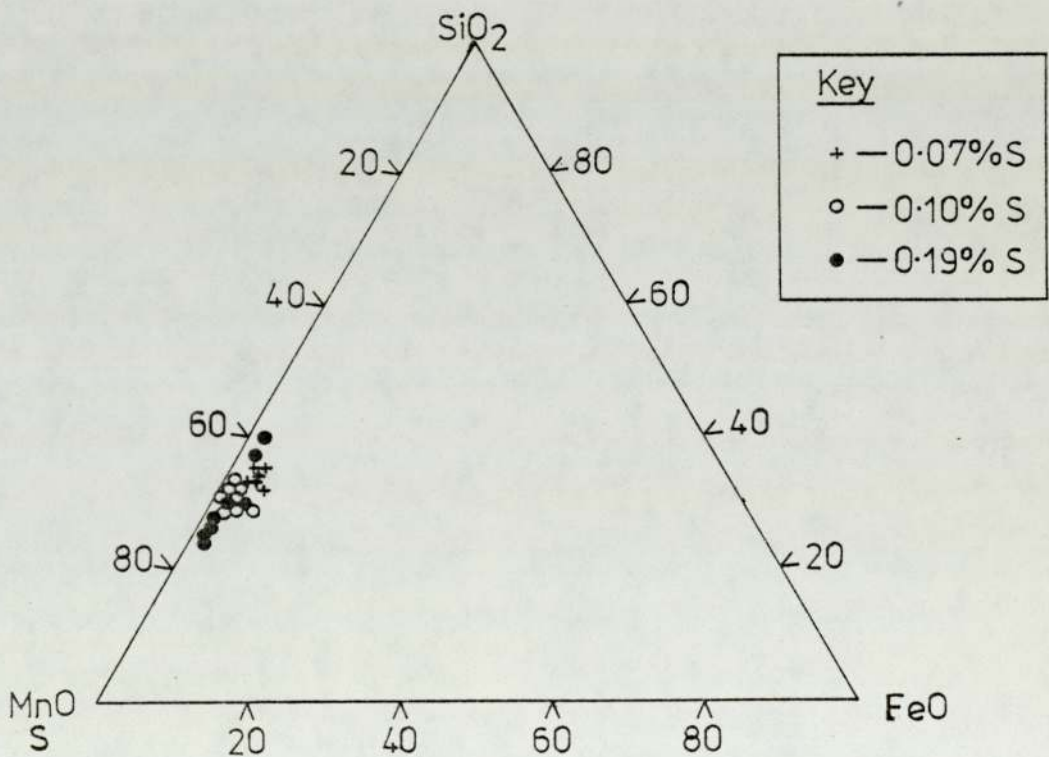


FIG-56 : 'As Cast' Inclusion Compositions [oxides]
In Steel 'D1' For Different Sulphur Contents

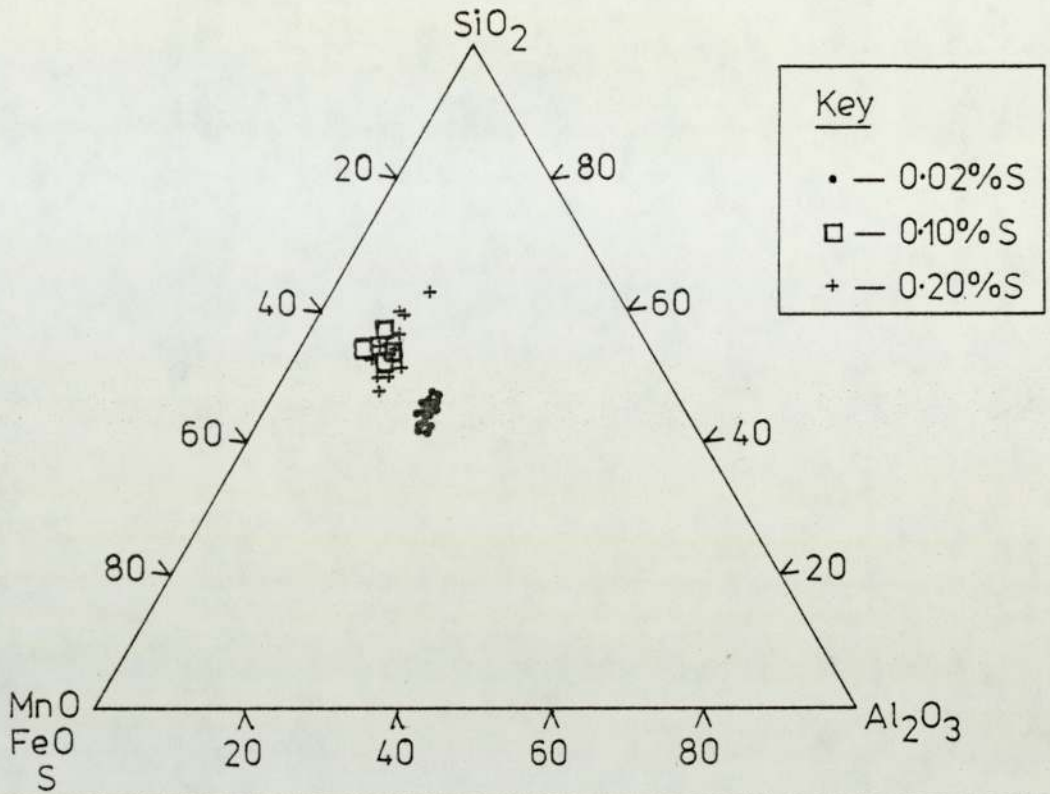


FIG-57 : 'As Cast' Oxide Inclusion Compositions In
Steel 'D2' For Different Sulphur Contents

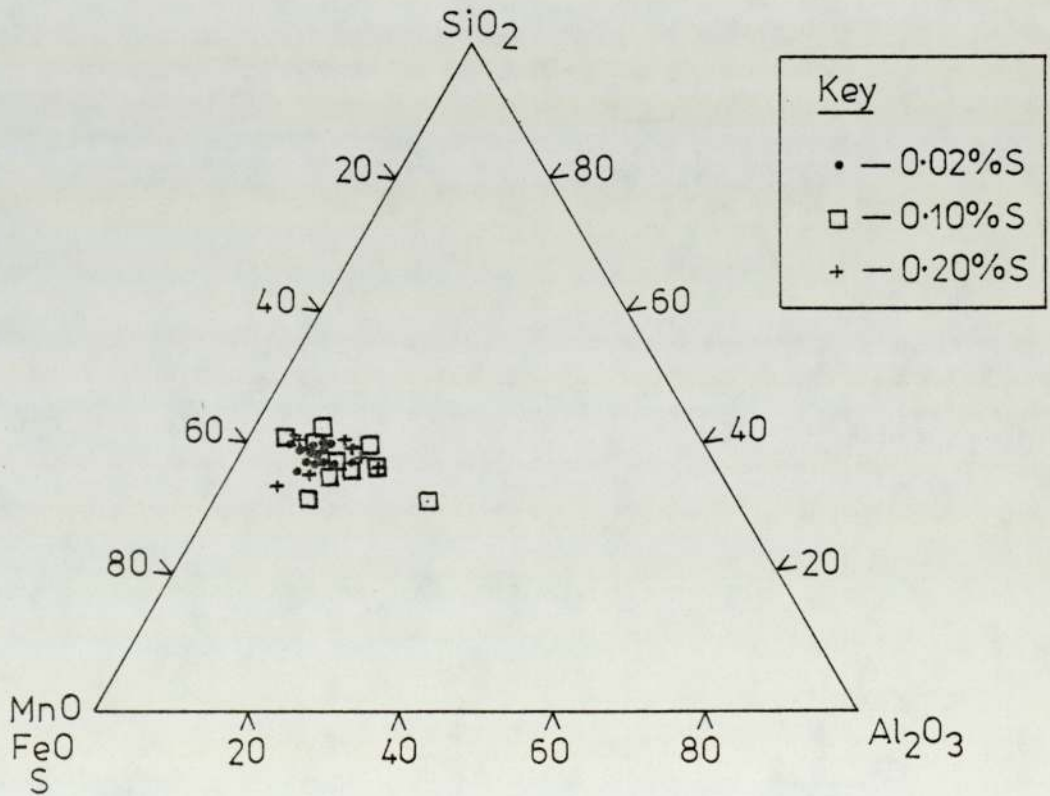


FIG-58: 'As Cast' Oxide Inclusion Compositions In Steel 'D3' For Different Sulphur Contents

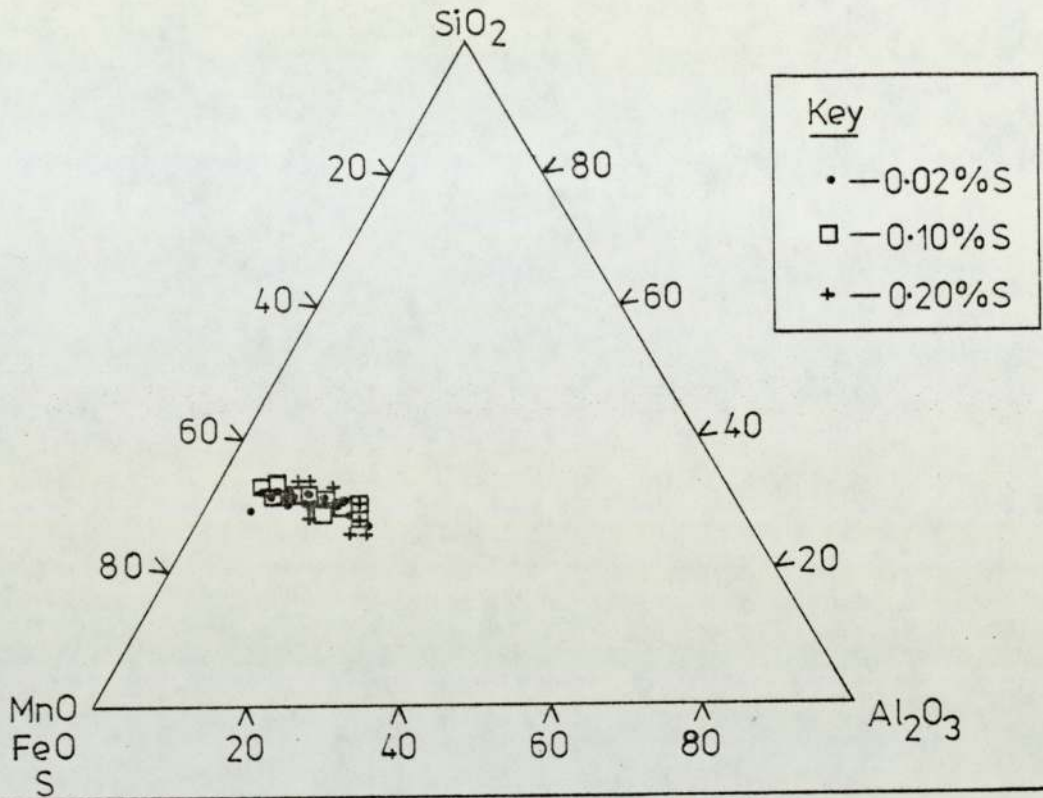
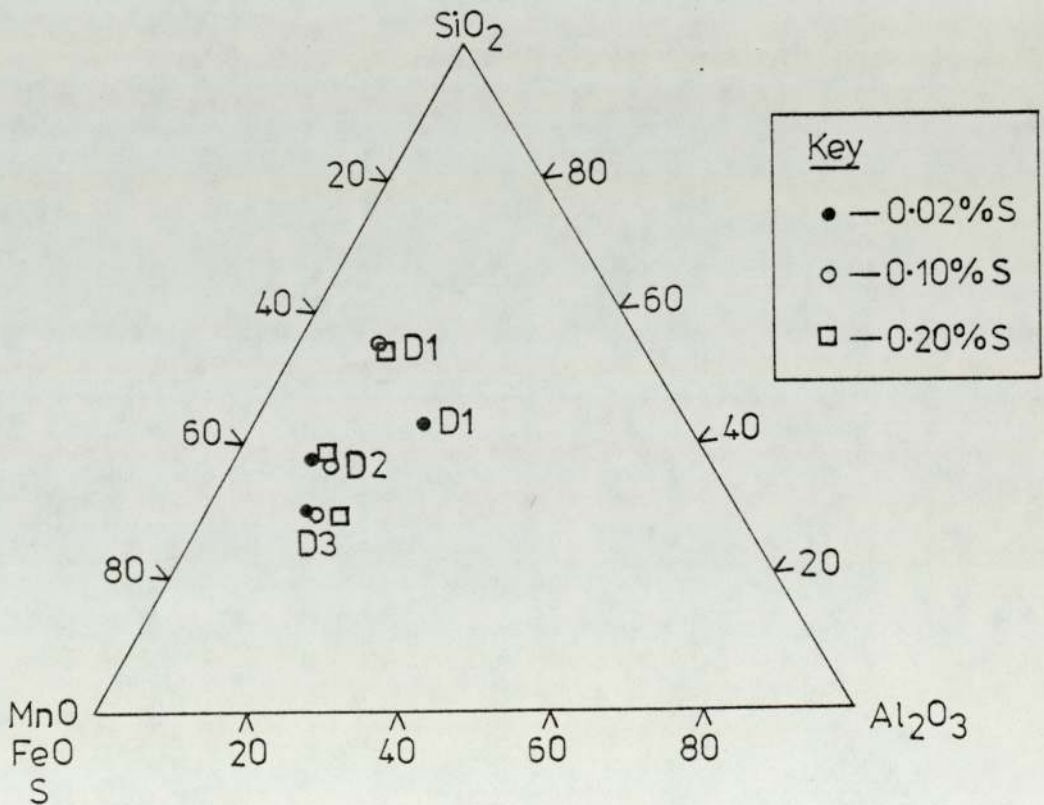
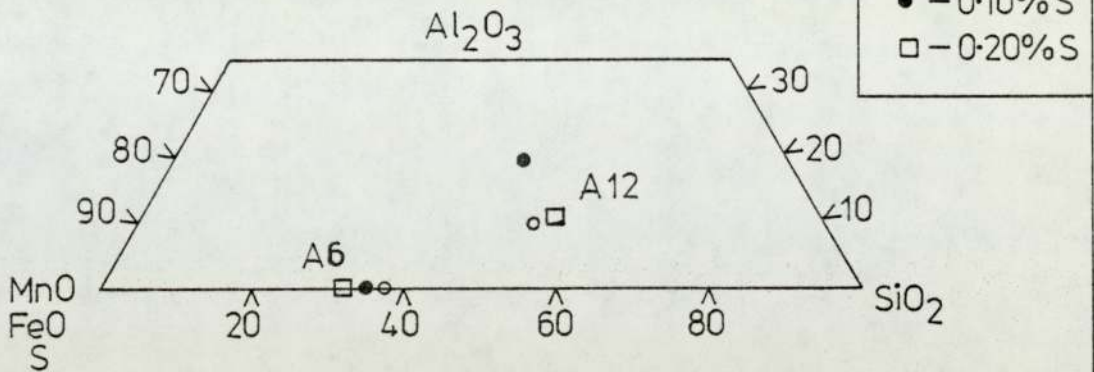


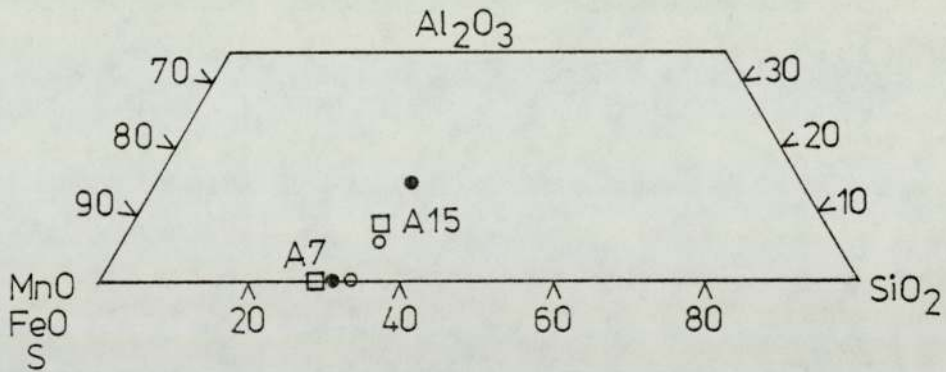
FIG-59 : Mean 'As Cast' Oxide Inclusion Compositions In Steels 'D1', 'D2', And 'D3' For Different Sulphur Contents



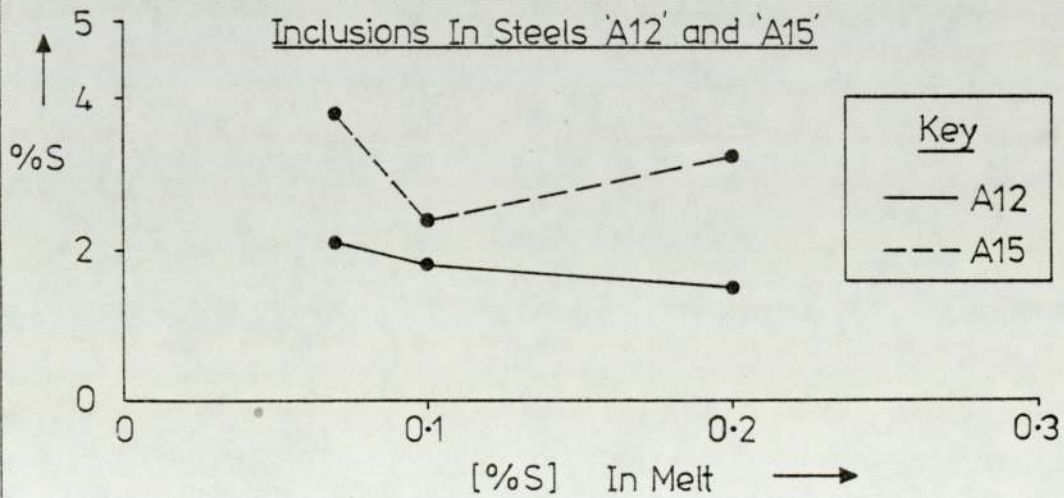
**FIG-60 : Mean 'As Cast' Oxide Inclusion Compositions
In Steels 'A6' and 'A12' For Different Sulphur
Contents**



**FIG-61 : Mean 'As Cast' Oxide Inclusion Compositions
In Steels 'A7' and 'A15' For Different Sulphur
Contents**



**FIG-62 : Mean Sulphur Contents Of 'As Cast' Oxide
Inclusions In Steels 'A12' and 'A15'**



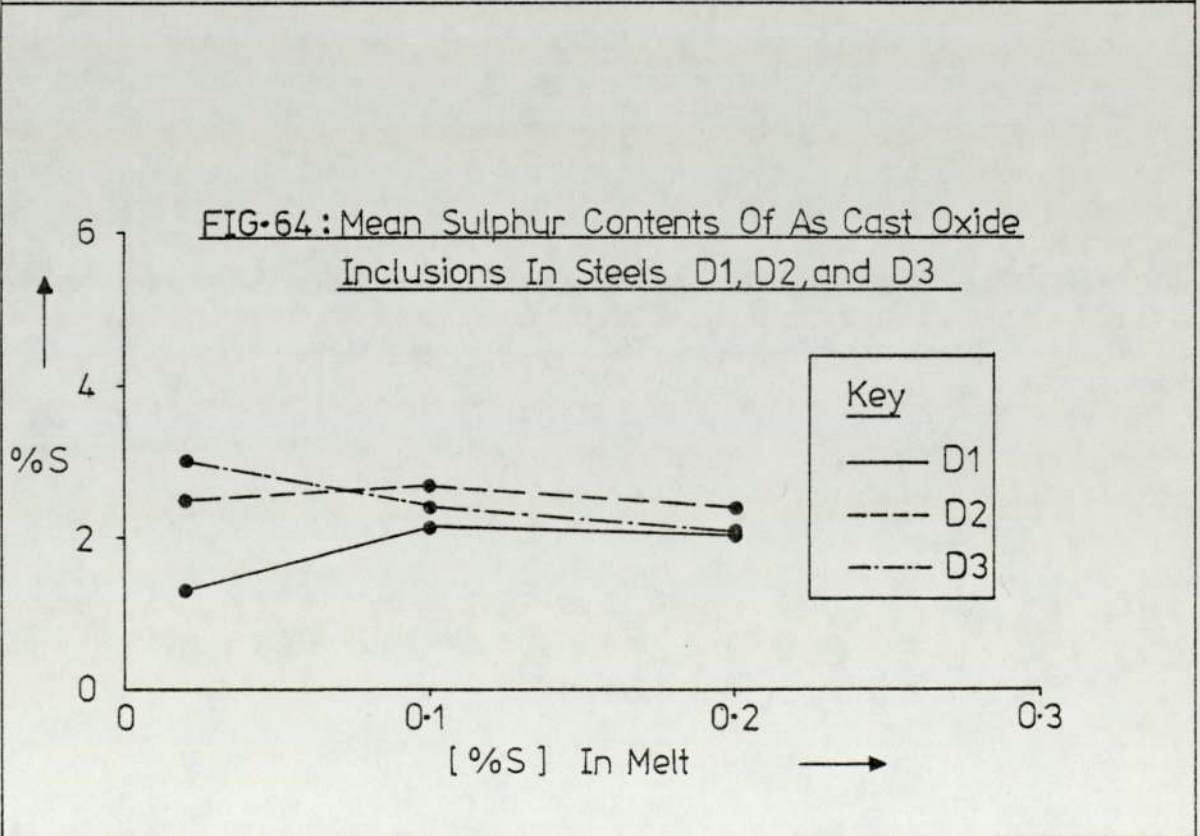
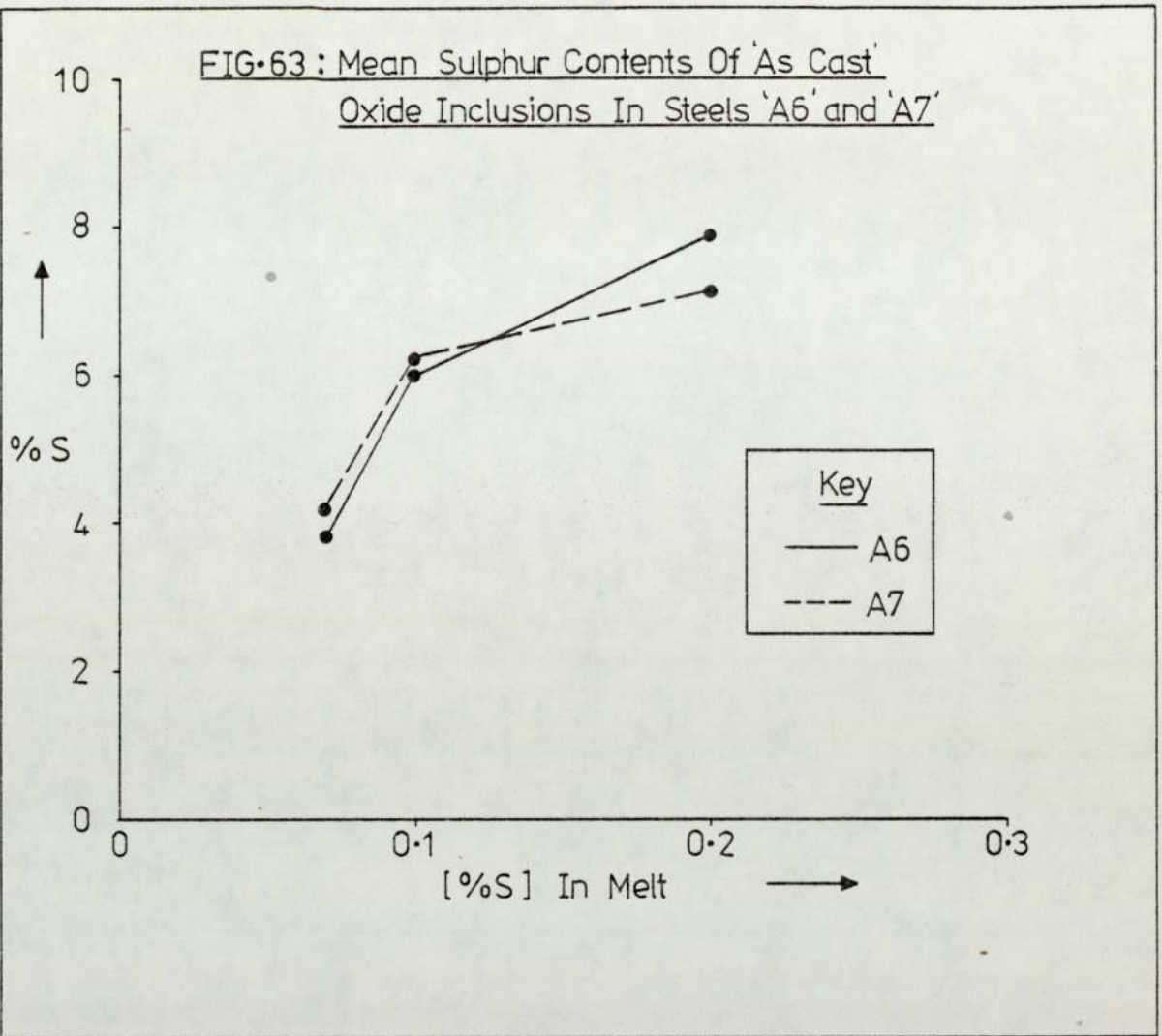


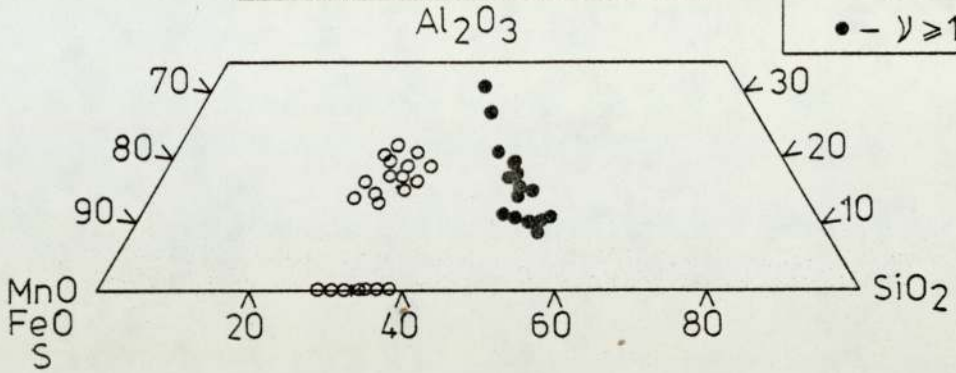
FIG-65: Oxide Inclusion Compositions

After Rolling Of Steels Containing 0.10% S

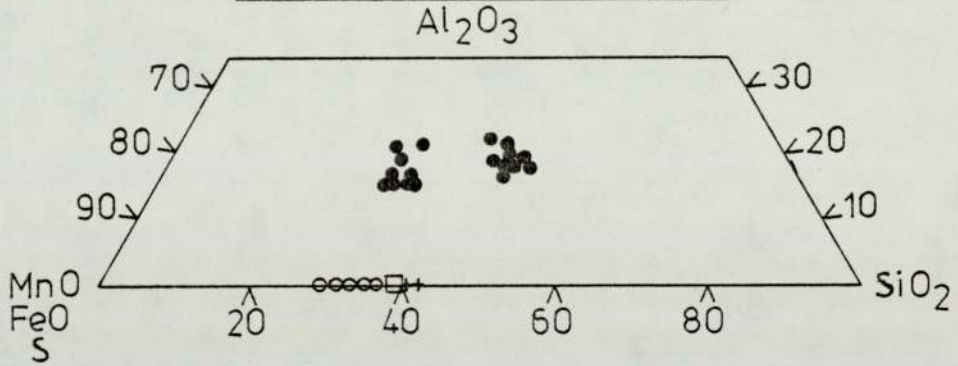
Key

- + - $0.1 \leq \nu < 0.5$
- o - $\nu < 0.1$
- - $0.5 \leq \nu < 1.0$
- - $\nu \geq 1.0$

(a) Rolling Temperature 900°C



(b) Rolling Temperature 1000°C



(c) Rolling Temperature 800°C

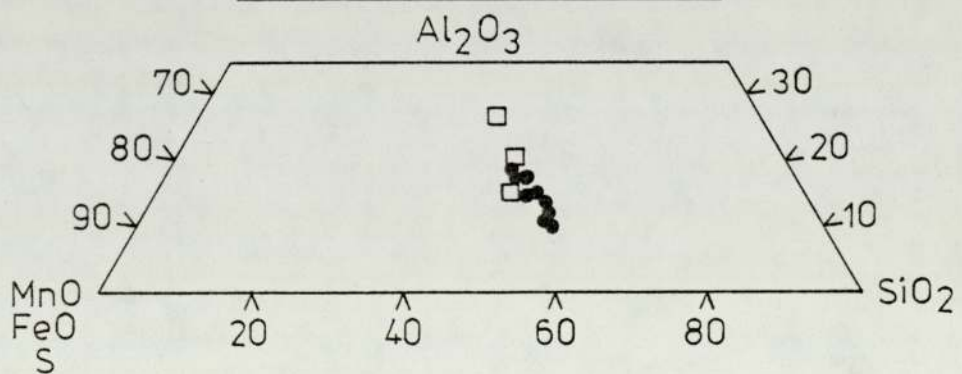
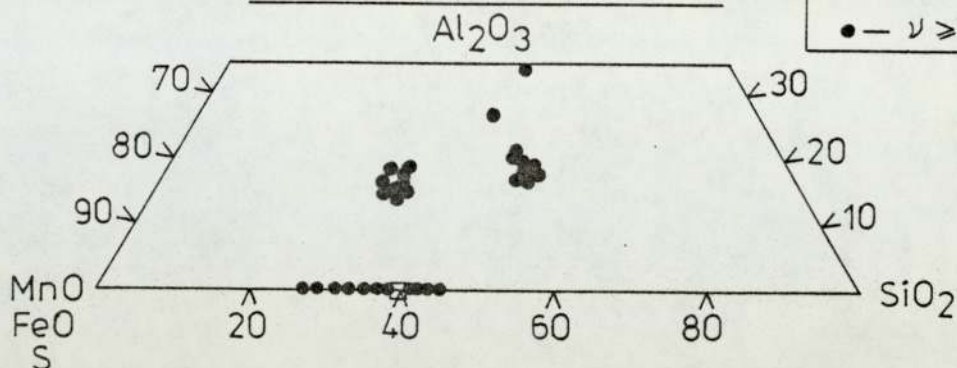


FIG.66:Oxide Inclusion Compositions After Rolling Of Steels Containing 0.10%S

Key

- — $\nu < 0.1$
- + — $0.1 \leq \nu < 0.5$
- — $0.5 \leq \nu < 1.0$
- — $\nu \geq 1.0$

(a) Rolling Temperature 1100°C



(b) Rolling Temperature 1200°C

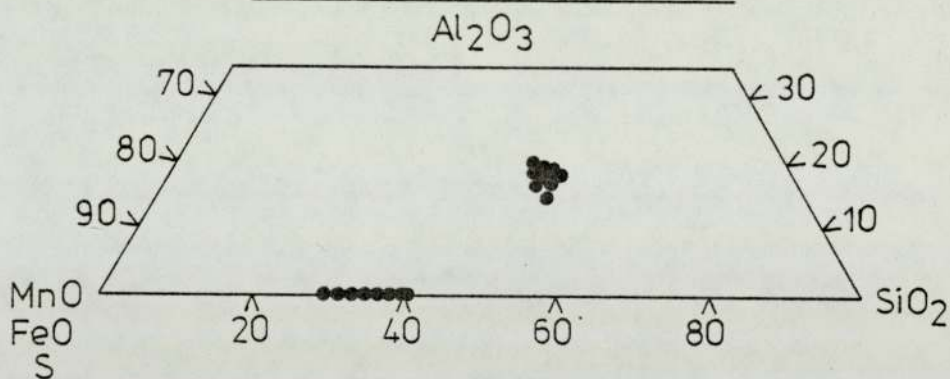


FIG.67:Oxide Inclusion Compositions After Rolling Of Steels Containing 0.07%S

Rolling Temperature 900°C

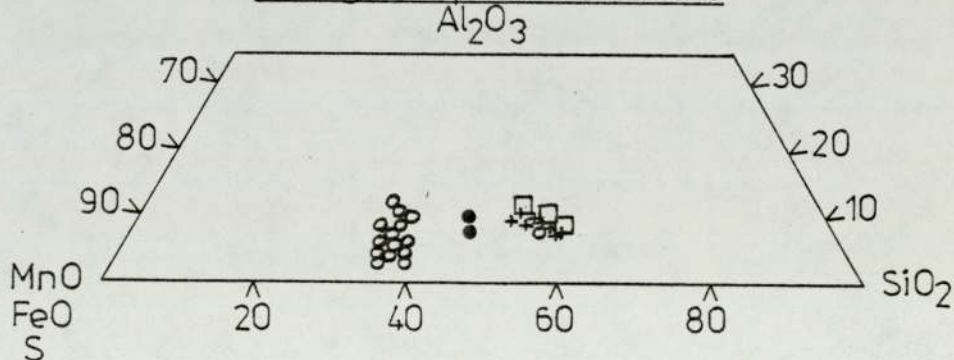


FIG-68:Oxide Inclusion Compositions After Rolling Of Steels Containing 0.07%S

Key

- - $\nu < 0.1$
- + - $0.1 \leq \nu < 0.5$
- - $0.5 \leq \nu < 1.0$
- - $\nu \geq 1.0$

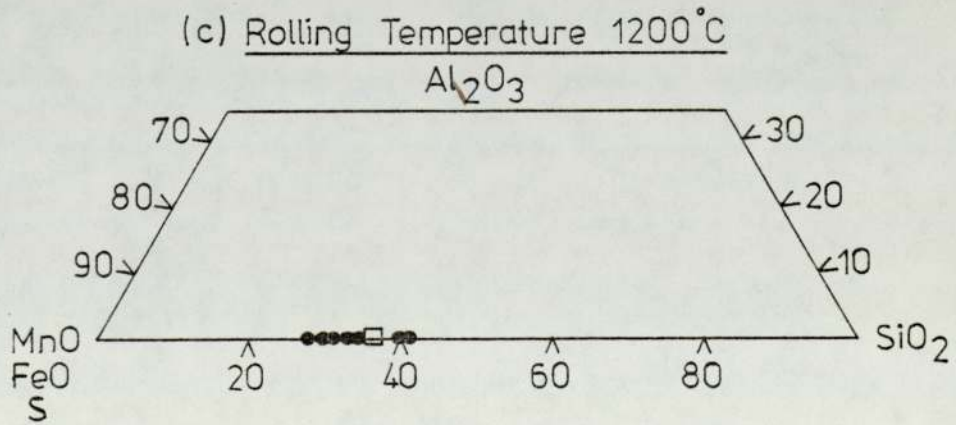
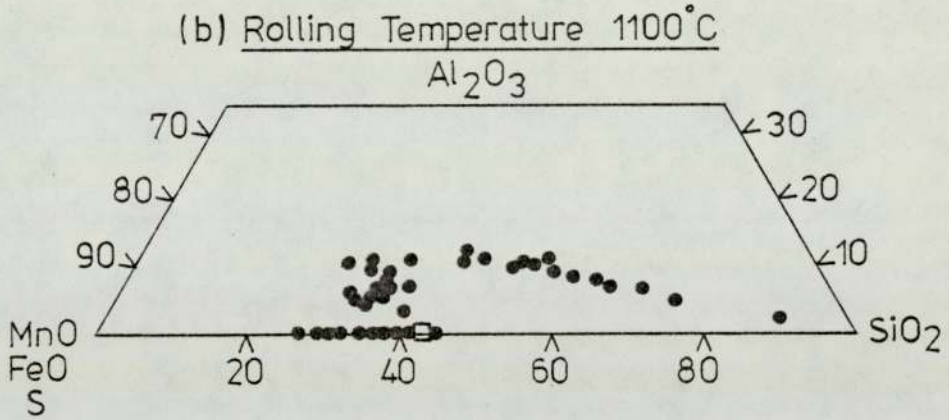
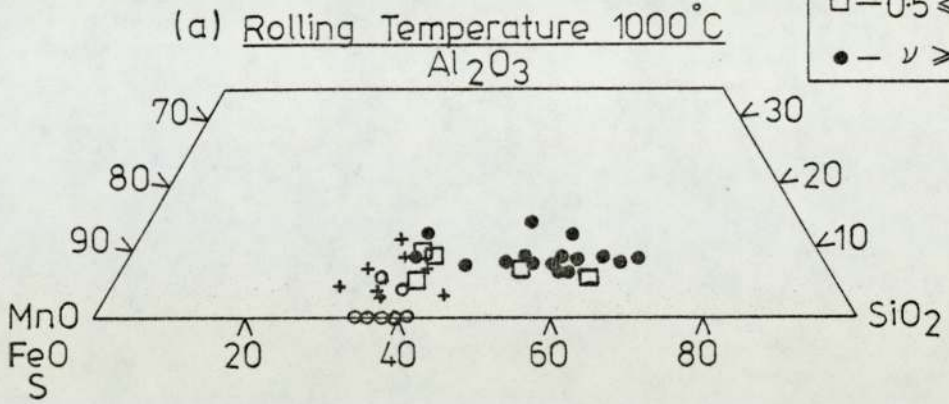


FIG-69:Oxide Inclusion Compositions After Rolling Of Steels Containing 0.07%S

Key

- — $\nu < 0.1$
- + — $0.1 \leq \nu < 0.5$
- — $0.5 \leq \nu < 1.0$
- — $\nu \geq 1.0$

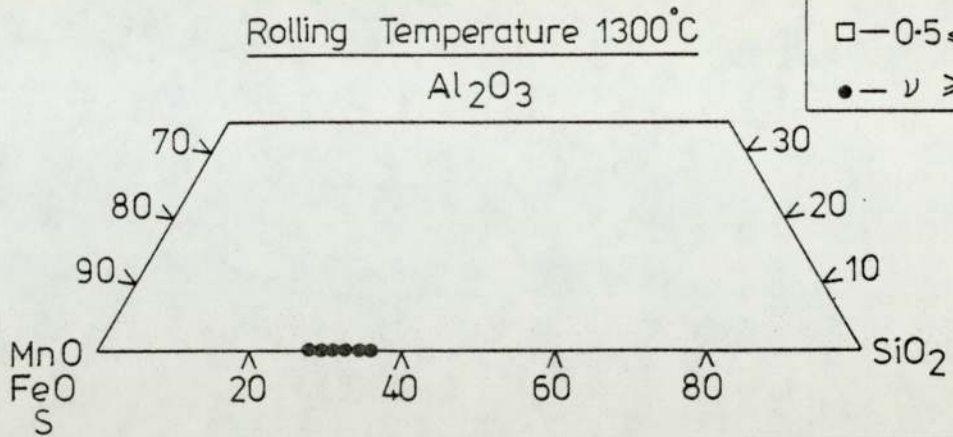
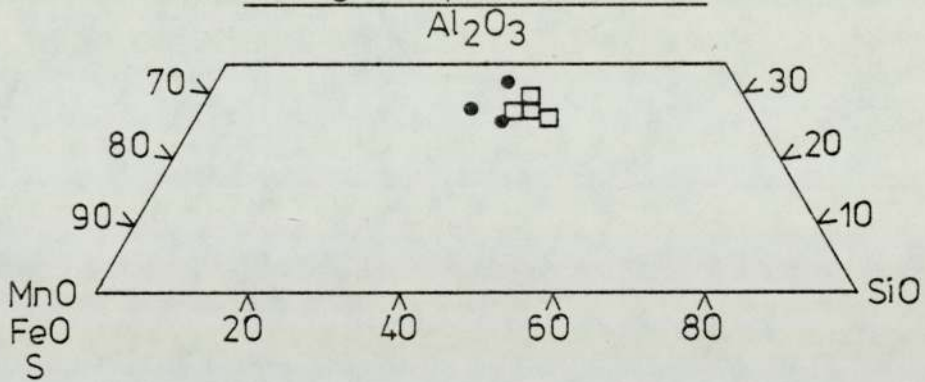


FIG-70:Oxide Inclusion Compositions After Rolling Of Steels Containing 0.20%S

(a) Rolling Temperature 800°C



(b) Rolling Temperature 900°C

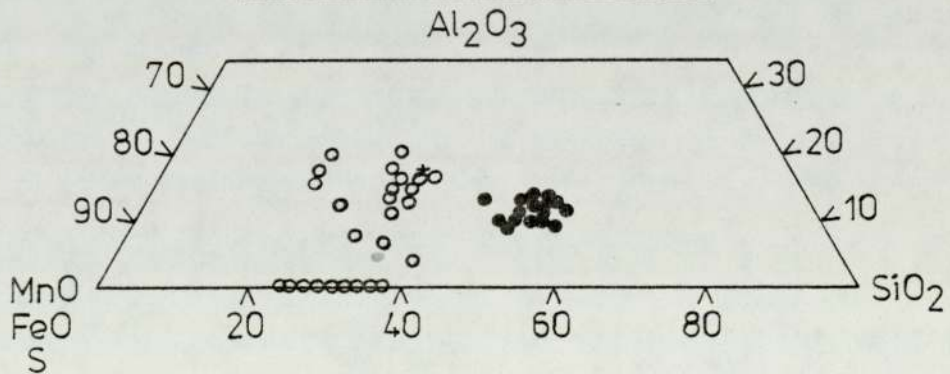
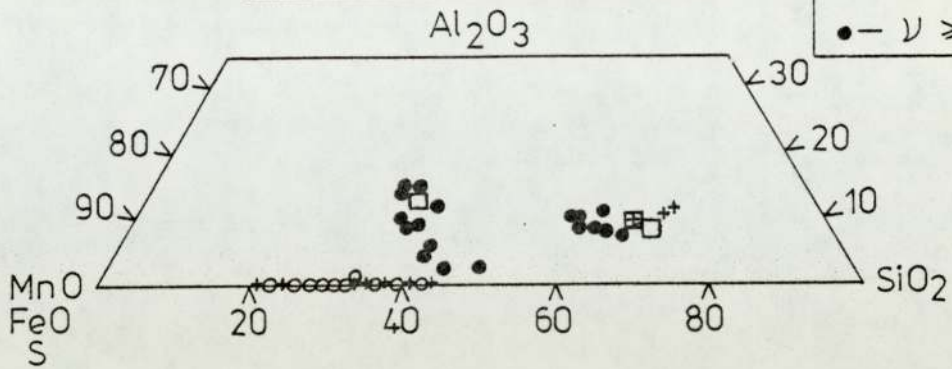


FIG-71:Oxide Inclusion Compositions After Rolling Of Steels Containing 0.20%

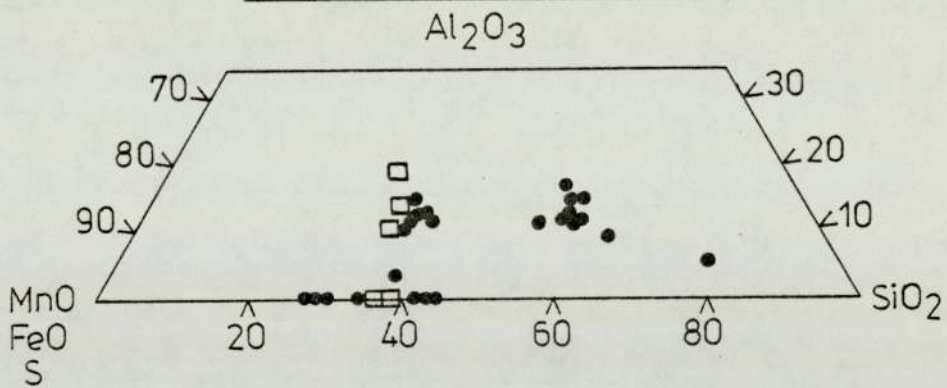
Key

- - $\nu < 0.1$
- + - $0.1 \leq \nu < 0.5$
- - $0.5 \leq \nu < 1.0$
- - $\nu \geq 1.0$

(a) Rolling Temperature 1000°C



(b) Rolling Temperature 1100°C



(c) Rolling Temperature 1200°C

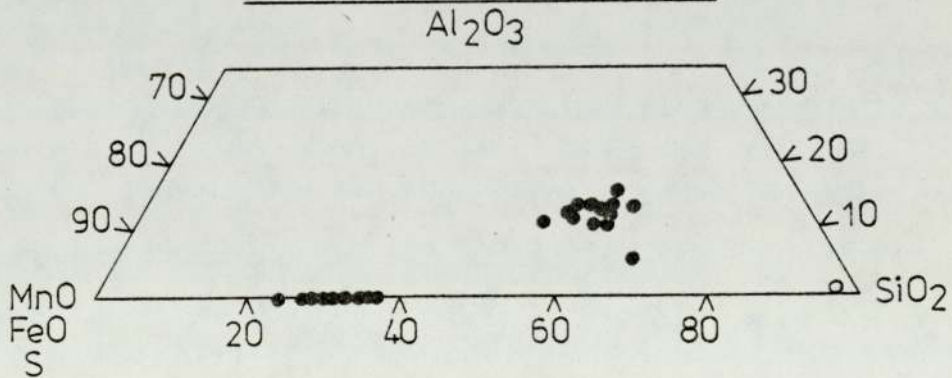


FIG.72:Oxide Inclusion Compositions After Rolling Of Steels Containing 0.20%S

Key

● — $v \geq 1.0$

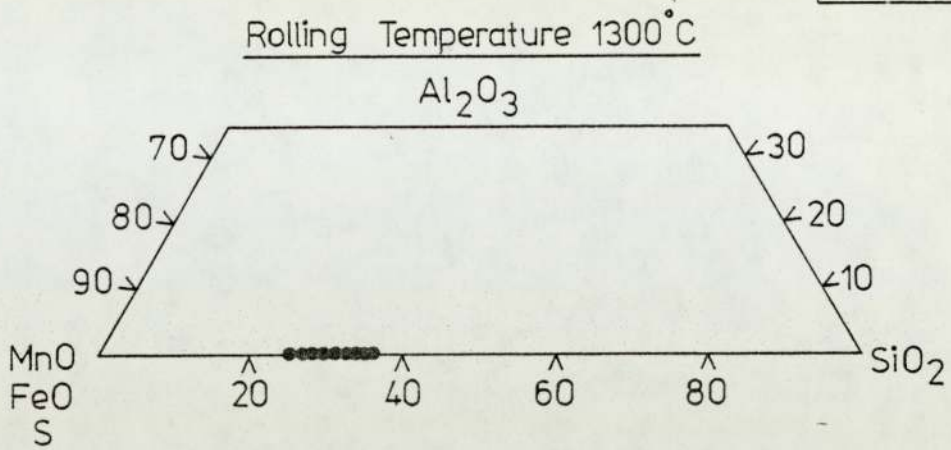


FIG.73:The Mean Sulphur Contents Of Oxide Inclusions In Steels Deoxidised By 'A6' After Rolling

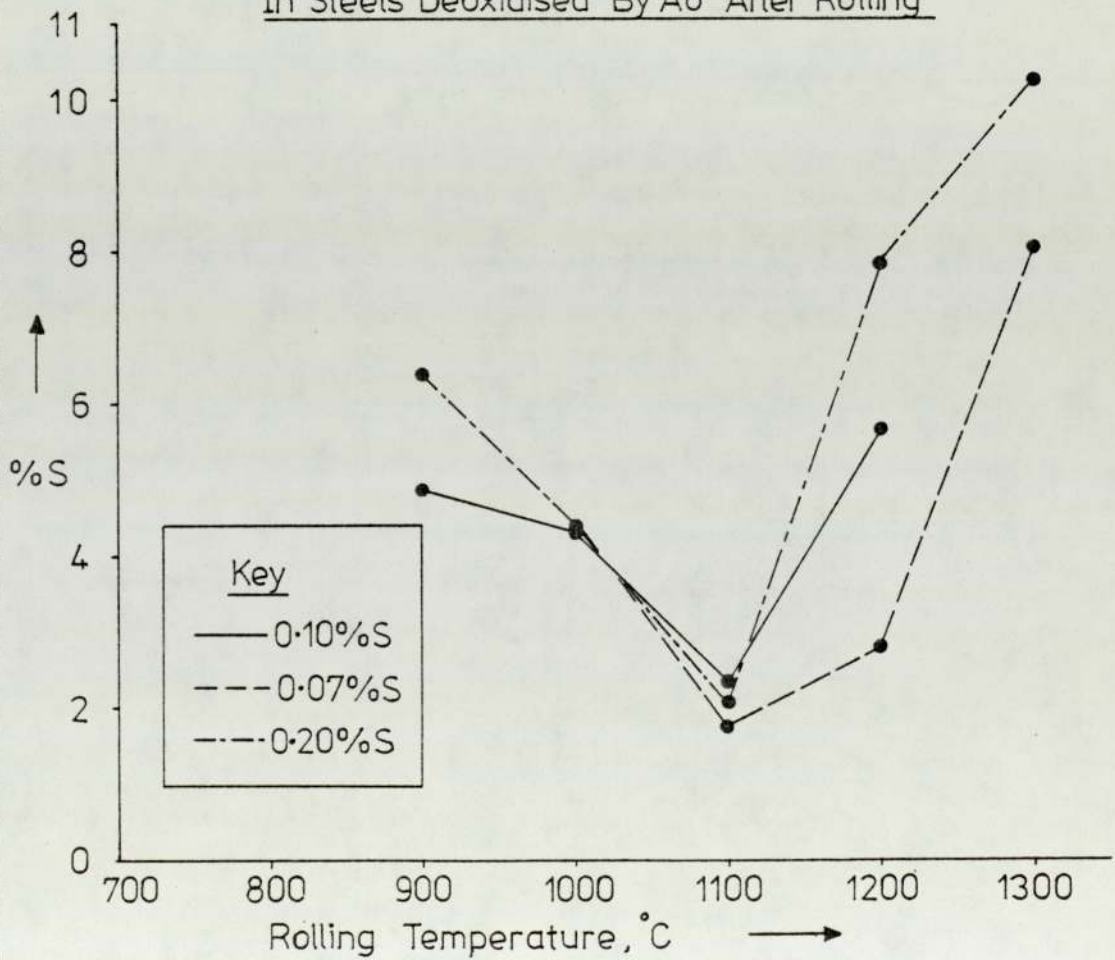


FIG.74: The Mean Sulphur Contents Of Oxide Inclusions In Steel 'A7' After Rolling

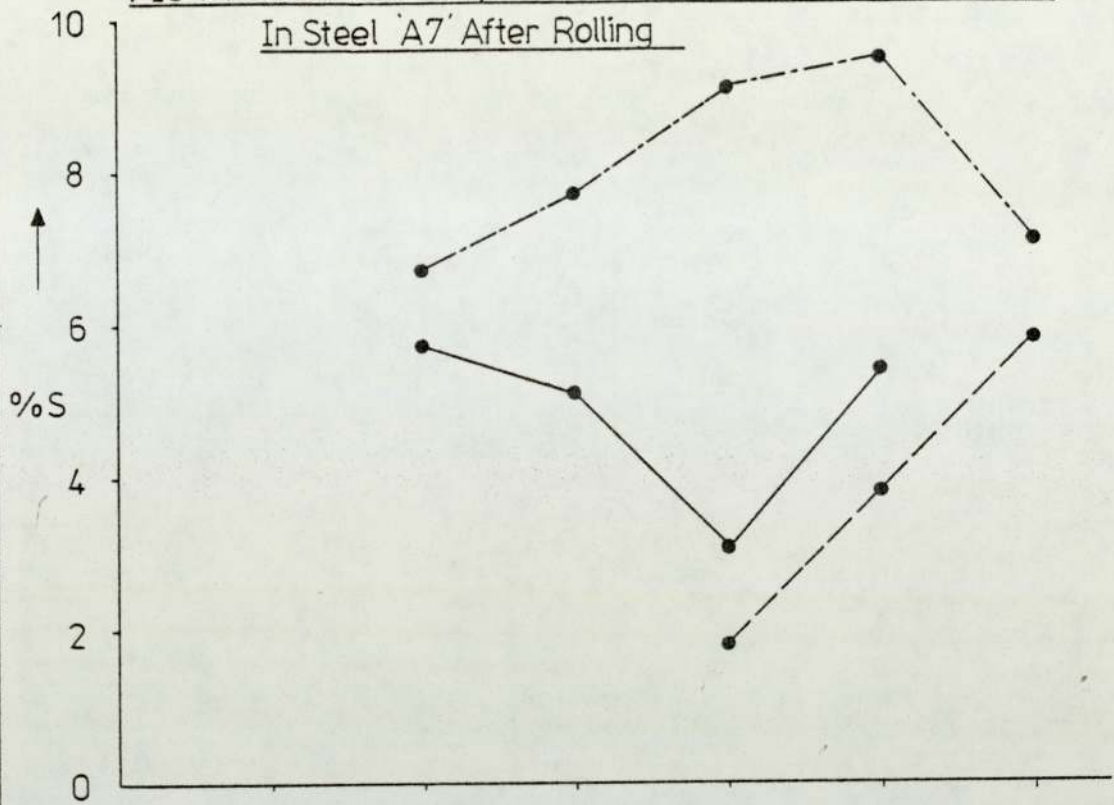
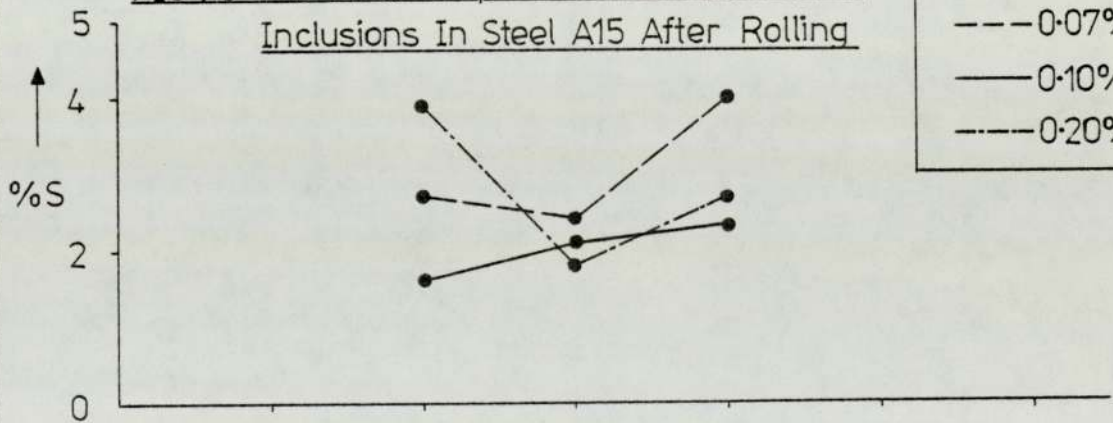


FIG.75: The Mean Sulphur Contents Of Oxide Inclusions In Steel A15 After Rolling



Key
 --- 0.07% S
 — 0.10% S
 - · - 0.20% S

FIG.76a: The Mean Sulphur Contents Of Oxide Inclusions In Steel A12 After Rolling

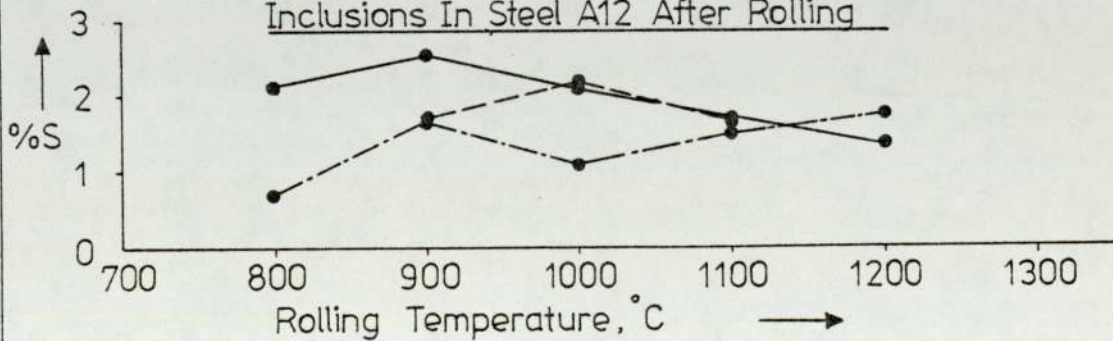
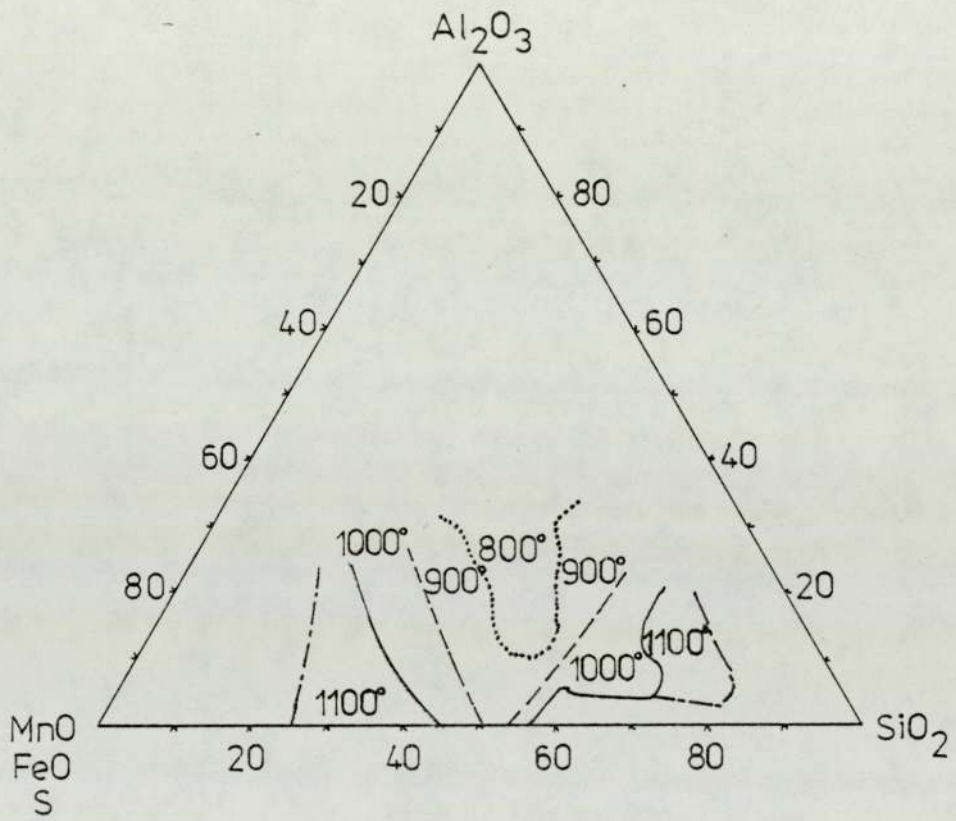


FIG.76b: Estimated Non-Deformable / Deformable
Inclusion Compositions At Different
Rolling Temperatures



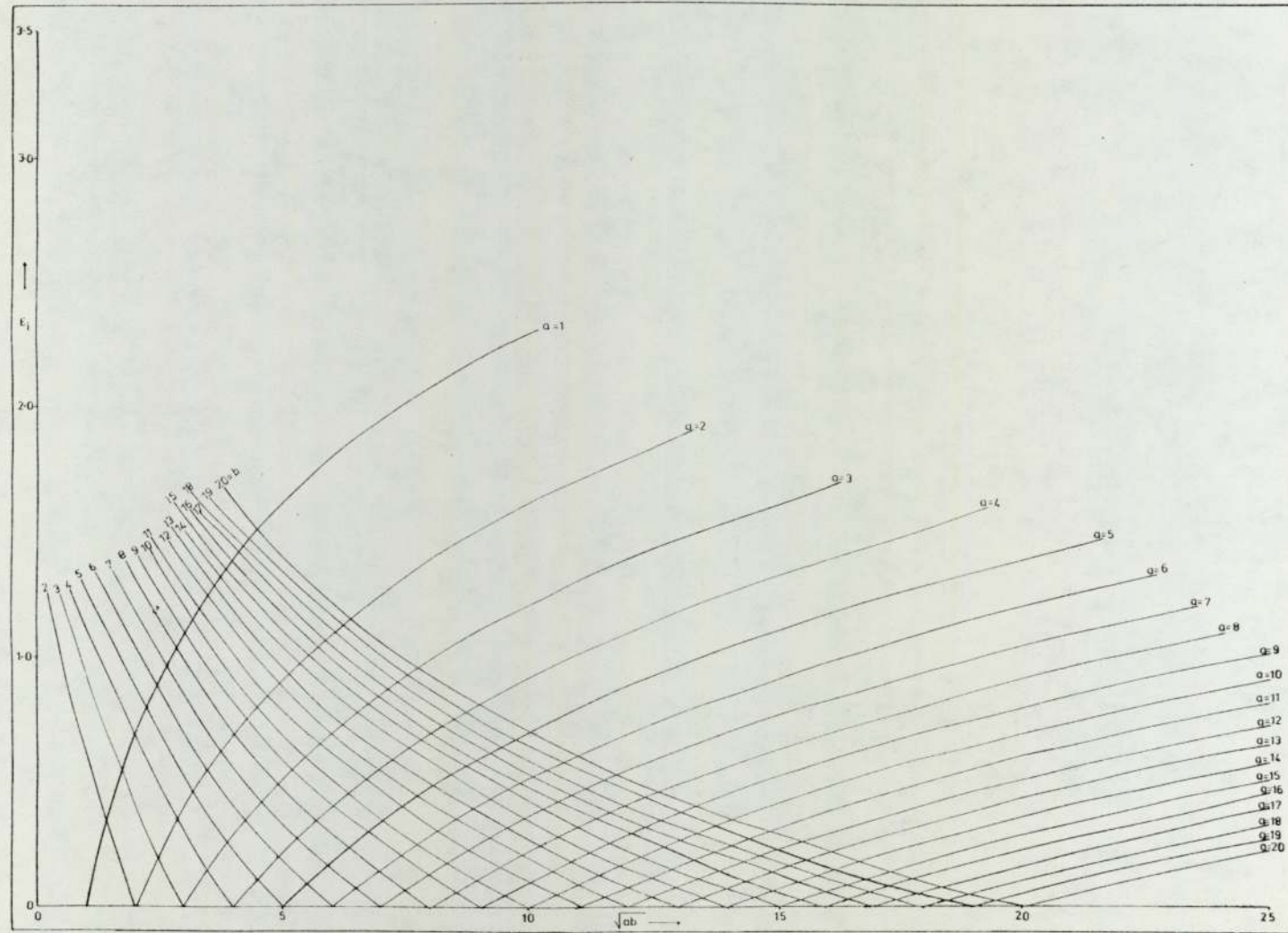


Figure 77A : THEORETICAL INCLUSION STRAIN, ϵ_i , VERSUS INCLUSION SIZE, \sqrt{ab}

FIG. 77: MELT A7 ROLLED AT 1100°C

(sulphur content = 0.07%)

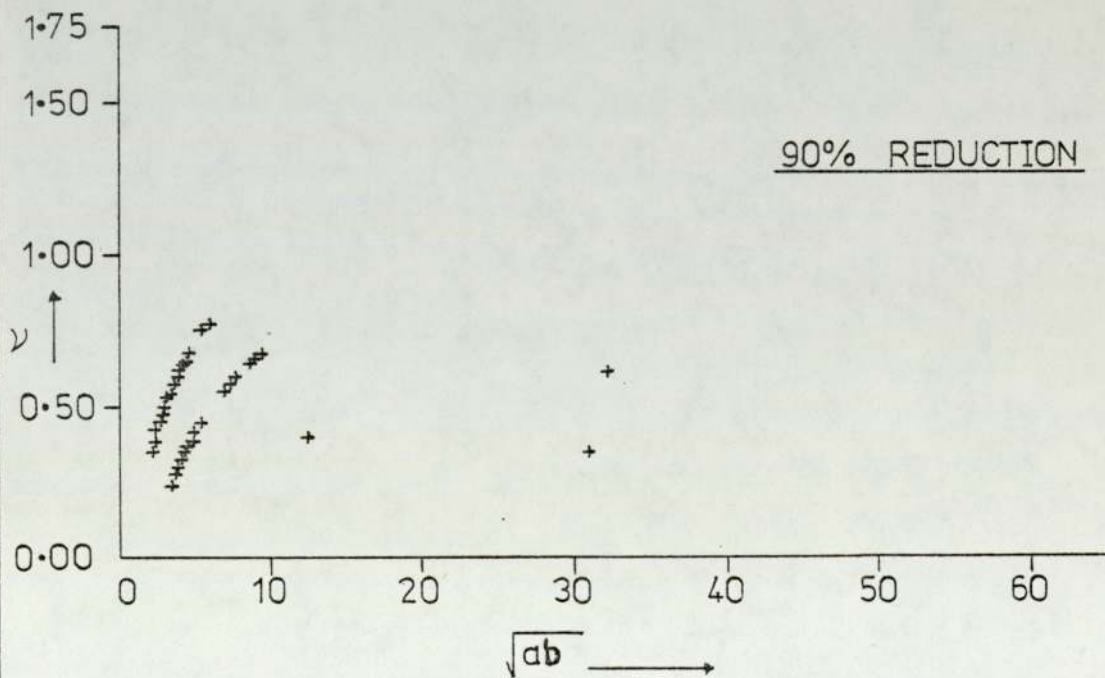
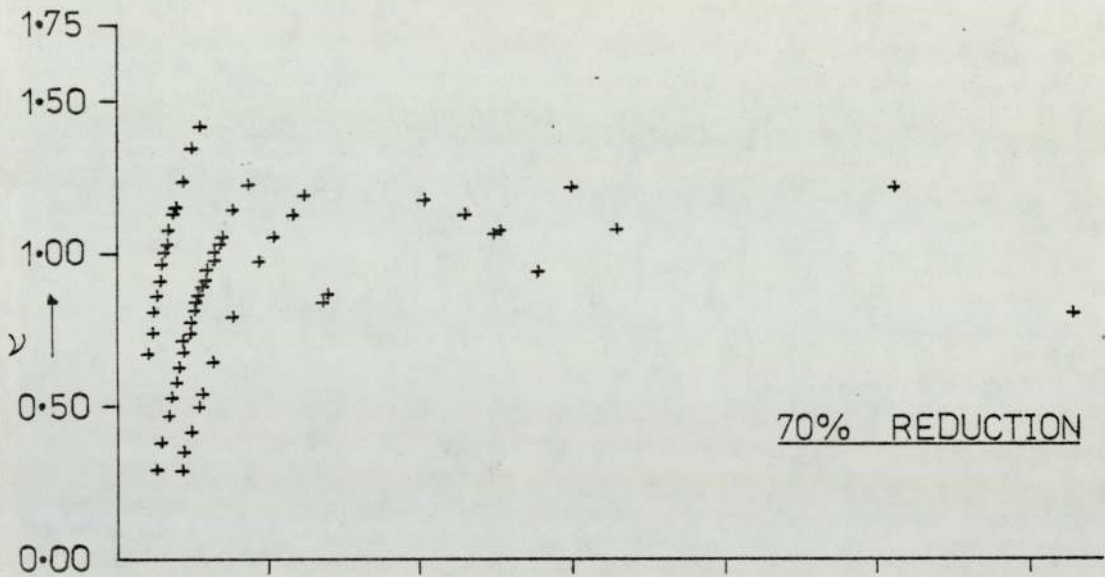
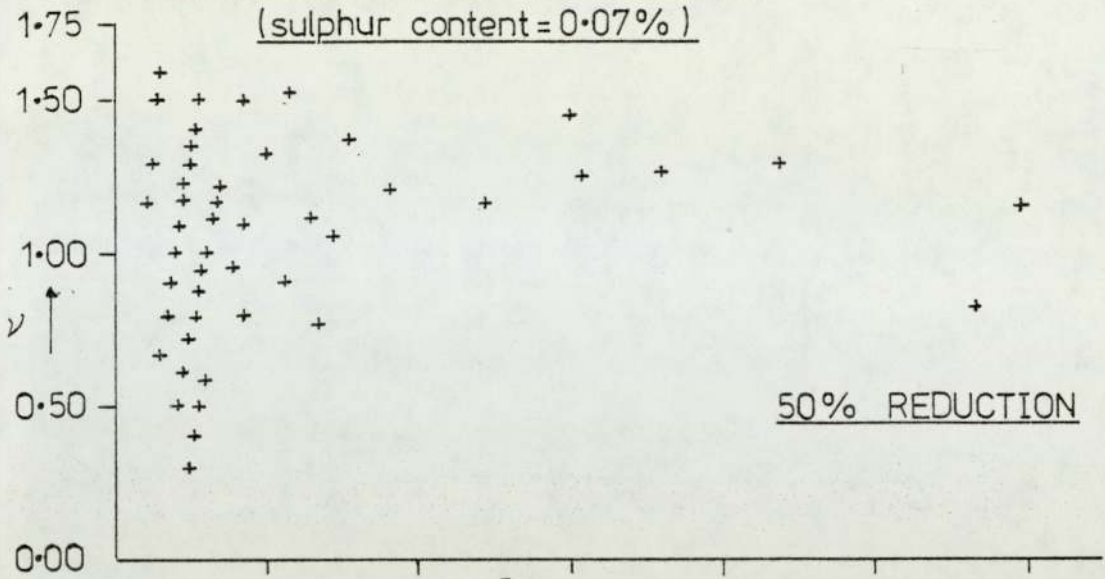


FIG-78 : MELT A7 ROLLED AT 1200°C

(sulphur content = 0.07%)

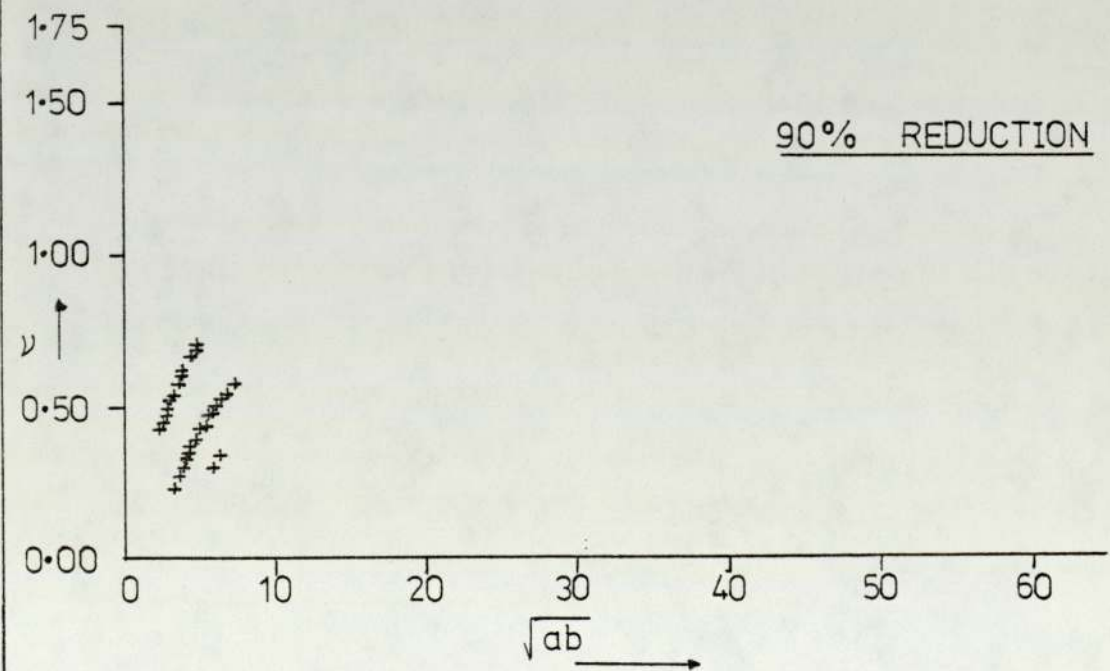
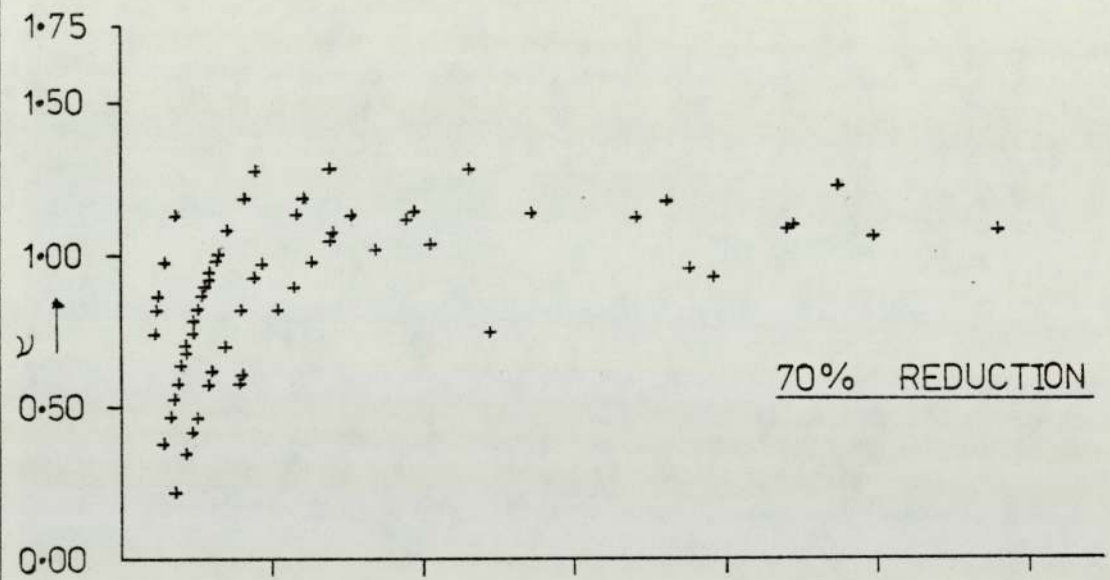
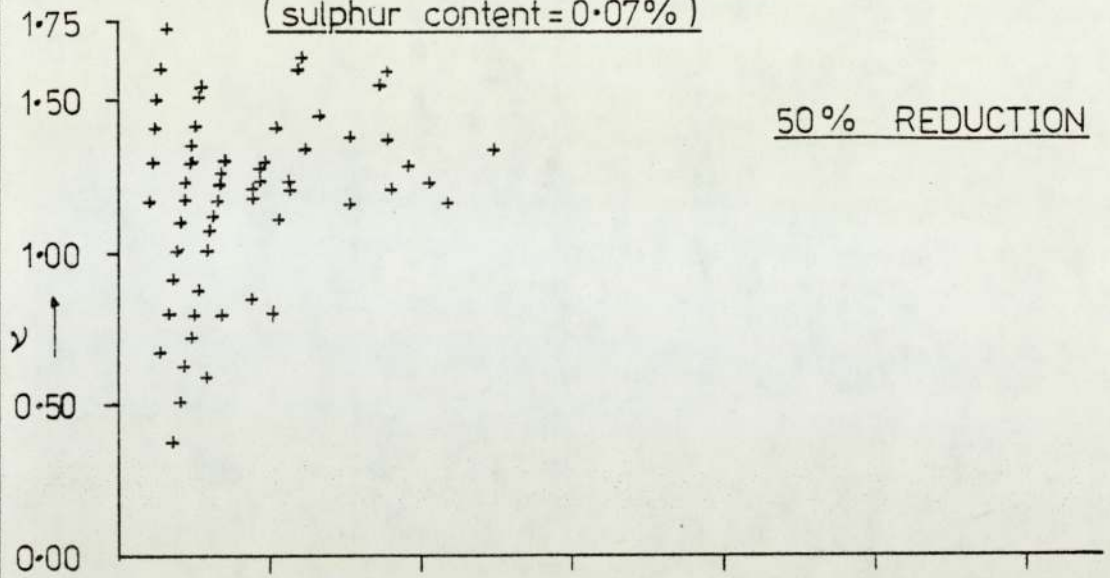


FIG-79 : MELT A7 ROLLED AT 1300°C
(sulphur content = 0.07%)

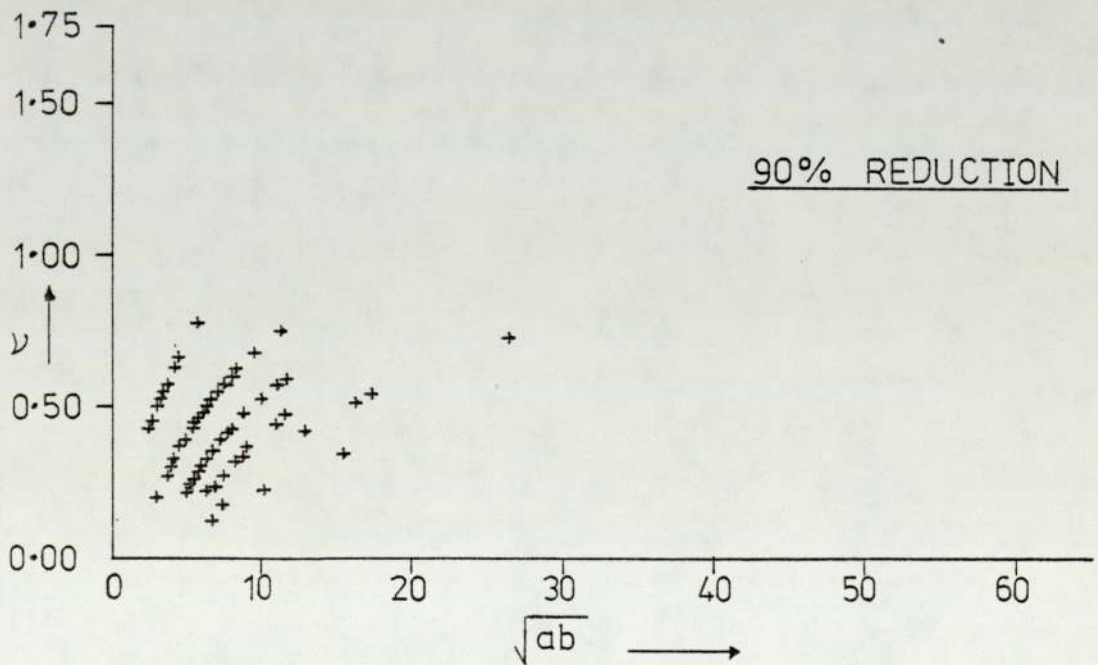
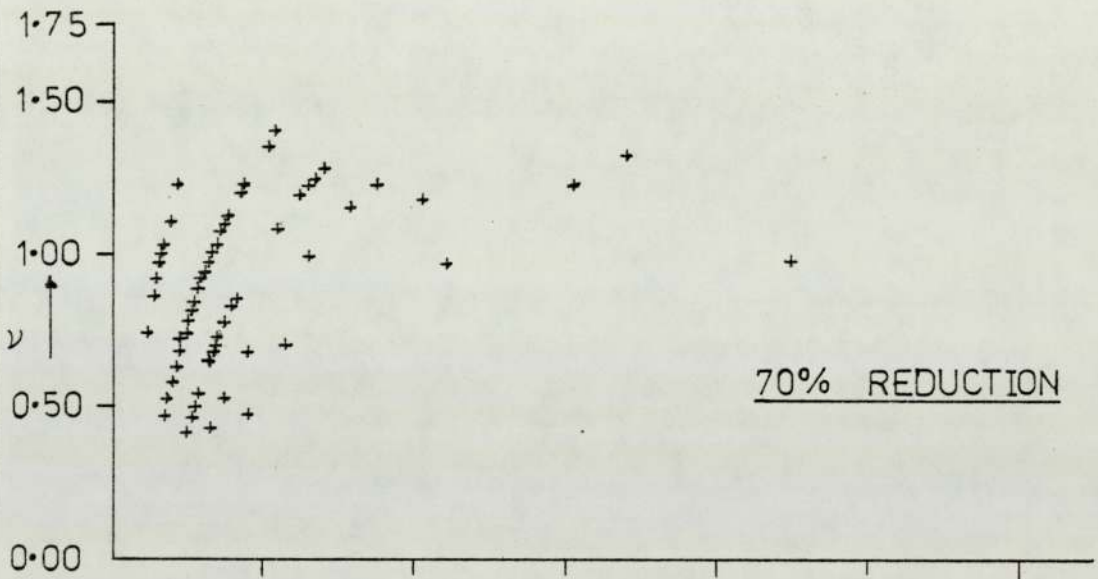
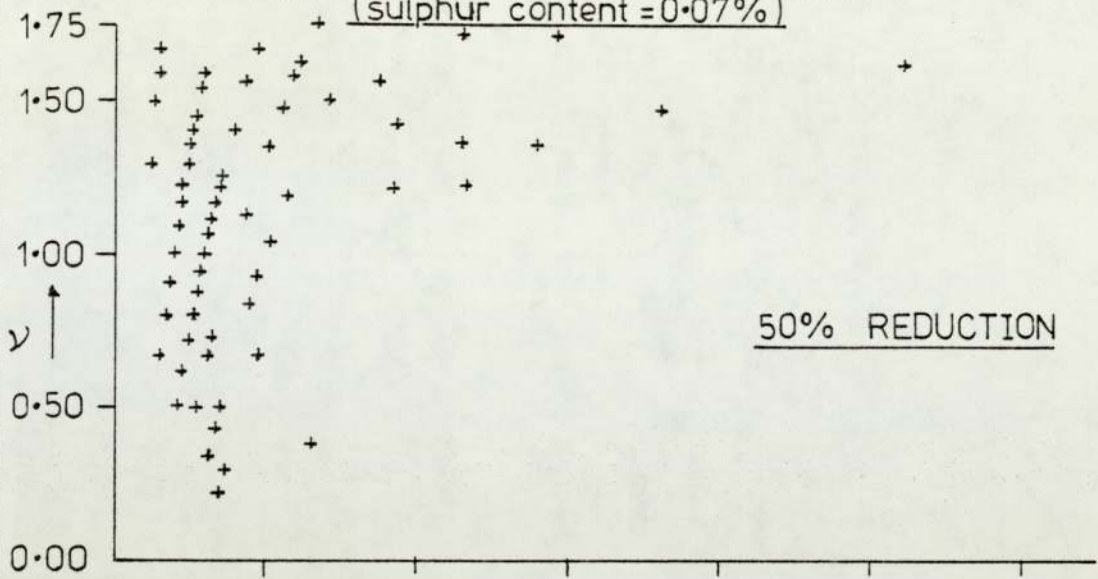


FIG. 80: MELT A6 ROLLED AT 1000°C
(sulphur content = 0.07%)

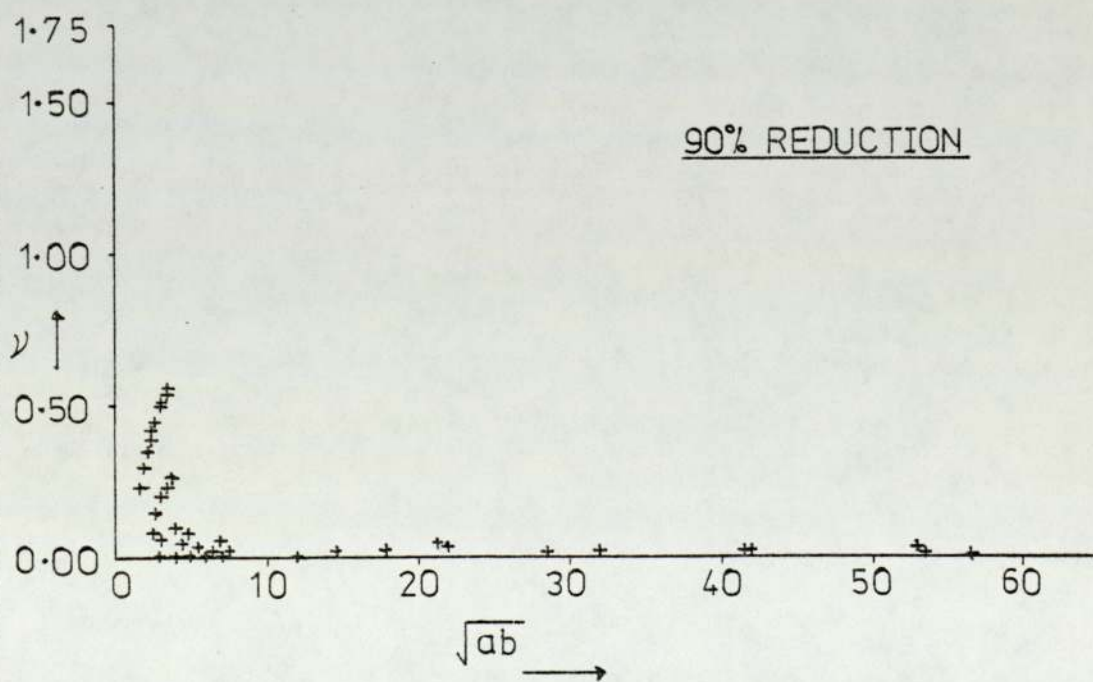
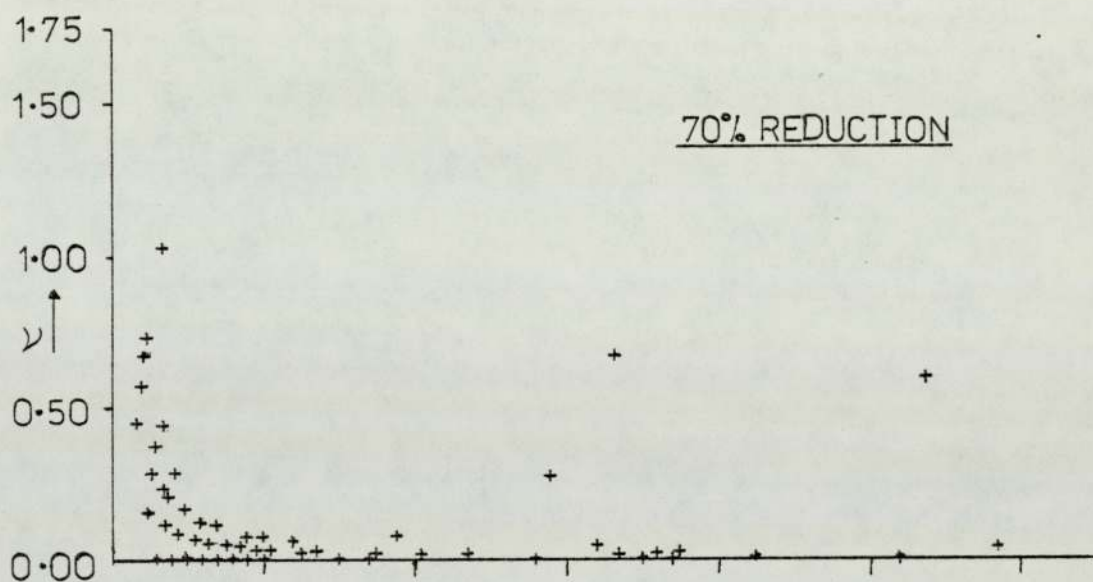
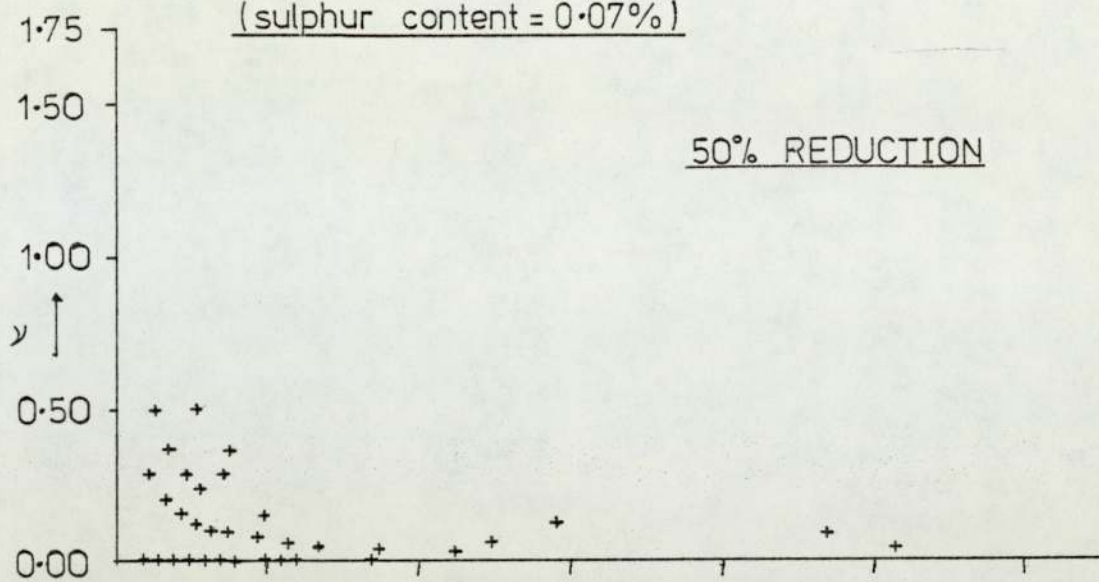


FIG-81: MELT A6 ROLLED AT 1100°C

(sulphur content = 0.07%)

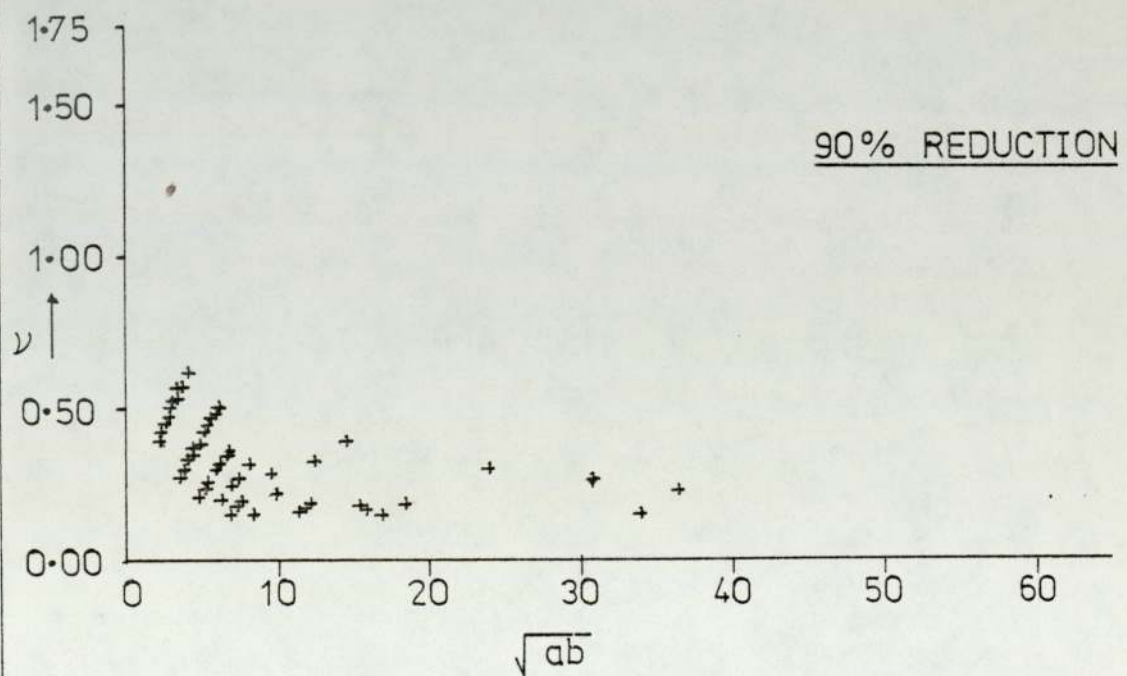
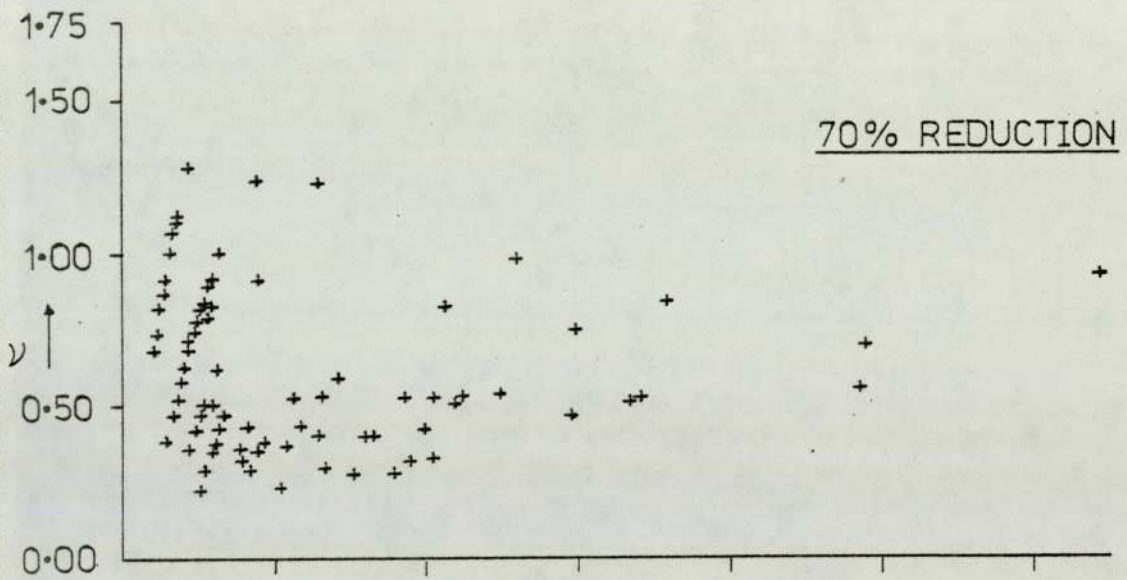
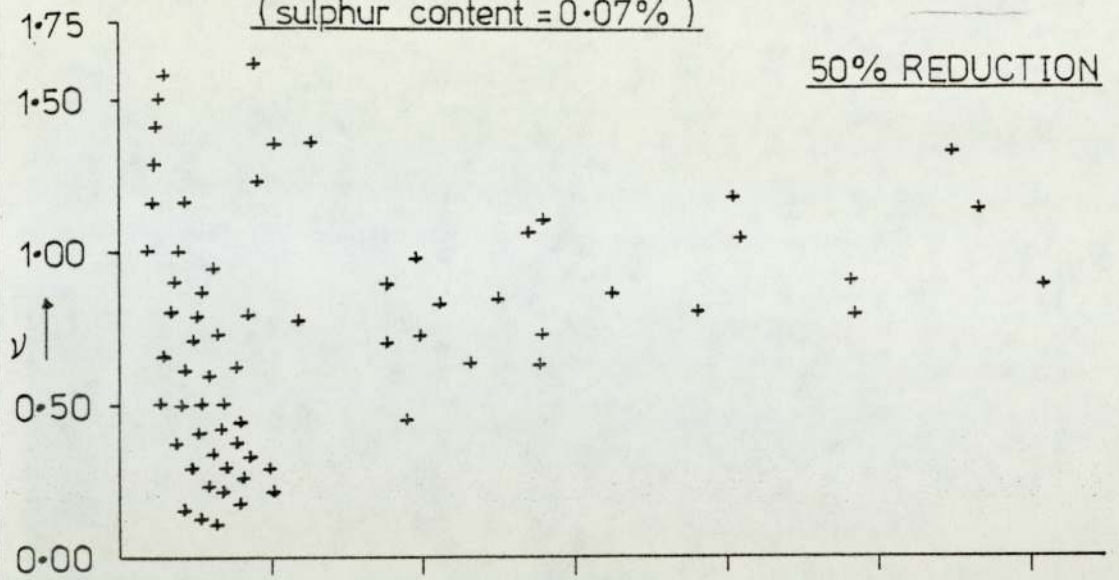


FIG.82: MELT A6 ROLLED AT 1200°C
(sulphur content=0.07%)

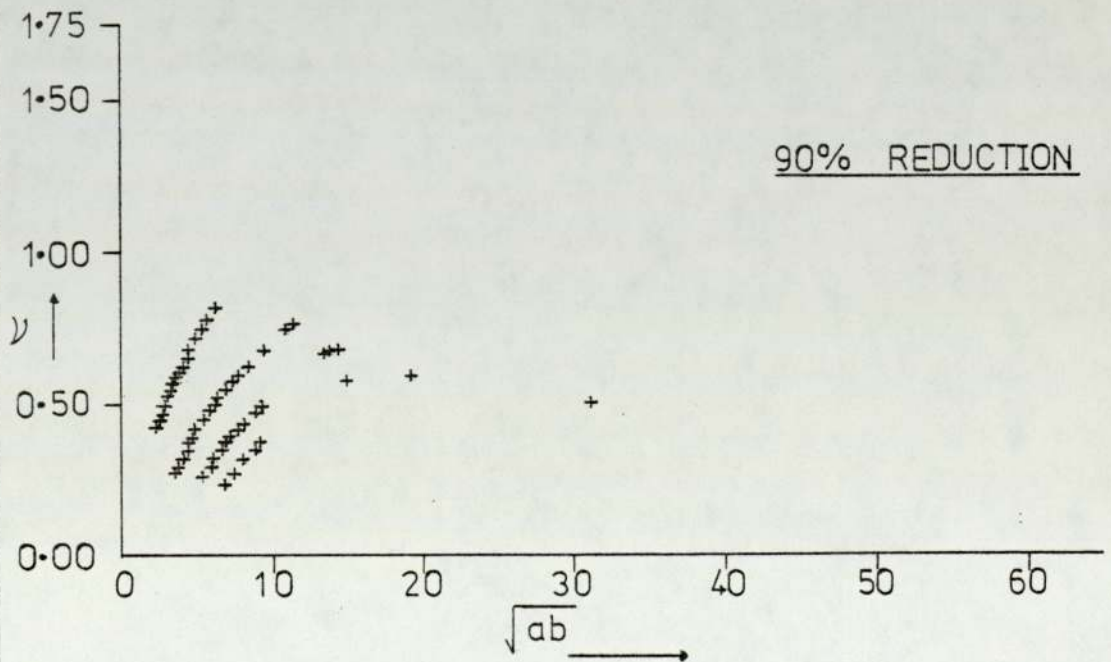
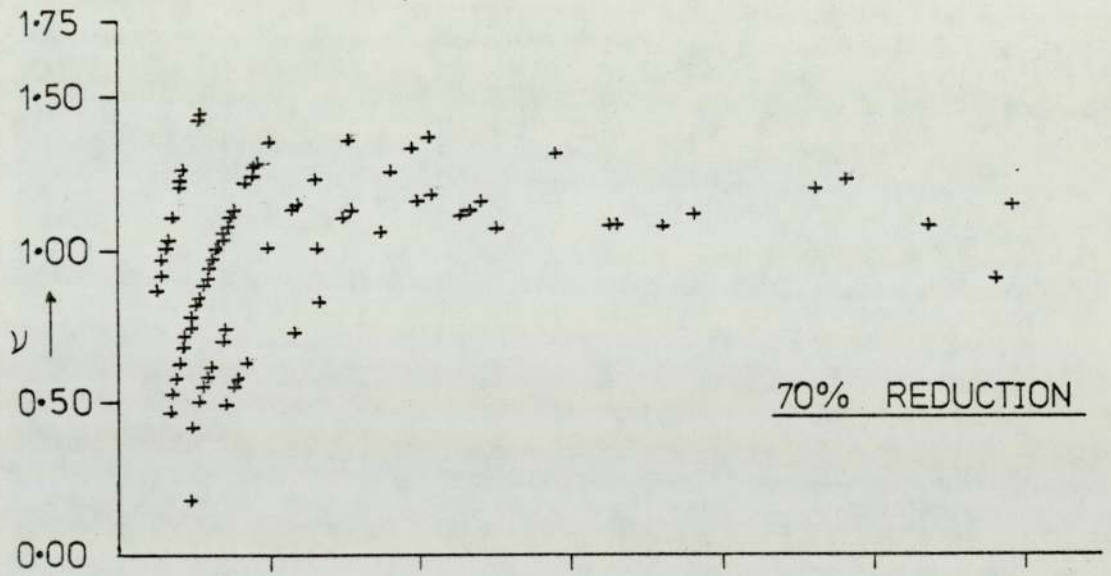
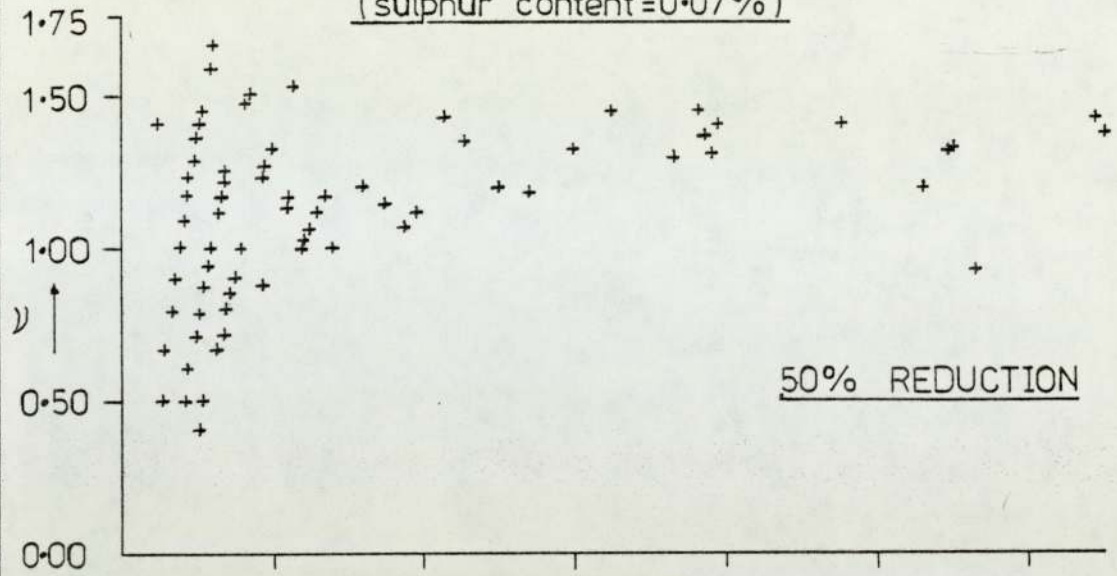


FIG-83: MELT A6 ROLLED AT 1300°C

(sulphur content=0.07%)

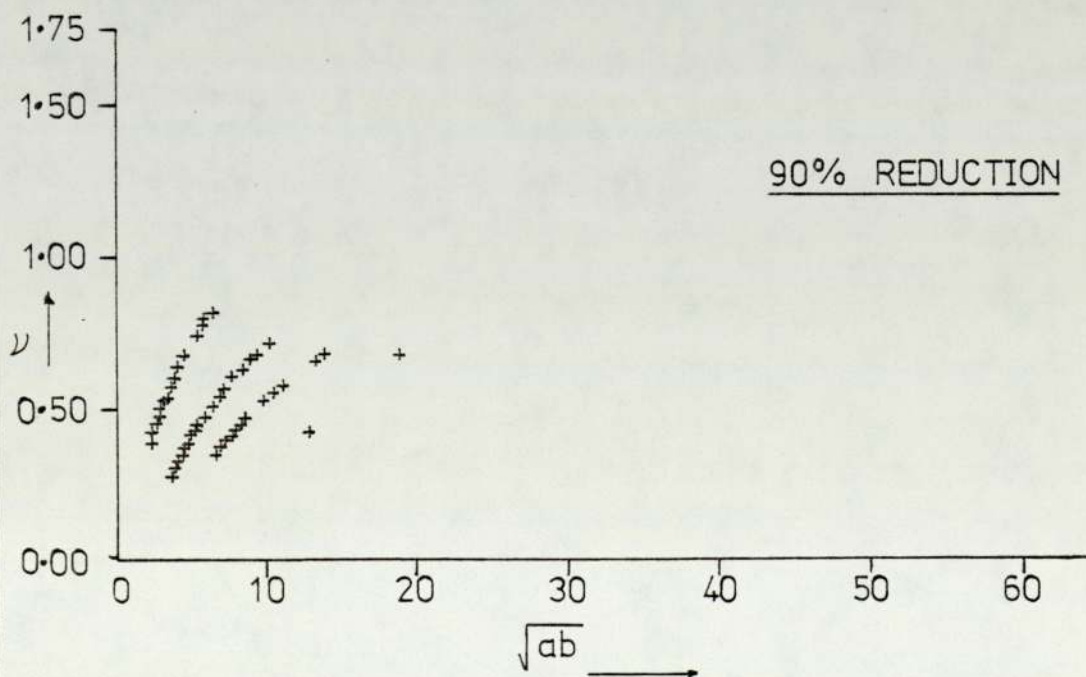
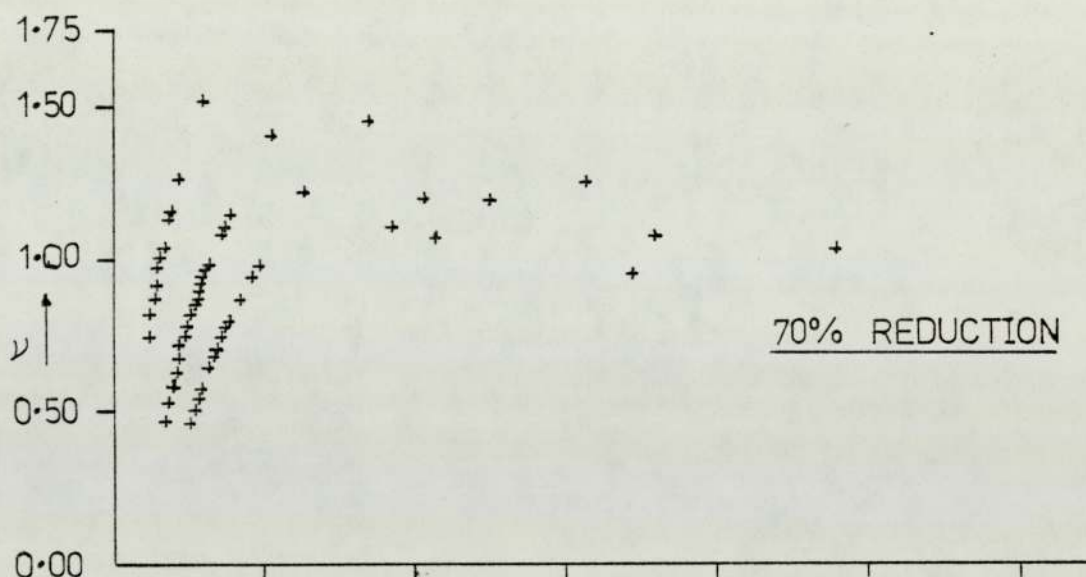
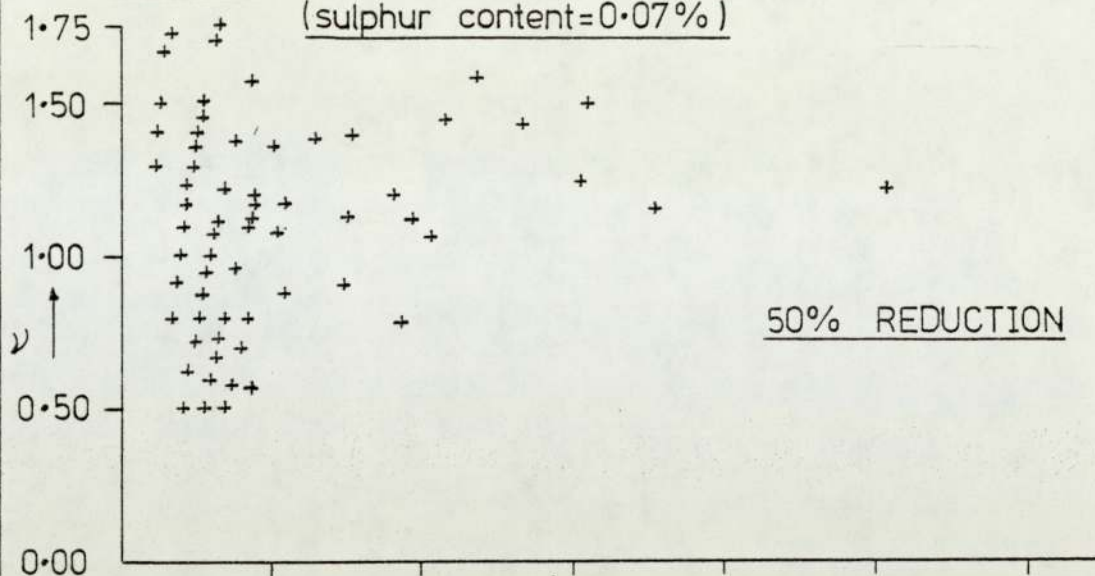


FIG. 84: MELT A12 ROLLED AT 900°C

(sulphur content = 0.07%)

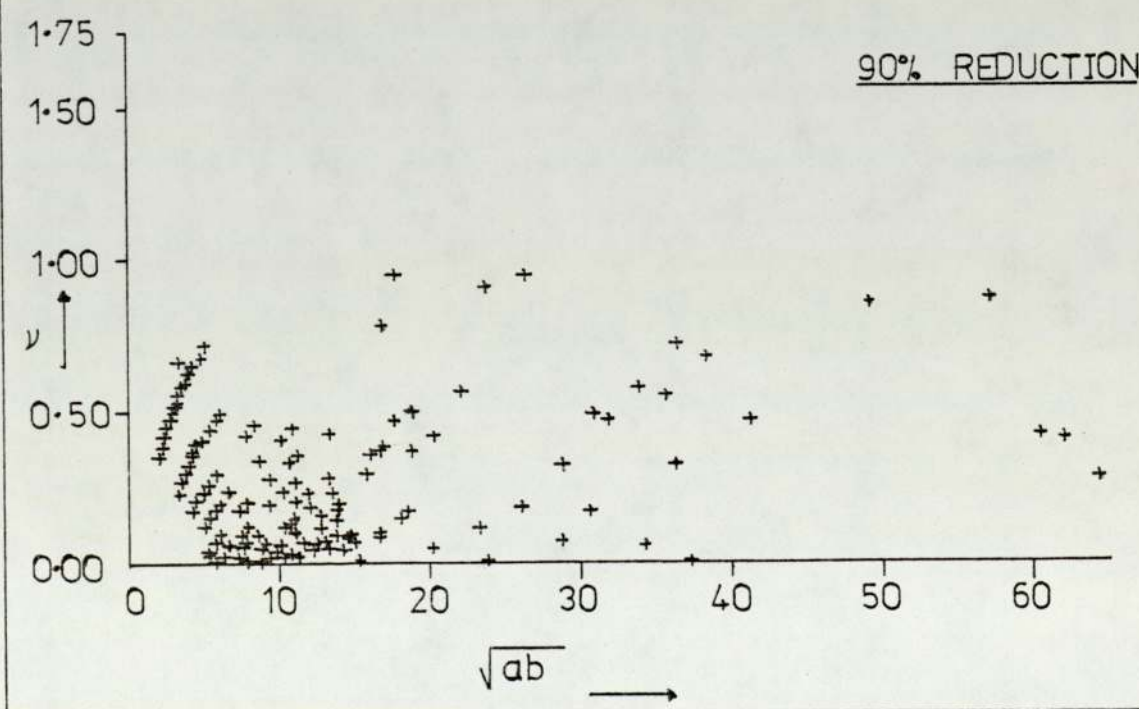
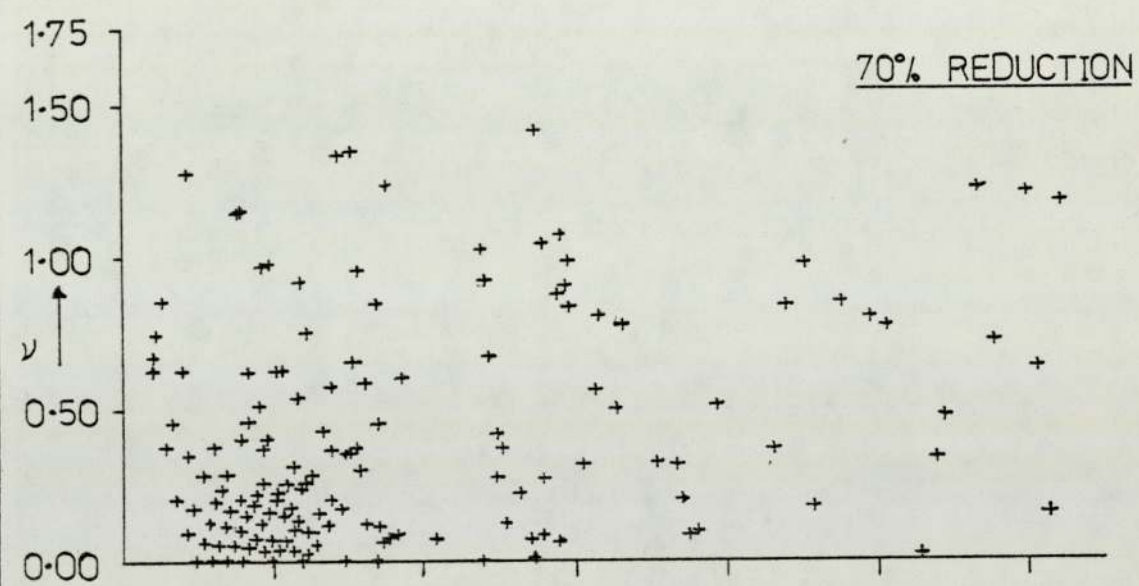
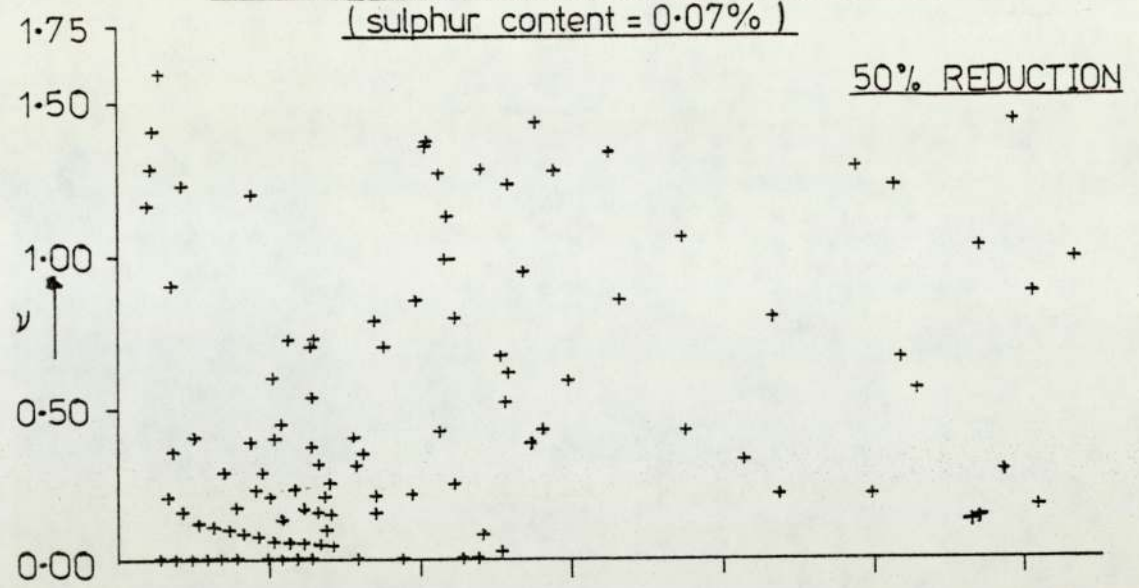


FIG. 85: MELT A12 ROLLED AT 1000°C
(sulphur content = 0.07%)

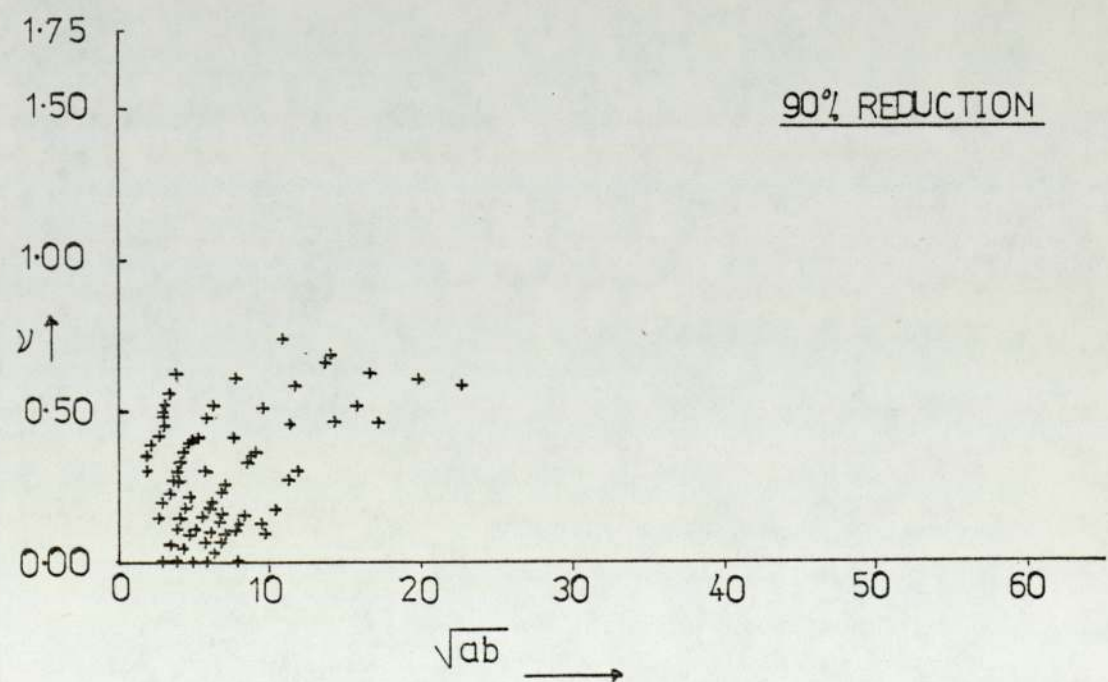
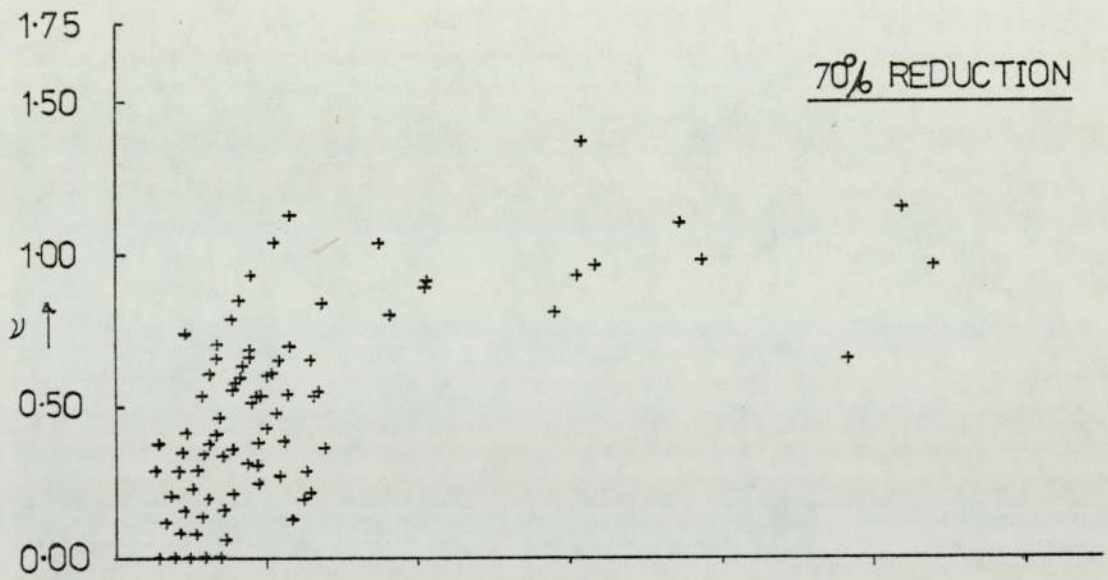
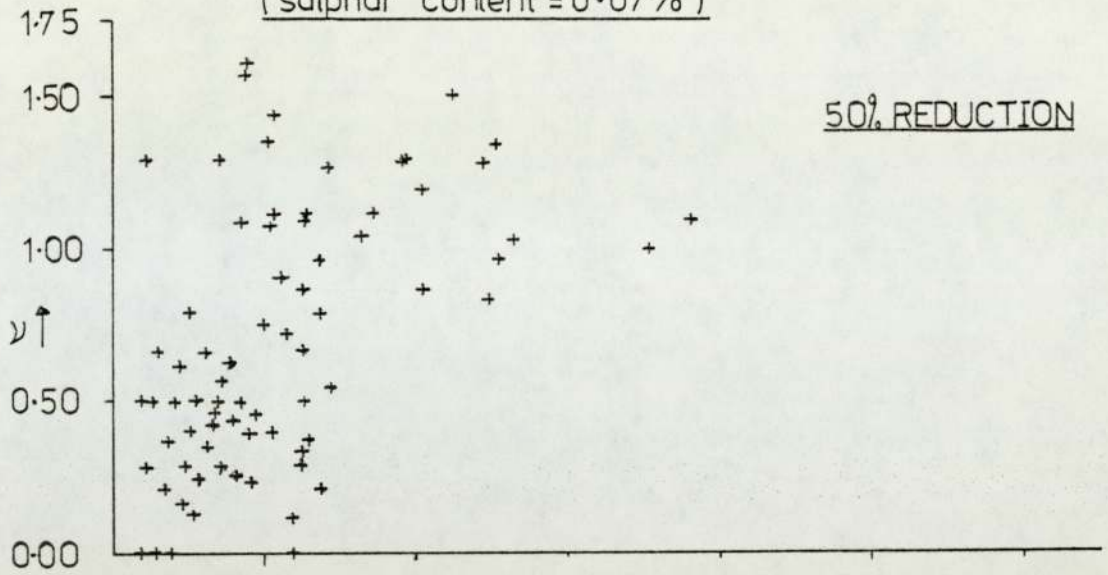


FIG-86: MELT A12 ROLLED AT 1100°C
(sulphur content = 0.07%)

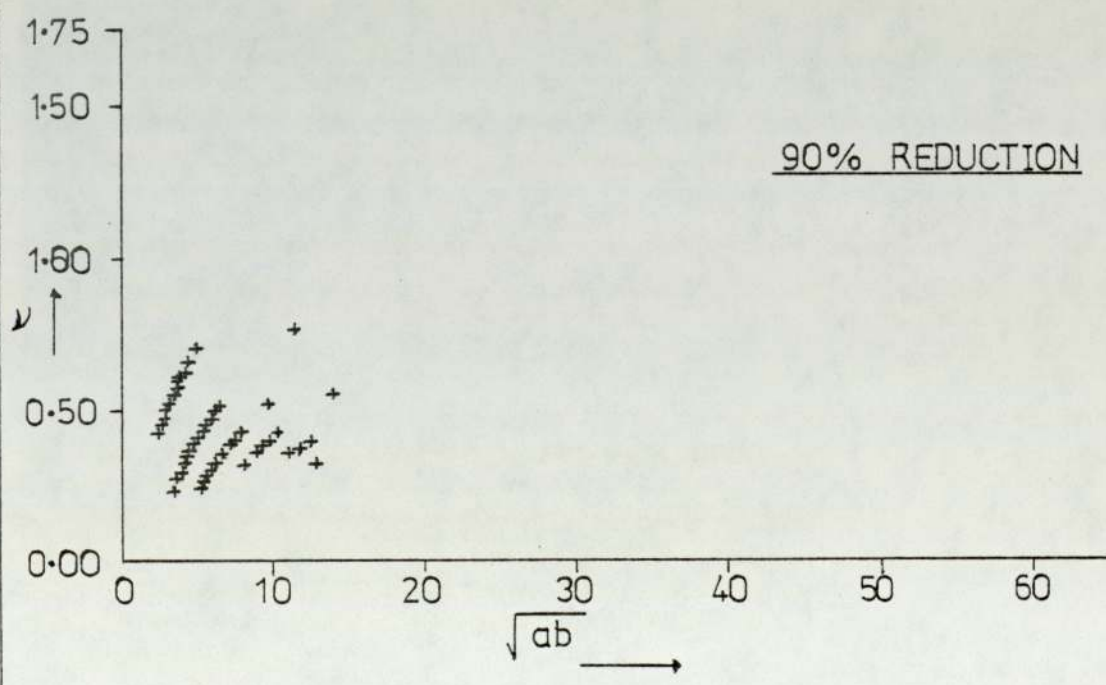
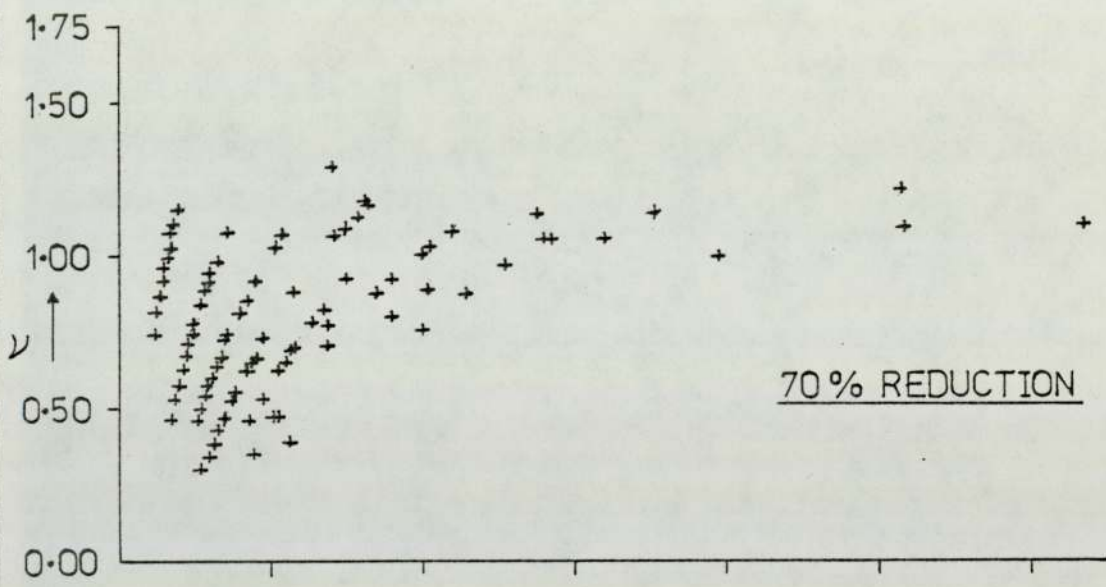
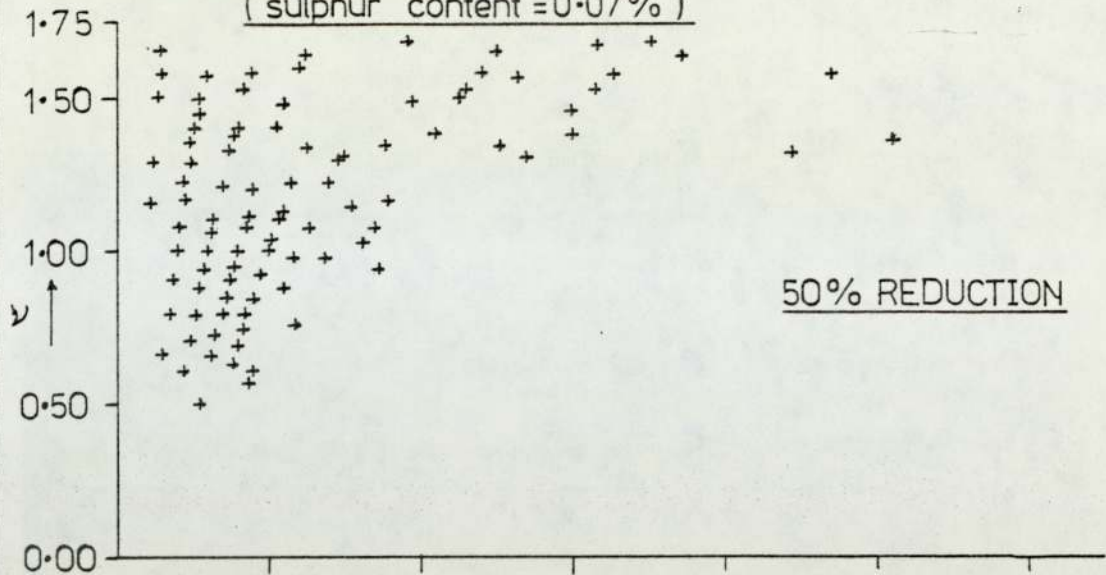


FIG.87: MELT A15 ROLLED AT 900°C
(sulphur content = 0.07%)

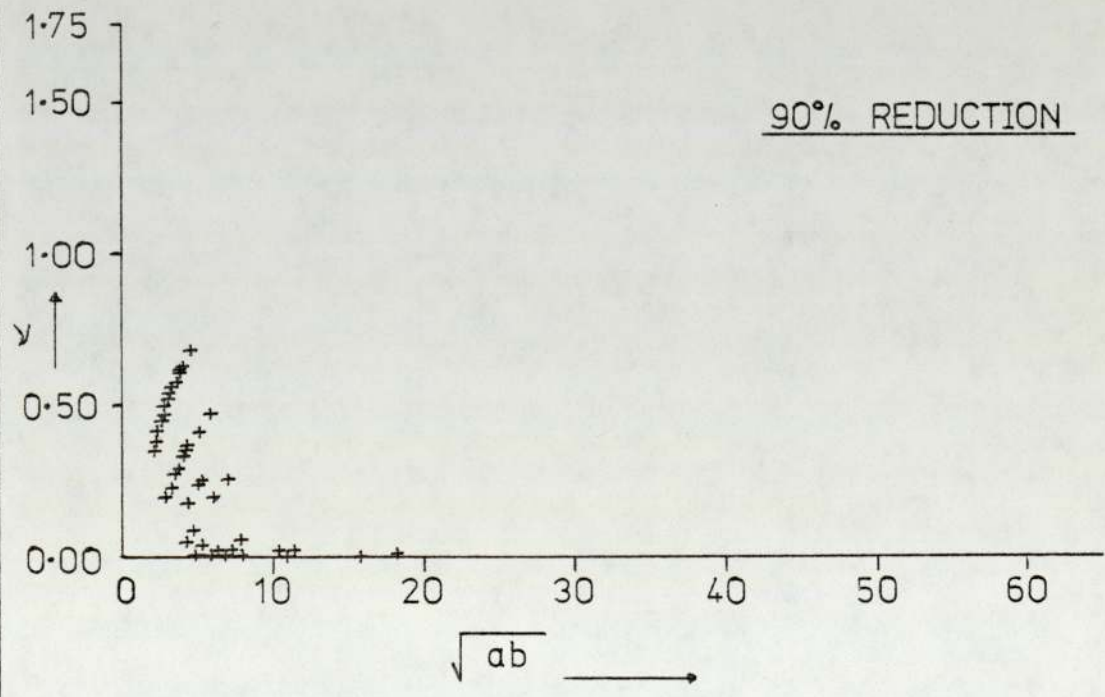
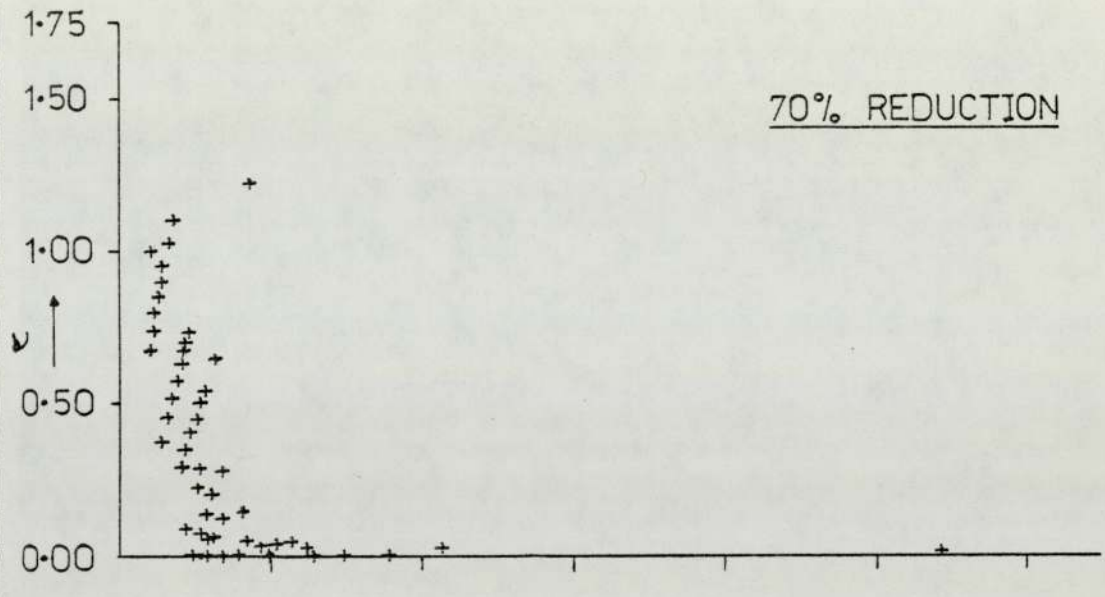
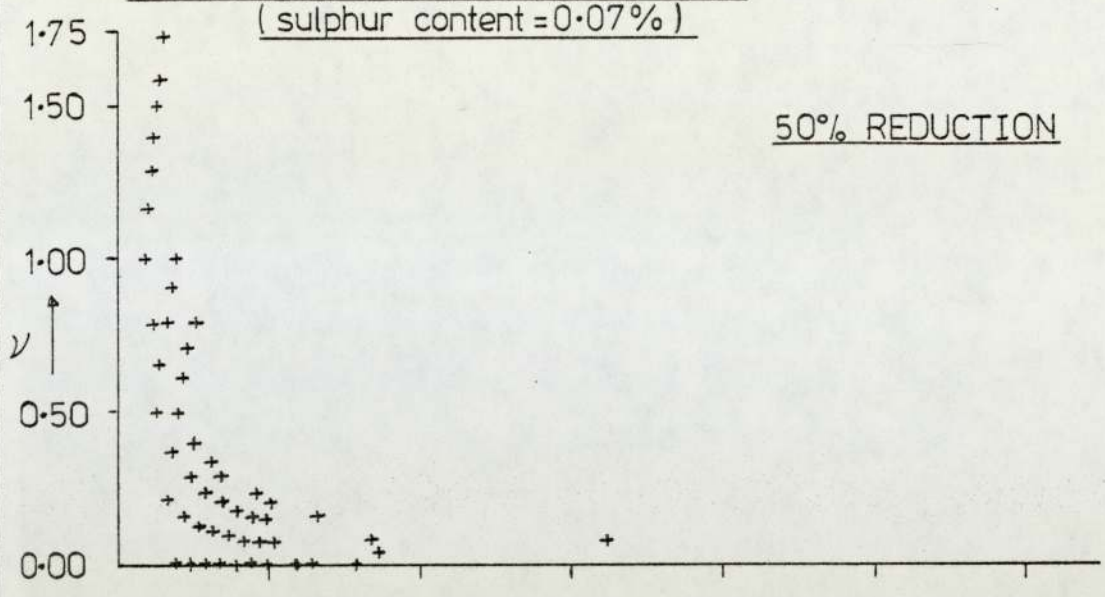


FIG-88: MELT A15 ROLLED AT 1000° C

(sulphur content=0.07%)

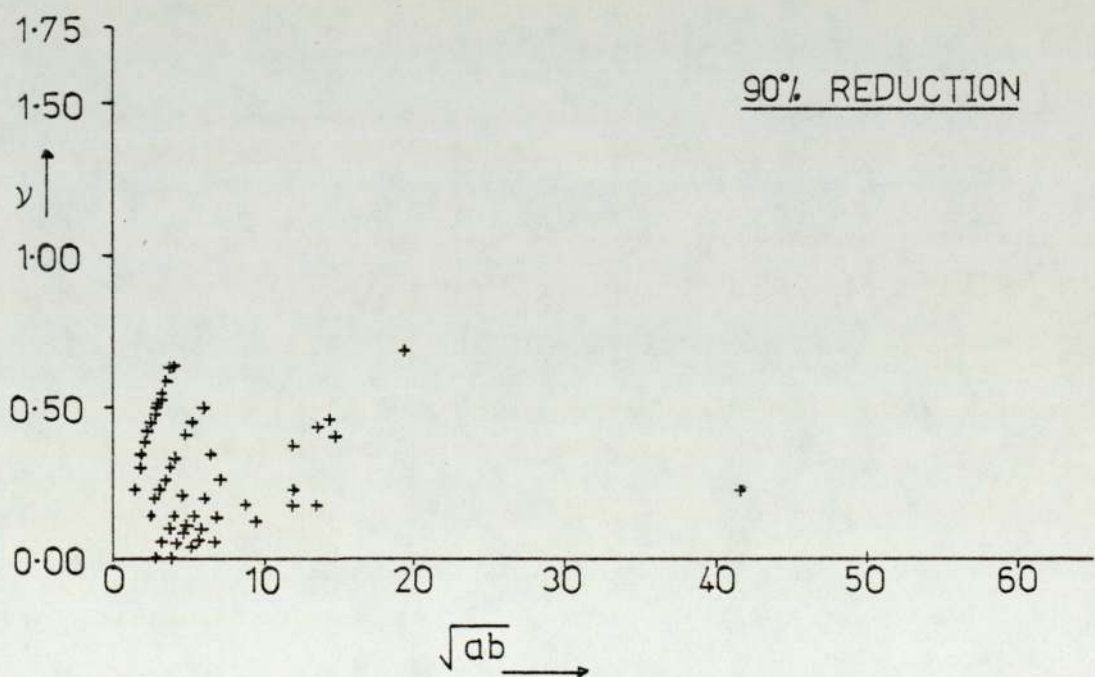
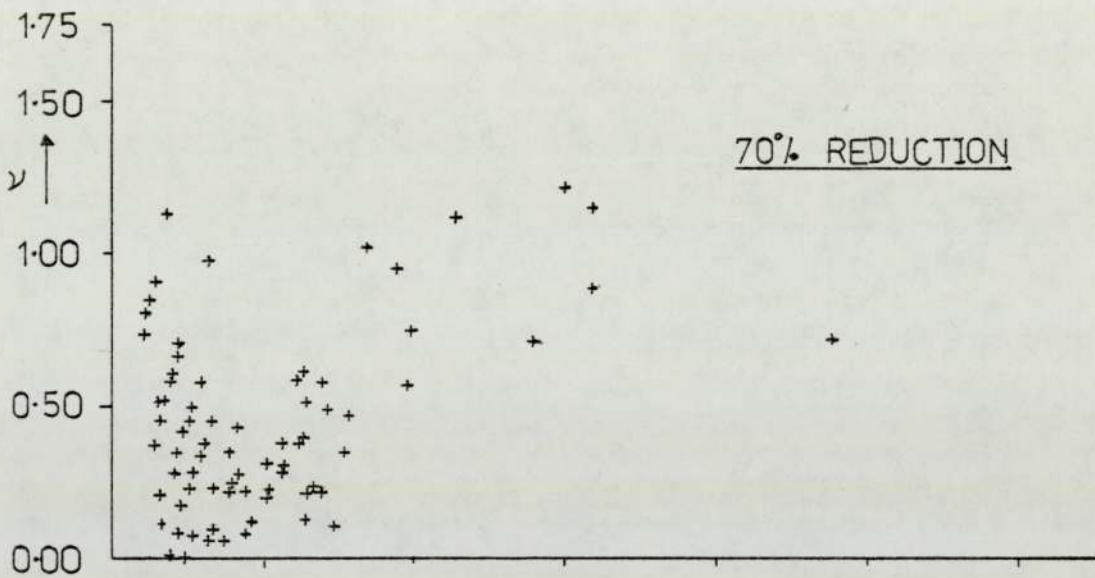
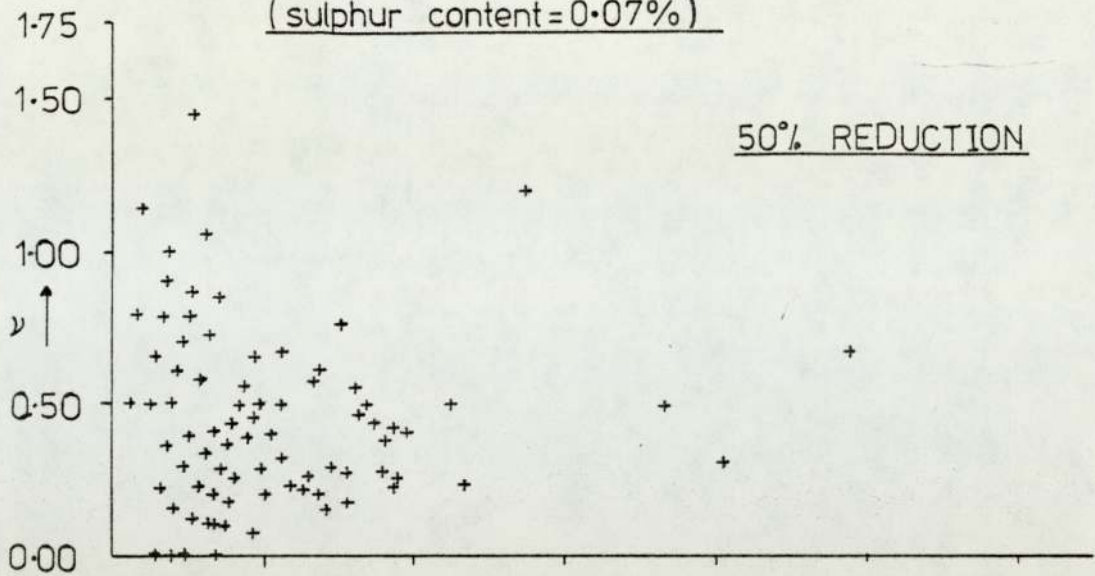


FIG.89:MELT A15 ROLLED AT 110°C

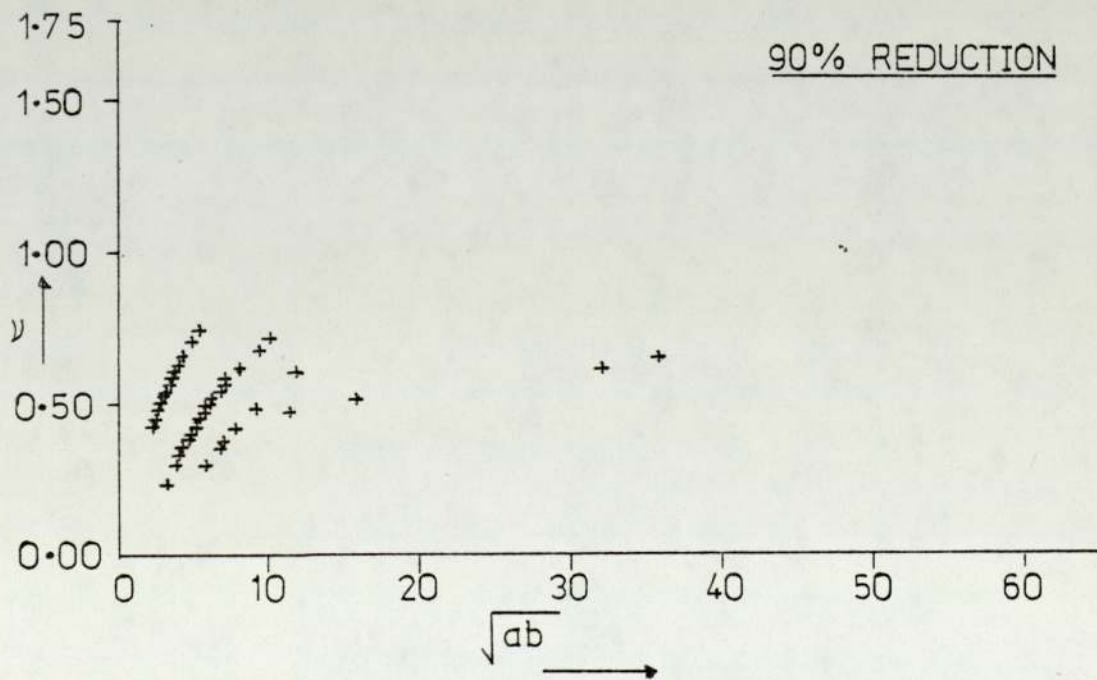
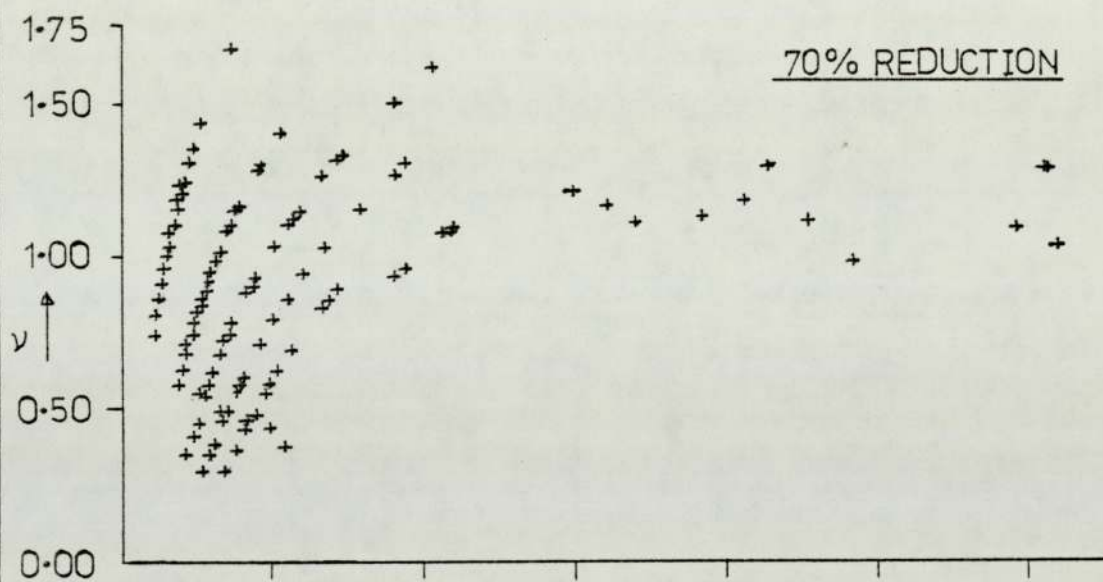
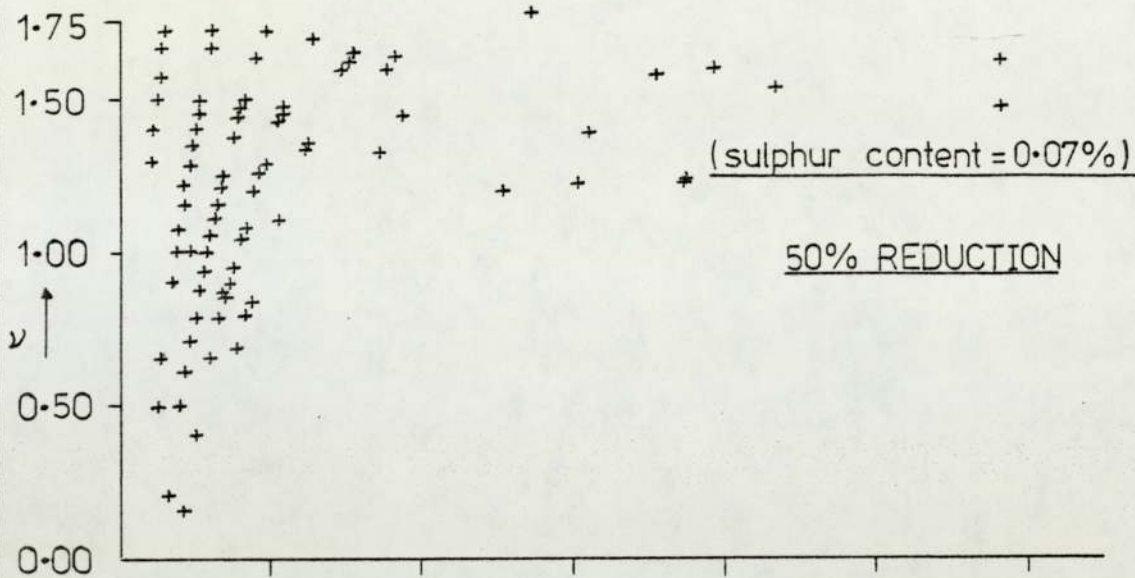


FIG-90: Melt A7 Rolled At 900°C
(sulphur content = 0.10%)

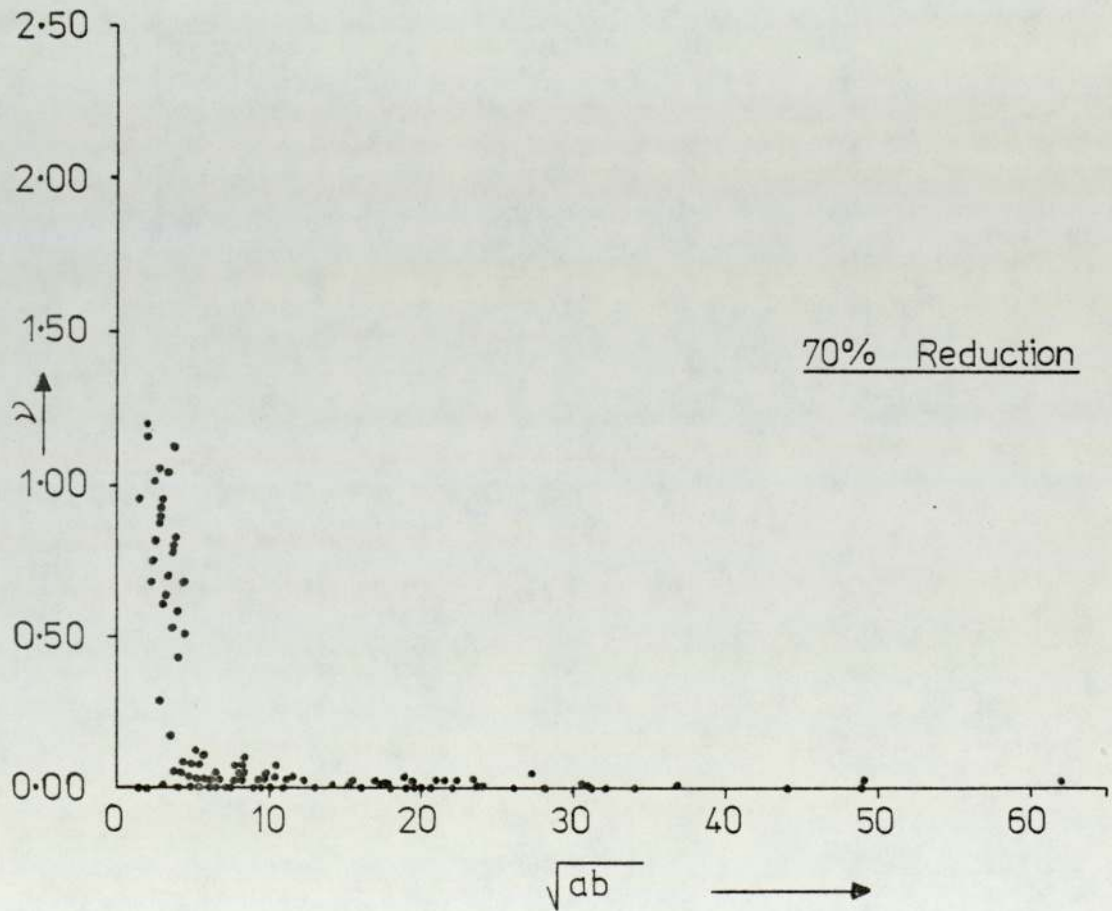
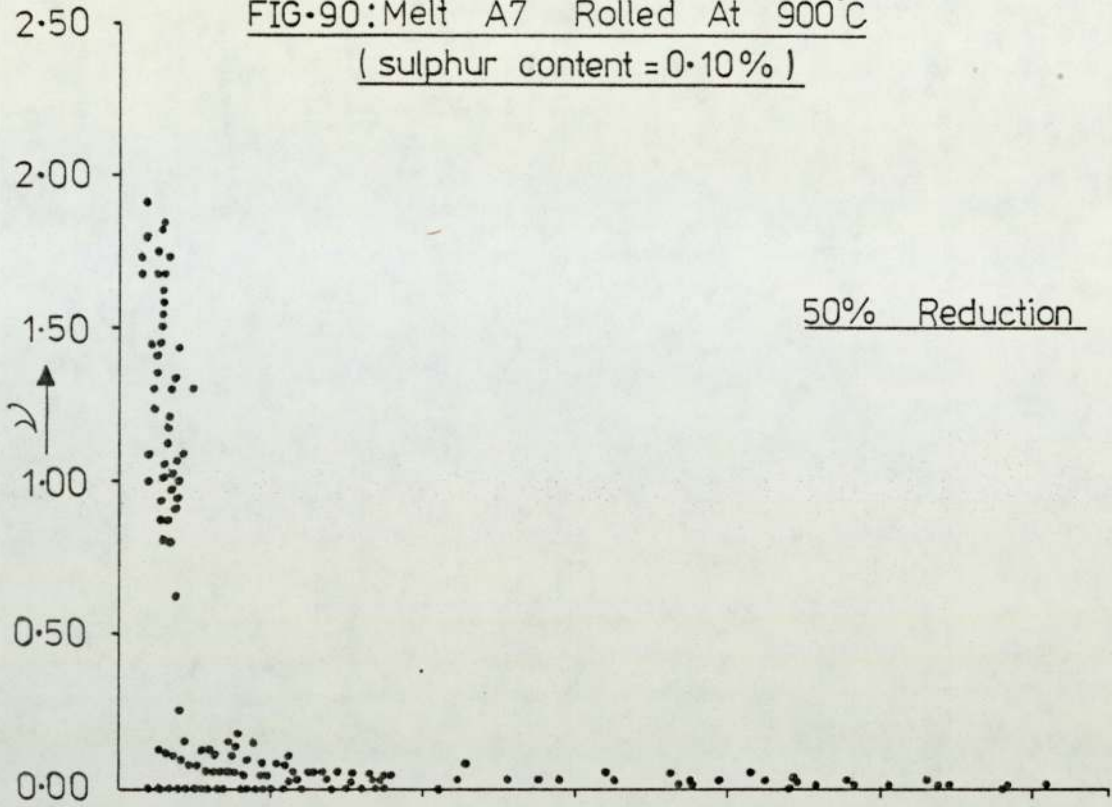


FIG.91: Melt A7 Rolled At 1000°C
(sulphur content = 0.10%)

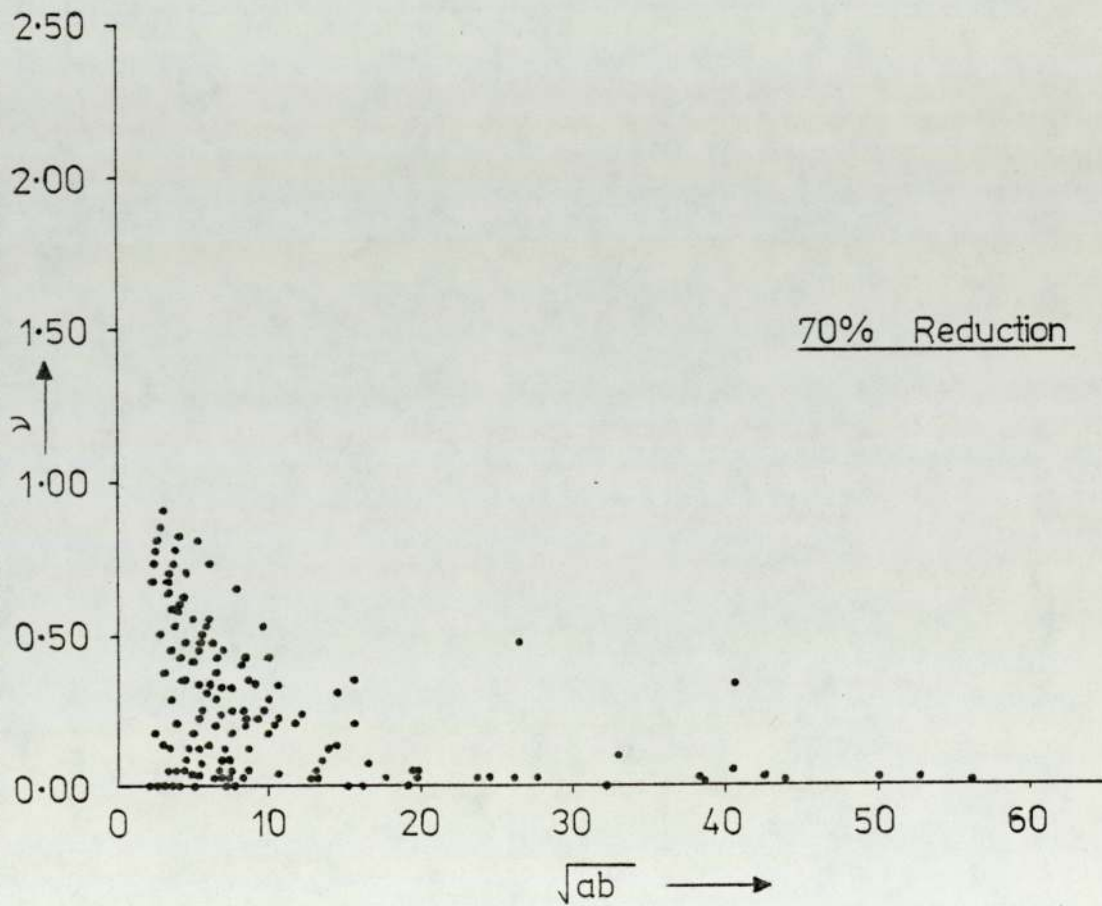
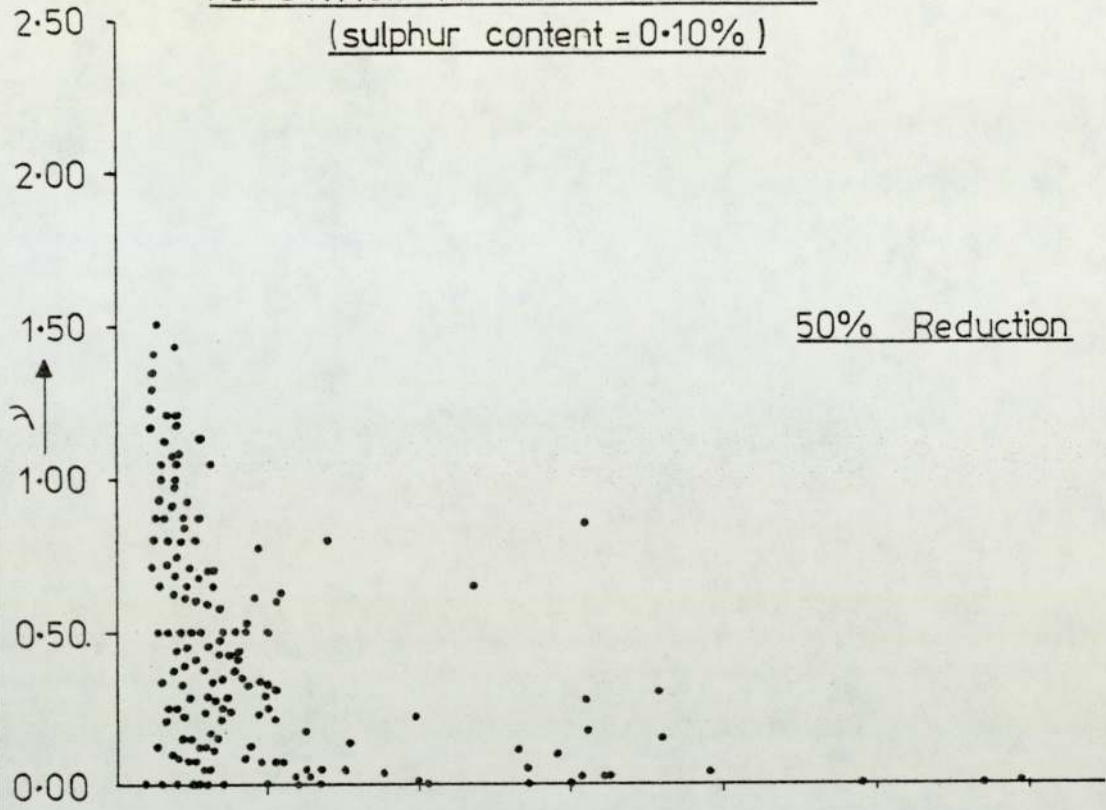


FIG-92: Melt A7 Rolled At 1100°C
(sulphur content = 0.10%)

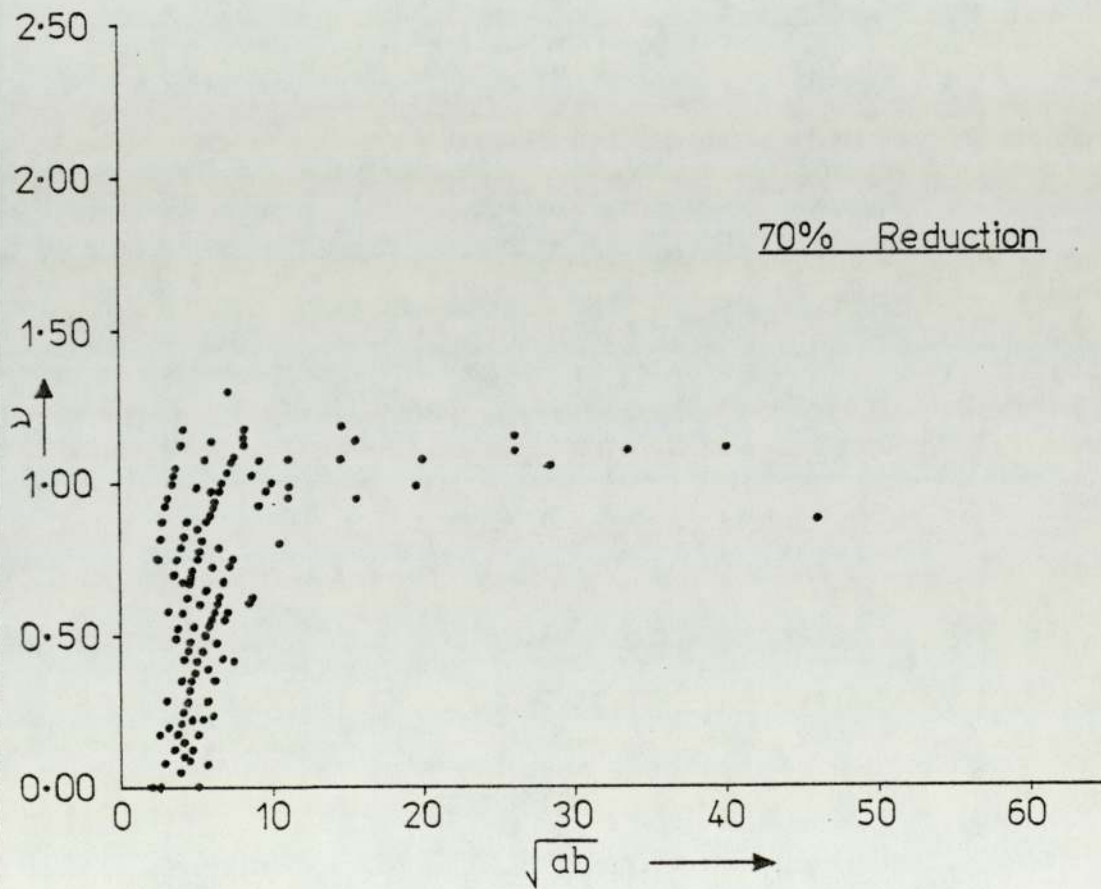
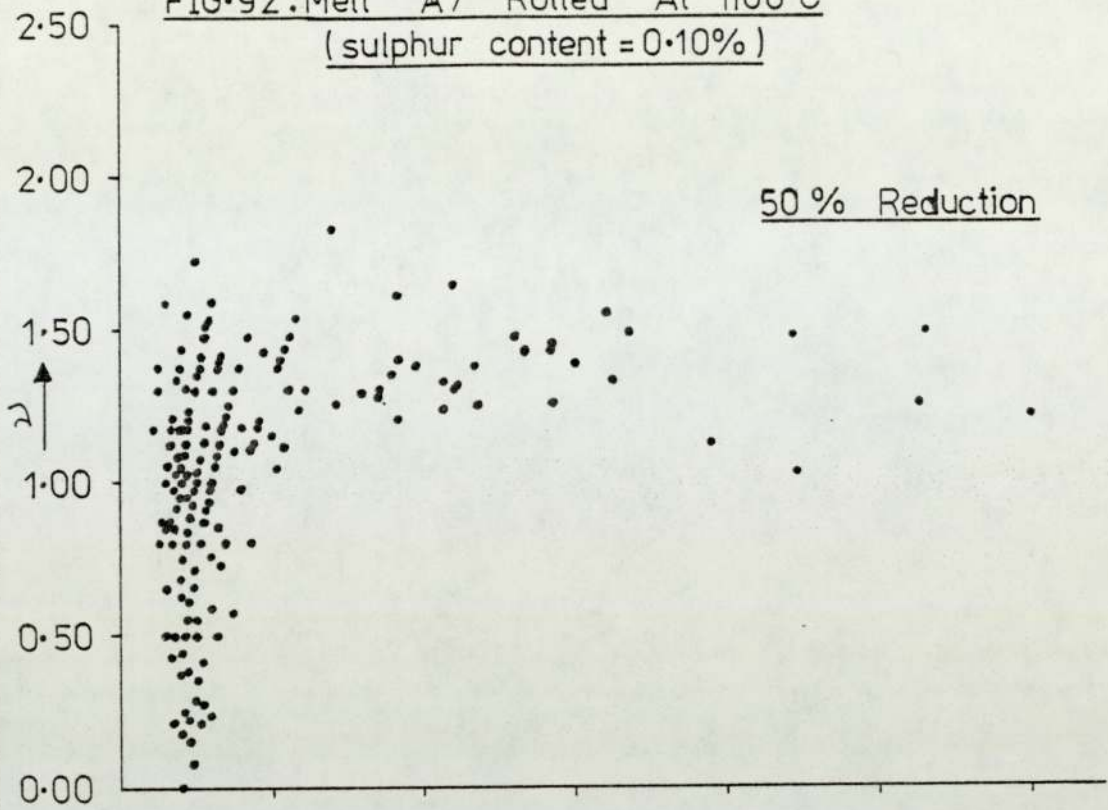


FIG. 93: Melt A7 Rolled At 1200°C
(sulphur content = 0.10%)

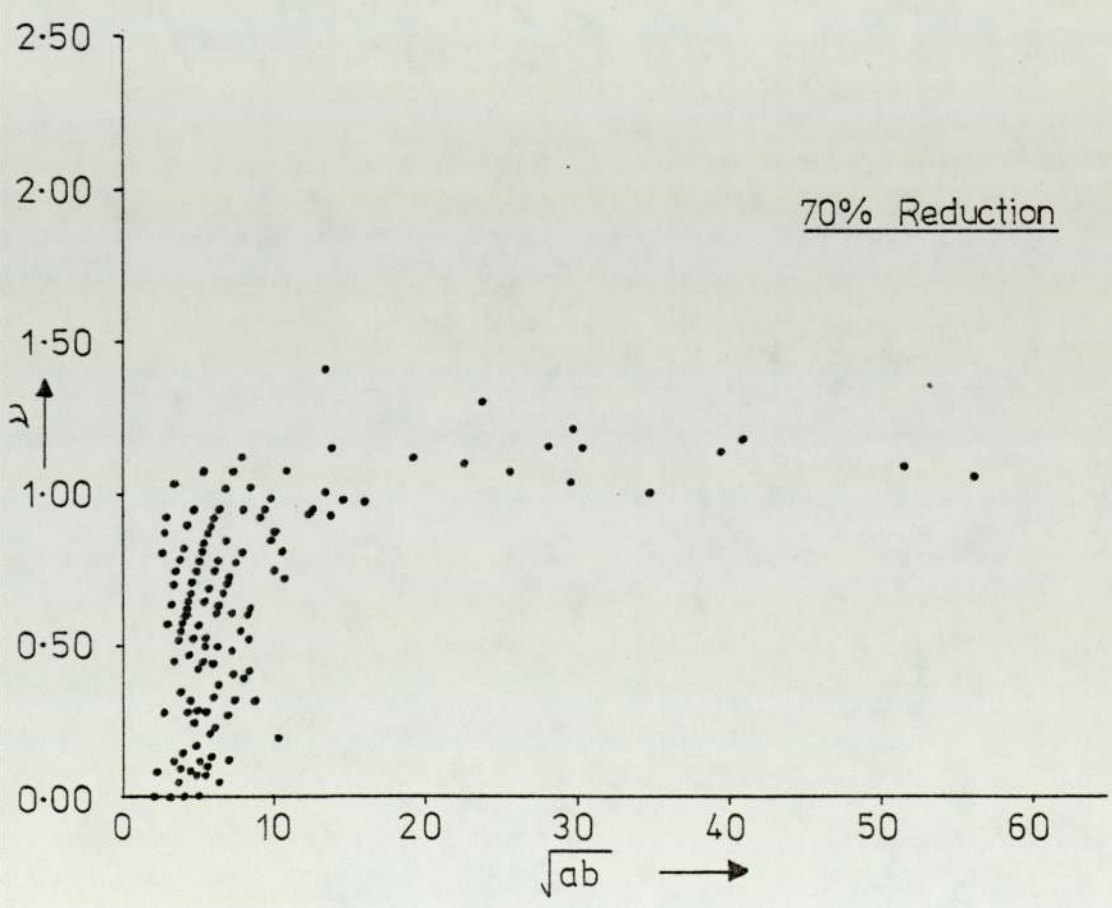
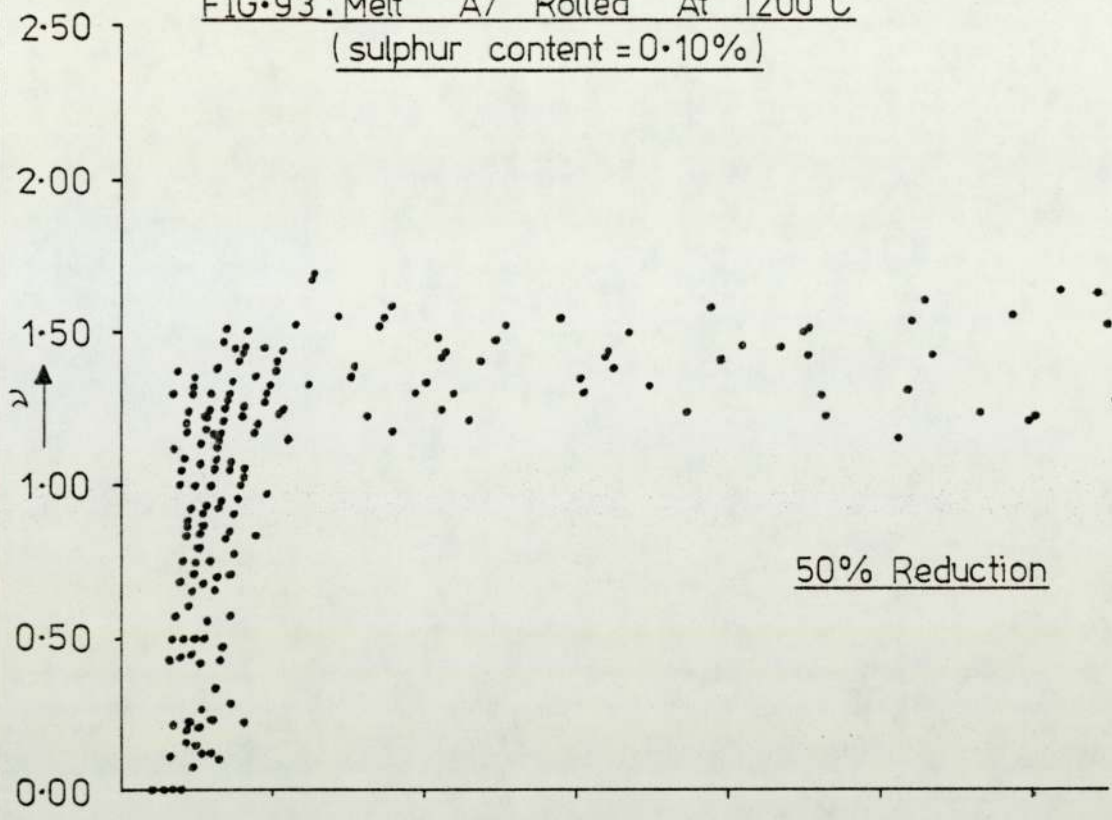


FIG.94 : Melt A6 Rolled At 900°C
(sulphur content = 0.10%)

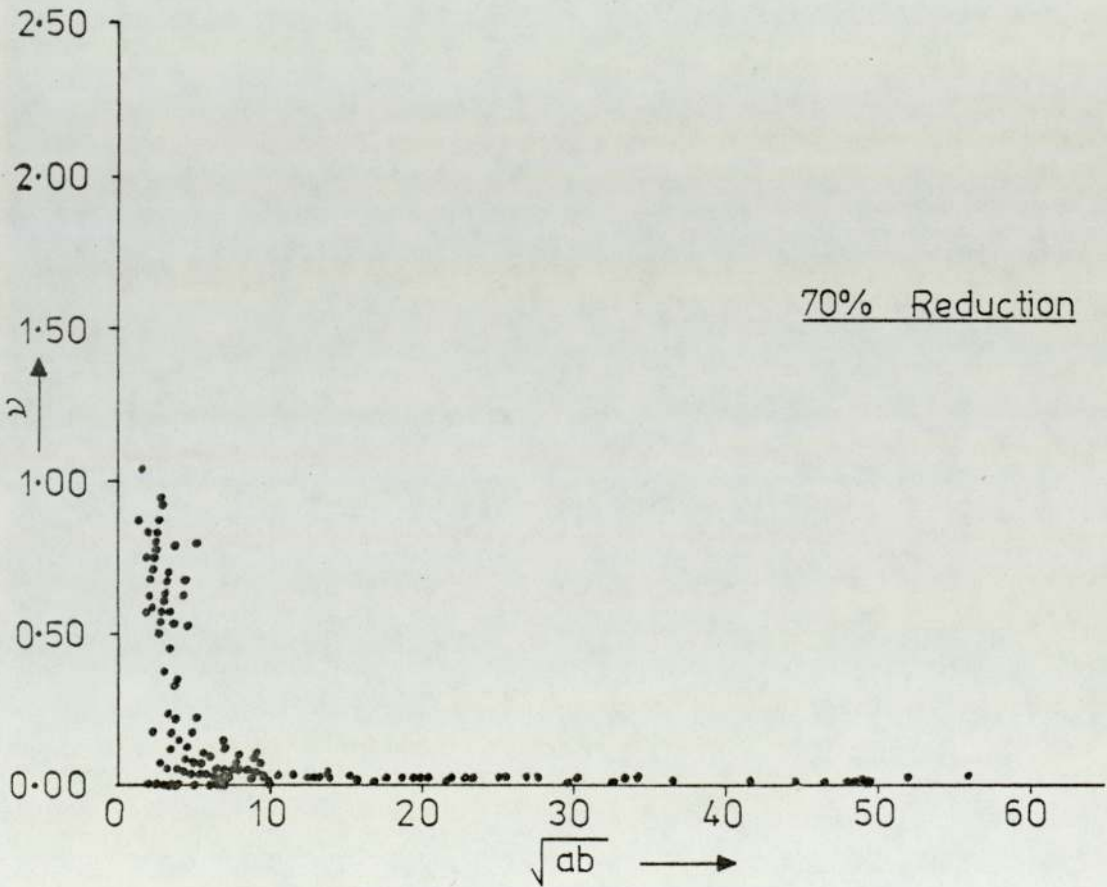
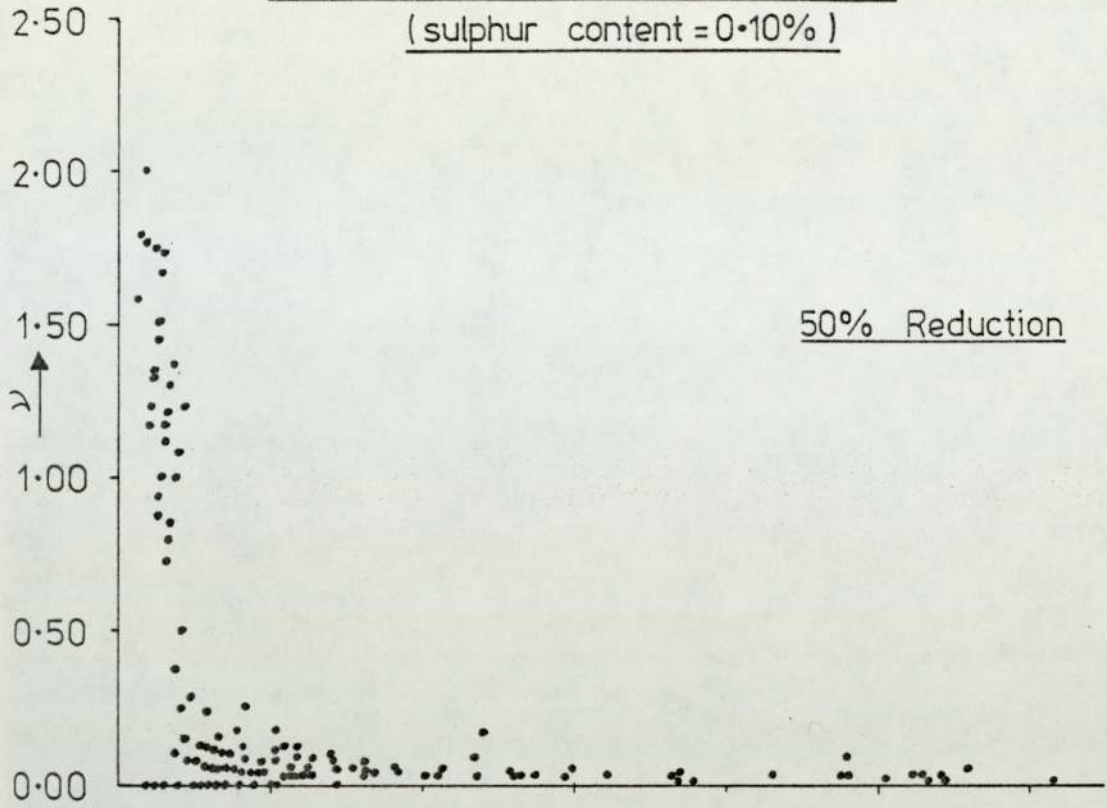
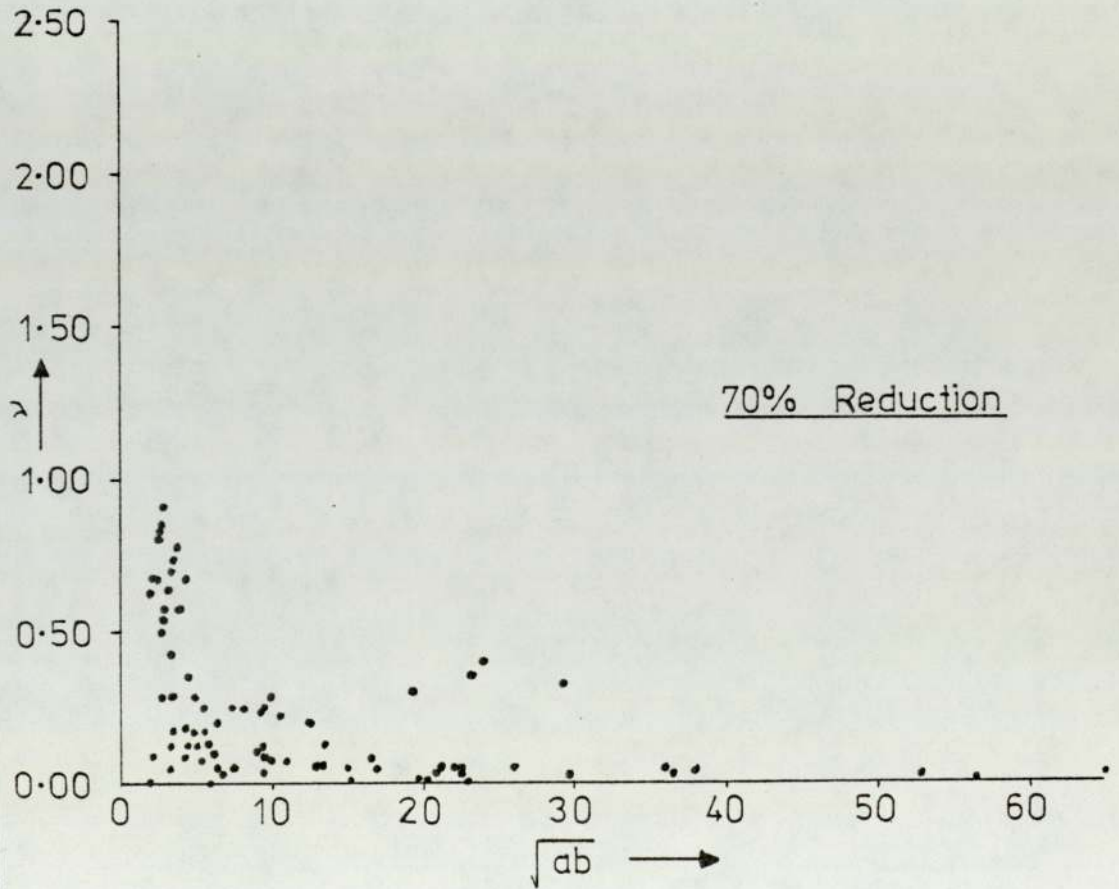
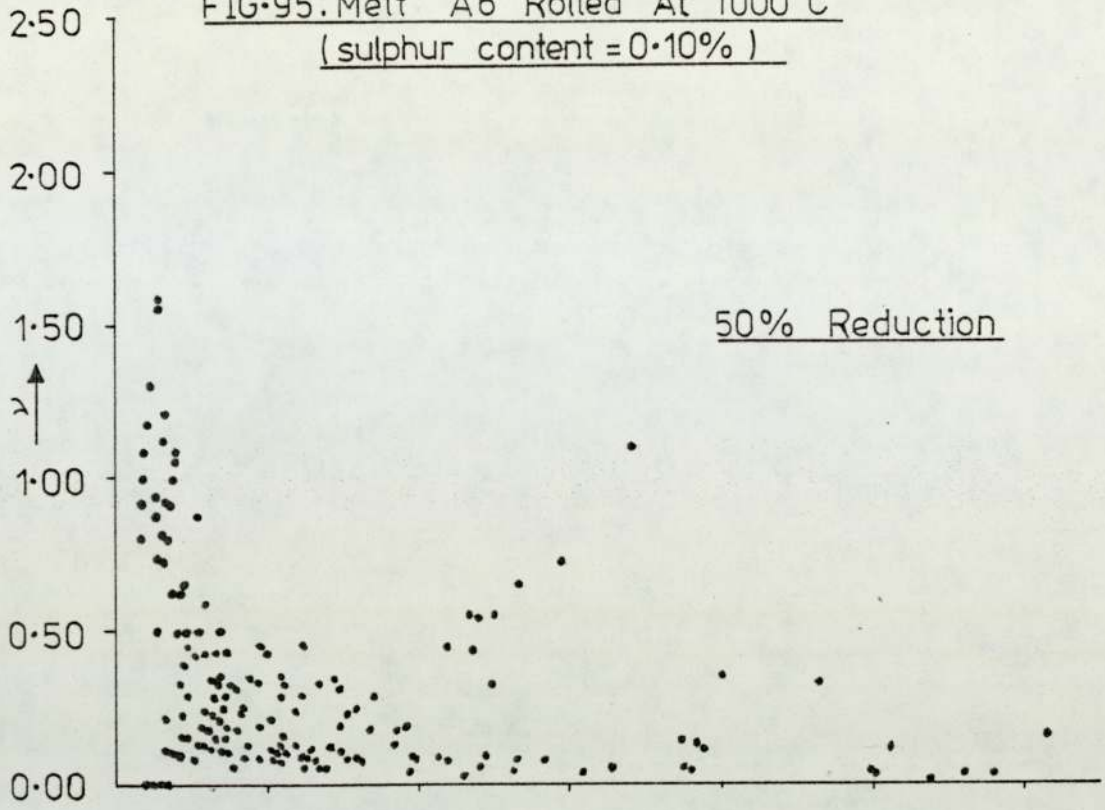


FIG-95: Melt A6 Rolled At 1000°C
(sulphur content = 0.10%)



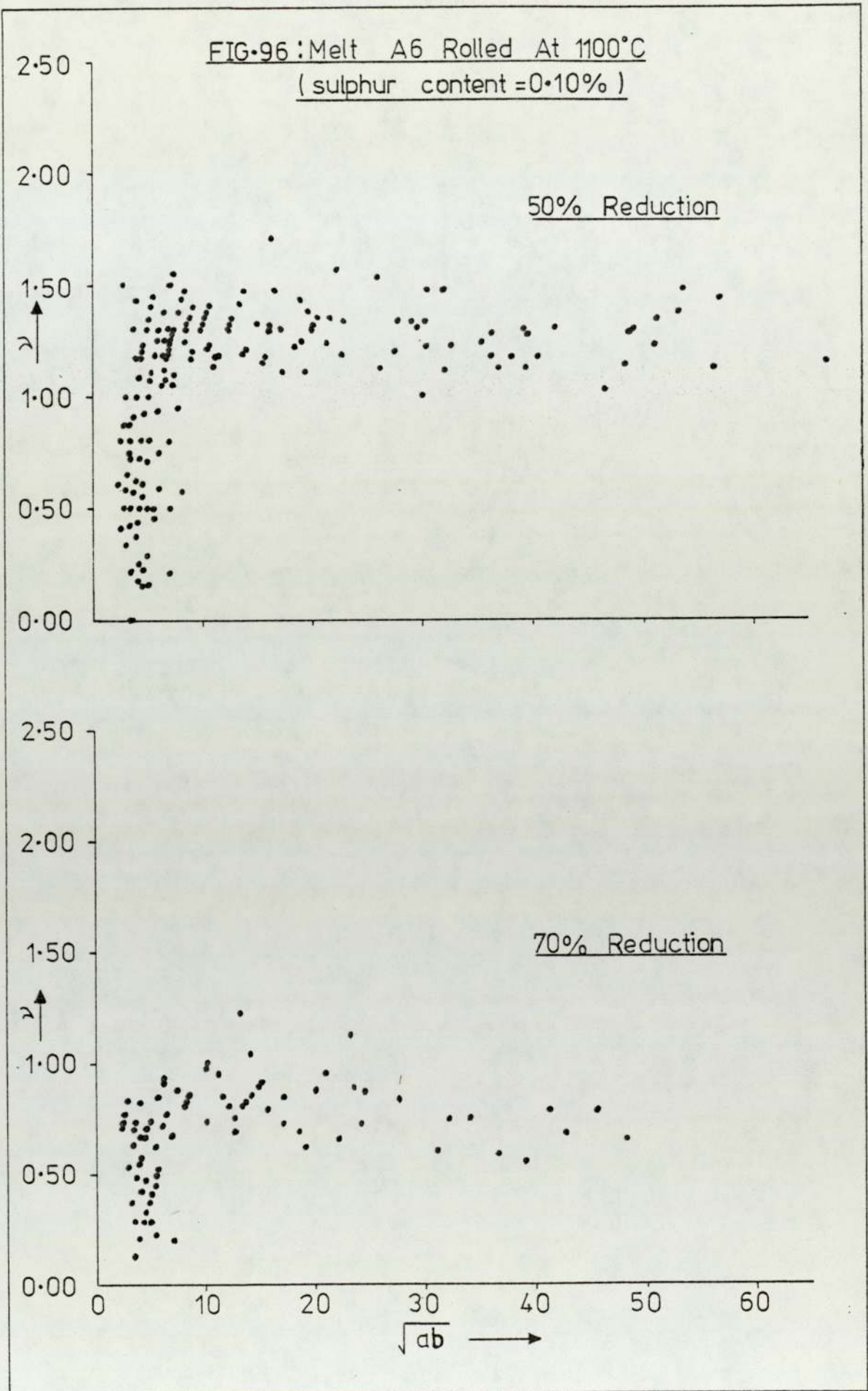


FIG-97: Melt A6 Rolled At 1200°C
(sulphur content = 0.10%)

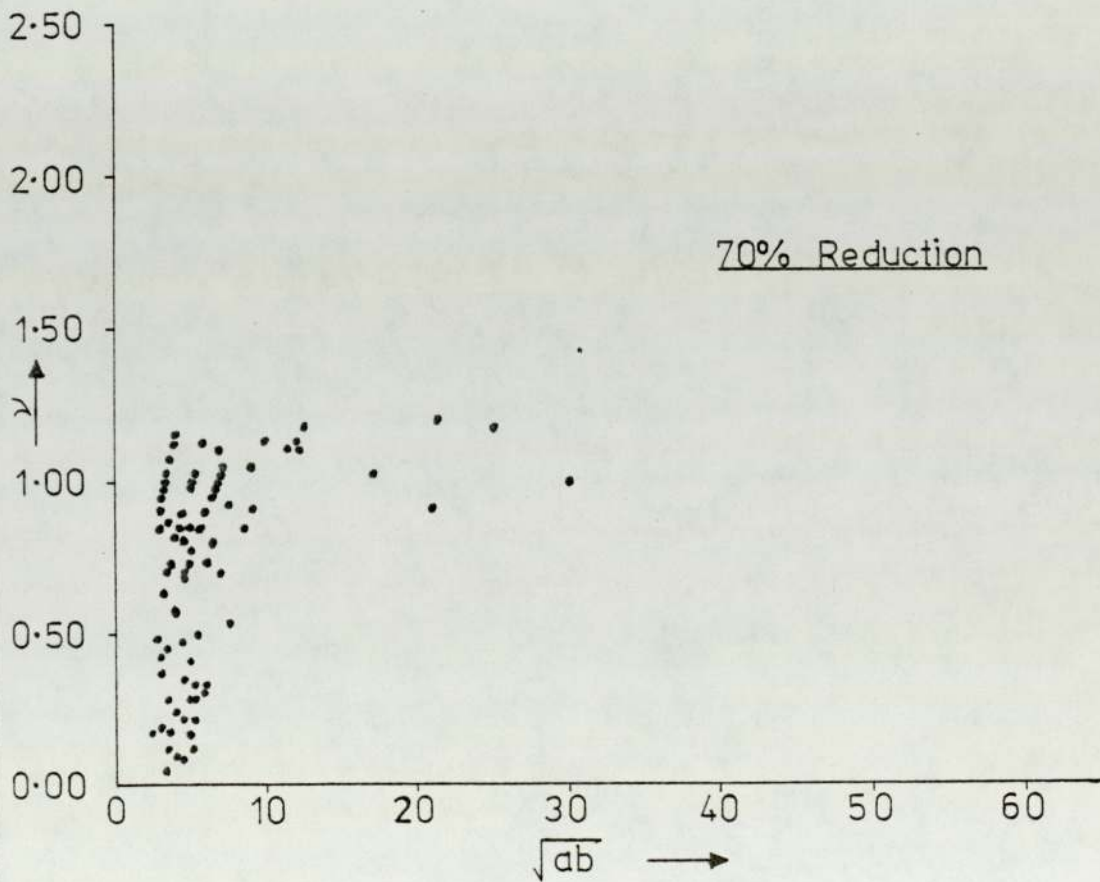
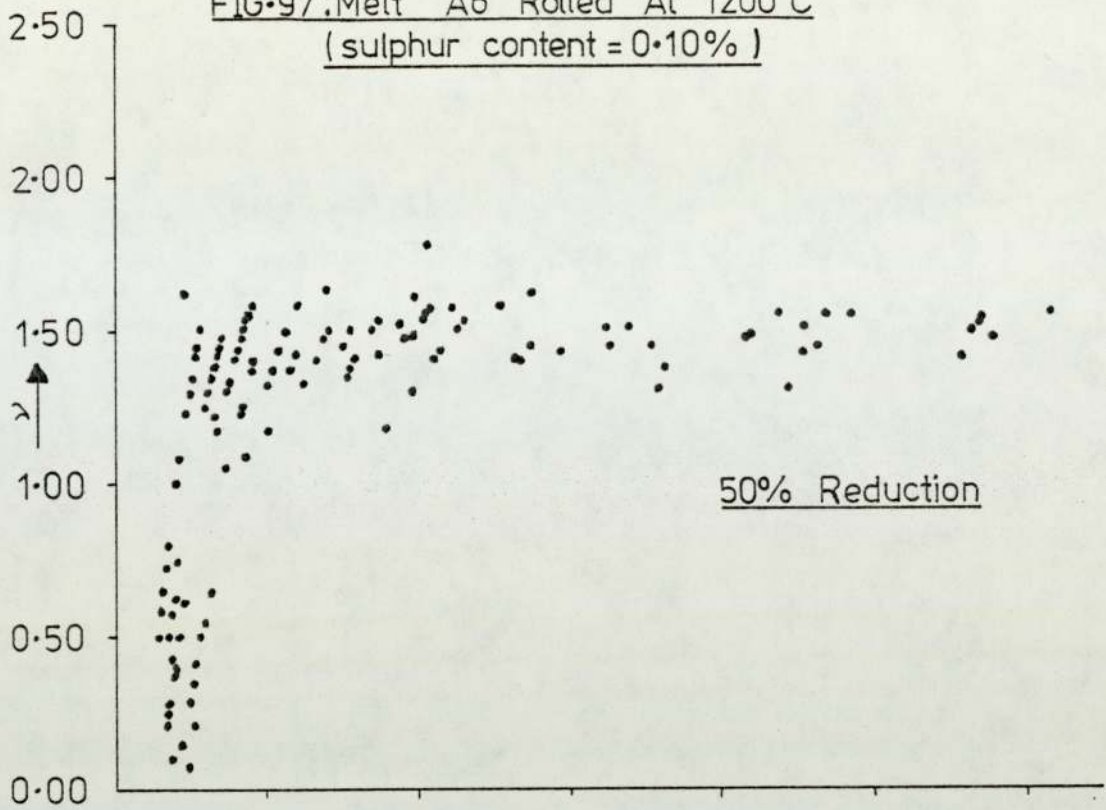


FIG-98: Melt A12 Rolled At 800°C
(sulphur content = 0.10%)

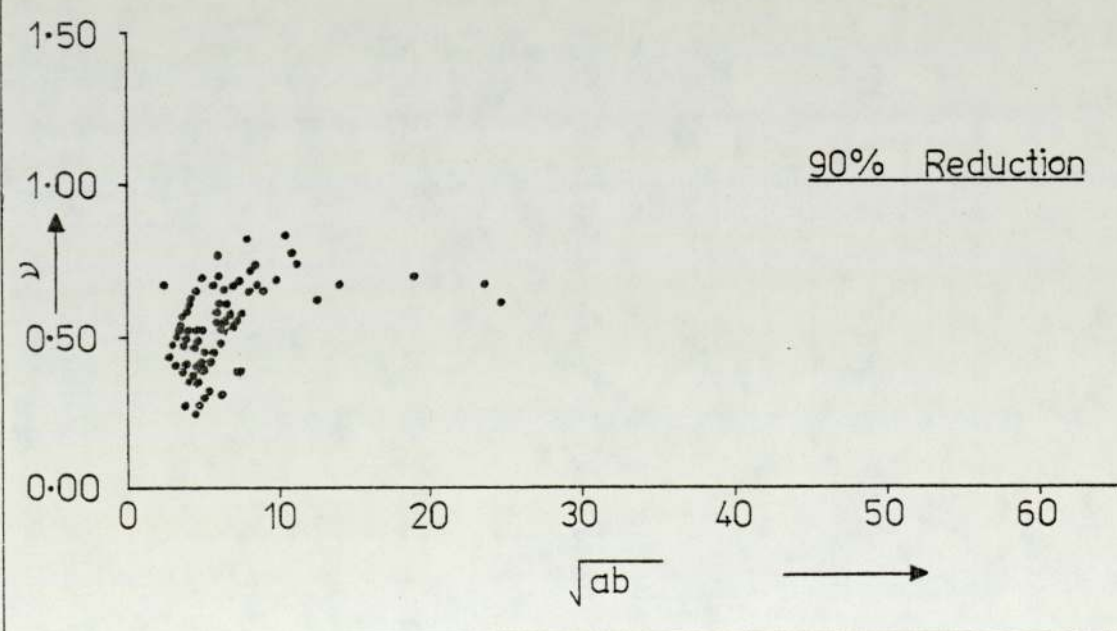
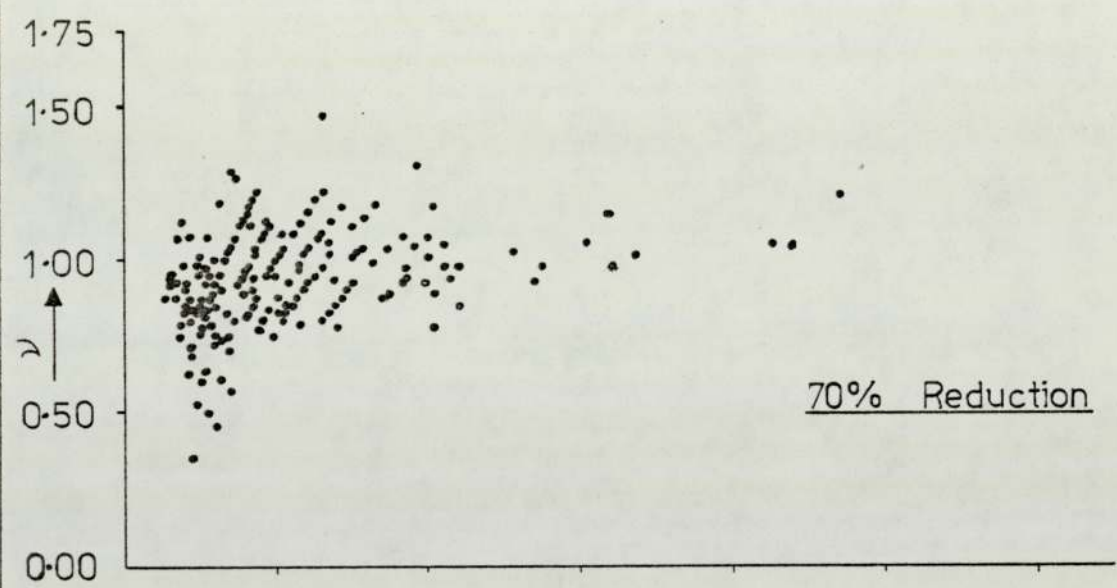
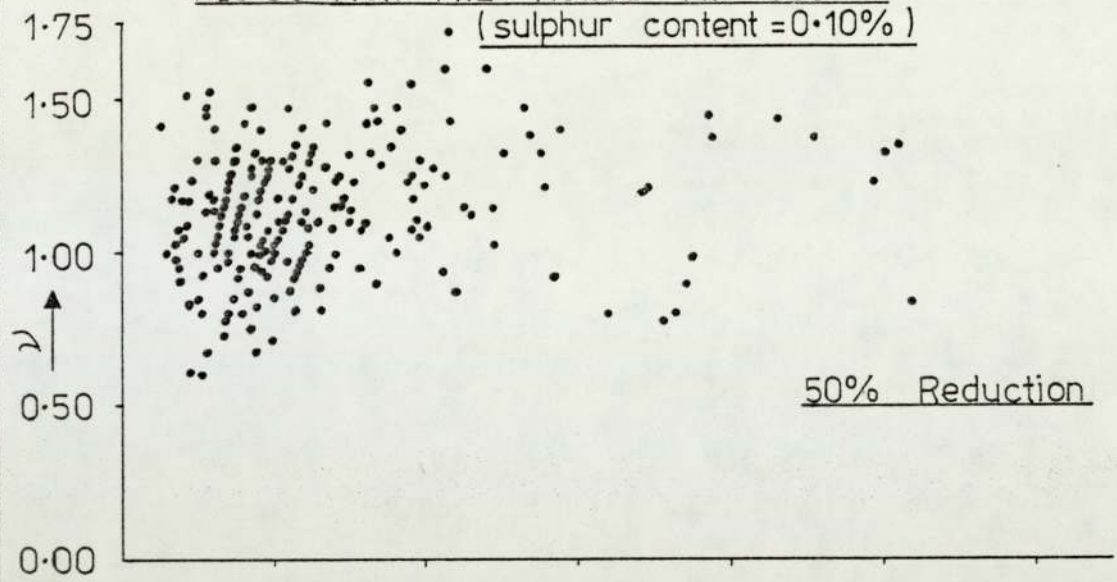


FIG-99: Melt A12 Rolled At 900°C

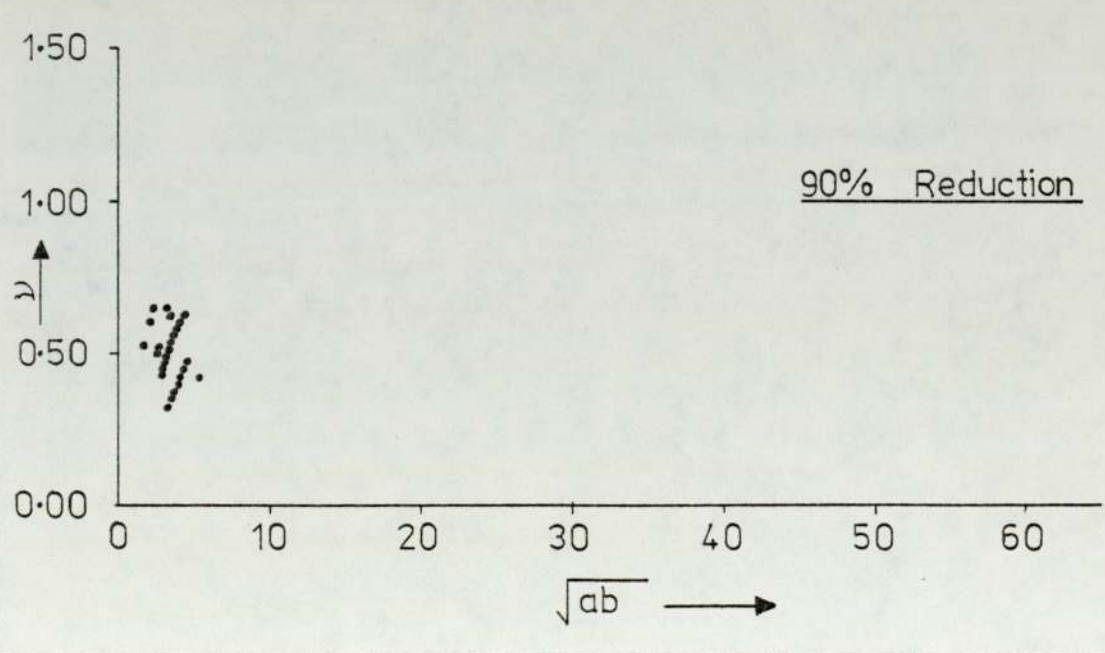
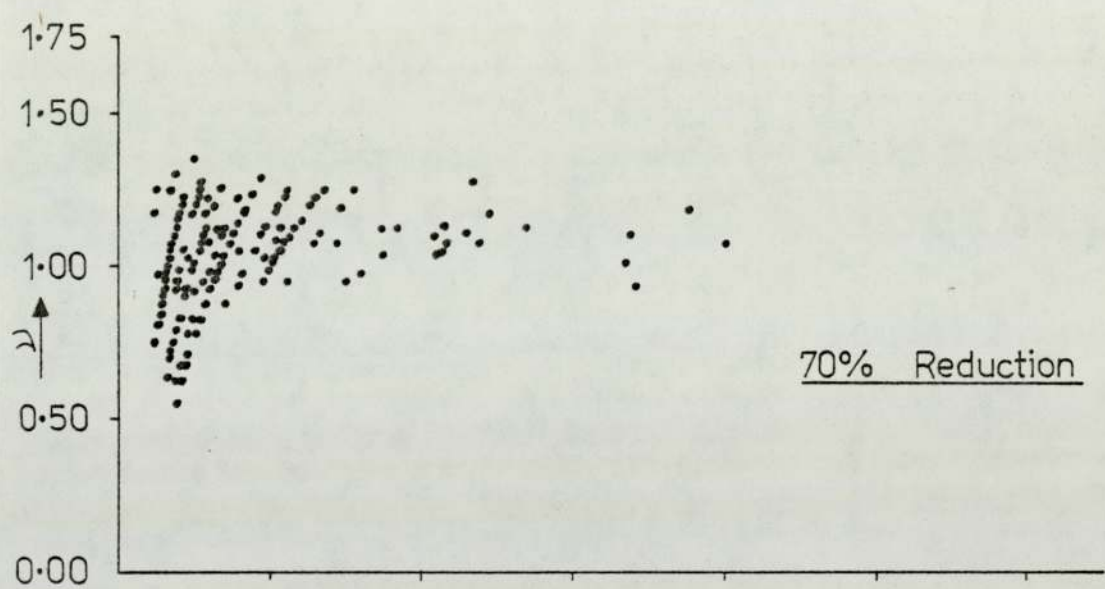
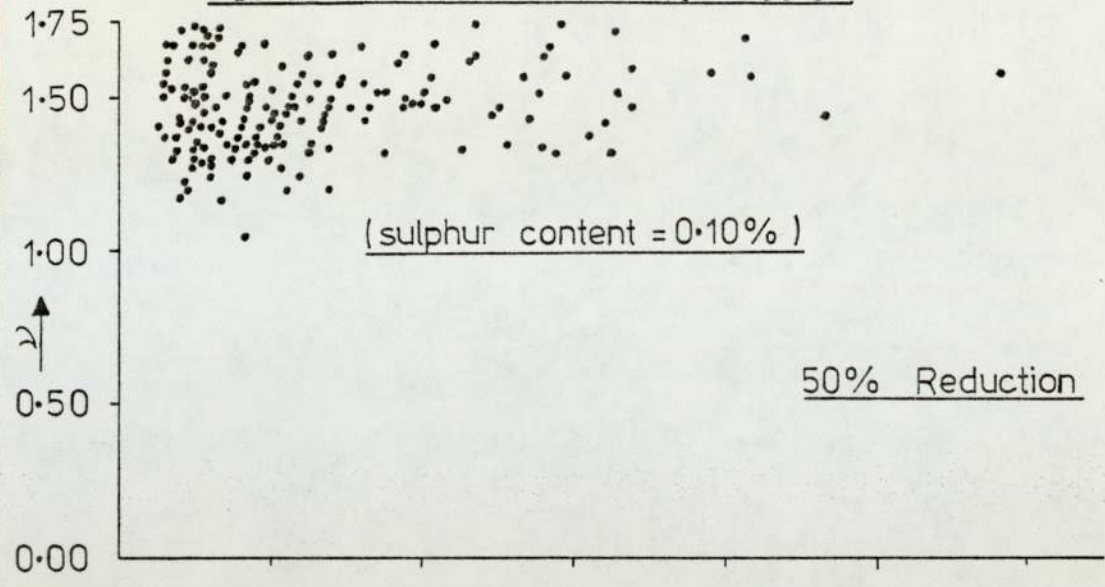


FIG-100:Melt A12 Rolled At 1000 °C

(sulphur content = 0.10%)

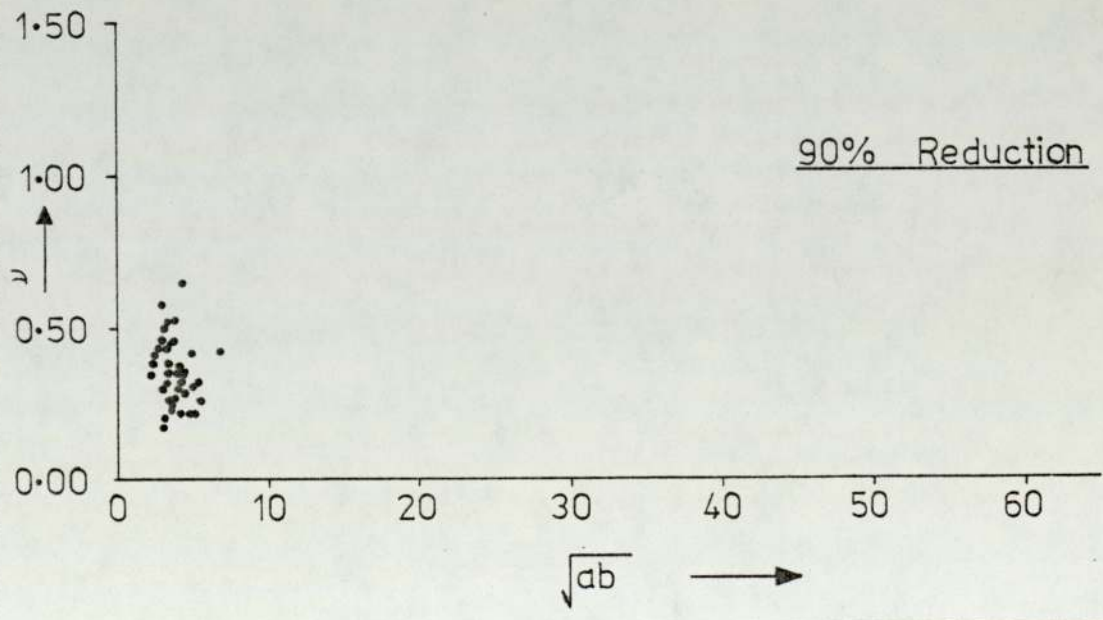
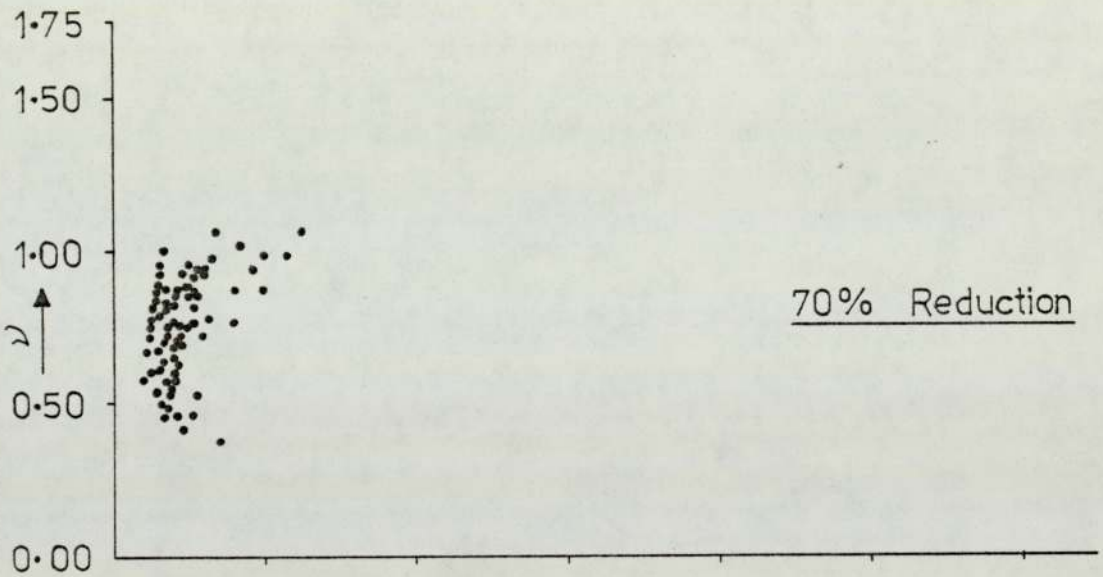
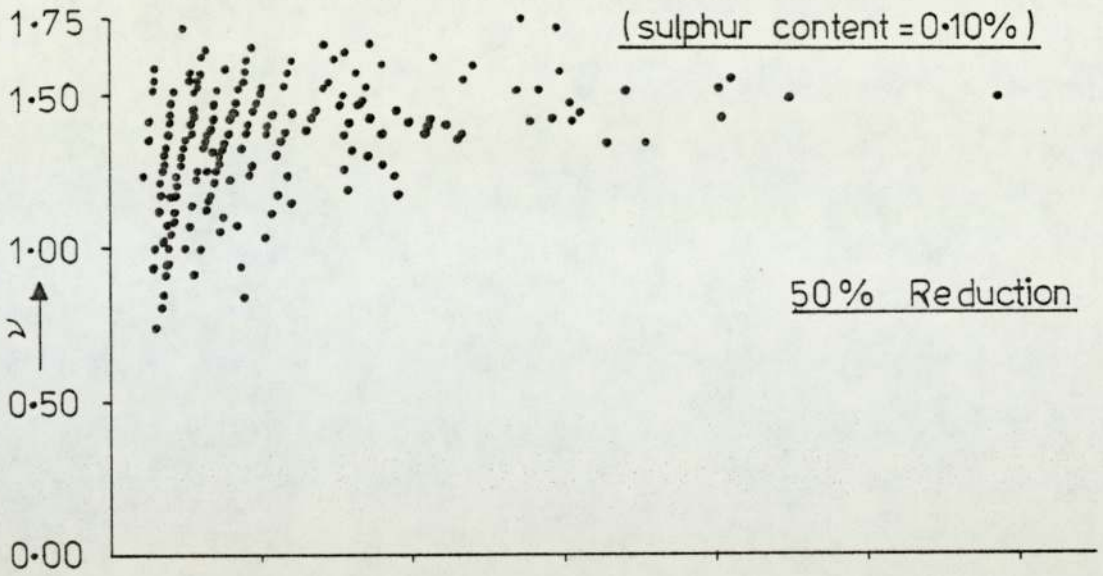


FIG-101: Melt A12 Rolled At 1100 °C

(sulphur content = 0.10%)

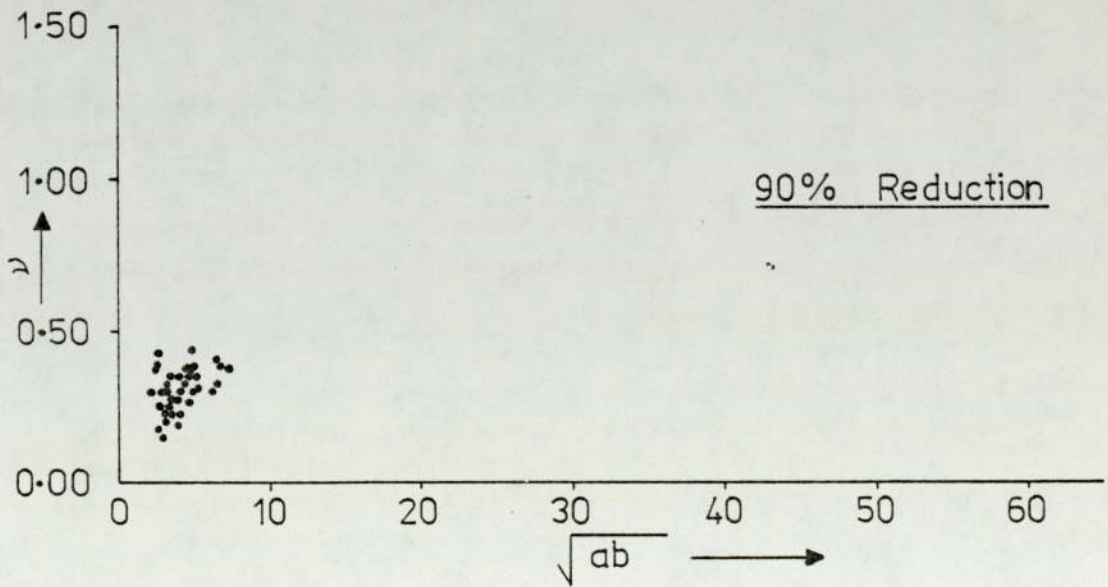
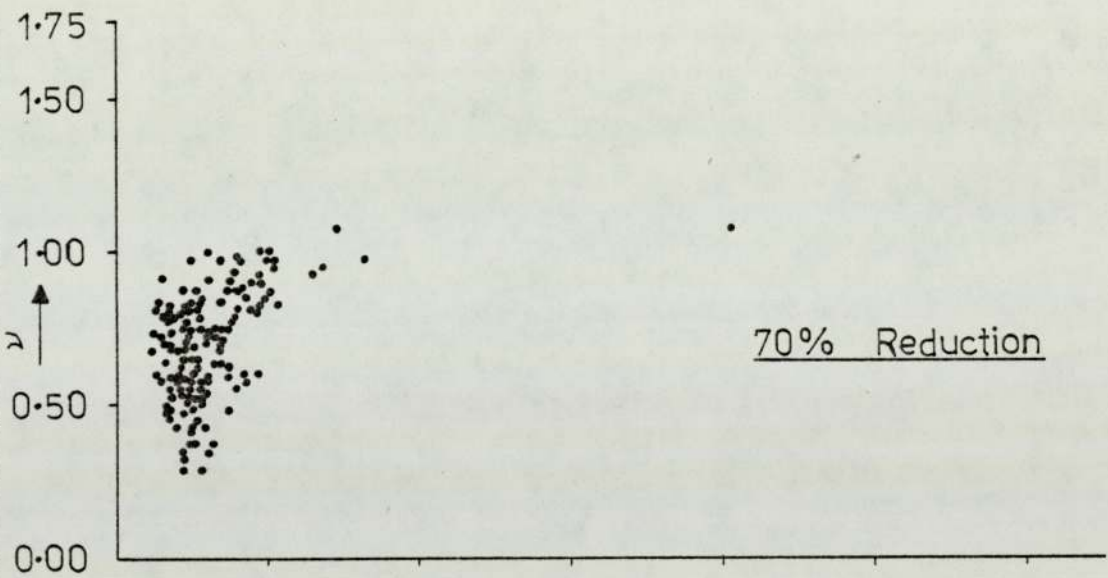
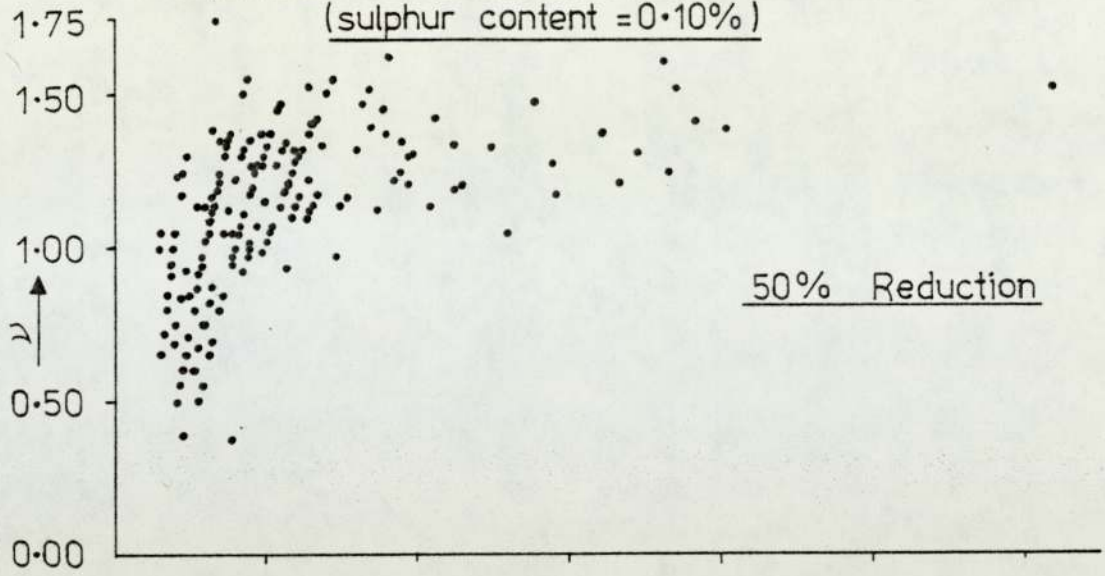


FIG-102: Melt A12 Rolled At 1200 °C
(sulphur content = 0.10%)

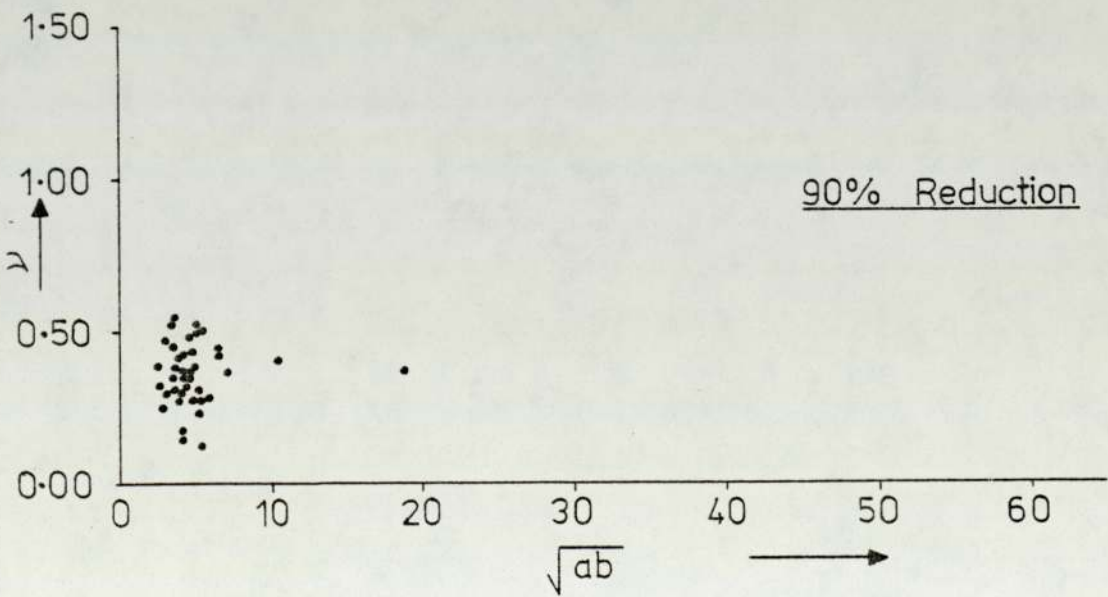
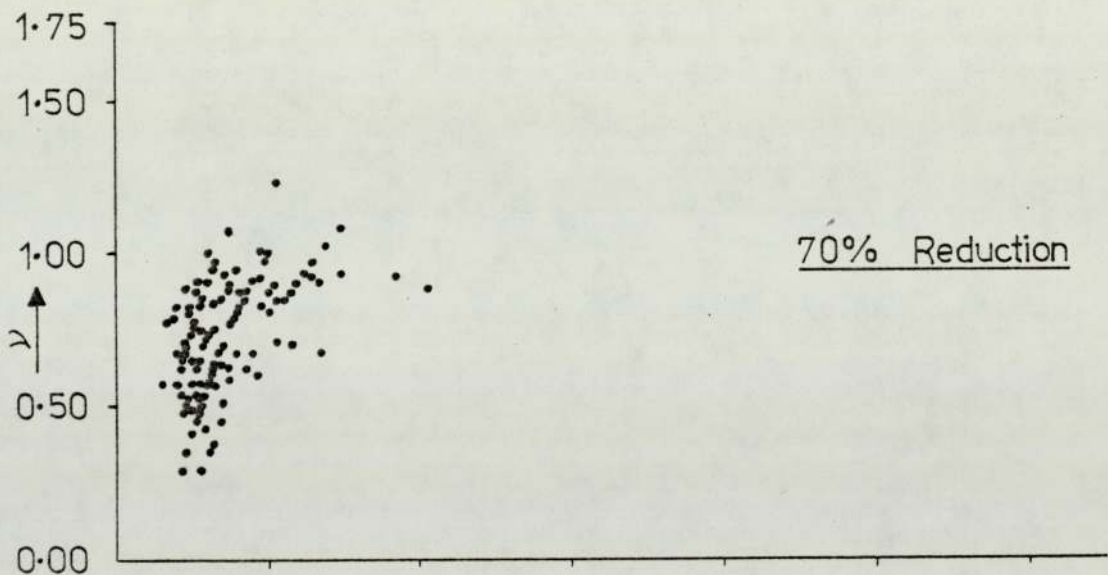
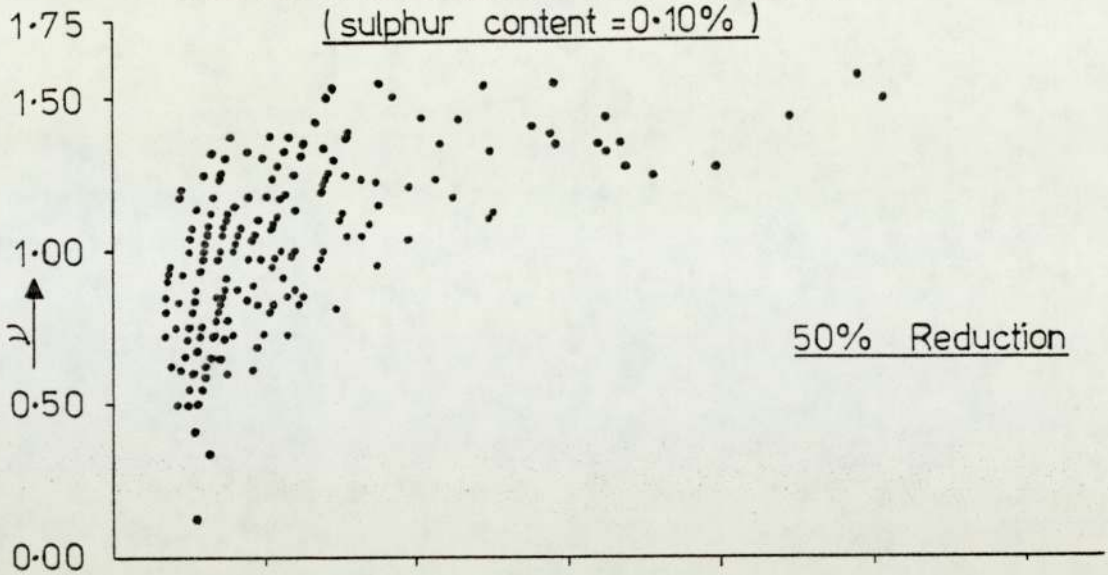
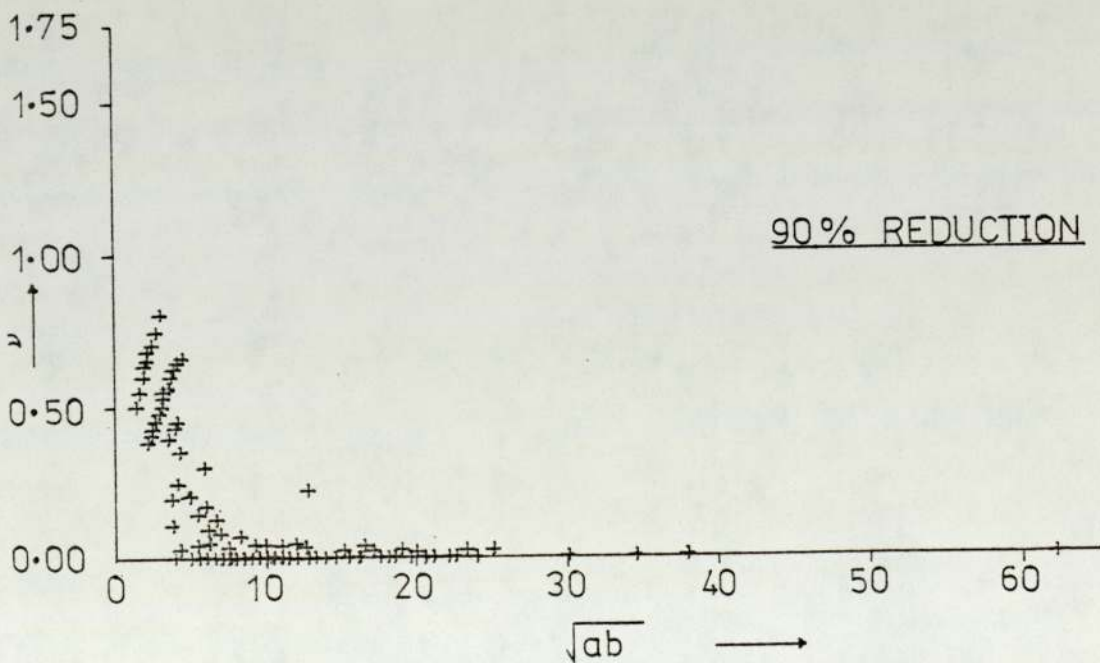
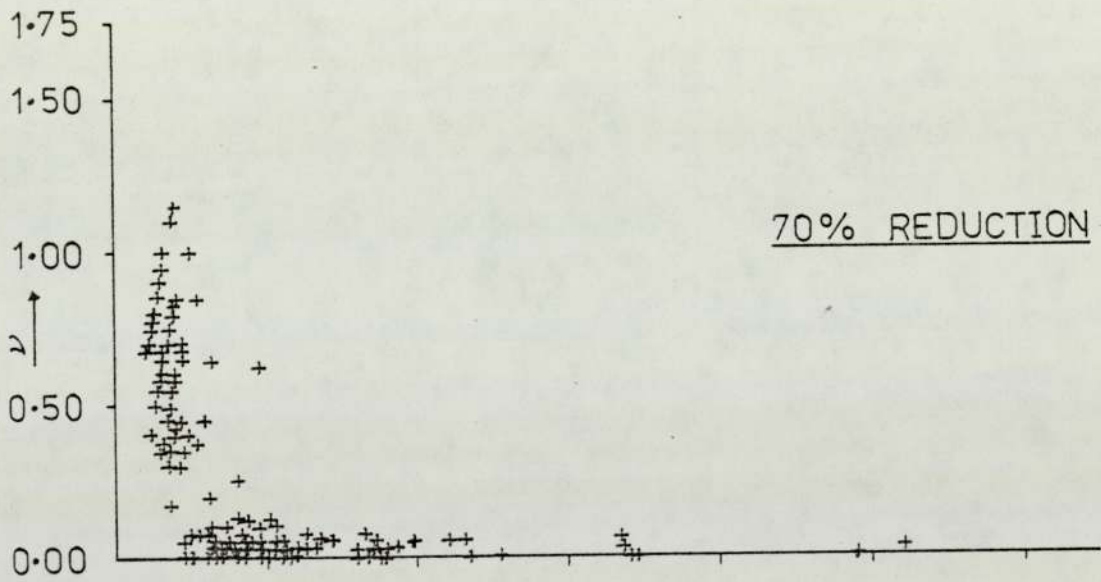
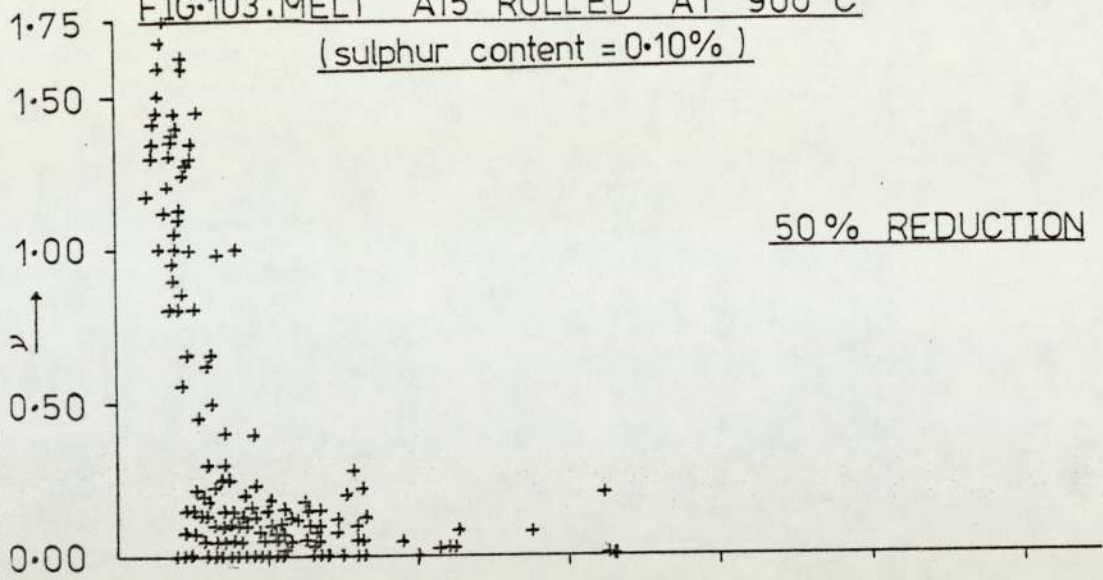


FIG.103:MELT A15 ROLLED AT 900° C

(sulphur content = 0.10%)



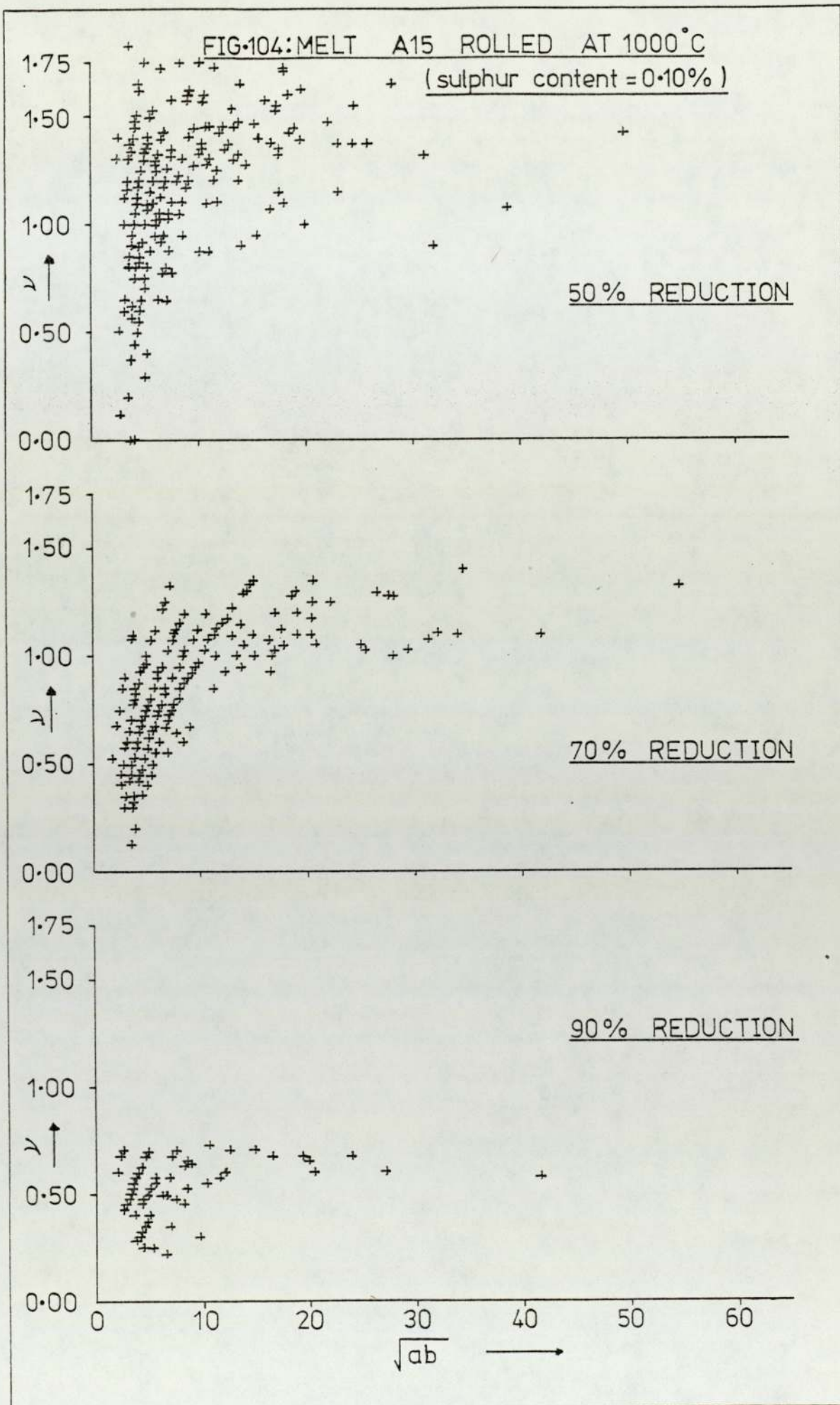
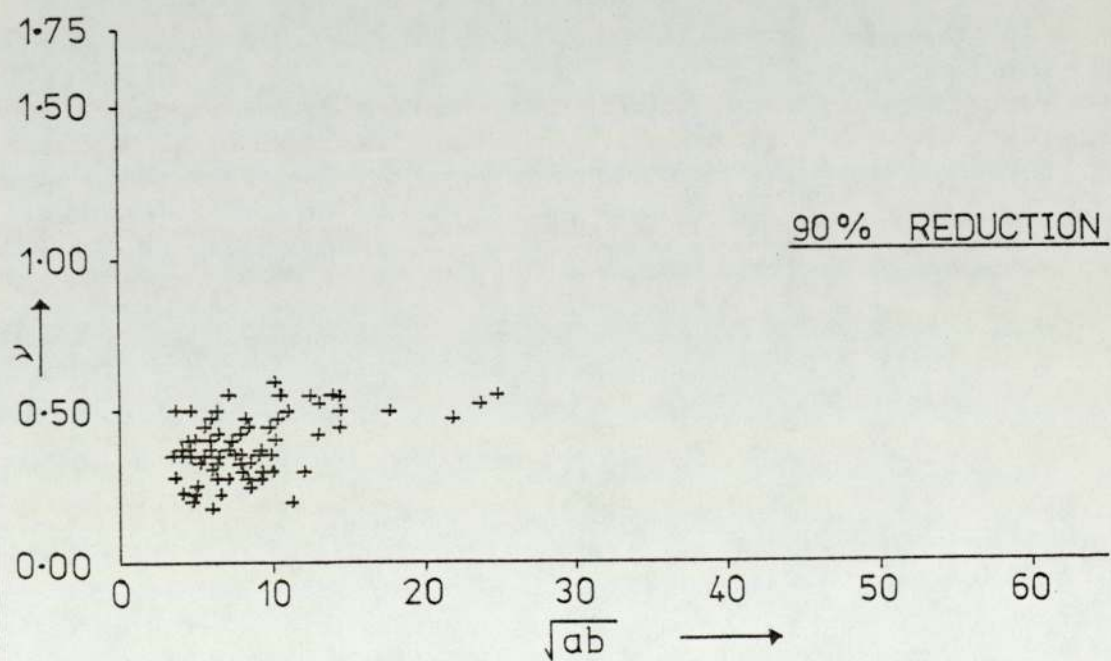
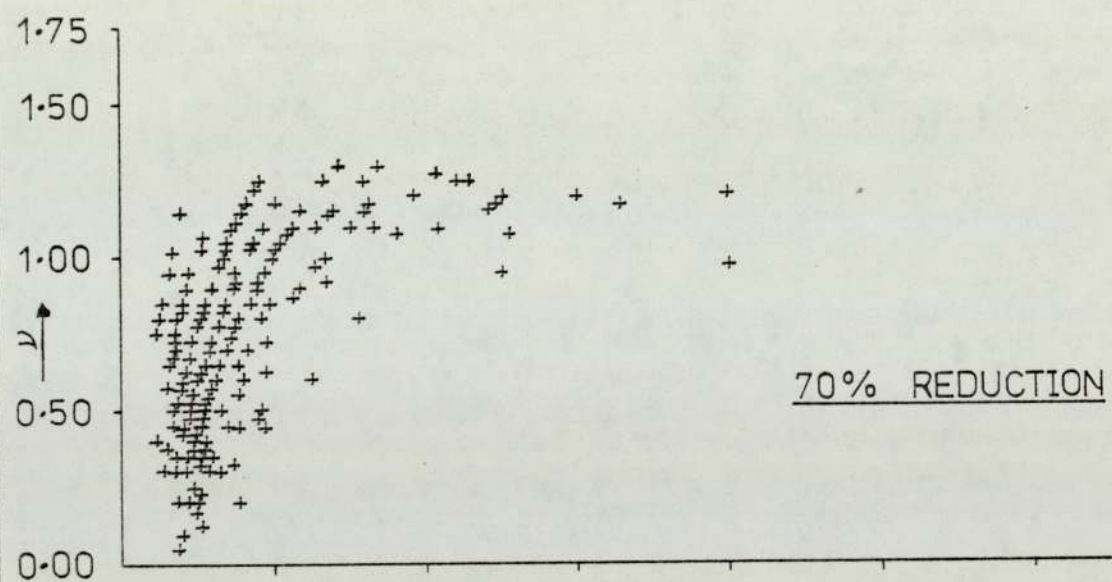
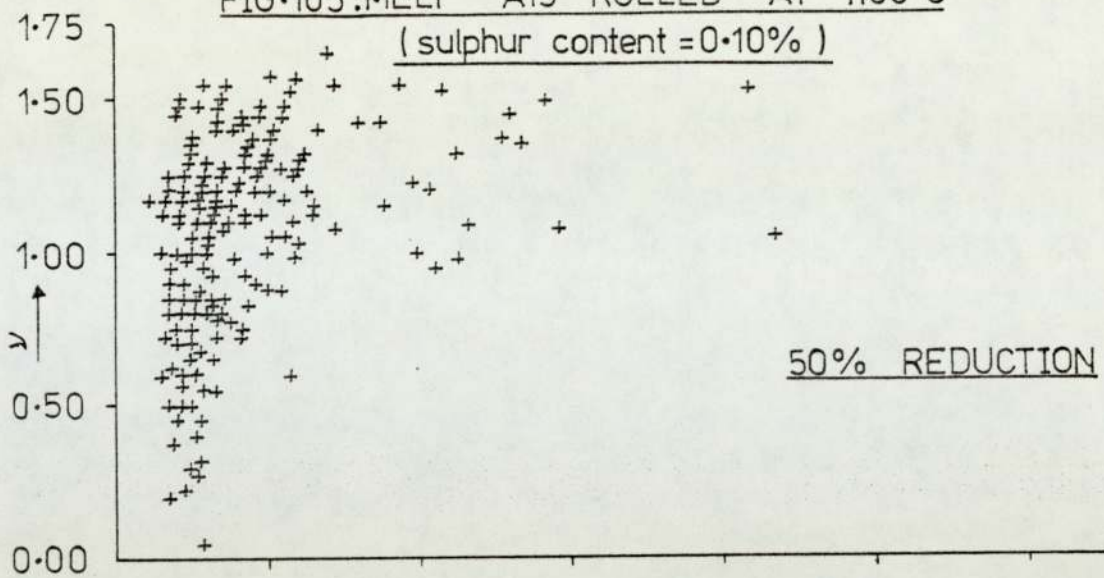
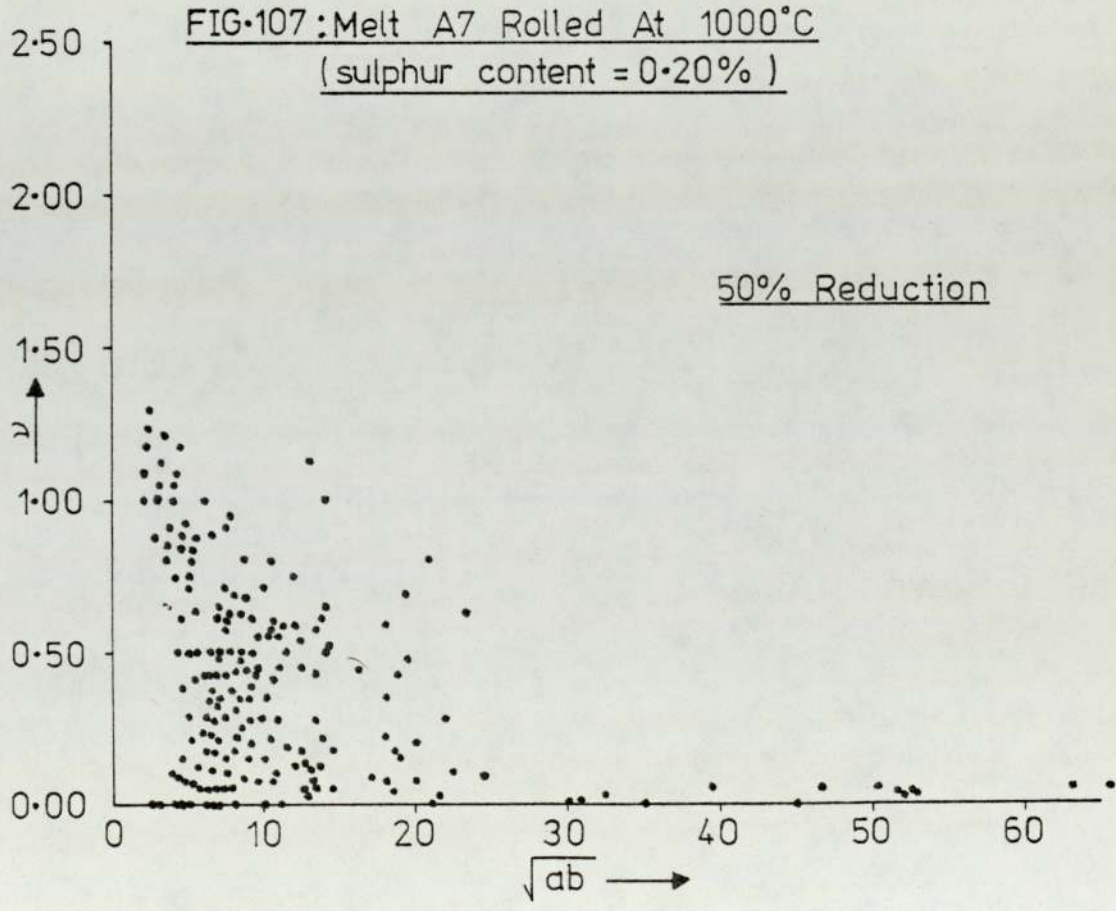
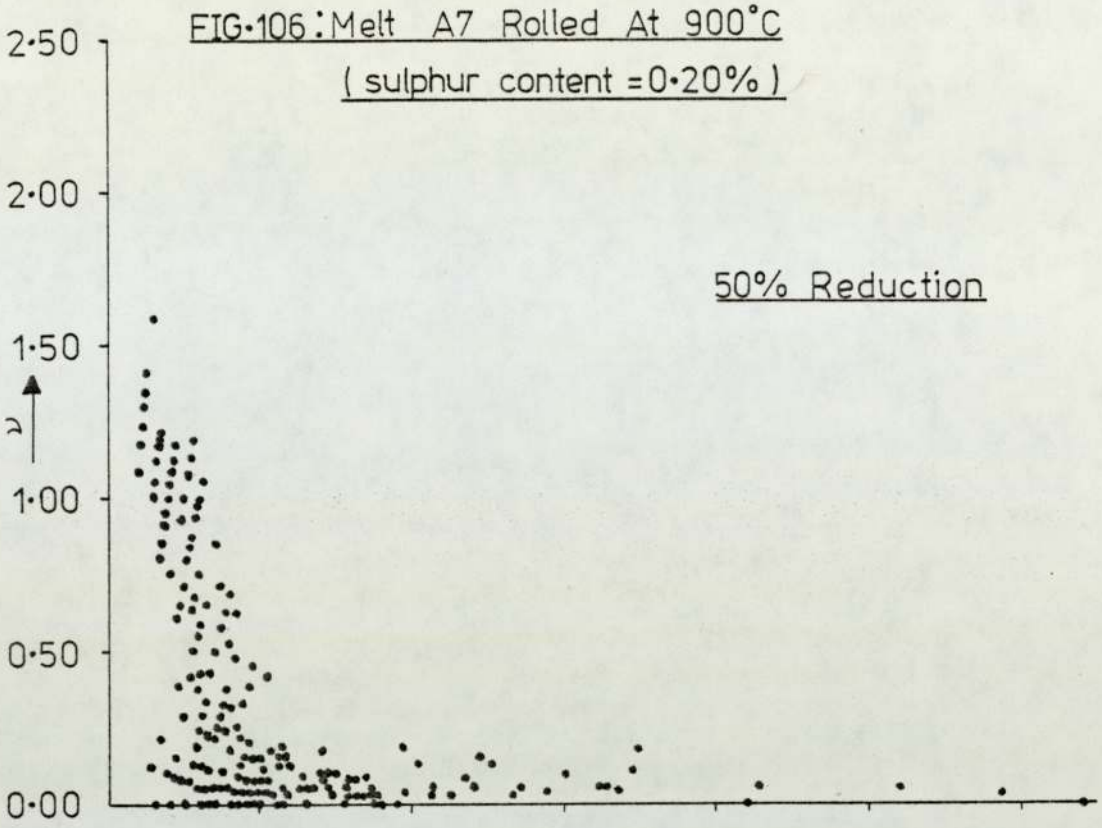
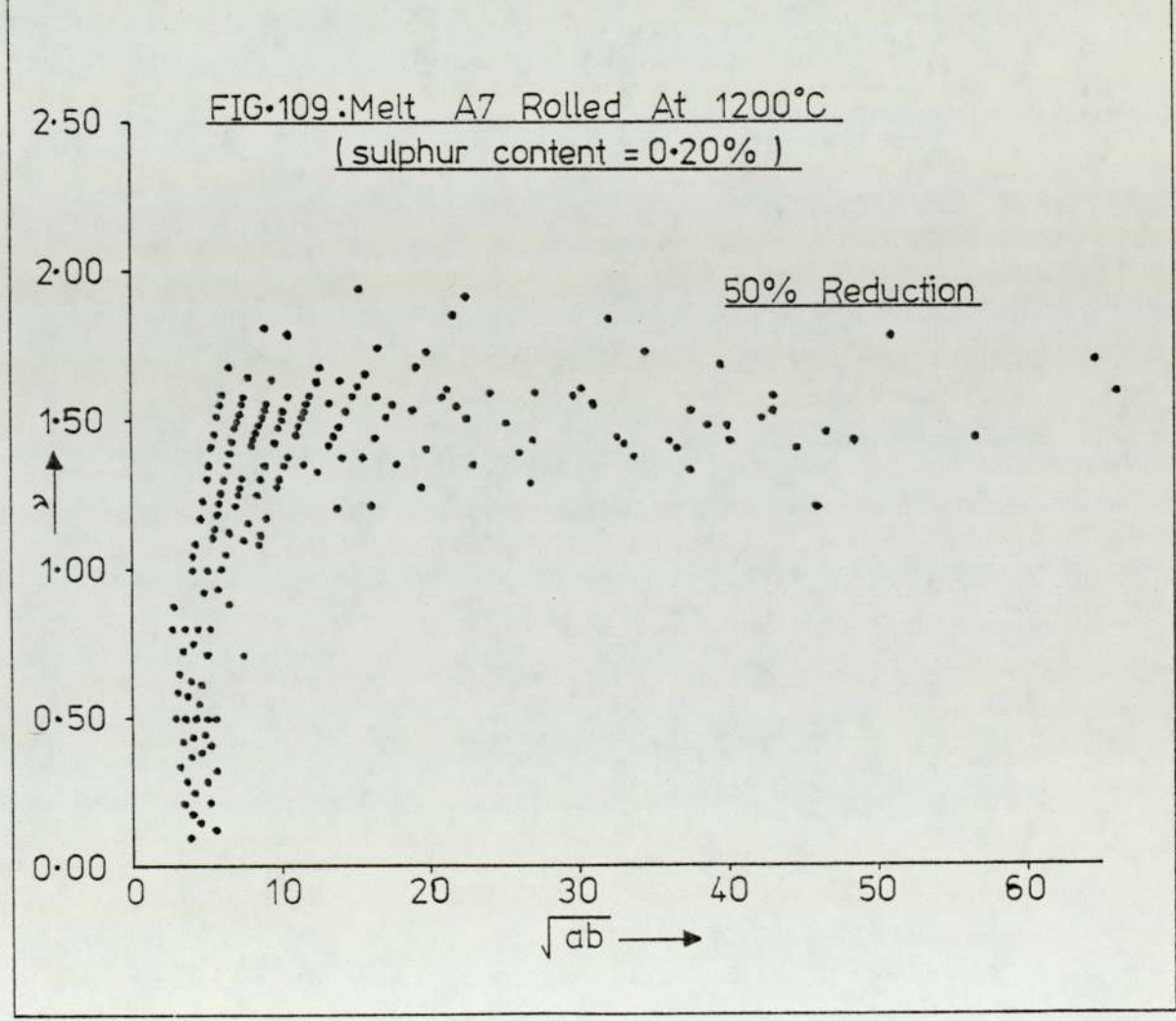
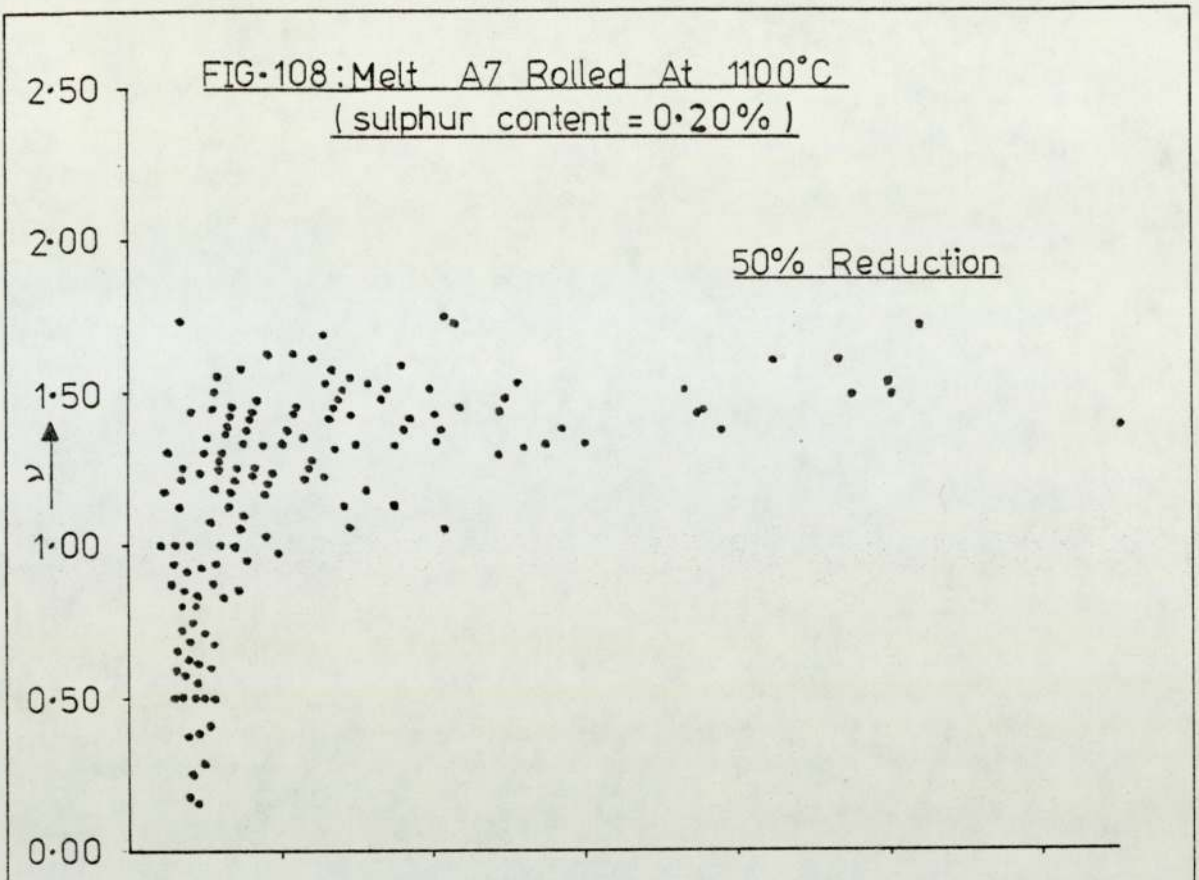


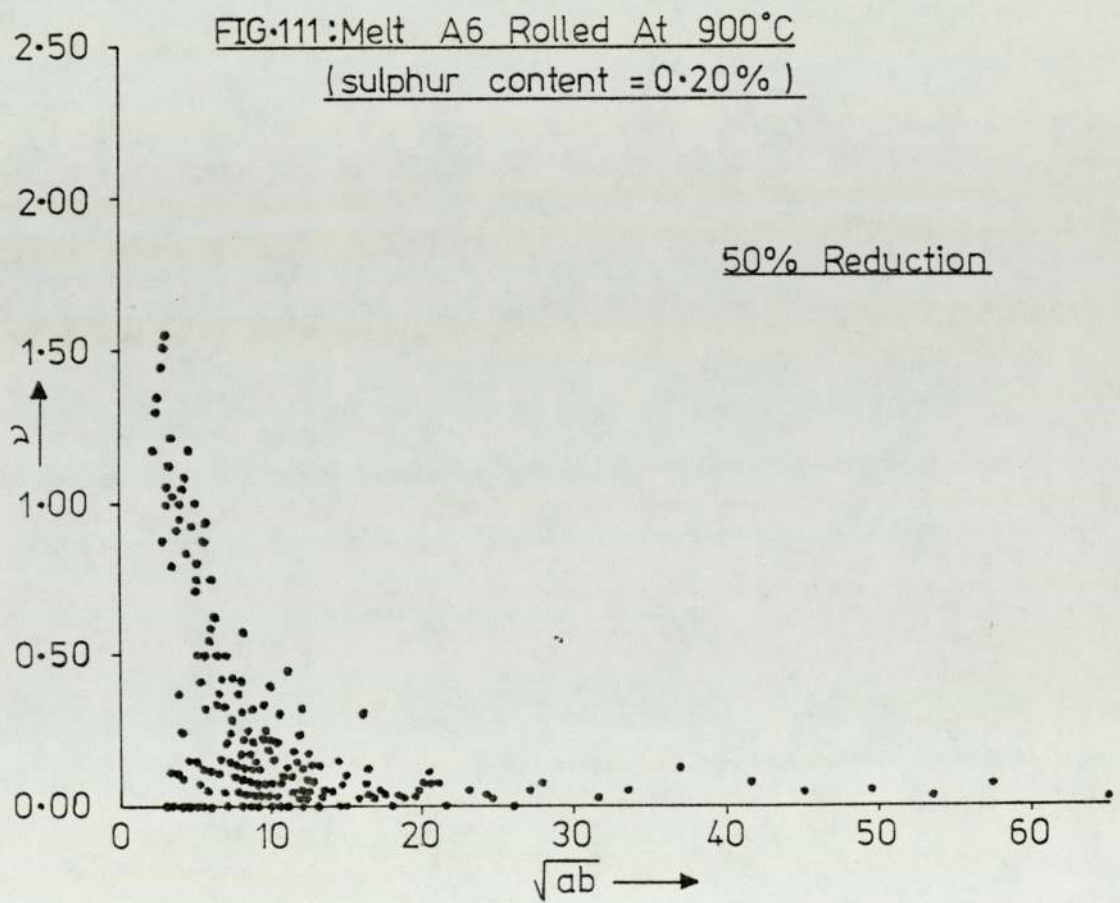
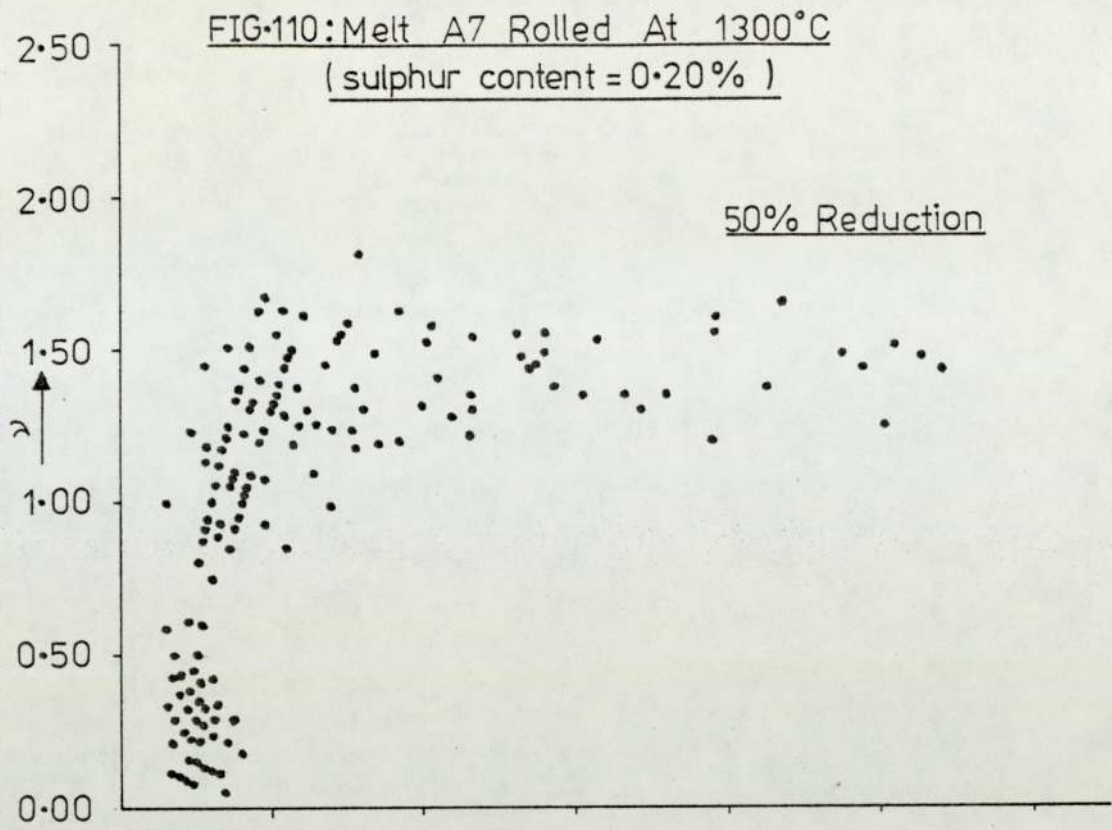
FIG.105:MELT A15 ROLLED AT 1100°C

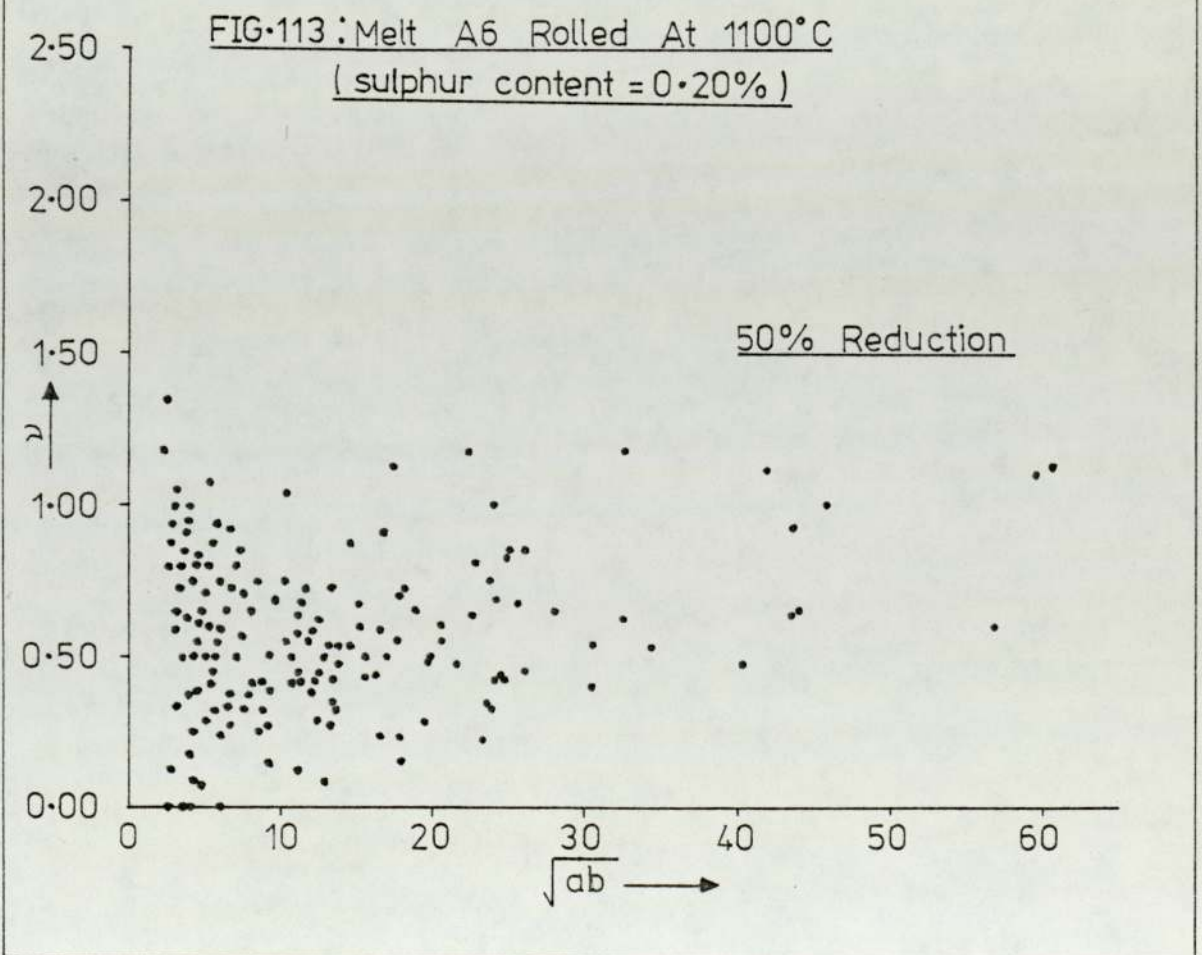
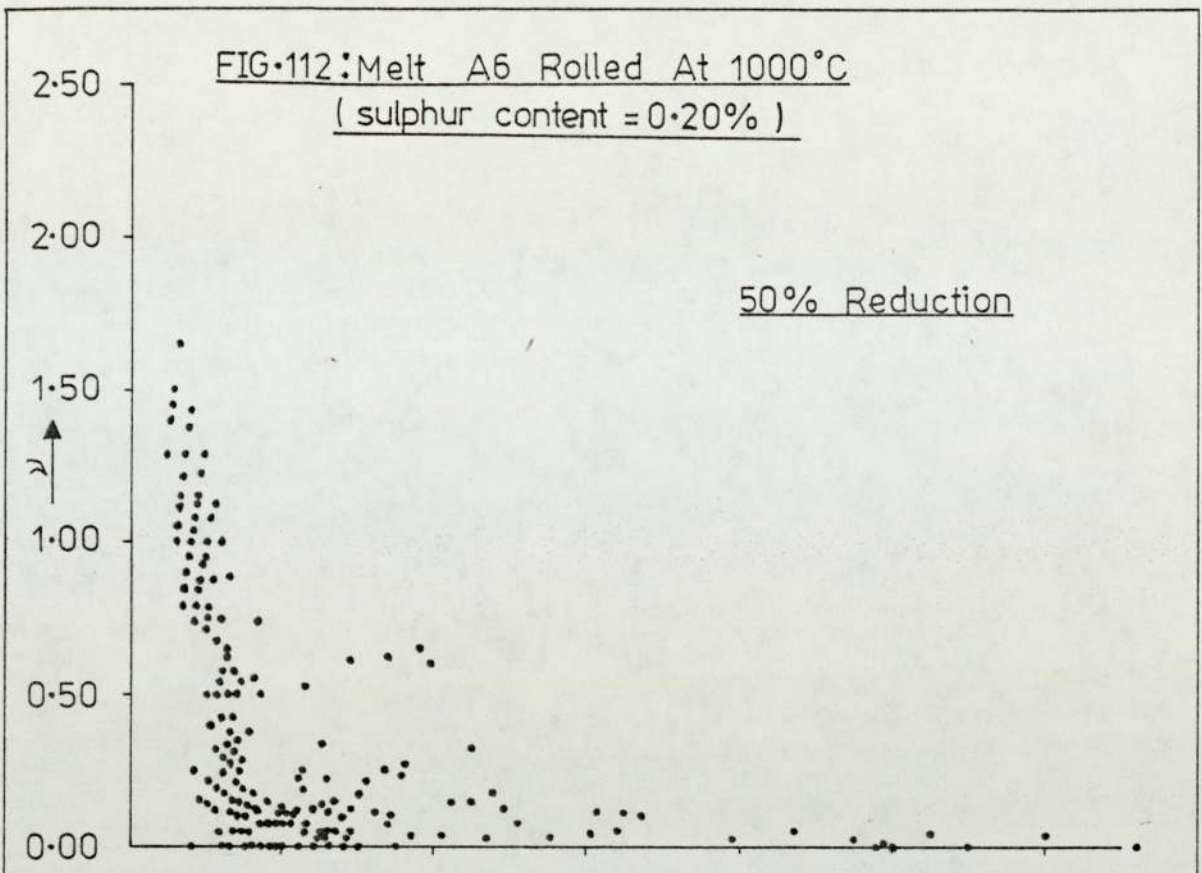
(sulphur content = 0.10%)

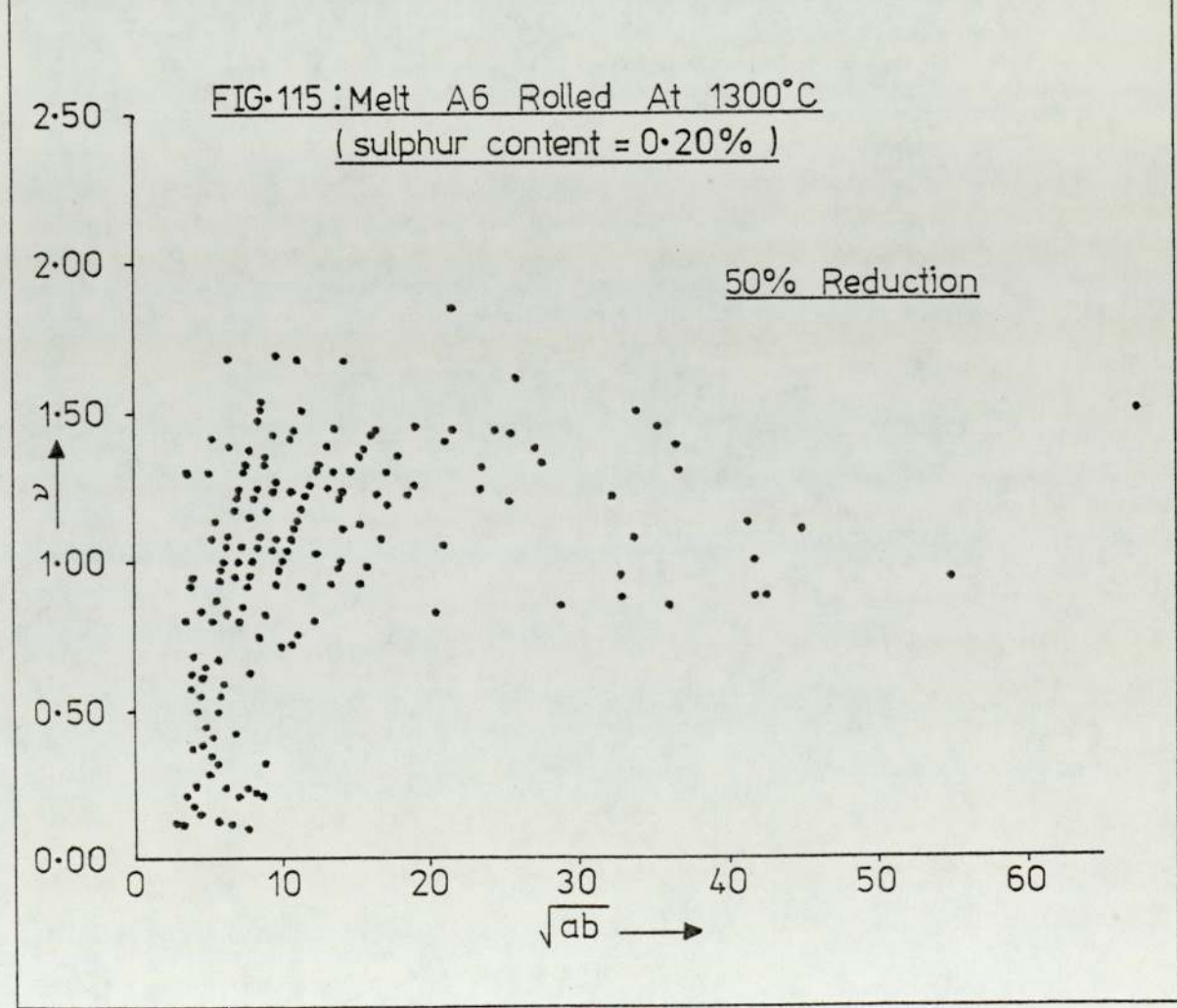
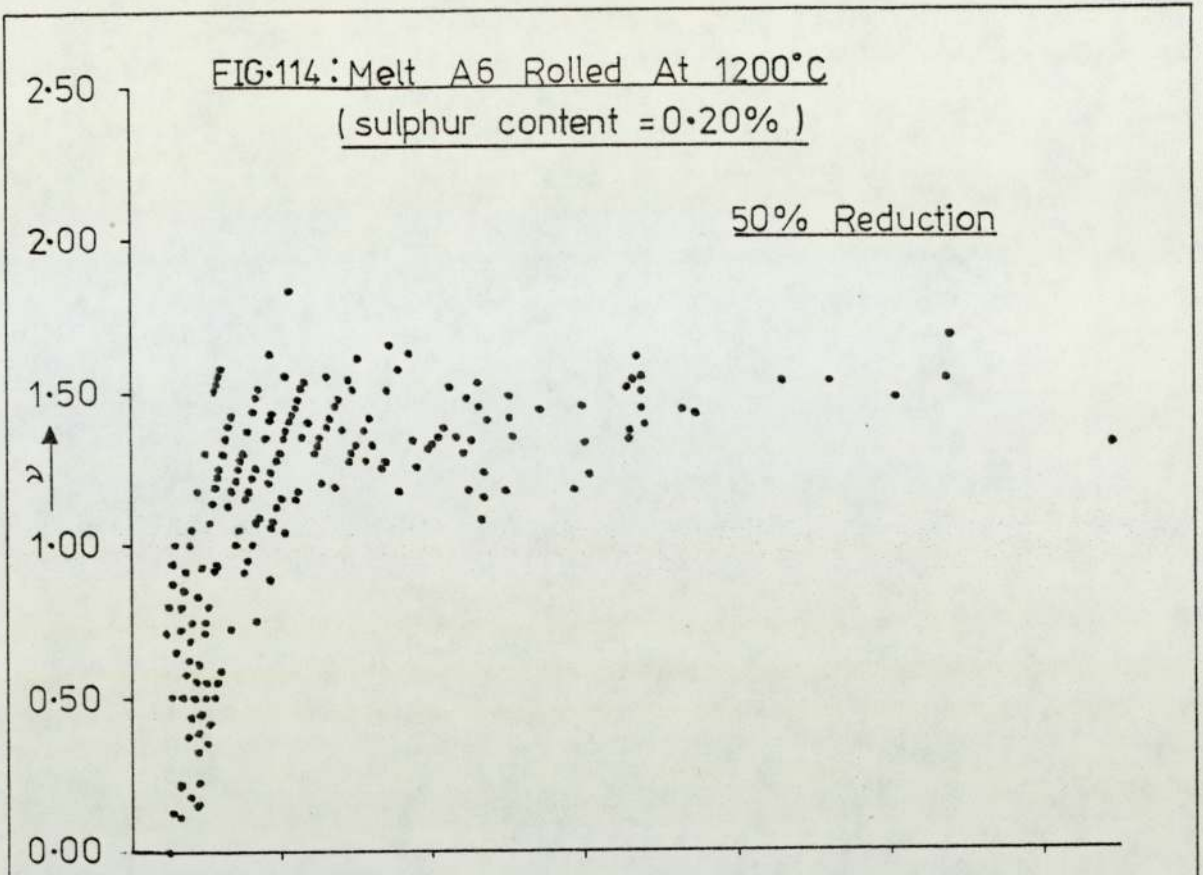


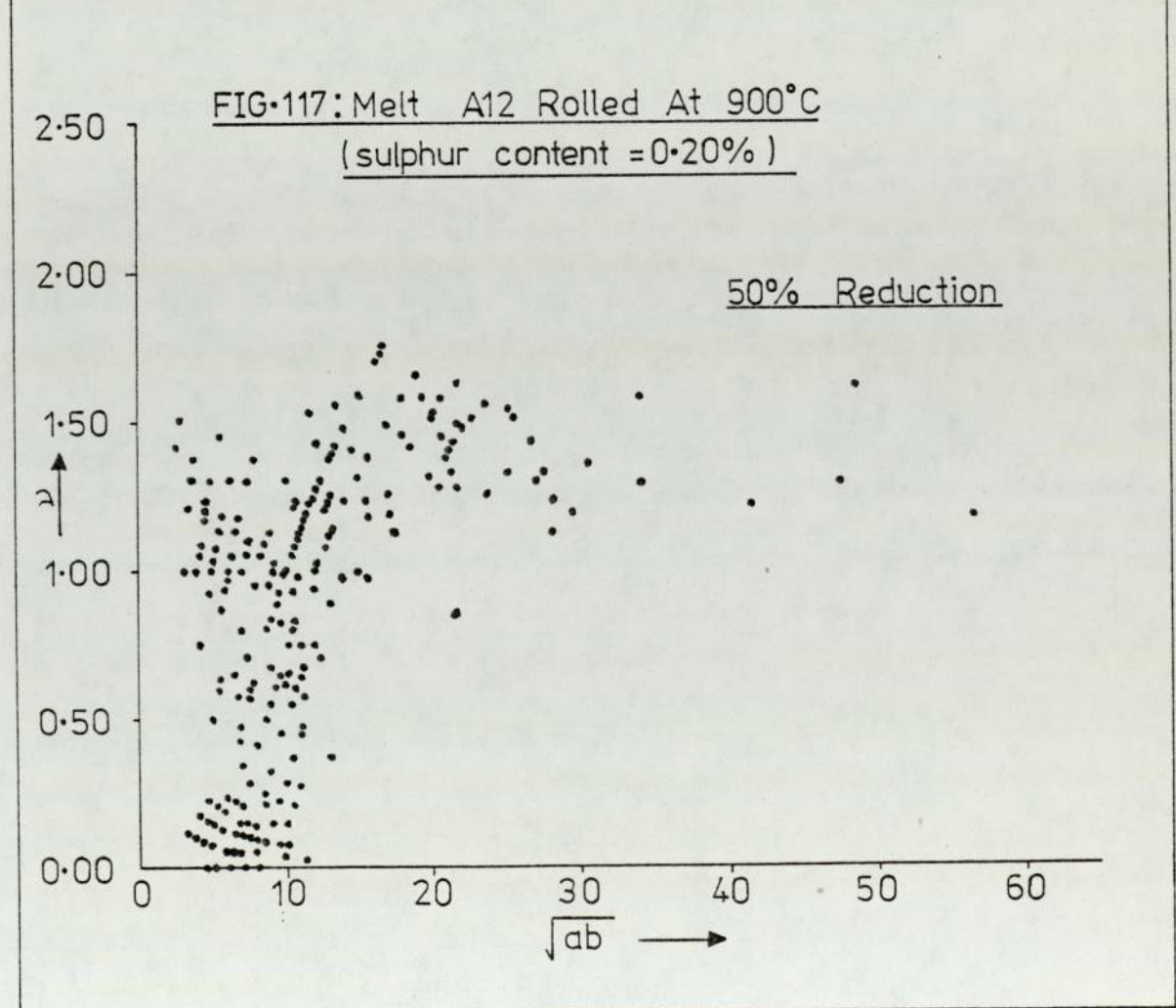
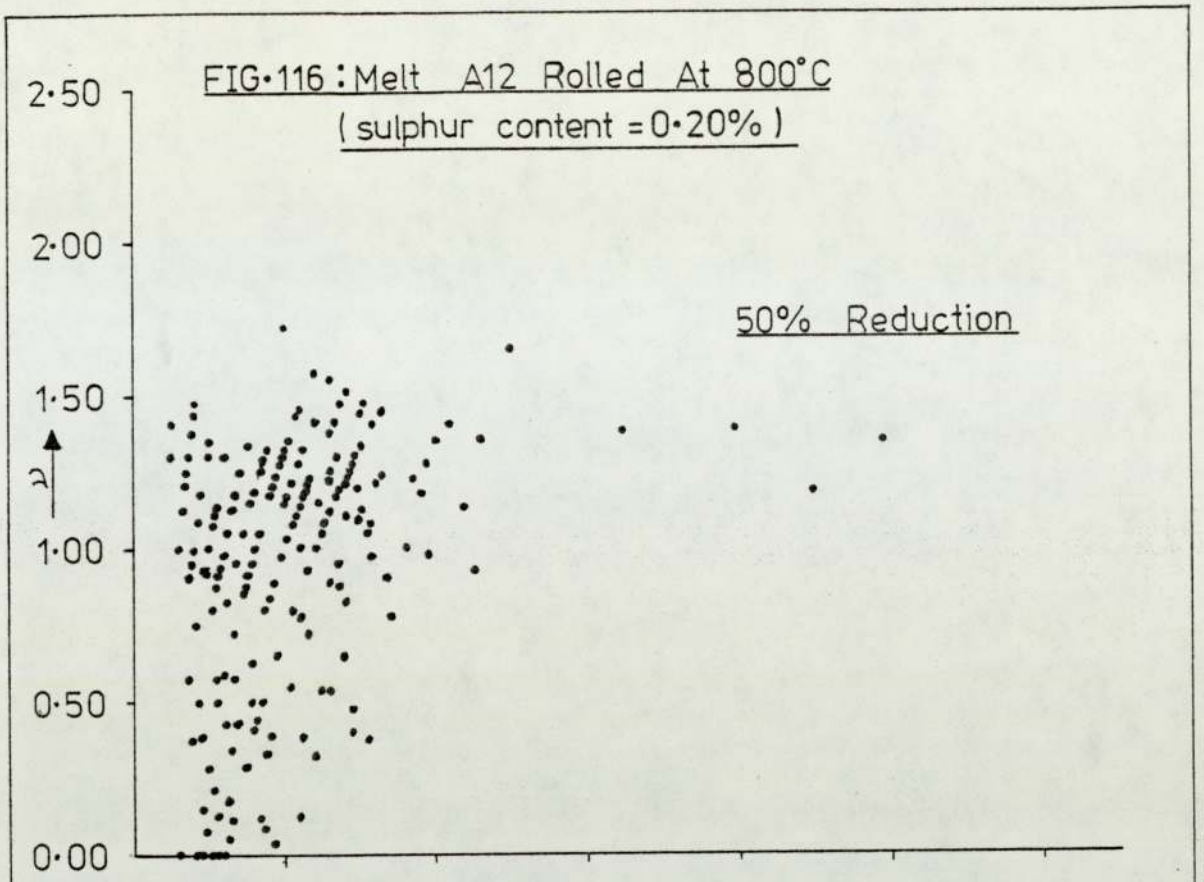


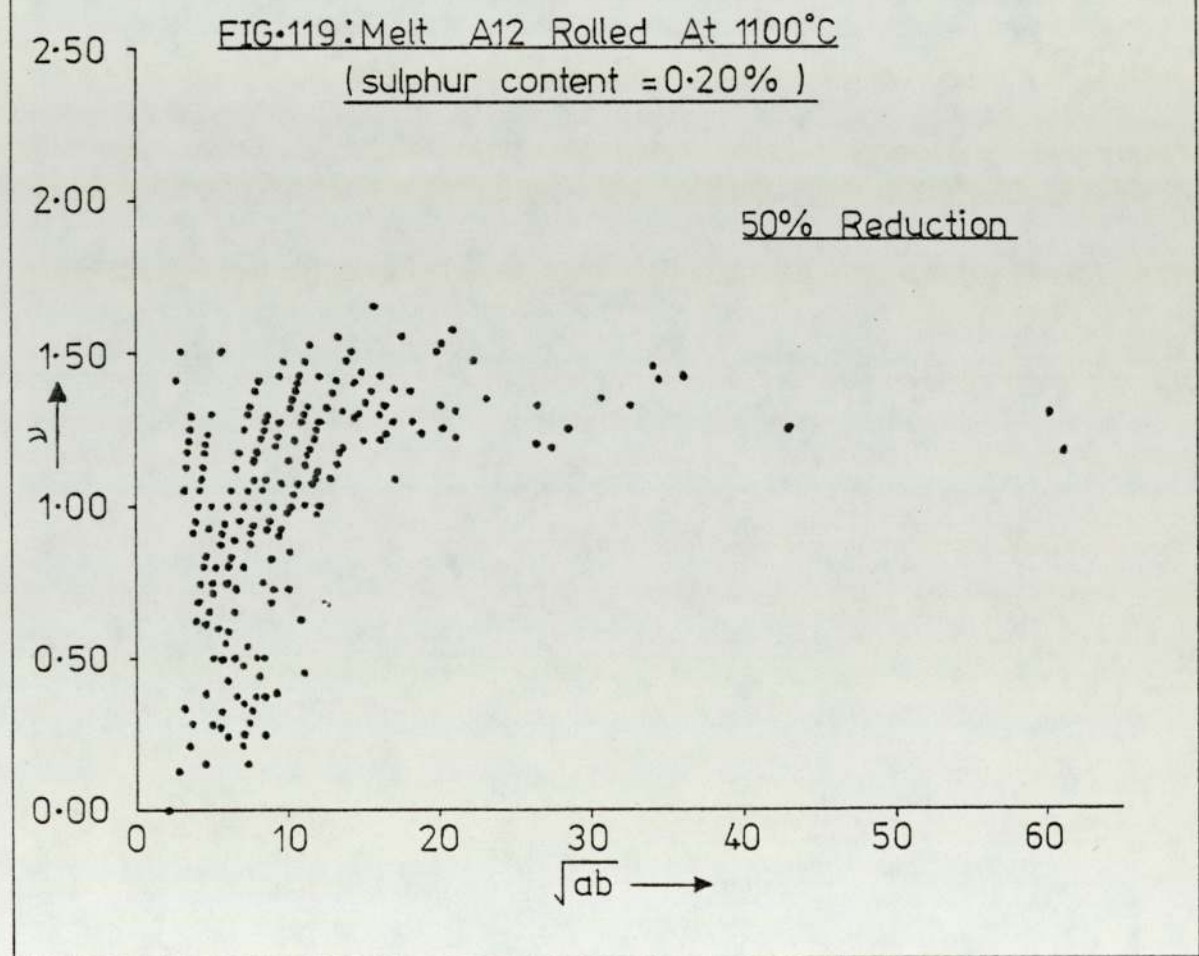
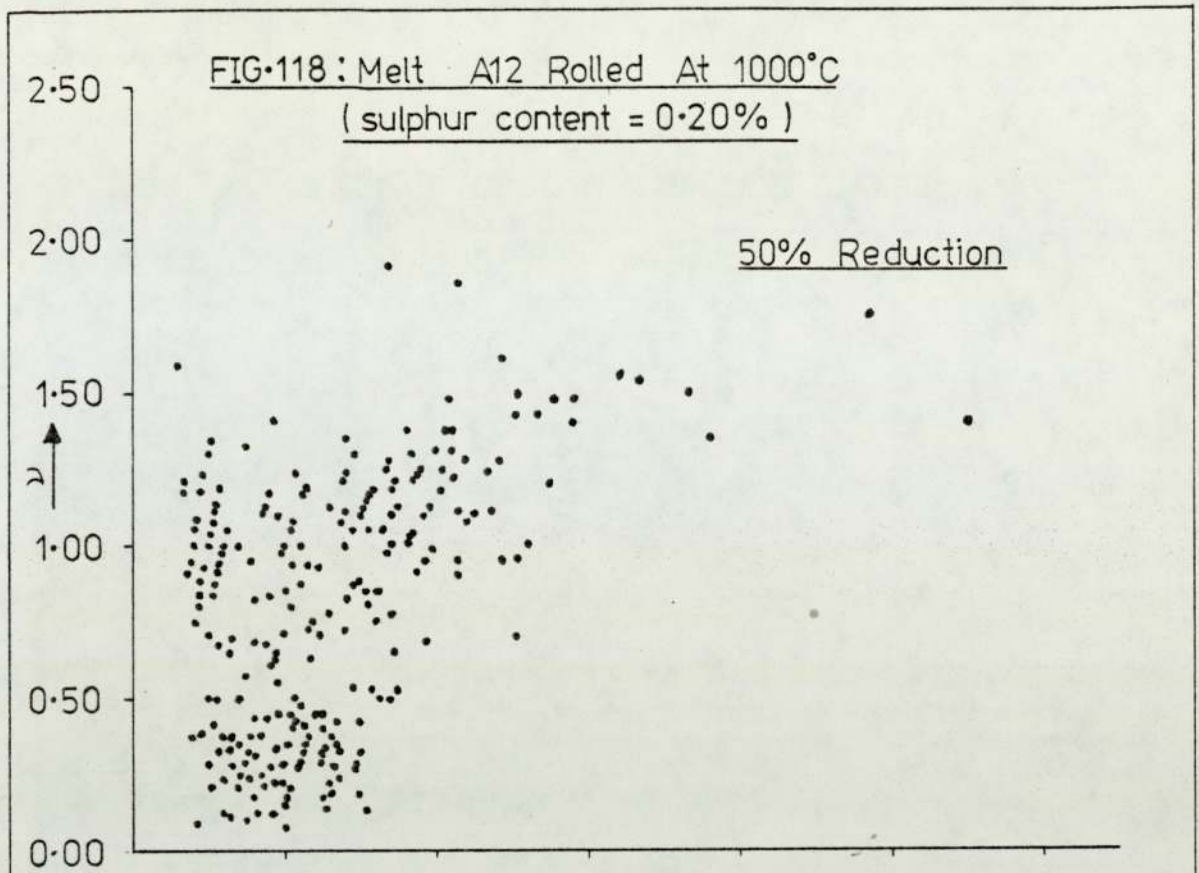


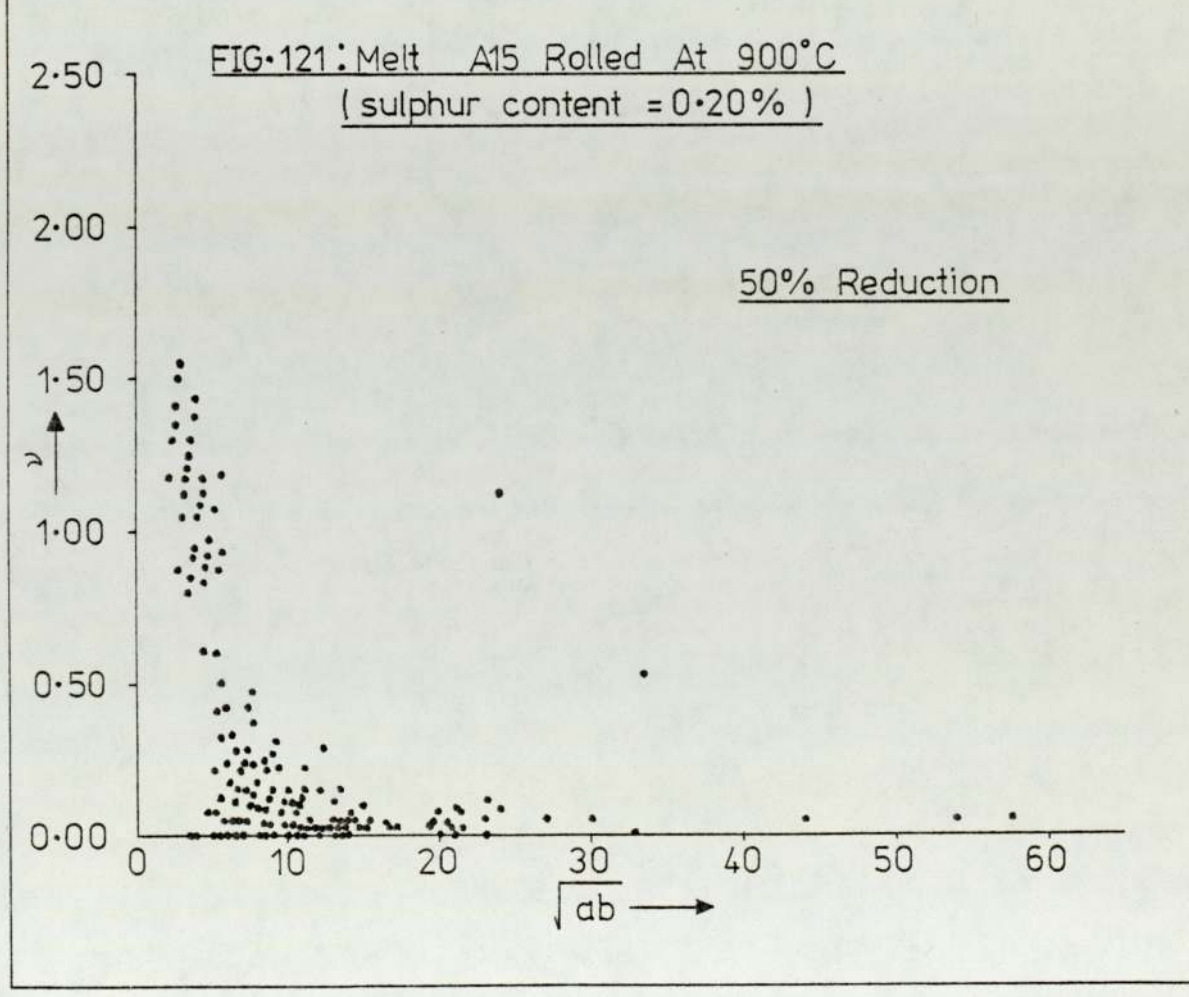
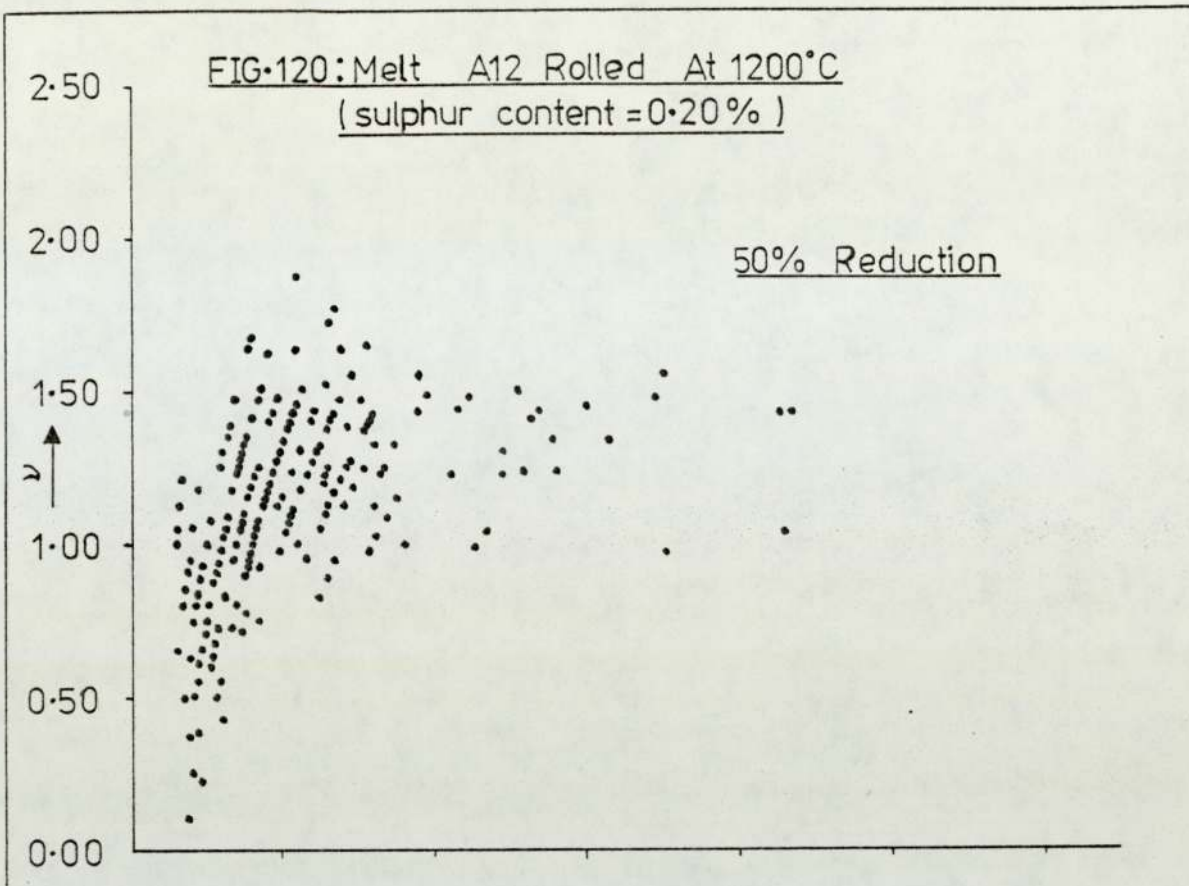












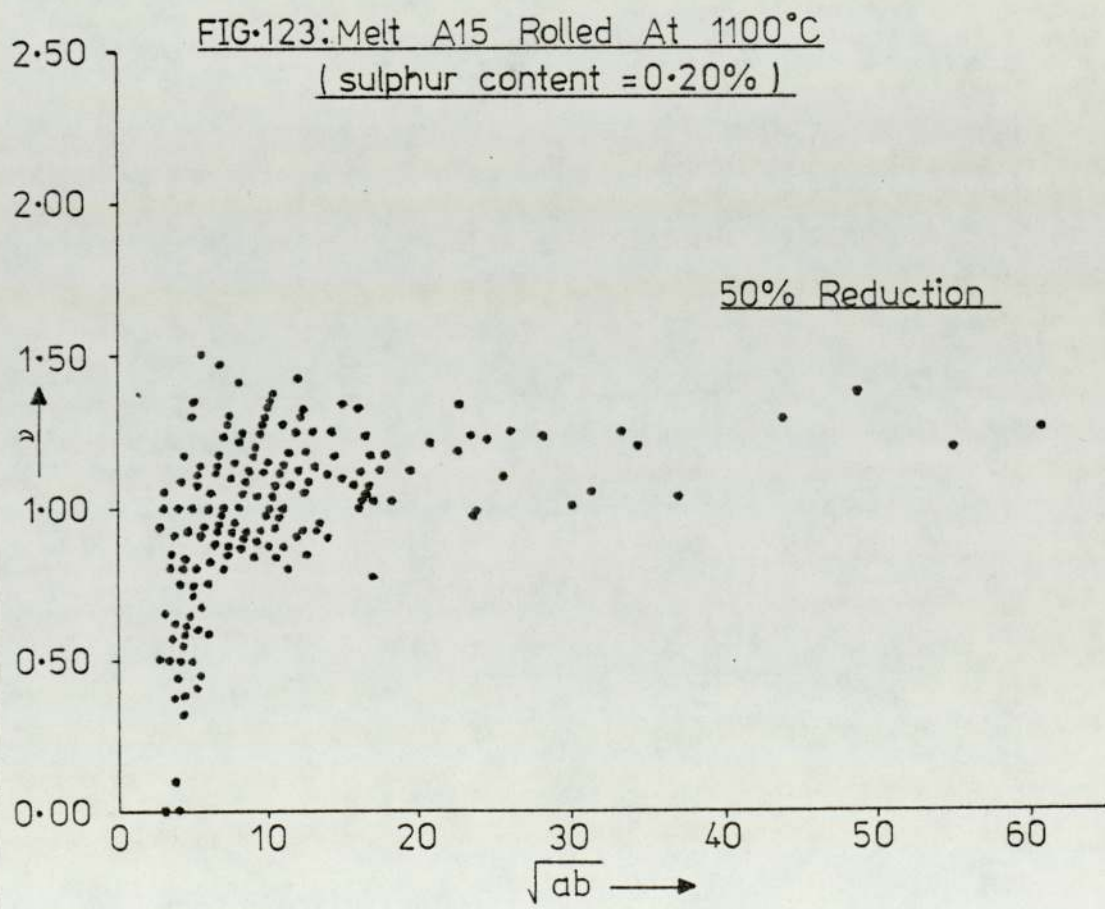
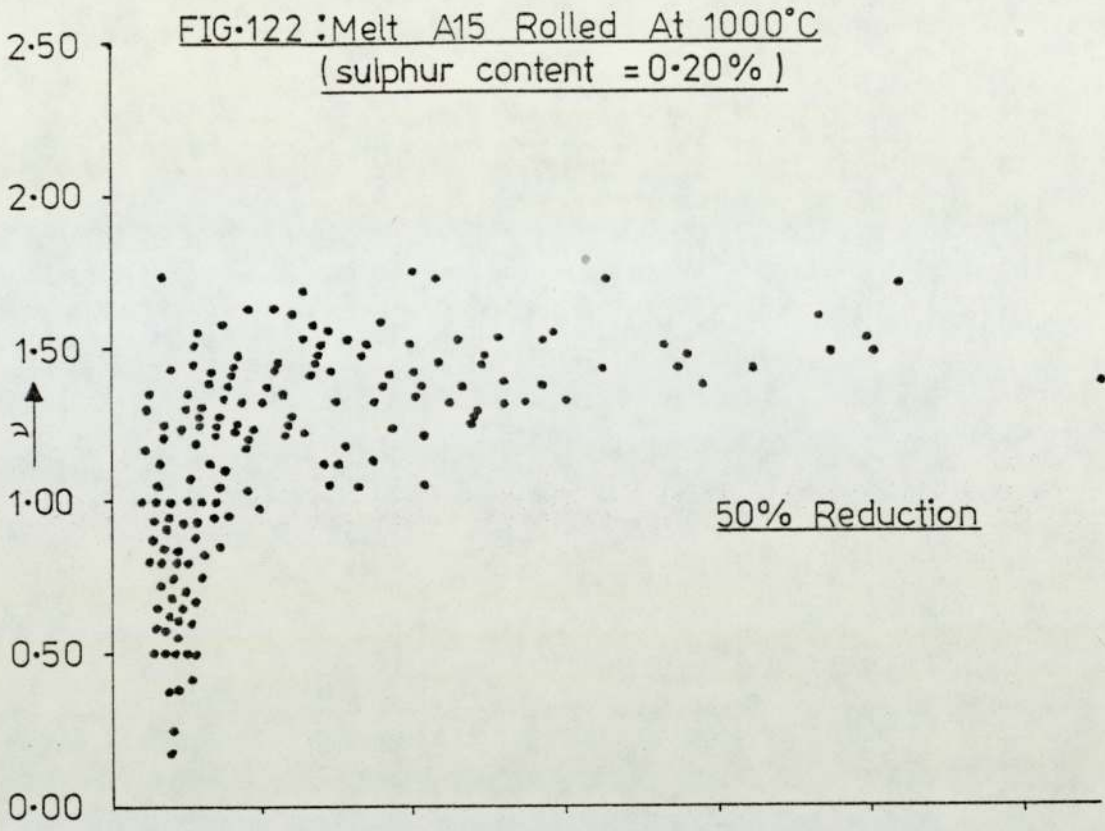


FIG-124:

Effect Of Rolling Temperature On
Relative Plasticity Of MnS Inclusions
In Melt A6

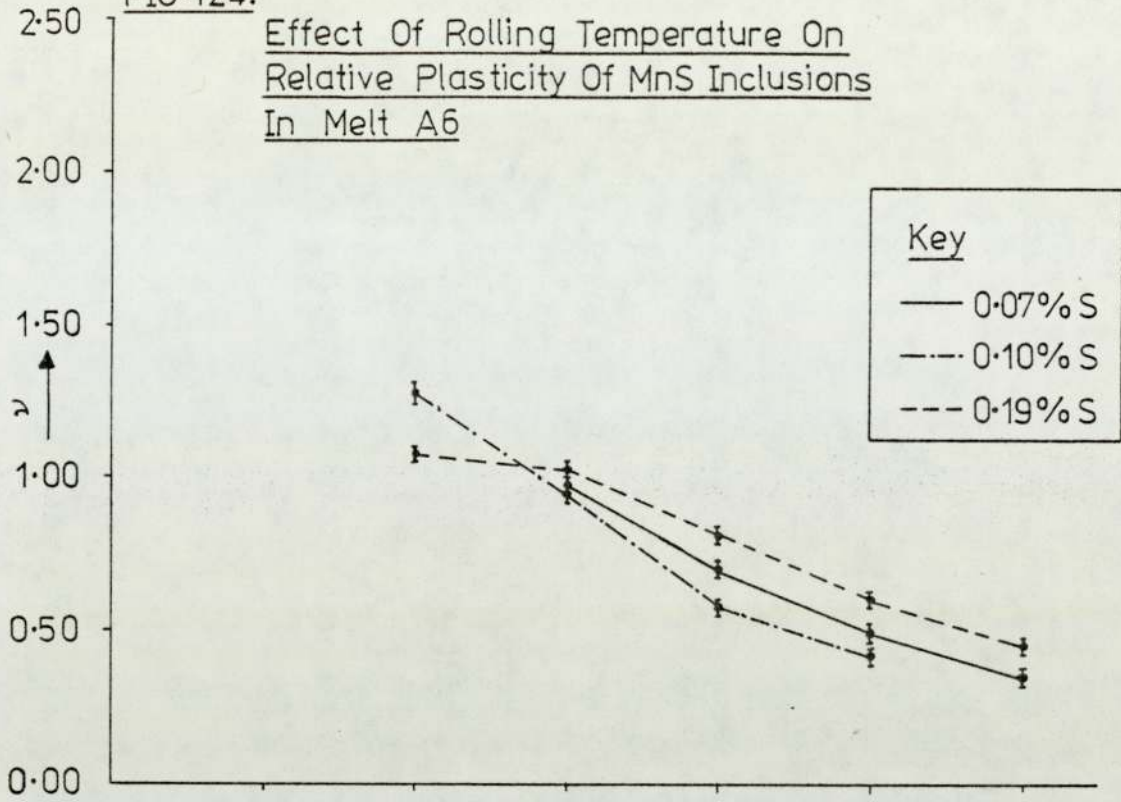
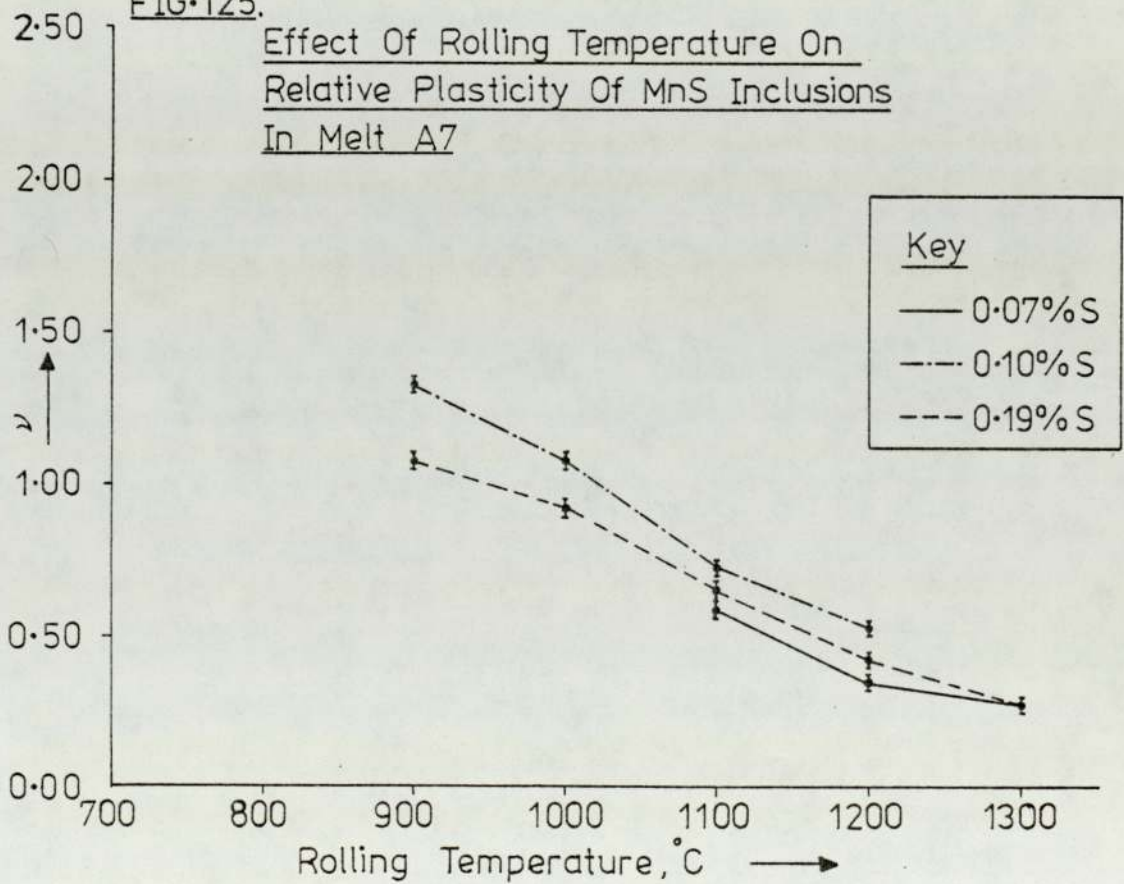
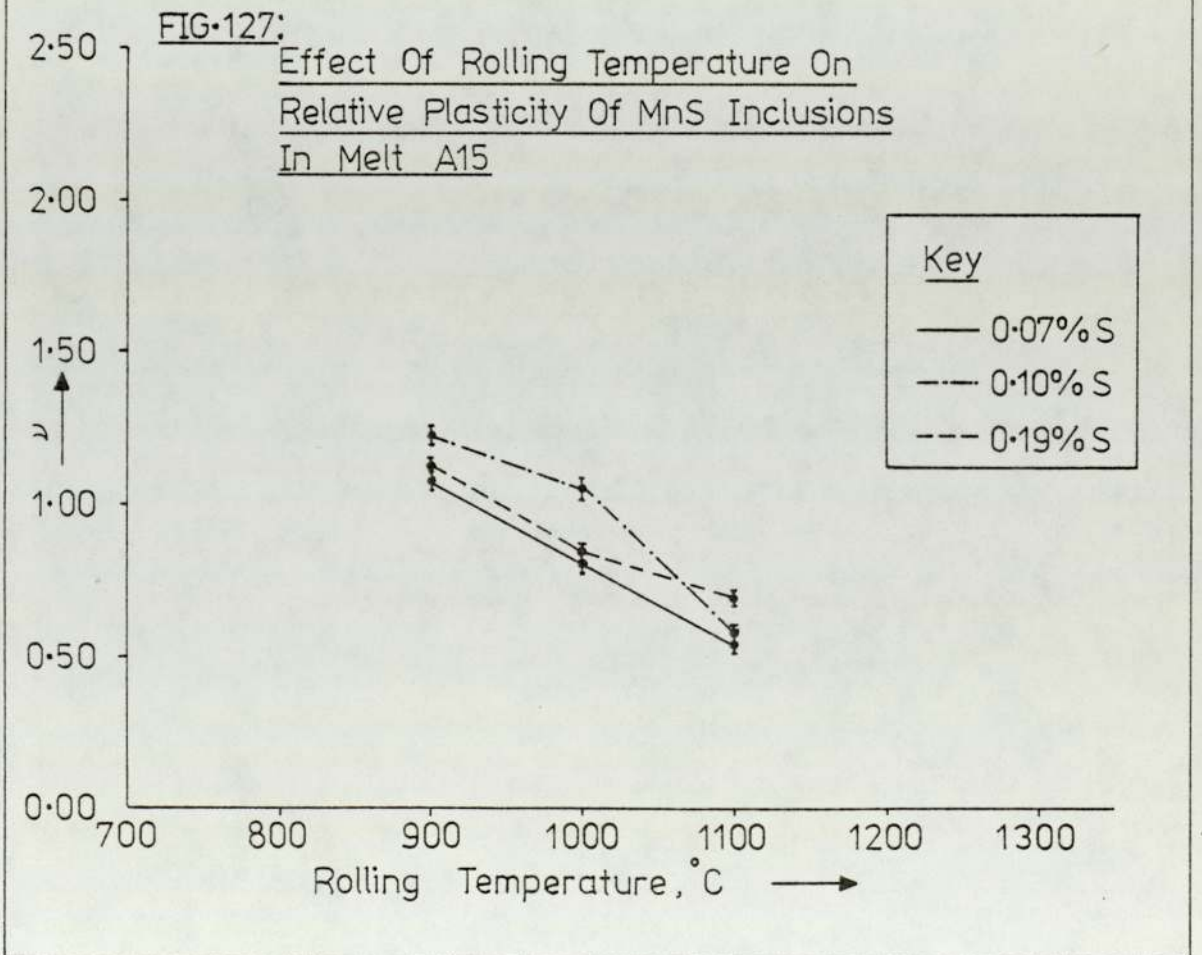
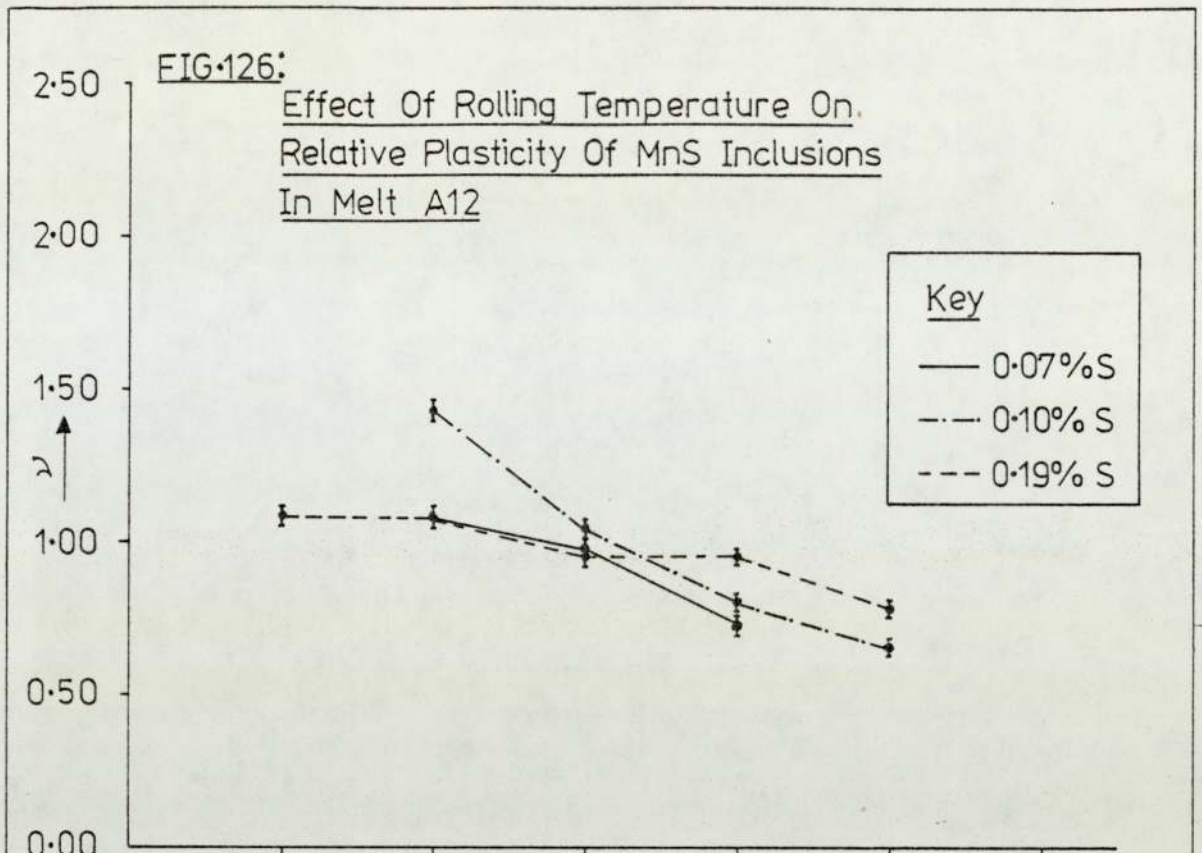
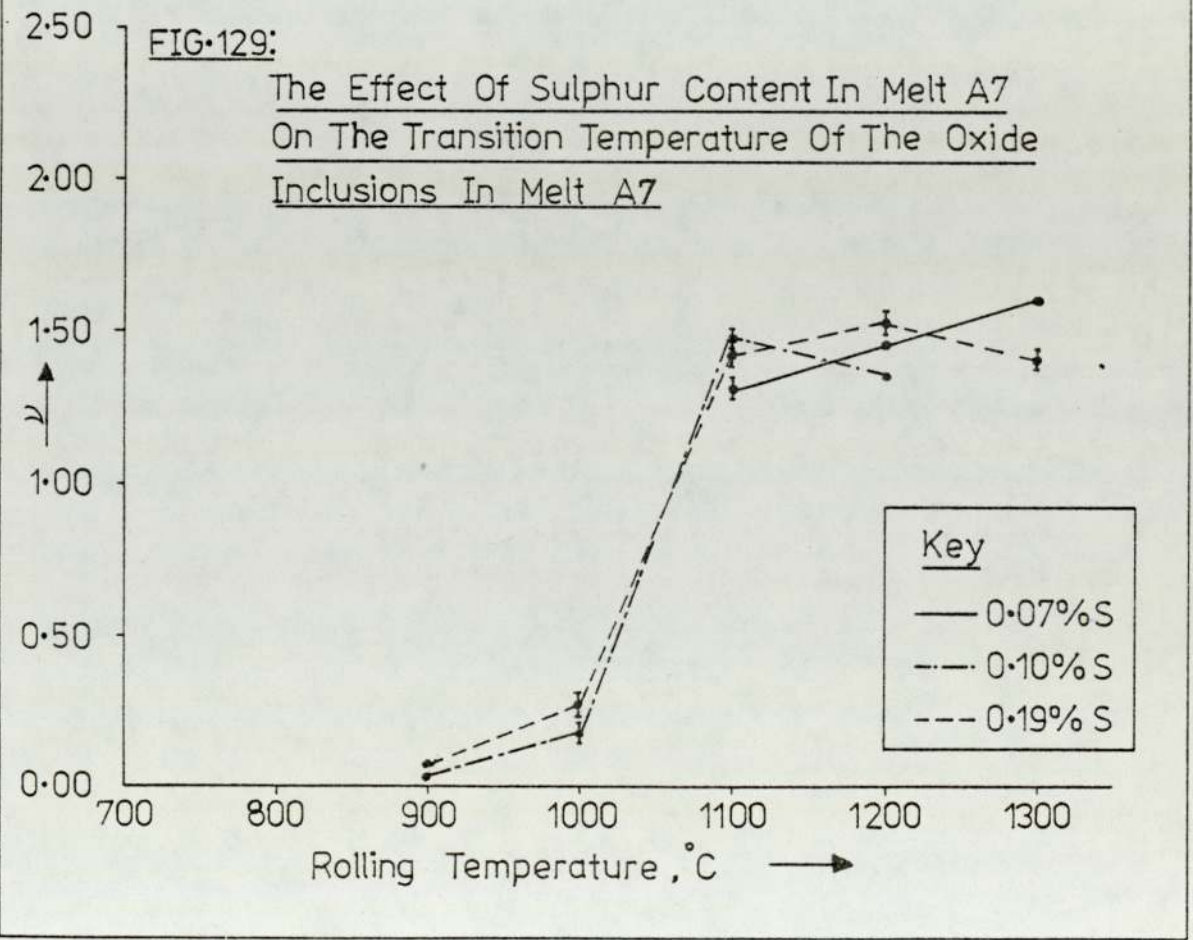
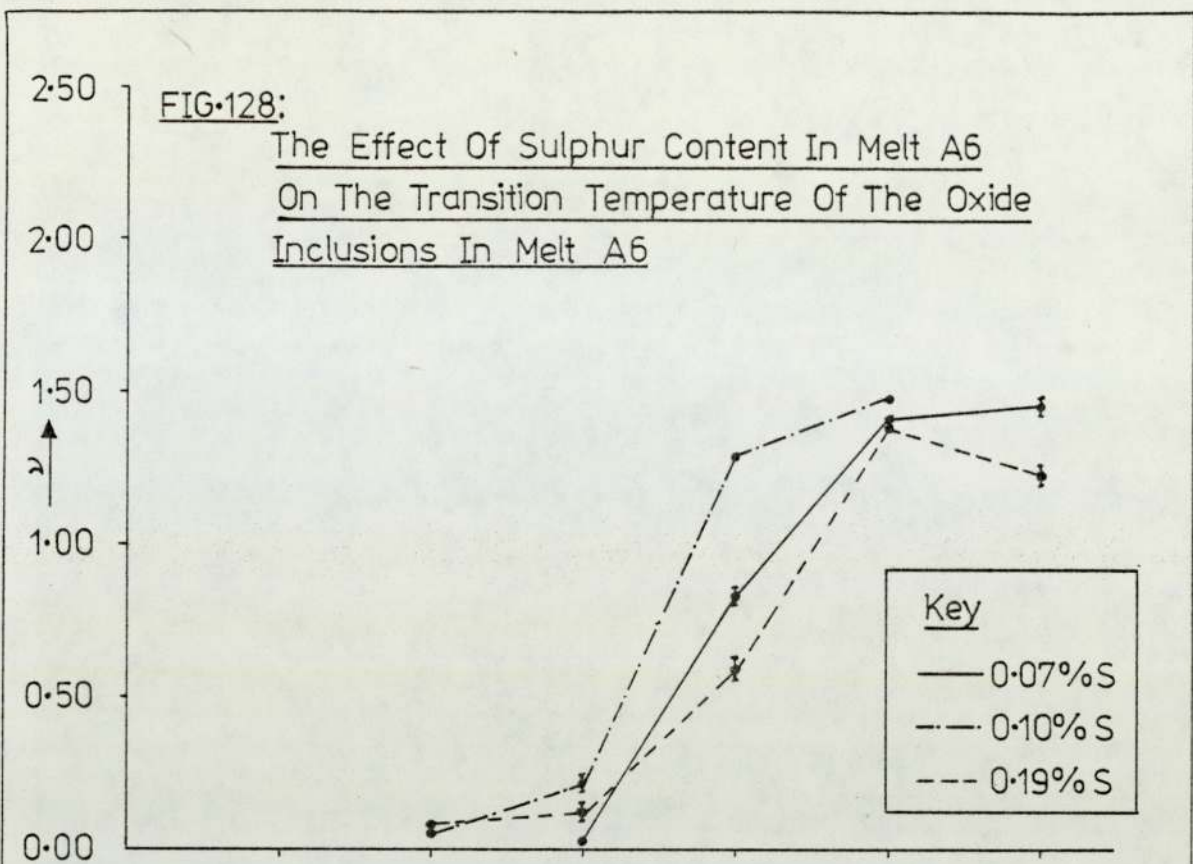


FIG-125:

Effect Of Rolling Temperature On
Relative Plasticity Of MnS Inclusions
In Melt A7







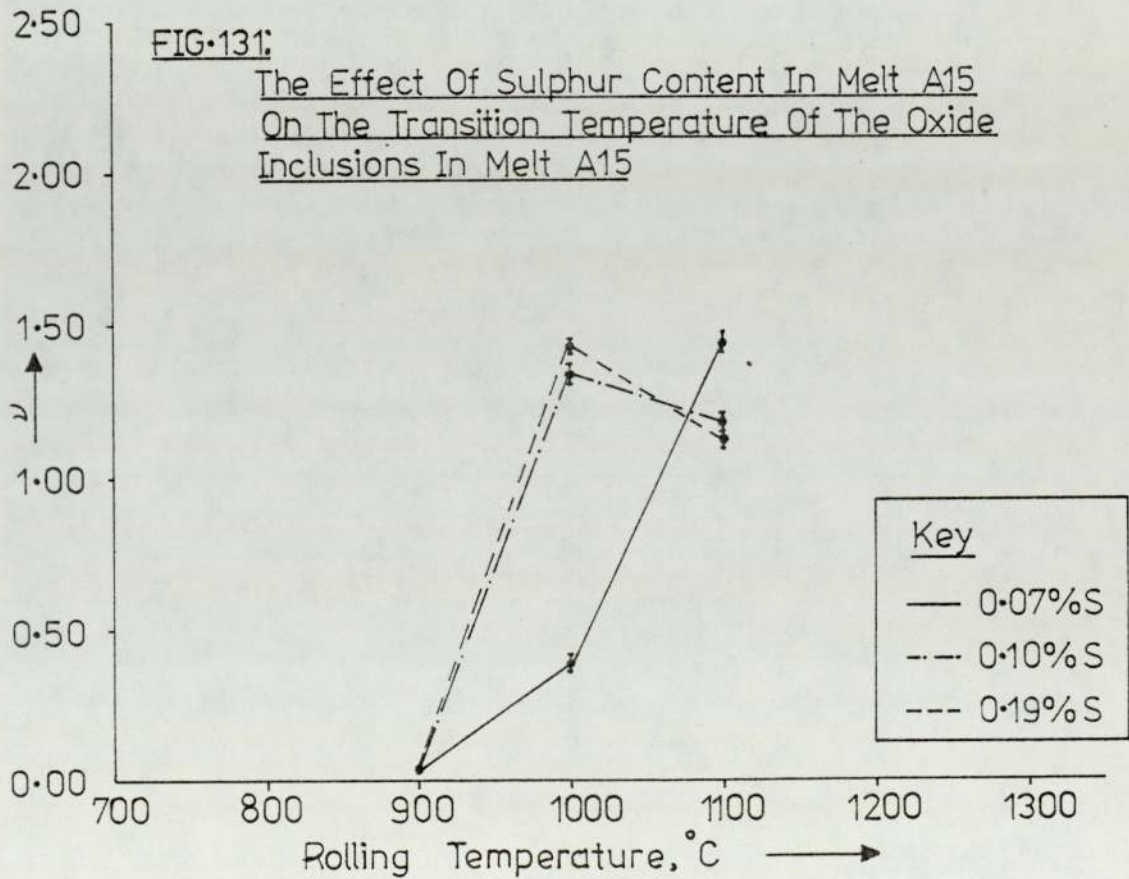
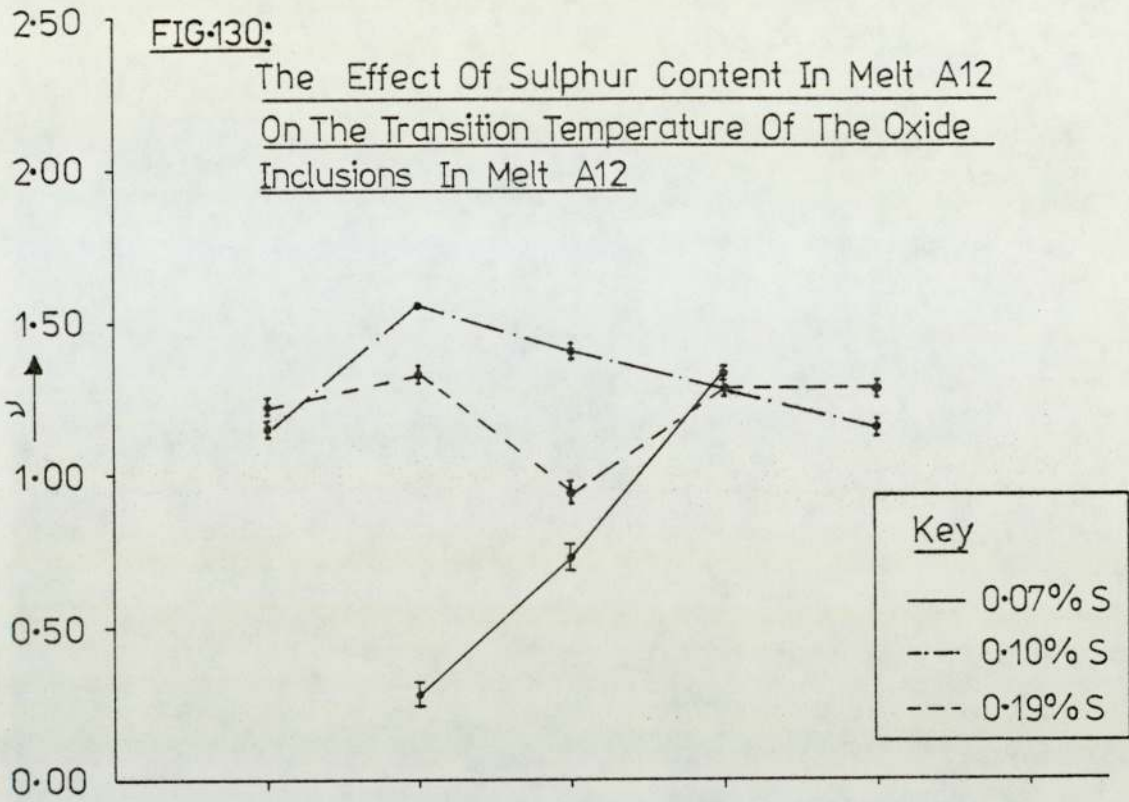


FIG.132:

Variation Of Plasticity Index With
Square Root Of Homogenisation Time
[specimen A12]

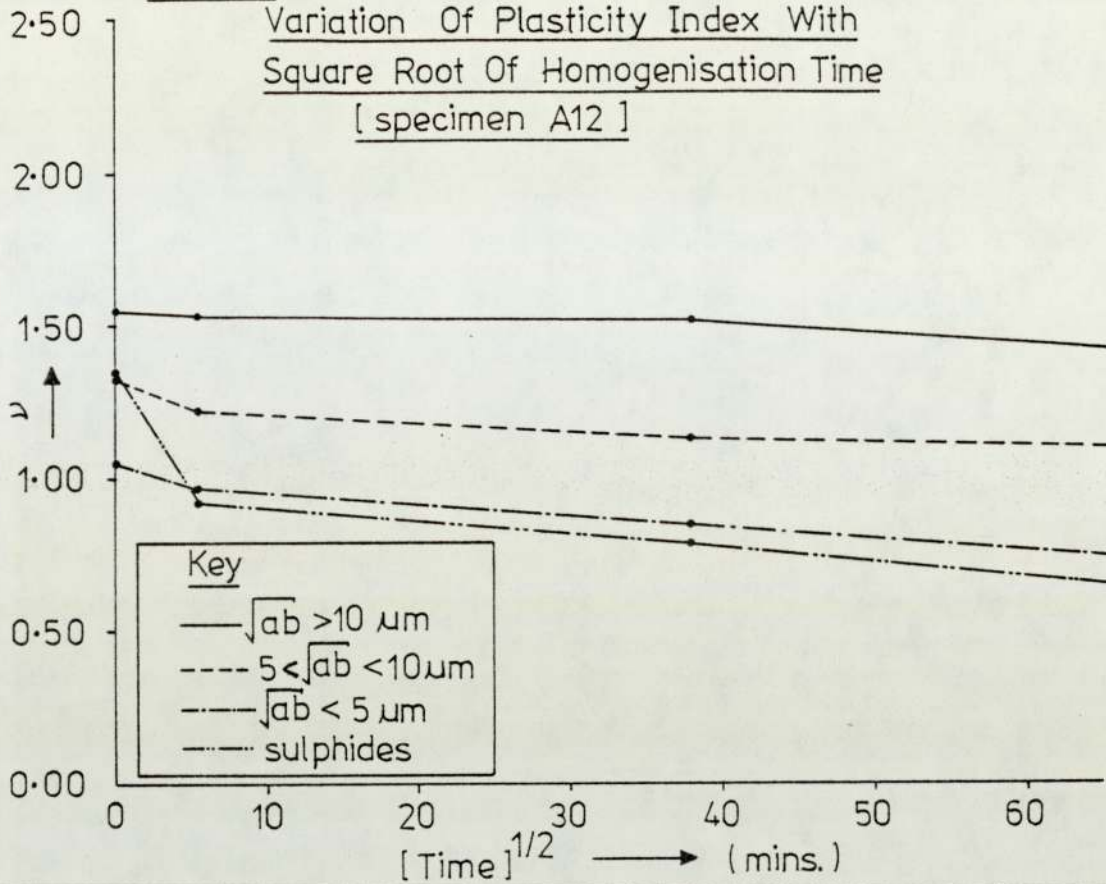
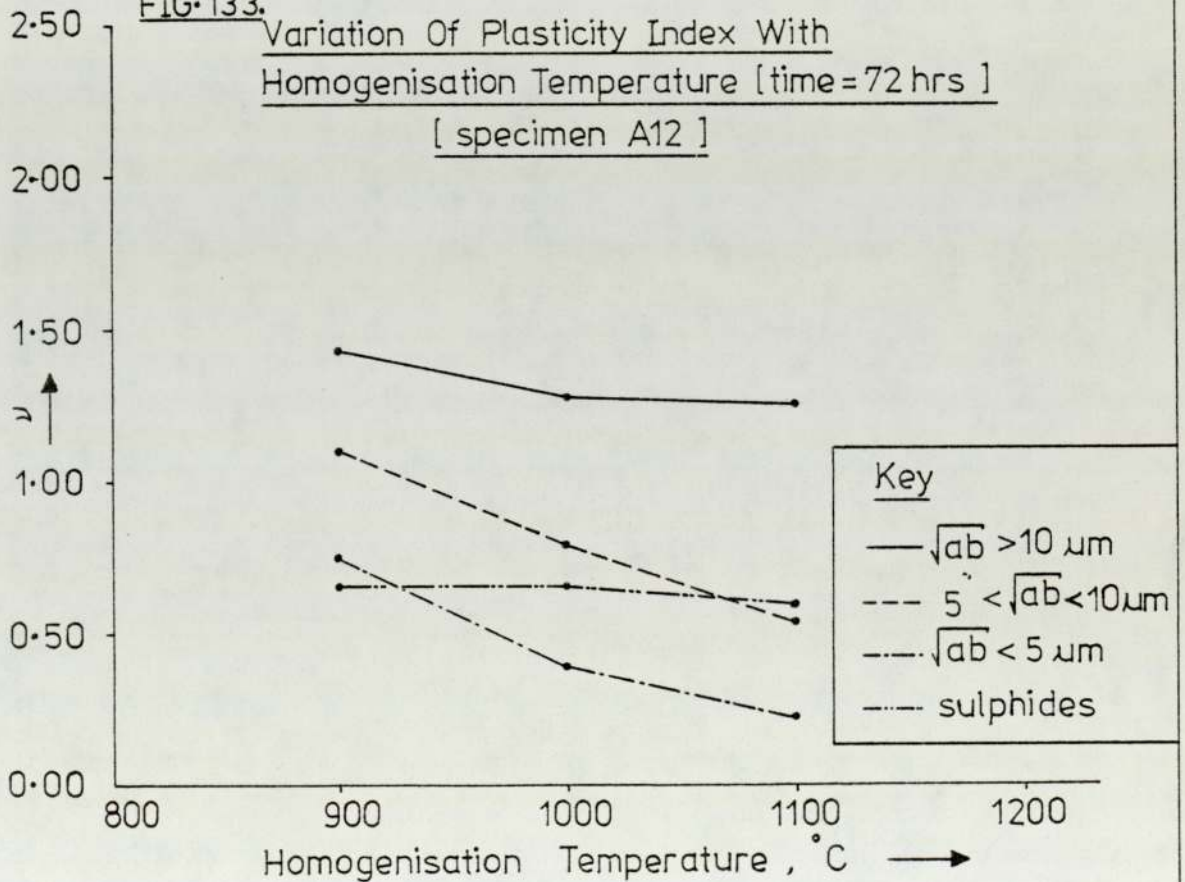
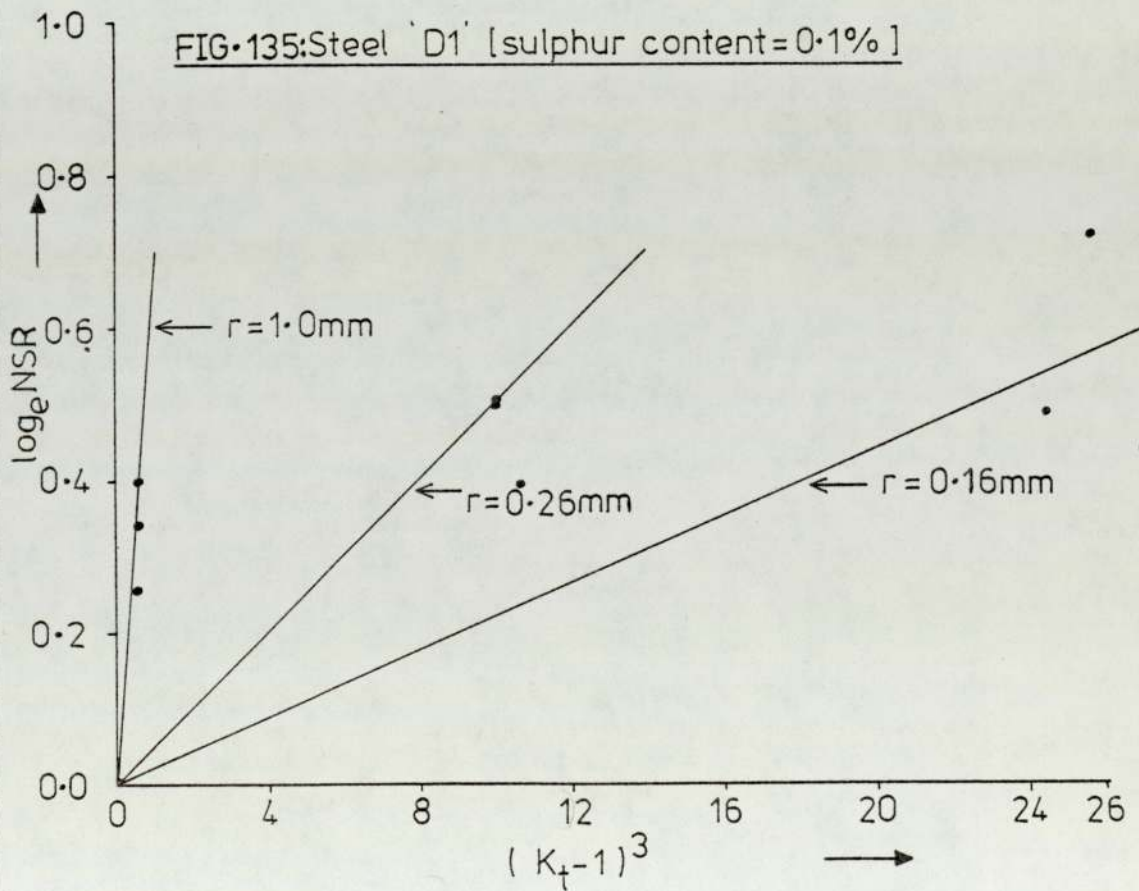
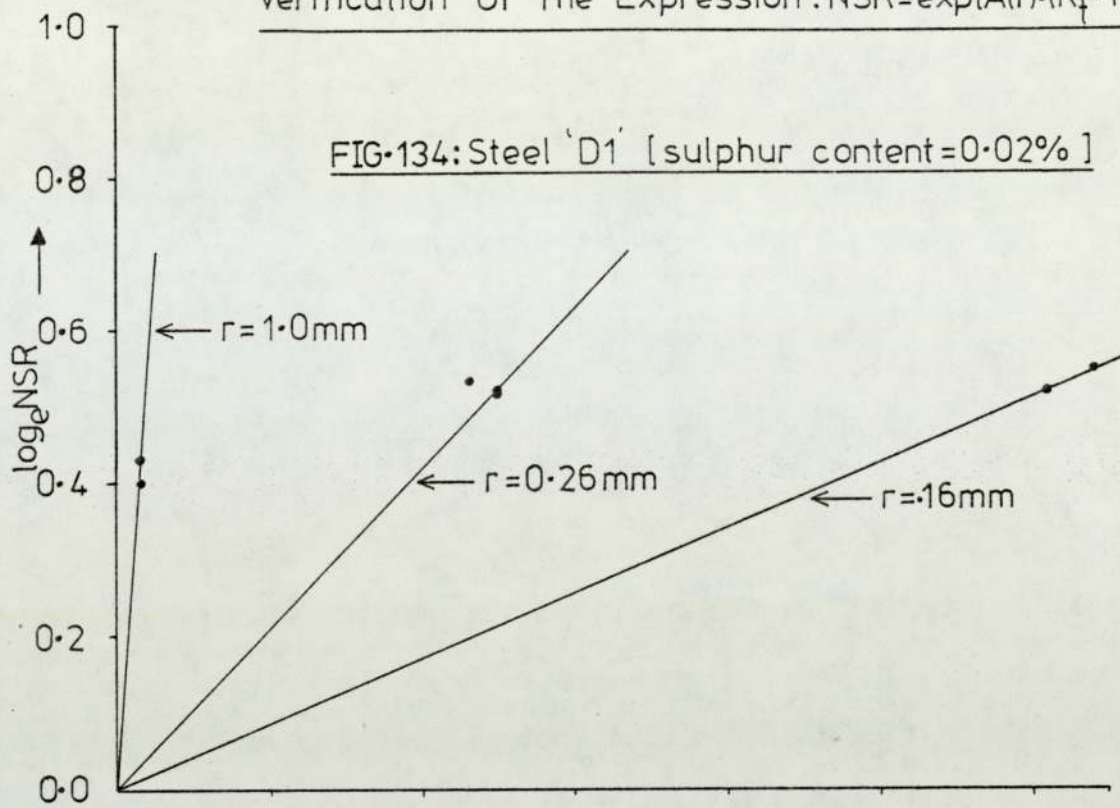


FIG.133:

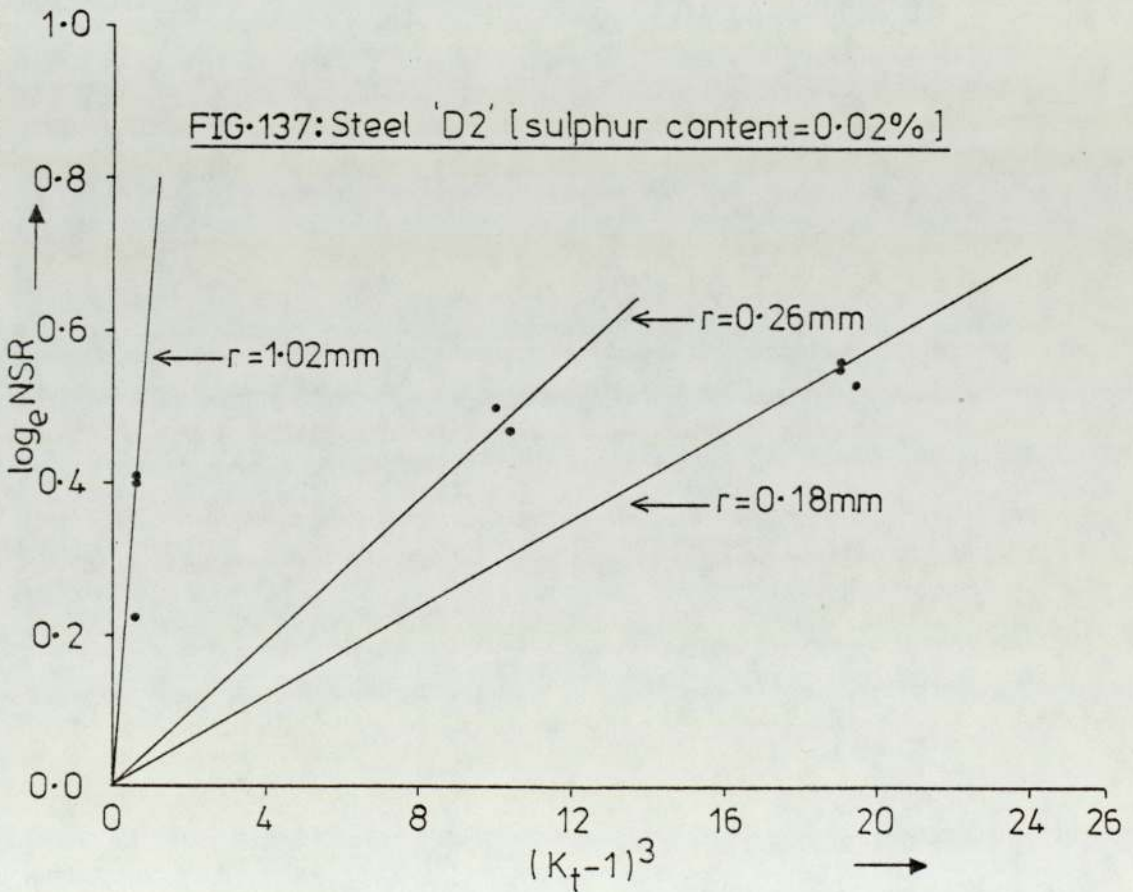
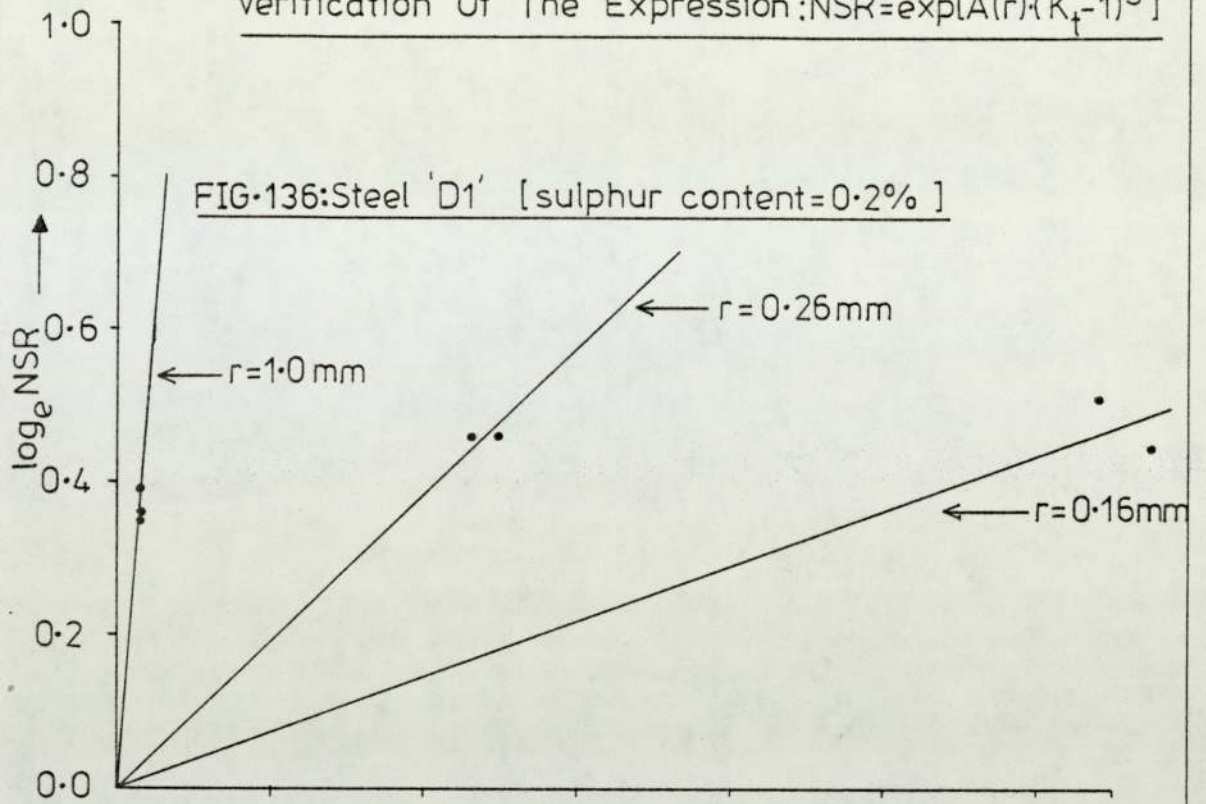
Variation Of Plasticity Index With
Homogenisation Temperature [time=72 hrs]
[specimen A12]



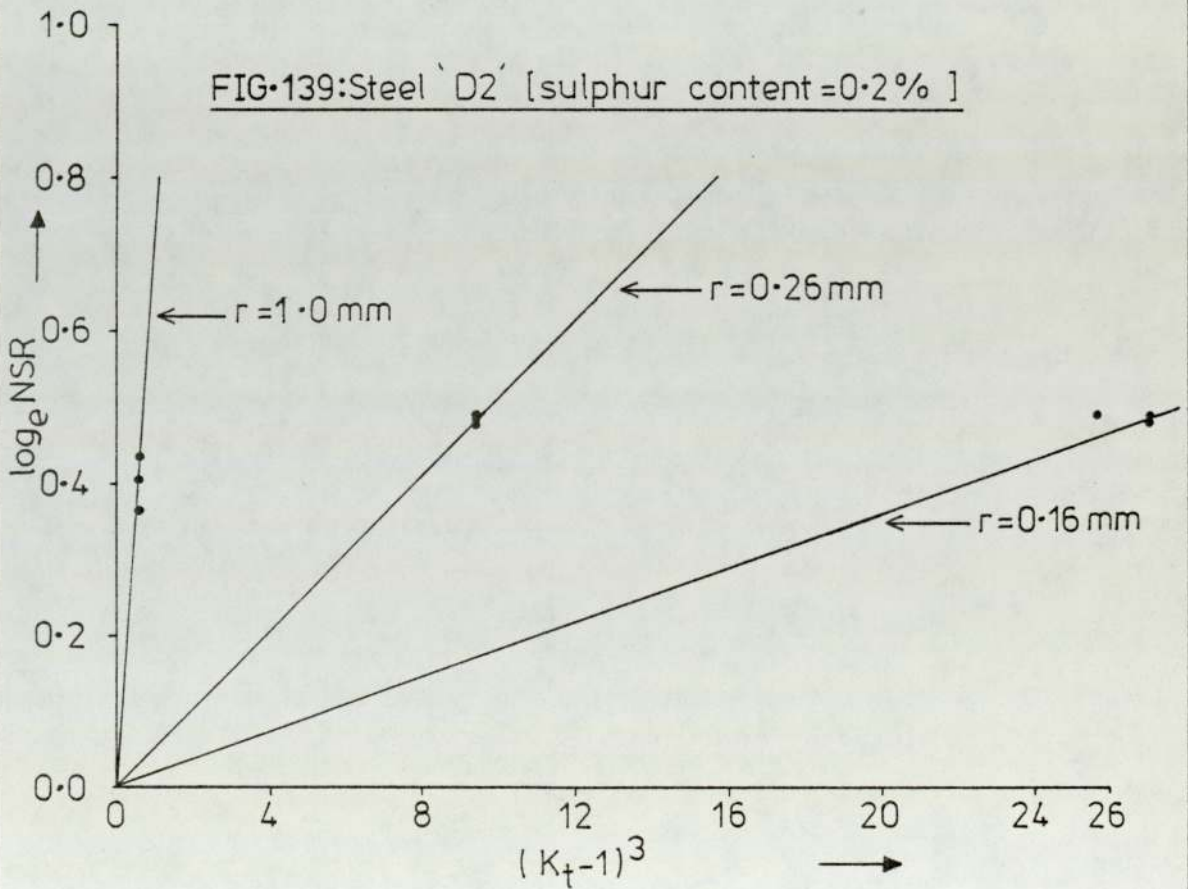
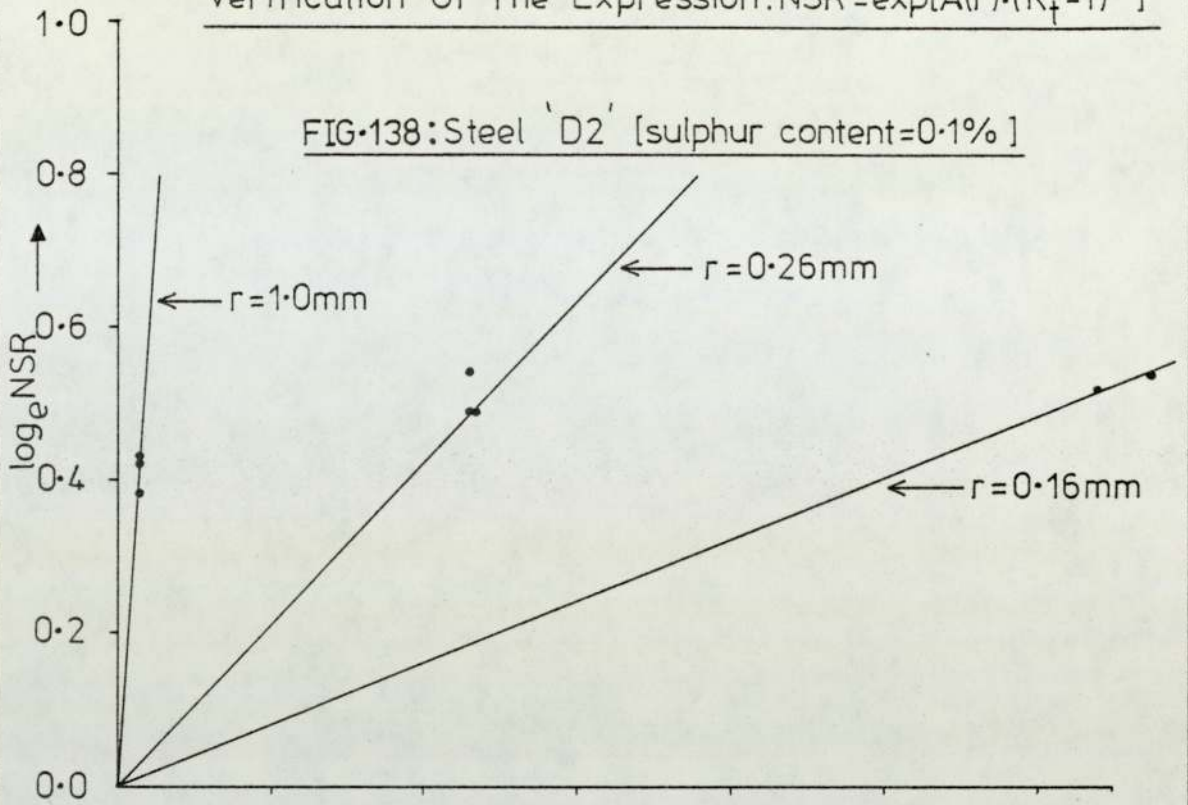
Verification Of The Expression : $NSR = \exp[A(r) \cdot (K_t - 1)^3]$



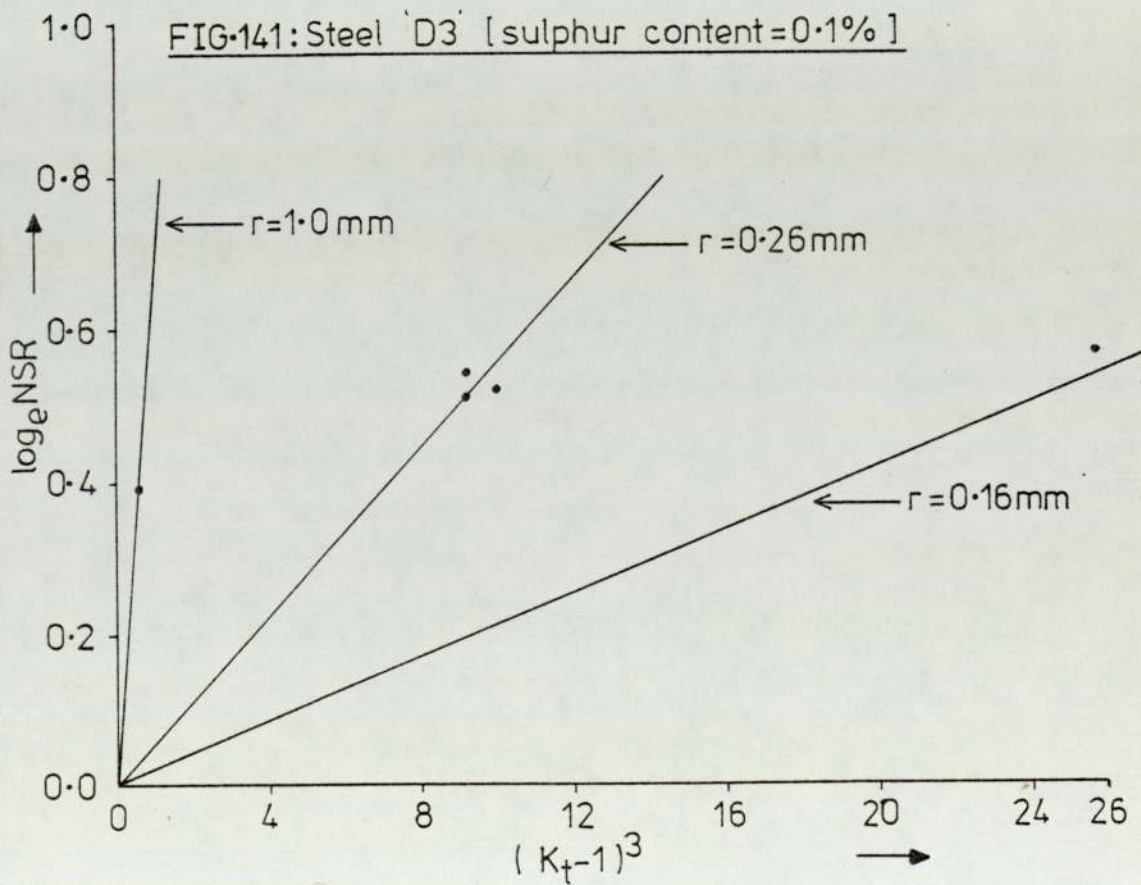
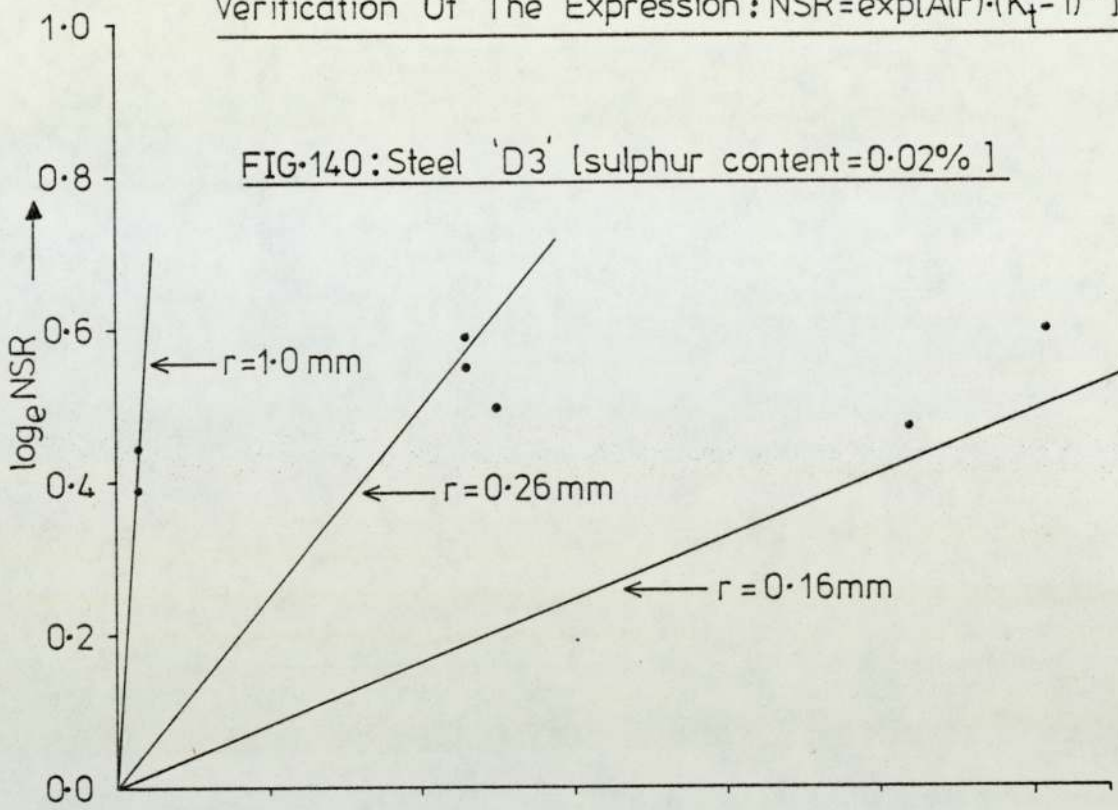
Verification Of The Expression : $NSR = \exp[A(r)(K_t - 1)^3]$

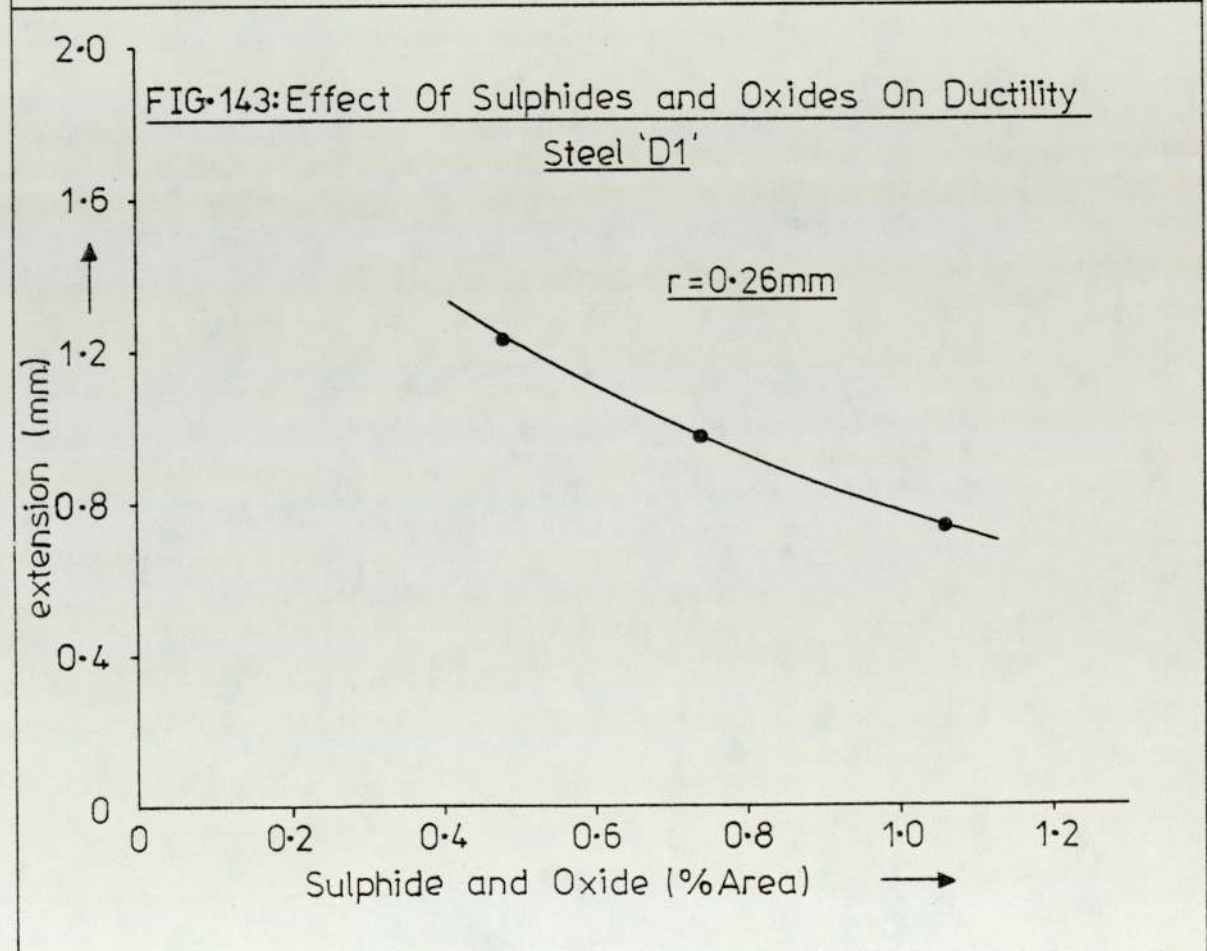
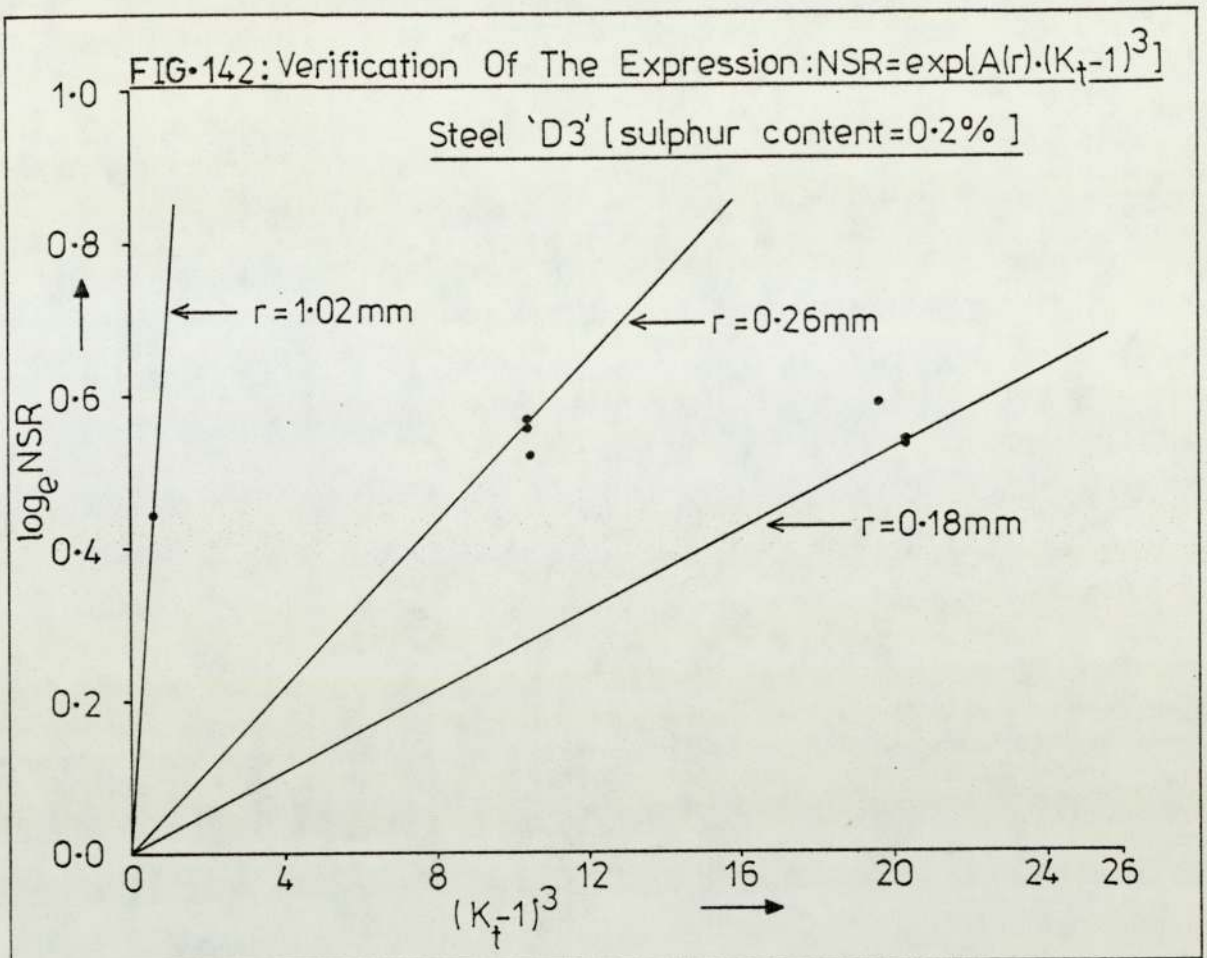


Verification Of The Expression: $NSR = \exp[A(r) \cdot (K_t - 1)^3]$



Verification Of The Expression : $NSR = \exp[A(r) \cdot (K_t - 1)^3]$





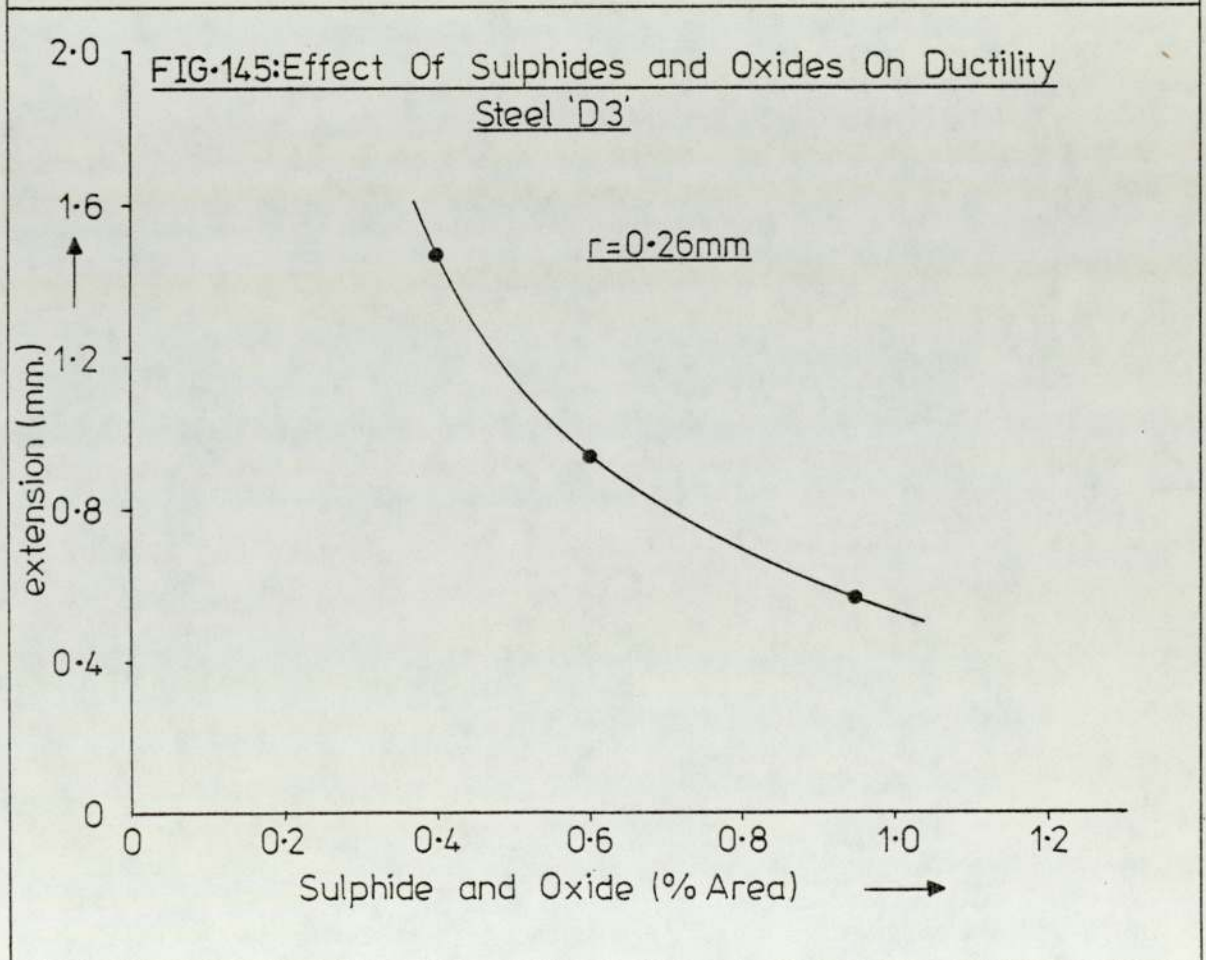
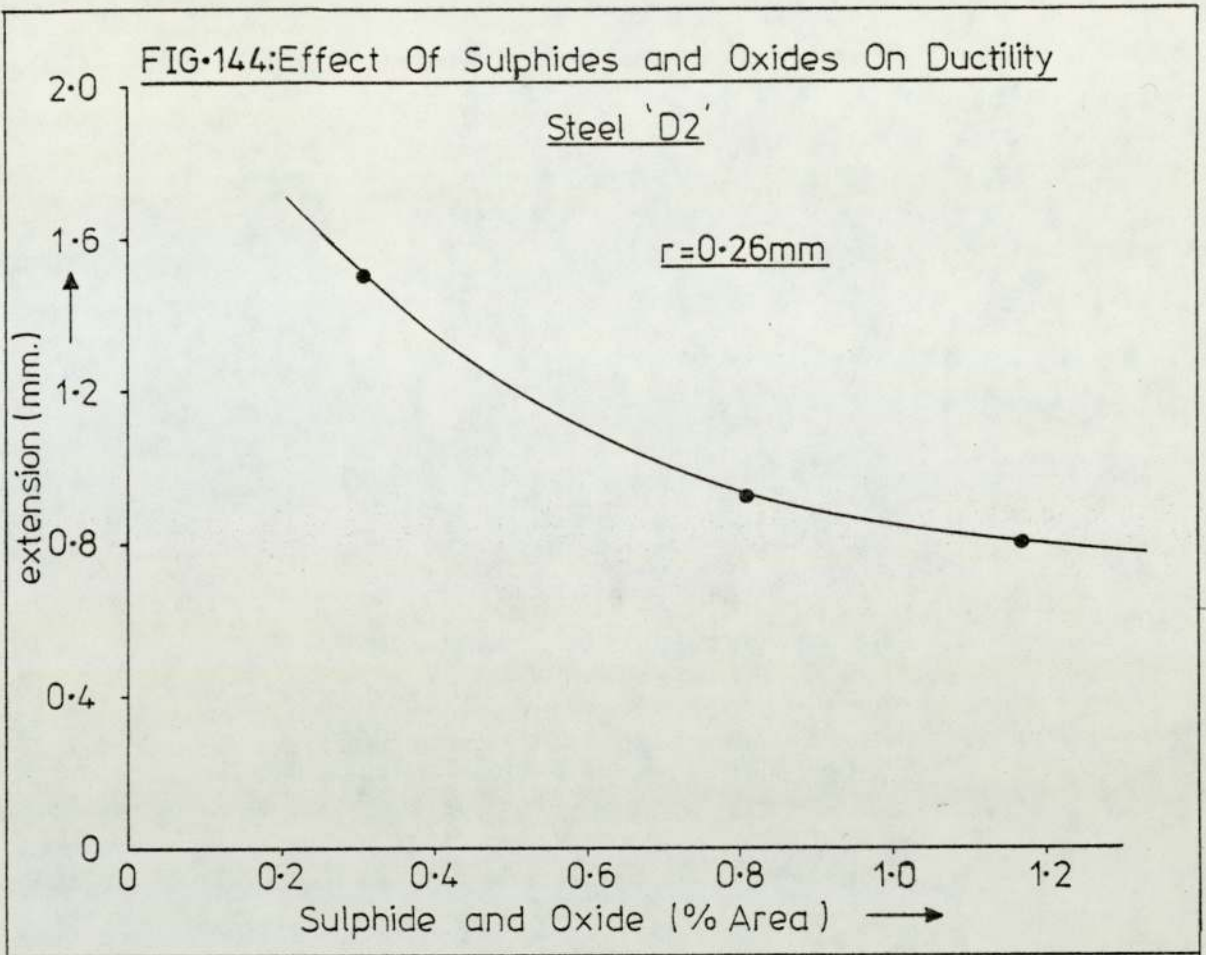
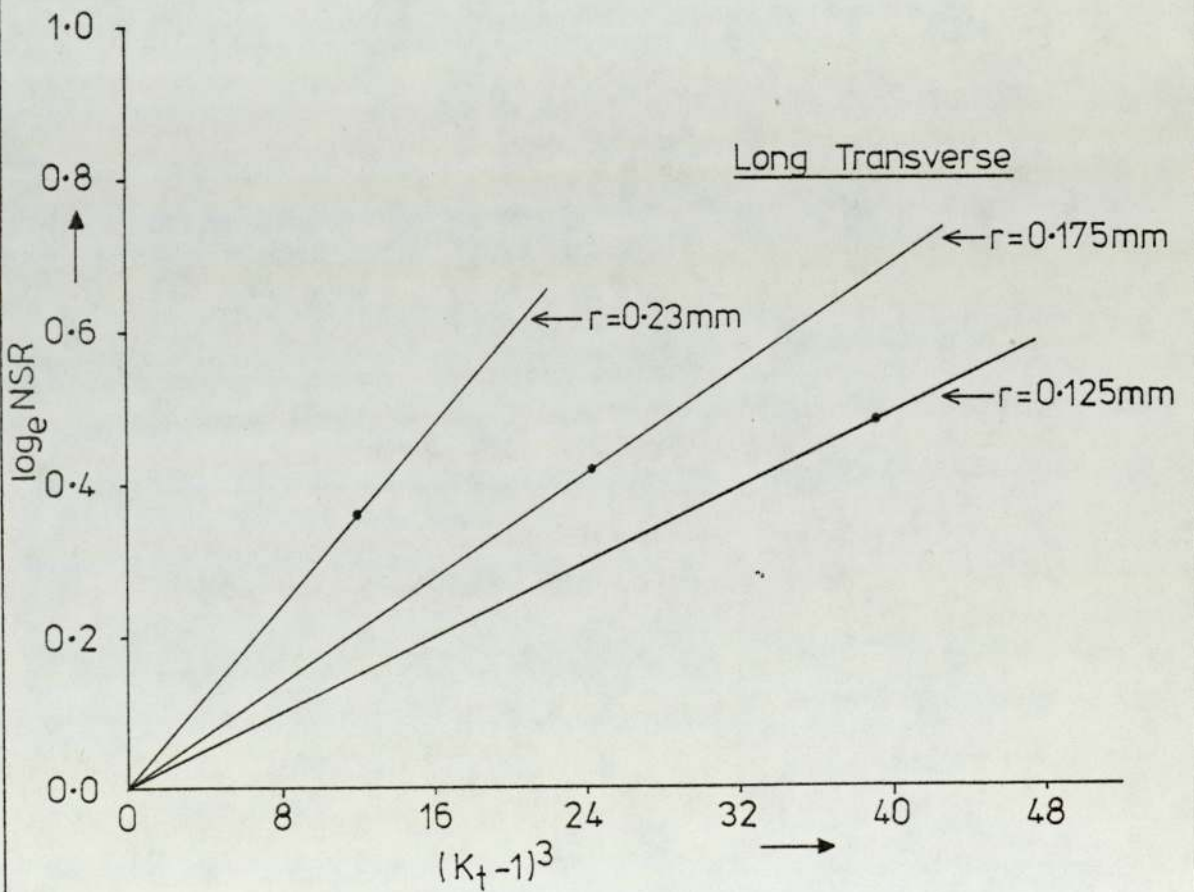
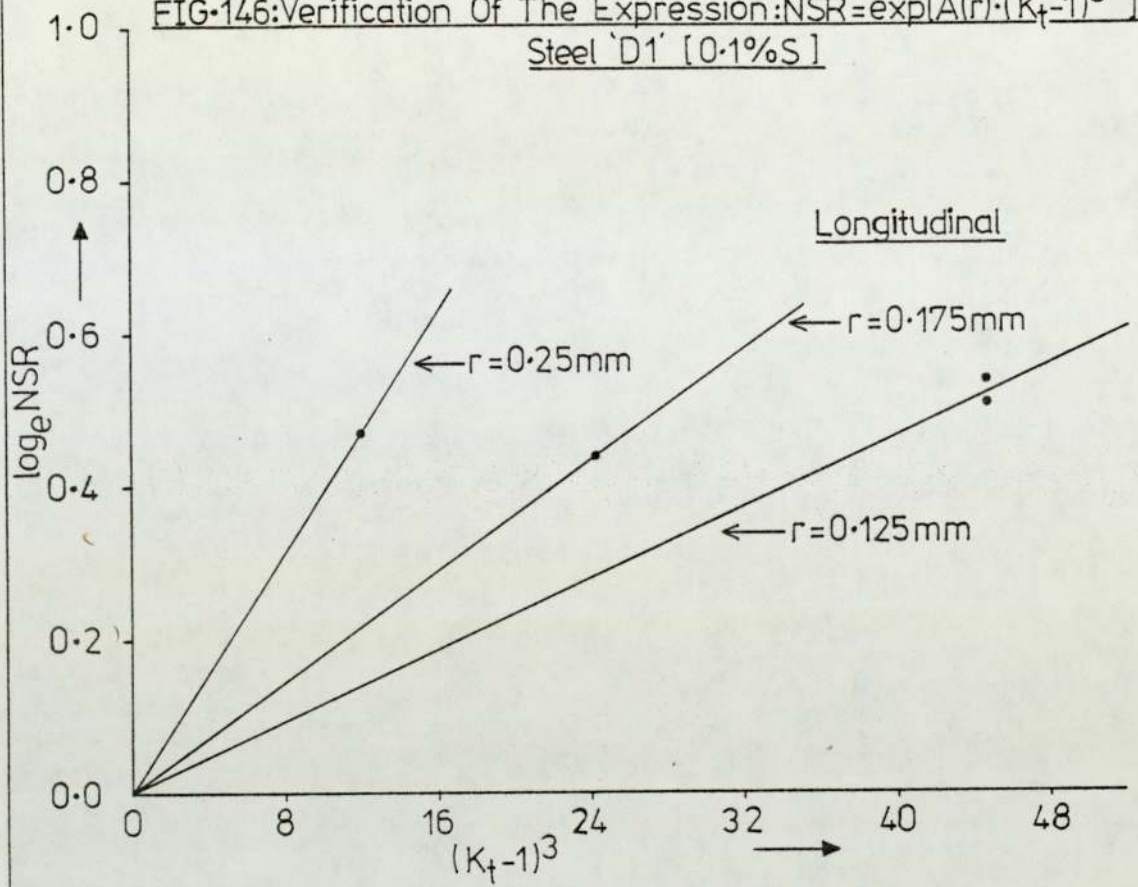
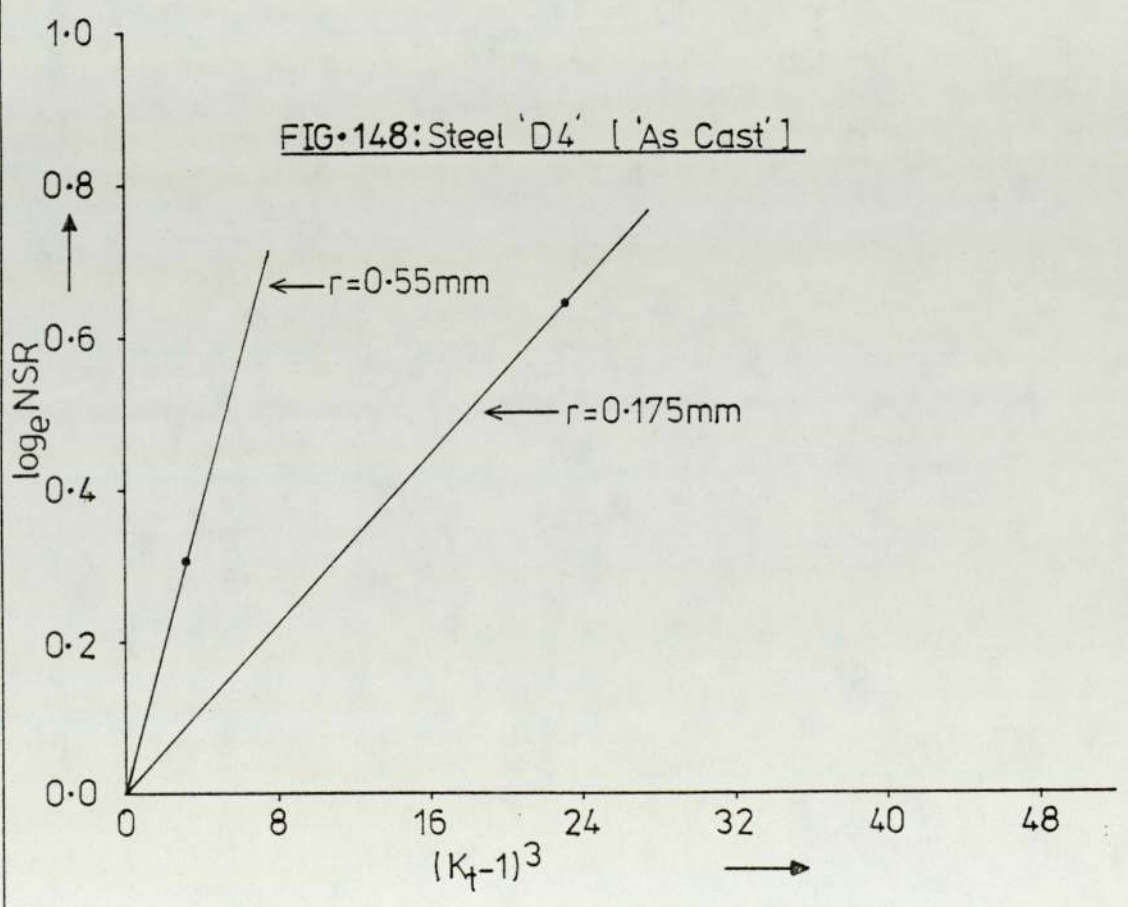
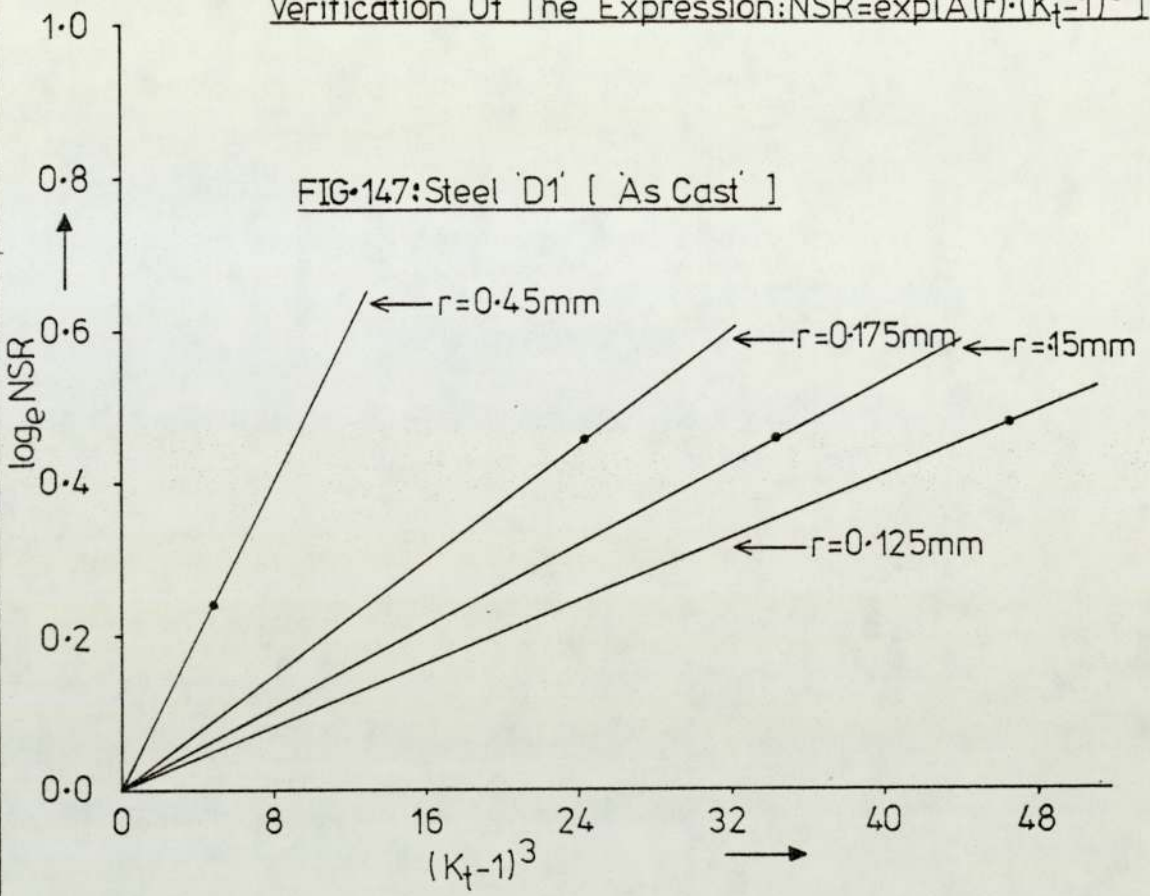
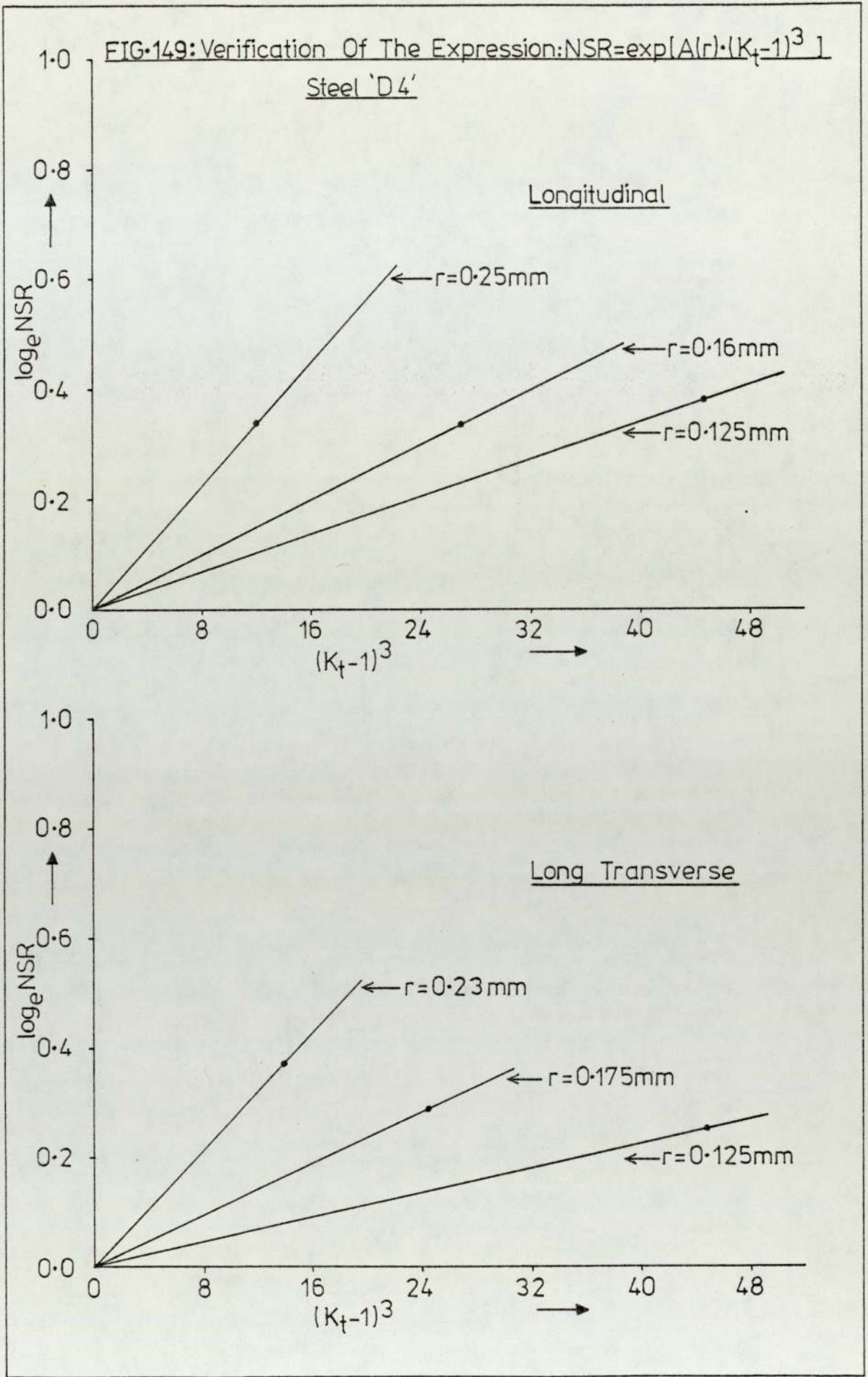


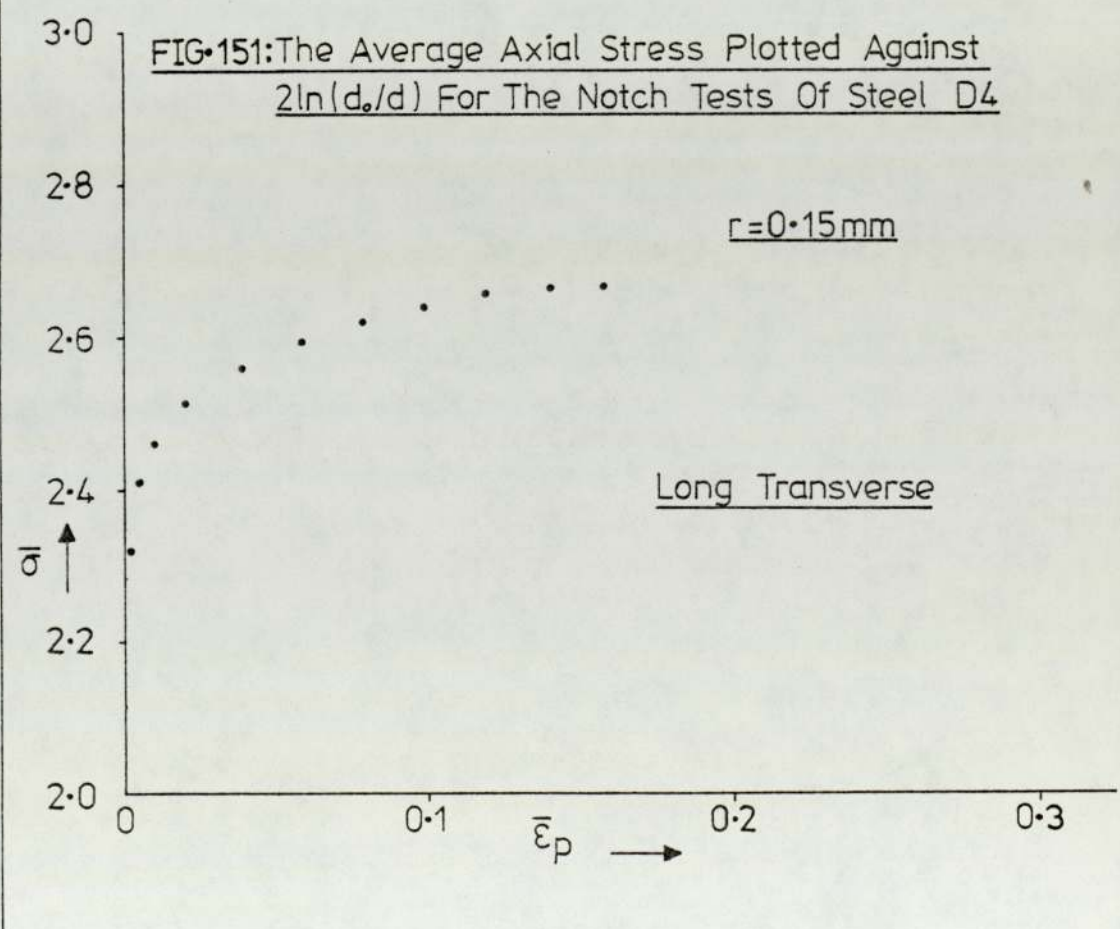
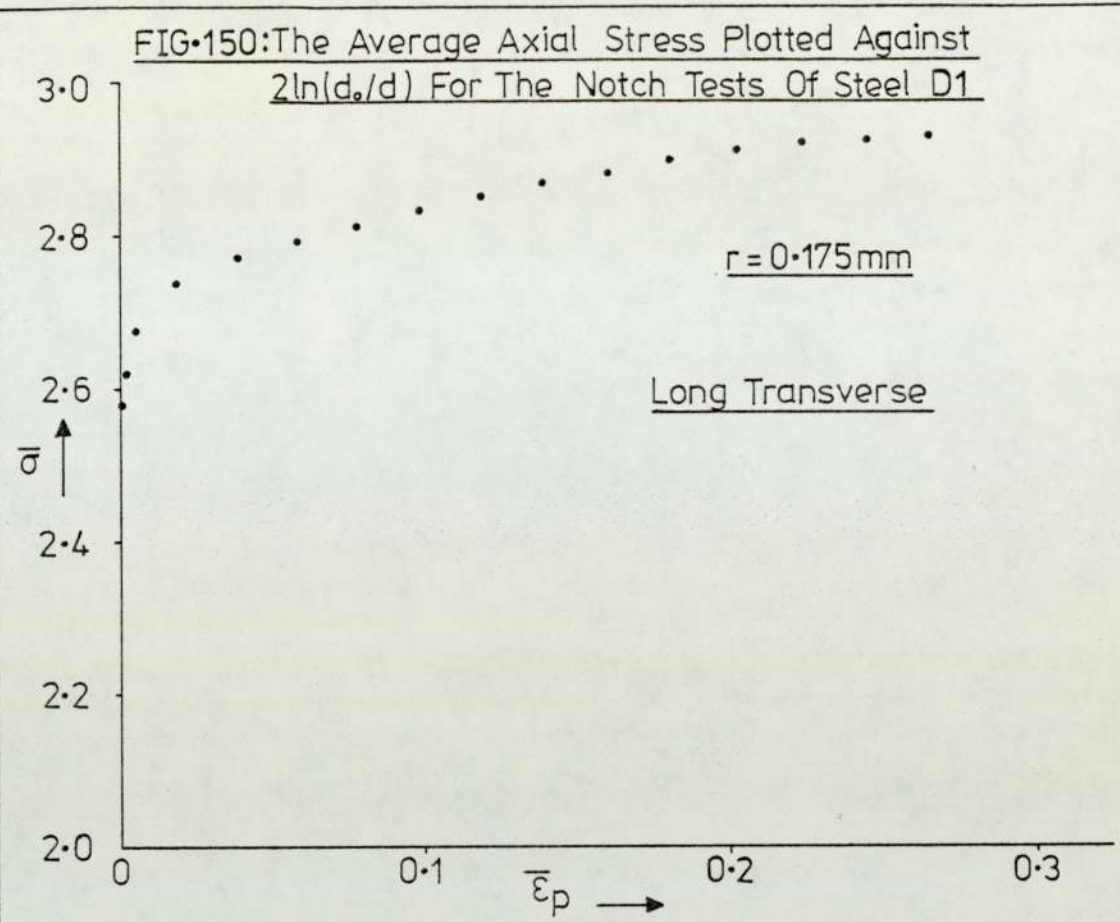
FIG-146: Verification Of The Expression: $NSR = \exp[A(r) \cdot (K_t - 1)^3]$
 Steel 'D1' [0.1% S]

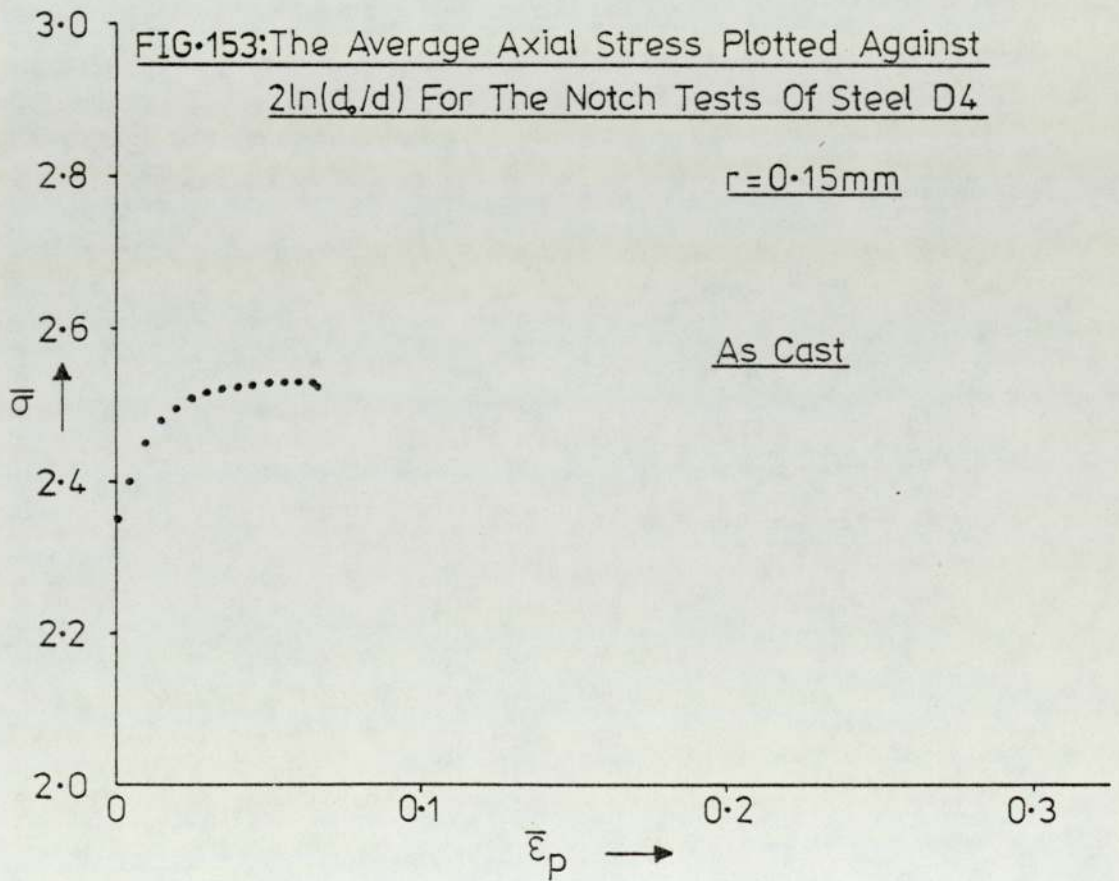
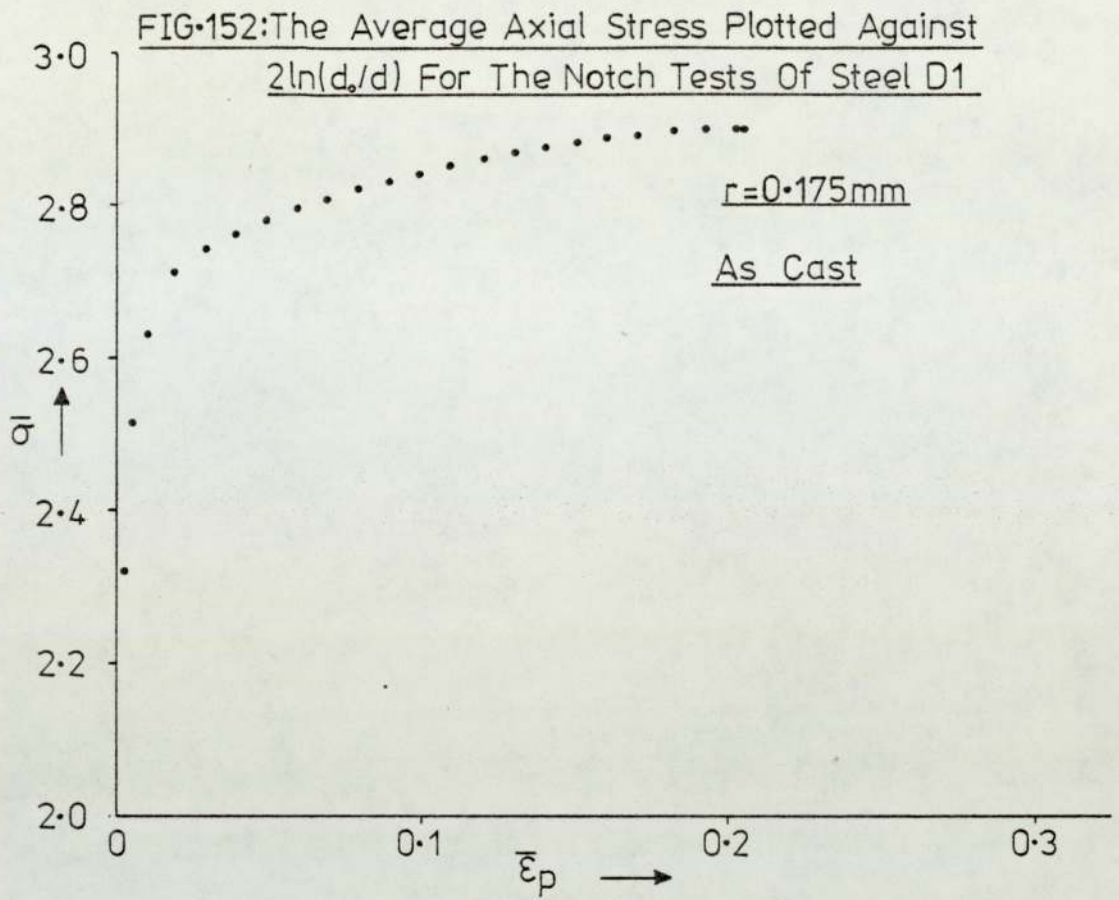


Verification Of The Expression: $NSR = \exp[A(r) \cdot (K_t - 1)^3]$









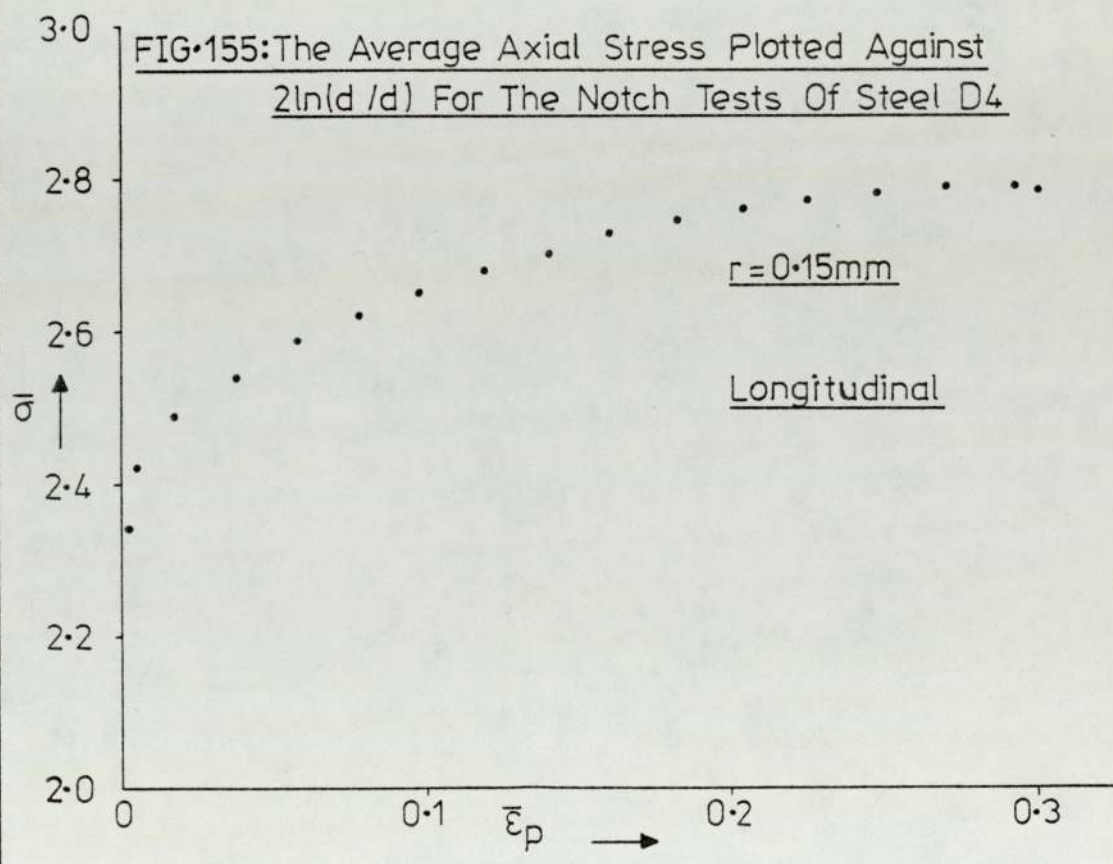
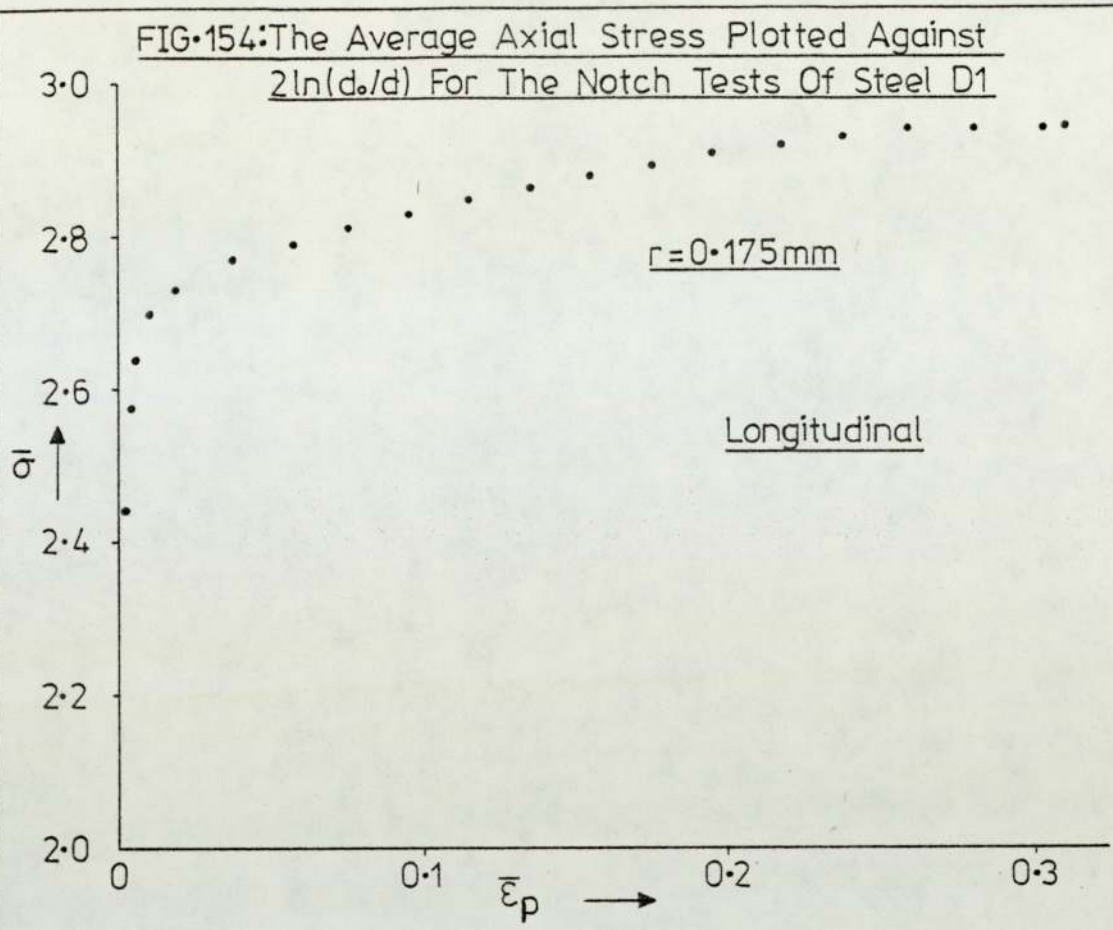


FIG-156:

Variation Of 'As Cast' Oxide Inclusion
Composition With Inclusion Size
Melt A7 (top), 0.1%S

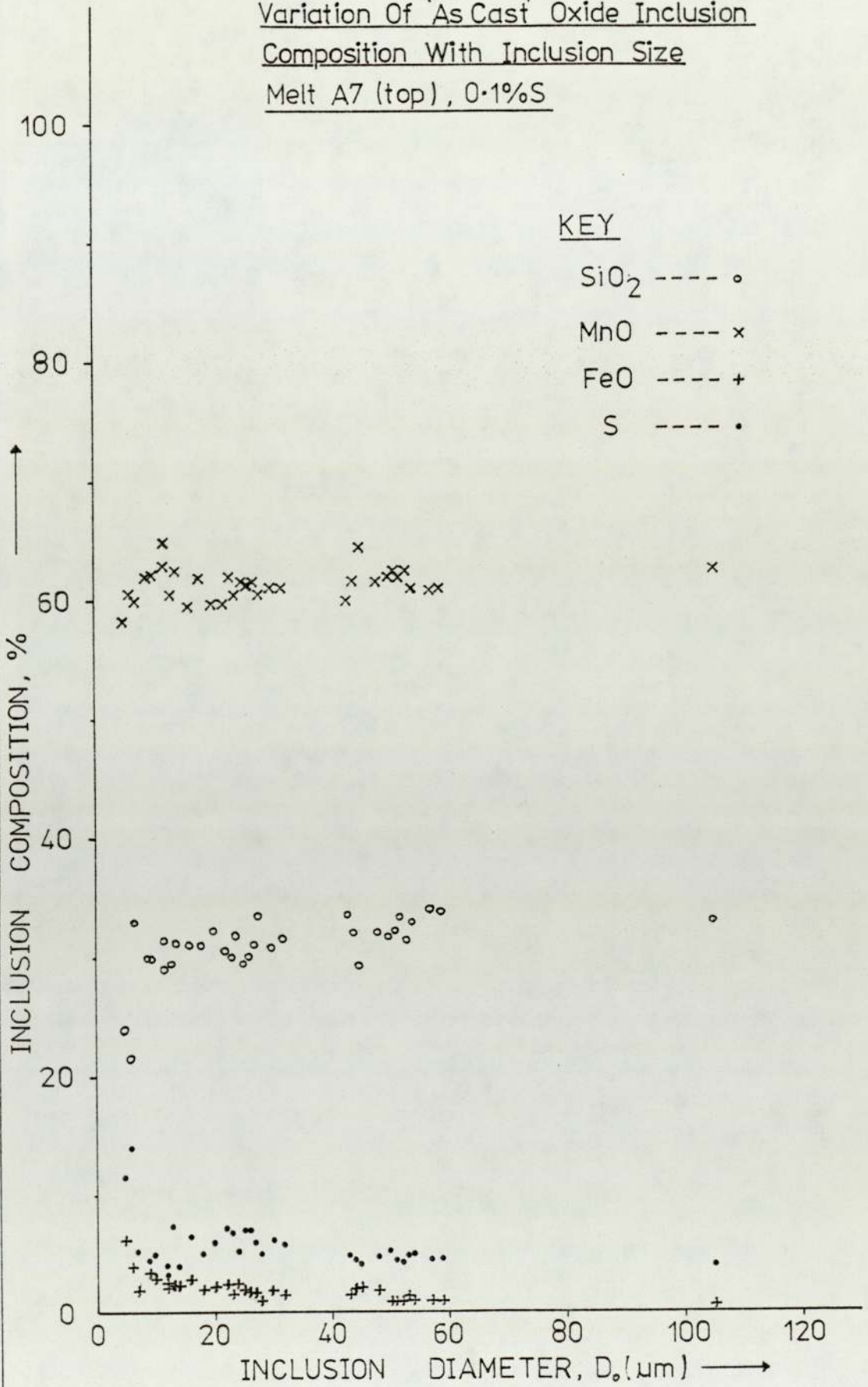


FIG-157:

Variation Of 'As Cast' Oxide Inclusion
Composition With Inclusion Size
Melt A7 (bottom), 0.1%S

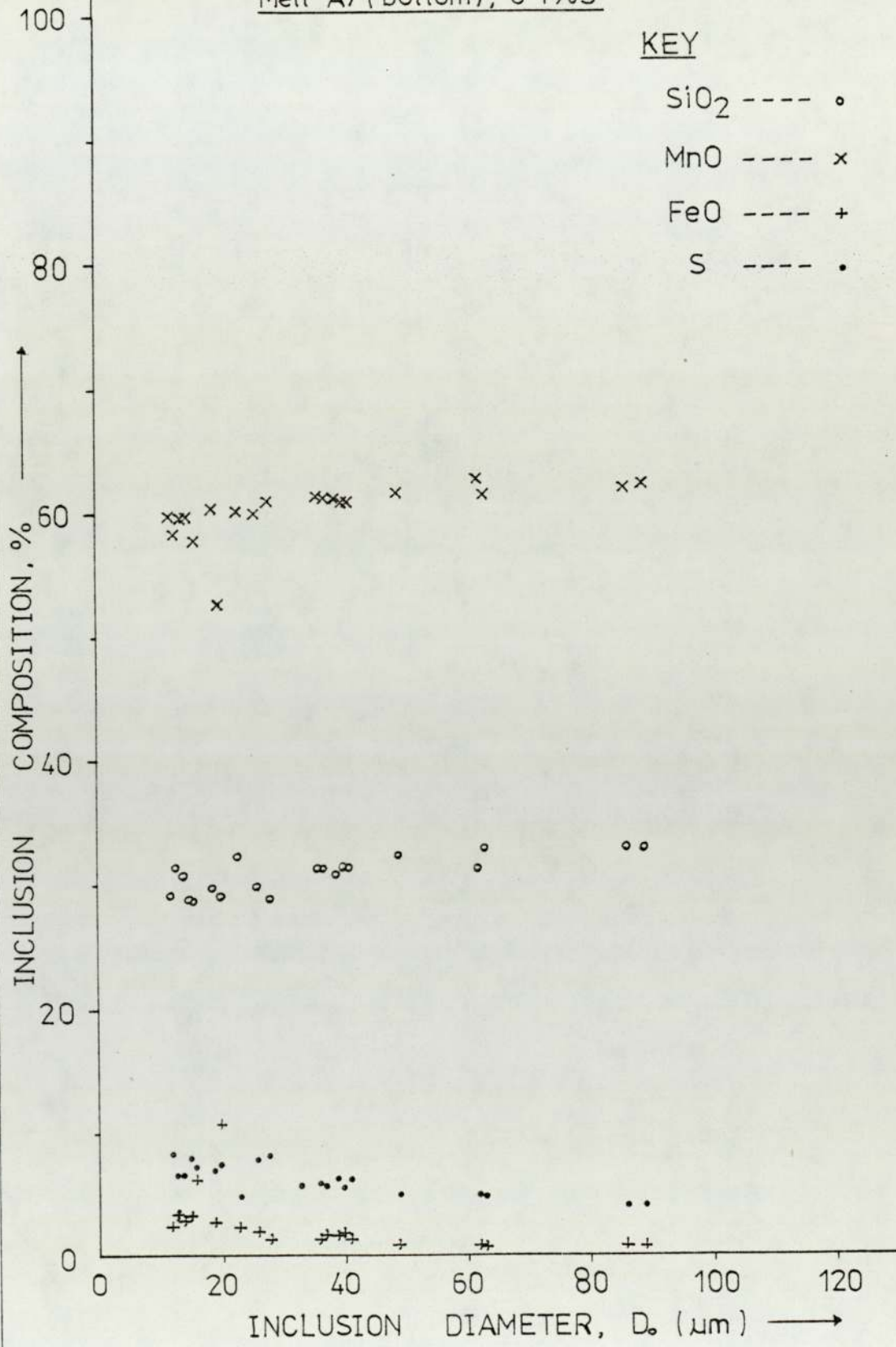


FIG-158:

Variation Of 'As Cast' Oxide Inclusion
Composition With Inclusion Size
Melt A6 (bottom) , 0.1%S

KEY

SiO₂ ---- o
MnO ---- x
FeO ---- +
S ---- •

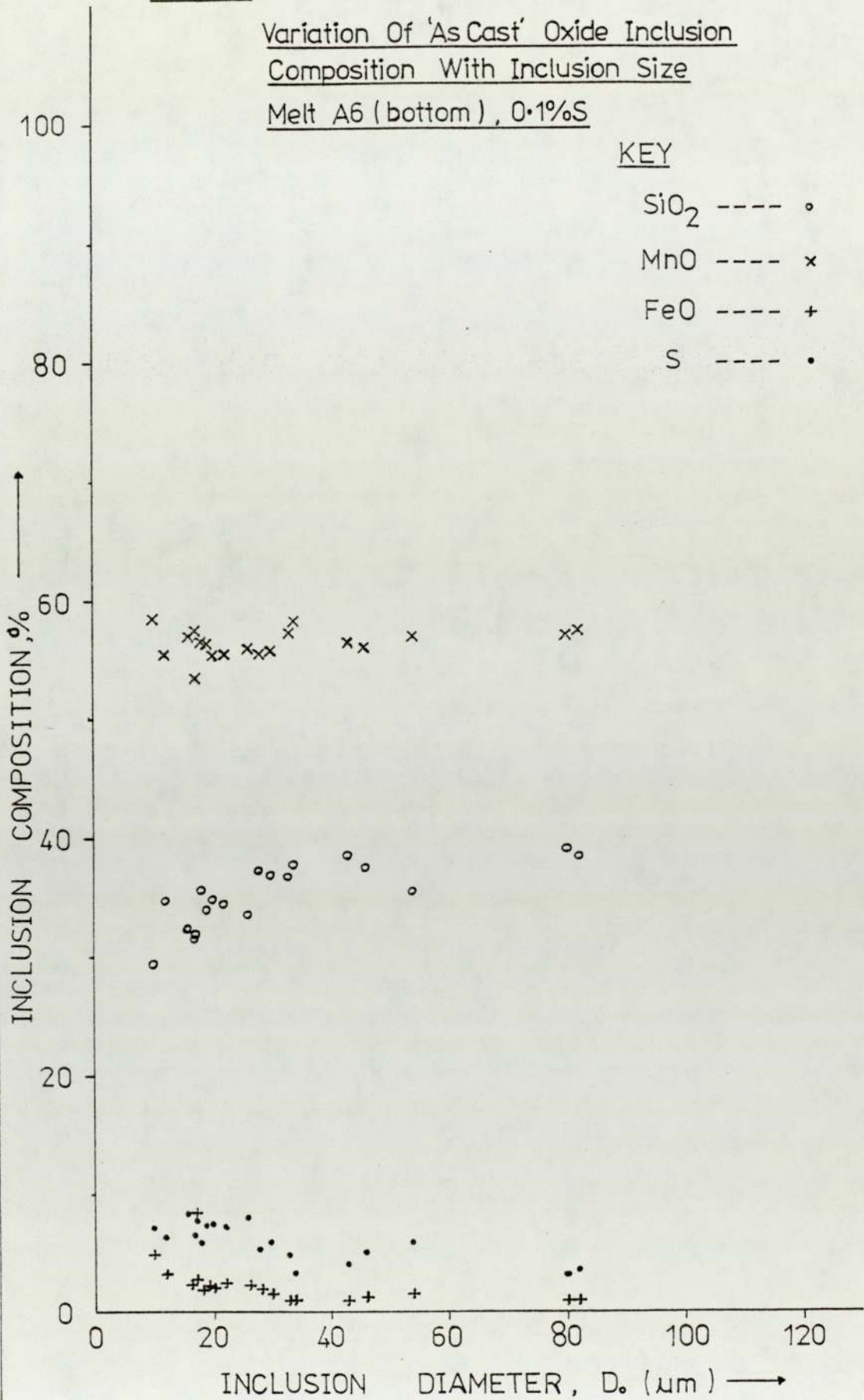


FIG-159:

Variation Of 'As Cast' Oxide Inclusion
Composition With Inclusion Size

Melt A15 (bottom), 0.1%S

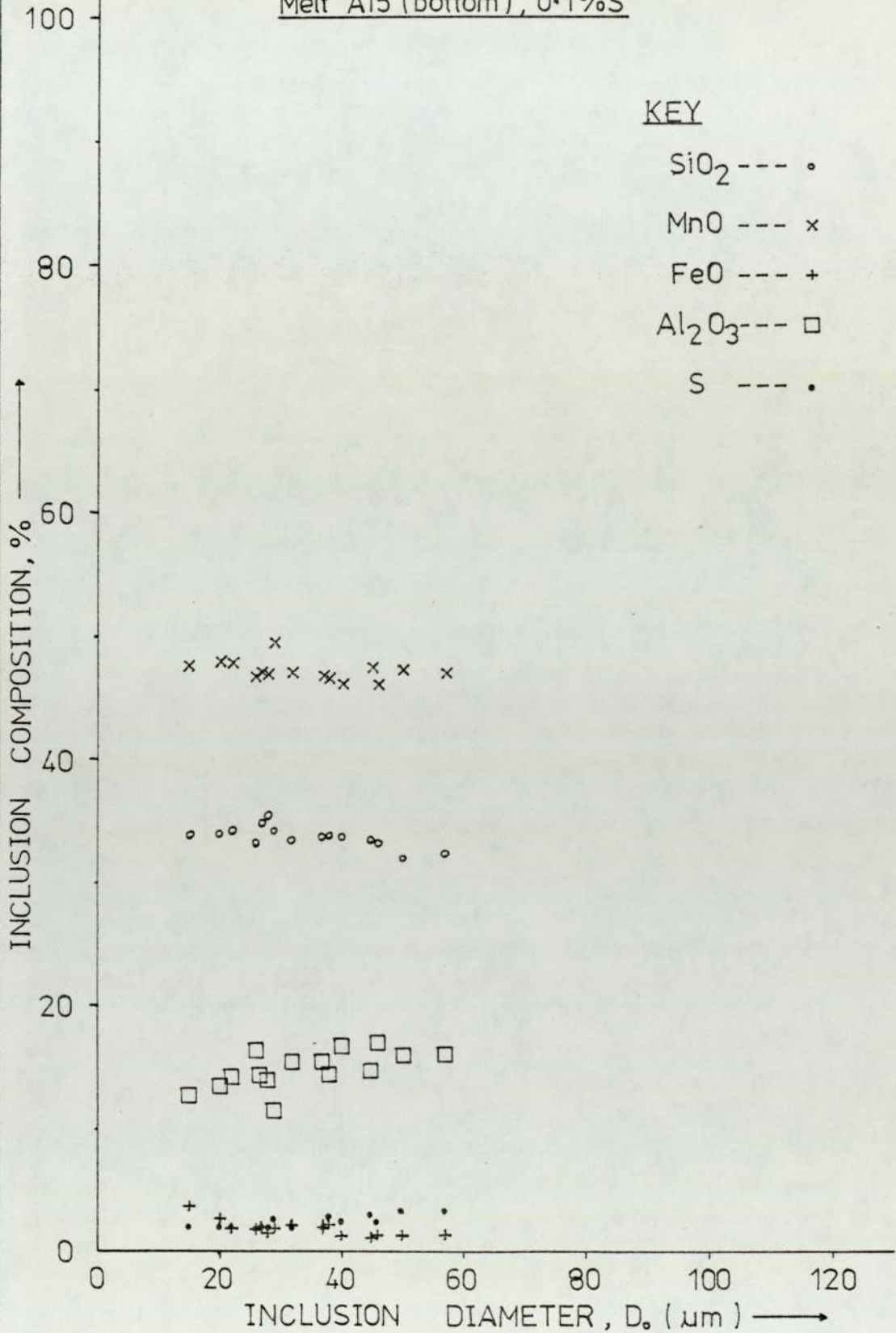


FIG. 160:

Variation Of 'As Cast' Oxide Inclusion
Composition With Inclusion Size

Melt A12 (bottom), 0.1%S

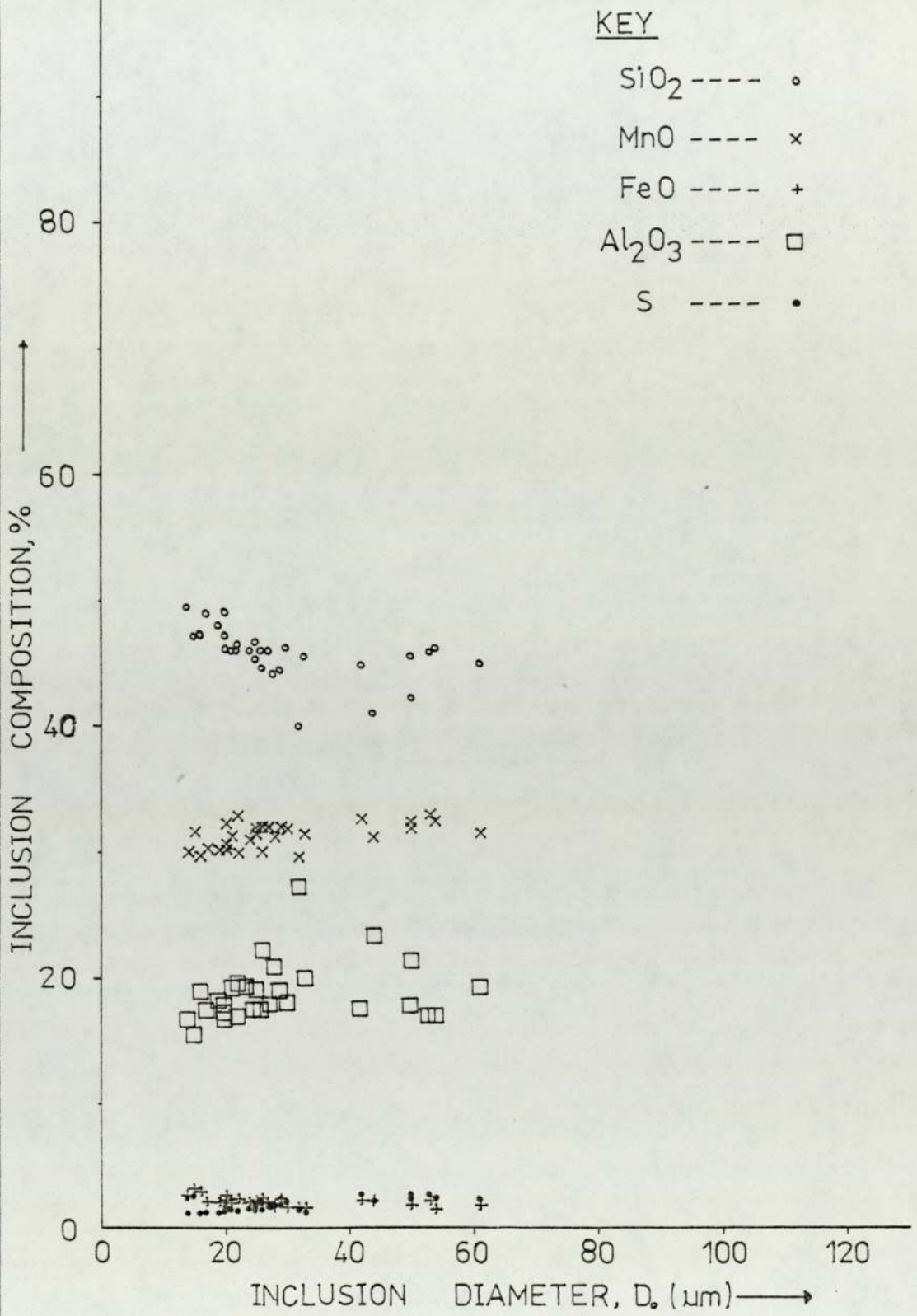


FIG-161: Distribution Of The Radii Appearing In
Planes Cutting Spherical Grain Of
Radius R_0 (ref. 199)

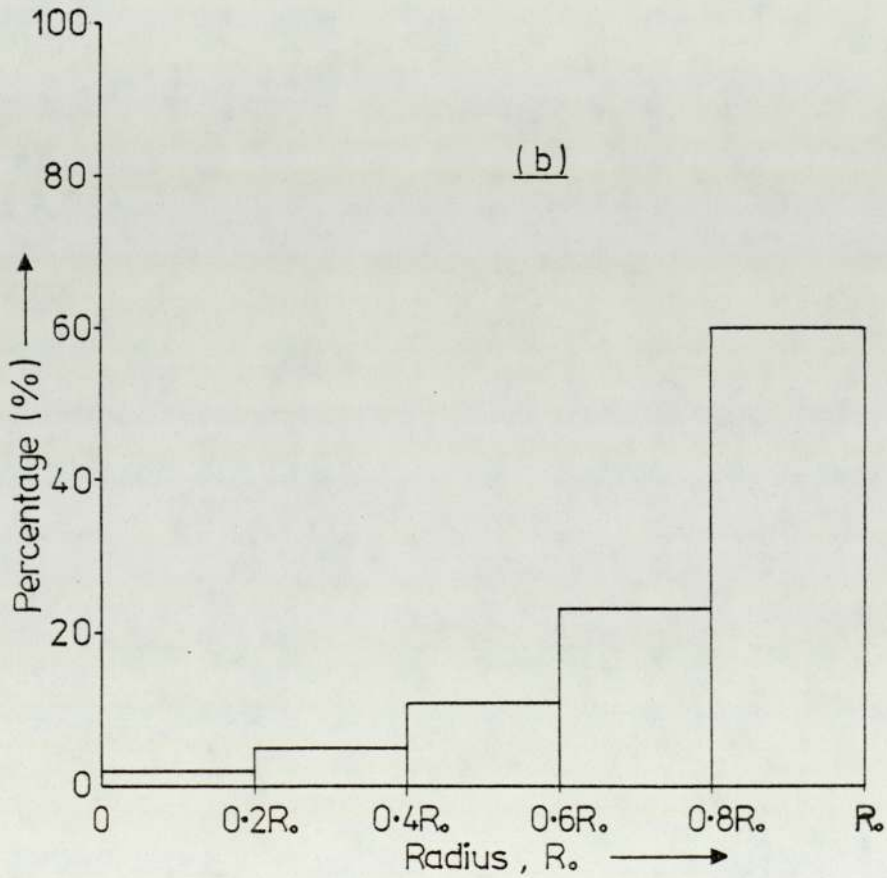
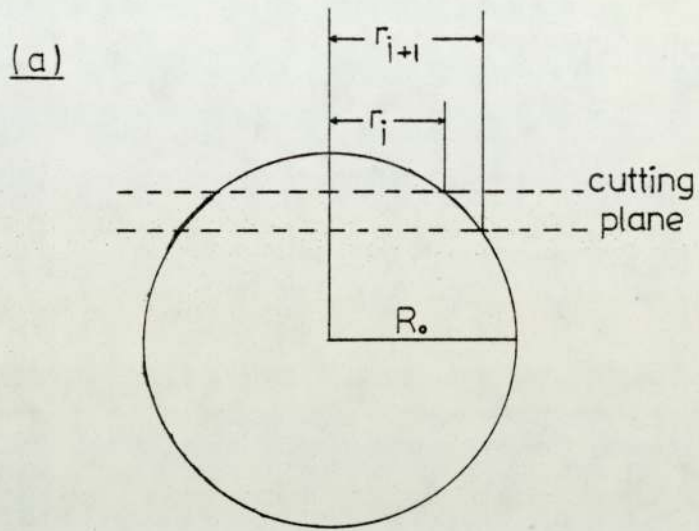


FIG.162 : Plasticity Index (or Factor) Versus Matrix Height Strain. (ref.100)

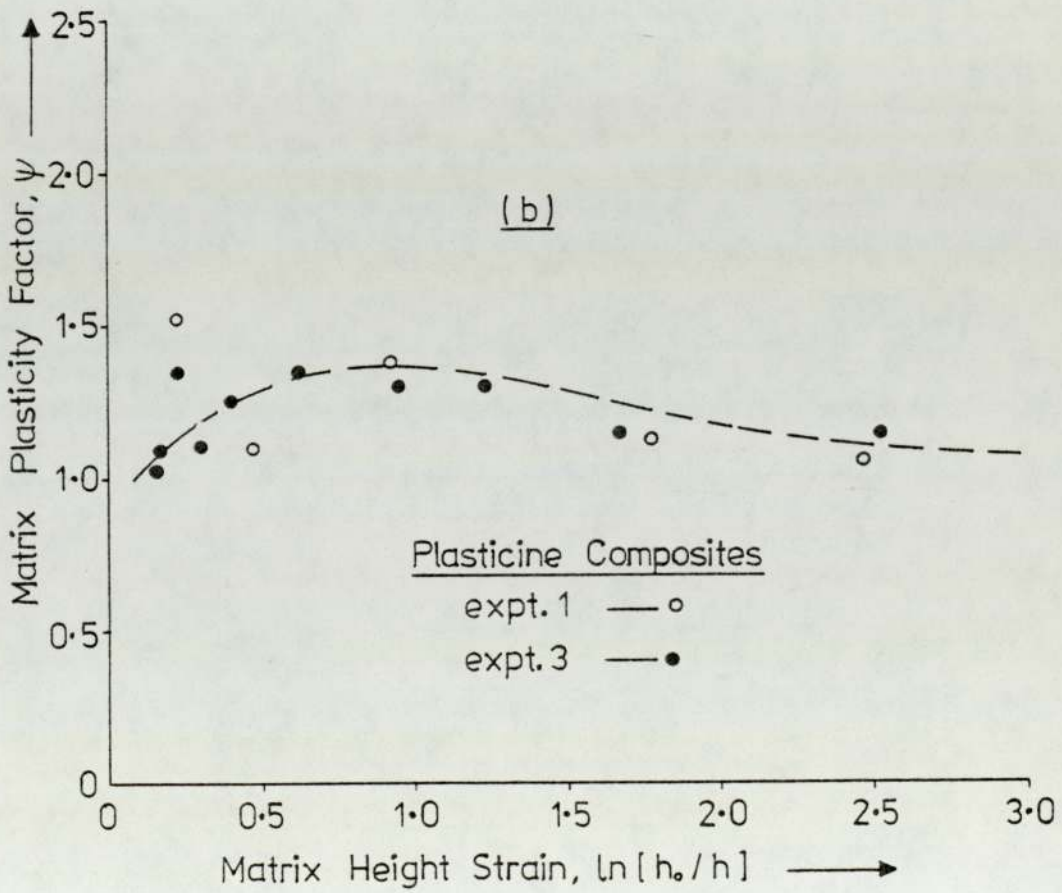
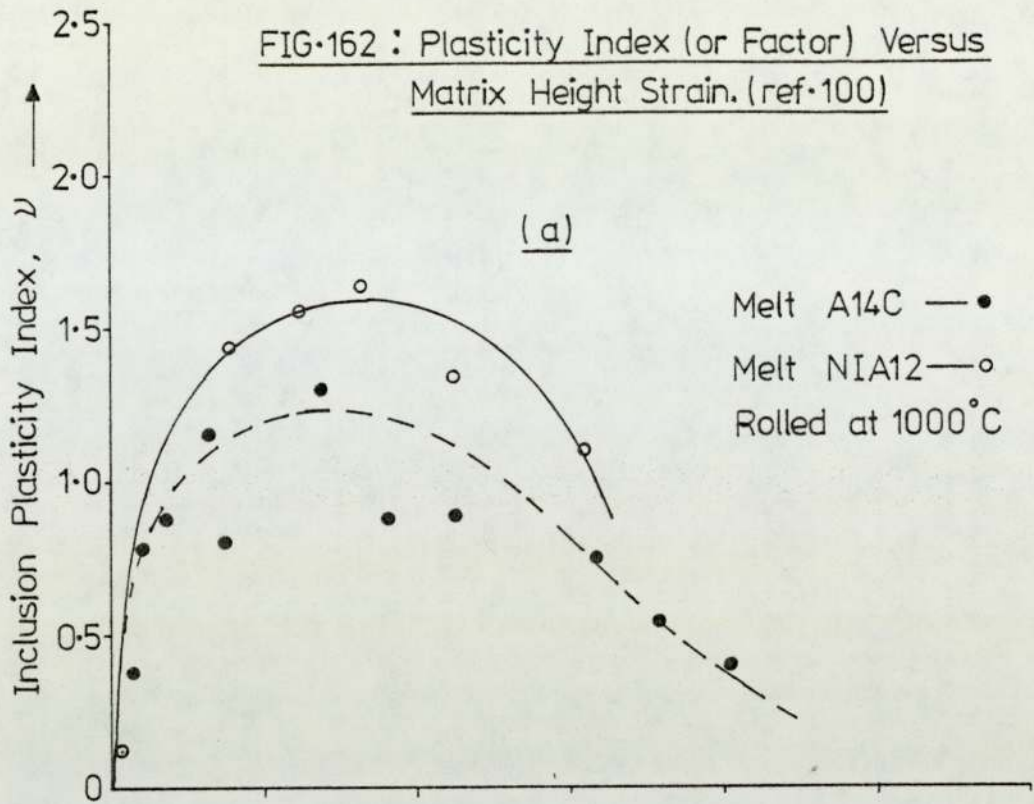


FIG.163 : Influence Of Ingoing Thickness On
Mean Rate Of Deformation (sticking friction)
Roll Speed - 430 mm/sec.

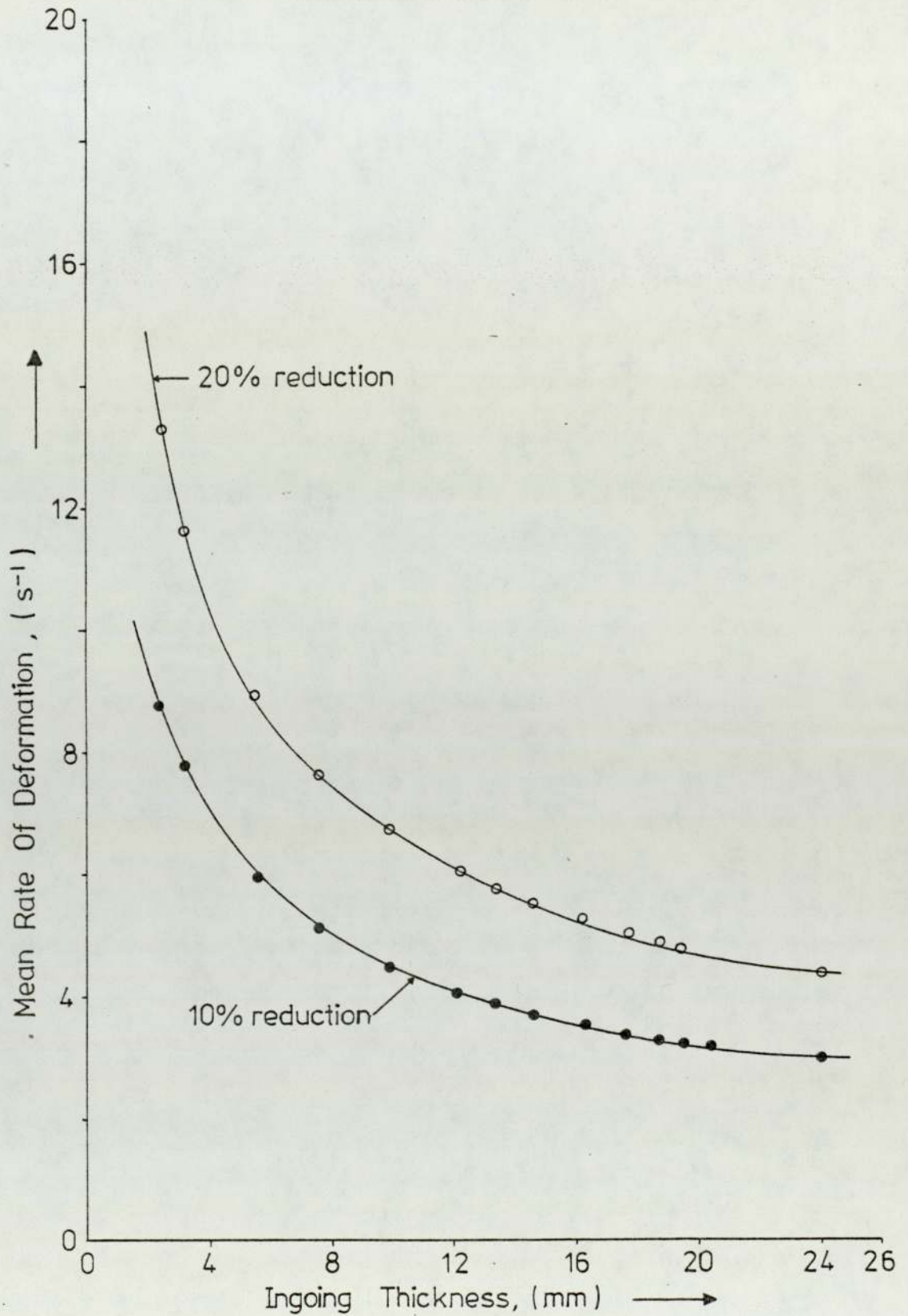


FIG-164: Mechanism Of The Ductile Fracture When
Elongated Inclusions Are Involved (Schematic)

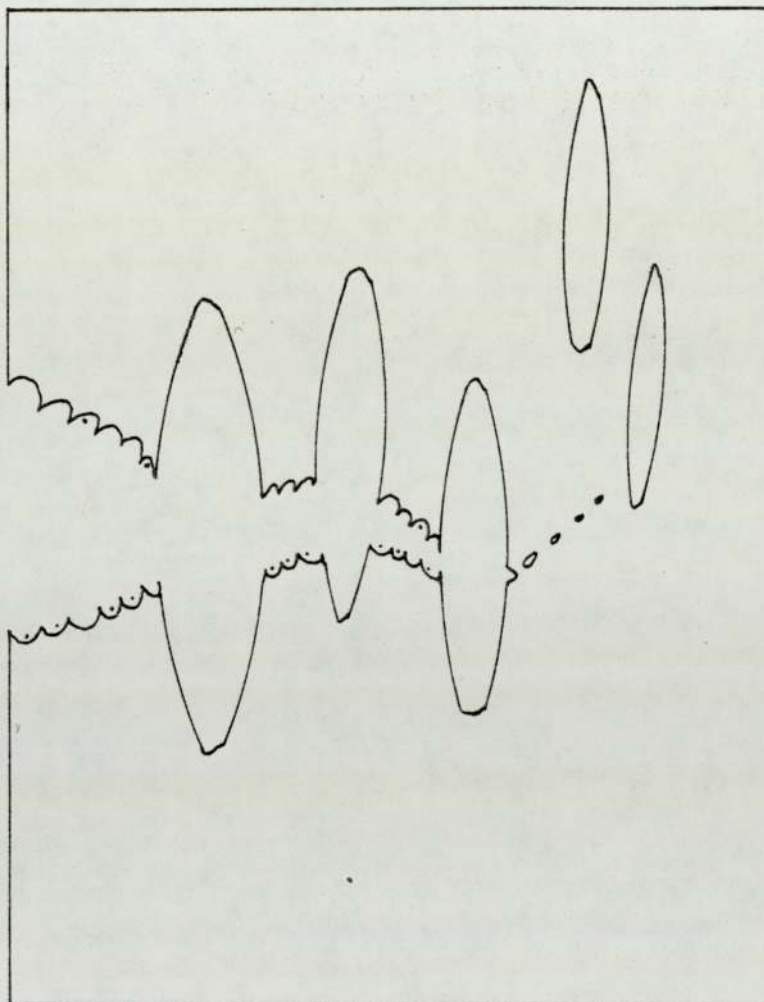




PLATE 1 : OPAQUE INCLUSION
FROM MELT A6
(0.07% S) x550

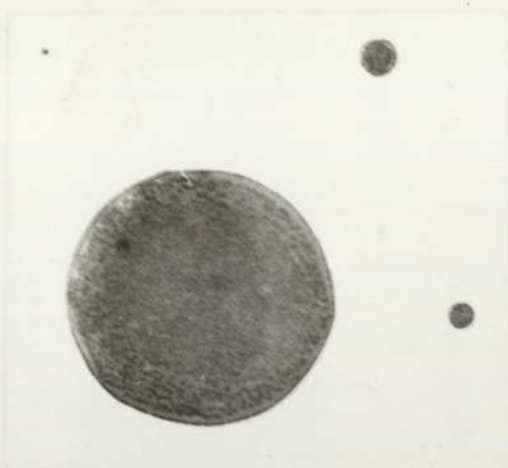


PLATE 2 : OPAQUE INCLUSIONS FROM
MELT A12 (0.07% S) WHICH
APPEARS TO CONTAIN VERY
FINE PRECIPITATES. x550

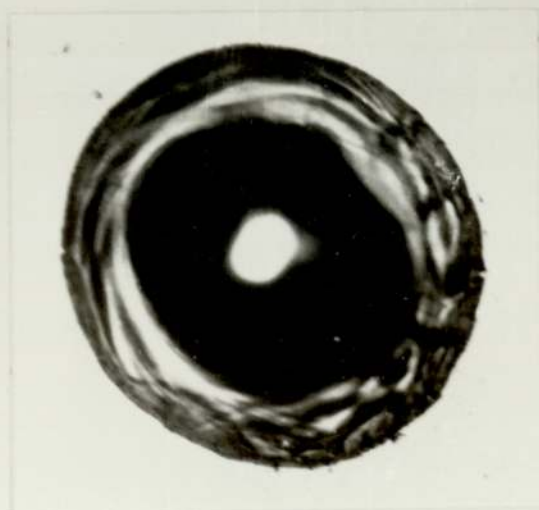


PLATE 3 : GLASSY INCLUSION FROM
MELT A12 (0.07% S). x400



PLATE 4 : OPAQUE INCLUSION
FROM MELT A15
(0.07% S) SHOWING
CRACKS IN THE AS
CAST INCLUSION.
x550

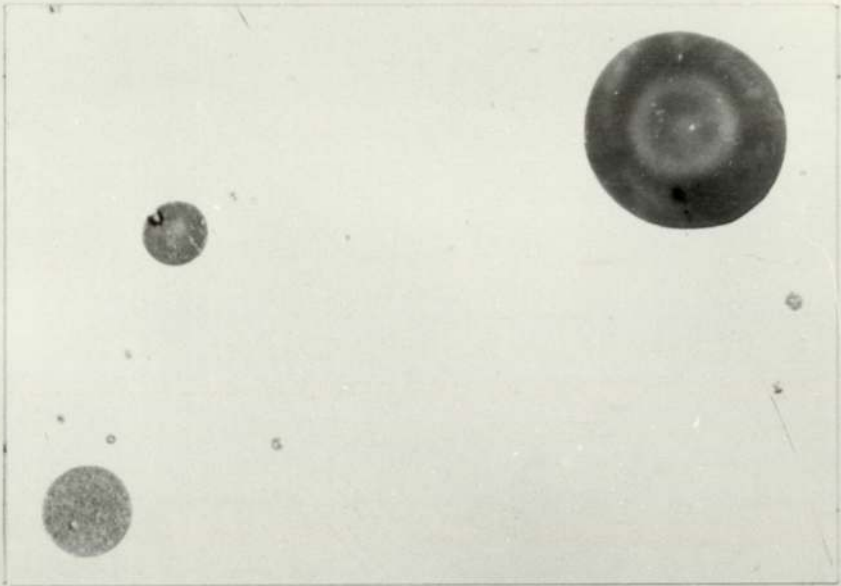


PLATE 5 : OPAQUE INCLUSIONS FROM MELT A15 (0.07% S).
THERE APPEARS TO BE FINE PRECIPITATION
WITH ONE OF THE INCLUSIONS. x550



PLATE 6 : OPAQUE INCLUSION FROM
MELT D3 (0.2% S). x720



PLATE 7 : GLASSY INCLUSION FROM
MELT D2 (0.02% S). x720

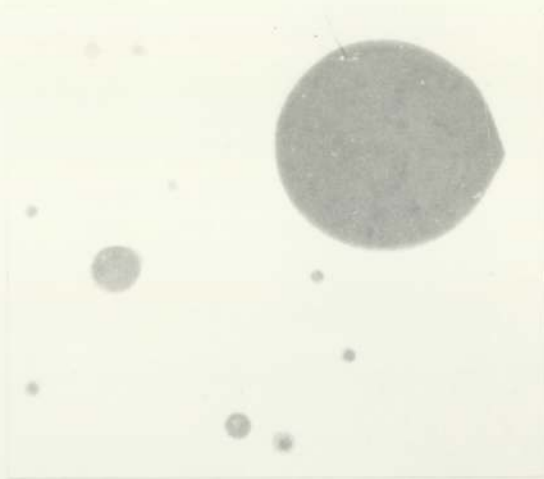


PLATE 8 : OPAQUE OXIDE INCLUSIONS
AND OXY-SULPHIDES FROM
MELT D2 (0.1%S). x720



PLATE 10 : OPAQUE OXIDE
INCLUSION FROM
MELT D2 (0.2%S).
x720

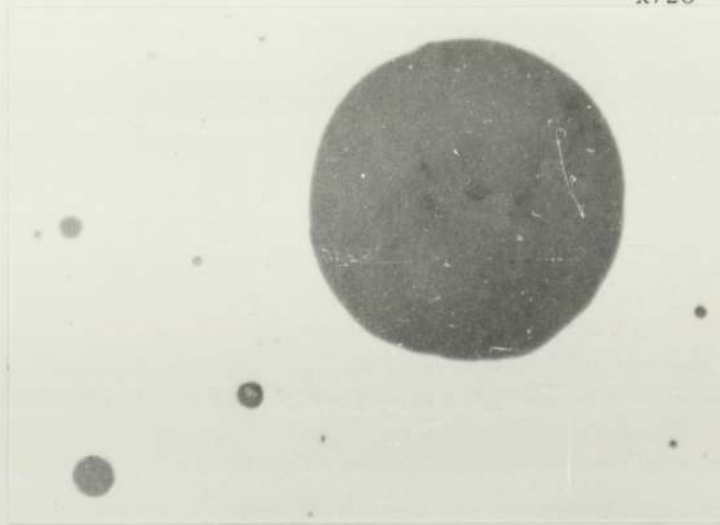


PLATE 9 : OPAQUE OXIDE INCLUSIONS FROM MELT D2
(0.2%S). x720



PLATE 11 : TYPE II MnS
INCLUSIONS FROM MELT
D4 . x500



PLATE 12 : TYPE I MnS INCLUSIONS.
x720



PLATE 13 : HOLE OCCUPIED
BY INCLUSION
WITH VOID.
TAKEN FROM
MELT A6
(0.07% S)
ROLLED AT
1000°C,
 $\epsilon_m = 0.69$ (50%)

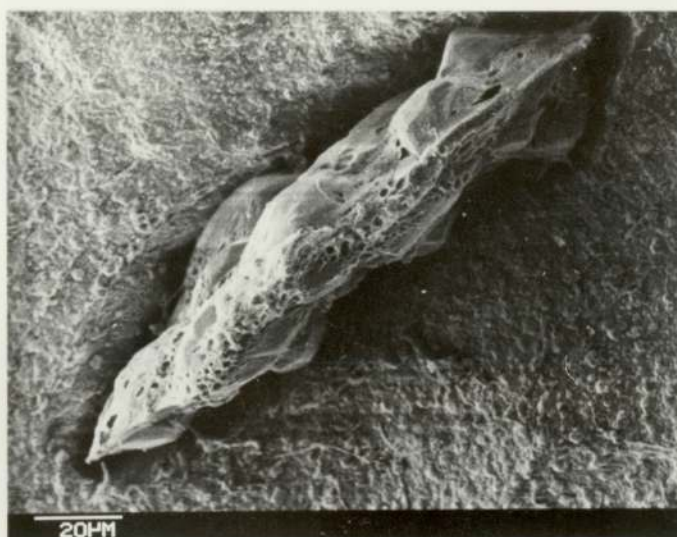


PLATE 14 : PLASTIC/
BRITTLE
BEHAVIOUR OF
A Mn-SILICATE
INCLUSION.
THIS IS A
CHARACTERISTIC
EXHIBITED
WHEN MELTS A6
AND A7 ARE
ROLLED AT
1100°C,
 $\epsilon_m = 0.69$ (50%)
TAKEN FROM
MELT A6
(0.1% S)

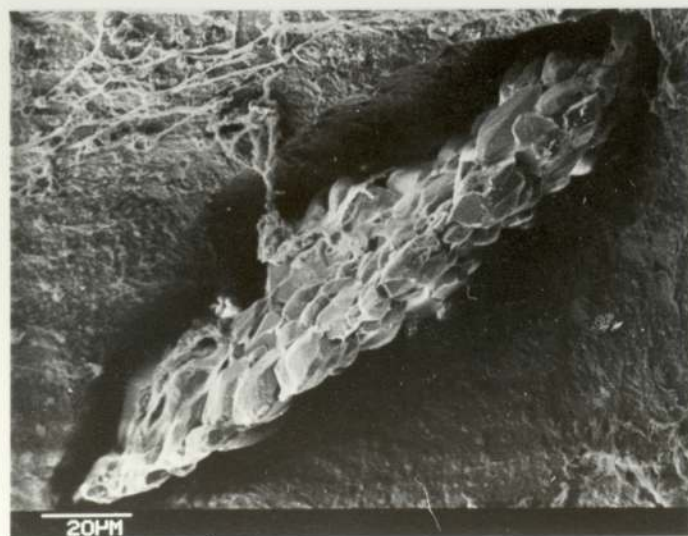


PLATE 15 : FRAGMENTED
ELONGATED Mn-
SILICATE
INCLUSION C
EXHIBITING
CRYSTALLISA-
TION. TAKEN
FROM MELT A6
(0.1% S)
ROLLED AT
1100°C,
 $\epsilon_m = 0.69$ (50%)

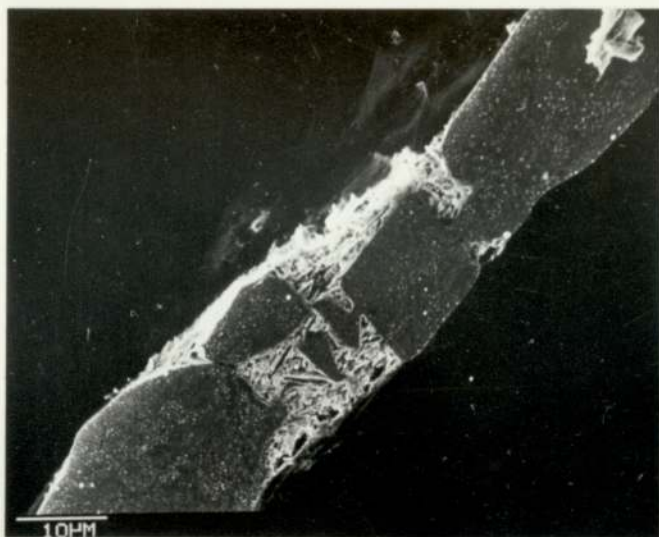


PLATE 16 : POLISHED SURFACE OF PLASTIC/
BRITTLE Mn-SILICATE INCLUSION.
TAKEN FROM MELT A6 (0.1%S) ROLLED
AT 1100°C, $\epsilon_m = 0.69$ (50%)



PLATE 17 : POLISHED SURFACE OF FRAGMENTED
ELONGATED Mn-SILICATE INCLUSION
SHOWING INTERNAL VOIDS WITHIN THE
INCLUSION. FROM MELT A6 (0.1%S)
ROLLED AT 1100°C, $\epsilon_m = 0.69$ (50%)



PLATE 18 : PLASTIC/
FRACTURE BEHAVIOUR OF A
Mn-SILICATE INCLUSION
FROM MELT A6 (0.1%S)
ROLLED AT 1200°C,
 $\epsilon_m = 0.69$ (50%)

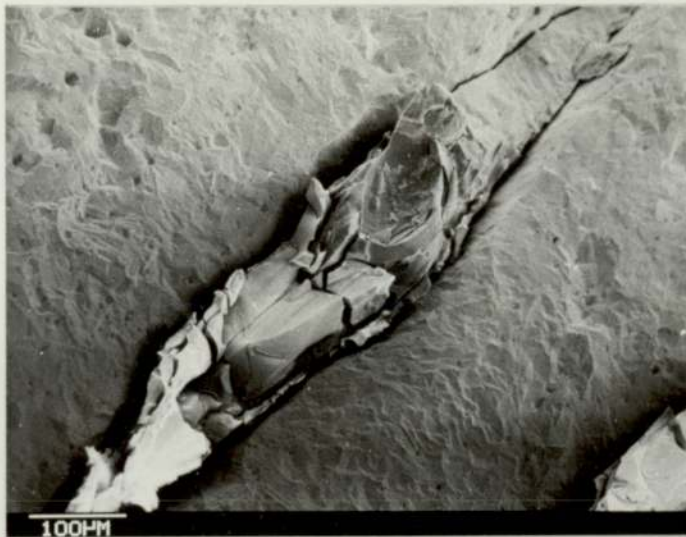


PLATE 19 : PLASTIC/
FRACTURE BEHAVIOUR OF
A Mn-SILICATE
INCLUSION. FROM MELT
A6 (0.1%S) ROLLED AT
1200°C,
 $\epsilon_m = 0.69$ (50%)



PLATE 20 : FLUID
BEHAVIOUR OF A Mn-
SILICATE INCLUSION.
FROM MELT A6 (0.1%S)
ROLLED AT 1300°C,
 $\epsilon_m = 0.69$ (50%)

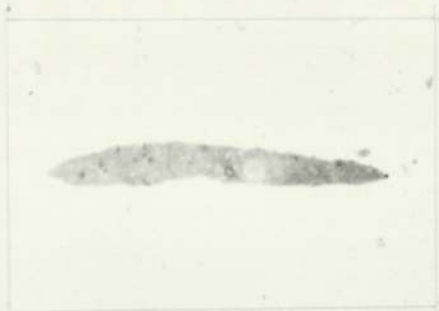


PLATE 21 : Mn SILICATE INCLUSION WITH
NO MnS ppt. FROM MELT A6
(0.2%S) ROLLED AT 1100°C,
 $\epsilon_m = 0.69$ (50%). x500



PLATE 22 : Mn-SILICATE INCLUSION
WITH MnS ppt WITHIN
IT. FROM MELT A6
(0.2%S) ROLLED AT
1200°C, $\epsilon_m = 0.69$
(50%). x500



PLATE 23 : Mn-SILICATE
INCLUSIONS WITH
MnS ppt WITHIN
THEM. FROM MELT A6
(0.2%S) ROLLED AT
1300°C, $\epsilon_m = 0.69$
(50%). x500



PLATE 24 : Mn-SILICATE INCLUSION
EXHIBITING INTERNAL VOIDS,
FROM MELT A7 (0.07%S) ROLLED AT
1100°C, $\epsilon_m = 0.69$ (50%). x680



PLATE 25 : DEFORMED Mn-SILICATE INCLUSION.
FROM MELT A7 (0.1%S) ROLLED AT
1000°C, $\epsilon_m = 0.69$ (50%)



PLATE 26 : PLASTIC/BRITTLE Mn-SILICATE
INCLUSIONS. FROM MELT A7 (0.1%S)
ROLLED AT 1000°C, $\epsilon_m = 0.69$ (50%)



PLATE 27 : PRECIPITATED INCLUSION
EXHIBITING CRACKING
CHARACTERISTICS FROM
MELT A12 (0.07%S)
ROLLED AT 900°C,
 $\epsilon_m = 0.69$ (50%). x680



PLATE 28 : DEFORMED AND PARTIALLY
DEFORMED INCLUSIONS
(LARGE) FROM MELT A12
(0.2%S) ROLLED AT 800°C
 $\epsilon_m = 0.69$. x400



PLATE 29 : DEFORMED
INCLUSIONS TAKEN FROM
MELT A12 (0.1%S) ROLLED
AT 800°C, $\epsilon_m = 2.3$ (90%)
THE UNDERFORMED
INCLUSION HAS VERY HIGH
SILICON CONTENT.



PLATE 30 : DEFORMED
INCLUSIONS TAKEN FROM MELT
A12 (0.1%S) ROLLED AT 900°C,
 $\epsilon_m = 0.69$ (50%).
SOME OF THE INCLUSIONS ARE
JOINED.

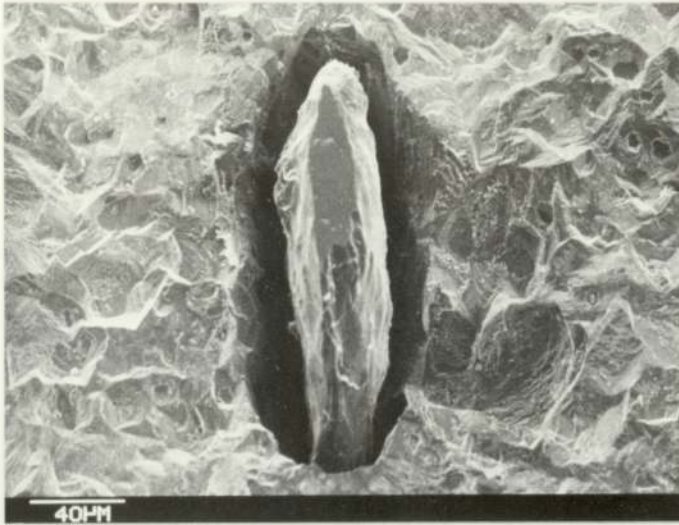


PLATE 31 : DEFORMED
OXIDE INCLUSION FROM
MELT A12 (0.1% S)
ROLLED AT 900°C,
 $\epsilon_m = 0.69$ (50%)

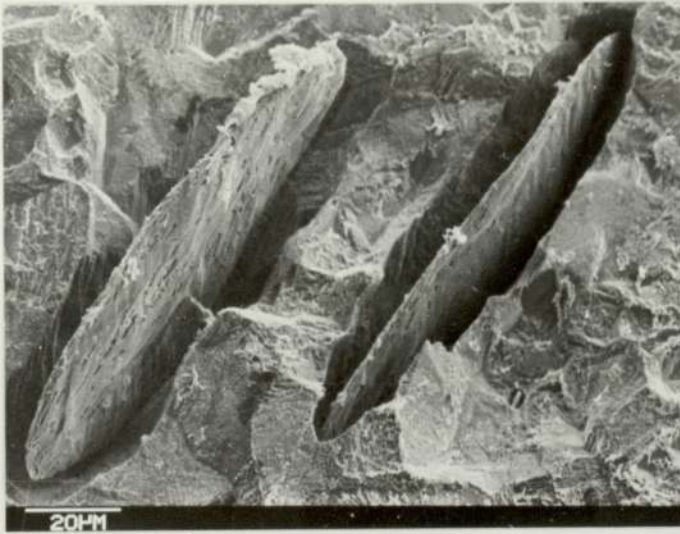


PLATE 32 : DEFORMED
INCLUSIONS TAKEN FROM
MELT A12 (0.1% S)
ROLLED AT 900°C,
 $\epsilon_m = 1.20$ (70%)

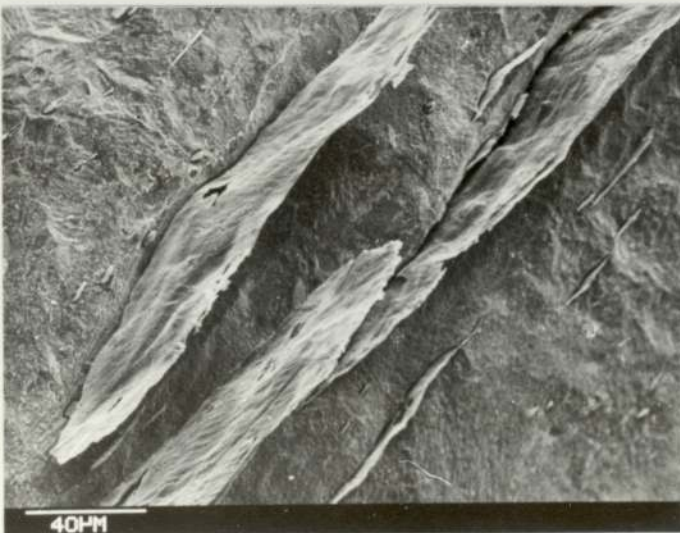


PLATE 33 : DEFORMED
INCLUSIONS SHOWING
SPLITTING AND ROPING
CHARACTERISTICS. FROM
MELT A12 (0.1% S)
ROLLED AT 900°C,
 $\epsilon_m = 2.30$ (90%)

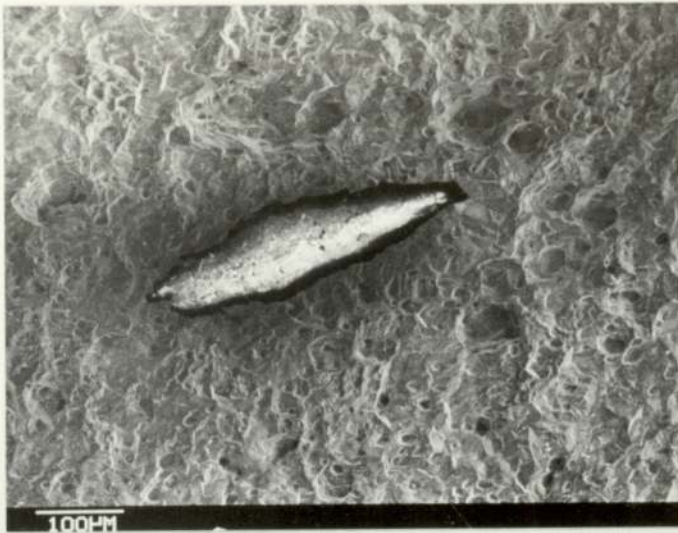


PLATE 34 : DEFORMED
OXIDE INCLUSION TAKEN
FROM MELT A12 (0.1% S)
ROLLED AT 900°C,
 $\epsilon_m = 0.69$ (50%)

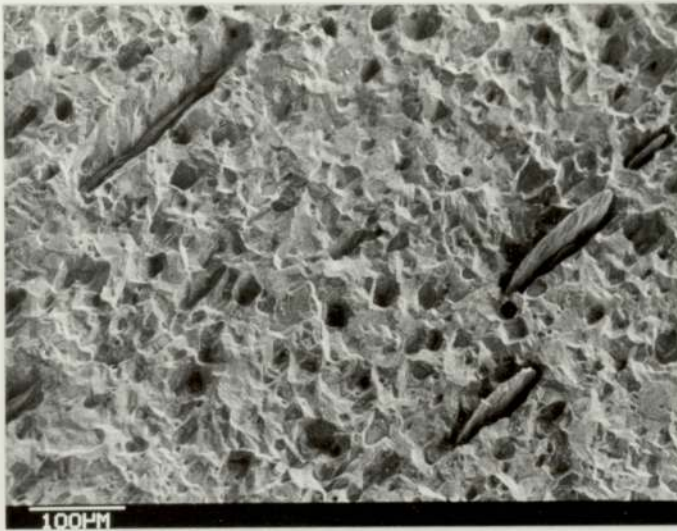


PLATE 35 : DEFORMED
OXIDE INCLUSIONS.
FROM MELT A12 (0.1% S)
ROLLED AT 900°C,
 $\epsilon_m = 1.20$ (70%)

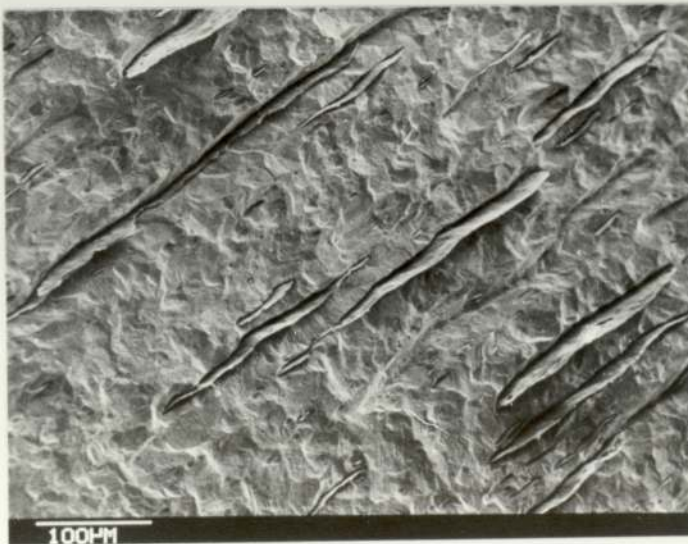


PLATE 36 : DEFORMED
INCLUSIONS SHOWING
ROPING CHARACTERISTICS
FROM MELT A12 (0.1% S)
ROLLED AT 900°C,
 $\epsilon_m = 2.30$ (90%)



PLATE 37 : UNDEFORMED
INCLUSIONS WITH PRECIPITATES
WITHIN THEM. TAKEN FROM MELT
A15 (0.07%S) ROLLED AT 900°C,
 $\epsilon_m = 0.69$ (50%). x680

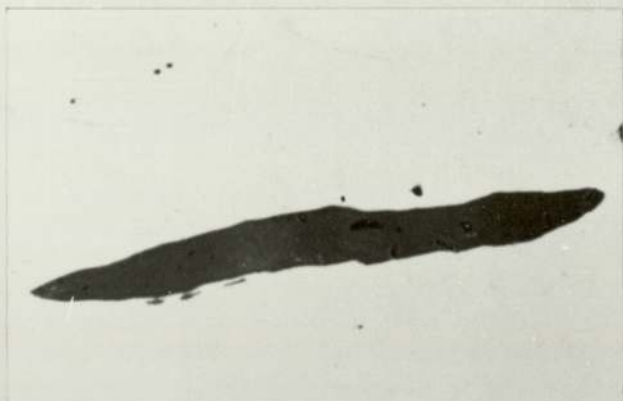


PLATE 38 : DEFORMED
INCLUSION TAKEN FROM MELT
A15 (0.07%S) ROLLED AT
1100°C, $\epsilon_m = 0.69$ (50%).
x690



PLATE 39 : SLIGHTLY
DEFORMABLE INCLUSION
HAVING COMPOSITION :
49%SiO₂, 38%MnO, 10%
Al₂O₃, 2%FeO, 1%S
FROM MELT A12 (0.1%S)
ROLLED AT 800°C,
 $\epsilon_m = 0.69$ (50%). x1000

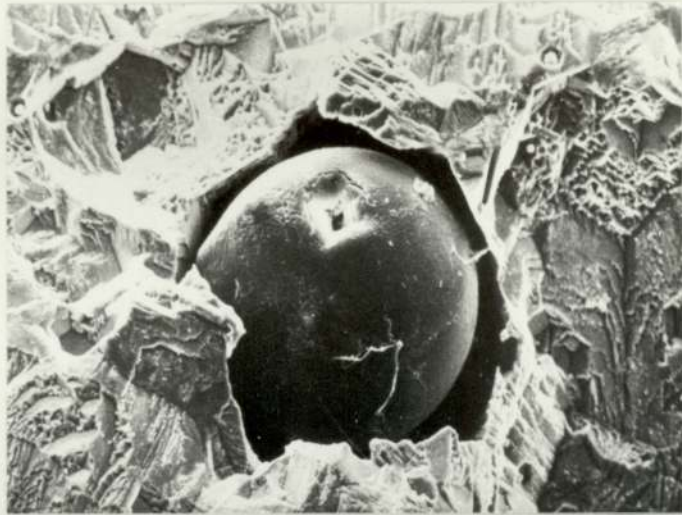


PLATE 40 : THE COMPOSITION OF THE UNDEFORMED INCLUSION IS 59%SiO₂, 30%MnO, 8%Al₂O₃, 2%FeO, 1%S.

TAKEN FROM MELT A12 (0.1%S) ROLLED AT 800°C, $\epsilon_m = 0.69$. x1000



PLATE 41 : THE COMPOSITION OF THE DEFORMED SECTION OF THE INCLUSION IS 45%SiO₂, 43%MnO, 10%Al₂O₃, 1%FeO, 1%S, .WHILST THE COMPOSITION OF THE UNDEFORMED SECTION IS 57%SiO₂, 31%MnO, 7%Al₂O₃, 3%FeO, 2 S. TAKEN FROM MELT A12(0.1%S) ROLLED AT 800°C, $\epsilon_m = 0.69$. x1000

MELT A12 (0.1% S)

AS CAST

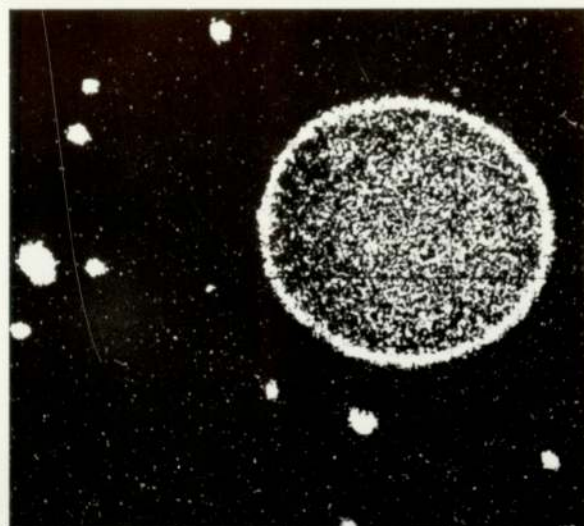


PLATE 42 : S X-RAY.
x1000

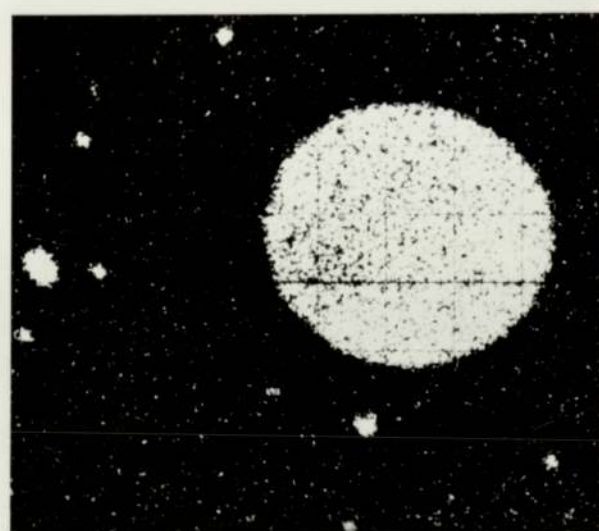


PLATE 43 : Mn X-RAY.
x1000

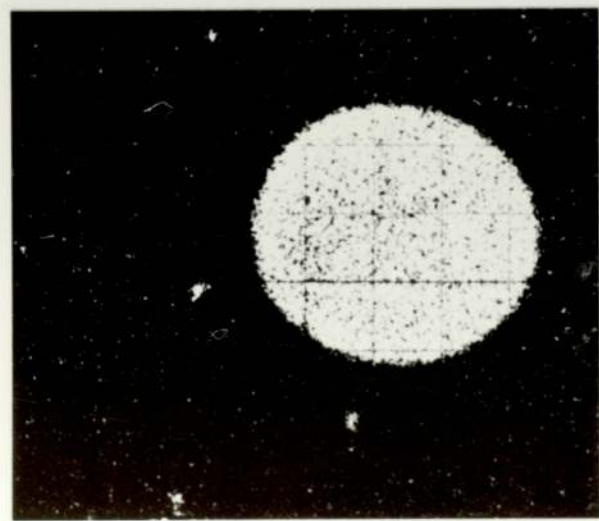


PLATE 44 : Si X-RAY.
x1000

MELT A12 (0.1%S)

AS CAST contd.

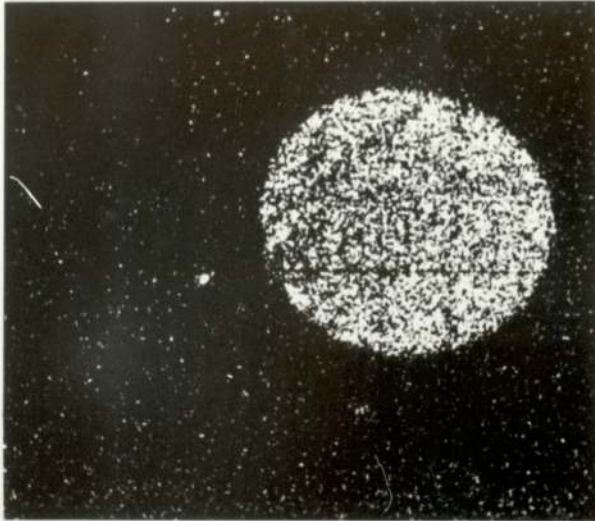


PLATE 45 : Al X-RAY.
x1000

MELT A6 (0.1%S)

AS CAST

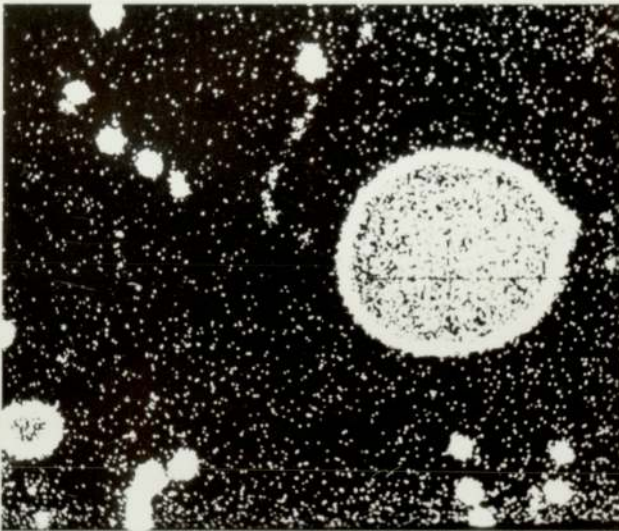


PLATE 46 : S X-RAY
x1000

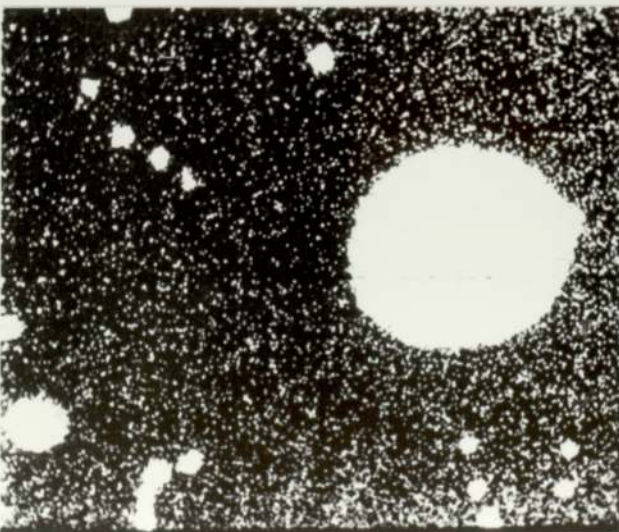


PLATE 47 : Mn X-RAY
x1000

MELT A6 (0.1%Si)

AS CAST contd.

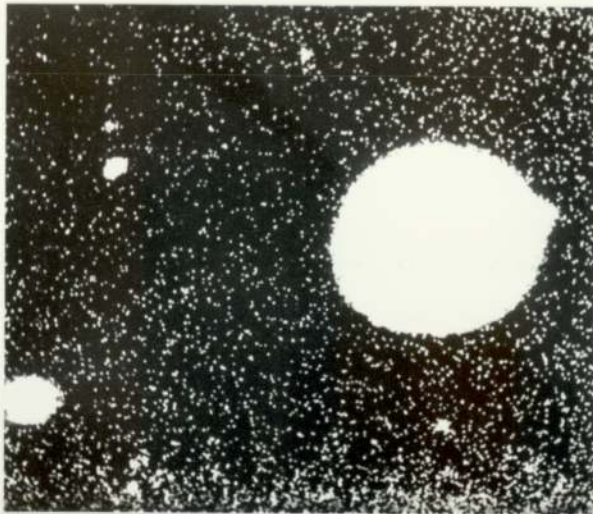


PLATE 48 : Si X-RAY
x1000

MELT A6 (0.2%Si)
ROLLED AT 1000°C,

$\epsilon_m = 0.69$



PLATE 49 : S X-RAY
x1000

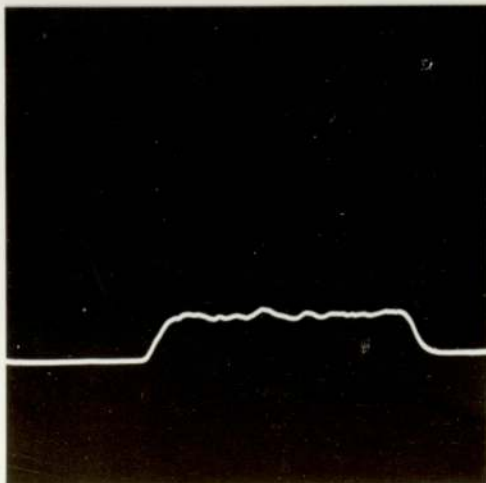


PLATE 50 : S-LINE SCAN
x1000

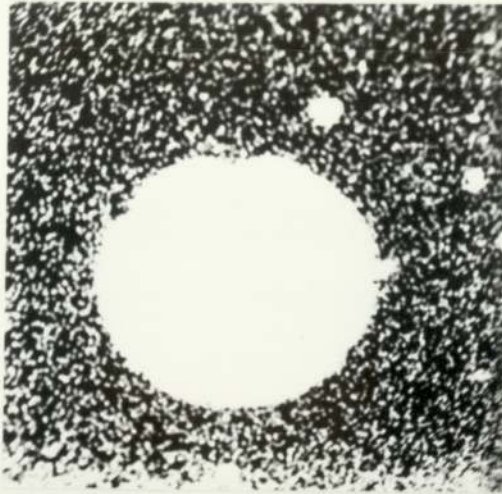


PLATE 51 : Mn X-RAY
x1000

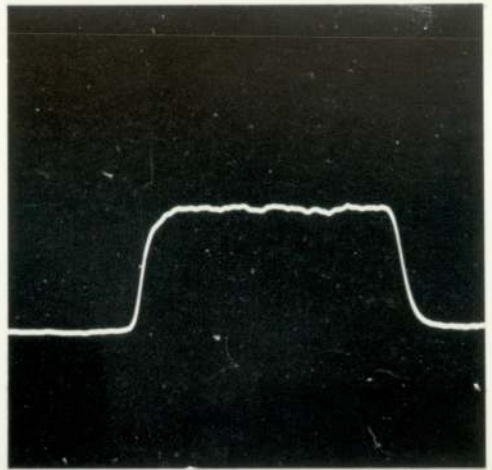


PLATE 52 : Mn-LINE SCAN
x1000

MELT A6 (0.2% S) ROLLED AT 1000°C, $\epsilon_m = 0.69$

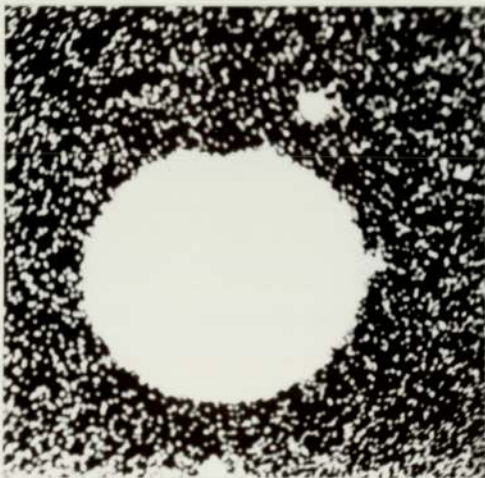


PLATE 53 : Si X-RAY
x1000

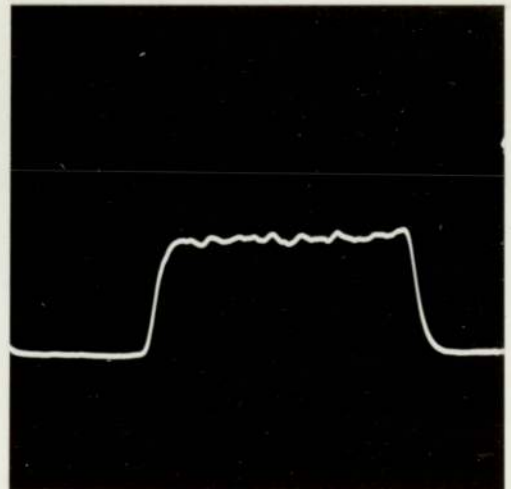


PLATE 54 : Si-LINE SCAN
x1000

MELT A6 (0.2% S) ROLLED AT 1000°C, $\epsilon_m = 0.69$



PLATE 55 : Al X-RAY
x1000

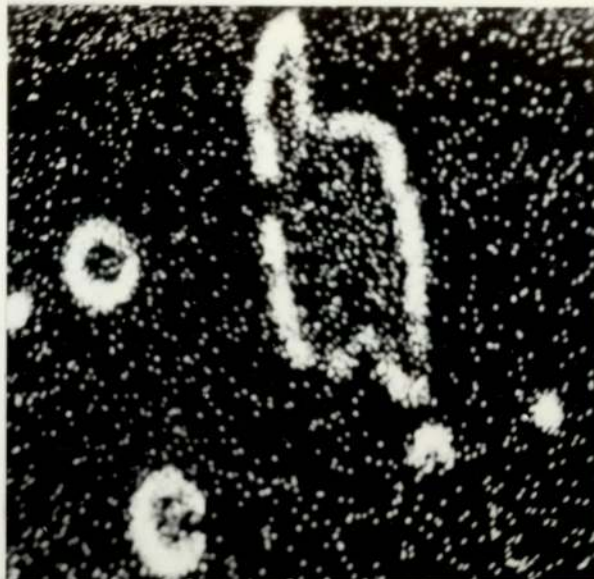


PLATE 56 : S X-RAY
x1000

MELT A12 (0.2% S) ROLLED AT 1000°C, $\epsilon_m = 0.69$

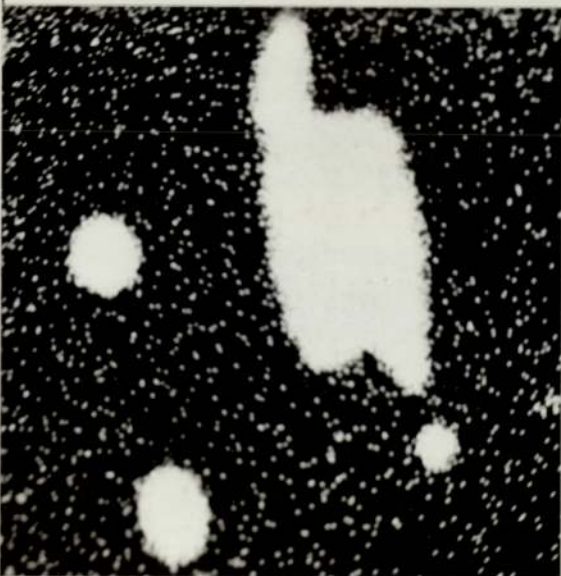


PLATE 57 : Si X-RAY
x1000

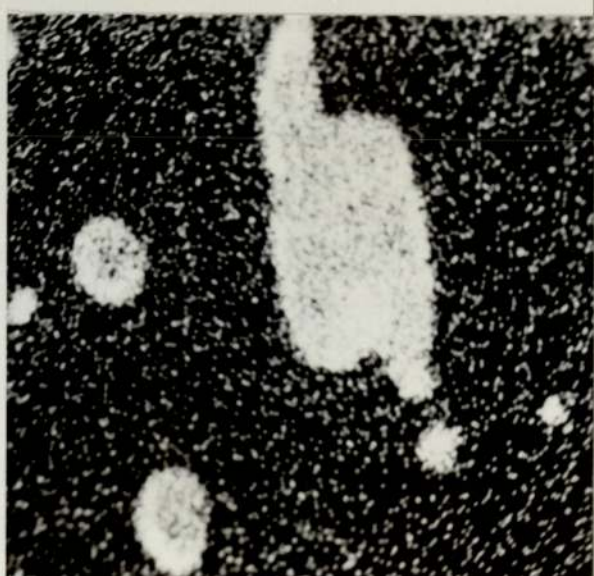


PLATE 58 : Mn X-RAY
x1000

MELT A12 (0.2 S) ROLLED AT 1000°C, $\epsilon_m = 0.69$

HEAT TREATMENT RESULTS

(MELT A12 (0.1% S) ROLLED AT
900°C, $\epsilon_m = 0.69$, BEFORE
HEAT TREATMENT)

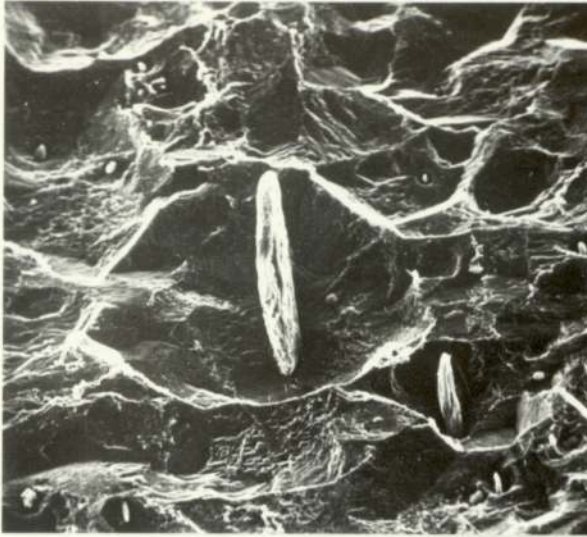


PLATE 59 : INITIAL
INCLUSIONS BEFORE
SPHEROIDISATION TREATMENT.
x650

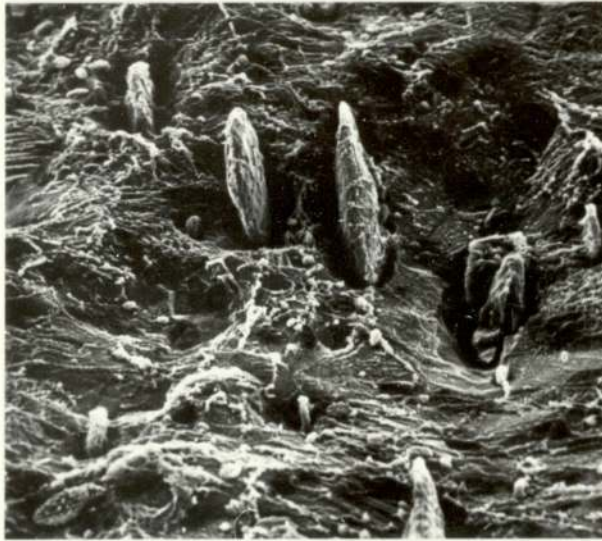


PLATE 60 : INCLUSIONS AFTER
HOMOGENISATION TIME = 72HRS
x600



PLATE 61 : INCLUSIONS
BEFORE SPHEROIDISATION
TREATMENT.
x780

HEAT TREATMENT RESULT

cont'd



PLATE 62 : HOMOGENISATION
TIME = 0 hrs.
x240



PLATE 63 : HOMOGENISATION
TIME = 72 HRS
x240



PLATE 64 : HOMOGENISATION
TIME = 72 HRS
x1320



PLATE 65A : CLEAVAGE FRACTURE
x3000

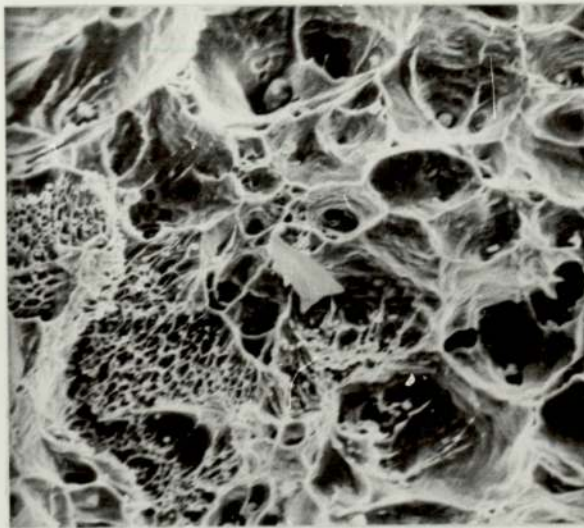


PLATE 65B : DUCTILE FRACTURE
SHOWING SUPERVOID.
x1000



PLATE 66A : DUCTILE FRACTURE
WITH VOID COALESCENCE.
x500

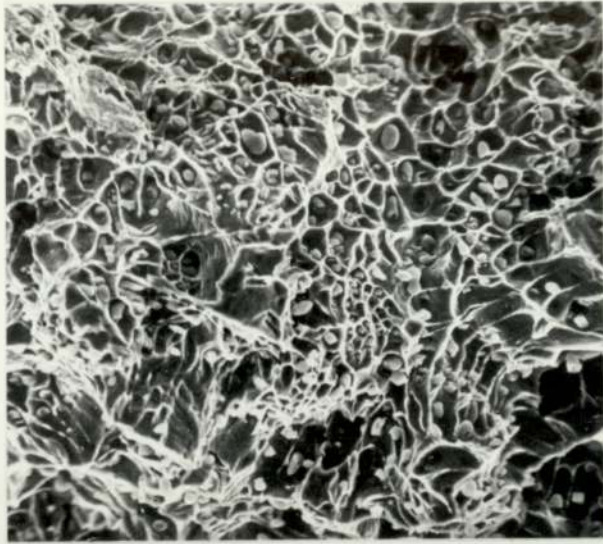


PLATE 66B : DUCTILE FRACTURE SURFACE OF
STEEL CONTAINING TYPE I MnS
INCLUSIONS. x1000



PLATE 67 : DUCTILE FRACTURE SURFACE OF STEEL
CONTAINING TYPE II MnS INCLUSIONS.



PLATE 68 : COALESCING INCLUSION
TAKEN FROM MELT A15
(0.07%S) AS CAST.
x550

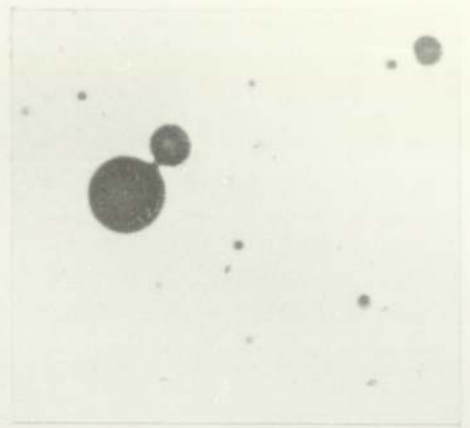


PLATE 69 : COALESCING OPAQUE
INCLUSION TAKEN
FROM MELT D2 (0.1%S)
AS CAST. x720



PLATE 70 : SEM PICTURE
OF PLATE 69.



PLATE 71 : SEM
PICTURE OF COALESCING
INCLUSION (FROM MELT
D1) (0.02%S)

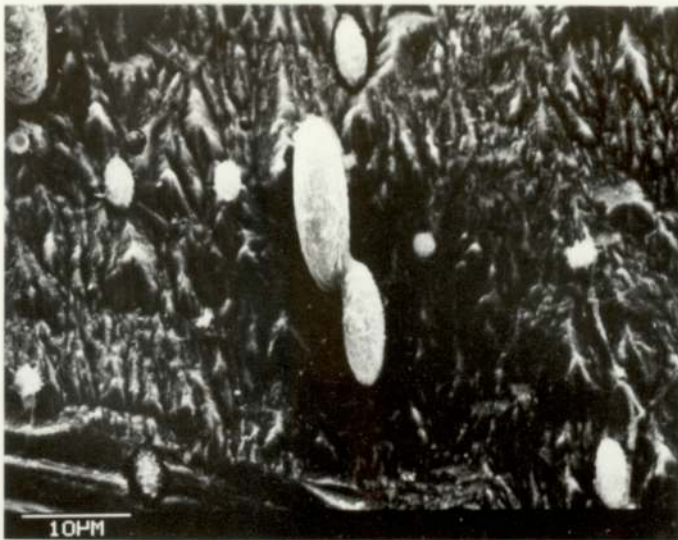


PLATE 72 : FLUID
(DEFORMED) INCLUSIONS
BEGINNING TO SHEAR FROM
MELT A12 (0.1% S) ROLLED
AT 1000°C, $\epsilon_m = 0.69$



PLATE 73 : FLUID
INCLUSIONS, LIKELY TO
HAVE BEEN PRODUCED BY
SHEARING FROM MELT A12
(0.1% S) ROLLED AT
1000°C, $\epsilon_m = 0.69$



PLATE 74 : FLUID
INCLUSION EXHIBITING
SPLITTING
CHARACTERISTICS. [A12
(0.1% S) ROLLED AT
1000°C, $\epsilon_m = 0.69$]

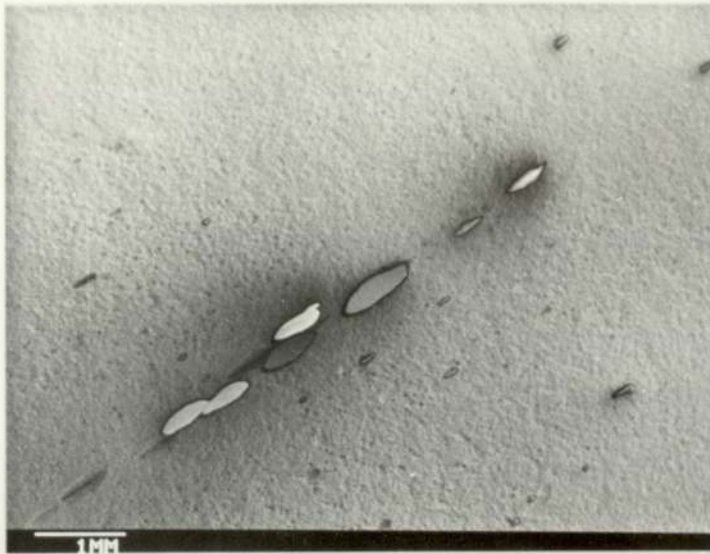


PLATE 75 : MELT A12
(0.2%S) ROLLED AT
800°C, $\epsilon_m = 0.69$
(50%)



PLATE 76 : MELT A12
(0.1%S) ROLLED AT
900°C, $\epsilon_m = 2.30$
(90%)



PLATE 77A : D1 (0.02%S)
THE DISTRIBUTION OF
OXIDE AND SULPHIDE
INCLUSIONS.



PLATE 77B : DISTRIBUTION
OF BOTH OXIDE AND
SULPHIDE INCLUSIONS
[MELT D1 (0.02%S)]

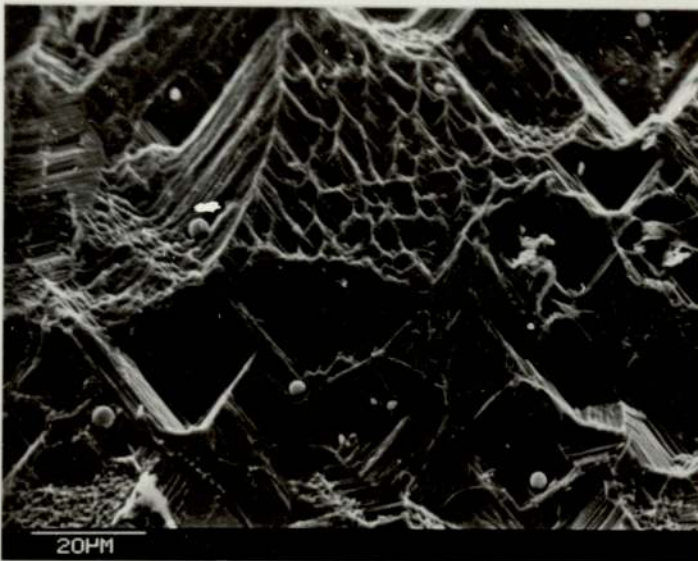


PLATE 78A : SULPHIDE
DISTRIBUTION TAKEN
FROM MELT D3 (0.2%S)



PLATE 78B : S X-RAY
OF PLATE 78A



PLATE 79A : MELT D3
(0.2%S) SHOWING
SULPHIDE INCLUSIONS
TRAPPED DURING
SOLIDIFICATION.

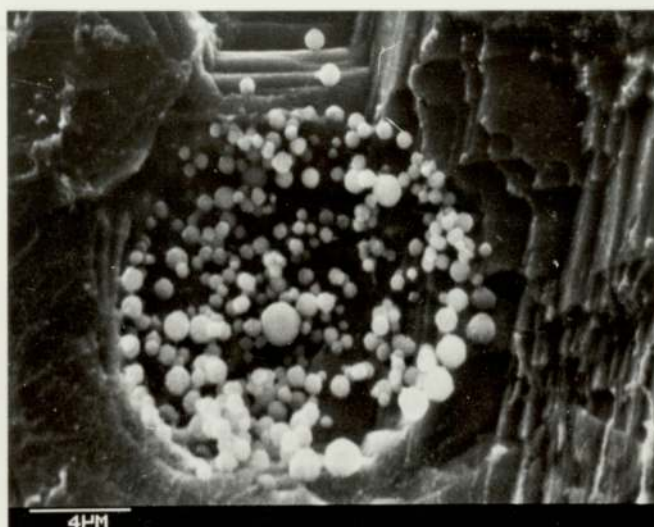


PLATE 79B : SAME AS
PLATE 79A.



PLATE 79C : S X-RAY
(SAME AS PLATE 79A)



PLATE 80 : INCLUSIONS SECTIONED SUCH THAT IT EXHIBITS ITS TRUE \vee IN THE POLISHED PLANE.

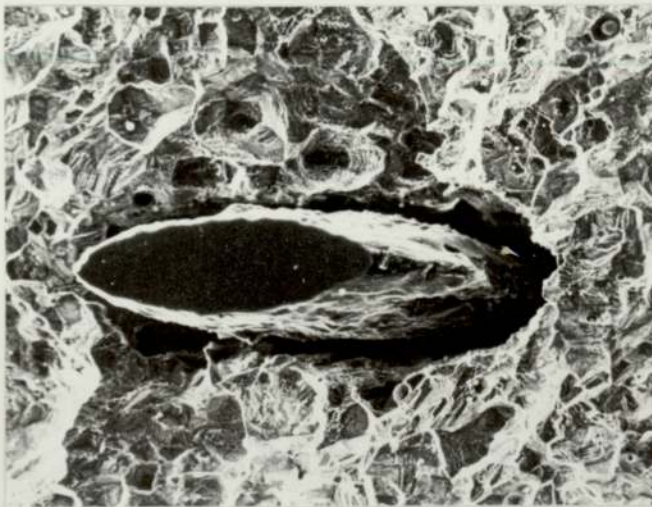


PLATE 81 : INCLUDING SECTIONED SUCH THAT IT EXHIBITS A LESSER \vee THAN ITS TRUE VALUE IN THE POLISHED PLANE



PLATE 82 : INCLUSIONS SECTIONED SUCH THAT IT EXHIBITS A GREATER \vee THAN ITS TRUE VALUE IN THE POLISHED PLANE.

REFERENCES

1. Bodsworth C. and Bell H.B.: 'Physical Chemistry of Iron and Steel Manufacture', 1963, 394.
2. Muan A. and Osborn E.: Phase equilibria among oxides in steelmaking, Addison-Wesley, London, 1965.
3. Kiessling R. and Lange N.: Non-metallic inclusions in steel, Parts I, II and III, I.S.I. Publns. 90, 100, 115.
4. Sicha M.: Hutnike Listy, 1963, 17, 479
5. Jørgensen C.: Inst. for Ferrous Metallurgy, Royal Inst. of Technology, Stockholm, Internal report.
6. Bell H.B.: Iron and Steel, 1954, 27, 493-559
7. Landon P.H.: Ph.D. Thesis, 1967, Aston University
8. Elliott J.F., Gleiser M., and Ramakrishna V.: Thermochemistry for Steelmaking, Vols. I and II, Addison-Wesley, 1963.
9. Kubaschewski O. and Evans E.: Metallurgical Thermochemistry, Pergamon Press Ltd.
10. As ref. 1.
11. Reeves G.: Unpublished work - Aston University
12. Chipman J. and Pillay T.C.M.: Trans. A.I.M.E., 1961, 221, 1277.
13. McLean A. and Ward R.J.: J.I.S.I., 1966, 204, 8.
14. Körber F. and Oelsen W.: Mitt. Kaiser-Wilhelm Inst. Eisenforsch, 1933, 15, 271-309.
15. Fischer W.A. and Fleischer H.J.: Arch. Eisenhüttenwese, 1961, 32, 1.

16. Forward G. and Elliott J.F.: Metall. Trans., 1970, 1, 2889.
17. Iyengar R.K. and Philbrook W.O.: *ibid*, 1973, 4, 2181
18. Gokcen N.A. and Chipman J.: Trans. A.I.M.E., 1953, 194, 131
19. Straube H., Kuhnelt G., and Plöckinger E.: Arch. Eisenh., July 1969, 509-518.
20. Plöckinger E.: Stahl U. Eisen., 1956, 76, 810-824
21. Plöckinger E. and Rosegger R.: *ibid.*, 1957, 77, 701-704
22. Plöckinger E. and Wahlster M.: *ibid.*, 1960, 80, 656-699
23. Sloman H.A. and Evans E.L.: J.I.S.I., May 1950, 81-90
24. Hilty D.C. and Crafts W.: Jnl of Metals, Feb. 1950, Trans A.I.M.M.E., 188, 414-425
25. Levin E.M. et al.: 'Phase diagrams for Ceramists'; 1964, Columbus, Ohio, The American Ceramic Society
26. Discussion of ref. 42: p.607-615
27. Bogdandy Von L., Meyer M. and Stanski I.N. _ Arch. Eisenh., 1963, 34, 235-241
28. Froberg M.G. and Potschke J.: Feiberger Forschung, 1969, B144, 31-51
29. Waudby P.E. and Salter W.J.M. _ J.I.S.I., July 1971, 518-522.
30. Rege R.A., Szekeres E.S. and Forgeng W.D.: Met. Trans. A.I.M.M.E., 1970, 1, 2652.

31. Lindon P.H. and Billington J.C.: Trans. Met. Soc. A.I.M.E., 1969, 245, 1775.
32. Kawawa T. and Ohkubo M.: Trans. I.S.I.J., 1968, 8, 203-219.
33. McLean A.: A.I.M.E. Elec. Furn. Steel Conf. Proc., 1967, 25, 56.
34. Kiessling R. and Lange N.: Non-metallic Inclusions in Steel, Part I, 1964, London, I.S.I.
35. Luyckx L. et al.: J. Met., 1974, 26, (6), 35.
36. Blickwede D.J.: Met. Progr., 1969, 96, 98
37. Iyengar R.K. and Philbrook W.O.: Metall. Trans., 1973, 4, 2181
38. Plöckinger E.: 'Clean Steel', 1963, 64, London, I.S.I.
39. Hilty D.C. and Crafts W.: Trans. A.I.M.E., 1950, 188, 425-431.
40. Walsh R.A. and Ramashandran S.: Trans. A.I.M.E., 1963, 227, 560-562.
41. Turkdogan E.T.: 'Chemical Metallurgy of Iron and Steel', 1973, 153, London, I.S.I.
42. Turkdogan E.T.: J.I.S.I., 1972, 210, 21
43. Turkdogan E.T.: Trans. A.I.M.E., 1965, 233, 2100-2112
44. Plöckinger E. and Wahlster M.: Stahl und Eisen, 1960, 80, 659-669.
45. Plöckinger E. and Wahlster M.: 'Clean Steel', I.S.I. Spec. Ref. No. 77, 1963, 51-56.

46. Torssell K.: Jernkonterets Ann., 1967, 151, 890
47. Gatellier G. and Olette M.: 'Chemical Metallurgy of Iron and Steel', 1973, 191, London, I.S.I.
48. Torssell K.: 'Clean Steel', Royal Swedish Academy of Engineering Sciences Report 169:1, 88, 1971, Stockholm
49. Pomey G. and Trentini B.: 'Production and Application of Clean Steels', 1972, 1, London, I.S.I.
50. Forster E. and Richter H.: *ibid.*, 24
51. Grethen E. and Philippe L.: *ibid.*, 29
52. Lindborg U. and Torssell K.: Trans. A.I.M.E., 1968, 242, 94
53. Matthew P.M. et al.: Arch. Eisenh., 1974, 45, 569
54. Bogdandy L. von. et al.: *ibid.*, 1961, 32, 451; 1963, 34, 235.
55. Turkdogan E.T.: J.I.S.I., 1966, 204, 914
56. Turpin M.L. and Elliott J.F.: *ibid.*, 217
57. Sigworth G.K. and Elliott J.F.: Can. Metall. Q., 1972, 11, 337
58. Olette M., Gatellier C., and Torssell K.: B.H.M., 1968, 113, (11), 484-492
59. Forward G. and Elliott J.F.: A.I.M.E. Elec. Furn. Steel Conf. Proc., 1966, 24, 16
60. Same as Ref. 16.

61. Same as Ref. 48
62. Torssell K. et al.: C.R. Hebd. Seances Acad. Sci., 1968, 267, 869.
63. Gatellier C. et al.: Rev. Metall., 1969, 66, 673.
64. Miyashita Y.: Trans. I.S.I.J., 1967, 7, 1.
65. Sakagami R. et al.: Tetsu-to Hagane, 1969, 55, 550
66. Miyashita Y.: Nippon Kokan Tech. Rep. (Overseas), 1965, 4, 41.
67. Kozakevitch P. and Olette M.: 'Production and Application of Clean Steel', 1972, 42, London, I.S.I.
68. Schenck H. et al.: Arch. Eisenh, 1970, 41, 131
69. Miyashita Y. et al.: Proc. Second Japan - U.S.S.R. Joint Symp. on Phys. Chem. Met., 1969, 101, Tokyo.
70. Iyengar R.K. and Philbrook W.O.: Metall. Trans., 1972, 3, 1823.
71. Knuppel V.H. et al.: Stahl Eisen, 1965, 85, 675
72. Kozakevitch P. and Lucas L.D.: Rev. Metall., 1968, 65, 589
73. Iyengar R.K. and Philbrook W.O.: 'Kinetic Metallurgischer Vorgänge bei der Stahlherstellung', 1972, 219, Düsseldorf, Verlag Stahleisen
74. Lunner S.E.: J.I.S.I., 1959, 124-136
75. Lindon P.H. and Billington J.C.: J.I.S.I., 1969, 207, 340-347

76. Waudby P.E.: 'Inclusions and their effects on steel properties'. B.S.C. Conference Bodington Hall, Leeds University, Sept. 1974
77. Dyson B.F.: Trans. A.I.M.E., 1963, 227, 1098
78. Halden F.A. and Kingery W.D.: Jnl. Phys. Chem., 1955, 59, 557
79. Linder S.: Scand. Jnl. Metall., 1974, 3, 137
80. Lindskog L. and Sandberg H.: ibid., 1973, 2, 71
81. Kiessling R and Lange N.: Special report 90 I.S.I., London, 1964
82. Kiessling R. and Lange N.: Special report 110, I.S.I., London
83. Pickering F.B.: Paper 3, Bodington Hall Conference, 1974, University of Leeds.
84. Robinson S.W.: Ph.D. Thesis, Sheffield Polytechnic, 1977
85. Rege R.A., Szekeres E.S. and Forgeng W.D.: Met. Trans. A.I.M.M.E., 1970, 1, 2652
86. Pickering F.B.: Iron and Steel, 1957
87. Fischer W.A. and Fleischer H.J.: Arch. Eisenh., 1961, 32, 305
88. Simms C.E. and Dahle F.B.: Trans. A.F.A., 1938, 86, 796
89. Baker T.J. and Charles J.A.: J.I.S.I., Sept. 1972, 702-706

90. Dahl W. et al.: Stahl u. Eisen., 1966, 86, 796
91. Same as Ref. 88
92. Fredriksson H. and Hillert M.: Scand. Jnl. Met., 1972, 2, 125-145
93. Buzek Z. et al.: Slevarenstui, 1969, (10), 17, 398-404
94. Duckworth W.E. and Inneson E.: 'The effects of externally introduced alumina particles on the fatigue life of En24 steel', 'Clean Steel', I.S.I. special report 77.
95. Same as Ref. 90
96. Same as Ref. 92
97. Ekerot S.: Scand. Jnl. Met., 1974, 3, 21-27
98. Scheil E and Schnell R., Stahl u. Eisen., 1952, 72, 683-687
99. Malkiewicz T. and Rudnik S.: J.I.S.I., Jan. 1963, 33-38
100. Wardle G.: Ph.D. Thesis, Aston University
101. Segal A. and Charles J.A.: Met. Tech., 1977, 177
102. Pickering F.B.: J.I.S.I., June 1958, 148-159
103. Baker T.J. and Charles J.A.: J.I.S.I., Sept. 1972, 680-690
104. Maunder P.J.H. and Charles J.A.: J.I.S.I., July 1968, 705-715

105. Van Vlack L.H.: Trans. A.S.M., 1953, 45, 741
106. Gladman T.: Paper 21, (as ref. 76)
107. Gove K.B. and Charles J.A.: Met. Tech., Sept. 1974, 425-431
108. Baker T.J., Charles J.A. and Gove K.B.: 'Met. Soc. Preprints', 'Directionality of Properties in wrought products'. Meeting 27-28th Nov. 1974, 75/716 Pt.1
109. Unkle H.: Jnl. Inst. Met., 1937, 61, 171
110. Zeisloft R.H. and Hosford W.F.: Trans. A.S.M., 1969, 62, 297-300
111. Sundström B.: Jnl. Composite Mats., 1971, 5, 277-278
112. McClintock J.: Jnl. Applied Mech., 1968, 35, 363
113. Klevebring B.I.: Scand. Jnl. Met., 1974, 3, 102-104
114. Mann G.S. and Van Vlack L.H.: Met. Trans. 1972, 3, 2005-2006
115. Charles J.A.: Paper 6 (as ref. 76)
116. Gay N.C.: Tectonophysics, 1968, 5, (3); 211-234
117. Ashok S.K.: Ph.D. Thesis, 1976, Cambridge University
118. Kiessling R.: Jerkont. Ann., 1969, 153, 295
119. Chao H.C., Van Vlack L.H., Oberin F. and Thomassen L. Trans. A.S.M., 1964, 57, 885-891
120. Chao H.C., Thomassen L. and Van. Vlack L.H.: Trans. A.S.M., 1964, 57, 386-398

121. Chao H.C. and Van Vlack L.H.: Trans. A.S.M. 1965, 58, 335-340
122. Baker T.J. and Charles J.A.: J.I.S.I., March 1973, 187-192
123. Gnanamuthu D., Katamis T.Z., Flemmings M.C., Mehrabain R.: Met. Trans., 1974, 5, 2557-2567
124. Wilson P.C., Murty Y.V., Katamis T.Z. and Mehrabain R.: Met. Tech., June 1975, 241-244
125. Murty Y.V., Marral J.E., Katamis T.Z. and Mehrabain R.: Met. Trans., 1975, 6A, 2031-2035
126. Ekerot S.: Scand. Jnl. Met., 1974, 3, 21-27
127. Ekerot S.: A.I.M.E. Fall Meeting on 'Inclusions in Steels', Cleveland, Ohio, 1970
128. Kiessling R.: 'Non-metallic inclusions in steel', Part II, I.S.I., Publ'n. 115
129. Shiraiwa T. et al.: 'The Sumitomo Search', 1974, 11, 85-100
130. Uchiyama I. and Sumita M.: Trans. Nat. Res. Inst. Met. (Japan)., 1965, 7, 233-241
131. Gove K.B., Baker T.J. and Charles J.A.: Met. Tech., April 1976, 183
132. Segal A. and Charles J.A.: Met. Tech., 1977, 177
133. Ekerot S. and Klevebring B.I.: Scand. Jnl. Met., 1974, 3, 151-152

134. Asante J.C.B.: M.Sc. Thesis, 1976, Aston University
135. Kiessling R.: I.S.I. Publication 115, 1968, 58
136. 'The effect of second phase particles on the mechanical properties of steels', I.S.I. Publication, 1971
137. 'Production and application of clean steel', I.S.I., 1972
138. 'Sulphide inclusions in steel', A.S.M., 1974, 273-360
139. Liu C.T. and Gurland J.: Trans. A.S.M., 1968, 61, 156-167
140. Gurland J. and Plateau J.: Trans. A.S.M., 1963, 56, 442-454
141. Embury J.D. et al.: Trans. A.I.M.E., 1967, 239, 114-118
142. Inoue T. and Kinoshita S.: Proc. 3rd Int. Conf. 'Strength of Metals and Alloys', Cambridge, 1973, 159
143. Kozasu I. and Kubota H.: Trans. I.S.I.J., 1971, 11, 321-330
144. Kozasu I. et al.: *ibid.*, 1973, 13, 20-28
145. Butcher J.H.: Trans. A.I.M.E., 1967, 239, 478
146. Palmer I.G. and Smith G.C.: 'Fracture of internally oxidised copper alloys', A.I.M.E. Conf. 'Oxide dispersion strengthening', Bolten Landing, New York, June 1966

147. Palmer I.G. et al.: 'Institute of Physics and Physical Society', London, 1967, P.53
148. Rogers H.C.: Trans. A.I.M.E., 1960, 218, 498-506
149. Cox T.B. and Low J.R.: Trans. Met., 1974, 5, 1457-1470
150. Same as Ref. 146
151. Barnby J.T.: Acta Met. 1967, 15, 903
152. Baker T.J. and Charles J.A.: B.S.C./I.S.I. Conf. 1971, 'Effect of second phase particles on the mechanical properties of steel', p.79
153. Gladman T. et al.: ibid., p.68
154. Tanaka T. et al.: Phil. Mag., 1970, 21, 267-279
155. Ashby M.F.: ibid., 1966, 14, 1157
156. Brown L.M. and Stobbs W.M.: ibid., 1971, 23, 1201
157. Klevebring B.I. and Mahrs R.: Scand. Jnl. Met., 1973, 2, 610
158. Sundström B.: Eng. Fract. Mech., 1974, 6, 483
159. Toya M.: Int. Jnl. Fract. Mech., 1973, 9, 463
160. Henry G. and Plateau J.: 'la Microfractographie', 1967, Editions Metreaux, IRSID.
161. Same as Ref. 153
162. McClintock F.A.: Int. Jnl. Fract. Mech., 1968, 4, 101

163. Tracy D.M. and Rice J.R.: Jnl. Mech. Phys. Solids., 1969, 17, 201
164. Thomason P.F.: Jnl. Inst. Metals, 1968, 96, 360-365
165. Fischmeister H.F. et al.: Metal Sci. Jnl., 1972, 6, 211-215
166. Knott J.F.: Paper 8 (as Ref. 76)
167. Baker T.J.: Paper 11 (As Ref. 76)
168. Gladman T. et al.: J.I.S.I., 1970, 208, 172
169. Clausing D.P.: Trans. A.S.M., 1967, 60, 504
170. Kozasu I. and Kubota H.: Proc. Int. Conf. Sci. and Tech. Iron and Steel (Sup. Trans. I.S.I.J.), 1971, 11, 1059
171. Thomason P.F.: Metal Science Jnl., 1971, 5, 64-67
172. Scott R.: Met. Tech., 1976, 3, 71-78
173. Grange R.A.: Trans. Met., 1971, 2, 417-426
174. Gouch A.J. and Dulieu D.: 'Effect of second-phase particles on the mechanical properties of steel', I.S.I. Publ., p.88
175. Mihelich J.L. et al.: J.I.S.I., 1971, 209, 469-475
176. Smith R.F. and Knott J.F.: Proc. Conf. 'Practical implication of fracture mechanics to pressure vessel technology', Inst. Mech. Eng., 1971, 65
177. Farrow R.J.: B.Sc. Project, 1975, Aston University

178. Trigwell N.: B.Sc. Project, 1976, Aston University
179. Roesch L.: Mem. Sci. Rev. Met., 1969, 66, 29
180. Gladman T. et al.: J.I.S.I., 1970, 208, 172
181. Edelson B.I. and Baldwin W.M.: Trans. A.S.M., 1962, 55, 230
182. Franklin A.G. et al.: J.I.S.I., 1964, 202, 588
183. Aydinceren A. and Kondic V.: Foundry Trade Jnl., 1969, 127, 345
184. Turkalo A.M. and Low J.R.: Trans. A.I.M.E., 1958, 212, 750-758
185. Cochrane R.C.: Same as Ref. 152, p.101-106
186. Gladman T.: J.I.S.I., 1969, 500
187. Baynes A.D.: ibid
188. Kinoshita T. et al.: Trans. I.S.I.J., 1975, 15, 45-54
189. Neuber H.: 'Theory of notch stresses, principles for exact calculation of strength with reference to structural form of material', Translated from a publication of Springer-Verlag, Berlin, Göttinger, Heidelberg, 1958.
190. Peterson R.E.: 'Stress concentration design factors', John Wiley and Sons Inc., New York, 1966
191. Hill R.: 'The Mathematical Theory of Plasticity', Clarendon Press, Oxford, 1967, p.245-252

192. Sachs G. and Fried M.L.: 'Notched bars tension tests on annealed carbon steel specimens of various sizes and contours', A.S.T.M. Symp. STP.87, 1948
193. Joubert F.L. and Valentin G.H.: Eng. Fract. Mech., 1976, 8, 669-676
194. Hancock J.W. and MacKenzie A.C.: Jnl. Mech. Phys. Solids, 1976, 24, 147-169
195. Bridgman P.W.: 'Studies in large plastic flow and fracture', p.9, McGraw-Hill, New York, 1952
196. Nichols F.A. and Mullins W.W.: Trans. T.M.S., A.I.M.E., 1965, 233, p.1840
197. GÖhler M.: Freiburger Forschungshefte, 1963, 1393, p.1
198. Kor G.J.W. and Turkdogan E.T.: Met. Trans., 1971, 2, 1561-1578; Met. Trans., 1972, 3, 1569-1578
199. Masui H. and Takechi H.: Trans. I.S.I.J., 1971, 16, 21-26
200. Larke E.C.: 'The rolling of strip, sheet and plate', 1957, Fletcher and Son Ltd., Norwich
201. Bradshaw J. and Jackson W.: Jnl. Research (SCRATA), 1970, 9, 11
202. Kawawa T. et al.: Tetsu-to-Hangane, 1966, 52, 1457
203. Alder J.F. and Phillips V.A.: Jnl. Inst. Met., 1954, 83, 80